

## Quantification of top soil moisture patterns

## **Nederlandse Geografische Studies / Netherlands Geographical Studies**

### **Redactie / Editorial Board**

Drs. J.G. Borchert (Editor in Chief)  
Prof. Dr. J.M.M. van Amersfoort  
Dr. P.C.J. Druijven  
Prof. Dr. A.O. Kouwenhoven  
Prof. Dr. H. Scholten

### **Plaatselijke Redacteuren / Local Editors**

Dr. R. van Melik,  
Faculteit Geowetenschappen Universiteit Utrecht  
Dr. D.H. Drenth,  
Faculteit der Managementwetenschappen Radboud Universiteit Nijmegen  
Dr. P.C.J. Druijven,  
Faculteit der Ruimtelijke Wetenschappen Rijksuniversiteit Groningen  
Drs. F.J.P.M. Kwaad,  
Fysich-Geografisch en Bodemkundig Laboratorium Universiteit van Amsterdam  
Dr. L. van der Laan,  
Economisch-Geografisch Instituut Erasmus Universiteit Rotterdam  
Dr. J.A. van der Schee,  
Centrum voor Educatieve Geografie Vrije Universiteit Amsterdam  
Dr. F. Thissen,  
Afdeling Geografie, Planologie en Internationale Ontwikkelingsstudies Universiteit van Amsterdam

### **Redactie-Adviseurs / Editorial Advisory Board**

Prof. Dr. G.J. Ashworth, Prof. Dr. P.G.E.F. Augustinus, Prof. Dr. G.J. Borger,  
Prof. Dr. K. Bouwer, Prof. Dr. J. Buursink, Dr. J. Floor, Prof. Dr. G.A. Hoekveld,  
Dr. A.C. Imeson, Prof. Dr. J.M.G. Kleinpenning, Dr. W.J. Meester,  
Prof. Dr. F.J. Ormeling, Prof. Dr. H.F.L. Ottens, Dr. J. Sevink, Dr. W.F. Slegers,  
T.Z. Smit, Drs. P.J.M. van Steen, Dr. J.J. Sterkenburg, Drs. H.A.W. van Vianen,  
Prof. Dr. J. van Weesep

Netherlands Geographical Studies 381

# Quantification of top soil moisture patterns

Evaluation of field methods, process-based modelling,  
remote sensing and an integrated approach

Johannes van der Kwast

Utrecht 2009

Koninklijk Nederlands Aardrijkskundig Genootschap  
Faculteit Geowetenschappen Universiteit Utrecht

Promotoren:  
Prof.dr. S.M. de Jong  
Prof.dr. Z. Su  
Prof.dr. V.G. Jetten

Co-promotor:  
Dr. D. Karssenbergh

Cover picture: Evapotranspiration from intensively irrigated crops (South-east of Kansas, USA), observed from space with the Landsat TM5 satellite sensor.

ISBN 978-90-6809-424-4

Graphic design, cartography and figures:  
GeoMedia (Faculty of Geosciences, Utrecht University)

Copyright © Johannes van der Kwast, c/o Faculty of Geosciences, Utrecht University, 2009

Niets uit deze uitgave mag worden vermenigvuldigd en/of openbaar gemaakt door middel van druk, fotokopie of op welke andere wijze dan ook zonder voorafgaande schriftelijke toestemming van de uitgevers.

All rights reserved. No part of this publication may be reproduced in any form, by print or photo print, microfilm or any other means, without written permission by the publishers.

Printed in the Netherlands by A-D Druk b.v. – Zeist

# Contents

Figures	9
Tables	15
Abbreviations and acronyms	17
List of Symbols Part II	21
List of Symbols Part III	24
List of Symbols Part IV	26
<b>1 Introduction</b>	<b>31</b>
1.1 Context	31
1.2 Problem definition	32
1.2.1 Soil moisture patterns	33
1.2.2 Field methods	35
1.2.3 Process-based models	37
1.2.4 Remote sensing	40
1.2.5 Data assimilation	42
1.2.6 Scaling issues	44
1.3 Study areas	45
1.4 Objective, research questions and thesis outline	46
<b>Part I Remote sensing data for soil moisture modelling</b>	
<b>2 Review of remote sensing techniques</b>	<b>51</b>
2.1 Remote sensing for soil moisture mapping	51
2.2 Optical reflectance of vegetation	52
2.3 Remote sensing image classification	54
2.4 Spectral vegetation indices	55
2.5 Radiation data from satellites	58
2.6 DEMs derived from Remote Sensing	59
<b>3 Case Study: DEM generation from Remote Sensing, a comparison between aerial photographs, ASTER and SRTM</b>	<b>63</b>
3.1 Introduction	63
3.2 Study area and datasets	64
3.3 Methodology	68
3.3.1 DEM extraction	68
3.3.2 Aerial Photography	68
3.3.3 ASTER imagery	71
3.4 Quality assessment	73

3.4.1	Mass point quality	74
3.4.2	Quality of interpolated DEMs	74
3.4.4	Variation at a transect	77
3.5	Discussion	78
3.6	Conclusions	81

## **Part II Evapotranspiration modelling using remote sensing**

<b>4</b>	<b>Surface energy balance theory</b>	<b>85</b>
4.1	Introduction	85
4.2	Global mean annual radiation and energy budget	85
4.3	The surface energy balance	89
4.4	Modelling the surface energy balance	94
4.5	The Surface Energy Balance System (SEBS)	96
4.5.1	Calculation of meteorological parameters	97
4.5.2	Submodel to derive energy balance terms	98
4.5.3	Submodel to derive stability parameters	99
4.5.4	Submodel to derive roughness length for heat transfer	101
4.5.5	Energy balance at limiting cases	103
<b>5</b>	<b>Acquisition of input data for SEBS from different satellite sensors and field measurements</b>	<b>107</b>
5.1	Introduction	107
5.2	Study area	107
5.3	Methods	110
5.3.1	Preprocessing Landsat TM5	110
5.3.2	Preprocessing ASTER	112
5.3.3	Preprocessing MODIS	114
5.3.4	Field measurement of emissivity	116
5.4	Results & Discussion	122
5.4.1	SEBS	122
5.4.2	Emissivity	122
5.5	Conclusions	125
<b>6</b>	<b>Evaluation of the Surface Energy Balance System (SEBS) using ASTER imagery at the SPARC 2004 site (Barrax, Spain)</b>	<b>127</b>
6.1	Introduction	127
6.2	SEBS	128
6.3	Data description	128
6.3.1	Remote Sensing data	129
6.3.2	Ground data	129
6.4	Results	131
6.4.1	Model output	131
6.4.2	Model evaluation	132
6.4.3	Model sensitivity	134

6.5	Discussion	138
6.6	Conclusions	139
<b>7</b>	<b>Comparison of MODIS and ASTER derived surface temperatures and energy fluxes at different resolutions</b>	<b>141</b>
7.1	Introduction	141
7.2	Approach	142
7.3	Remote Sensing and Field Data	143
7.4	Methods	144
7.4.1	SEBS	144
7.4.2	UniTrad	144
7.4.3	DisTrad	144
7.4.4	Analysis methods	147
7.5	Results	149
7.5.1	Temperatures	149
7.5.2	Energy fluxes	157
7.6	Discussion	162
7.7	Conclusions	163

### Part III Soil moisture modelling with a process-based model

<b>8</b>	<b>Process-based soil moisture modelling using the Soil Moisture System (SOMS) model</b>	<b>167</b>
8.1	Introduction	167
8.2	Site description	168
8.2.1	Climate	168
8.2.2	Geomorphology and soils	169
8.2.3	Land cover	171
8.3	Methods	172
8.3.1	The SOMS model	172
8.3.2	Field data	180
8.3.3	Model calibration	189
8.4	Results, calibration and evaluation	190
8.4.1	Calibration	190
8.4.2	Evaluation	192
8.4.3	Spatial results	194
8.5	Discussion	197
8.6	Conclusions	198

### Part IV Integration of remote sensing data in a soil moisture model

<b>9</b>	<b>Error propagation in SEBS and SOMS using Monte Carlo simulations</b>	<b>201</b>
9.1	Introduction	201
9.2	Methods	202
9.2.1	SOMS – Data Rich Scenario	203

9.2.2	SOMS – Data Poor Scenario	213
9.2.3	SEBS – Large Error scenario	214
9.2.4	SEBS – Small Error scenario	217
9.3	Results and discussion	217
9.3.1	SOMS – Data Rich Scenario	217
9.3.2	SOMS – Data Poor Scenario	222
9.3.3	SEBS error propagation results	224
9.3.4	Comparison of SOMS and SEBS	229
9.4	Conclusions	231
<b>10</b>	<b>Integrating remote sensing observations in soil moisture modelling by means of a particle filter</b>	<b>235</b>
10.1	Introduction	235
10.2	Methods	236
10.2.1	Particle Filter	236
10.2.2	Implementation	238
10.3	Results	239
10.3.1	Filter results for actual evapotranspiration	239
10.3.2	Filtering results for Volumetric Moisture Content (VMC)	243
10.4	Discussion	249
10.4.1	Variance versus distribution of AET	249
10.4.2	Correlation between AET and VMC	250
10.4.3	Spatial variability of VMC after filtering	256
10.4.4	Technical restrictions of the Particle Filter	256
10.5	Conclusions	257
<b>11</b>	<b>Conclusions</b>	<b>259</b>
11.1	Remote sensing data as input to process-based models	259
11.2	Evapotranspiration modelling using remote sensing	261
11.3	Soil moisture prediction using process-based models	264
11.4	Uncertainty analysis of SEBS and SOMS	264
11.5	Integrating remote sensing derived AET in a soil moisture model by means of a particle filter	266
11.6	Main research question	267
	<b>References</b>	<b>271</b>
	<b>Summary</b>	<b>287</b>
	<b>Samenvatting</b>	<b>291</b>
	<b>Résumé</b>	<b>295</b>
	<b>خلاصة</b>	<b>301</b>
	<b>Acknowledgements</b>	<b>305</b>
	<b>Curriculum Vitae</b>	<b>308</b>
	<b>Publications</b>	<b>309</b>

# Figures

1.1	a: A one-dimensional soil water balance and surface energy balance. b: A two-dimensional conceptualisation of a hillslope.	34
1.2	Potential use of remote sensing derived products in process-based soil moisture modelling.	41
1.3	Flowchart of the research.	47
2.1	Typical spectral reflectance curves between 300 and 2700 nm for water, soil and vegetation.	52
2.2	Time series of NDVI images derived from MODIS showing the green biomass development during the growing season in the Sehoul study area in Morocco.	53
2.3	Land cover map of northern Sehoul, Morocco. Derived from an ASTER image (October 2004) using image segmentation in combination with a minimum distance to mean classification.	55
2.4	Normalized Difference Vegetation Index as a function of the Leaf Area Index (LAI) of a spring-wheat canopy for growth (solid line) and senescent (dashed line) periods of the growing season.	56
2.5	NDVI image of north Sehoul, derived from ASTER (October 20 <sup>th</sup> 2004).	57
2.6	Albedo image of north Sehoul, derived from ASTER (October 20 <sup>th</sup> 2004), using the method of Liang (2000).	59
2.7	Oued Arjat Kebir, Sehoul (Morocco) in June 1996. Orthorectified aerial photograph mosaic draped over the SRTM DEM.	60
3.1	The location of the study area Peyne in southern France.	65
3.2	Spatial heterogeneity of agricultural land and <i>Maquis</i> as observed by aerial photography and ASTER.	66
3.3	Land cover map of the Peyne study area.	67
3.4	Diagram of the workflow for DEM extraction.	70
3.5	Possible rotation angles of airborne sensor platforms.	71
3.6	Simplified diagram of the imaging geometry for ASTER along-track stereo.	72
3.7	Average difference of mass points per land cover class.	75
3.8	Histograms of absolute differences in meters between the DEMs and the reference IGN DTM after subtraction.	78
3.9	Mass point distribution in the aerial photographs.	79
3.10	Mass point density histograms for aerial photographs and ASTER.	79
3.11	Profile through different land cover types illustrating the deviations of elevation per DEM type.	80
4.1	Radiation and energy fluxes of the earth-atmosphere system.	86
4.2	Soil temperature profiles in the Sehoul study area, Morocco.	90
4.3	The atmospheric boundary layer and its diurnal changes.	91

4.4	Radiosonde sounding from a weather balloon at the SPARC 2004 field campaign in Barrax (Spain) showing profiles of virtual potential temperature, wind direction, wind speed and a LIDAR profile.	91
4.5	Conceptual model of the oasis effect.	92
4.6	Diurnal cycle of radiation budget components for a vineyard in the SPARC 2004 study area (Barrax, Spain).	93
4.7	Diurnal cycle of energy budget components for a vineyard in the SPARC 2004 study (Barrax, Spain).	93
4.8	Schematization of a single-source (left) and a dual-source (right) model.	96
4.9	Flowchart of the SEBS model.	97
4.10	Concept of the surface energy balance at limiting cases illustrated for an ASTER surface temperature image of the Barrax field site in Spain (July 18 <sup>th</sup> 2004, 11.004 UTC).	104
5.1	Location of the Sehoul study area.	108
5.2	(a) Submersion irrigation for mint, (b) drip irrigation.	109
5.3	Cork oak ( <i>Quercus suber</i> ) and doum palm ( <i>Hyphaene thebaica</i> ) at the Forest of Sehoul.	109
5.4	Flowchart of the pre-processing steps for Landsat TM5.	110
5.5	Flowchart of the pre-processing steps for ASTER.	113
5.6	Flowchart of the pre-processing steps for MODIS.	114
5.7	The two-lid box method in use in the Sehoul study area (Morocco).	117
5.8	Procedure for measuring emissivity with the two-lid box method.	118
5.9	Calibration curve between a black body and the Raytek Raynger ST60.	119
5.10	Filter function (Nominal bandpass curve) for the optical filter of the Raytek ST60.	120
5.11	Temperature (a) and radiance (b) error when using eq. 5.18.	121
5.12	Latent heat flux calculated with SEBS for (a) ASTER (October 20 <sup>th</sup> 2004), (b) Landsat TM5 (September 15 <sup>th</sup> 2003) and (c) MODIS (October 20 <sup>th</sup> 2004).	123
5.13	Results of the empirical derivation of emissivity for (a) ASTER (October 20 <sup>th</sup> 2004), (b) Landsat TM5 (September 15 <sup>th</sup> 2003) and (c) MODIS (October 20 <sup>th</sup> 2004).	124
6.1	Top: ASTER image of July the 18 <sup>th</sup> 2004 at 11.008 GMT with the positions of the ground measurements and fields used for experiments during the SPARC 2004 field campaign. Bottom: landuse map with 90 m cells.	130
6.2	Net radiation flux ( $R_n$ ) (upper left), soil heat flux ( $G_o$ ) (upper right), latent heat flux ( $\lambda E$ ) (lower left) and sensible heat flux ( $H$ ) (lower right) as modelled by SEBS for 18 July 2004 at Barrax, Spain.	132
6.3	Measured versus modelled sensible heat flux ( $H$ ) for various land cover types.	133
6.4	Sensitivity of sensible heat flux ( $H$ ) to 25% deviation in shortwave incoming radiation ( $K_s^{\downarrow}$ ), for all measurements.	135
6.5	Mean sensitivity of sensible heat flux ( $H$ ) to most sensitive input parameters of SEBS (except for shortwave incoming radiation (figure 6.4) and surface temperature (figure 6.6)).	135
6.6	Sensitivity of sensible heat flux to surface temperature.	136
6.7	Mean sensitivity of sensible heat flux to $z_{0M}$ (left), $d_0$ and $b_c$ (right).	136

6.8	Modelled sensible heat flux ( $H$ ) compared to measured values. A comparison between $H$ modelled with remote sensing based empirical functions and field measurement/literature values for $z_{0M}$ , $h_c$ and $d_0$ .	137
7.1	The relation between NDVI and surface temperature.	145
7.2	An experimental semivariogram with a fitted spherical semivariogram model.	148
7.3	Part of the RGB ASTER composite of July 18 <sup>th</sup> 2004, 11.004 UTC over the SPARC 2004 site.	148
7.4	Scatterplots of NDVI-Temperature relations. Top: ASTER; bottom: MODIS.	150
7.5	Radiometric surface temperatures from MODIS and ASTER at original resolution (left) and calculated with DisTrad (right).	151
7.6	Histograms of the frequency distribution of the radiometric surface temperature for ASTER (bottom) and MODIS (top) at original resolution (left) and calculated with DisTrad (right).	152
7.7	Difference between coarse resolution radiometric surface temperature and DisTrad results for ASTER and MODIS expressed in RMSE.	153
7.8	Scatterplots of radiometric surface temperatures: (a) ASTER 90 vs. MODIS 1000; (b) ASTER 250 vs. MODIS 250 DisTrad; (c) ASTER 250 vs. MODIS 250 UniTrad.	154
7.9	Experimental semivariogram (crosses) of radiometric surface temperature from ASTER 90 (top) and ASTER 15 DisTrad (bottom). The line shows the fitted variograms.	155
7.10	Experimental semivariograms (crosses) of radiometric surface temperature from MODIS 1000 (top) and MODIS 250 DisTrad (bottom). The lines show the fitted variograms.	156
7.11	Sensible heat fluxes ( $H$ ) modelled with SEBS at different resolutions.	158
7.12	Histograms of sensible heat flux ( $W\ m^{-2}$ ) distribution. Clockwise starting from upper left: ASTER 90, ASTER 15 DisTrad, ASTER 15 UniTrad and MODIS 250 DisTrad.	159
7.13	Relation between ASTER 90 radiometric surface temperature and corresponding sensible heat flux, modelled with SEBS.	159
7.14	Scatterplots of sensible heatflux calculations.	160
7.15	Sensible heatflux per land cover type at different resolutions.	161
8.1	Left: the location of the Sehoul study area in Morocco. Right: The Sehoul study area.	168
8.2	Top: Potential evapotranspiration (PET) and actual evapotranspiration (AET) for a wet and a dry year (Rabat/Salé). Bottom: Precipitation in Sehoul in 2003.	169
8.3	Cross section through Oued Arjat Seghir in the south of the Plateau of Mamora at Rouichat.	170
8.4	Generalised soil map of northern Sehoul, based on Watfeh (1986) and Nafaa (2002).	171
8.5	6 layer soil moisture model: arrows are the fluxes simulated in the model.	172
8.6	TDR with handheld GPS.	181
8.7	The double ring infiltrometer.	182
8.8	Example curves of infiltration at the four calibration sites.	182
8.9	Soil Water Retention Curves for two samples from the sable beige de Mamora.	183

8.10	Hemispherical photographs of <i>Quercus suber</i> (left) and <i>Eucalyptus</i> (right).	184
8.11	The meteorological field station in the Schoul study area.	185
8.12	Daily precipitation and volumetric soil moisture content measured late morning at the calibration sites, winter 2004.	187
8.13	Daily precipitation and volumetric soil moisture content measured late morning at the calibration site, winter 2005 (C01), the cork oak Forest of Mamora.	187
8.14	Land cover map with calibration sites and location of the meteorological station.	188
8.15	Measured and modelled top soil moisture for the four reference sites C01, C02, C03 and C04.	191
8.16	Scatterplots of measured versus modelled soil moisture values.	192
8.17	Validation sites.	193
8.18	Scatterplot of validation of the model results for site C02.	194
8.19	Modelled versus measured volumetric soil moisture content (VMC) at the validation sites V02, V03 and V04.	195
8.20	Spatial modelling of top soil moisture using PCRaster.	196
9.1	Example realisations along a transect of a spatial attribute satisfying the: (a) Discrete Model of Spatial Variation (DMSV), (b) Continuous Model of Spatial Variation (CMSV), (c) Mixed Model of Spatial Variation (MMSV).	205
9.2	Map of unique land cover and soil type combinations within the study area used for the error modeling of $\theta_0, k_{sat}, \zeta$ using DMSV.	206
9.3	Nested pooled semivariogram model calculated from standardized non-zero square root transformed daily rainfall data.	211
9.4	Regression between variance in radiometric surface temperature at 250 meter resolution and NDVI for the three MODIS overpasses (a to c). In d the soil moisture content at calibration site C04 is plotted against the temperature variance at the three overpasses.	216
9.5	Timeseries of the average volumetric soil moisture content (VMC) in the first model layer (0-15 cm) at the calibration and validation sites for the SOMs-Data Rich Scenario.	218
9.6	Timeseries of the Coefficient of Variation for VMC for locations C01, C02, C03 and C04 for the SOMs-Data Rich Scenario.	220
9.7	Average VMC (upper) and its <i>CV</i> (lower) at 4 model layers as modelled at location C01 using the SOMs-Data Rich Scenario.	221
9.8	Actual evapotranspiration at locations C01 to C04 for the SOMs – Data Rich Scenario. Evapotranspiration estimated by both SEBS scenarios is also indicated in the graph.	224
9.9	Timeseries of the average volumetric soil moisture content (VMC) in the first model layer (0-15 cm) at the calibration and validation sites for the SOMs-Data Poor Scenario.	226
9.10	Average actual evapotranspiration and its standard deviation at locations C01 to C04 after 200 Monte Carlo runs for the SOMs – Data Poor Scenario. The actual evapotranspiration estimated for these locations by both SEBS scenarios are also indicated in the graph.	230

9.11	Realisation of actual evapotranspiration at three overpass times (2, 17 and 23 November 2004) for the soil moisture model, SEBS – Large Error Scenario and SEBS – Small Error Scenario of the SEBS error propagation model.	232
10.1	a) the posterior density ( $k_i$ ) before resampling, multiplied by the ensemble size (100); b) the modified posterior density ( $k_{i,r}$ ) after subtraction of the integer values in histogram a). The remainder of the ensemble is drawn from this density.	238
10.2	Modelled actual evapotranspiration (AET) at location C03 using four scenarios. A) SOMS – Data Rich Scenario filtered with the SEBS – Large Error filter data; B) SOMS – Data Rich Scenario filtered with the SEBS – Small Error filter data; C) SOMS – Data Poor Scenario filtered with the SEBS – Large Error filter data; D) SOMS – Data Poor Scenario filtered with the SEBS – Small Error filter data.	240
10.3	$\sigma_{\text{VMCfilter}}/\sigma_{\text{VMC}}$ ratio timeseries results.	242
10.4	Left column: timeseries of model output for the average VMC in the first model layer (0-15 cm) after 200 Monte Carlo runs. Right column: $\sigma_{\text{VMCfilter}}/\sigma_{\text{VMC}}$ ratio timeseries results.	244
10.5	Average VMC map at $t = 445$ (one timestep after the first filter moment) for a) Data Poor error propagation scenario without filtering, b) Data Poor error scenario with large error filter data.	248
10.6	Goodness of fit of different model scenarios at the calibration sites C02, C03 and C04 and validation sites V02, V03 and V04.	250
10.7	Effect of filtering on the frequency distribution of actual evapotranspiration at $t = 445$ , one hour after the first filter moment. a) SOMS – Data Poor error propagation scenario without filtering, b) SOMS – Data Poor Scenario with SEBS – Small Error filter data.	251
10.8	Regression analysis between VMC and AET at location C02 for a) original Data Rich scenario, b) No meteo error scenario, c) No meteo and no pore space error scenario, d) Fixed $\zeta$ scenario.	252
10.9	Scatterplot of VMC versus slope of the regression curve with AET for a) SOMS – Data Rich error propagation scenario and b) Fixed $\zeta$ error propagation scenario.	254
10.10	Distribution of the number of clones (y-axis) over the different realisations during the SOMS – Data Poor Scenario with the SEBS – Large Error filter data.	255



# Tables

1.1	Lateral support and coverage for data and models used in this research.	44
1.2	Chances of available and usable MODIS and ASTER images in the Netherlands and Morocco, based on the evaluation of meteorological data on cloud cover and visual inspection of images.	45
3.1	Mean height of land cover classes, derived from field estimates.	67
3.2	Polynomial orders for estimation of exterior orientation.	72
3.3	RMSE of triangulation.	72
3.4	Mass points compared to reference DTM.	74
3.5	Statistics of the difference between the DEMs and the reference DTM.	76
3.6	Statistics of the difference between the DEMs and the reference DTM per land cover unit.	76
4.1	Constants in the stability correction functions.	100
5.1	Radiometric range of bands and resolution for the Landsat TM5 sensor.	111
5.2	Radiometric range of bands and resolution for the ASTER sensor.	114
5.3	Radiometric range of bands and resolution for the MODIS sensor.	115
5.4	Comparison between emissivities derived from ASTER, Landsat TM5 and MODIS using the empirical relation with NDVI and field measurements of emissivity using the box method.	125
6.1	Surface parameters for the different land cover types	129
6.2	Input parameters of SEBS for which the sensitivity of sensible heat flux ( $H$ ) is less than 10% when a deviation of 25% is applied.	134
6.3	Field observations ( $h_c$ ) and literature-based ( $z_{0M}$ and $d_0$ ) versus land use averaged modelled surface parameters.	136
8.1	Soil profile of the <i>Sols isohumique gris couvrant les sols sableux fersiallitiques lessivés</i> .	170
8.2	Soil profile of the <i>Sols fersiallitique lessivé à galets</i> .	171
8.3	Input variables and parameters used in the SOMS model.	173
8.4	Calibration sites.	180
8.5	Measurement periods of top soil moisture content with a TDR ( $\theta_0$ ), residual soil moisture content ( $\theta_r$ ) and saturated soil moisture content ( $\theta_s$ ) from samples, saturated hydraulic conductivity ( $k_{sat}$ ) with the double ring infiltrometer and leaf area index ( $\chi$ ) with hemispherical photographs at the calibration sites.	180
8.6	Measured saturated hydraulic conductivity ( $k_{sat}$ ).	181
8.7	LAI estimations using WINPHOT on four samples per vegetation type.	185
8.8	Average land cover properties assigned to the land cover map. Albedo ( $\alpha$ ), fractional vegetation cover ( $f_v$ ) and leaf area index ( $\chi$ ).	188
8.9	Goodness of fit of the calibration.	193
8.10	Evaluation results with an independent dataset of 2004.	193
9.1	Input variables and parameters modelled with error in the soil moisture model.	204

9.2	Non-Spatial Error Model (NSEM) parameters for the meteorological measurements.	204
9.3	Land cover and soil type combinations.	207
9.4	Parameters used in the application of DMSV for $\theta_0(x)$ .	208
9.5	Parameters for the DMSV model applied to the correlated variables $k_{sat}(x)$ and $\zeta(x)$ .	208
9.6	Model restrictions for initial volumetric soil moisture content ( $\theta_0$ ), saturated hydraulic conductivity ( $k_{sat}$ ), and the soil water retention curve parameter ( $\zeta$ ).	208
9.7	Semivariogram models used in this chapter.	209
9.8	Parameter values for the application of CMSV to saturated volumetric soil moisture content.	210
9.9	Semivariogram model parameters used in the CMSV for precipitation.	211
9.10	MMSV parameters for maximum interception storage.	212
9.11	Parameters of semivariogram model for potential evaporation.	212
9.12	Parameters for the DMSV model applied to the correlated variables $k_{sat}(x)$ and $\zeta(x)$ for the SOMS – Data Poor Scenario.	214
9.13	Assumed parameter values for the application of CMSV to $\theta$ , [-] in the SOMS – Data Poor Scenario.	214
9.14	Coefficients of the regression function.	216
9.15	Goodness of fit of error propagation results for the SOMS – Data Rich Scenario at the calibration sites C02, C03 and C04 and independent validation sites V02, V03 and V04.	220
9.16	Goodness of fit of error propagation results of the SOMS – Data Poor Scenario at the calibration sites C02, C03 and C04 and validation sites V02, V03 and V04.	223
9.17	AET [ $\text{cm h}^{-1}$ ] and standard deviation modelled by SEBS using the Small Error Scenario and the Large Error Scenarion for all overpasses ( $t = 444$ , $t = 805$ and $t = 948$ ).	231
10.1	Analysis of the change of mean estimated VMC after filtering.	239
10.2	Analysis of the change of standard deviation of VMC after filtering.	249
11.1	Resolutions of different applications of remote sensing sensors.	261
11.2	Performance of different methods for the estimation of soil moisture patterns in space and time, in terms of uncertainty, resolution and coverage.	268

# Abbreviations and acronyms

1D	One-dimensional
2D	Two-dimensional
3D	Three-dimensional
ABL	Atmospheric Boundary Layer
AET	Actual Evapotranspiration
AHS	Airborne Hyperspectral Scanner
ANEM	Adjusted Normalized Emissivity Method
ASL	Atmospheric Surface Layer
a.s.l.	Above sea level
ASTER	Advanced Spaceborne Thermal Emission and Reflection Radiometer
AVHRR	Advanced Very High Resolution Radiometer
BAS	Bulk Atmospheric boundary layer Similarity theory
BATS	Biosphere-Atmosphere Transfer Scheme
BOREAS	Boreal Ecosystem-Atmosphere Study
CMSV	Continuous Model of Spatial Variation
CV	Coefficient of Variation
DEM	Digital Elevation Model
DGPS	Differential Global Positioning System
DMSV	Discrete Model of Spatial Variation
DN	Digital Number
DPS	Digital Photogrammetry System
DSM	Digital Surface Model
DTM	Digital Terrain Model
EC	Eddy Correlation system
ESA	European Space Agency
GCP	Ground Control Point
GDAS	Global Data Assimilation System
GIS	Geographical Information System
GLUE	Generalized Likelihood Uncertainty Estimation
GMSV	General Model of Spatial Variation
GOES	Geostationary Operational Environmental Satellites
GPS	Global Positioning System
HAPEX-Sahel	Hydrological and Atmospheric Pilot Experiment in the Sahel
HMM	Hidden Markov Model
HRS	High Resolution Stereo
IDL	Interface Description Language
IGN	Institute Géographique National
INRA	Institut Scientifique de Recherché Agronomique

InSAR	interferometric synthetic aperture radar
IRS-1C	Indian Remote Sensing Satellite
ISA	International Standard Atmosphere
ITAP	Provincial Technical Agronomical Institute
JNP	Jarvis, Noilhan and Planton scheme
KNMI	Koninklijk Nederlands Meteorologisch Instituut (Royal Netherlands Meteorological Institute)
LAI	Leaf Area Index
LAS	Large Aperture Scintillometer
LIDAR	Light Detection and Ranging
LPDAAC	Land Processes Distributed Active Archive Center
LPS	Leica Photogrammetry Suite
MISR	Multiangle Imaging SpectroRadiometer
MMD	Min-Max Difference emissivity algorithm
MMSV	Mixed Model of Spatial Variation
MODIS	Moderate Resolution Imaging Spectroradiometer
MODTRAN	Moderate resolution atmospheric transmission
MOS	Monin-Obukhov Similarity theory
MSG	Meteosat Second Generation
NASA	National Aeronautics and Space Administration
NCEP	National Centers for Environmental Prediction
NDVI	Normalized Difference Vegetation Index
NEM	Normalized Emissivity Method
NIMA	National Imagery and Mapping Agency
NIR	Near Infrared
NOAA	National Oceanic and Atmospheric Administration
NRL	Naval Research Laboratory
NSEM	Non-Spatial Error Model
PAR	Photosynthetically Active Radiation
PBL	Planetary Boundary Layer
pdf	Probability density function
PEST	Parameter Estimation algorithm
PET	Potential Evapotranspiration
PF	Particle Filter
POLDER	POLarization and Directionality of the Earth's Reflectances
POTRAD	Potential Radiation model
PVI	Perpendicular Vegetation Index
RMSE	Root Mean Square Error
RR	Residual resampling
RTC	Radiative Transfer Code
SA	Sonic Anemometer
SAVI	Soil Adjusted Vegetation Index
SEBAL	Surface Energy Balance Algorithm for Land
SEBS	Surface Energy Balance System
SEVIRI	Spinning Enhanced Visible and Infrared Imager

SGP97	Southern Great Plains 1997 Hydrology Experiment
SiB	Simple Biosphere model
SIR	Sampling Importance Resampling
SIS	Sequential Importance Sampling
SMOS	Soil Moisture and Ocean Salinity Mission
SOMS	Soil Moisture System
SPARC	SPectra bARrax Campaign
SPOT	Satellite Pour l'Observation de la Terre
SRTM	Shuttle Radar Topography Mission
SVAT	soil-vegetation-atmosphere transfer schemes
SWATRE	Soil Water and Actual Transpiration Rate Extended model
SWIR	Shortwave radiation
SWRC	Soil Water Retention Curve
TES	Temperature Emissivity Separation Algorithm
TIN	Triangular Irregular Network
TIROS	Television & Infrared Observation Satellite
TM	Thematic Mapper
TOVS	TIROS Operational Vertical Sounder
TSEB	Two-Source Energy Balance model
TVDI	Temperature Vegetation Dryness Index
TVX	Temperature-Vegetation Index Plot
UTC	Coordinated Universal Time
UTM	Universal Transverse Mercator
VMC	Volumetric Moisture Content
VNIR	Visual and Near Infrared
XT	Crosstalk



# List of Symbols Part II

Symbol	Meaning	Unit
$B^{-1}$	inverse Stanton number or Margoulis number	-
$B_w$	bulk stability functions for momentum transfer in Atmospheric Boundary Layer	-
$c$	speed of light ( $=3.0 \cdot 10^8$ )	$m s^{-1}$
$C_d$	foliage drag coefficient	-
$C_p$	specific heat of air at constant pressure	$J kg^{-1} K^{-1}$
$C_t$	heat transfer coefficient of the leaf	-
$C_t^*$	heat transfer coefficient of the soil	-
$C_w$	bulk stability functions for heat transfer in Atmospheric Boundary Layer	-
$d_0$	zero plane displacement height	m
$\langle d\epsilon \rangle$	vegetation structure parameter	-
$E$	actual evapotranspiration	m
$e_a$	actual vapour pressure	Pa
$e_s$	saturation vapour pressure	Pa
$f$	frequency	Hz
$f(\lambda)$	spectral response function, or filter function	-
$f_c$	canopy fraction	-
$f_s$	soil fraction	-
$g$	acceleration due to gravity	$m s^{-2}$
$G_0$	soil heat flux density	$W m^{-2}$
$H$	sensible heat flux density	$W m^{-2}$
$h$	constant of Planck ( $= 6.626069311 \cdot 10^{-34}$ )	J s
$h_c$	height of the canopy	m
$H_{dry}$	dry limit sensible heat flux density	$W m^{-2}$
$H_f$	relative humidity	-
$h_i$	height of the boundary layer	m
$h_s$	roughness height of the soil	m
$h_{st}$	height of Atmospheric Surface Layer	m
$H_{wet}$	wet limit sensible heat flux density	$W m^{-2}$
$I$	spectral radiance	$J s^{-1} m^{-2} sr^{-1} Hz^{-1}$
$k$	Von Karman constant ( $= 0.41$ )	-
$K_{aa}^{\uparrow}$	shortwave scatter and reflection into space by atmospheric constituents	$W m^{-2}$
$K_{aa}^+$	absorption of shortwave radiation by atmospheric constituents	$W m^{-2}$
$K_{ac}^{\uparrow}$	shortwave reflection of clouds	$W m^{-2}$
$K_{ac}^+$	shortwave cloud absorption	$W m^{-2}$
$K_{exo}^{\downarrow}$	shortwave average annual extra-terrestrial incoming solar radiation	$W m^{-2}$
$K_S^{\uparrow}$	shortwave surface reflection	$W m^{-2}$
$K_S^{\downarrow}$	shortwave radiation received at the surface	$W m^{-2}$
$K_S^*$	absorption of shortwave radiation at the surface	$W m^{-2}$
$K_n$	net incoming shortwave radiation	$W m^{-2}$

Symbol	Meaning	Unit
$L$	Monin-Obukhov length	m
$L_{1, \dots, L_4}$	box measurements of radiance	$W m^{-3} sr^{-1}$
$L_{8-14}$	band integrated radiance for 8-14 $\mu m$	$W m^{-3} sr^{-1}$
$L_d$	Monin-Obukhov length under dry-limit condition (dry-bound)	m
$L_n$	net longwave radiation	$W m^{-2}$
$L_w$	Monin-Obukhov length under wet-limit condition (wet-bound)	m
$L_s^{\downarrow}$	downward longwave radiation received at the surface	$W m^{-2}$
$L_s^{\uparrow}$	longwave emitted surface radiation	$W m^{-2}$
$L_\lambda$	spectral radiance received by the sensor	$W m^{-2} sr^{-1} \mu m^{-1}$
$M$	amount of energy radiated per unit surface area of a black body per unit time	$W m^{-2}$
$n$	within-canopy wind speed profile extinction coefficient	-
$NDVI_{max}$	NDVI for full vegetation cover	-
$NDVI_{min}$	NDVI for bare soil	-
$NDVI_n$	NDVI image of resolution $n$	-
$p$	pressure	Pa
$P$	box specific parameter	-
$p_0$	reference pressure (=1013)	mbar
Pr	Prandtl number	-
$q$	specific humidity	$kg kg^{-1}$
$Q$	box specific parameter	-
$r_{ah}$	aerodynamic resistance for heat transfer	$s m^{-1}$
$R_d$	specific gas constant for dry air (= 287.1)	$J kg^{-1} K^{-1}$
$r_e$	external (aerodynamic) resistances	$s m^{-1}$
$Re_*$	roughness Reynolds number	-
$r_{ew}$	external resistance at the wet-limit	$s m^{-1}$
$r_i$	bulk internal (or surface, or stomatal) resistances	$s m^{-1}$
$R_n$	surface net radiation	$W m^{-2}$
$R_v$	specific gas constant water vapour (= 461.5)	$J kg^{-1} K^{-1}$
$S_i$	sensitivity to a fraction $i$ deviation of a parameter	-
$T$	ambient temperature	K
$t_a$	air temperature	$^{\circ}C$
$T_a$	air temperature for a standard atmosphere	K
$T_B$	effective at-satellite brightness temperature	K
$T_b$	blackbody temperature	K
$T_R$	radiometric surface temperature	K
$\hat{T}_{Rn}$	estimated radiometric surface temperature as a function of NDVI at resolution $n$	K
$T_s$	atmospherically corrected surface temperature	K
$u$	windspeed at height $z$	$m s^{-1}$
$u_*$	friction velocity	$m s^{-1}$
$w$	water vapour content	$g cm^{-2}$
$w_i$	weight of location $i$	-
$x_i$	modelled flux at location $i$	$W m^{-2}$
$z$	measurement height	m
$Z$	surface elevation	m
$z_{0H}$	roughness length for heat transfer	m
$z_{0M}$	roughness length for momentum transfer	m
$Z_{pbl}$	height of Planetary Boundary Layer	m

Symbol	Meaning	Unit
$\alpha$	albedo	-
$\alpha_n$	normalized reflectance of band $n$	-
$\alpha_{sw}$	broadband shortwave surface albedo	-
$\gamma$	psychrometric constant (= 0.67)	Pa K <sup>-1</sup>
$\Gamma_c$	ratio of soil heat flux to net radiation for full vegetation canopy	-
$\Gamma_s$	ratio of soil heat flux to net radiation for bare soil	-
$\Delta$	rate of change of saturation vapour pressure with temperature	Pa K <sup>-1</sup>
$\Delta \hat{T}_R$	regression correction term for radiometric temperature estimation	K
$\delta L$	second order correction function for band integrated radiance	W m <sup>-3</sup> sr <sup>-1</sup>
$\delta NDVI$	NDVI correction factor	-
$\delta \varepsilon$	geometry dependent correction factor for emissivity measurement with the box-method	-
$\varepsilon$	emissivity	-
$\varepsilon_0$	emissivity of an ideal box	-
$\varepsilon_c$	emissivity of cold lid	-
$\varepsilon_g$	emissivity of bare soil	-
$\varepsilon_h$	emissivity of hot lid	-
$\varepsilon_s$	emissivity of sample or surface	-
$\varepsilon_v$	emissivity for full vegetation cover	-
$\theta$	potential temperature	K
$\theta_0$	potential temperature at the surface	K
$\theta_a$	potential temperature of the overlying air at reference height $z$	K
$\theta_v$	potential virtual temperature near the surface	K
$\Lambda$	evaporative fraction	-
$\lambda$	latent heat of vaporization (= 2.501·10 <sup>6</sup> )	J kg <sup>-1</sup>
$\lambda E$	latent heat flux density	W m <sup>-2</sup>
$\lambda E_{dry}$	dry limit latent heat flux density	W m <sup>-2</sup>
$\lambda E_{wet}$	wet limit latent heat flux density	W m <sup>-2</sup>
$\Lambda_r$	relative evaporation	-
$\hat{\mu}$	weighted average of modelled flux within footprint of field measurement	W m <sup>-2</sup>
$\rho_a$	air density	kg m <sup>-3</sup>
$\rho_w$	density of water	kg m <sup>-3</sup>
$\sigma$	Stefan-Boltzmann constant (=5.670400·10 <sup>-8</sup> )	J s <sup>-1</sup> m <sup>-2</sup> K <sup>4</sup>
$\hat{\sigma}^2$	footprint weighted variance of the modelled fluxes	W m <sup>-2</sup>
$\tau$	atmospheric transmissivity	-
$\tau_0$	surface shear stress	N
$\nu$	kinematic viscosity of the air	Pa s
$\Psi_H$	stability correction function for sensible heat transfer	-
$\Psi_M$	stability correction function for momentum transfer	-
$\omega$	mixing ratio between moist air and dry air	-

# List of Symbols Part III

Symbol	Meaning	Unit
$C$	intercepted amount of rain	m
$C_f$	cloud factor	-
$C_p$	specific heat of air at constant pressure	J kg <sup>-1</sup> K <sup>-1</sup>
$D$	throughfall	m
$d_0$	zero plane displacement height	m
$d_{met}$	displacement height at $z_{met}$	m
$E$	actual evapotranspiration flux	m s <sup>-1</sup>
$E_0$	actual surface evapotranspiration	m s <sup>-1</sup>
$e_a$	actual vapour pressure	Pa
$E_{int}$	evaporation from interception	m
$E_p$	potential evapotranspiration flux	m s <sup>-1</sup>
$e_s$	saturation vapour pressure	Pa
$f(t)$	functions for the calculation of the JNP scheme	-
$F_1, \dots, F_4$	functions for the calculation of the JNP scheme	-
$f_c$	canopy fraction	-
$h$	matric suction	m
$h_{50}$	matrix potential at a 50% reduction of the potential evapotranspiration	m
$h_A$	air entry matric suction	m
$h_c$	height of the canopy	m
$H_f$	relative humidity	-
$l_i$	percolation from layer $i$ to the next layer	m s <sup>-1</sup>
$l_{i-1}$	percolation received from the layer above or from the surface storage for $i = 0$	m s <sup>-1</sup>
$k$	Von Karman constant (= 0.41)	-
$k(\theta_E)$	unsaturated hydraulic conductivity	-
$k_r(\theta_E)$	relative unsaturated hydraulic conductivity	-
$K_S^\downarrow$	shortwave radiation received at the surface	W m <sup>-2</sup>
$k_{sat}$	saturated hydraulic conductivity	m s <sup>-1</sup>
$K_p^\downarrow$	potential incoming shortwave radiation	W m <sup>-2</sup>
$L_n$	net longwave radiation	W m <sup>-2</sup>
$L_p$	potential longwave radiation	W m <sup>-2</sup>
$P_n$	net precipitation	m s <sup>-1</sup>
$r(t)$	residual at timestep $t$	-
$r_a$	aerodynamic resistance	s m <sup>-1</sup>
$R_n$	surface net radiation	W m <sup>-2</sup>
$R_p$	minimum radiation for photosynthesis	W m <sup>-2</sup>
$r_s$	stomatal resistance	s m <sup>-1</sup>
$r_{s,max}$	maximum stomatal resistance	s m <sup>-1</sup>
$r_{s,min}$	minimal stomatal resistance	s m <sup>-1</sup>
$S$	interception	m

Symbol	Meaning	Unit
$S_{max}$	maximum canopy storage capacity	m
$t_a$	air temperature	°C
$T_b$	blackbody temperature	K
$T_i$	actual transpiration from layer $i$	$\text{m s}^{-1}$
$T_p$	potential transpiration	$\text{m s}^{-1}$
$T_{p,i}$	potential transpiration from each rootzone layer $i$	$\text{m s}^{-1}$
$T_r$	the potential transpiration that remains for the root zone	$\text{m s}^{-1}$
$u$	windspeed	$\text{m s}^{-1}$
$V_p$	potential evaporation for the unvegetated fraction of a grid cell	$\text{m s}^{-1}$
$w(t)$	calibration weights of measurements at timestep $t$	-
$w_i$	transpiration from roots in layer $i$	$\text{m s}^{-1}$
$X$	surface storage	m
$Z_0$	aerodynamic roughness	m
$Z_{0met}$	aerodynamic roughness at $z_{met}$	m
$Z_{meso}$	height of the mesostrophic wind	m
$Z_{met}$	wind measurement height	m
$\alpha$	albedo	-
$\alpha_n$	surface reflection of ASTER band $n$	-
$\beta_i$	moisture dependent evapotranspiration reduction factor	-
$\gamma$	psychrometric constant (= 0.67)	$\text{Pa K}^{-1}$
$\delta$	rate of change of saturation vapour pressure with temperature	$\text{Pa K}^{-1}$
$\Delta t$	model time interval	s
$\Delta z$	model layer thickness	m
$\eta$	wind extrapolation factor	-
$\hat{\theta}_0$	predicted top soil moisture content	$\text{m m}^{-1}$
$\theta_E$	relative degree of saturation	-
$\theta_i$	volumetric soil moisture content of layer $i$	$\text{m m}^{-1}$
$\theta_r$	residual moisture content	$\text{m m}^{-1}$
$\theta_s$	saturated moisture content	$\text{m m}^{-1}$
$\lambda$	latent heat of vaporization (= $2.501 \cdot 10^6$ )	$\text{J kg}^{-1}$
$\upsilon$	vapour pressure deficit of the air	Pa
$\Xi$	modelling efficiency	-
$\rho_a$	air density	$\text{kg m}^{-3}$
$\zeta$	dimensionless slope of the log-linear relationship between $\ln(h/h_\lambda)$ and $(1-\theta_E)$	-
$\sigma$	Stefan-Boltzmann constant (= $5.670400 \cdot 10^{-8}$ )	$\text{J s}^{-1} \text{m}^{-2} \text{K}^{-4}$
$\sigma_0^2$	variance of the measured soil moisture	$\text{m m}^{-1}$
$\sigma_E^2$	error variance	-
$\tau$	tortuosity	-
$\chi$	leaf area index	$\text{m}^2 \text{m}^{-2}$

# List of Symbols Part IV

Symbol	Meaning	Unit
$A$	a set of state variables	-
$a$	range of variogram	-
$C$	$\text{var}(\varepsilon(t))$	-
$C_0(k)$	$\text{var}(\varepsilon(k))$	-
$C_g$	$\text{var}(\varepsilon_g)$	-
$C_r$	$\text{var}(\varepsilon_r)$	-
$C_{z_1z_2}(k)$	covariance between $\varepsilon_1(k)$ and $\varepsilon_2(k)$	-
$D$	domain	-
$\mathbf{d}$	vector of filter data	-
$D_k$	stratum $k$ of domain $D$	-
$E$	expectation	-
$E$	modelling efficiency	-
$E_0(t)$	actual surface evapotranspiration	$\text{m s}^{-1}$
$E_p$	potential evapotranspiration flux	$\text{m s}^{-1}$
$ET_{ps}(x)$	random field of potential evoptranspiration calculated by SEBS	$\text{m s}^{-1}$
$ET_{ptot}(t)$	temporal stochastic variable for potential evapotranspiration	$\text{m s}^{-1}$
$ET_{ptot}(x,t)$	spatio-temporal random potential evapotranspiration field	$\text{m s}^{-1}$
$f$	scaling factor for precipitation variograms	-
$f()$	function	-
$f_d(\mathbf{d} \Psi)$	probability density function of $\mathbf{d}$ assuming that random variable $\underline{\psi} = \psi$	-
$f_m(\psi)$	prior probability density function	-
$h$	lag distance	$\text{m}$
$H$	measurement operator	-
$H_f$	relative humidity	-
$I$	set of stochastic input variables	-
$i_n$	realization $n$ of $I$	-
$k$	number of Monte Carlo runs	-
$K$	number of strata	-
$k_j$	integer number of clones	-
$k_{j,r}$	residual of integer number of clones	-
$K_S^{\downarrow}$	shortwave radiation received at the surface	$\text{W m}^{-2}$
$k_{sat}$	saturated hydraulic conductivity	$\text{m s}^{-1}$
$p$	air pressure	$\text{Pa}$
$P$	precipitation	$\text{m}$
$P$	set of stochastic input parameters	-
$P_i(m,t)$	amount of precipitation measured at the time step $t$	$\text{m}$
$P_i(x,t)$	amount of precipitation at a time step $t$ at location $x$ for event $i$	$\text{m}$
$p_n$	realization $n$ of $P$	-
$s$	Monte Carlo run, $s=1..k$	-

Symbol	Meaning	Unit
$s^2(k)$	sample variance	-
$s_x^2(k)$	variance of mean $X$ in stratum $k$	-
$s^2$	sill of variogram	-
$S_{int}$	maximum canopy storage capacity	m
$t$	discrete model timestep	s
$T_a$	air temperature	K
$\hat{T}_{R250}$	surface temperature image from MODIS at 250 meter resolution after application of DisTrad	K
$u$	windspeed	$m\ s^{-1}$
$w_i$	weight of particle $i$	-
$x$	spatial index	-
$Z(t)$	non-spatial, temporal stochastic input variable or parameter	-
$Z(x)$	spatial random field	-
$\beta(k)$	unit-dependent mean	-
$\gamma(h)$	semivariance	-
$\gamma_U$	nested semivariogram	-
$\varepsilon(k)$	unit-dependent noise term	-
$\varepsilon(t)$	random variable that represents the non-systematical error in the measured variable	-
$\varepsilon(x)$	zero-mean, spatially autocorrelated residual that represents the small-scale fluctuation	-
$\varepsilon_g$	random variable representing the systematic error or bias	-
$\varepsilon_r(t)$	random variable that represents the non-systematical error in the measured variable, relative to the measured value	-
$\theta_0$	top soil moisture content	$m\ m^{-1}$
$\theta_s$	saturated soil moisture content	$m\ m^{-1}$
$\mu(t)$	measured deterministic variable at timestep $t$	-
$\mu(x)$	(deterministic) mean, or trend, of attribute $Z(x)$	-
$\sigma$	standard deviation	-
$\zeta$	dimensionless slope of the log-linear relationship between $\ln(h/h_A)$ and $(1-\theta_E)$	-
$\Psi$	unknown model evolution, which is a value of random variable $\underline{\Psi}$	-
$\overline{\Psi}$	mean posteriori pdf	-



You see that pale, blue dot? That's us. Everything that has ever happened in all of human history, has happened on that pixel. All the triumphs and all the tragedies, all the wars all the famines, all the major advances... it's our only home. And that is what is at stake, our ability to live on planet Earth, to have a future as a civilization. I believe this is a moral issue, it is your time to seize this issue, it is our time to rise again to secure our future.

*Al Gore*

*An Inconvenient Truth (2006)*



# 1 Introduction

## 1.1 Context

Precipitation has decreased in the last decades of the past century throughout the southern Mediterranean region, while the demands for fresh water are rising due to expansion of irrigated areas and urban development (Grenon and Batisse, 1988; Zeng et al., 1999; Van Dijck et al., 2005). Climate models predict even a further reduction in precipitation and an increase of the annual temperature (Van Dijck et al., 2005). To cope with this scarcity and the economic pressure on water resources due to a changing climate, scientists need to provide water management tools to guarantee a sustained availability of fresh water.

Operational environmental models are important tools for decision makers. These models use a combination of all available up-to-date data, from satellites and field measurements, for predictions of environmental variables at short time scales. Timescales ranging from hours to days after an event of interest, such as a rainstorm, are important for many natural hazard predictions as flooding and drought. Satellite data allows us to make distributed predictions at short timescales over large areas.

A key variable both in agricultural land use and in land degradation processes such as erosion and desertification is the spatial and temporal distribution of soil moisture after a rainfall event, at the scale of agricultural communities. In this thesis different approaches in the spatio-temporal modelling of soil moisture are evaluated.

An operational model for the prediction of spatio-temporal patterns of top soil moisture, here defined as the upper 15 cm of the soil profile (see section 1.2.1), is useful for early drought prediction (Engman, 1990), drought monitoring (Jackson et al., 1981, 1987) and evaluation of drought impact on agricultural production (Newton et al., 1983) for management of rural subsidy schemes (Walker, 1999). It can also be useful for the optimization of irrigation schemes (Jackson et al., 1981, 1987; Jackson, 1982; Saha, 1995) and crop yield through optimizing soil moisture conditions at pre-planting and during the growing season (Topp et al., 1980; Jackson et al., 1987; Saha, 1995), e.g. precision irrigation.

The temporal and spatial distribution of soil moisture in the top soil also affects runoff generation and is therefore important for erosion predictions (Beecham, 1995; Western et al., 1997; Van Asch et al., 2001) and flood forecasting (Entekhabi et al., 1993; Su et al., 1995). Other examples for the usefulness of an operational soil moisture model are (Walker, 1999): improvement of weather predictions through improved modelling of the interaction of land surface processes (Fast and McCorcle, 1991; Engman, 1992; Betts et al., 1994; Su et al., 1995), selective application of pesticides for soil moisture dependent insects and diseases (Engman, 1990), monitoring of global climate change through persistence of high or low soil moisture content (Engman, 1992), management of cultural practices, including trafficability in the fields (Wigneron et al., 1998) and predictions of reduction in recharge of aquifers due to climate change (Van Dijck et al., 2005). In arid and semi-arid climates soil moisture plays a significant

role in determining vegetation patterns and the type of vegetation cover, which makes it of major importance in ecosystems in these zones (Grayson et al., 2006).

Spatio-temporal soil moisture patterns are currently derived from field measurements, process-based modelling or remote sensing data. The main objective of this research is to develop an approach that combines advantages of process-based soil moisture modelling, with field measurements as input data, and remote sensing data. It will be evaluated if this combined approach can improve the predictions of top soil moisture (0-15 cm) in space and time compared to conventional methods.

## 1.2 Problem definition

The urgent need of operational models that can accurately predict soil moisture patterns in space for hours to days after a rainfall event, using generally available data, is made clear in the previous section. Accurate spatio-temporal modelling of soil moisture patterns, however, is complicated. Any method of predicting soil moisture is complicated since it has to deal with a high degree of spatio-temporal variation in soil moisture, which is caused by an interaction of processes. Four different approaches can be used to estimate soil moisture patterns: (1) field measurements, (2) remote sensing, (3) process-based modelling, and (4) statistical modelling.

Samples of field measurements of soil moisture are traditionally at a small spatial support, which makes it laborious and time-consuming to get a good spatial and temporal coverage (Giacomelli et al., 1995; Van Oevelen, 2000). The term support is defined here as the area (or volume) and time interval for which the measured properties are considered homogeneous, and for which only the average value is measured and not the variation within (Bierkens et al., 2000; Karssenber, 2002). Coverage is defined as the sampling intensity in space and/or time (Bierkens et al., 2000). The poor support and coverage necessitates upscaling and downscaling of the soil moisture measurements by means of geostatistical interpolation techniques. Upscaling is the conversion of data or model results to a higher resolution, while downscaling refers to the conversion from higher resolution to lower resolution.

Direct remote sensing of soil moisture is limited, because the methods rely on indirect and complex relationships between remote sensing data and soil moisture, e.g. evapotranspiration estimated with surface energy balance models. Although the spatial coverage of remote sensing derived data is good for many applications, the temporal coverage can be poor for high resolution imagery (see section 1.2.6).

Process-based modelling has the specific problem of estimating inputs and parameters with their appropriate spatial and temporal distribution. Another problem with process-based modelling is the choice of an appropriate model structure.

Examples of statistical models are geostatistical models, stochastic models and data assimilation models. Geostatistical models are used to interpolate and/or downscale field measurements of soil moisture, e.g. (block) kriging. They are also used to create spatial realisations of input parameters and variables in a stochastic model. Stochastic modelling of soil moisture involves the propagation of errors in input variables and parameters through a process-based model. By analyzing statistics from many realisations of the model, the error in the predicted soil moisture can be estimated. A data assimilation model provides a stochastic model with the best estimate of the model state at a timestep when measurements are available.

In this thesis the advantages of process-based soil moisture modelling, with field measurements as input data, and remote sensing data will be combined, using data assimilation, in order to improve the predictions of top soil moisture (0-15 cm) in space and time compared to the result of each method separately. The model will predict top soil moisture with timesteps of one hour and grid cells of 125 m. This is considered as the minimum resolution needed to model dynamic patterns in soil moisture for agricultural fields.

In section 1.2.1 the processes causing spatial and temporal variability of soil moisture will be explained. Next, in section 1.2.2 field methods for measuring the soil moisture content will be explained, followed by a review of process-based modelling of soil moisture in section 1.2.3. Section 1.2.4 discusses the use of remote sensing for the estimation of soil moisture patterns. Section 1.2.5 reviews the use of data assimilation techniques in combining process-based soil moisture modelling with remote sensing data. Finally, in section 1.2.6 scale issues in combining field measurements and remote sensing based data in a process-based model will be discussed.

### 1.2.1 Soil moisture patterns

Soil moisture can be defined as the water in the unsaturated part of the soil profile, i.e. between the soil surface and the ground water level. In this thesis, the term soil moisture refers to top soil moisture, unless stated otherwise. Top soil moisture is defined here as the upper 15 cm of the unsaturated soil profile. This is considered as the soil layer that actively interacts with surface processes and surface evapotranspiration. A depth of 15 cm also corresponds with the limits of soil moisture measurements from the soil surface for most common measuring methods (section 1.2.2). Note that the Soil Moisture System (SOMS) model (chapter 8), used in this study, also includes deeper soil layers in order to model the transpiration from the root zone.

At a particular point in time the soil moisture content is determined by boundary conditions and the fluxes in the soil profile (Gomez-Plaza et al., 2001; Mohanty and Skaggs, 2001; Van Asch et al., 2001; Williams et al., 2003). The boundary conditions are: the precipitation history, runoff and runoff fluxes determined by the topography of the land surface, and the depth to the ground water table. The water fluxes in the soil profile are: infiltration determined by the texture of the soil and evapotranspiration determined by vegetation cover, meteorological, and radiation conditions. In addition, horizontal flow occurs due to water routing processes.

The relative importance of these fluxes depends on the dominance of either vertical or horizontal (lateral) water fluxes. Derived from this, Grayson et al. (1997) introduced the notion of local and non-local controls on soil moisture patterns. In dry conditions local controls determine the soil moisture patterns by means of vertical fluxes as shown in figure 1.1a. Under these conditions, soil properties and local terrain properties, in particular areas of high local convergence, are the most important factors having effect on soil moisture. In wet conditions, non-local controls occur, causing lateral water flows through both surface and subsurface paths (figure 1.1b). In this case the topography of the catchment determines the drainage paths and therefore the spatial soil moisture patterns. In the transition from wet to dry circumstances, the potential evapotranspiration increases, which will dry the soils until lateral flow is no longer possible. The system will switch from non-local to local controls.

Local controls prevail in arid and semi-arid regions associated with sparse vegetation, soil crusts and subtle variations in soil characteristics in combination with the effect of micro-topographic features (Fitzjohn et al., 1998; Gomez-Plaza et al., 2001). Since these factors either retain soil water or promote infiltration and evapotranspiration, the soil moisture pattern in the

transition from wet to dry can be very heterogeneous. Vegetation for example can influence the soil moisture pattern directly by its transpiration properties, or indirectly by influencing soil properties like infiltration capacity, soil water retention and repellancy (Gomez-Plaza et al., 2001).

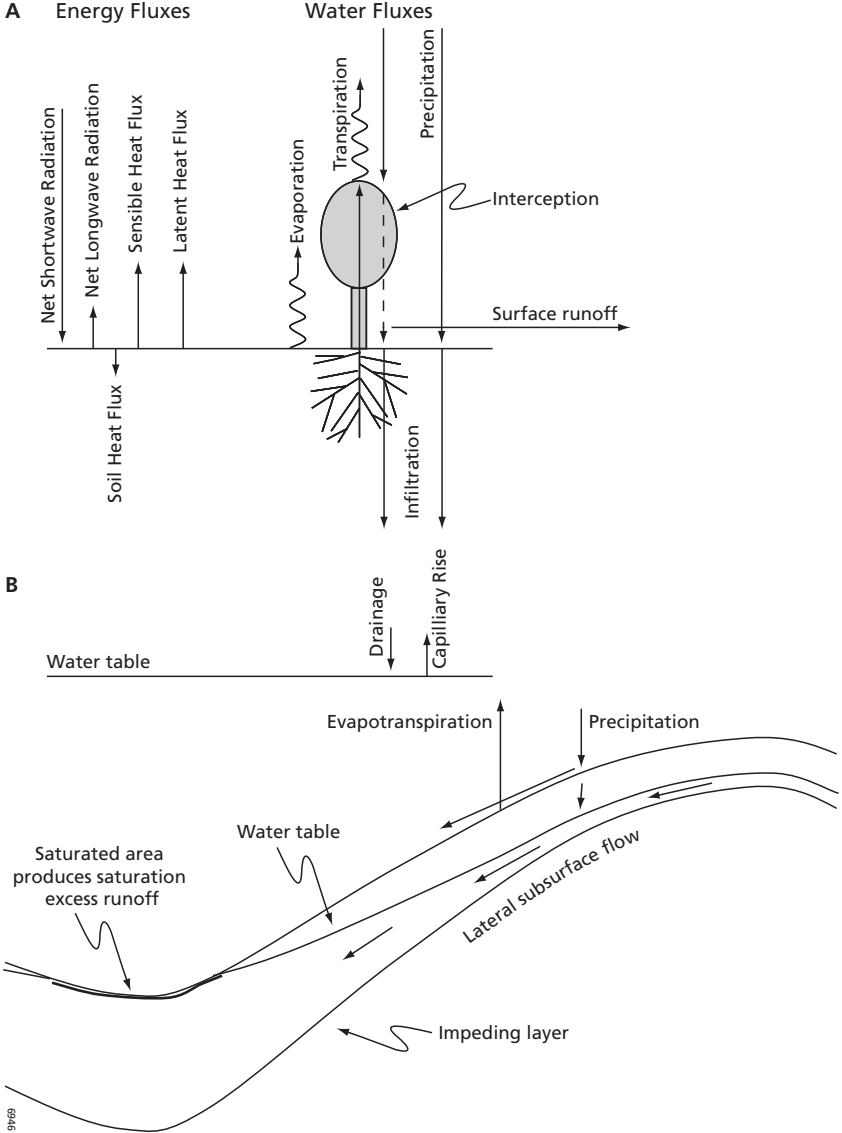


Figure 1.1 a: A one-dimensional soil water balance and surface energy balance. This is applicable where lateral flows are insignificant. b: A two-dimensional conceptualisation of a hillslope where both subsurface and surface flow can redistribute precipitation and affect the local soil water balance. Source: Western et al. (2002).

Typical behaviour of local controls occurs at the end of a dry season. At this moment the soils are extremely dry and soil moisture patterns will be closely related to the spatial variability in wilting point, which is the soil moisture content at which plants can no longer recover their turgidity and start wilting. When lateral flows are absent, as is the case on plateaus, the spatial variability of rainfall will determine the soil moisture patterns until the soil saturates. After saturation the pattern of porosity or field capacity will determine the soil moisture patterns (Grayson et al., 2006). This is the case in the Sehoul study area used for hydrologic modelling in this research. In agricultural areas land management and cultivation practices can largely determine the texture (Beckett and Webster, 1971) and structure (Rowell, 1994) of soils and influence the spatial pattern.

When topography is present in arid and semi-arid regions non-local controls only exist immediately after a rainfall event. In these regions infiltration excess overland flow (Hortonian overland flow) is the most important non-local control, because vegetation is absent or sparse, the soils are thin and have low infiltration capacities (Van de Griend and Engman, 1985).

From this section we can conclude that soil moisture patterns are highly variable in space and time. The scale of variability depends on the dominance of local and non-local controls on soil moisture patterns. Depending on the dominant control, different processes act on the spatial and temporal distribution of soil moisture and its spatial correlation. Since all these processes should be included in soil moisture models, the accurate modelling of soil moisture patterns in space and time is a difficult task.

### 1.2.2 Field methods

The most common methods to measure soil moisture content directly in the field, or from field samples in the laboratory are the gravimetric method, the neutron probe, the capacitance probe and Time Domain Reflectometry (TDR) or Frequency Domain Reflectometry (FDR) (Kutilek and Nielsen, 1994). All these methods have a limited support and coverage.

#### *Gravimetric method*

A frequently used method for estimating the soil moisture content in the field is the gravimetric analysis of soil samples. The soil samples are dried 24 hours in an oven at 105°C. After drying the loss in weight is determined. The weight analysis has to be done in the laboratory, it is laborious and sensitive to errors in sampling and weighing. The method does not differentiate between 'structural' and 'non-structural' water (Ward and Robinson, 1989): after drying in the oven, clay particles can still adsorb a considerable amount of water from the air causing an underestimation of the soil moisture content. Overestimation may also occur when organic particles oxidize at temperatures larger than 50°C (Ward and Robinson, 1989). Gardner (1986) recognised these two disadvantages and started the discussion about the reliability of the widespread and often undiscussed acceptance of the gravimetrically determined soil moisture contents. An additional disadvantage is that the method is destructive for the sample location, which makes it impossible to reproduce measurements at the same location (Ward and Robinson, 1989).

#### *Neutron probe*

The neutron probe uses a radioactive source of 'fast', i.e. high energy, neutrons. The radioactive source is lowered into a borehole in the soil, and the number of 'fast' neutrons that are slowed

down or thermalized by collisions with hydrogen nuclei, mainly present in the soil water, is counted by a detector (Kutilek and Nielsen, 1994). The spatial support of this method varies inversely with the soil water content. It is a soil cylinder with a radius between 10 cm for wet soil and 25 cm for dry soil. There is a fairly linear relationship between the detector count and the soil water content, but this is soil specific. Usually, the measurements are calibrated against gravimetric measurements, to obtain the soil specific relation. The neutron probe is mostly used to measure moisture differences rather than absolute soil moisture contents (Ward and Robinson, 1989).

#### *Capacitance probe*

The capacitance probe uses the dielectric constant of the soil as a measure of its soil moisture. The dielectric constant of soil is for 80% determined by the soil water content (Van Oevelen, 2000). Also, this method requires calibration with gravimetric samples in order to establish the soil specific relationship between dielectric constant and soil water content. Therefore it is best suited to measure changes in soil water content. Because the support of the capacitance probe is small, it is possible to make measurements close to the soil surface and over different horizons of a soil profile (Kutilek and Nielsen, 1994). On the other hand, the small support makes the method sensitive to local inhomogeneities and the access tube should be installed very carefully, because air gaps can bias the results (Ward and Robinson, 1989). In general, the neutron probe is preferred over the capacitance probe at depths greater than 0.15 m in clays and 0.2 m in loamy soils (Boucher, 1997).

#### *Time Domain Reflectometry (TDR) and Frequency Domain Reflectometry (FDR)*

Time Domain Reflectometry (TDR) and Frequency Domain Reflectometry (FDR) also use the dielectric properties of the soil. Originally, the technique is used to characterize and locate faults in metallic cables (cable tester). Hoekstra and Delaney (1974) and Topp et al. (1980) demonstrated the use for the measurement of soil water content. Both methods use two or more parallel metal rods that are placed in the soil. An electromagnetic wave is propagated through the rods. The apparent permittivity, which is related to the dielectric properties of the soil, is calculated from the change of an electromagnetic wave when it propagates through the rod, the soil and back to the measuring device. TDR calculates the difference in travel time, in nanoseconds, between the impulse that has been sent into the soil and that has been reflected. With FDR the oscillator frequency is matched with the resonant frequency of the soil, i.e. the amplitude of the reflected wave is greatest for the soil under consideration. This frequency is a measure of the soil water content.

The rods or probes are usually between 10 and 30 cm. Early results were encouraging and had an accuracy comparable to that of gravimetric samples (Topp and Davis, 1985). Today, TDR is widely accepted and used in many hydrological studies, e.g. Gómez-Plaza et al. (2001), Van Asch et al. (2001), Western et al. (1999). The method is non-destructive and non-radioactive. Furthermore, it can easily be set up for either manual or automatic operation with a datalogger (Ward and Robinson, 1989). However, a calibration with gravimetric samples is important when accurate absolute results are required. In this research soil moisture is measured with a TDR, which will be discussed in chapter 8.

### 1.2.3 Process-based models

From section 1.2.1 it can be concluded that soil moisture is highly variable in both space and time, depending on the domination of local and non-local controls. In section 1.2.2 the most common soil moisture measurement techniques have been discussed. The limited spatial support of the measurements makes it time consuming and laborious to measure soil moisture patterns at scales larger than plot scale. A large temporal coverage of field measurements requires dataloggers. Therefore it is hard to measure actual soil moisture patterns in space and time with traditional field measurements alone. In addition, prediction of soil moisture is not possible from field measurements without a model. Geostatistical space-time interpolation and extrapolation techniques can be useful, but the accuracy of the result depends much on the spatial autocorrelation and the density and location of the samples. With these techniques processes causing the spatial and temporal distribution of soil moisture are not taken into account. Process-based models, where field data is used as input data and for calibration, have been developed to take processes into account that determine the redistribution of soil moisture.

#### *Model structure*

Many numerical process-based models have been developed to model soil moisture patterns in space and time, based on mathematical descriptions and a set of input data. Mathematical descriptions in process-based models are derived from lower level physical laws for which it is assumed that they are valid under all known circumstances (Karssenberg, 2002). These models can be divided in lumped models and distributed models. In lumped models the state variables are homogeneous for the modelled area. In distributed models states are heterogeneous in the model area, because spatial variability in input data and parameters is included. Distributed process-based models, however, are often discretized in a grid, so in reality each model gridcell lumps subgrid processes and results cannot be obtained at subgrid scales (Beven, 1989).

Models that simulate only vertical fluxes are called one-dimensional (1D) models. Models that also include lateral fluxes are called three-dimensional (3D) models. When modelling soil moisture in an area where only vertical exchanges of soil moisture take place (local controls) and the lateral flows are negligible, e.g. on plateaus, 1D soil moisture models are well capable of predicting the temporal behaviour of soil moisture if soil physical parameters and meteorological parameters are known at a point in a landscape for which the model is representative. In order to perform distributed modelling for situations with local controls, the 1D model is run for many representative points in the area of interest. The model parameters and variables may be interpolated, using geostatistical techniques, like kriging (Burrough and McDonnell, 1998). The model can also be distributed using strata derived from a combination of land cover and soil maps.

The choice of the model structure depends on the desired spatial and temporal scale of the predictions, the relevant processes in the study area, the amount of available data and the available computational power. These factors determine the complexity and level of detail that should be included in the model parameterization.

#### *Input data*

Distributed process-based modelling can be done in a dynamic Geographical Information System (GIS) (Wesseling et al., 1996; Burrough and McDonnell, 1998), e.g. PCRaster (PCRaster, 2008). In this case input data are digital maps.

Most soil moisture models need the following inputs:

1. Meteorological data. Temperature, relative humidity, wind speed, air pressure and incoming solar radiation are used to calculate evapotranspiration. Precipitation data provides the main input of moisture in the model.
2. Soil physical data. Initial soil moisture, hydraulic conductivity, parameters of the soil water retention curve and porosity are required to model water fluxes in the unsaturated zone.
3. Vegetation data. Leaf Area Index (LAI) and fractional vegetation cover are important in the calculation of interception and evapotranspiration. Vegetation data is also used for calculation of transpiration from the soil profile.
4. Elevation data. Digital Elevation Models (DEMs) are required for modeling the pattern and velocity of runoff and locations of possible re-infiltration of runoff downstream (Burrough and McDonnell, 1998). Furthermore, elevation data is used to calculate the incoming solar radiation at the surface that is required for the calculation of evapotranspiration (Van Dam, 2000, 2001).

It is hard to acquire high quality spatial input data at a sufficiently large spatial and temporal coverage with field methods. Meteorological data are usually available from one to a small number of meteorological stations. When data from more stations is available, the data is spatially interpolated. The spatial coverage of meteorological data is poor, but the temporal coverage can be high due to the use of data loggers at the meteorological stations. Distributed soil physical data are usually derived from a small number of fields. These data have a poor spatial and temporal coverage. Hence, spatio-temporal interpolation is required to retrieve spatially and temporally continuous inputs for the model. LAI and fractional vegetation cover can be derived by linking land cover maps to literature values of LAI and fractional vegetation cover. These maps are not always available, have a low temporal coverage and a coarse resolution. DEMs can be derived from interpolation of height measurements in the field or interpolation of digitized contour lines, when accurate maps are available. Both methods are labourious for large areas. In Part II of this thesis and section 1.2.4 it will be shown that remote sensing can provide spatial data on vegetation and elevation.

When a parameterization method has been chosen and proper input data and parameters have been collected in the field, the following steps need to be done before applying a process-based model: calibration, validation and uncertainty analysis.

### *Calibration*

Since a model is an approximate representation of reality, errors are introduced by the model structure. Additionally, uncertainty in available data on parameters, initial conditions and boundary conditions causes deviations of predicted variables from field observations (Beven, 2002). Therefore, process-based models should be calibrated by comparing predicted and observed soil moisture values and optimizing model parameters to fit the predictions to the observations as closely as possible. The accuracy of the calibration, however, is much dependent on the quality of the input data and the propagation of errors through the model (Heuvelink, 1998). Another problem concerning the calibration of process-based models is the fact that the higher the level of detail in a model, the greater the risk of overparameterization. In the case of overparameterization too many tuning parameters are used to calibrate the model, causing a perfect fit with the reference data. When the model inputs are changed, the model gives

unrealistic results. Furthermore, there is the problem of equifinality, when different combinations of parameters can give a good fit with the observations (Beven, 1989).

In general, there are four ways to calibrate process-based models (Beven, 2002):

1. Manual tuning of parameters, until the predicted data resembles more or less the measured data. This is usually done by trial-and-error, using subjective 'eye-ball fitting' or an objective function. Although with a small number of parameters good results can be reached, this method lacks exactness, reproducibility and objectivity (Janssen, 1995).
2. Automatic optimization methods like hill-climbing techniques, simulated annealing and genetic algorithms. These methods assume an optimum parameter set, while ignoring the estimation of predictive uncertainty (Beven, 2002). The goal of automatic optimization methods is to maximize or minimize an objective function. An example of these methods is the Parameter Estimation (PEST) algorithm (Doherty, 2002), which has been used in chapter 8 of this thesis.
3. Reliability analysis methods. These methods assume an optimum parameter set, while estimating the parameter uncertainty, based on assumptions about the parameter response surfaces (Beven, 2002). Most of these methods are based on Monte Carlo simulations or approximations to save computation time.
4. Conditioning methods. These are methods that reject the assumption of an optimum parameter set, but accept equifinality (Beven, 2002). These models evaluate the likelihood of each possible parameter set and the uncertainty of its predictions. An example of these methods is the Generalized Likelihood Uncertainty Estimation (GLUE) (Beven and Binley, 1992).

The choice of one of these methods depends on computing time, the model objectives, model structure and data availability. In practice, parameters to which the model predictions are very sensitive and that are difficult to measure in the field are used for calibration. For distributed models, for each gridcell an effective parameter is needed that represents the heterogeneity within a gridcell. Since the measurement and calibration of each gridcell independently is practically impossible, in many process-based models parameters are assumed to vary only with combinations of land cover and soil type. Examples of these models are LISEM (De Roo et al., 1992) and SHE (Abbott et al., 1986). The newly developed SOMS model uses the same principles when run as a process-based model (chapter 8).

### *Validation*

After calibration the model should be validated with an independent set of field measurements that have not been used in the calibration procedure. Goodness of fit measures are used to express the quality of model predictions. Oreskes et al. (1994) argued however, that validation of numerical models of natural systems is impossible, because natural systems are never closed systems and because results of these models are never unique. Therefore in this thesis the term evaluation is preferred over validation.

The problem with both calibration and evaluation is the support of field measurements (section 1.2.2) compared to the support of model gridcells. Bierkens et al. (2000) and Blöschl and Sivaplan (1995) give a detailed description of up- and downscaling concepts. Scaling issues in this research are discussed in section 1.2.6.

Another problem is that field sampling should be done at a small number of representative locations that cover all combinations of soil and land cover types included in the model. Spatial heterogeneity makes it in practice very difficult to determine in the field which locations are representative.

With the development of remote sensing techniques it is possible to determine effective parameter values at the scale of individual grid cells. However, the resolution of the remote sensing derived parameter should match the model requirements. Resampling of grid cells to other resolutions is complicated, because many variables show a non-linear response, and cannot be simply averaged over areas. Furthermore, remote sensing derived parameters are often results of models itself, introducing the same problems as described above.

#### *Uncertainty analysis*

A calibrated model should not only give predictions and goodness of fit measures with validation data, but also an estimation of the uncertainty of the model predictions. This is called uncertainty analysis or error propagation modelling. Spatio-temporal models can contain six types of error sources: attribute errors, positional errors, lineage, logical consistency, completeness and temporal accuracy (DCDSTF, 1988; Guptill and Morrison, 1995). Heuvelink (1998) describes a number of approaches to model errors in model inputs and parameters. Usually the error propagation is modelled using Monte Carlo runs in which the uncertainty of parameters is propagated through the model. This results in the mean and variance estimate of the output variables. Chapter 9 of this thesis contains an uncertainty analysis of a process-based soil moisture model, SOMS, and the chosen remote sensing based evapotranspiration model, SEBS (Surface Energy Balance System, (Su, 2002)).

#### **1.2.4 Remote sensing**

Nowadays remote sensing images can provide the basis of the spatial data requirements of distributed soil moisture models. Since the launch of the first earth observation satellite in 1972 many earth observation systems have been brought into orbit by various space agencies like NASA, ESA and NASDA. A number of missions and platforms are of specific interest for hydrological studies. These are mainly sensor systems that combine thermal infrared and optical data, and active and passive radar systems. Thermal infrared sensors register mainly the emission of radiation in wavelengths ranging from 3 to 50  $\mu\text{m}$ . Optical sensors register mainly the reflection of sunlight from objects, which is in the visible and near infrared part of the electromagnetic spectrum. This ranges from 0.4 to 1.1  $\mu\text{m}$ . Radar or microwave remote sensing refers to the part of the electromagnetic spectrum ranging from  $10^3$  to  $10^5$   $\mu\text{m}$ . Apart from the sensor's spectral definition, revisit time and spatial resolution are important considerations to determine whether a sensor is suitable for hydrological monitoring and modelling. Revisit time is the temporal coverage of a remote sensing sensor and refers to the time span between the image acquisitions of the same area, which is normally in the order of 1 to 16 days. Important missions for hydrological studies are the currently operational ASTER (Yamaguchi et al., 1988; ASTER, 2008) and MODIS (Justice et al., 1998; MODIS, 2008) sensors aboard the TERRA platform, the SMOS mission of ESA (Soil Moisture and Ocean Salinity mission), planned for 2009 and the Landsat series (LANDSAT, 2008). Apart from satellite sensors, there are also many airborne sensors available that acquire data at different spatial and spectral resolutions. Examples are standard survey aerial photography and hyperspectral sensors like HyMap (HyVista, 2008) and

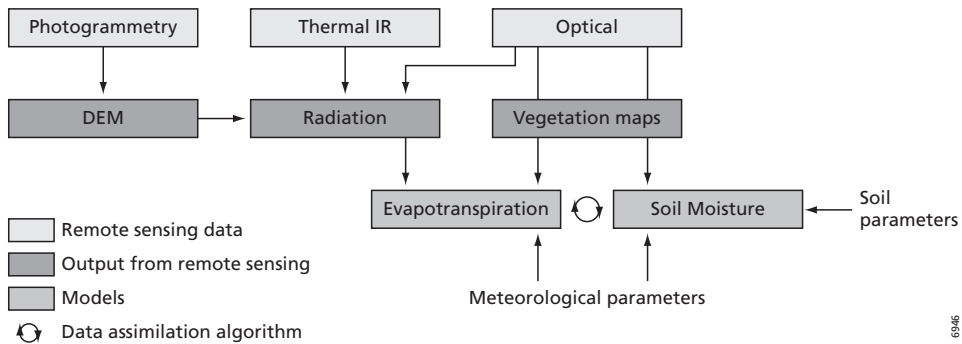


Figure 1.2 Potential use of remote sensing derived products in process-based soil moisture modelling.

DAIS7915 (Strobl et al., 1996) that acquire data in many small spectral bands, which can be used for imaging spectroscopy (Van der Meer and De Jong, 2001).

In the flowchart of figure 1.2 the potential use of remote sensing in process-based soil moisture modelling is schematized. The use of microwave remote sensing for the retrieval of soil moisture falls outside the scope of this research. Many examples of soil moisture retrieval by microwave remote sensing can be found in literature (Jackson, 1982; Engman, 1990; Entekhabi et al., 1993; Engman and Chauhan, 1995; Giacomelli et al., 1995; Su et al., 1995, 1997; Ulaby et al., 1996; Srivastava et al., 1997; Wigneron et al., 1998; Galantowicz et al., 1999; Van Oevelen, 2000; Narayanan and Hirsave, 2001; Reichle et al., 2001c; Zribi and Dechambre, 2003).

Following figure 1.2 remote sensing provides a means of extracting vegetation parameters, digital elevation models, and surface energy balance components. Remote sensing makes it possible to extract these inputs over large areas and provides information of their changes over time. It is important to keep in mind that remote sensing cannot replace ground observations. Earth observation imagery does not give direct values for variables or parameters used in hydrological modelling, but always require an interpretative model. Remote sensing observations assist in determining the temporal and spatial distribution of hydrological state variables or process controlling variables, but will always require evaluation and verification by field measurement or ground station data. In data poor areas, where ground truth is difficult to acquire due to a lack of instrumentation, poor infrastructure or non-cooperative authorities, remote sensing is the only data source.

Important variables that can be retrieved from imagery with varying accuracy are: land cover, natural vegetation cover, LAI, above ground biomass, elevation, and surface energy balance parameters. The accuracy of the derived variables varies from sensor to sensor, from area to area and as a function of local conditions of the atmosphere and the surface.

In this research remote sensing data will be used to estimate input variables and parameters of the Surface Energy Balance System (SEBS) and SOMS model. These data consist of DEMs and vegetation parameters. Remote sensing will also be used for the estimation of actual evapotranspiration, by means of SEBS. SEBS is a static surface energy balance model that estimates atmospheric turbulent fluxes and evapotranspiration fluxes from thermal and optical remote sensing. The evapotranspiration output of SEBS will be compared with evapotranspiration output of SOMS at times that satellite data are available in order to optimize

the prediction of soil moisture. This is called data assimilation and will be explained the next section. Direct derivation of soil moisture states, using microwave remote sensing, will not be used in this research, because the resolution is too low for modelling of agricultural fields in the study areas.

### 1.2.5 Data assimilation

From section 1.2.1 it can be concluded that soil moisture is highly variable in both space and time, depending on whether local or non-local controls are dominant. In section 1.2.2 the most common soil moisture measurement techniques have been discussed. The limited spatial support of the measurements makes it time consuming and laborious to measure soil moisture patterns at scales larger than plot scale. A high temporal coverage of field measurements requires dataloggers. Therefore it is hard to measure actual soil moisture patterns in space and time with traditional field measurements alone. Geostatistical space-time interpolation techniques can be useful, but the accuracy of the result depends much on the spatial autocorrelation and the density and location of the samples. Section 1.2.3 discussed the problems with distributed process-based modelling of soil moisture, which are related to the support and coverage of input parameters, the choice of model structure, calibration and evaluation. In section 1.2.4 the possibilities of using remote sensing for the derivation of input parameters and variables for process-based models have been discussed. In this section a statistical optimization technique called data assimilation will be introduced, which makes it possible to combine remote sensing derived actual evapotranspiration with the result of soil moisture modelling.

Data assimilation is a method for estimating an unknown probability density function (pdf) recursively over time using incoming measurements and a process-based model. It is also known as recursive Bayesian estimation (Doucet et al., 2000) and is based on the assumption that the true state of a model variable is an unobserved Markov process. The Markov property of a stochastic process assumes that a conditional probability distribution of future states of the process, given the present state and all past states, solely depends upon the present state and not on any past states. The measurements that are available during certain timesteps are assumed to be observed states of a hidden Markov model (HMM). A HMM models a Markov process, but the parameters are unknown and should be determined from observations (Doucet et al., 2000).

The purpose of a data assimilation algorithm is to provide the process-based model with the best estimate of the model state at the timestep of the measurement (Walker, 1999). Recently, data assimilation in process-based models has been used to assimilate uncertain remote sensing data instead of field measurements (Errico, 1999; Errico et al., 2000).

Data assimilation methods were applied successfully in numerical weather predictions and oceanography (Evensen and Van Leeuwen, 1996; Houtekamer and Mitchell, 1998; Lermusiaux, 1999; Madsen and Canizares, 1999; Keppenne, 2000). For soil moisture predictions, many studies have assimilated microwave remote sensing data with promising results, e.g. Reichle et al. (2001b, 2001c), Pauwels et al. (2001), Margulis et al. (2002), Houser et al. (1998), Hoeben and Troch (2000), Walker et al. (2001). The spatial resolution of microwave remote sensing images, however, is not appropriate for the level of detail needed in predictions of soil moisture at the scale of agricultural areas and small catchments. Much less studies have been published on the use of thermal and optical remote sensing data through evapotranspiration modelling, which can give results at higher resolutions compared to microwave remote sensing. Schuurmans et al. (2003) and Ottlé and Vidal-Madjar (1994) demonstrate the use of 1 km resolution NOAA-

AVHRR data. Research on data assimilation of remote sensing derived evapotranspiration in a soil moisture model should now focus on the scale of Landsat TM 5 (120 m), Landsat TM 7 (60 m) or ASTER (90 m) images. These methods use optical and thermal channels. This research focuses on the use of these relatively high resolution sensors as well as the disaggregation of low resolution images for the derivation of actual evapotranspiration using SEBS and its assimilation in the SOMS model.

The most common types of data assimilation are: the Kalman Filter, the Extended Kalman Filter, the Ensemble Kalman Filter and the Particle Filter.

#### *Kalman Filters*

Kalman filters (Kalman, 1960) assume linear dynamical systems that are discretised in the time domain. For each timestep it is assumed that the states have the Markov property and therefore form a Markov chain, which is built on linear operators perturbed by Gaussian noise (Gelb, 1974). If an observation is available, the filter estimates a statistically optimal update of the system states, using the covariances of both the model system state predictions and the observations (Walker, 1999). Hydrological processes, however, are non-linear. Therefore, the Extended Kalman Filter has been developed, which is based on a first-order linearization of non-linear functions (Gelb, 1974). In the case when non-linearities are strong, the Extended Kalman Filter will give inaccurate results (Weerts and El Serafy, 2006). The Ensemble Kalman Filter (Evensen, 1994; Burgers et al., 1998; Margulis et al., 2002; Reichle et al., 2002) can be used in that case. In this algorithm errors are propagated with the non-linear model equations in Monte Carlo simulations, resulting in an ensemble of model runs. All Kalman Filters modify system states at the observation moment, meaning that the physical laws of conservation of mass, momentum, and energy might be violated.

#### *Particle Filters*

Particle filters, or sequential Monte Carlo methods, popular in the fields of object recognition (Zhou et al., 2004), target tracking (Hue et al., 2002), financial analysis (Yu, 2005) and robotics (Fox et al., 1999) have only recently been introduced in the field of hydrology (Moradkhani et al., 2005; Weerts and El Serafy, 2006). The main advantage of particle filters is that no assumptions are made on the prior pdf of the model states and that the full prior density is used (Weerts and El Serafy, 2006), while Kalman filters assume a Gaussian distribution. With sufficient samples, particle filters can approach the Bayesian optimal estimate and are therefore more accurate than the first-order approach of Kalman filters.

The most common particle filters are based on either Sequential Importance Sampling (SIS) or Sampling Importance Resampling (SIR). SIS approximates the posterior density function by a set of weighted random samples, which are called *particles* (Weerts and El Serafy, 2006). The SIR algorithm (Gordon et al., 1993) has been developed to avoid that all except one of the importance weights are close to zero, which causes degeneracy of the algorithm. The particles are therefore resampled. Resampling duplicates particles with a high weight according to their weight and largely ignores particles with a low weight (Van Leeuwen, 2003).

In the case of a particle filter, data assimilation is not an inverse problem. The best set of particles is propagated, resulting in state predictions accompanied by its uncertainty, while preserving physical consistency, i.e. conservation of mass, momentum, and energy. Because of these advantages over a Kalman Filter, a particle filter approach was chosen for this study.

Chapter 10 will further explain the particle filter and its implementation in a process-based soil moisture model, using remotely sensed evapotranspiration as filter data.

### 1.2.6 Scaling issues

From the previous sections it can be derived that field measurements, process-based models, remote sensing input data and remote sensing derived evapotranspiration (SEBS results) are different in terms of support and coverage. Table 1.1 shows these differences for the datasets and the SOMS model used in this research.

The data assimilation model uses the resolution of SOMS, i.e. grid cells of 125 x 125 m. In this research it is necessary to take into account the different supports and coverages where combinations of datasets are used. This is the case for calibration and evaluation of SOMS, input data for SOMS derived from field data and remote sensing, input for SEBS from field data and remote sensing and the assimilation of SEBS and SOMS in the data assimilation model. Some of the methods of upscaling and downscaling discussed in Bierkens et al. (2000) will be applied, like geostatistical interpolation techniques (see chapters 8, 9 and 10). For the radiometric surface temperature needed as input to SEBS, a different method will be applied in chapter 7, which estimates subpixel temperatures using higher resolution optical channels of a remote sensing sensor. The use of disaggregated coarse resolution images is needed, because Landsat and ASTER images have a poor temporal coverage due to their repeat cycles of 16 days (table 1.1). Moreover, the number of available images will in practice be much lower than 16 days, because unfavourable atmospheric circumstances hamper the accurate retrieval of radiometric surface temperature. A further limiting factor is that, for some of these satellite sensors like ASTER, the acquisition schedule is on-demand, meaning that data only will be collected over a location after a user request.

Satellites with a much better temporal coverage are available, but the spatial resolution of the thermal bands (1-5 km) is poor for the detailed modelling of agricultural communities, e.g. MODIS in table 1.1. Table 1.2 shows that even when daily images, like MODIS, are used, the success rate is low (5.2%) in temperate areas like the Netherlands. The values for the Netherlands are based on local weather data of cloud cover and visual inspection of 1436 MODIS possible

*Table 1.1* Lateral support and coverage for data and models used in this research. VNIR = Visual and Near Infrared, TIR = Thermal Infrared.

	Lateral spatial support [m <sup>2</sup> ]		Spatial coverage [samples or gridcells/ha]		Temporal coverage (sampling interval)
Field measurements (moisture, TDR)	0.002		20		Daily
Field measurements (meteorological)	Depends on height of measurements, wind speed and surface properties		1 station for the entire study area		10 min
Process-based model (SOMS)	15625		0.64		1 h
Remote sensing data	VNIR	TIR	VNIR	TIR	
ASTER	225	8100	44.4	1.23	≥ 16 days
Landsat TM 5	900	14400	11.1	0.69	≥ 16 days
MODIS	62500	1000000	0.16	0.01	≥ Daily

*Table 1.2* Chances of available and usable MODIS and ASTER images in the Netherlands and Morocco, based on the evaluation of meteorological data on cloud cover and visual inspection of images.

Location	Number of days analysed	MODIS	ASTER
Langbroekerwetering, the Netherlands	1436	5.2%	0.56%
Sehoul, Morocco	47	29.8%	2.1%

images from 2003 to 2006. In Mediterranean zones the success rate is much higher. A visual inspection of MODIS images during 47 days in the rain season of 2004 in the Sehoul study area in Morocco reveals that the chances are better, but still low (29.8%). The distribution of images appropriate for surface energy balance modelling is also a problem, because cloudless days are clustered and not always available at model timesteps where filter data could largely improve the results of soil moisture predictions. Table 1.2 also shows that one should not heavily rely on the availability of ASTER images in either temperate or Mediterranean climates.

### 1.3 Study areas

In this research three study sites have been used for different purposes. The sites are Barrax (Spain), Sehoul (Morocco) and La Peyne (France).

The Barrax field site is located in the La-Mancha region in Spain. This flat agricultural area shows a large contrast between pivot irrigated crops and dry areas, which made it very suitable for the evaluation of SEBS, which is explained in Part II of the thesis. During the ESA funded SPARC 2004 field campaign all necessary input and validation data for the SEBS model have been collected. Su et al. (2005) gives an overview of the field measurements done in this ‘data rich’ field site. Because the water balance in this area is human controlled, this site has not been used for soil moisture modelling.

The Sehoul study area is located in the north of the agricultural community of Sehoul in Morocco. The site lies about 20 km south-east from Rabat. Although Sehoul is located in the same climate zone as the Barrax study site, i.e. Csa climate according to the climate classification of Köppen (Köppen, 1936), the differences in land use are clear. Land use comprises rainfed wheat, maize and horticulture. Some traditional irrigation is present. Because soils are relatively homogeneous and the spatial variability is low, this site was chosen for the application of the soil moisture model, which is explained in Part III and IV of this thesis. Furthermore, Sehoul, which is Arabic for plateau, does not have large differences in elevation, except for the river valleys. Meteorological measurements, soil moisture measurements and land cover mapping have been done during several field campaigns from 2003 to 2006. Nevertheless, this study area is ‘data poor’ in the sense that only inexpensive practical measurements have been done and the use of remote sensing data is necessary for the spatio-temporal predictions of soil moisture.

The La Peyne study area is only used in the case study on DEM generation by remote sensing in chapter 3. It is located in southern France, approximately 60 km west of the city of Montpellier. This area was selected because a large set of high quality aerial photographs was

available as well as ASTER images. Furthermore, a large ground truth database exists for this area, based on research by Sluiter (2005).

The study areas are described in more detail in the relevant chapters.

## 1.4 Objective, research questions and thesis outline

The main objective of this research is to evaluate the performance of different methods that can be used for the estimation of top soil moisture patterns in space and time. The methods that will be evaluated are field measurements, process-based modelling and remote sensing based modelling. Apart from evaluating each method separately, a data assimilation approach that combines the advantages of each method for operational soil moisture modelling will be developed and evaluated.

The prediction of top soil moisture (0-15 cm below the soil surface) will be done at a specific resolution of 125 m and timesteps of 1 h, which is in accordance with processes related to agriculture in the study area.

The central research question is:

- a) *Top soil moisture patterns in space and time can be estimated using field methods, process-based models and remote sensing data. What is the performance, in terms of accuracy, resolution and coverage of operational spatio-temporal estimation of top soil moisture, of each method separately and a combined approach that uses a particle filter data assimilation algorithm?*

In order to answer the central research question, other questions must first be answered. This will be done according to the flowchart in figure 1.3, which also explains the structure of this thesis. The thesis consists of four parts. Each part focuses on one of the main research questions that will be introduced in this section.

Part I of the thesis describes in what way remote sensing can contribute to the modelling of soil moisture. This leads to the following research questions that will be answered in this part of the thesis:

- b) *Which spatial inputs for a process-based soil moisture model and a remote sensing based evapotranspiration model can be derived from remote sensing? Are these inputs available at a sufficient temporal and spatial resolution for the modelling of agricultural areas like the study sites?*

Chapter 2 gives a review of remote sensing techniques that are useful in soil moisture modelling, including remote sensing image classification, spectral vegetation indices, derivation of radiation data and Digital Elevation Models (DEMs). Part I concludes with a case study on the derivation of DEMs from remote sensing in the La Payne study area, which is explained in chapter 3.

In addition to model inputs, also the actual evapotranspiration, a model output variable, can be derived from remote sensing. In Part II, SEBS will be introduced and evaluated in order to answer the following questions:

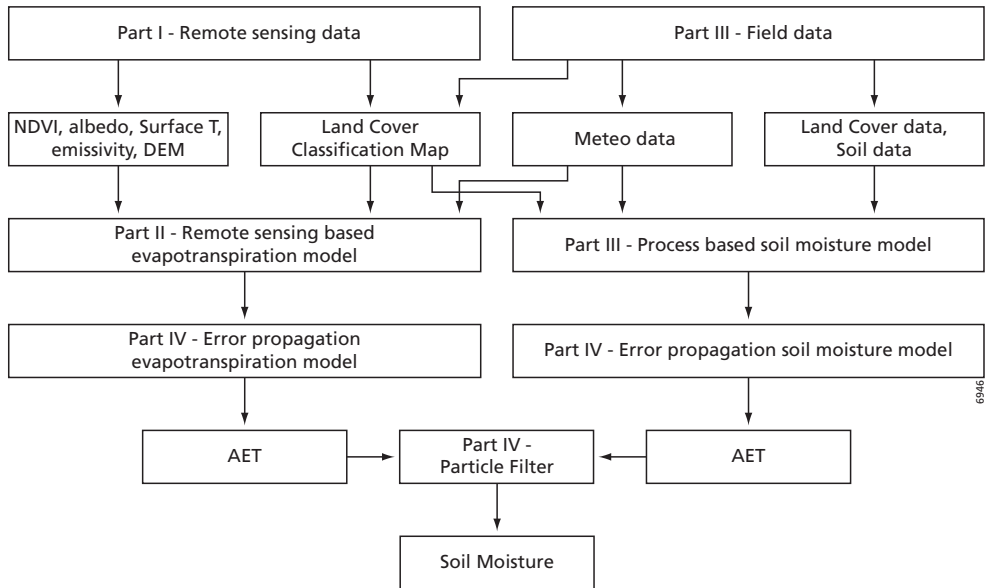


Figure 1.3 Flowchart of the research. NDVI = Normalized Difference Vegetation Index, AET = actual evapotranspiration, DEM = Digital Elevation Model.

- c) *How can SEBS, the model selected for derivation of evapotranspiration from remote sensing, derive fluxes from satellite data and how accurate is this for different land cover types?*
- d) *Can we derive the inputs for SEBS from different satellite data, in order to include remote sensing based evapotranspiration in operational models?*
- e) *Can we improve the spatial resolution of daily remote sensing images in order to provide data for an operational model at an appropriate scale?*

Question c will be answered with a literature review on the surface energy balance and its modelling in chapter 4. Chapter 4 will conclude with the description of the SEBS model. Question d will be answered in chapter 5, which shows different procedures for the acquisition of input data for SEBS, using different satellite images. In chapter 6 SEBS will be evaluated with field data in order to answer question c. Part II concludes with the application and evaluation of a disaggregation algorithm for the improvement of the resolution of radiometric surface temperature images. This answers question e.

For the purpose of this research a process-based spatio-dynamic soil moisture model will be developed that is feeded and calibrated using field observations. In Part III the process-based soil moisture model SOMS will be explained. Chapter 8 describes the study site in the community of Sehoul in Morocco. Furthermore, the model and field data are described. This chapter concludes with the calibration and evaluation of the model and should answer the following question:

- f) *What is the accuracy of top soil moisture patterns predicted by a deterministic process-based soil moisture?*

The effect of error propagation through the process-based soil moisture model (SOMS) and SEBS is studied in part IV, chapter 9, in order to answer the following questions:

- g) *What is the accuracy of the predictions of top soil moisture and actual evapotranspiration of the process-based soil moisture model and what are the most important sources of uncertainty?*
- h) *What is the accuracy of SEBS predictions of actual evapotranspiration and what are the most important sources of uncertainty?*

Finally, in chapter 10, SEBS derived actual evapotranspiration will be integrated in the soil moisture model by means of a particle filter. Different modelling scenarios should answer the main research question and indicate the limitations of the chosen method:

- i) *Can the particle filter data assimilation of remote sensing based predictions of actual evapotranspiration in a process-based soil moisture model improve the prediction of soil moisture patterns in space and time compared to methods that use field measurements, process-based models and remote sensing separately?*
- j) *What are the requirements for successful application of a particle filter for the prediction of top soil moisture patterns?*

Chapter 11 gives the synthesis of the thesis.

**Part I**  
**Remote sensing data for soil moisture  
modelling**



## 2 Review of remote sensing techniques

### 2.1 Remote sensing for soil moisture mapping

In section 1.4.2 the potential use of remote sensing in process-based soil moisture modelling has been introduced. The direct retrieval of soil moisture from remote sensing, however, is not straightforward, because indirect relations exist between the signal received by a sensor and the soil moisture near the earth's surface.

Either a combination of optical and thermal sensors or microwave (radar) remote sensing can be used to map soil moisture content. It is not feasible to derive soil moisture maps from optical sensors alone for several reasons (Moran et al., 2004). First, the signal received by optical sensors is reflected or emitted by only the top millimetres of the earth's surface, so it does not contain information about the upper 15 cm of the soil profile, which is studied in this research. Furthermore, the reflection received by the sensor is not only a function of soil moisture, but is also related to soil composition and soil physical properties. In addition, the received signal is influenced by vegetation and atmospheric conditions.

Better results can be obtained by combining data from optical sensors with data from thermal sensors. Thermal sensors can be used to derive surface temperature, which spatial variation is highly correlated with soil moisture variability for bare soils (Schmugge, 1978; Friedl and Davis, 1994). For (partially) vegetated areas a combination between thermal imagery and spectral vegetation indices (see section 2.4) can improve the estimation of soil moisture. These methods use the negative correlation that exists between radiometric surface temperature and a spectral vegetation index like the Normalized Difference Vegetation Index (NDVI, eq. 2.1) (Moran et al., 2004). Examples are the triangle method (Carlson et al., 1995), temperature-vegetation contextual approach (TVX, (Czajkowski et al., 2000)), surface temperature-vegetation index space (Lambin and Ehrlich, 1996), temperature-vegetation dryness index (TVDI, (Sandholt et al., 2002)), moisture index (Dupigny-Giroux and Lewis, 1999). Strong correlations and low standard errors have been found (Nemani et al., 1993; Goward et al., 2002; Sandholt et al., 2002; Hassan et al., 2007). Although the results are promising, these methods are hampered by atmospheric conditions. The empirical relationships should be calibrated for different seasons or crop growing stages, for each land cover type, topography and different meteorological conditions in order to get accurate absolute values of soil moisture (Smith and Choudhury, 1991; Nemani et al., 1993; Gillies and Carlson, 1995).

Some investigations have been done to relate the evaporative fraction, defined as the ratio between actual evaporation and the available energy (Su, 2002), to soil moisture. Only weak non-linear relations have been found (Nichols and Cuenca, 1993; Basara and Crawford, 2002). The correlation was higher when moisture in the entire rootzone was considered (Basara and Crawford, 2002), making this method less useful in areas with low vegetation covers.

Microwave remote sensing of soil moisture content is based on the contrast in dielectric properties between dry soil and water. The backscattered signal at the radar receiver, however,

depends not only on this contrast between dry and wet soils, but also on topography, surface roughness and vegetation cover. The received signal is also related to the frequency of the observation, polarisation of the waves and the incidence angle of the radiation. The use of microwave remote sensing falls outside the scope of this thesis, because of the coarse resolutions of passive microwave and the low temporal coverage of active microwave sensors. Many examples of soil moisture retrieval by microwave remote sensing can be found in literature (Jackson, 1982; Engman, 1990; Entekhabi et al., 1993; Engman and Chauhan, 1995; Giacomelli et al., 1995; Su et al., 1995, 1997; Ulaby et al., 1996; Srivastava et al., 1997; Wigneron et al., 1998; Galantowicz et al., 1999; Van Oevelen, 2000; Narayanan and Hirsave, 2001; Reichle et al., 2001c; Zribi and Dechambre, 2003).

Because of the limitations of direct soil moisture mapping from remote sensing, this chapter focuses on the derivation of data from optical and thermal remote sensing that can be used as spatial input for a process-based soil moisture model.

## 2.2 Optical reflectance of vegetation

Vegetation and crops play an important role in hydrological processes. Large volumes of water are transported by plants from the soil into the atmosphere by means of transpiration. Transpiration is essential for photosynthesis and respiration processes of a plant. Transpiration is controlled by the opening and closing of the stomata in the leaves of plants. Environmental factors, like water availability, temperature, humidity of the air and plant status, can control the opening and closing of stomata. The spatial distribution and phenological status of plants, which changes over the seasons and by environmental conditions, are important controlling factors in the process of evapotranspiration. In order to incorporate the spatio-temporal behaviour of

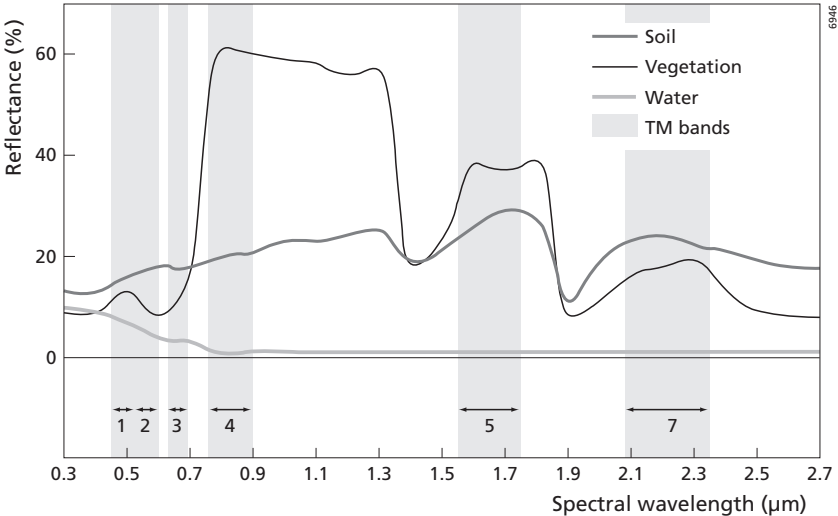
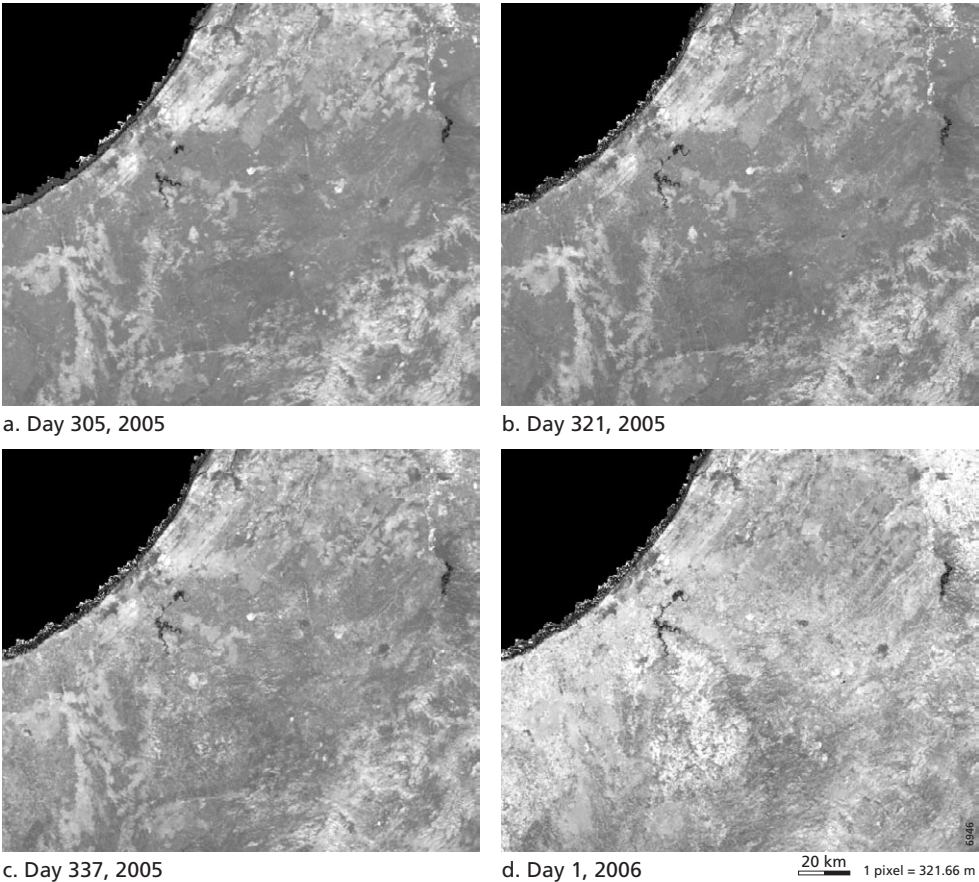


Figure 2.1 Typical spectral reflectance curves between 300 and 2700 nm for water, soil and vegetation. In gray the wavelengths of the Landsat bands are indicated, see also table 5.1.

plants in hydrological models, their features should be mapped in a quantitative manner. Remote sensing is a suitable tool to acquire vegetation properties such as vegetation cover, Leaf Area Index (LAI, the total canopy leaf area per unit ground area), aboveground biomass and structure. It is also possible to identify crop and vegetation types. Most hydrological models use LAI or coverage.

Figure 2.1 shows the spectral properties of vegetation, water and soil. Reflectance of vegetation in the visible wavelengths (0.4-0.6  $\mu\text{m}$ ) is generally low and reflection in near infrared (0.7-1.1  $\mu\text{m}$ ) is generally high. Three leaf characteristics strongly affect the reflectance properties of leaves: chemical composition, physiological structure and water content (Huete, 1989; Lambers et al., 1998). Pigments (chlorophyll a and b) absorb radiation of the visible wavelengths, while some narrow absorption bands due to lignin, cellulose and other constituents are present in near and short-wave infrared wavelengths. Water content of the leaves reduces



*Figure 2.2* Time series of NDVI images derived from MODIS showing the green biomass development during the growing season in the Sehoul study area in Morocco. Light values indicate high biomass volumes, dark values low biomass volumes.

overall leaf reflectance and causes some narrow water absorption bands. Due to these factors healthy vegetation has the characteristic reflection curve of figure 2.1. Reflection properties of a vegetation canopy are affected by its physiological structure: the spatial distribution of vegetated and non-vegetated areas, the number of layers of the vegetation cover, the species composition, the LAI, the leaf angle distribution and the vegetation conditions.

Combinations of visible and near infrared bands enable us to discriminate bare soil surfaces or water bodies from vegetation and to assess the percentage of vegetation cover. The living leaves and canopy show a dynamic behaviour through their growing cycle as a function of their environment. Remote sensing allows to detect this dynamic behaviour. Figure 2.2 shows an example of monitoring the dynamics of vegetation and crops for an area near Rabat in Morocco using NDVI values (explained in section 2.4) derived from the Moderate Resolution Imaging Spectroradiometer (MODIS) sensor. The series of images shows the development of crop biomass during the rain season from late October 2005 to January 2006.

### 2.3 Remote sensing image classification

A widely used product derived from remote sensing images is the thematic vegetation or thematic crop type map retrieved by image classification. Thematic classification of an image involves (Schowengerdt, 1997): 1) training: extract pixels from the image to characterize certain categories or classes (e.g. crop types, soil types, water, urban), 2) determine the discriminant functions in the feature space allowing assignment of a class label to each pixel, and 3) apply the discriminant function to the entire image to label all pixels with unknown land cover type. Widely used functions for image classification are the maximum likelihood decision rule or the minimum distance to mean decision rule. Thematic classification of remotely sensed images results in raster-based maps. Using lookup tables containing relevant land cover properties from field measurements or literature, these maps can provide spatial inputs for dynamic distributed models that simulate hydrological processes. Examples can be found in Boegh et al. (2004), Burrough and McDonnell (1998) and Dankers (2002).

Until recently, classification of remote sensing images was done using only pixel based methods. As long as the spectral response of the objects is spatially homogeneous, these methods are appropriate. For open heterogeneous vegetation patterns, as commonly found in Mediterranean and semi-arid regions, newly developed contextual classification algorithms may yield better results (De Jong and Van der Meer, 2004; Sluiter et al., 2004). There are three categories of contextual classification methods:

1. Methods based on spectral information captured by the image like the Spatial Co-occurrence method (Franklin and Peddle, 1990), variogram methods (Curran, 1988; Woodcock et al., 1998) and fractal methods (De Jong and Burrough, 1995);
2. Methods that apply segmentation algorithms on images to identify objects to be classified, for example e-Cognition (Blaschke et al., 2004; Definiens-Imaging, 2008);
3. Methods refining previously classified images; these methods are referred to as contextual re-classifiers. Examples are the local frequency distribution method (Wharton, 1982), the Spatial Reclassification Kernel (SPARK) method (Barnsley and Barr, 1996; De Jong et al., 2000; Sluiter et al., 2004; SPARK, 2008) and the Spatial and Spectral Classification method (De Jong et al., 2001).

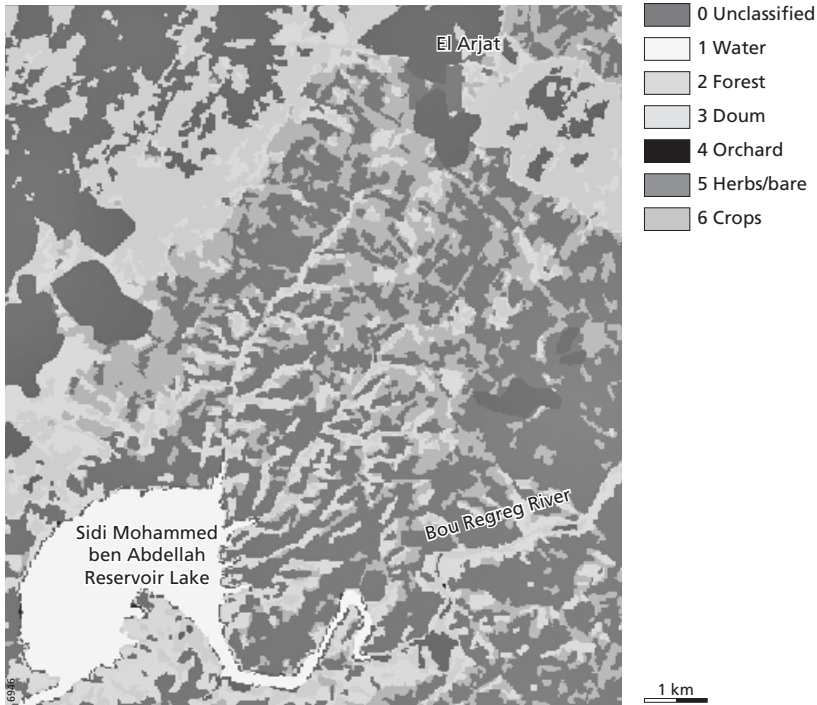


Figure 2.3 Land cover map of northern Shouf, Morocco. Derived from an ASTER image (October 2004) using image segmentation in combination with a minimum distance to mean classification.

In Part III, chapter 8 (figure 8.14) a generalized land cover map is used based on the classification of an image from the Advanced Spaceborne Thermal Emission and Reflection Radiometer (ASTER). This was done in two steps. First, segments were determined using e-Cognition. Next, the mean and standard deviation of each segment was calculated for each VNIR and SWIR ASTER band. These 18 channels are used in a minimum distance to mean classification. The result is shown in figure 2.3.

### 2.4 Spectral vegetation indices

A second, widely used method to extract information on land use properties from imagery are spectral vegetation indices. Vegetation indices are quantitative measures, based on digital values, that aim at measuring and mapping variables such as aboveground biomass (De Jong et al., 2003) and vegetative cover and/or LAI (De Jong, 1994). LAI and vegetative cover are important variables in hydrological models and surface energy balance models like the Surface Energy Balance System (SEBS).

Spectral vegetation indices enhance the spectral contribution of green vegetation while they minimize contributions from soil background, solar irradiance, sun angle, senescent vegetation

and atmosphere by transforming the axes of the multi-dimensional space (Asrar, 1989). Usually a spectral vegetation index is formed by combining several spectral values that are added, divided, or multiplied. High values of the vegetation index identify pixels covered by substantial proportions of healthy and active vegetation. The most widely used vegetation index is the Normalized Difference Vegetation Index or NDVI (Tucker, 1979; Asrar, 1989; Hurcom and Harrison, 1998). Much research was carried out to these spectral vegetation indices in the late seventies and eighties of the last century for sensor systems such as NASA's Landsat Thematic Mapper (TM), launched in 1984 and for NOAA's Advanced Very High Resolution Radiometer (AVHRR). The NDVI is calculated from an image by taking the ratio of the difference of the near infrared (high reflectance by vegetation) and red reflection (strong absorption by vegetation) and the sum between these two bands using:

$$NDVI = \frac{NIR - R}{NIR + R} \tag{2.1}$$

Where *NIR* is near infrared reflectance (700-1100 nm) and *R* is red reflectance (600-700 nm). Figure 2.4 shows an example of the relation between the NDVI and an agricultural crop. Note that the predictive value of the NDVI for crop cover is good for values of the LAI between 0

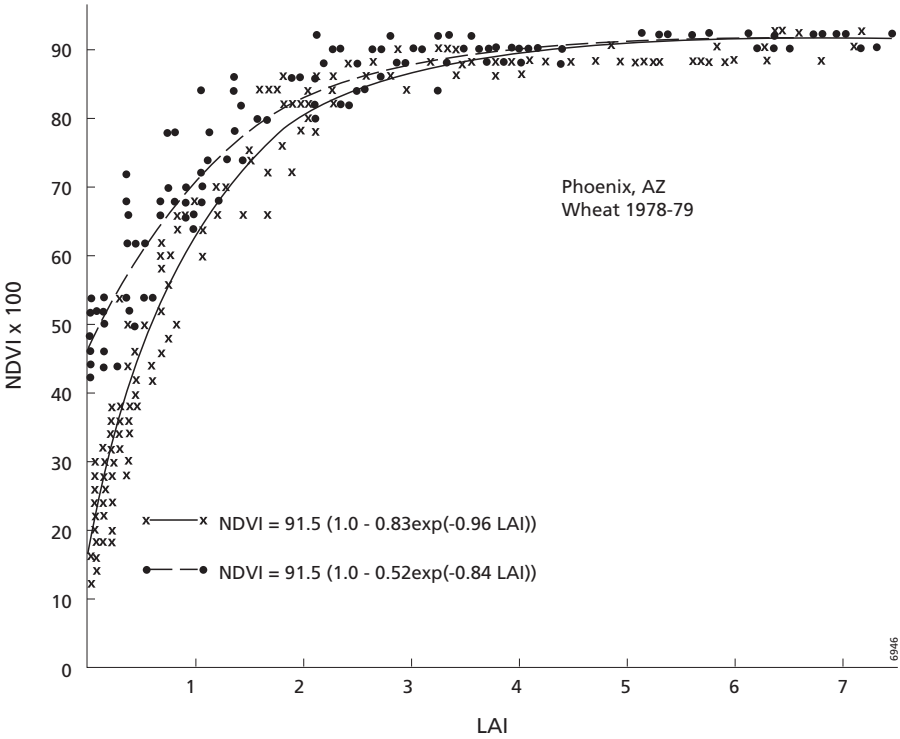


Figure 2.4 Normalized Difference Vegetation Index as a function of the Leaf Area Index (LAI) of a spring-wheat canopy for growth (solid line) and senescent (dashed line) periods of the growing season. Source: Asrar (1989).

and 3. However, the NDVI curve tends to become saturated at higher LAI values. An advantage of using ratio band combinations for quantitative assessments of vegetation variables is that the band ratios like the NDVI compensate for changing illumination conditions, surface slope and aspect factors.

Figure 2.5 shows an NDVI image of the northern part of the community of Sehoul in Morocco. It was derived from an ASTER image of October 20<sup>th</sup> 2004, 11:13 UTC using the following equation:

$$NDVI = \frac{Band3 - Band2}{Band3 + Band2} \tag{2.2}$$

where Band 3 is the NIR band of ASTER and Band 2 is the red band.

It can clearly be seen that the Forest of Mamora and wet valleys have high NDVI values. The agricultural area south of El Arjat has low values of NDVI, except for irrigated fields. Most agricultural fields lie fallow because the image was acquired at the end of the dry season. Clouds and water have very low or even negative values of NDVI.

Other often used spectral vegetation indices are the Soil Adjusted Vegetation Index: SAVI (Huete, 1989) and the Perpendicular Vegetation Index: PVI (Richardson and Wiegand, 1977). A more advanced approach is presented by the Tasseled Cap transformation (Christ and Cicone, 1984; Christ and Kauth, 1986). The Tasseled Cap transformation was originally developed as a linear transformation of spectral data space. In this plane the major spectral components, i.e.

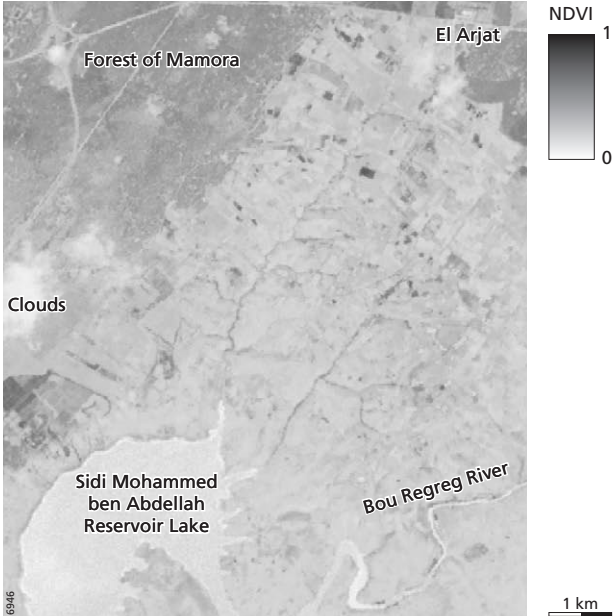


Figure 2.5 NDVI image of north Sehoul, derived from ASTER (October 20<sup>th</sup> 2004). The image is acquired after a long dry period. Most agricultural land lies fallow and has a low NDVI. The cork oak (*Quercus suber*) forests in the north have a relatively high NDVI as well as irrigated agricultural fields and wet valley bottoms. Water, clouds and roads have the lowest values.

axes of maximum variance, are displayed in two dimensions. The transformation results in three principal variables: brightness, greenness and wetness showing generally a reasonable correlation with soil brightness, abundance of vegetation and moisture or noise, respectively. Although such spectral vegetation indices have been shown to be powerful tools for studying vegetation, they must be used with care if the values are to be rigorously, rather than qualitatively, interpreted. Values of these ratios and spectral vegetation indices can be influenced by many factors unrelated to vegetation characteristics, such as viewing angle, soil background, atmospheric conditions, and row direction and spacing in the case of agricultural crops.

## 2.5 Radiation data from satellites

So far we discussed vegetation and land cover derived from the optical wavelengths of visible, near infrared and middle infrared parts of the electromagnetic spectrum. The radiation measured by satellite sensors within these wavelengths is reflected shortwave solar radiation. The amount of reflection depends on the albedo of the earth's surface and clouds in the atmosphere. Therefore surface albedo is an important variable for solving the surface energy balance. It determines the net shortwave radiation at the surface. Modelling the surface energy balance is important in hydrological studies, because evapotranspiration can be calculated for each pixel. By coupling the soil water balance to the surface energy balance it is possible to incorporate earth observation techniques for surveying complex spatial and temporal patterns of top soil moisture.

Albedo refers to the ratio of energy reflected from a surface to the energy incident on that surface. Usually it refers to the entire part of the spectrum from 400 to 2500 nm. Various empirical studies have been carried out to understand the relation between radiation measured by remote sensing sensors and surface albedo, especially for sensor systems such as Landsat TM. One of the most widely used empirical relations, between optical Landsat Thematic Mapper spectral bands after radiometric calibration, and the surface albedo ( $\alpha$ ) is developed for the central US by Duguay and LeDrew (1991):

$$\alpha = 0.256R_2 + 0.362R_4 + 0.112R_7 \quad (2.3)$$

where  $R_i$  are reflectance values registered by the Landsat Thematic Mapper channel  $i$ .

Liang (2000) applied an approach that decouples surface reflectance spectra from real-time radiative transfer simulations in order to incorporate many different surface reflectance spectra and atmospheric conditions. Liang (2000) provides the conversion formulae for a wide range of sensors, based on extensive radiative transfer simulations. These equations can be used to calculate the total shortwave albedo, total-, direct-, and diffuse-visible, and near-infrared broadband albedos for the following narrowband sensors: ASTER, AVHRR, ETM+/TM, GOES, MODIS, MISR, POLDER, and VEGETATION.

Figure 2.6 shows the total shortwave albedo of the northern part of the community of Schoul in Morocco. It has been derived using the conversion formula of Liang (2000) with an ASTER image of October 20<sup>th</sup> 2004. It can be seen that the agricultural plots that lie fallow at the end of the dry season have a high albedo, compared to the Forest of Mamora. Clouds have a high albedo, while their shadows and water bodies have a low albedo.

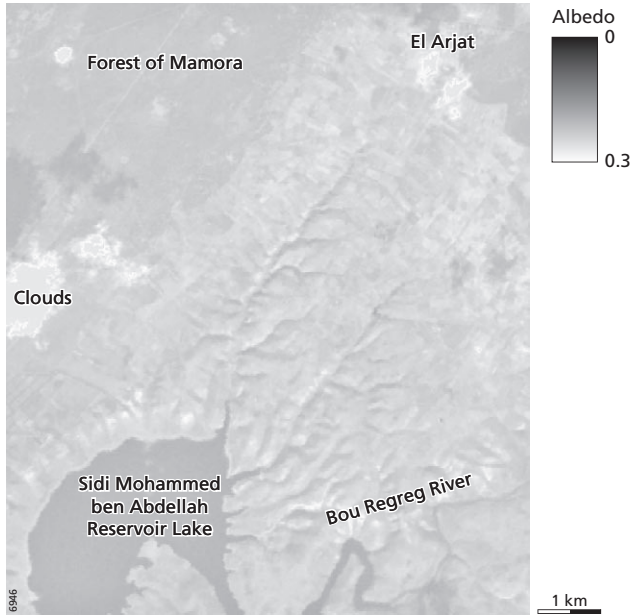


Figure 2.6 Albedo image of north Sehoul, derived from ASTER (October 20<sup>th</sup> 2004), using the method of Liang (2000). The agricultural plots that lie fallow at the end of the dry season have a high albedo, compared to the Forest of Mamora. Clouds have a high albedo, while their shadows and water bodies have a low albedo.

The thermal part of the spectrum (3 to 50  $\mu\text{m}$ ) provides also interesting data for the modelling of the surface energy balance. The thermal part of the spectrum has two atmospheric windows: 3 to 5 and 8 to 14  $\mu\text{m}$ . Thermal infrared imagery provides us with information about the radiant temperature of the earth's surface. This radiant temperature is a function of the kinetic or internal temperature and the emissivity of an object. With satellite data of surface temperature and other radiation data it is possible to model the surface energy balance at the moment of satellite overpass and calculate evapotranspiration for each image pixel. Part II of this thesis will explain the theory and modelling of the surface energy balance in detail. Albedo, NDVI and thermal data are important remote sensing inputs in surface energy balance models like SEBS (Su, 2001), SEBAL (Bastiaanssen, 1995) and TSEB (Norman et al., 1995).

## 2.6 DEMs derived from Remote Sensing

Digital elevation models (DEMs) are important datasets for hydrological studies. DEMs are used to determine a wide range of hydrology-related terrain variables. Examples of the use of DEMs are computation of local and regional drainage networks, quantitative assessment of volumes and energy of surface runoff, calculation of surface ponding, assessment of solar incoming radiance, computation of wetness indices, deriving the shape of slopes. Burrough and McDonnell (1998) provide an excellent overview of the use and generation of DEMs and error sources related to

their use and application for spatio-dynamic modelling. Traditionally, elevation information was derived from overlapping stereo aerial photographs (Mikhail et al., 2001). Nowadays, various other, remote sensing based sources for DEMs are available comprising radar data acquired by NASA's Shuttle Radar topography Mission (SRTM), a variety of LIDAR or laser data collected by airborne systems and optical data acquired by the French SPOT satellite and ASTER.

In February 2000 the space shuttle Endeavour carried a dual band radar system aboard comprising a C and an X band system, with wavelengths of 5.5 and 3.1 cm, respectively. These systems acquired interferometric radar images for the earth surface between 60°N and 56°S latitude. From these images it is possible to produce a DEM by interferometry. Imaging radar interferometry is based on analysis of the phase of the radar signal as received by two antennas located at different positions in space. The phase difference between the signal as recorded by the two antennas contains information about the elevation of the surface that reflected the signal. Based on these interferometric images, it is possible to compute fairly accurate digital elevation data. SRTM DEMs (Rabus et al., 2003) have a pixel size of 1 arc second (only freely available for the USA) or 3 arc seconds. The overall estimated vertical accuracy is 16 m. The SRTM DEMs form an interesting dataset for regional hydrological studies and are freely available. Figure 2.7 shows a mosaic of orthorectified aerial photographs, draped over the SRTM DEM. The image makes it possible to analyse in detail the geomorphology of the Oued Arjat Kébir (Large Arjat River), which incises the plateau of Mamora in the Sehoul study area.

Light Detection and Ranging (LIDAR) or laser altimetry is also an active remote sensing system (Lillesand and Kiefer, 1994). It involves the use of pulses of laser light (~1040 nm)

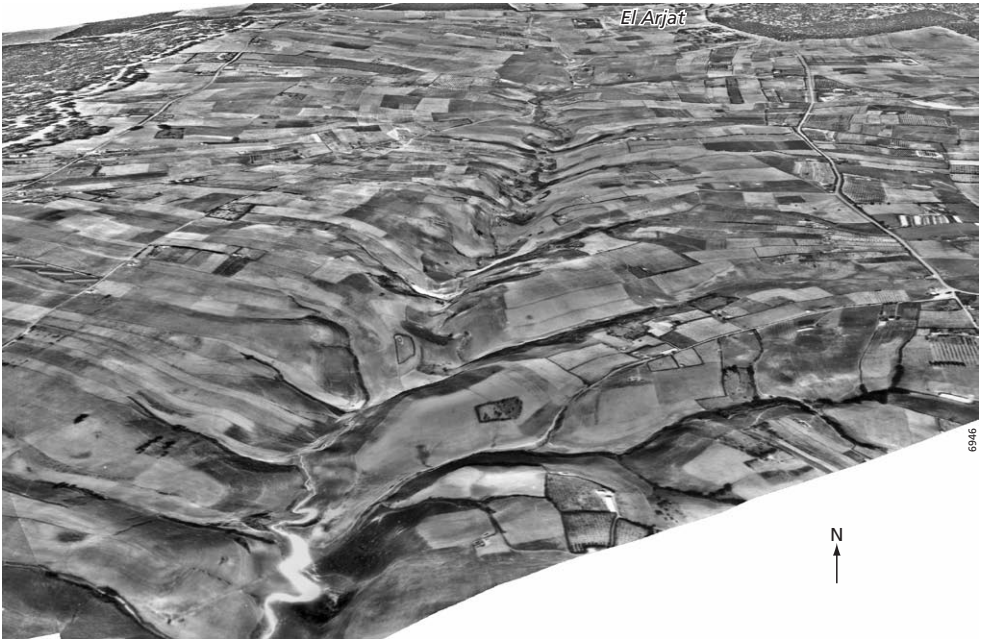


Figure 2.7 Oued Arjat Kebir, Sehoul (Morocco) in June 1996. Orthorectified aerial photograph mosaic draped over the SRTM DEM. The relief has been exaggerated three times.

directed toward the ground and the measuring of the return time of the pulse back to the sensor. For each pulse this return time is processed to calculate the distances between the sensor's platform and the various objects on, or above the ground. Point density can go up to 25 laser points per square meter and the vertical accuracy may reach a few centimetres. However, these laser techniques merely measure a Digital Surface Model, i.e. they determine the elevation of trees, houses and other objects rather than the elevation of the ground surface. For hydrological studies the ground surface is of prime interest and Digital Terrain Models are required (DTMs). Laser altimetry systems are currently developing towards full-waveform scanners, meaning that they do not only measure the first pulse returned to the platform, e.g. stemming from a tree top, but that they also register the later returned pulses from e.g. branches and the ground surface (Wagner et al., 2005). These new data types will allow to construct Digital Surface Models, based on first pulse data and to construct DTMs based on the last returned pulse.

Each of the remote sensing sources mentioned in this section is capable of delivering continuous elevation information after interpolation. Radar interferometry produces a continuous DEM directly. The horizontal and vertical resolution and accuracy is significantly different from sensor type to sensor type. SRTM data is more suitable for regional studies while laser altimetry and stereo photography are suitable for local and more detailed hydrological studies. The next chapter presents a case study about the comparison of DEMs derived from remote sensing.



# 3 Case Study: DEM generation from Remote Sensing, a comparison between aerial photographs, ASTER and SRTM

## 3.1 Introduction

Digital Elevation Models (DEMs) and their derivatives are important input variables for quantitative models used by a wide range of geoscientists involved with the simulation of land surface processes such as hydrological surface runoff and soil erosion (Burrough and McDonnell, 1998). DEMs are furthermore an important input variable in the orthorectification process and radiometric calibration of aerial photography and satellite imagery.

Since the '80s and '90s of the last century the performance of personal computers increased, while the cost of equipment decreased. With this development Digital Photogrammetric Systems (DPS) became widely available for geoscientists (Baltsavias, 1996). Since the early 1930s, analogue stereo photographs were acquired from airborne platforms. The first space platform was the CORONA satellite. This was a US imaging reconnaissance satellite, which made panoramic analogue stereo photographs between 1960 and 1972 (McDonald, 1997). DEM generation from declassified CORONA images, using a DPS, was demonstrated by Altmaier and Kany (2002).

Since 1986 the System Probatoire d'Observation de la Terre (SPOT) satellites were launched, which (SPOT 1 to 4) have the ability of tilting the sensor up to 30 degrees off nadir. Using multi-temporal imagery, digital cross-track stereo images can be acquired for DEM extraction which was demonstrated by Al-Rousan and Petrie (1998) and Zomer et al. (2002). Another platform is the Indian Remote Sensing (IRS-1C) satellite (Rao et al., 1996). However, the use of multi-temporal imagery causes differences between the images (e.g. differences in cloud cover), which hamper the DEM extraction process (Kääb, 2002). With the launch of the Advanced Spaceborne Thermal Emission and Reflection Radiometer (ASTER) sensor in 1999 and the SPOT 5 HRS in 2002 this problem was overcome. These sensors are capable to acquire along-track stereo images, using a nadir- and aft-looking telescope on the same platform (Abrams et al., 2002). DEM extraction from ASTER images has been used in recent geoscientific studies (Kääb, 2002; Cheng, 2003; Hirano et al., 2003). Other sensors with along-track stereo capability followed (IKONOS, Quickbird).

Nowadays, geoscientists have a large choice of platforms for DEM generation, resulting in DEMs with different resolution and quality. Over the last years photogrammetry software became available for the desktop computer. Desktop A3 scanners for digitising aerial photos are affordable and computing power is not a limiting factor anymore. The use of DEM extraction techniques became available for the entire geoscientific community and is not any more reserved for geodetics. In addition, DEMs derived from the Shuttle Radar Topography Mission (SRTM) (Rabus et al., 2003) are freely available through the internet.

The main objective of this chapter is to investigate and compare the quality of DEMs originating from three different sources: stereo aerial photographs, images from the Advanced Spaceborne Thermal Emission Radiometer (ASTER), and Shuttle Radar Topography Mission (SRTM) data enabling the end-user to make a well-balanced choice what type of DEM to use for specific applications. For soil moisture mapping and modelling DEMs are important for determining the incoming solar radiation and the redistribution of moisture after a rainfall event by routing the surface runoff.

The quality of the derived DEMs will also be discussed, not from a geodetic point of view, but from a DEM user point of view and with emphasis on mass point extraction and land cover type. Since this research was performed in a Mediterranean area in southern France, it only applies to regions with a similar relief and land cover.

We first present the available datasets and the selected study area. We discuss a number of essential steps of the DEM extraction process from aerial photographs, ASTER image and SRTM data. An understanding of this extraction process is essential for understanding the results of the quality assessment for the different platforms. Many DEM extraction algorithms are based on pattern matching in the overlapping images; therefore this research puts emphasis on the effect of different land cover types on the accuracy of DEM extraction. It is hypothesised that the contrast differences caused by land cover, and hence the pattern matching results, have an effect on the quality of the DEM. This effect is different for the investigated platforms as will be discussed in section 3.4.3.

Some confusion exists between the different definitions of terrain models and must be clarified here. A Digital Elevation Model or DEM is a quantitative representation of a part of the earth's surface in digital form (Burrough and McDonnell, 1998). This description may refer to the elevation of the ground surface, but also to the elevation of terrain features like trees or buildings. A Digital Terrain Model (DTM) is a DEM that refers only to ground elevation, while a Digital Surface Model (DSM) refers to the highest elevation at each point, either ground surface or terrain objects (Paparoditis and Polidori, 2002). Although for many purposes the goal of DEM extraction algorithms applied to stereo imagery is to derive a DTM, they cannot always distinguish ground objects from the ground surface and usually generate a DSM. Therefore in this study the term DEM will be used for all generated elevation models. This research focuses on the spatial variation in quality of the different DEMs, compared to a reference DTM.

## 3.2 Study area and datasets

The three remotely sensed DEMs and the reference DTM were all acquired for one specific test site to evaluate their practical use and accuracy. The selected study area is the Peyne area and is located in southern France approximately 60 km west of the city of Montpellier with centre coordinates: 43°33'N and 3°18'E. Figure 3.1 shows its location. This area was selected because a large set of high quality aerial photographs was available as well as ASTER images. Furthermore, a large ground truth database exists for this area, based on research by Sluiter (2005).

Large spatial heterogeneity makes the study area interesting for DEM extraction at different scales. Large variation at short distances in geology, elevation ranging from 50 to 1250 m above sea level, climate and human disturbance is responsible for a wide range of growing conditions and hence a large variety of vegetation types in this region (Sluiter et al., 2004). The area is

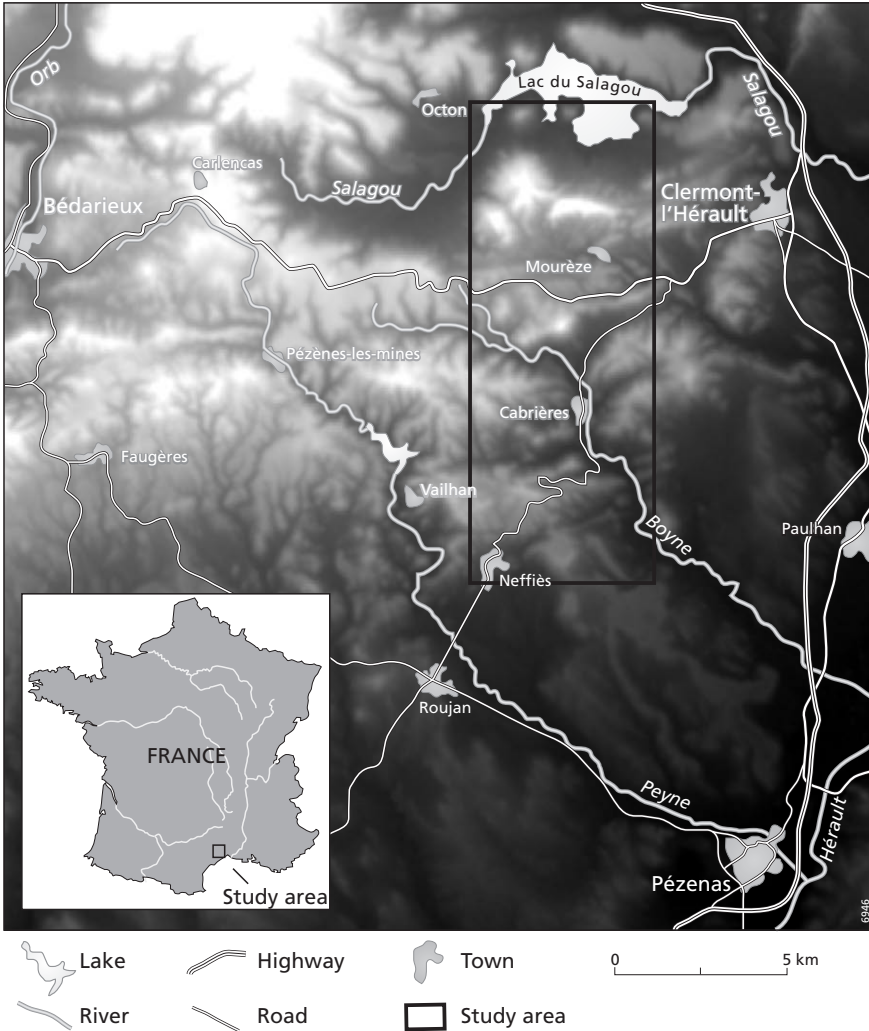


Figure 3.1 The location of the study area Peyne in southern France.

covered by matorral vegetation. According to Tomaselli (1981) matorral is ‘a formation of woody plants, whose aerial parts are not differentiated into trunk and leaves, because they are much ramified from the base, and are of shrubby habit’. Matorral is classified according to height, density and species composition:

- *Maquis* consists of dense thickets of tall shrubs. The dominant species are *Quercus ilex* and *Arbutus unedo*, which is considered as a regional climax. This vegetation type has a height ranging from 2 to 5 m. Because there is little penetration of light, undergrowth of herbaceous species is usually absent (Sluiter, 2005).
- *Garrigue* consists of low scattered bushes with a height ranging from 0.6 to 2 m. The bushes are interspersed with bare patches of rock, sand or stony ground (Sluiter, 2005). When the

vegetation density permits enough light penetration, undergrowth of herbaceous species may be present.

- *Landes* is the shortest vegetation type in the Peyne area and has a height < 0.6 m. The dominant vegetation is herbaceous.

Scattered around the area crops, vineyards, orchards and coniferous plantations are found.

Figure 3.2 shows an example of different land cover types in the study area and their spatial pattern. The pattern-matching algorithm will be hampered by the homogeneous reflectance pattern of the *Maquis*, while the spatial pattern of agricultural lots enable an accurate matching result. Additionally, the height of the land cover (table 3.1) will bias the DEM extraction results. Trees in a forest, well elevated over the terrain, will yield other absolute terrain elevation values than will be obtained for bare soil areas or for areas with agricultural crops having a limited elevation above the terrain surface.

A land cover map of the study area is required to assess the effect of land cover type on the pattern-matching algorithm and on the accuracy of the produced DEM. A land cover map was produced using land use and land cover information collected during various field campaigns (Sluiter et al., 2004). The land cover map of the study area was derived from the ASTER image

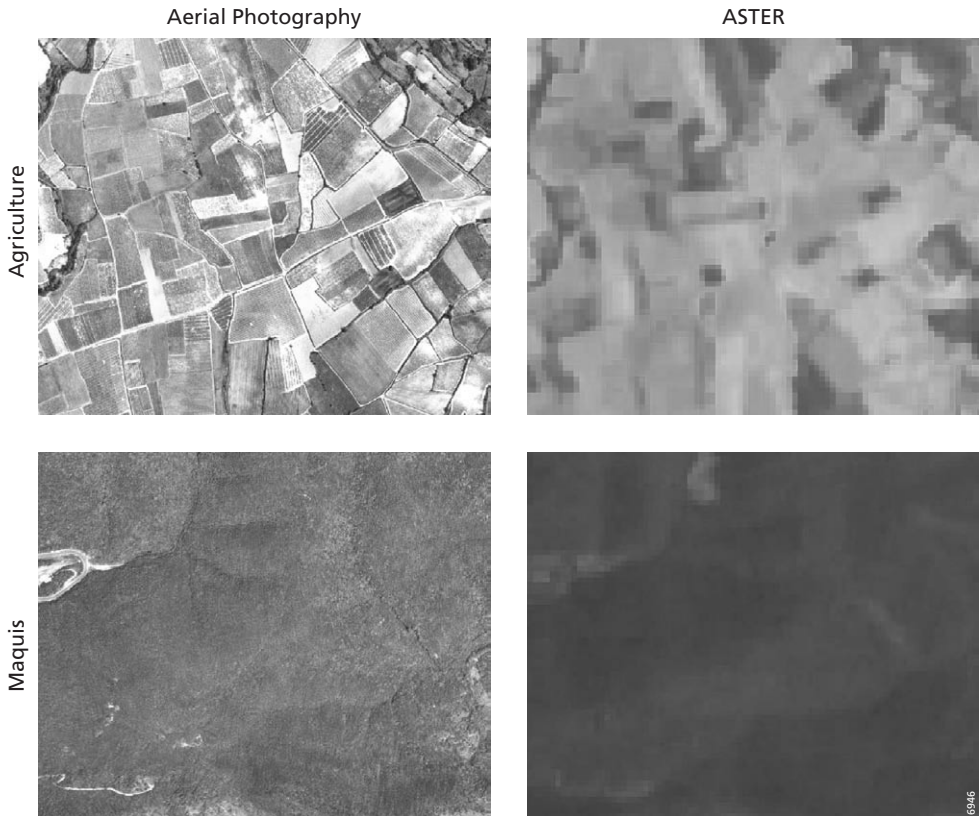


Figure 3.2 Spatial heterogeneity of agricultural land and *Maquis* as observed by aerial photography and ASTER.

using a maximum likelihood classification on the visual, near infrared and shortwave infrared bands. The land cover map is shown in figure 3.3. Seven classes were distinguished, based on field data: coniferous forest, *Maquis*, *Garrigue*, *Landes*, agricultural, urban and water. The classification has an overall accuracy of 88% and a kappa value of 0.86.

In this research five types of data were used. The datasets are all covering the same area in the Peyne study area (figure 3.1). The source data for the DEMs are:

- Contact prints of 12 colour aerial photographs from the *Institut Geographique National* (IGN, 2008), France, June 5<sup>th</sup> 2001. The approximate scale of the contact prints is 1: 25000. The photographs were scanned at 800 dpi using an EPSON GT-12000 A3 scanner.

Table 3.1 Mean height of land cover classes, derived from field estimates.

Land cover Type	Height [m]
Maquis	>2
Garrigue	0.6 -2.0
Landes	< 0.6
Coniferous Plantation	6 – 7
Urban	6
Agricultural	1

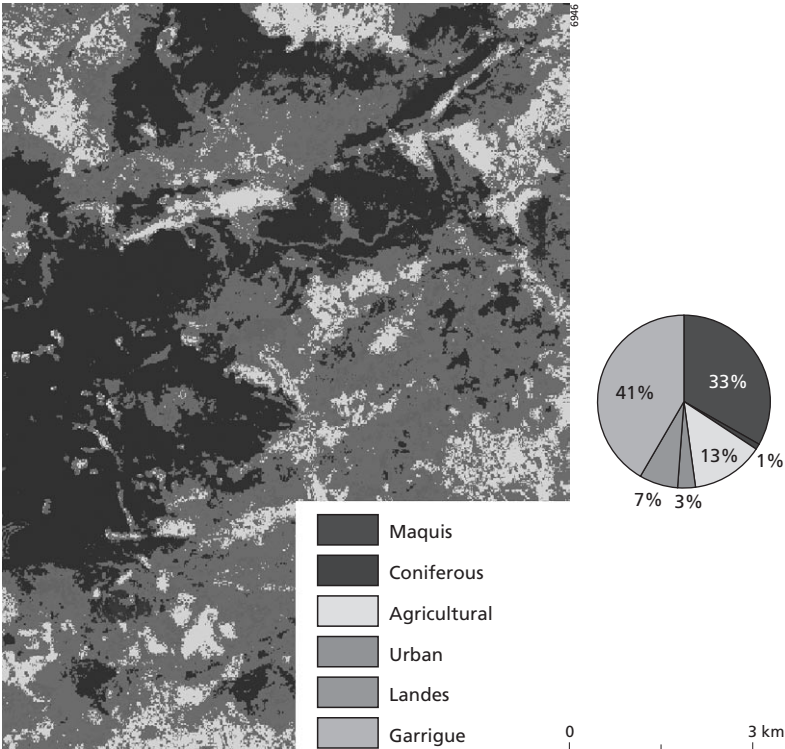


Figure 3.3 Land cover map of the study area produced as described in Sluiter et al. (2004).

- Stereo images of the Advanced Spaceborne Thermal Emission Radiometer (ASTER) of June 13<sup>th</sup> 2002. Channel 3 is acquired for along track stereo purposes and consists of a nadir and a backward channel. Its wavelengths are within the near infrared (NIR, 0.78-0.86  $\mu\text{m}$ ) at a spatial resolution of 15 m.
- DEM from the Shuttle Radar Topography Mission (SRTM), which was acquired from the NASA internet database (NASA, 2008). The SRTM-3 data is a near-global DEM of the earth, processed from radar interferometry by the National Aeronautics and Space Administration (NASA) and the National Imagery and Mapping Agency (NIMA), as well as the participation of the German and Italian space agencies (Farr and Kobrick, 2000). It was acquired with the Shuttle Radar Topography Mission, using interferometric synthetic aperture radar (InSAR). SRTM-3 data is collected using the C-band. The resolution of the SRTM-3 product is 3 arc-second, which is approximately 68 m in the study area. Technical details of the mission are available in Rabus et al. (2003).

The reference data used for quality assessment of elevation and georeferencing of all datasets are:

- Reference DTM from IGN: BD TOPO MNT (IGN, 2008). The DTM has a resolution of 25 meters. The reported vertical accuracy is 2 to 4 m.
- Topographical maps 1:25000 from IGN (IGN, 2008). These maps were scanned on 300dpi using an A0 scanner (Contex ScanPlus III 810C). The digital topographical maps were georeferenced to the UTM Zone 31 coordinate system with WGS-84 datum. All georeferencing in this study has been based on this projection.

Although the datasets are acquired at different dates, it is assumed that differences in land cover between the different data sets are very small and could be neglected.

### 3.3 Methodology

#### 3.3.1 DEM extraction

The DPS Leica Photogrammetry Suite (LPS) (Leica, 2003) was used for extracting DEMs from the aerial photographs and from the ASTER image. The SRTM DEM was processed by NASA and downloaded from the NASA internet database (NASA, 2008). For technical details about SRTM processing we refer to Rabus et al. (2003). The next paragraphs describe respectively DEM generation from aerial photography and from ASTER imagery.

#### 3.3.2 Aerial Photography

The scanned contact prints of the aerial photographs are imported in LPS. The workflow of LPS is followed as shown in the 7 steps of figure 3.4 (Leica, 2003):

1. Calculation of pyramid layers, a data storage method for faster processing and displaying. The full image resolution is resampled to three images of a lower resolution. The calculation of pyramid layers has two purposes:
  - it increases the display performance during the collection of ground control points in the viewer;
  - it reduces the computation time of image matching and increases the matching reliability (see points 5 and 7).

2. Definition of interior orientation, which is the internal geometry of the camera: lens distortion, focal length and location of the principal point. This information is needed in order to convert the image pixel coordinate system to the image space coordinate system (mm), i.e. the coordinates on the contact print of the aerial photograph. Location of the principle point and the focal length were obtained from the camera calibration report from the Deutscher Kalibrierdienst (DKD, 1996). The software estimated the lens distortion.
3. Definition of exterior orientation, which is the position and angular rotation of the exposure station. These parameters ( $X$ ,  $Y$ ,  $Z$ ,  $\Omega$ ,  $\Phi$  and  $\kappa$ ) (figure 3.5) describe the relation between the ground coordinate system and the image space coordinate system (mm). In our case no data from an on-board GPS/INS system were available, so these parameters need to be estimated by the bundle block adjustment. Prior to bundle block adjustment, ground control points and tie points are needed to estimate the position of the photographs relative to each other and to the ground coordinate system.
4. Ground Control Point (GCP) collection. DGPS field measurements and additional  $x$ ,  $y$ ,  $z$  locations from topographical maps (IGN) are used as GCPs, to link image pixel coordinates to the ground coordinate system.
5. Tie point collection. Tie points link similar objects in stereo pairs and only have image space coordinates. The LPS software can automatically calculate up to 500 tie points a time, based on a multiple resolution area correlation matching. A first estimate of the exterior orientation is necessary. This is calculated on the fly, using the GCPs. All colour photographs were converted to panchromatic images in order to maximize the contrast. A disadvantage of the automatic tie point calculation is that it only detects tie points in pairs and not on all overlapping photographs.
6. In order to establish the exterior orientation of all images and ground coordinates of the tie points, a bundle block adjustment is performed. This is a triangulation, based on the collinearity equations, which determines the relationship among image coordinates, ground coordinates, and orientation parameters.
7. The final step is the DEM extraction itself. The LPS software uses a multi-resolution area-based matching algorithm for the extraction of mass points (points with  $x$ ,  $y$  and  $z$  coordinates that are used as a base for DEM interpolation). The results of matching depends, among other factors, on the contrast of the land cover types as discussed previously. Little contrast hampers the matching process, as is the case for *Maquis* forest shown in figure 3.2. Significant contrast as shown for the agricultural lots in figure 3.2 yields good results for matching. More details about image matching can be found in Paparoditis and Dissard (2002). Three strategy parameters can be set:
  - a) The size of the search window (in pixels), which is used to find corresponding image points in the overlap of a stereo pair. This window is applied to an epipolar stereo pair, in which the  $Y$  parallax is minimized during triangulation, while the  $X$  parallax remains. The  $X$  dimension is the number of pixels along the epipolar line and the smaller  $Y$  dimension is perpendicular to this line. As the  $X$  parallax is a function of elevation, the

X dimension of the search window should be set larger for a larger range of ground elevation. With good triangulation results a Y dimension of one to three pixels should be sufficient. The default window with X dimension = 21 pixels and Y dimension = 3 pixels is used here.

- b) The size of the correlation window, which defines the local neighbourhood for which the correlation coefficient between common points in the overlap is calculated. The settings of this size depend on the variation in elevation and contrast. Areas with homogeneous land cover or low relief need a larger window size. The default size of 7 x 7 pixels is used.
- c) The correlation coefficient limit is the threshold for accepting candidate points in the overlap as a matched pair. Only these points are used in the DEM extraction. The default value of 0.80 is used.

At the end of these 7 steps the 3D coordinates of the mass points are computed with space forward intersection, based on the triangulated interior and exterior orientation parameters. The mass points are then interpolated using a Triangular Irregular Network (TIN) and converted to a continuous grid with a resolution of 25 meters. Outside LPS it is possible to use other interpolation techniques, which might give better results.

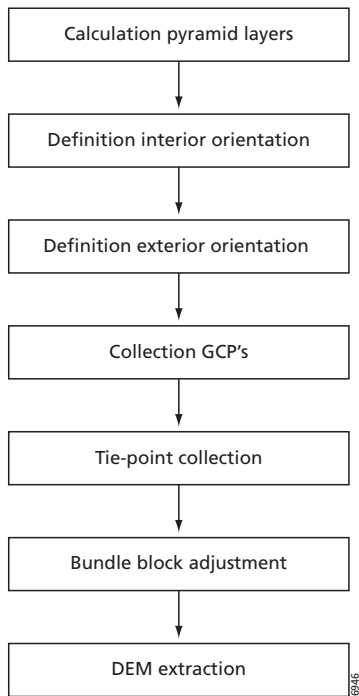


Figure 3.4 Diagram of the workflow for DEM extraction in 7 steps. Details are given in the text.

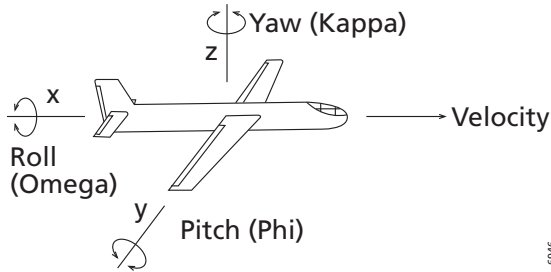


Figure 3.5 Possible rotation angles of airborne sensor platforms, modified from Curran (1985).

### 3.3.3 ASTER imagery

The DEM extraction procedure from the ASTER image requires only the use of spectral band 3 nadir and 3 backward. Prior to photogrammetric analysis, these two ASTER bands need to be pre-processed. Pre-processing consists of de-stripping, which is performed automatically when importing the ASTER channels into the software of ERDAS (Leica, 2003). The procedure for DEM extraction is slightly different from aerial photography and comprises the following steps:

1. Calculation of pyramid layers (see procedure for aerial photography and figure 3.4).
2. Automatic import of interior orientation parameters: focal length, principal point and pixel size from the ASTER metadata into LPS.
3. Importing the exterior orientation parameters from the ASTER metadata. Useful ephemeris data are: position of the satellite in geocentric coordinates, velocity vector, attitude changes and exact time of exposure of the centre scan line. The ASTER pushbroom sensor moves smooth in its orbit, resulting in a unique perspective centre and rotation for each scan line. A low-order polynomial model can be used to estimate the perspective centre and rotation angle per scan line (Leica, 2003). The polynomial coefficients are calculated after triangulation. The polynomial order ( $P$ ) determines the number of polynomial coefficients ( $C$ ):  $C = P + 1$ . This requires a minimum number of GCPs to estimate the polynomial coefficients. For one stereo pair, this means that the minimum number ( $N$ ) of required GCPs is:  $N = 2 * C$  for each model parameter (i.e.  $X, Y, Z, \text{Omega}, \text{Phi}, \text{Kappa}$ ). In table 3.2 the polynomial orders used in this study are presented. This configuration requires a minimum of 32 evenly distributed full (containing  $x, y$  and  $z$  coordinates) GCPs. Furthermore, some additional ephemeris information is extracted from the header of the images, for instance the side incidence and track incidence.

The side incidence angle is defined as the angle between the vertical position of the satellite and the direction of the scanner. This direction is perpendicular to the orbit of the satellite. The track incidence angle, or look angle, ( $\alpha$ ) is the angle between the nadir and the backward ASTER VNIR channels, along the orbit of the satellite (figure 3.6). This value can be calculated from the base-to-height ratio:  $B/H = \tan \alpha$ . The base,  $B$  [m], is the distance between the stereo observations and  $H$  [m] is the height of the observations. The  $B/H$  ratio for the ASTER stereo channels is 0.6, which results in a  $\alpha$  of 30.96 degrees (ERSDAC, 2002; Hirano et al., 2003).

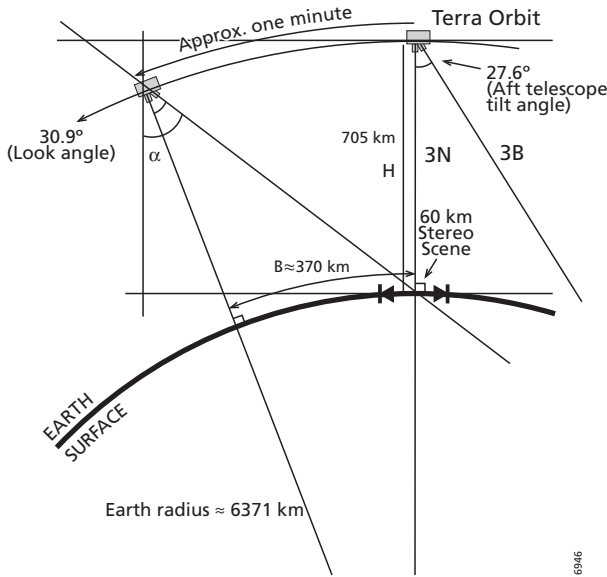


Figure 3.6 Simplified diagram of the imaging geometry for ASTER along-track stereo (Hirano et al., 2003). In order to create a stereo scene, first an image is acquired at nadir using channel 3 (Near Infrared) of ASTER, referred to as band 3N. Approximately one minute later the backward looking channel 3, band 3B, of ASTER acquires the second image of the stereo pair. The angle between the nadir and backward sensor is the look angle or track incidence angle  $\alpha$ .

Table 3.2 Polynomial orders for estimation of exterior orientation. For explanation of symbols, see text.

Parameter	Polynomial Order 3N	Polynomial Order 3B
X [m]	2	2
Y [m]	2	2
Z [m]	2	2
Omega [degrees]	1	1
Phi [degrees]	1	1
Kappa [degrees]	2	2

Table 3.3 RMSE of triangulation. Between brackets the number of GCPs used in the triangulation.

	Aerial photographs	ASTER DEM
Total image RMSE	0.03 mm	0.01 pixels
Ground x RMSE [m]	2.6 (25)	23.4 (202)
Ground y RMSE [m]	2.0 (25)	40.0 (202)
Ground z RMSE [m]	2.5 (25)	29.72 (202)
Image x RMSE [mm]	0.06 (36)	0.5 (403)
Image y RMSE [mm]	0.07 (36)	0.1 (403)

4. Step 4 is the same as described for aerial photographs.
5. Step 5 is also the same as described for aerial photographs.
6. The bundle adjustment is calculated in a similar way as the block bundle adjustment of aerial photographs. The only difference is that for ASTER, the ground coordinates and rotation angles of the perspective centre of the centre scan line are estimated. Next, the polynomial coefficients are computed and used to calculate the perspective centre and rotation angles of the other scan lines of the sensor.
7. The same DEM extraction algorithm is applied as with aerial photogrammetry described under step 7. This semi-automatic product will be referred to as ASTER.

LPS can automatically calculate a relative DEM from ASTER imagery without the input of GCPs and tie points, based on only metadata included with the imagery. In this chapter the automatically derived ASTER DEM will be referred to as AUTO-ASTER DEM.

The root mean square error (RMSE) of the triangulations is presented in table 3.3. The values are calculated using the x, y and z coordinates of the GCPs:

$$RMSE = \sqrt{\frac{\sum_{i=1}^N (X_i - Y_i)^2}{N}} \quad (3.1)$$

where  $N$  is the number of GCPs and  $i$  is the x, y or z coordinate.  $X$  refers to the estimated coordinates using the triangulated model and  $Y$  is the reference location of the GCP as measured in the field.

No independent set of check points is used in this study. It is assumed that the horizontal errors are of the same order for the DEMs with a resolution of 25 meters. The analyses will concentrate on the vertical discrepancies between the datasets.

### 3.4 Quality assessment

In this section we describe how we carried out a quality assessment of the remote sensing derived DEMs. Generally the terms accuracy and precision are used to describe the quality of data. Accuracy is defined as the extent to which an estimated value approaches the true value. Here the accuracy is expressed as the average difference  $\bar{d}$ :

$$\bar{d} = \frac{\sum_{i=1}^N X_i - Y_i}{N} \quad (3.2)$$

where  $X_i$  is the value of variable  $X$  at the  $i^{\text{th}}$  observation,  $Y_i$  is the  $i^{\text{th}}$  observation of reference variable  $Y$ .  $N$  is the number of observations. Precision refers to the dispersion of observations around a mean and can be expressed by RMSE (eq. 3.1).

In this quality assessment  $X$  is the remote sensing derived DEM and  $Y$  is the reference, which is the DTM produced by the French *Institut Géographique Nationale* (IGN). The given

vertical accuracy of this IGN DTM is between 2 to 4 meters. The quality assessment comprises three steps: 1) evaluation of the extracted mass points that are the individual spot elevations of the DEM, 2) assessment of the quality of the interpolated DEMs, 3) analysis of the spatial distribution of differences between the different DEM sources. Prior to the accuracy assessment, all DEM and land cover datasets were subsetting to the area covered by the aerial photographs. Additionally, the size of this area was decreased with 10% to reduce any possible edge effects of the interpolation. The resulting analysis area of 96 square kilometres is represented in figure 3.1.

**3.4.1 Mass point quality**

The elevation values of the mass points extracted from ASTER and aerial photography were sampled in the reference DTM (IGN) and their values were compared. Table 3.4 summarizes the results. This analysis was not possible for SRTM as InSAR techniques were used to derive the DEM. Interferometry uses the phase information of every pixel to measure the parallaxes. No mass points are extracted and interpolated (Rabus et al., 2003).

It can be observed that on average the mass point extraction results in an overestimation of elevation values for ASTER and an underestimation for aerial photography. The results are generally good. Next, an analysis was made of the average difference of computed elevation per land cover type by using the land cover map as a mask for extracting elevation mass points. The average difference per land cover type is presented in figure 3.7 and reveals that this systematic error is true for all classes except coniferous forest. The absolute errors differ slightly, but it is expected that the difference in the amount of extracted mass points will have an effect on the quality of the interpolated DEMs as will be discussed in the next paragraph. Errors in the retrieval of mass points can be related to the quality of the GCPs and, in the case of aerial photography, the geometric accuracy of the A3 scanner.

**3.4.2 Quality of interpolated DEMs**

The quality assessment of the interpolated DEMs was carried out after the interpolation from point data to spatial continuous DEMs. As presented in section 3.3.2, the extracted mass points are interpolated using the Triangulated Irregular Network algorithm (TIN) and then converted to a 25-meter grid, which is the resolution of the reference DTM (Leica, 2003). In order to quantify the overall accuracy of the extracted DEMs and the SRTM-3 DEM, the DEMs were subtracted from the reference DTM (IGN). Table 3.5 summarizes the overall accuracy for the difference maps. It is obvious that the interpolated DEM from the underestimated mass points in the case of aerial photography results in an underestimation for the interpolated DEM too. In the case of ASTER however, the overestimated mass points result in an unexpected underestimated interpolated grid. A possible explanation for this might be the small number of mass points compared to the size of the study area. This causes large TIN triangles. It can be concluded that the SRTM-3 DEM has the best overall accuracy, followed by the aerial

*Table 3.4* Mass points compared to reference DTM.

	Number of Mass Points	$\bar{d}$ [m]	RMSE [m]
ASTER	21844	4.7	9.6
Aerial Photography	309192	-3.0	9.1

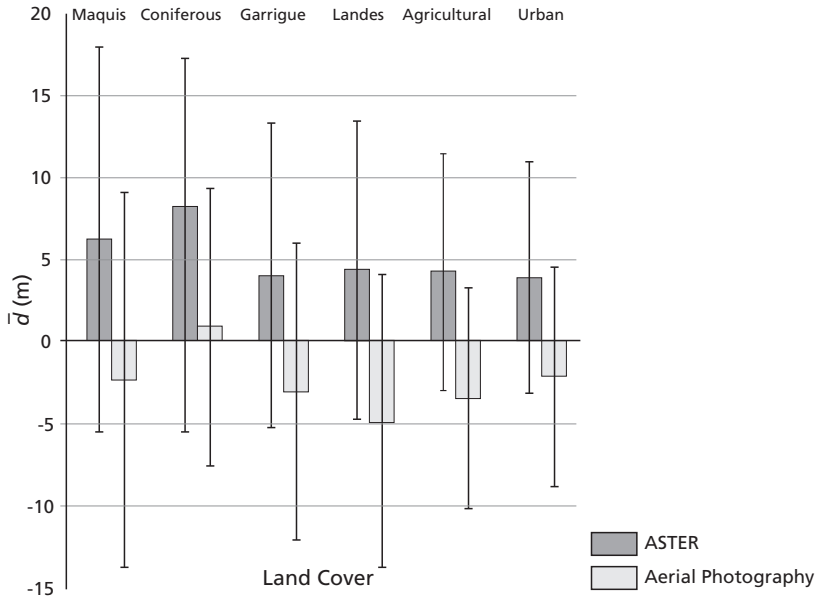


Figure 3.7 Average difference  $\bar{d}$  of mass points per land cover class. The whiskers indicate the RMSE.

photography DEM in spite of the lower spatial resolution. The semi automatically derived ASTER DEM seems to underestimate the elevation, while the automatically generated ASTER DEM overestimates the elevation compared to the reference DTM. However, the difference maps of both ASTER DEMs have almost the same RMSE. This can be expected as both ASTER derived DEMs have the same input (channel 3 nadir and 3 backward). With the same contrast within the stereo pair, the DEM extraction algorithm performs in the same manner. However, the semi- automatic ASTER DEM extraction procedure uses GCPs to perform a better fit of the ASTER pushbroom model and a better fit with the ground coordinate system. Therefore, there is a difference with the automatically derived ASTER DEM, which uses only header information. The difference in overall accuracy between ASTER and aerial photographs can be explained by the total amount of mass points used in the DEM extraction.

Rabus et al. (2003) discusses possible error sources in SRTM data like shadows, layover effects and ripples on water bodies.

### 3.4.3 Spatial variation of accuracy

The DEM extraction algorithm compares the reflectance pattern of a stereo dataset in a window of  $7 \times 7$  pixels as discussed before. The difference in scale and degree of spatial heterogeneity as registered by the different sensors aboard the platforms (figure 3.2) causes a large and significant difference in the number of extracted mass points as is illustrated in table 3.4. This significant difference in mass points does not only result in accuracy differences for the DEM as a whole, but since the extraction process of mass points is hampered by certain land cover types, the accuracy of the DEM will differ from one land cover type to another. The land cover map (figure

Table 3.5 Statistics of the difference between the DEMs and the reference DTM.

Platform	$\bar{d}$ [m]	Max. underestimation [m]	Max. overestimation [m]	RMSE [m]
ASTER	-11.49	-279.45	195.21	32.76
ASTER AUTO	12.47	-262.47	154.33	35.77
Aerial Photography	-6.90	-199.46	65.41	17.87
SRTM	0.08	-40.00	50.00	7.47

Table 3.6 Statistics of the difference between the DEMs and the reference DTM per land cover unit.

ASTER	$\bar{d}$ [m]	Max. underestimation [m]	Max. overestimation [m]	RMSE [m]
Garrigue	-9.4	-279.5	146.9	30.3
Landes	-6.1	-253.5	110.7	24.0
Coniferous forest	-16.7	-240.4	95.5	37.9
Urban	1.2	-248.8	195.2	25.0
Agriculture	4.8	-252.0	171.0	20.4
Maquis	-23.0	-271.5	114.8	37.6

ASTER AUTO	$\bar{d}$ [m]	Max. underestimation [m]	Max. overestimation [m]	RMSE [m]
Garrigue	11.7	-262.5	147.6	34.4
Landes	13.3	-204.5	83.7	31.0
Coniferous forest	1.8	-226.3	75.7	39.3
Urban	26.5	-230.0	92.1	18.0
Agriculture	28.4	-250.2	108.8	16.3
Maquis	5.5	-244.9	154.3	42.4

Aerial Photographs	$\bar{d}$ [m]	Max. underestimation [m]	Max. overestimation [m]	RMSE [m]
Garrigue	-6.3	-222.3	83.7	16.4
Landes	-7.5	-209.0	57.8	10.7
Coniferous forest	-8.0	-193.8	64.6	26.4
Urban	-2.1	-213.5	42.8	7.4
Agriculture	-3.7	-205.5	67.5	7.5
Maquis	-11.7	-212.7	77.9	23.5

SRTM	$\bar{d}$ [m]	Max. underestimation [m]	Max. overestimation [m]	RMSE [m]
Garrigue	-0.3	-40.0	50.0	7.4
Landes	-1.4	-37.0	23.0	6.5
Coniferous forest	1.0	-24.0	31.0	9.1
Urban	0.4	25.0	38.0	4.9
Agriculture	-0.1	-15.0	30.0	4.0
Maquis	1.0	-33.0	38.0	8.7

3.3) was used to calculate statistics of the DEM derived difference maps per land cover class. Table 3.6 gives the results.

Figure 3.8 contains the histograms with the distribution of the differences between the DEMs and the reference DTM for each class.

DEM extraction algorithms have difficulties separating terrain objects from ground surface and therefore they actually create DSMs. In heterogeneous vegetation types, for example, the algorithms will identify mass points at the top of individual trees, causing a systematic overestimation of the surface elevation (table 3.1). When the vegetation is very closed and dense, preventing the algorithm from identifying mass point within the forest, the interpolation of mass points surrounding the forest causes an underestimation of the ground elevation below the forest. This is the case in the Peyne study area for the *Maquis* forest and Coniferous forest as shown in figure 3.9. The mass point density graph per land cover type for aerial photographs, presented in figure 3.10, confirms that few mass points are found in the *Maquis* area and this relates to the relative high errors found for the class *Maquis*. The errors are, however, in many cases larger than the height of vegetation or other surface objects. Table 3.6 suggests a systematic overestimation of the elevation by ASTER AUTO and an underestimation by ASTER and aerial photography. This systematic component of the average difference  $\bar{d}$  could be removed by normalizing the DEMs to the reference DTM. In this way only local errors remain.

A second error source is edge effects of the interpolation algorithm. When few mass points are identified in a land cover type, the interpolation algorithm uses points at a large distance and as a result interpolation uncertainty increases. Only elevation values for *Landes* land cover types and urban areas are more accurate in the ASTER DEM than for the DEM extracted from aerial photography. From table 3.6 and figure 3.10 it is clear that for the ASTER DEM land cover classes with fewer mass points are less accurate, except for the land cover type *Landes*. The overall average difference  $\bar{d}$  and per land cover class are larger in the case of the ASTER DEM, because of fewer mass points.

#### 3.4.4 Variatiation at a transect

A profile through different land cover types is presented in figure 3.11 and confirms that under dense *Maquis* forest, the DEM extraction algorithm fails to identify terrain summits. In the case of aerial photography forested valleys are missed as indicated in figure 3.11. The profile for *Maquis* suggests that also the planimetric geometry is distorted as peaks seem to be shifted away from the IGN DTM. Under agricultural land the DEM extraction algorithms perform much better. However, it must be kept in mind that small differences are more important in the flat agricultural regions than in the hilly *Maquis* landscapes. In the case of heterogeneous slopes the results for the different platforms are similar. Generally, we conclude that aerial photography DEMs underestimate the relief, except in case of densely vegetated valleys. The AUTO ASTER DEM shows the opposite, but the errors are much larger, especially in agricultural areas where elevations values are overestimated. The 5.6 cm wavelength of the C-band used to collect SRTM data is not capable of penetrating vegetation very well. This explains why the SRTM DEM slightly overestimates the relief in the case of *Maquis* and *Garrigue*.

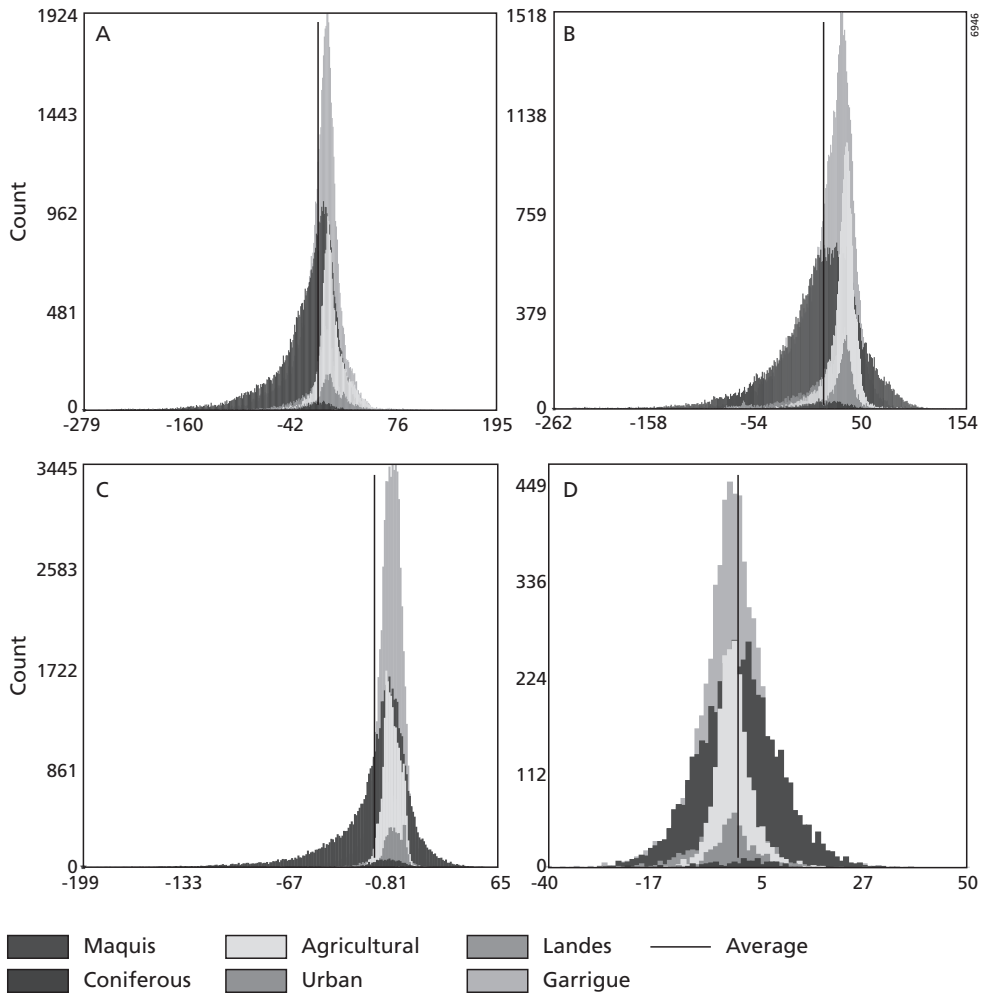


Figure 3.8 Histograms of absolute differences in meters between the DEMs and the reference IGN DTM after subtraction. A. ASTER, B. ASTER AUTO, C. Aerial Photography, D. SRTM-3.

### 3.5 Discussion

The results show that land cover is an important factor in determining the quality of DEMs for this area. The spatial distribution of mass points depends on the type of land cover and is not proportional when ASTER and aerial photography are compared (figure 3.9). *Maquis* and Coniferous plantations influence the DEM extraction algorithms negatively in two ways:

1. Mass point extraction is difficult because dense, homogeneous vegetation lacks the contrast needed for optimal contrast matching, resulting in less mass points for these land cover classes. The difference with other land cover classes is larger for aerial photography than for

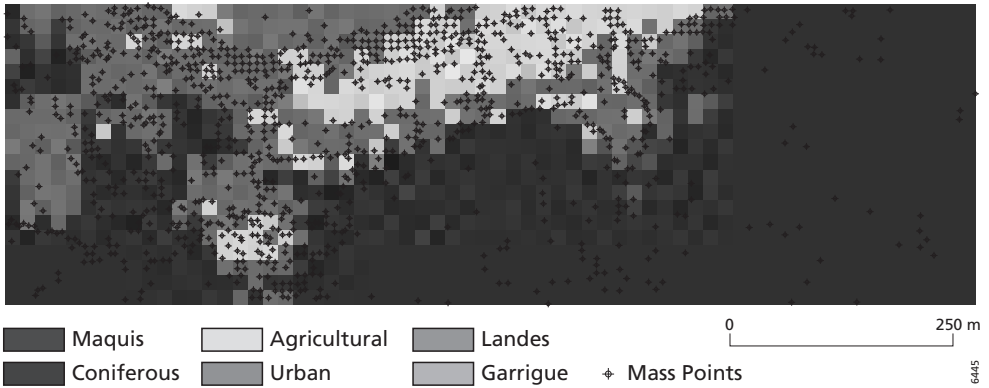


Figure 3.9 Mass point distribution in the aerial photographs.

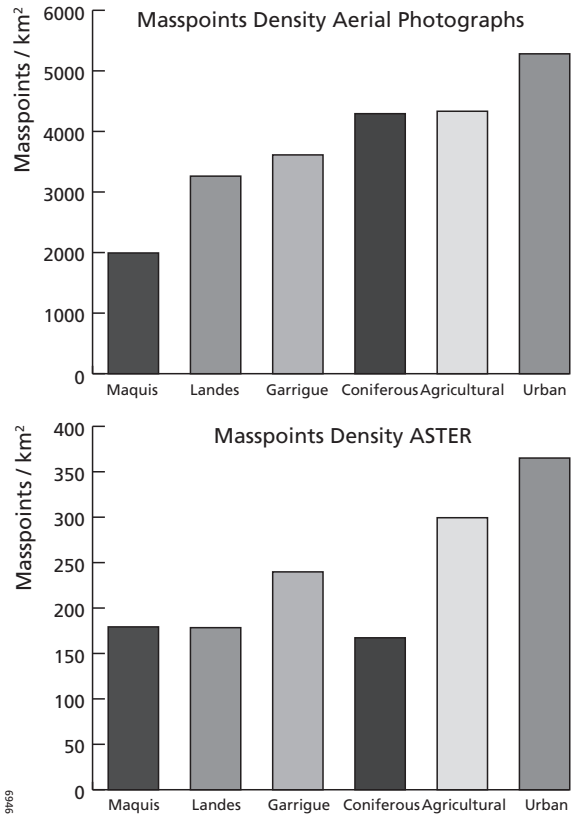


Figure 3.10 Mass point density histograms for aerial photographs and ASTER.

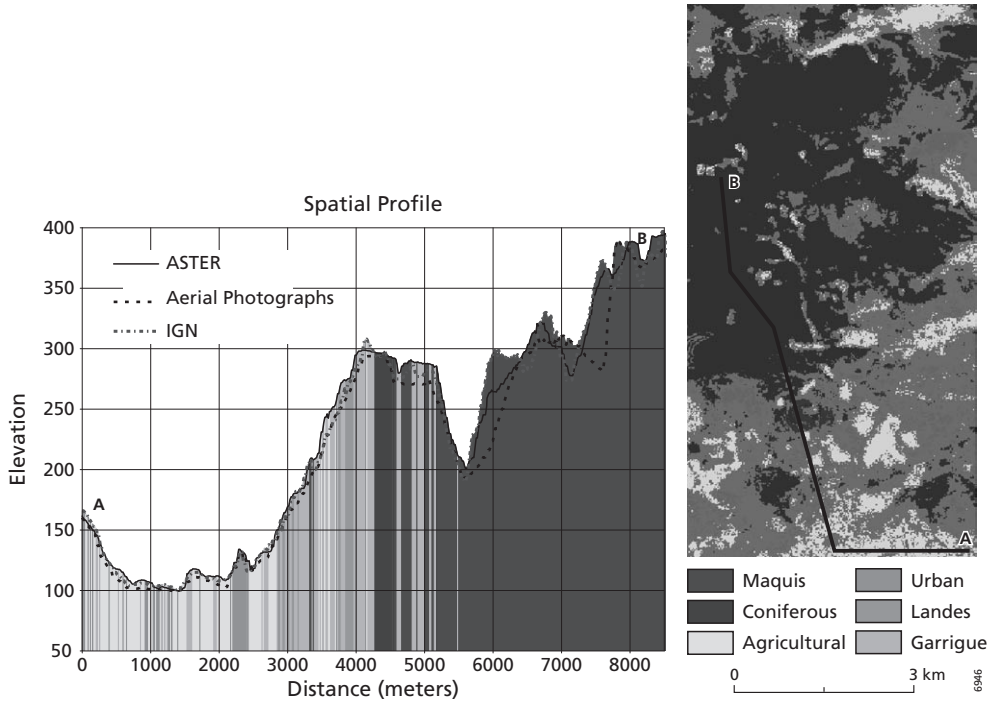


Figure 3.11 Profile through different land cover types illustrating the deviations of elevation per DEM type.

ASTER as shown in figure 3.5. On the scale of aerial photography Coniferous plantations are heterogeneous, while for ASTER *Maquis*, *Landes* and Coniferous plantations have approximately the same homogeneity (i.e. mass point density).

- The height of *Maquis* and Coniferous plantations biases the terrain elevation. It is suspected that the large elevation overestimation of mass points from ASTER is related to vegetation height. With aerial photography this effect is not visible (figure 3.7). The overestimation of mass points in *Maquis* and Coniferous land cover is compensated after interpolation, because the few mass points lead to an underestimation both in ASTER and aerial photography. Terrain summits in these land cover classes are underestimated and valleys are overestimated. DEM extraction algorithms perform well in *Garrigue* as the land cover is heterogeneous and the vegetation is low. Both for ASTER and aerial photography the mass point density is higher and the average difference  $\bar{d}$  between the interpolated DEM and the reference DTM is smaller than for *Maquis* and Coniferous plantations. *Landes* is more homogeneous than *Garrigue*, but the vegetation height is low. Therefore it takes an intermediate position in accuracy. The heterogeneity of agricultural and urban land cover results in a relatively high mass point density for both ASTER and aerial photography. In combination with scarce, low vegetation, the interpolated DEMs are best for these classes. It can also be concluded that the quality of the DEM generated from SRTM-3 is not much influenced by land cover, as  $\bar{d}$  is comparable for each class as shown in table 3.6. From a practical point of view we conclude that for studies

in comparable areas where DEMs of resolutions coarser than 25 m are needed, the SRTM-3 data is the best choice: the DEM is accurate and freely available. In cases where DEMs with a resolution of 25 meter or higher are needed, either aerial photography or ASTER is a good option. The automatically generated ASTER DEM is the most cost-effective option and the absolute quality per land cover unit is comparable with the semi automatic ASTER DEM, although the automatic ASTER DEM overestimates elevation and the semi-automatic ASTER DEM gives an underestimation. However, for agricultural areas the semi-automatic ASTER DEM performs much better. Further research should investigate if the bias in the ASTER DEMs can be removed by normalizing with the SRTM DEM.

The best results are obtained from aerial photography, but the improvement for 25-meter resolution is minimal. It is anticipated that with the 309192 mass points extracted from aerial photography, a much more accurate and a higher resolution DEM can be generated. However, based on the comparison with the 25-meter reference DTM and based on the amount of DGPS measurements this could not be confirmed.

For the purpose of surface runoff modelling, smooth DEMs are preferable, since erroneous spikes and pits in the DEM can give unexpected results for routing algorithms. Often DEMs are corrected for spikes and pits before they are used in hydrological models (Burrough and McDonnell, 1998).

### 3.6 Conclusions

Digital Elevation Models and their derivatives are important input data for a wide range of environmental simulation models. Understanding and investigating the quality of such DEMs and a careful evaluation of the various available sources for DEMs are currently important research issues. We compared DEMs derived from aerial photography, ASTER and SRTM-3 with a reference DTM at 25-meter resolution. From the analysis of extracted mass points from ASTER and aerial photography we conclude that the RMSE and average difference  $\bar{d}$  compared to the reference DEM are of the same order and result in an overestimation for ASTER and an underestimation for aerial photography. After interpolation, the overall RMSE and  $\bar{d}$  of ASTER and aerial photography differs more. This is related to the amount of extracted mass points which for ASTER is 10 percent of the amount extracted from the aerial photographs. We hypothesized that land cover has an effect on DEM quality and from this study we conclude that the type of land cover has an impact on the generation and the accuracy of DEMs. For soil moisture modelling at resolutions coarser than 25 meters, the smooth SRTM-3 DEM is the best option. SRTM-3 is capable of accurately detecting the elevation trends at a coarse resolution. When the systematical errors in ASTER are known, the ASTER DEM could potentially be used to improve the resolution of the SRTM-3 DEM by adding small-scale elevation trends, like valleys or hilltops, to the SRTM-3 data.

At finer resolutions ASTER or aerial photographs should be used, with pit and spike removing algorithms or a smooth interpolation of the mass points instead of the TIN interpolation. Further research should focus on different interpolation techniques and filtering in combination with land cover, since mass points contain elevation data of the surface as well as surface objects. Optimization of the criteria for the contrast-matching algorithm per land cover type may increase the number of mass points and may yield better interpolation results. In

addition to the quality of the DEMs, the effect on the quality of hydrological products derived from these DEMs, should be quantified in future research.

The quality of high resolution DEM derivation from aerial photography using higher resolution reference data (e.g. LIDAR) should be assessed. Further research should investigate if land cover is also an important factor controlling the accuracy of DEMs in areas with subtle or extreme relief.

In the models used in Part II, III and IV of this thesis, the SRTM-3 DEM will be used, because it is appropriate for the spatial resolutions used in the models, which is 90 meters or coarser.

## **Part II**

# **Evapotranspiration modelling using remote sensing**



# 4 Surface energy balance theory

## 4.1 Introduction

In the previous chapter it was discussed that the estimation of evapotranspiration by solving the surface energy balance on the basis of earth observation data could be of great importance to the modelling of top soil moisture. The objective of this chapter is first to present the theory of surface energy balance and its modelling. Next, the Surface Energy Balance System (SEBS; (Su, 2002)) model will be explained in detail.

Two study sites are used in this part of the thesis: the SPARC 2004 experimental site and the Schoul study area. Both sites are agricultural areas located in a sub-humid to semi-arid climate. Agricultural practices and available field data of each site, however, are very different. The land cover at the SPARC 2004 site is dominated by pivot irrigation. At this site many energy balance and land cover properties were measured during the ESA SPARC (Spectra Barrax Campaign) 2004 field experiment conducted at the Las Tiesas Experimental Farm test site at Barrax in the La-Mancha region in Spain (Su et al., 2005). The Schoul study area is dominated by rainfed agriculture. It is located 20 km southeast from Rabat in Morocco. Field data on soils, soil moisture and meteorology has been collected by several researchers from the Mohammed V University in Rabat, and Alterra and Utrecht University in the Netherlands. Relevant details on the study areas and field measurements will be given in the sections where the specific sites and methods are mentioned.

Chapter 5 will give details on the acquisition of input data for SEBS from MODIS, ASTER and Landsat TM 5 images and field methods. In chapter 6 SEBS derived fluxes are evaluated on a landscape scale using ASTER imagery at the SPARC 2004 site in Barrax, Spain. In chapter 7 an algorithm for the estimation of subpixel surface radiometric temperatures will be presented and evaluated.

## 4.2 Global mean annual radiation and energy budget

Solar radiation provides the main energy input to the earth-atmosphere system. On an annual basis, the extra-terrestrial short-wave radiation influx must equal the loss of energy into space in order to sustain the earth's climate by means of the earth's energy balance. Incoming solar radiation is lost into space by scattering and reflection from atmospheric gasses and aerosols, clouds and reflection from the earth's surface. This amount is controlled by the albedo of the earth's surface and the atmosphere. In summary, the incoming solar radiation is dissipated by the atmosphere and earth's surface according to the following equation (Oke, 1978):

$$\overline{K}_{exo}^{\downarrow} = K_{ac}^{\uparrow} + K_{aa}^{\uparrow} + K_{ac}^* + K_{aa}^* + K_s^{\uparrow} + K_n \quad (4.1)$$

$$100 = 19 + 6 + 5 + 20 + 3 + 47$$

Atmospheric reflection
Atmospheric absorption
Surface reflection
Net incoming shortwave radiation

where  $\overline{K}_{exo}^{\downarrow}$  is the average annual extra-terrestrial incoming solar radiation, which is short-wave,  $K_{ac}^{\uparrow}$  is the reflection of clouds and  $K_{aa}^*$  is the absorption by clouds,  $K_{ac}^{\uparrow}$  is the scatter and reflection into space by atmospheric constituents and  $K_{aa}^*$  the absorption by these particles.  $K_s^{\uparrow}$  is the part of the solar radiation that reaches the earth's surface and is reflected back into space as a result of the earth surface albedo.  $K_n$  is the net incoming solar radiation that is absorbed at the earth's surface and converted into thermal energy. The absorbed shortwave radiation can be reradiated as longwave radiation or by heat transfer.

Figure 4.1 gives the relative size of each component relative to the average annual incoming solar radiation and divided into shortwave, longwave and convective energy components.

The amount of radiation that is converted into thermal energy at the earth's surface is relatively large: 47%. This net radiation must also be re-radiated into space in order to maintain the earth's equilibrium energy budget. The absorbed solar radiation is partly radiated back into the atmosphere as longwave radiation ( $L_s^{\uparrow}$  in figure 4.1) as a function of their temperature and emissivity. The kinetic energy of the moving molecules gives earth surface objects a kinetic

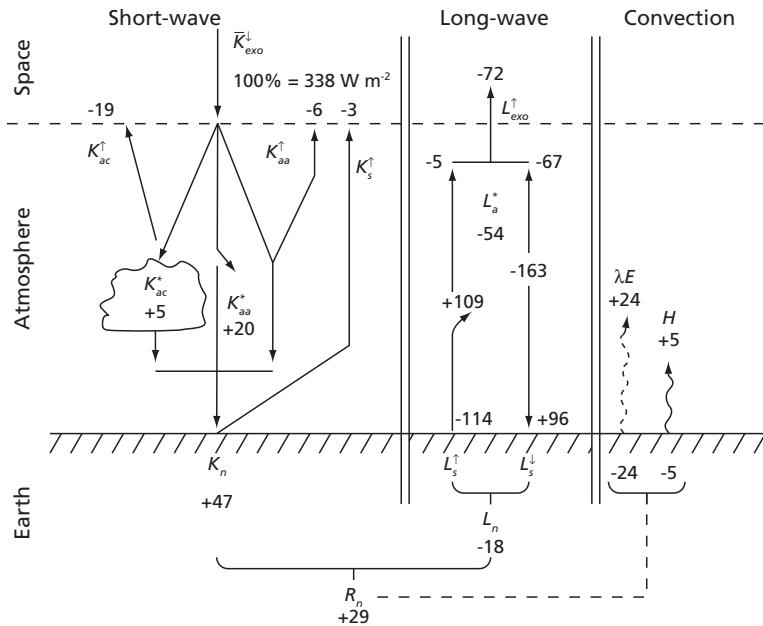


Figure 4.1 Radiation and energy fluxes of the earth-atmosphere system. Values are percentages of the average annual extra terrestrial solar radiation ( $K_{exo}^{\downarrow} = 338 \text{ W m}^{-2}$ ), spread over the outer surface of the atmosphere (Oke, 1978). Positive values indicate radiation or energy directed towards the earth's surface, negative values indicate radiation or energy directed away from the earth's surface.

temperature. According to the law of Stefan-Boltzmann (Stefan, 1879; Boltzmann, 1884), the total amount of energy radiated per unit surface area of a black body per unit time,  $M$  [ $\text{W m}^{-2}$ ], is directly proportional to the fourth power of the object's kinetic temperature,  $T$  [K]. Since real objects are not black bodies, the result should be corrected for the object's emissivity,  $\epsilon$  [-]:

$$M = \epsilon \sigma T^4 \quad (4.2)$$

where  $\sigma$  is the Stefan-Boltzmann constant. Emissivity,  $\epsilon$ , is the ability of a material to absorb and radiate energy. According to Planck's law of black body radiation most electromagnetic radiation at the temperature of earth surface objects is in the longwave part of the spectrum:

$$I = \frac{2bf^3}{c^2} \frac{1}{e^{\frac{hf}{\sigma T}} - 1} \quad (4.3)$$

where  $I$  is the spectral radiance [ $\text{J s}^{-1}\text{m}^{-2}\text{sr}^{-1}\text{Hz}^{-1}$ ],  $f$  is the frequency [Hz],  $h$  is the constant of Planck,  $c$  is the speed of light.

The remaining part of the absorbed solar radiation is transferred into the atmosphere through convective transport of sensible heat (5%) and latent heat (24%). Latent heat ( $\lambda E$  [ $\text{W m}^{-2}$ ]) is the amount of energy that is required to evaporate water, sensible heat ( $H$  [ $\text{W m}^{-2}$ ]) is the energy used to heat the atmosphere. Latent heat plays an important role in the hydrological cycle by coupling the energy balance to the water balance. It is the latent heat of vaporization ( $\lambda$ ) times the actual evapotranspiration ( $E$  [m]):

$$\lambda E = \lambda \cdot E \quad (4.4)$$

Transport of heat by means of convection is the vertical interchange of heat by currents within liquids and gasses (Oke, 1978). Sensible and latent heat are transported from the earth's surface into the air as parcels of air, called eddies. Since these eddies move in a turbulent manner, the fluxes of sensible and latent heat are called the turbulent heat fluxes. They are characterised by chaotic, stochastic behaviour and have a low momentum diffusion, high momentum convection and a rapid variation of pressure and velocity in space and time. The turbulence is caused by either free or forced convection. Free convection takes place when the density of an eddy is different from its surroundings. For example, an eddy warmer than its surroundings has a lower density and will rise, while cooler eddies sink. A strong heating of the earth's surface lowers the density of air close to the surface and causes a free convective flux from the surface to the atmosphere. In this case the atmosphere is unstable. The atmosphere is called stable if the air parcel has the same temperature as its surroundings. Motion of eddies in a stable atmosphere is suppressed, since the eddy will lose heat faster than its surroundings when it is moved upwards. Because of its higher density it will move down to its original position and will stay in a stable equilibrium with its surroundings.

Apart from free convective motion, eddies can also start a turbulent motion when air flows over obstacles at the earth's surface (Oke, 1978). Over smooth surfaces the air flow is laminar. The turbulence of the flow will increase when surface roughness increases and the speed of the horizontal flow over the obstacles increases. This is called forced, or mechanical convection. Often both forms of convection are responsible for heat transfer. In that case the transporting process

is called mixed convection. Modelling turbulent heat transfer and turbulent flow, however, is an important challenge in physics.

Thus, the surplus of radiative energy received by the earth's surface is balanced by the convective transport of sensible and latent heat from the earth's surface into the atmosphere. The atmosphere's radiation deficit is balanced by the release of sensible heat when it mixes with the cooler air (second law of thermodynamics) and by condensation of water vapour by using latent heat. The amount of sensible heat flux depends on the state of atmospheric turbulence and the magnitude of the vertical temperature difference. The amount of latent heat flux depends on the state of atmospheric turbulence and the strength of the vertical moisture difference. Without vertical motion the air above the surface saturates quickly with water vapour and no more energy can be exchanged from the surface to the atmosphere.

In summary, the surface net radiation,  $R_n$  [ $\text{W m}^{-2}$ ], can be stated as the balance among all incoming and outgoing radiation:

$$R_n = K_n + L_n \quad (4.5)$$

where  $K_n$  and  $L_n$  are the net incoming shortwave and longwave radiation respectively, as indicated in figure 4.1. They are calculated with:

$$K_n = K_s^\downarrow - K_s^\uparrow \quad (4.6)$$

$$L_n = L_s^\downarrow - L_s^\uparrow \quad (4.7)$$

where  $K_s^\downarrow$  [ $\text{W m}^{-2}$ ] is the downward solar radiation. A part of  $K_s^\downarrow$  is reflected at the earth's surface as upward shortwave radiation,  $K_s^\uparrow$  [ $\text{W m}^{-2}$ ] (see eq. 4.1 and figure 4.1). The amount of reflection depends on the albedo,  $\alpha$  [-], of the surface:

$$K_s^\uparrow = \alpha \cdot K_s^\downarrow \quad (4.8)$$

$L_s^\uparrow$  [ $\text{W m}^{-2}$ ] is the upward longwave radiation (see figure 4.1), which is a function of emissivity,  $\varepsilon_s$  [-], and the temperature,  $T_s$  [K] of the earth's surface according to the law of Stefan-Boltzmann (eq. 4.2):

$$L_s^\uparrow = \varepsilon_s \cdot \sigma \cdot T_s^4 \quad (4.9)$$

Similarly, the downward longwave radiation,  $L_s^\downarrow$  [ $\text{W m}^{-2}$ ], can be calculated from the emissivity  $\varepsilon_a$  [-], and temperature  $T_a$  [K] of the atmosphere:

$$L_s^\downarrow = \varepsilon_a \cdot \sigma \cdot T_a^4 \quad (4.10)$$

When equations 4.5 to 4.10 are combined, the net radiation can be stated as:

$$R_n = (1 - \alpha) \cdot K_s^\downarrow + \varepsilon_a \cdot \sigma \cdot T_a^4 - \varepsilon_s \cdot \sigma \cdot T_s^4 \quad (4.11)$$

The annual average net radiation received by the earth's surface, as calculated with eq. 4.5 or 4.11, should equal the mean annual energy budget of the earth's surface (figure 4.1), which can be written as the sum of the soil heat flux, the sensible heat flux and the latent heat flux (Oke, 1978):

$$R_n = G_0 + H + \lambda E \text{ [W m}^{-2}\text{]} \quad (4.12)$$

The soil heat flux,  $G_0$  [W m<sup>-2</sup>], representing the exchange of heat with the subsurface, can be assumed zero at an average annual timescale. The biochemical storage of energy due to photosynthesis is negligible.

### 4.3 The surface energy balance

Until now we have considered the mean annual situation. For our purpose of modelling regions or catchments at shorter timescales we have to look at the surface energy balance at appropriate scales. At this scale the soil heat flux in eq. 4.12 is not negligible. This is not a turbulent flux since the heat in the soil is mainly transported by conduction. Some convection can take place depending on the air and moisture content of the soil. Also some evaporation can take place in the soil, causing a small latent heat flux (Koorevaar et al., 1983). The soil heat flux depends on the thermal properties of the soil, i.e. volumetric heat capacity, heat conductivity and the temperature gradient across the material. Apart from soil physical properties, the thermal soil properties are strongly dependent on soil water content.

Figure 4.2 shows soil temperature profiles in time. Temperatures are measured at the surface and at 3, 8, 12, 17 and 22 cm below the surface using calibrated LM35 semi-conductor sensors with an accuracy < 0.1 °C. From figure 4.2 it is obvious that the effect of the heating of the earth's surface during daytime is attenuated with depth. The amplitude of the temperature attenuates and shifts with depth. At 17 cm depth, the diurnal variation is almost nihil. Damping out of the soil temperature cycle is determined by its moisture content and soil physical properties. The highest air temperature, 33.1 °C, occurred at 2.20 pm. At 3 cm depth the maximum temperature is reached at 4.00 pm and is 27.6 °C. At 22 cm the amplitude is very small (0.8 °C) and reaches its maximum of 24.4 °C at midnight. From 5.40 pm to 8.40 am the soil is warmer than the air and the soil heat flux is directed towards the soil surface. Also, small temporal changes in air temperatures are smoothed with depth. Generally, during daytime the soil heat flux is directed away from the surface into the soil.

Next, we consider the atmosphere compartment. The atmosphere can be divided in several layers. The part of the atmosphere influenced by the earth's surface is called the troposphere (Oke, 1978), which is the lowest 10 km of the atmosphere. The part of the troposphere that is influenced by the earth's surface on timescales of an hour or less is called the planetary or atmospheric boundary layer, or simply boundary layer. The boundary layer is schematized in figure 4.3. In the boundary layer the Coriolis forces, caused by the earth's rotation, are negligible compared to the influence of earth surface processes. The turbulent heat transfer, i.e. sensible heat flux and latent heat flux, is restricted to this layer, more precisely the mixed layer. All moisture and much of the heat in the boundary layer are transferred from the earth's surface by means of turbulence.

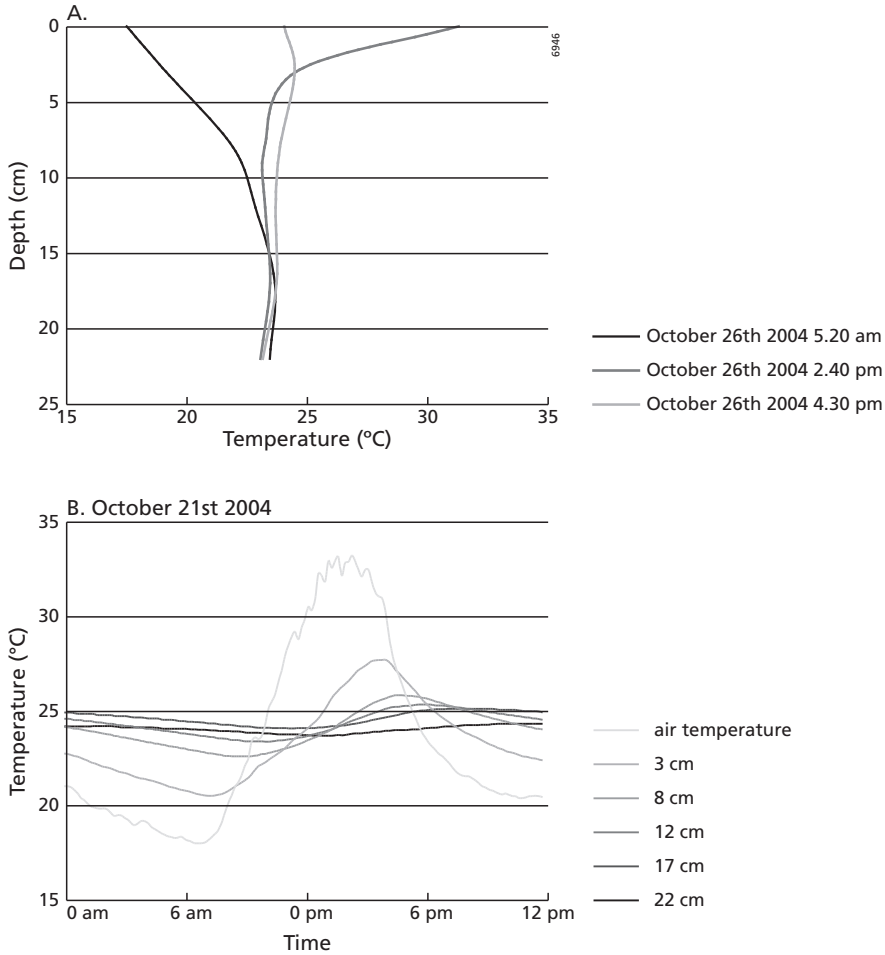


Figure 4.2 Soil temperature profiles in the Sehoul study area, Morocco.

Within the mixed layer, potential temperature, humidity and wind speed are nearly constant with height (figure 4.4). Potential temperature is used to correct for air pressure differences within the atmosphere. Potential temperature is the temperature that a parcel of air would acquire when it is adiabatically brought to a standard reference pressure (Oke, 1978). Above the mixed layer the turbulent eddies reach the entrainment layer where they mix with the laminar processes in the free atmosphere.

Below the mixed layer the surface layer exists. This layer is a few meters to a few tens of meters thick, close to the ground. In this layer the forced convection exceeds the free convection. In this layer the Monin-Obukhov similarity hypothesis (Monin and Obukhov, 1954) can be applied to describe the profiles of wind, temperature and humidity. This hypothesis states that wind, temperature and humidity profiles in the surface layer above extensive horizontal homogeneous terrain are similar.

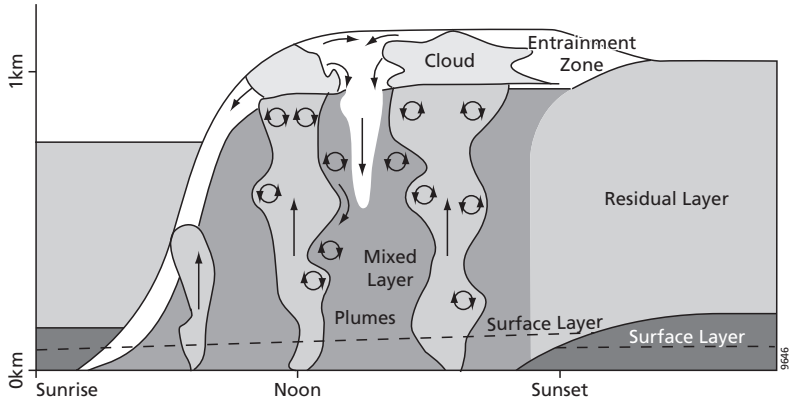


Figure 4.3 The atmospheric boundary layer and its diurnal changes. Source: Piironen (1994).

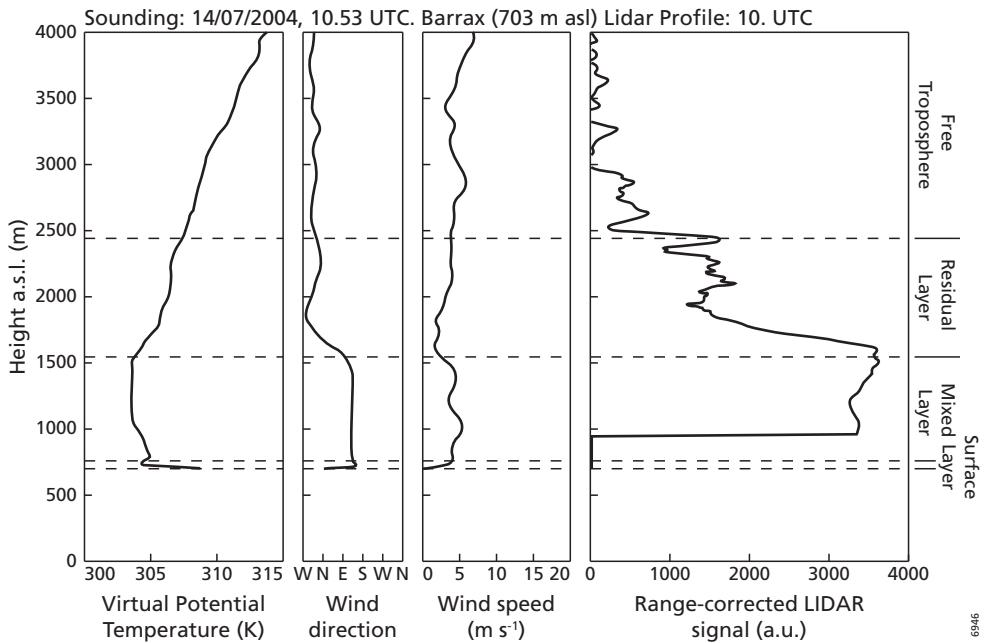


Figure 4.4 Radiosonde sounding from a weather balloon at the SPARC 2004 field campaign in Barrax (Spain) showing profiles of virtual potential temperature, wind direction, wind speed and a LIDAR profile. A higher LIDAR signal is caused by a higher concentration of aerosols in the atmosphere. The virtual temperature is the temperature that a parcel of dry air would have if it had the same pressure and density as moist air. The surface is at 700 m a.s.l. Source: Molero et al. (2005).

Below the surface layer a very small laminar boundary layer exists of only a few millimetres thick. In this layer all heat is transferred by means of conduction, which is controlled by molecular diffusion.

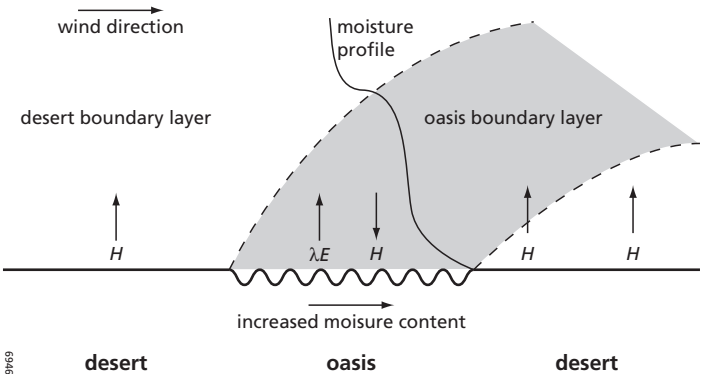
The height of the boundary layer varies with the strength of the convective transport (figure 4.4). Generally at daytime the convection is largest since the earth's surface is heated more by the sun than the atmosphere. In this case the boundary layer depth can be around 1 to 2 km. By night, when the earth's surface cools quicker than the atmosphere, there is a downward heat flux and the boundary layer can be less than 100 m.

A downward sensible heat flux can also take place during daytime when wet surfaces cool rapidly by evapotranspiration and enough dry air is supplied to keep the high evapotranspiration rates. This is called the "oasis effect" (Brutsaert, 1982; Stull, 1988) (figure 4.5).

Horizontally, the largest variation in sensible and latent heat flux is found in the turbulent surface layer. Above a heterogeneous surface horizontal advection takes place. The height at which turbulence becomes more or less independent of surface properties, is the blending height (Wieringa, 1986).

In many studies concerned with modelling the surface energy balance, it is decided to give the energy fluxes a positive value when they are directed away from the earth's surface. The net radiation is given a positive value when directed towards the surface. In this thesis the same convention will be used.

Figure 4.6 and figure 4.7 show an example of the diurnal cycle of the radiation and energy budget as measured over a vineyard in the SPARC 2004 study area (Barrax, Spain). During daytime the incoming shortwave solar radiation is large and partly reflected. Absorption of the shortwave radiation by the atmosphere and earth's surface causes a heating of the surface and atmosphere. According to the law of Stefan-Boltzmann this causes the emission of energy, which according to Planck's law will take place in the longwave part of the spectrum. The outgoing



**9969** **desert** **oasis** **desert**  
*Figure 4.5* Conceptual model of the oasis effect. When very dry air reaches a wet area, evaporative cooling due to heat advection can take place. Heat is advected from surrounding warmer surfaces and subsidence of hot airmasses from higher in the atmosphere, resulting in a negative sensible heat flux ( $H$ ). In these areas the latent heat flux ( $\lambda E$ ) can be two times higher than the locally available radiative flux. The oasis effect is not only present in deserts, but also a common phenomenon with water bodies in arid surroundings, melting snow patches, irrigated fields in arid areas, or irrigated urban lawns and parks (Glickman, 2000).

longwave radiation from the surface is partly absorbed by the atmosphere, which gets warmer. The heated atmosphere causes the incoming longwave radiation, which is less than the outgoing longwave radiation. At night the shortwave radiation is absent, and the surface and atmosphere are cooling, resulting in a decreasing longwave radiation.

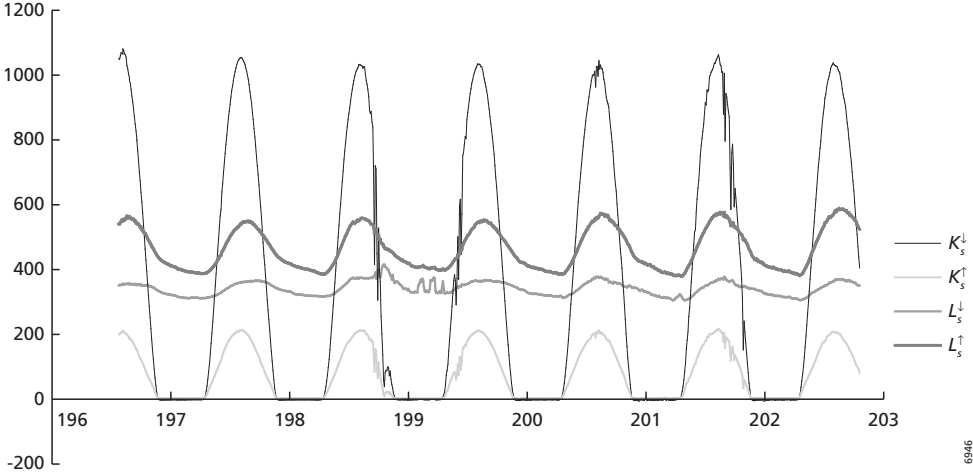


Figure 4.6 Diurnal cycle of radiation budget components for a vineyard in the SPARC 2004 study area (Barrax, Spain).  $K_s^{\downarrow}$  is shortwave incoming radiation,  $K_s^{\uparrow}$  is shortwave outgoing radiation,  $L_s^{\downarrow}$  is longwave incoming radiation and  $L_s^{\uparrow}$  is longwave outgoing radiation. Source: Su et al. (2005).

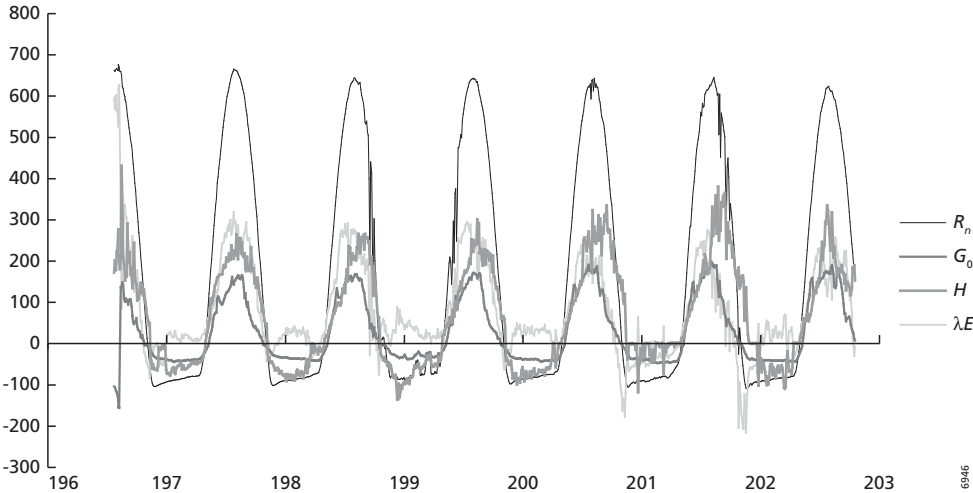


Figure 4.7 Diurnal cycle of energy budget components for a vineyard in the SPARC 2004 study area (Barrax, Spain).  $R_n$  is net surface radiation,  $G_0$  is soil heat flux,  $H$  is sensible heat flux and  $\lambda E$  is latent heat flux. Source: Su et al. (2005).

The net radiation (figure 4.7) is positive during daytime and has a maximum at noon. The sensible, latent and soil heat flux show the same periodicity, but have a smaller amplitude. At night the net radiation is directed towards the sky. The soil heat flux is, in general, directed towards the surface since the surface cools quicker than the subsoil. Additionally, the sensible heat flux is directed towards the surface to compensate the surface cooling. The latent heat flux can be small at night, because heat is added to the surface by the other fluxes. However, a stable atmosphere impedes the upwelling of turbulent fluxes at night. Sometimes the latent heat flux is negative, caused by the condensation of moisture in the air.

#### 4.4 Modelling the surface energy balance

In the previous paragraph the theory of the surface energy balance was described. In order to model the surface energy balance, a number of models have been developed recently with varying complexity, e.g. SEBAL (Bastiaanssen, 1995), SEBS (Su, 2001), TSEB (Norman et al., 1995).

Various surface energy balance models calculate the net radiation, soil heat flux and sensible heat flux separately. The latent heat flux, which links the soil water balance with the surface energy balance, is estimated as the rest term to close the energy balance (eq. 4.12). This latent heat flux can be used to link surface energy balance models to soil moisture models.

These models describe the sensible heat flux as a physically based resistance network of energy exchanges between bare soil and vegetation and their exchange with the surrounding air (Kustas and Norman, 2000):

$$H = \frac{\rho_a \cdot C_p}{r_{ab}} \cdot (\theta_0 - \theta_a) \quad (4.13)$$

where  $\rho_a$  is the air density [ $\text{kg m}^{-3}$ ],  $C_p$  [ $\text{J kg}^{-1} \text{K}^{-1}$ ] is the specific heat of air at constant pressure,  $\theta_0$  [K] represents potential temperature at the surface and  $\theta_a$  [K] is the potential temperature of the overlying air at reference height  $z$  [m].  $r_{ab}$  [ $\text{s m}^{-1}$ ] is the aerodynamic resistance to heat, given by (Timmermans et al., 2005b):

$$r_{ab} = \frac{\left[ \ln\left(\frac{z-d_0}{z_{0M}}\right) - \Psi_M(z, L) \right] \cdot \left[ \ln\left(\frac{z-d_0}{z_{0H}}\right) - \Psi_H(z, L) \right]}{k^2 \cdot u} \quad (4.14)$$

where  $d_0$  [m] is the zero displacement height,  $z_{0M}$  [m] the roughness height for momentum transfer,  $z_{0H}$  [m] the scalar roughness height for heat transfer,  $k$  the Von Karman constant (0.41),  $u$  the windspeed [ $\text{m s}^{-1}$ ] at height  $z$  [m],  $\Psi_M$  and  $\Psi_H$  the stability correction functions for momentum and sensible heat transfer respectively, and  $L$  [m], the Monin-Obukhov length. This is the height above the ground where forced convection is in balance with the dissipative effect of downward buoyancy. The Monin-Obukhov length is defined as (Timmermans et al., 2005b):

$$L = -\frac{\rho_a \cdot C_p \cdot u_*^3 \theta_v}{k \cdot g \cdot H} \quad (4.15)$$

where  $g$  [ $\text{m s}^{-2}$ ] is the acceleration due to gravity,  $\theta_v$  [K] is the potential virtual temperature near the surface and  $u_*$  [ $\text{m s}^{-1}$ ] is the friction velocity. When  $R_n$ ,  $G_0$  and  $H$  are known, the latent heat flux can be calculated as a rest term, closing the energy balance.

The different types of energy balance models derive these fluxes in a different way. Surface energy balance models can be one-dimensional or multi-dimensional, lumped or distributed, single-source or dual-source.

A one-dimensional energy balance model simulates the vertical distribution of water content, and sometimes temperature, within a schematized soil profile. Vertical moisture and heat fluxes between these layers are estimated. The surface energy balance is calculated from the interaction between the atmosphere and the subsurface moisture and heat fluxes. Examples of these type of models are: BATS (Dickinson, 1986), SiB (Sellers et al., 1986) and SWATRE (Belmans et al., 1983). These models can be coupled to atmospheric models to describe the effect of horizontal interferences on the vertical exchanges at the land surface (Kroon and de Bruin, 1993).

One-dimensional models can be lumped models that predict area-average flux densities for each grid cell by assuming uniform processes within a grid cell. They can also be semi-distributed by using stochastic-dynamic approaches that account for spatial variability. One-dimensional models may give incorrect results when lateral transport of surface water by streams, overland flow in sloping terrain and groundwater movement is important.

According to Bastiaanssen (1995) the combination of two- and three-dimensional land surface parameterization schemes with PBL models that apply to similar length scales is still a challenge. It requires a lot of data and computational power.

The heterogeneity of canopies causes a complex three-dimensional heat transfer. The surface temperature of foliage and soil varies significantly and the vertical distribution of foliage temperature is a function of solar elevation, density of the leaves and the angle distribution of leaves (Jia, 2004). Figure 4.8 schematizes the difference between single-source and dual-source models. Single-source (also one-layer or one-source) models make no distinction between the energy balance, temperature and vapour regimes of the vegetation canopy and the soil surface (Friedl, 2002). Some models use an excess resistance term that accounts for the fact that the roughness lengths for heat and momentum are different, e.g. the  $kB^{-1}$  parameter that will be explained in the next section, which is highly variable in space and time. Dual-source (also two-source or two-layer) models use two sets of resistances across which individual, local, single-source models are applied: a bare soil resistance scheme and a vegetation resistance scheme. Within the canopy interaction between soil and vegetation components is included. Finally, a single aerodynamic resistance connects the combined canopy with the atmosphere. A single-source model uses only one resistance and assumes that all the surfaces can be represented by one effective temperature and humidity value.

Although dual-source models have a greater physical realism, and therefore should reflect the surface energy fluxes more accurately than single-source models, they also require more ancillary data. Furthermore, many researchers have found that, after appropriate tuning of the model parameters, single-source models can describe the overall surface energy balance satisfactorily (Kustas et al., 1996; Troufleau et al., 1997; Bastiaanssen, 1998). A simple but correctly calibrated single-source model might well perform better than an ill-parameterized dual-source model (Kustas, 1990). Therefore, often the simpler single-source schemes are utilized for operational monitoring and forecasting (Timmermans et al., 2005b). Examples of single-source models are: SEBAL (Bastiaanssen, 1995) and SEBS (Su, 2002). TSEB (Norman et al., 1995) is an example

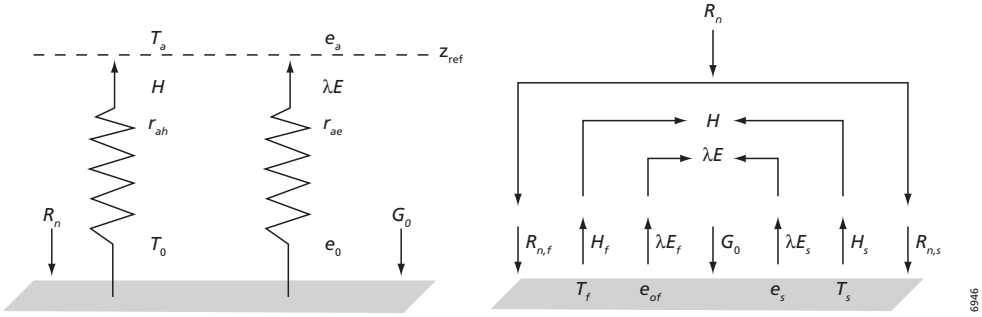


Figure 4.8 Schematization of a single-source (left) and a dual-source (right) model.  $Z_{ref}$  is the reference height in the overlaying atmosphere,  $T_0$  is the surface temperature,  $T_a$  is the air temperature,  $e_0$  is the surface water vapour pressure,  $e_a$  is the air water vapour pressure,  $r_{ah}$  and  $r_{ae}$  are the aerodynamic resistance of heat transfer and of water vapour transfer respectively. In the right figure, subscript  $f$  indicates foliage and  $s$  indicates soil. Source: Jia (2004)

of a dual-source model. Timmermans et al. (2005b) evaluated the differences between one-source and dual-source models used at the SPARC 2004 site in Barrax (Spain).

#### 4.5 The Surface Energy Balance System (SEBS)

In this thesis the Surface Energy Balance System (SEBS) (Su, 2002) will be evaluated and used in soil moisture modelling. SEBS is a single-source model, which estimates atmospheric turbulent fluxes and surface evaporative fraction from remote sensing data.

In the current setup SEBS requires three sets of input data: (1) Data derived from remote sensing: albedo, emissivity, temperature and Normalized Difference Vegetation Index (NDVI) to derive surface roughness parameters. Instead of remote sensing data a land cover map can be used in conjunction with lookup tables for surface roughness parameters; (2) Meteorological parameters at a reference site (air pressure, temperature, relative humidity, wind speed); (3) Radiation data (downward solar radiation, downward longwave radiation).

The SEBS algorithm, which is described in detail in Su (2002), has been implemented with the PCRaster Python Library (Karsenberg, 2006). The input-output relations have been checked with a SEBS version programmed in IDL by other researchers and revealed no differences.

The model consists of three modules: (1) Submodel to derive energy balance terms (section 4.5.2); (2) Submodel to derive stability parameters (section 4.5.3) and (3) Submodel to derive roughness length for heat transfer (section 4.5.4). Using these three modules, the energy balance for limiting cases (i.e. completely wet or dry pixels) can be resolved, which will be explained in section 4.5.5. Consequently, the energy balance terms, relative evaporation, evaporative fraction and evaporation flux can be derived for all pixels. Figure 4.9 shows the concept of SEBS.

First, the preprocessing of the meteorological parameters that are used in the three submodels will be explained in section 4.5.1. Next, the three submodels and the energy balance for limiting cases will be described from which the actual evapotranspiration flux can be calculated. The derivation of input data for SEBS from satellite images will be explained in the next chapter.

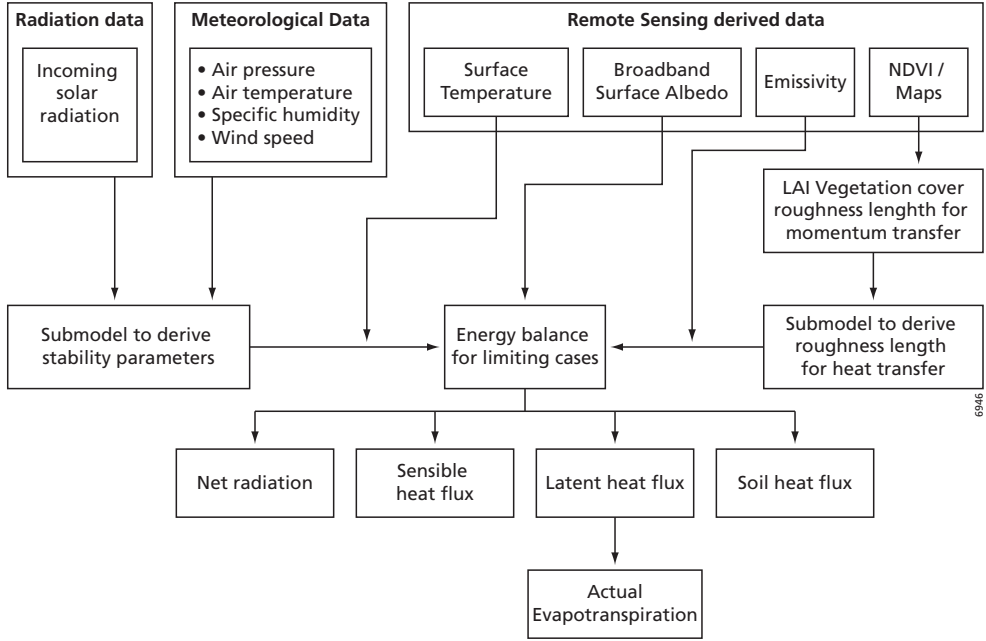


Figure 4.9 Flowchart of the SEBS model.

#### 4.5.1 Calculation of meteorological parameters

Standard meteorological stations provide SEBS inputs of air temperature, air pressure, relative humidity and incoming solar radiation. From these parameters the model derives saturation vapour pressure, potential temperature, virtual potential temperature, specific humidity and (moist) air density and distributes these parameters spatially.

The saturation vapour pressure,  $e_s$  [kPa], is calculated with:

$$e_s = 0.611 \cdot e^{\frac{17.502t_a}{t_a + 240.97}} \quad (4.16)$$

where  $t_a$  is the air temperature in degrees Celcius. When the relative humidity,  $H_f$  [-], is multiplied with  $e_s$  the actual vapour pressure  $e_a$  [kPa] is obtained:

$$e_a = H_f \cdot e_s \quad (4.17)$$

The potential temperature,  $\theta$  [K], is calculated with:

$$\theta = T \left( \frac{p_0}{p} \right)^{0.286} \quad (4.18)$$

where  $T$  [K] is the air temperature,  $p$  [mbar] is the air pressure and  $p_0 = 1013$  mbar, which is the reference pressure. The virtual potential temperature,  $\theta_v$  [K], can then be calculated with:

$$\theta_v = (1 + 0.61q)\theta \quad (4.19)$$

where  $q$  [ $\text{kg kg}^{-1}$ ] is the specific humidity:

$$q = \left( \frac{R_d}{R_v} \right) \cdot \frac{e_a}{p} \quad (4.20)$$

In this equation  $R_d = 287.1 \text{ J kg}^{-1} \text{ K}^{-1}$  and  $R_v = 461.5 \text{ J kg}^{-1} \text{ K}^{-1}$ . These are the specific gas constants for dry air and water vapour respectively.

Air temperature and pressure measured at a meteorological station is extrapolated horizontally, using relationships with elevation from a DEM, defined in terms of the properties of the International Standard Atmosphere (ISA) (ICAO, 1993). For pressure this relation is:

$$p(Z) = p \left( \frac{44331 - Z}{44331 - z} \right)^{\frac{1}{0.1903}} \quad (4.21)$$

and for temperature:

$$T(Z) = \frac{T}{\left( 1 - \frac{Z}{44331} \right)^{1.5029}} \quad (4.22)$$

where  $Z$  [m] is the elevation derived from a DEM and  $z$  [m] is the measurement height. The air density  $\rho_a$  [ $\text{kg m}^{-3}$ ] is calculated with:

$$\rho_a = \frac{p}{R_d \theta_v} \quad (4.23)$$

The moist air density  $\rho_w$  [ $\text{kg m}^{-3}$ ] is calculated using the mixing ratio  $\omega$ :

$$\rho_w = \rho_a \cdot \omega \quad (4.24)$$

where

$$\omega = 0.622 \frac{e_a}{p - e_a} \quad (4.25)$$

#### 4.5.2 Submodel to derive energy balance terms

The submodel to derive the energy balance terms (eq. 4.12) calculates the net radiation,  $R_n$ , from equation 4.11 by balancing the radiation terms. Albedo, emissivity and surface temperature as derived from remote sensing and measured incoming solar radiation are used to calculate the net radiation. Next, the soil heat flux,  $G_0$ , is estimated by:

$$G_0 = R_n \cdot [\Gamma_c + (1 - f_c) \cdot (\Gamma_s - \Gamma_c)] \quad (4.26)$$

which assumes that the ratio of soil heat flux to net radiation  $\Gamma_c = 0.05$  for full vegetation canopy (Kustas and Daughtry, 1990) and  $\Gamma_s = 0.315$  for bare soil (Brutsaert, 1982). The fractional canopy coverage,  $f_c$  [-], is then used to interpolate between these limiting cases. The variable  $f_c$  can be derived from mapped field data or NDVI. The derivation from NDVI will be explained in the next chapter. In order to calculate the sensible heat flux,  $H$  (eq. 4.13), equations 4.14 and 4.15

need to be solved. The stability correction functions needed in equation 4.14 are derived in the submodel that calculates the atmospheric stability parameters.

### 4.5.3 Submodel to derive stability parameters

The submodel for the derivation of the atmospheric stability parameters derives friction velocity,  $u_*$ , the Monin-Obukhov stability length,  $L$  (eq. 4.15) and the sensible heat flux,  $H$ , iteratively, using boundary layer similarity theory. The atmospheric boundary layer (ABL) (or Planetary Boundary Layer) consists of two layers as has been described in section 4.3: the inner atmospheric surface layer (ASL) and the outer mixed layer, therefore two stability correction functions are required to relate surface fluxes to surface variables and the mixed layer atmospheric variables. In the ASL flow mainly depends on surface characteristics, while in the mixed layer the effect of the surface is little and mean profiles of wind and potential temperature are assumed constant with height under free convective conditions.

In this submodel first the Monin-Obukhov similarity (MOS) hypothesis (Monin and Obukhov, 1954; Brutsaert, 1982) is used, which states that wind, temperature and humidity profiles in the surface layer above extensive horizontal homogeneous terrain are similar. This makes it possible to relate surface fluxes to surface variables and variables in the atmospheric ASL. In order to relate surface fluxes to the mixed layer variables, the MOS functions are replaced with the bulk atmospheric boundary layer (ABL) similarity (BAS) (Brutsaert, 1999) functions.

The similarity principle in the ASL for mean wind speed  $u$  and mean potential temperature ( $\theta_0 - \theta_a$ ), are usually written in integral form as (Su, 2002):

$$u = \frac{u_*}{k} \left[ \ln \left( \frac{z - d_0}{z_{0M}} \right) - \Psi_M \left( \frac{z - d_0}{L} \right) + \Psi_M \left( \frac{z_{0M}}{L} \right) \right] \quad (4.27)$$

$$\theta_0 - \theta_a = \frac{H}{ku_* \rho_a C_p} \left[ \ln \left( \frac{z - d_0}{z_{0H}} \right) - \Psi_H \left( \frac{z - d_0}{L} \right) + \Psi_H \left( \frac{z_{0H}}{L} \right) \right] \quad (4.28)$$

where

$$u_* = (\tau_0 / \rho_a)^{1/2}$$

$\tau_0$  is the surface shear stress [N]. The roughness length for heat transfer,  $z_{0Hp}$  is calculated in the submodel explained in section 4.5.4.

The equations 4.15, 4.27 and 4.28 are solved numerically to find  $L$ ,  $H$  and  $u_*$ .

For meteorological measurements at a few meters above the ground, the MOS stability correction functions for momentum and sensible heat transfer of Brutsaert (1999) are used (Su, 2001):

$$\Psi_i(y) = \int_0^y [1 - \phi_i(x)] \frac{dx}{dy} \quad (4.29)$$

with  $y = -(z - d_0)/L$

where  $i = M$  for momentum heat transfer or  $i = H$  for sensible heat transfer. The variable  $\phi_M$  is calculated as:

$$\phi_M(y) = \frac{\left(a + b \cdot y^{m+1/3}\right)}{a + y^m} \quad (4.30)$$

$$\phi_M(y) = \frac{(c + d \cdot y^n)}{c + y^n}$$

The constants can be found in table 4.1.

After integration of equation 4.29, using equation 4.30, the MOS stability function for free convective, unstable conditions is obtained:

$$\Psi_M(y) = \ln(a + y) - 3 \cdot b \cdot y^{1/3} + \frac{b \cdot a^{1/3}}{2} \ln \left[ \frac{(1+x)^2}{(1-x+x^2)} \right] + 3^{1/2} \cdot b \cdot a^{1/3} \tan^{-1} \left[ \frac{(2 \cdot x - 1)}{3^{1/2}} \right] + \Psi_0 \quad (4.31)$$

Where  $x = (y/a)^{1/3}$  and the integration constant  $\Psi_0 = (-\ln a + 3^{1/2} \cdot b \cdot a^{1/3} \cdot \pi/6)$ .

In the case that  $y \leq b^{-3}$ :

$$\Psi_M(y) = \Psi_M(b^{-3}) \quad (4.32)$$

When  $y > b^{-3}$ :

$$\Psi_H(y) = \left[ \frac{(1-d)}{n} \right] \ln \left[ \frac{(c + y^n)}{c} \right] \quad (4.33)$$

For stable conditions the following equations are used (Beljaars and Holtslag, 1991):

$$\Psi_M(y) = - \left[ a_s \cdot y_s + b_s \left( y_s - \frac{c_s}{d_s} \right) \cdot e^{(-d_s \cdot y_s)} + \frac{b_s \cdot c_s}{d_s} \right] \quad (4.34)$$

$$\Psi_H(y_s) = - \left[ \left( 1 + \frac{2a_s}{3} y_s \right)^{1.5} + b_s \cdot \left( y_s - \frac{c_s}{d_s} \right) \cdot e^{(-d_s \cdot y_s)} + \left( \frac{b_s \cdot c_s}{d_s} - 1 \right) \right] \quad (4.35)$$

Where  $y_s = (z-d_0)/L$ . For constants see table 4.1.

Within an unstable atmospheric boundary layer, the MOS functions can be used for the surface layer. In the mixed layer the mean profiles of wind and potential temperatures are nearly constant with height under free convective conditions. The MOS functions should be appropriately scaled using the bulk atmospheric boundary layer similarity functions (BAS) (Brutsaert, 1982, 1999). The height of the surface layer,  $h_{st}$  [m], should be scaled with the thickness of the boundary layer

*Table 4.1* Constants in the stability correction functions. Constants with subscript  $s$  are used in stable conditions (eq. 4.34 and 4.35).

$a = 0.33$	$b = 0.41$	$m = 1.0$	$c = 0.33$	$d = 0.057$
$n = 0.78$	$a_s = 1$	$b_s = 0.667$	$c_s = 5$	$d_s = 1$

over moderately rough surfaces. Over rough terrain  $h_{st}$  should be scaled with surface roughness (Brutsaert, 1999). This is modelled with the following equations:

$$h_{st} = \alpha_b \cdot h_i \text{ [m]} \quad (4.36)$$

$$h_{st} = \beta_b \cdot z_0 \text{ [m]} \quad (4.37)$$

where  $h_i$  is the height of the boundary layer [m],  $\alpha_b$  can range from 0.10 to 0.15 and  $\beta_b$  can range from 100 to 150. The largest value of  $h_{st}$  is used. Typical values are:  $\beta_b/\alpha_b = 10^3$ ,  $h_i = 10^3$  m. This results in a  $z_0$  of 1 m, which separates rough terrain from moderately rough terrain (Su, 2001).

The model distinguishes three possibilities:

1. Unstable atmosphere, moderately rough terrain

In this case  $z_0 < (\alpha_b / \beta_b) \cdot h_i$  and the surface layer will be joined with the mixed layer resulting in the same windspeed and potential temperature at the height of the surface layer as the average of the lower half of the mixed layer. Mathematically:  $u(z-d_0) = u_m$ ,  $\theta_a(z-d_0) = \theta_m$  and  $z-d_0 = h_{st}$ . The lower average windspeed and potential temperature of the lower half of the mixed layer is used since the upper half is biased by the entrainment of warmer air into the boundary layer. The BAS functions for this case are:

$$\begin{aligned} B_w &= -\ln(\alpha_b) + \Psi_M(\alpha_b \cdot h_i / L) - \Psi_M(z_0 / L) \\ C_w &= -\ln(\alpha_b) + \Psi_H(\alpha_b \cdot h_i / L) - \Psi_H(z_{0H} / L) \end{aligned} \quad (4.38)$$

2. Unstable atmosphere, rough terrain

In this case  $z_0 \geq (\alpha_b / \beta_b) \cdot h_i$ , which causes a well defined separation between the surface layer and the mixed layer. The BAS functions for this case are:

$$\begin{aligned} B_w &= -\ln(h_i / (\beta_b \cdot z_0)) + \Psi_M(\beta_b \cdot z_0 / L) - \Psi_M(z_0 / L) \\ C_w &= -\ln(h_i / (\beta_b \cdot z_0)) + \Psi_H(\beta_b \cdot z_0 / L) - \Psi_H(z_{0H} / L) \end{aligned} \quad (4.39)$$

3. Stable conditions

In this case  $h_i / L > 0$  and mean potential virtual temperature increases with altitude. The BAS functions for this case are (Brutsaert, 1982):

$$\begin{aligned} B_w &= -2.2 \cdot \ln(1 + h_i / L) \\ C_w &= -7.6 \cdot \ln(1 + h_i / L) \end{aligned} \quad (4.40)$$

#### 4.5.4 Submodel to derive roughness length for heat transfer

To calculate the MOS and BAS functions, the roughness length for momentum transfer,  $z_{0M}$ , and the roughness length for heat transfer,  $z_{0H}$ , need to be known (eq. 4.27 and 4.38). The derivation of  $z_{0M}$  will be explained below in equation 4.49. SEBS uses a submodel to derive  $z_{0H}$  using a simplified localized near-field Lagrangian theory (Massman, 1999a):

$$z_{0H} = z_{0M} / \exp(kB^{-1}) \text{ [m]} \quad (4.41)$$

where  $B^{-1}$  is the inverse Stanton number. The Stanton number is the ratio of heat transferred into a fluid to the thermal capacity of the fluid and is used to characterize heat transfer in forced convective conditions, i.e. heat transfer by the motion of the fluid. It is also known as the Margoulis number.  $kB^{-1}$  is a measure for the different mechanisms that determine heat and momentum transfer (Thom, 1972). Molecular diffusion is the main mechanism for heat transfer near the surface. Momentum transfer depends on both viscous shear and the pressure gradient (Brutsaert, 1982). According to Su (2001)  $kB^{-1}$  cannot be negative, since the heat transfer coefficient can not be negative in any physical system. Many researchers, however, show a wide range of  $kB^{-1}$  values, which differ for the same land cover. Some authors even report negative values (Verhoef et al., 1997). Troufleau et al. (1997) concluded that site specific average  $kB^{-1}$  values are not representative for observed instantaneous variations. From a review of  $kB^{-1}$  calculations Verhoef et al. (1997) concluded that most of the equations are only valid on either bare soil or high vegetation cover. They should not be applied to sparse canopies. Furthermore they concluded that the equations are not able to describe the diurnal variation in  $kB^{-1}$  that has been observed. They concluded that the  $kB^{-1}$  concept should be avoided in models. Su et al. (2001), however improved the  $kB^{-1}$  concept, to overcome issues mentioned by Verhoef et al. (1997). SEBS determines the  $kB^{-1}$  value using a model of Su et al. (2001) which is a modification of Massman (1999a):

$$kB^{-1} = \frac{kC_d}{4C_t \frac{u_*}{u(h_c)} (1 - e^{-n/2})} f_c^2 + 2f_c^2 f_s^2 \frac{k \cdot \frac{u_*}{u(h_c)} \cdot \frac{z_{0M}}{h_c}}{C_t^*} + kB_s^{-1} f_s^2 \quad (4.42)$$

where  $f_s$  is the fraction of unvegetated soil ( $1-f_c$ ),  $C_d$  is the foliage drag coefficient (0.2),  $C_t$  is the heat transfer coefficient of the leaf (0.01),  $u(h_c)$  is the horizontal wind speed at the top of the canopy,  $h_c$  is the height of the canopy [m],  $C_t^*$  is the heat transfer coefficient of the soil, which is calculated with:

$$C_t^* = \text{Pr}^{-2/3} \text{Re}_*^{-1/2} \quad (4.43)$$

where Pr is the Prandtl number, which has been set to 0.71, a typical value for air (Massman, 1999b). It approximates the ratio of momentum diffusivity and thermal diffusivity.  $\text{Re}_*$  is the roughness Reynolds number, which is the ratio of inertial force to viscous forces. It is used to separate between laminar and turbulent flow. It is calculated with:

$$\text{Re}_* = \frac{h_s u_*}{\nu} \quad (4.44)$$

Where  $h_s$  [m] is the roughness height of the soil (typical values: 0.009-0.024 m),  $\nu$  is the kinematic viscosity of the air [ $\text{Pa} \cdot \text{s}$ ], which is calculated with (Massman, 1999b):

$$\nu = 1.327 \cdot 10^{-5} (p_0 / p) (T/T_0)^{1.81} \quad (4.45)$$

Where  $p$  [kPa] and  $T$  [K] are the ambient pressure and temperature respectively, and  $p_0 = 101.3$  kPa and  $T_0 = 273.15$  K.  $kB_s^{-1}$  in eq. 4.42 is  $kB^{-1}$  for bare soil surface, which is calculated following Brutsaert (1982):

$$kB_s^{-1} = 2.46(\text{Re}_s)^{1/4} - \ln(7.4) \quad (4.46)$$

The within-canopy wind speed profile extinction coefficient,  $n$ , needed in equation 4.42, can be calculated by:

$$n = \frac{C_d \cdot LAI}{2u_*^2 / u(b_c)^2} \quad (4.47)$$

where  $LAI$  is the Leaf Area Index.  $LAI$  is derived from  $NDVI$  (Su, 1996, 2000):

$$LAI = \sqrt{\left( NDVI \cdot \frac{1 + NDVI}{1 - NDVI} \right)} \quad (4.48)$$

Because  $NDVI$  saturates at high  $LAI$  values (see chapter 2, figure 2.4), eq. 4.48 is only valid for low vegetation covers. For high vegetation covers  $LAI$  is underestimated. In this case it is better to use field measurements of  $LAI$ .

Field estimates of roughness length of momentum transfer,  $z_{0M}$ , can be used in eq. 4.41. When field data is not available a lookup table with literature values can be used or a derivation from remote sensing images. In the SEBS model used here, the empirical relationship with  $NDVI$  is used (Su, 2001):

$$z_{0M} = 0.005 + 0.5 \cdot \left( \frac{NDVI}{\max(NDVI)} \right)^{2.5} \quad (4.49)$$

where  $\max(NDVI)$  is the maximum  $NDVI$  in the study area.

The height of the canopy,  $h_c$ , used in eq. 4.42 is derived with (Brutsaert, 1982):

$$h_c = \frac{z_{0M}}{0.136} \quad (4.50)$$

The displacement height,  $d_0$ , used in eq. 4.27 and 4.28 can be calculated with (Brutsaert, 1982):

$$d_0 = \frac{2}{3} h_c \quad (4.51)$$

#### 4.5.5 Energy balance at limiting cases

The energy balance at limiting cases is used to calculate the evaporative fraction (Su, 2002), from which the actual evapotranspiration is derived. The concept is illustrated in figure 4.10. At the dry-limit, soil moisture is limited and no evapotranspiration can take place. The latent heat flux  $\lambda E_{dry}$  [ $\text{W m}^{-2}$ ] will be zero and the sensible heat flux  $H_{dry}$  [ $\text{W m}^{-2}$ ] will have its maximum value. From eq. 4.12 we can derive:

$$\lambda E_{dry} = R_n - G_0 - H_{dry} \equiv 0 \quad (4.52)$$

$$H_{dry} = R_n - G_0$$

At the wet-limit, where the soil water supply is unlimited, evapotranspiration takes place at the potential rate:  $\lambda E_{wet}$  [ $\text{W m}^{-2}$ ]. The potential evaporation is only limited by the energy available under the given surface and atmospheric conditions. In that case  $H_{wet}$  [ $\text{W m}^{-2}$ ] is very low:

$$\lambda E_{wet} = R_n - G_0 - H_{wet}$$

$$H_{wet} = R_n - G_0 - \lambda E_{wet} \quad (4.53)$$

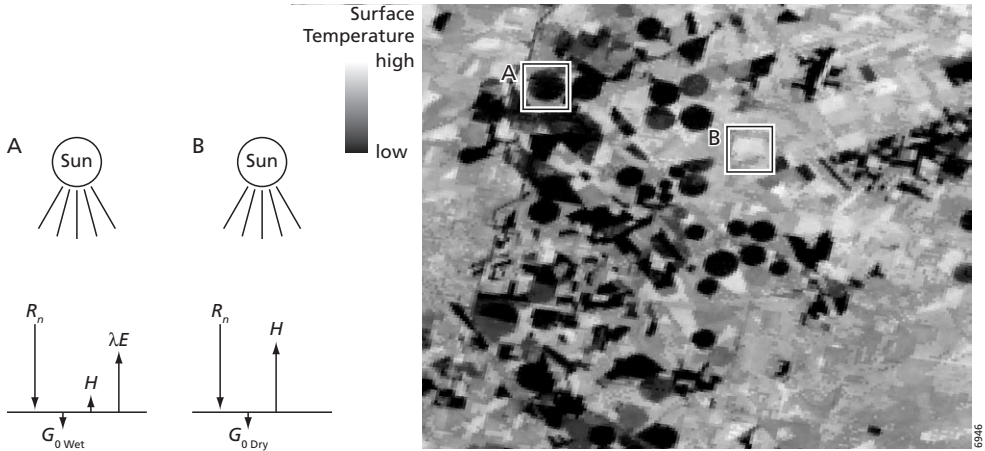


Figure 4.10 Concept of the surface energy balance at limiting cases illustrated for an ASTER surface temperature image of the Barrax field site in Spain (July 18<sup>th</sup> 2004, 11.004 UTC). The circular structures are pivot irrigation sites. Because the pivots are well irrigated, the evapotranspiration of the irrigated crops is maximal, causing a low sensible heat flux ( $H$ ), giving low temperatures in the image (A). This is the *wet-limit*. In the dry surrounding areas no moisture is present for evapotranspiration.  $\lambda E = 0$  and  $H$  is maximal (B). This is the *dry-limit*.

The ratio between the latent heat flux for the actual evapotranspiration and the wet-limit latent heat flux,  $\lambda E_{wet}$ , is called the relative evaporation  $\Lambda_r$  [-]. It is calculated with:

$$\Lambda_r = \frac{\lambda E}{\lambda E_{wet}} = 1 - \frac{\lambda E_{wet} - \lambda E}{\lambda E_{wet}} \quad (4.54)$$

When eq. 4.12, 4.52 and 4.53 are substituted in eq. 4.54,  $\Lambda_r$  can be expressed in terms of sensible heat flux,  $H$ :

$$\Lambda_r = 1 - \frac{H - H_{wet}}{H_{dry} - H_{wet}} \quad (4.55)$$

It is clear that the actual sensible heat flux  $H$ , used in eq. 4.28, is confined between the wet-limit  $H_{wet}$  and dry-limit  $H_{dry}$ .  $H_{dry}$  is calculated with eq. 4.52. The equation for the calculation of  $H_{wet}$  is derived from an equation similar to the Penman-Monteith combination equation (Monteith, 1965). Menenti (1984) derived the following equation for  $\lambda E$  by grouping the resistance terms into the bulk internal (or surface, or stomatal) resistances,  $r_i$  [ $s\ m^{-1}$ ], and the external (aerodynamic) resistances,  $r_e$  [ $s\ m^{-1}$ ], under the assumption that roughness lengths for heat and vapour transfer are equal (Brutsaert, 1982):

$$\lambda E = \frac{\Delta \cdot r_e \cdot (R_n - G_0) + \rho C_p \cdot (e_s - e_a)}{r_e \cdot (\gamma + \Delta) + \gamma \cdot r_i} \quad (4.56)$$

where  $\Delta$  [ $Pa\ K^{-1}$ ] is the rate of change of  $e_s$  with temperature and  $\gamma = 0.67\ Pa\ K^{-1}$  is the psychrometric constant. The variable  $r_e$  depends on the Monin-Obukhov length  $L$  (eq. 4.15),

which is also a function of friction velocity  $u_*$  and sensible heat flux  $H$  (eq. 4.27 and 4.28). When  $L$  and  $u_*$  are solved iteratively,  $r_e$  can be derived from eq. 4.28 as (Su, 2002):

$$r_e = \frac{1}{ku_*} \left[ \ln \left( \frac{z-d_0}{z_{0,b}} \right) - \Psi_b \left( \frac{z-d_0}{L} \right) + \Psi_b \left( \frac{z_{0,b}}{L} \right) \right] \quad (4.57)$$

Unlike the Penman-Monteith equation, eq. 4.56 is not only valid for vegetation, but also for bare soils when  $r_i$  is properly defined.  $r_i$ , however, is controlled by the soil moisture content. Because SEBS does not include data on soil moisture,  $r_i$  cannot be used directly in SEBS to estimate  $\lambda E$ . Because at the wet-limit  $r_i \equiv 0 \text{ s m}^{-1}$ ,  $H_{wet}$  can be derived from eq. 4.54, 4.55 and 4.56 (Su, 2002):

$$H_{wet} = \left( (R_n - G_0) - \frac{\rho C_p}{r_{ew}} \cdot \frac{e_s - e_a}{\gamma} \right) / \left( 1 + \frac{\Delta}{\gamma} \right) \quad (4.58)$$

where  $r_{ew} [\text{s m}^{-1}]$  is the external resistance at the wet-limit, which can be expressed similar to eq. 4.57:

$$r_{ew} = \frac{1}{ku_*} \left[ \ln \left( \frac{z-d_0}{z_{0,b}} \right) - \Psi_b \left( \frac{z-d_0}{L_w} \right) + \Psi_b \left( \frac{z_{0,b}}{L_w} \right) \right] \quad (4.59)$$

The wet-limit Monin-Obukhov length,  $L_w$  [m], is derived from eq. 4.15 as:

$$L_w = - \frac{\rho_w u_*^3}{kg \cdot 0.61 \cdot (R_n - G_0) / \lambda} \quad (4.60)$$

$\Lambda_r$  is solved from eq. 4.54 and used in the calculation of the evaporative fraction  $\Lambda$  [-]:

$$\Lambda = \frac{\lambda E}{R_n - G} = \frac{\Lambda_r \cdot \lambda E_{wet}}{R_n - G} \quad (4.61)$$

The latent heat flux  $\lambda E$  is calculated by inverting eq. 4.61:

$$\lambda E = \Lambda \cdot (R_n - G_0) \quad (4.62)$$

Using eq. 4.4 the actual evapotranspiration flux  $E$  [ $\text{m s}^{-1}$ ] is calculated for each model grid cell:

$$E = \frac{\lambda E}{\lambda \cdot \rho_w} \quad (4.63)$$

where  $\rho_w$  [ $\text{kg m}^{-3}$ ] is the density of water (e.g.  $998 \text{ kg m}^{-3}$  at  $25 \text{ }^\circ\text{C}$ ).

This chapter explained the theory of the surface energy balance and how it is modelled with SEBS. In the next chapter a procedure for the derivation of the inputs for SEBS from different satellite images will be proposed. In chapter 6 the model will be applied to the SPARC 2004 site in Barrax, Spain. An ASTER image and field measurements will provide the inputs. The model will be evaluated using measurements of fluxes at different locations in the study area. Furthermore, a sensitivity analysis will be done.



# 5 Acquisition of input data for SEBS from different satellite sensors and field measurements

## 5.1 Introduction

The SEBS model, described in the previous chapter, needs three sets of input data:

1. Data derived from remote sensing: albedo ( $\alpha$ , eq. 4.11), surface emissivity ( $\epsilon_s$ , eq. 4.11), surface temperature ( $T_s$ , eq. 4.11) and Normalized Difference Vegetation Index (NDVI, eq. 4.48 and 4.19) to derive surface roughness parameters. Instead of remote sensing data a land cover map can be used in conjunction with lookup tables for surface roughness parameters;
2. Meteorological parameters collected at a reference site: air pressure ( $p$ , eq. 4.20, 4.21 4.23, 4.25, 4.45), air temperature ( $T$ , eq. 4.18, 4.22), relative humidity ( $H_p$ , eq. 4.17) and wind speed ( $u$ , eq. 4.27);
3. Radiation data: global radiation (downward solar radiation,  $\kappa_s^\downarrow$ , eq. 4.11) and downward longwave radiation (eq. 4.10).

The objective of this chapter is to derive input data, mentioned under 1, from remote sensing. For each satellite sensor the derivation of temperature, emissivity and albedo is different. Here we present an operational preprocessing procedure for data from the Moderate Resolution Imaging Spectroradiometer (MODIS), Advanced Spaceborne Thermal Emission and Reflection Radiometer (ASTER) and Landsat Thematic Mapper 5 (Landsat TM5). The SEBS results for the latent heat flux calculated from input data derived from ASTER, Landsat TM5 and MODIS will be compared for the Sehouli study area.

As the accurate estimation of emissivity is important in surface energy balance modelling, the remote sensing derived emissivities will be compared with field measurements using the box-method (Rubio et al., 1997, 2003). The in-situ measurements of emissivity collected during a field campaign in 2004 in the Sehouli study area will be evaluated. The results will be compared with emissivity derived from the different satellite images.

SEBS input data mentioned under item 2 and 3 are derived from a meteorological station (figure 5.1).

## 5.2 Study area

The presented methods are evaluated using in-situ measurements in the Sehouli study area. First a description of the study area is given to facilitate the understanding of fluxes calculated with SEBS.

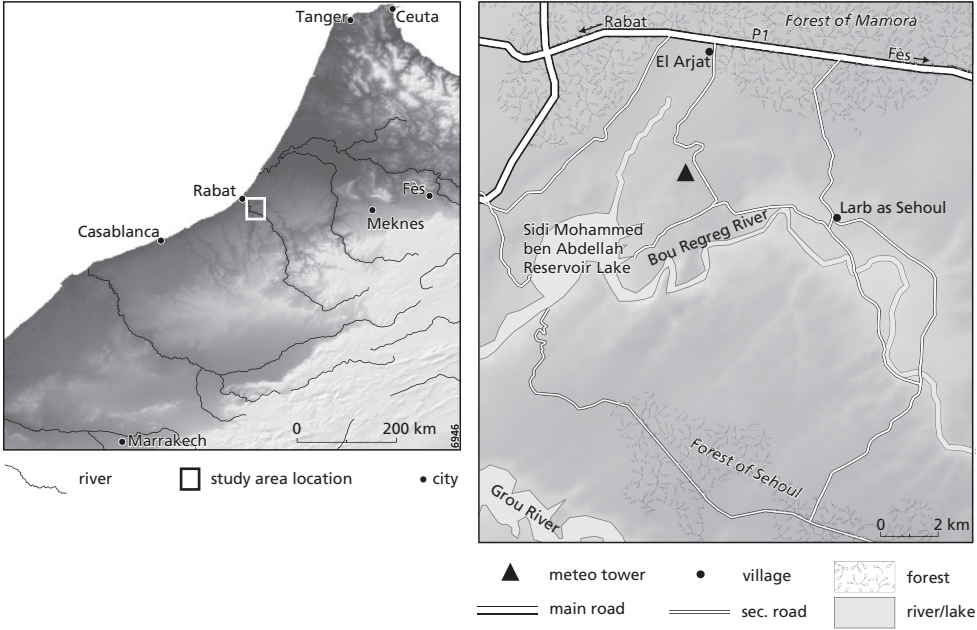


Figure 5.1 Location of the Sehoul study area.

The area is located at the Atlantic Meseta, in the community of Sehoul, province of Sala al Jadida, about 20 km south-east of Rabat (Morocco) (figure 5.1). The climate in this region is between sub-humid and semi-arid, with a mean annual precipitation of 500 to 550 mm. Most of the precipitation falls in winter and spring.

Most of the study area is a plateau used for agriculture. Land use in this area consists of rainfed wheat and maize, horticulture (mint, beans, peanuts and courgette) and orchards. Some fields are irrigated using traditional irrigation systems like submersion irrigation or drip irrigation (figure 5.2). The northern and western border of the study area is fringed by the Forest of Mamora, which extends further to the north and covers 144000 ha of plio-quaternary dunes with cork oak (*Quercus suber*). In the south of the study area another cork oak forest exists, the Forest of Sehoul (figure 5.3). Some communal grazing areas consist of short doum palm (*Hyphaene thebaica*). Furthermore, little *Eucalyptus* plantations for fire wood and construction can be found in the area. The Bou Regreg River and the Grou River cross the study area and supply water to the Sidi Mohammed ben Abdellah reservoir lake. Near the rivers and the reservoir lake, steep gullies have eroded the plateau of Sehoul. In the valley bottoms ephemeral streams and springs can be found.



A



B

Figure 5.2 (a) Submersion irrigation for mint, (b) drip irrigation.



Figure 5.3 Cork oak (*Quercus suber*) and doum palm (*Hyphaene thebaica*) at the Forest of Sehoul.

### 5.3 Methods

#### 5.3.1 Preprocessing Landsat TM5

Remote sensing input data, as required for the SEBS model, has been derived from a Landsat Thematic Mapper 5 image of September 15<sup>th</sup> 2003, 10:40 UTC. This is at the end of the dry season in the Sehoul study area. The Landsat TM5 sensor (LANDSAT, 2008) has a resolution of 30 meters in the visual, near- and shortwave infrared wavelengths and 120 meters in the thermal channel (table 5.1).

The pre-processing steps are summarized in the flowchart of figure 5.4. First the Level 1R Landsat TM5 image has been orthorectified, using a Digital Elevation Model (DEM) of the Shuttle Radar Topography Mission (SRTM (Rabus et al., 2003), see also chapter 3), and ground control points measured with a differential GPS.

Next, an atmospherical correction has been applied to the image. For the atmospherical correction of the thermal band (band 6) the mono-window algorithm has been used (Qin et al., 2001):

$$T_s = [a \cdot (1 - C - D) + (b \cdot (1 - C - D) + C + D) \cdot T_b - D \cdot T_a] / C$$

$$C = \epsilon_s \cdot \tau$$

$$D = (1 - \tau)[1 + (1 - \epsilon_s) \tau]$$
(5.1)

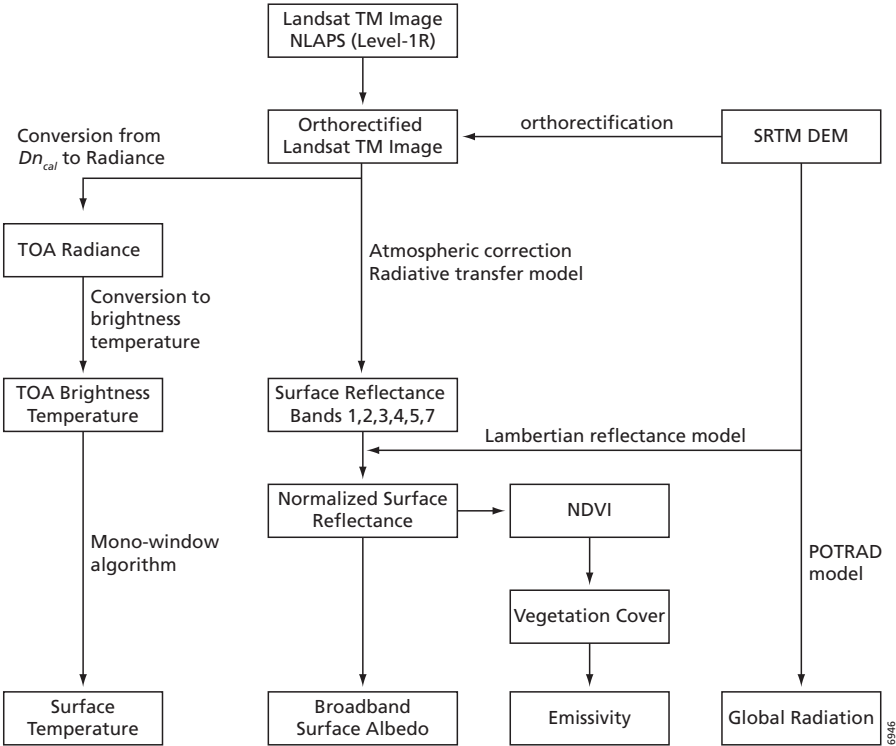


Figure 5.4 Flowchart of the pre-processing steps for Landsat TM5.

Table 5.1 Radiometric range of bands and resolution for the TM5 sensor (LANDSAT, 2008).  
 VIS = Visual, NIR = Near Infrared, TIR = Thermal Infrared, SWIR = Shortwave Infrared.

Band no.		Wavelength [ $\mu\text{m}$ ]	Resolution [m]
1	VIS	0.45-0.52	30
2		0.52-0.60	30
3		0.63-0.69	30
4	NIR	0.76-0.90	30
5		1.55-1.75	30
6	TIR	10.40-12.50	120
7	SWIR	2.08-2.35	30

where  $T_s$  [K] is the atmospherically corrected surface temperature,  $a$  and  $b$  are empirical parameters with values of respectively  $a = -67.355351$ ,  $b = 0.458606$ ,  $T_B$  [K] is the effective at-satellite brightness temperature,  $T_a$  [K] is the mean atmospheric temperature,  $\epsilon_s$  [-] is the surface emissivity and  $\tau$  [-] is the atmospheric transmissivity.

In order to calculate  $T_B$  the digital number (DN) values of band 6 should be converted to spectral radiance received by the sensor,  $L_\lambda$  [ $\text{W m}^{-2} \text{sr}^{-1} \mu\text{m}^{-1}$ ], using (Markham and Barker, 1986):

$$L_\lambda = 0.55158 \cdot DN + 1.2378 \quad (5.2)$$

Then,  $T_B$  can be calculated with:

$$T_B = \frac{K_2}{\ln\left(\frac{K_1}{L_\lambda} + 1\right)} \quad (5.3)$$

where  $K_1$  is calibration constant 1 in  $\text{W m}^{-2} \text{sr}^{-1} \mu\text{m}^{-1}$ , and  $K_2$  is calibration constant 2 in Kelvin. For Landsat TM5 the values for  $K_1$  and  $K_2$  are respectively 607.76 and 1260.56 (Markham and Barker, 1986).

$T_a$  has been calculated for a standard atmosphere, mid-latitude summer, using the following equation (Brutsaert, 1999):

$$T_a = 16.0110 + 0.92621 \cdot T \quad (5.4)$$

where  $T$  [K] is the air temperature at reference height. Atmospheric transmissivity,  $\tau$ , has been estimated with (Brutsaert, 1999):

$$\tau = 0.974290 - 0.08007 \cdot w \quad (5.5)$$

where  $w$  [ $\text{g cm}^{-2}$ ] is the water vapour content. The value of  $w$  has been derived from a meteorological station in the field.

The optical bands were atmospherically corrected using MODTRAN 4 (Anderson et al., 1999) in combination with atmospheric visibility and fixed water vapour amount, estimated from

the meteorological measurements. The reflection values have been topographically normalized with the SRTM DEM, using a Lambertian model (Smith et al., 1980; Colby, 1991).

Broadband shortwave surface albedo,  $\alpha_{sw}$ , has been calculated from the normalized reflection values of Landsat TM5 channels 1, 3, 4, 5 and 7, using the following equation (Liang, 2000):

$$\alpha_{sw} = 0.356 \alpha_1 + 0.130 \alpha_3 + 0.373 \alpha_4 + 0.085 \alpha_5 + 0.072 \alpha_7 - 0.0018 \quad (5.6)$$

where  $\alpha_n$  is the normalized reflectance of band  $n$ .

Surface emissivity,  $\epsilon_s$  [-], has been calculated accounting for vegetation cover (Caselles and Sobrino, 1989; Valor and Caselles, 1996):

$$\epsilon_s = \epsilon_v f_c + \epsilon_g (1 - f_c) + 4 \langle d\epsilon \rangle f_c (1 - f_c) \quad (5.7)$$

where  $f_c$  [-] is the fractional vegetation cover, and  $\epsilon_v$  and  $\epsilon_g$  are emissivity for full vegetation cover and bare soil in the 10.5 to 12.5  $\mu\text{m}$  range of Landsat TM5 band 6.  $\epsilon_v = 0.985$  and  $\epsilon_g = 0.960$  were used (Caselles and Sobrino, 1989). The vegetation structure parameter  $\langle d\epsilon \rangle$  was assumed to be zero, because most of the agricultural part of the study area has a low vegetation cover at the end of the dry season. For the cork oak forests  $\langle d\epsilon \rangle$  can be large, but also here it is assumed that  $\langle d\epsilon \rangle = 0$ , because no data exists for vegetation structure effects on emissivity for cork oak forest. This will probably give larger errors in the emissivities calculated for cork oak forest than for the agricultural area.

The value of  $f_c$  is derived from NDVI, using the following equation (Carlson and Ripley, 1997):

$$f_c = \left( \frac{NDVI - NDVI_{\min}}{NDVI_{\max} - NDVI_{\min}} \right)^2 \quad (5.8)$$

where  $NDVI_{\min}$  is the NDVI for bare soil and  $NDVI_{\max}$  is the NDVI for full vegetation cover.

Downward solar radiation has been calculated using the POTRAD model (Van Dam, 2000, 2001) in combination with the SRTM DEM. The POTRAD model input variables are latitude, DEM, date, time and atmospheric transmissivity. The atmospheric transmissivity parameter has been calibrated with pyranometer data from the meteorological station.

The resulting input maps for SEBS that have a resolution of 30 m pixels have been resampled to 120 m pixels by averaging 16 pixels, which is the resolution of the thermal band that is used to derive surface temperature.

### 5.3.2 Preprocessing ASTER

The ASTER data (ASTER, 2008) has been acquired on October 20<sup>th</sup> 2004, 11:13:42 UTC. The ASTER sensor system has 3 bands of 15 m resolution in the visible and near infrared region, 6 bands of 30 m resolution in the shortwave infrared region and 5 bands of 90 m resolution in the thermal infrared region (table 5.2).

The ASTER On-Demand L2 Surface Kinetic Temperature (AST\_08) product provided the surface temperature in Kelvin. This ASTER product has been calculated from the five thermal infrared bands between 8 and 12  $\mu\text{m}$  using the Temperature-Emissivity Separation (TES)

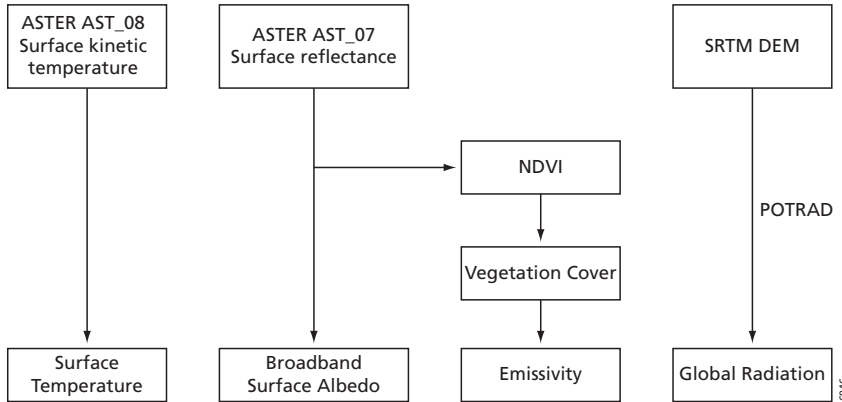


Figure 5.5 Flowchart of the pre-processing steps for ASTER.

algorithm (Gillespie et al., 1998). We refer to Gillespie et al. (1999) for a detailed description of the TES algorithm.

The derivation of other SEBS inputs is summarized in the flowchart of figure 5.5.

Broadband surface albedo,  $\alpha_{sw}$ , has been calculated from the ASTER On-Demand L2 Surface Reflectance products (AST\_07VD, AST\_07SD), using the empirical relation of Liang (2000):

$$\alpha_{sw} = 0.484 \alpha_1 + 0.335 \alpha_3 - 0.324 \alpha_5 + 0.551 \alpha_6 + 0.305 \alpha_8 - 0.367 \alpha_9 - 0.0015 \quad (5.9)$$

where  $\alpha_n$  is the reflectance of ASTER band  $n$ .

The ASTER surface reflectance images in the visible and near-infrared (VNIR) and shortwave-infrared (SWIR) channels have been atmospherically corrected. This correction uses a look-up table approach with data derived from a Gauss-Seidel iteration radiative transfer code (RTC) (Herman and Browning, 1965). In this calculation the following parameters are used: solar zenith angle, satellite view angle, relative azimuth angle between the satellite and sun, molecular scattering optical depth, aerosol scattering optical depth, aerosol single scatter albedo, aerosol size distribution parameter, and surface reflectance. Atmospheric scattering and optical depths and aerosol parameters are provided by other sources than ASTER (Thome, 1999).

The input of ozone data is provided by the NCEP/TOVS (National Centers for Environmental Prediction/TIROS (Television & Infrared Observation Satellite) Operational Vertical Sounder) that acquire data from a NOAA satellite two times a day. Aerosol input data is provided by the Aerosol Climatology data of NRL (Naval Research Laboratory). Data on temperature, atmospheric pressure and moisture profile are provided by the NCEP-GDAS (Global Data Assimilation System).

For a detailed description of the process of deriving surface reflectance for ASTER VNIR and SWIR bands, the reader is referred to Thome (1999).

In the data acquired by the ASTER SWIR sensor the crosstalk (XT) phenomenon can be observed in places where there is a sharp contrast in DN values, like in coastal areas. XT causes a dispersion of the incident electromagnetic radiation and leaks to other bands. For ASTER

SWIR this is mainly a leakage from band 4 to bands 5 and 9. Recently ASTER Surface Reflectance products are available that have been XT corrected (AST07\_XTS).

Emissivity and global radiation have been calculated in the same way as with the Landsat TM 5 image.

The resulting input maps for SEBS have been resampled to 90 m pixels by area-averaging 36 15 m pixels, which is the resolution of the surface temperature product.

**5.3.3 Preprocessing MODIS**

The Moderate Resolution Imaging Spectroradiometer (MODIS) has 36 spectral channels: 2 bands at 250 meter, 5 bands at 500 meter and 29 bands at 1000 m resolution (table 5.3).

*Table 5.2 Radiometric range of bands and resolution for the ASTER sensor (Abrams et al., 2002; ASTER, 2008). VNIR = Visual and Near Infrared, SWIR = Shortwave Infrared and TIR = Thermal Infrared.*

Band no.		Wavelength [μm]	Resolution [m]
1	VNIR	0.52-0.60	15
2		0.63-0.69	15
3N/3B		0.76-0.86	15
4	SWIR	1.60-1.70	30
5		2.145-2.185	30
6		2.185-2.225	30
7		2.235-2.285	30
8		2.295-2.365	30
9		2.360-2.430	30
10	TIR	8.125-8.475	90
11		8.475-8.825	90
12		8.925-9.275	90
13		10.25-10.95	90
14		10.95-11.65	90

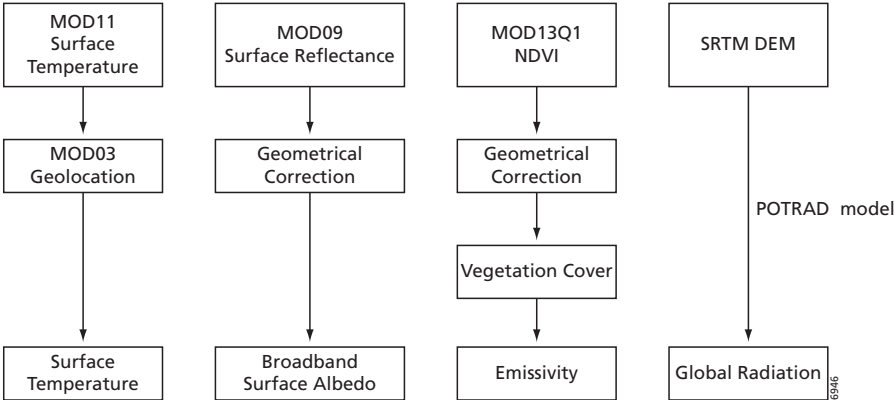


*Figure 5.6 Flowchart of the pre-processing steps for MODIS.*

In order to use MODIS data as an input for SEBS, different dataproducts provided by NASA's Land Processes Distributed Active Archive Center (LPDAAC) have been used as indicated in the flowchart of figure 5.6.

The Land Surface Temperature/Emissivity 5-min L2 Swath 1 km (MOD11\_L2) product provides data on surface temperature at 1000 m resolution. The temperature data has been projected to a sinusoidal projection, using the ModisSwathTool (LPDAAC, 2006) and the Geolocation Fields 5-Min L1A Swath 1km data (MOD03). The MOD03 product contains data

*Table 5.3* Radiometric range of bands and resolution for the MODIS sensor (MODIS, 2008).

Band no.	Wavelength [ $\mu\text{m}$ ]	Resolution [m]
1	620-670	250
2	841-876	250
3	459-479	500
4	545-565	500
5	1230-1250	500
6	1628-1652	500
7	2105-2155	500
8	405-420	1000
9	438-448	1000
10	483-493	1000
11	526-536	1000
12	546-556	1000
13	662-672	1000
14	673-683	1000
15	743-753	1000
16	862-877	1000
17	890-920	1000
18	931-941	1000
19	915-965	1000
20	3.660-3.840	1000
21	3.929-3.989	1000
22	3.929-3.989	1000
23	4.020-4.080	1000
24	4.433-4.498	1000
25	4.482-4.549	1000
26	1360-1390	1000
27	6.535-6.895	1000
28	7.175-7.475	1000
29	8.400-8.700	1000
30	9.580-9.880	1000
31	10.780-11.280	1000
32	11.770-12.270	1000
33	13.185-13.485	1000
34	13.485-13.785	1000
35	13.785-14.085	1000
36	14.085-14.385	1000

on geodetic latitude and longitude, surface height above geoid, solar zenith and azimuth angles, satellite zenith and azimuth angles, and a land/sea mask for each 1 km sample.

Broadband surface albedo,  $\alpha_{sw}$ , has been calculated from Surface Reflectance Daily L2G Global 250 m data in the VNIR wavelengths (MOD09GQK) and 500 m data in the SWIR wavelengths (MOD09GHK) using the empirical relation of Liang (2000):

$$\alpha_{sw} = 0.160\alpha_1 + 0.291\alpha_2 + 0.243\alpha_3 + 0.116\alpha_4 + 0.112\alpha_5 + 0.081\alpha_7 - 0.0015 \quad (5.10)$$

where  $\alpha_n$  is the reflectance of band  $n$ .

Emissivity has been derived from the NDVI channel in the Vegetation Indices 16-Day L3 Global 250 m (MOD13Q1) product using the same equations as with the Landsat TM5 image (eq. 5.7 and 5.8). Also the same derivation of global radiation has been used.

The resulting input maps for SEBS have been resampled to 1000 m pixels, which is the resolution of the surface temperature product.

### 5.3.4 Field measurement of emissivity

Surface emissivity in the 8-14  $\mu\text{m}$  window is important in the calculation of the surface energy balance, because it determines the emission of longwave radiation from the earth's surface into space. The net longwave radiation ( $L_n$  [ $\text{W m}^{-2}$ ]) can be written as (Rubio et al., 1997):

$$L_n = \epsilon_s \sigma T_s^4 + (1 - \epsilon_s) L \downarrow \quad (5.11)$$

where  $\epsilon_s$  [-] is the emissivity of the surface,  $\sigma$  is the Stefan-Boltzmann constant,  $T_s$  [K] is the surface temperature and  $L \downarrow$  is the downward longwave radiation coming from the atmosphere. The equation assumes a Lambertian emission. Since  $L_n$  is proportional with  $\epsilon_s$ , a 10% error in  $\epsilon_s$  gives a 10% error in  $L_n$  (Ogawa et al., 2003).

The radiance registered at the satellite sensor is a combination of temperature and emissivity and affected by the atmosphere. Therefore it is impossible to separate temperature and emissivity without knowledge of the thermal radiative properties of the surface (Rubio et al., 1997). This means that the accurate estimation of surface emissivity at the satellite pixel level is important for satellite-based models of the surface energy balance.

Some surface energy balance studies use a constant and uniform emissivity or lookup tables to relate data from a spectral library (Salisbury and D'Aria, 1992) to land cover maps. These methods ignore the spatial variability of emissivity between individual pixels.

Many methods have been developed to estimate emissivity from satellite imagery. In the previous sections emissivity has been derived from an empirical relation with fractional cover, which has been derived from NDVI. Other frequently used methods to derive emissivity from satellite images are NEM (Gillespie, 1986), ANEM (Coll et al., 2003), TES (Gillespie et al., 1998), MMD (Schmugge et al., 1998) and split-window techniques (Becker and Li, 1990; Sobrino et al., 1994). Less research has been done in the estimation of broadband, or window, emissivity. The use of narrow band emissivity instead of broad band emissivity can lead to errors up to 100  $\text{W m}^{-2}$  in the calculation of net longwave radiation (Wang et al., 2005). Regression functions for broadband emissivity have been derived for ASTER (Ogawa et al., 2002, 2003) and MODIS (Wang et al., 2005), but need further validation over a broad range of land cover types.

Field measurement of emissivity is difficult and the extrapolation of in-situ measurements to effective values for heterogeneous pixels of a remote sensing image is an important issue (Rubio et al., 1997). Also the relationship between field measurements with broadband radiometers and the narrow bands within remote sensing data is difficult.

The most used field method for the in situ determination of emissivity of natural surfaces is the so-called box-method. There are two variants of this method: the two-lid (Buettner and Kern, 1965) and the one-lid (Combs et al., 1965) box-method. Here the two-lid box method will be explained and applied to the Sehoul study area.

The two-lid box method has originally been developed for laboratory measurements of emissivity (Buettner and Kern, 1965; Dana, 1969), but Sobrino and Caselles (1993) proposed the application to in-situ field measurements. Rubio et al. (1997) reported emissivity values for different vegetation covers and soils in a 8-14  $\mu\text{m}$  bandwidth that have been derived from in-situ measurements with the one-lid and two-lid box method. Rubio et al. (2003) improved the method and added new measurements of vegetation and soils in the 8-14  $\mu\text{m}$  bandwidth and other narrow bandwidths.

The two-lid box method (figure 5.7) uses a sequence of measurements of radiance in a box. Two interchangeable lids are used to cover the top of the box: a 'hot lid' and a 'cold lid'. Ideally, the interior of the box and the two cold lids are perfect specular reflectors, i.e. with  $\epsilon_c = 0$ , and the hot lid is a perfect blackbody Lambertian emitter, i.e. with  $\epsilon_b = 1$ . In reality the interior of the box and the cold lid are made of polished aluminium with  $\epsilon_c \approx 0.03$ . The hot lid consists of rough anodized aluminium coated with black paint (NEXTEL-Velvet-Coating 811-21) with  $\epsilon_b \approx 0.98$ . All sides and lids of the box are covered with 4 cm thick sheets of isolation material (Roofmate styrofoam/polystyrene) to prevent environmental disturbances during the measurement. The hot lid has a heating system that consists of six heating elements of approximately 12 W each (foil type with adhesive backing), powered by a 12V-40Ah car battery. The temperature of the hot lid



*Figure 5.7* The two-lid box method in use in the Sehoul study area (Morocco).

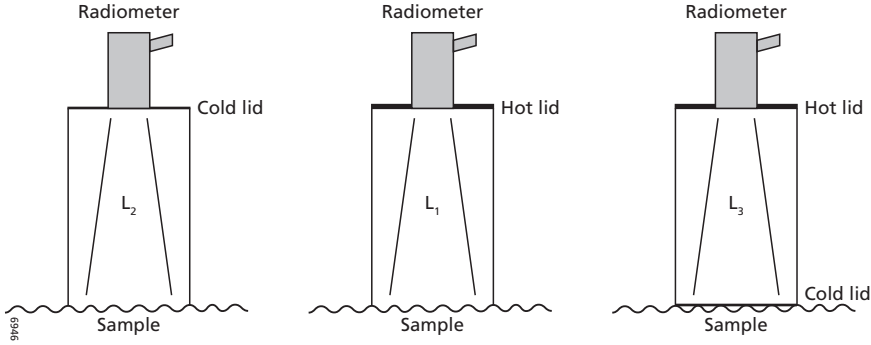


Figure 5.8 Procedure for measuring emissivity with the two-lid box method. The sequence of measurements is from left to right ( $L_2, L_1, L_3$ ). Source: Rubio et al. (1997).

can be controlled by an electronic temperature controller (Carel IR32D2L000) in combination with a thermocouple wire (J-type) taped to the hot lid. The hot lid and one of the cold lids have a hole through which a sequence of three measurements is made using a hand-held infrared radiometer (figure 5.8). The cold lid without a hole has been scoured in a small area in the centre of the lid to prevent the narcissus effect (Rubio et al., 2003), i.e. the effect of measuring the radiation emitted by the infrared radiometer itself.

When a sample is measured by a hand-held radiometer, the measured radiance is a combination of the sample kinetic temperature, its emissivity and the environmental downwelling longwave radiance that is reflected from the sample (eq. 5.11, Rubio et al., 2003). In order to know the emissivity, three measurements are needed under controlled conditions.

The measurements can be done with two persons, but works most efficiently with three persons. One person makes the instantaneous measurements with the hand-held radiometer, another person moves the box and changes the lids and a third person writes down the measured sequence.

The measurement procedure is as follows (Rubio et al., 1997, 2003) (figure 5.8). First the hot lid is heated to 30 K above the sample temperature. The box is placed over the sample in order to isolate the sample from its surroundings. The specular walls translate the radiance, but do not contribute to the signal. The first measurement,  $L_2$ , is made through the cold lid at the top of the box. In this case, the system box-sample is assumed to be equivalent to a black body with the sample's temperature. For the next measurement,  $L_1$ , the cold lid is replaced by the hot lid. In this case the radiance emitted by the sample and by the environmental irradiance is simulated. The environmental irradiance is the radiance emitted by the hot lid and reflected by the sample towards the sensor. For the last measurement,  $L_3$ , the whole box, still covered with the hot lid, is placed over the cold lid without a hole. In this case the system represents a black body with the hot lid temperature.

Based on this sequence of measurements, emissivity can be calculated for an ideal box (i.e.  $\epsilon_c = 0$  and  $\epsilon_b = 1$ ) with the following equation (Conaway and Van Bavel, 1967; Dana, 1969):

$$\epsilon_0 = \frac{L_3 - L_1}{L_3 - L_2} \quad (5.12)$$

Because a real box is not ideal, a fourth measurement is needed to calculate a corrective factor,  $\delta\epsilon$ , that depends on the geometry of the box, the temperature of the polished aluminium and the emissivities of the box and its lids (Rubio et al., 1997). It can be calculated with:

$$\delta\epsilon = (1 - \epsilon_0) \left\{ 1 - \frac{(L_3 - L_2)(1 - \epsilon_c)}{(L_3 - L_2) - (L_3 - L_4)P + (L_2 - L_4)Q} \right\} \tag{5.13}$$

Rubio et al. (1997) have determined the box specific parameters  $P = 0.1460$  and  $Q = 0.2921$ . In this study the same values have been used, because the measurements have been performed with a box with the same dimensions and emissivity properties. The value for  $L_4$  can be obtained by a fourth measurement, for which we replace the hot lid directly after the third measurement with the cold lid and measure the radiance emitted from the polished aluminium of the walls of the box.

The emissivity of the sample can now be calculated as:

$$\epsilon_s = \epsilon_0 + \delta\epsilon \tag{5.14}$$

An important assumption in this method is that the kinetic temperatures of the box walls, lids and the sample do not change during the measurement sequence (Rubio et al., 2003). Therefore the consecutive measurements should be taken quickly and repeated many times to calculate proper average values and standard deviations of the sample emissivity.

In this research a Raytek Raynger ST 60 infrared thermometer has been used, which measures the radiance temperature (when emissivity is set to 1) within the 8-14  $\mu\text{m}$  bandwidth. In order to convert the measured temperature to radiance, first the temperature has been

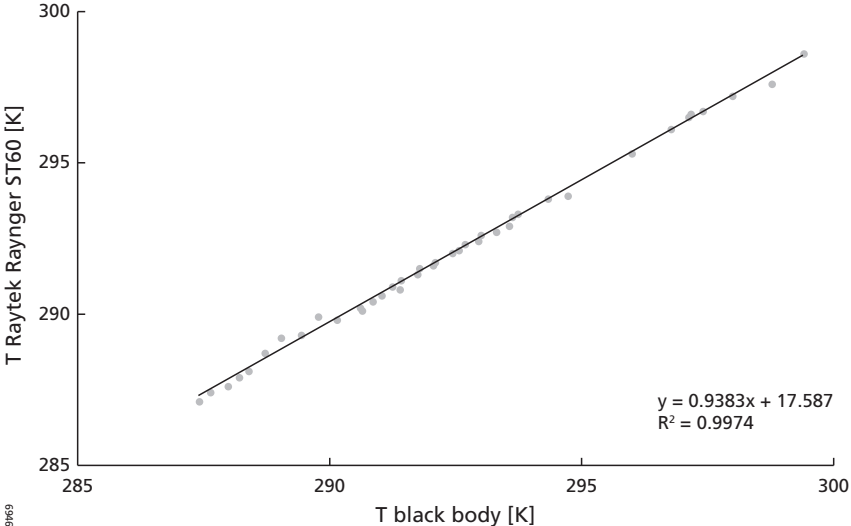


Figure 5.9 Calibration curve between a black body and the Raytek Raynger ST60. Measurements are derived from laboratory experiments ( $n = 40$ ) at the Thermodynamics Department, Faculty of Physics, University of Valencia (R. Niclos & J. van der Kwast).

calibrated with a black body. Figure 5.9 shows the calibration curve. The RMSE is 0.5 K and the  $r^2$  is 0.9974.

Next, the Planck's function (eq. 4.3, chapter 4) should be approximated for the spectral interval of the used infrared thermometer, i.e. 8-14  $\mu\text{m}$ . Radiance ( $L_{8-14}$  [ $\text{W m}^{-3} \text{sr}^{-1}$ ]) and measured blackbody temperature ( $T_b$  [K]) has been fitted to the following equation:

$$L_{8-14} = p \cdot e^{\left(\frac{-q}{T_b^s}\right)} \tag{5.15}$$

The coefficients  $p$ ,  $q$  and  $s$  have been determined by a regression between the band integrated radiance, taking into account the spectral response function of the instrument and temperature in Kelvin.

The band-integrated radiance is defined as:

$$L_{8-14} = \frac{\int_8^{14} L_\lambda \cdot f(\lambda) \cdot d\lambda}{\int_8^{14} f(\lambda) \cdot d\lambda} \tag{5.16}$$

where  $f(\lambda)$  is the spectral response function, or filter function that is provided by the manufacturer (Raytek cooperation). The response function is given in figure 5.10. The total spectral filtering which is applied to the signal (including lens transmission, detector substrate characteristics, electronic circuit filters) is considered proprietary of the manufacturer and could not be included for determination of the conversion function. It is assumed that this has a negligible effect on the determination of the measured radiation.

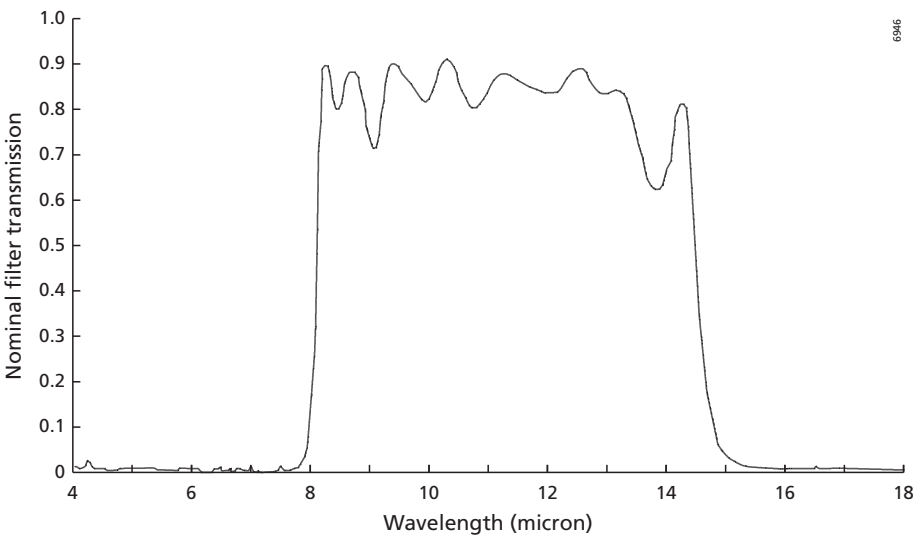


Figure 5.10 Filter function (Nominal bandpass curve) for the optical filter of the Raytek ST60. Source: Raytek cooperation.

A lookup table of band-integrated radiances for different temperatures has been calculated within the temperature range from 240-340 K in steps of 0.1 K. The coefficients of eq. 5.15 are finally determined by a regression between the band-integrated radiances and temperatures in the lookup table, following the expression in eq. 5.15. It has been determined that  $p = (1.07 \pm 0.02) \cdot 10^9 \text{ W m}^{-3} \text{ sr}^{-1}$ ,  $q = 1011 \pm 19$ , and  $s = 0.939 \pm 0.004$  with an  $r^2$  of 0.9999.

Figure 5.11 shows that eq. 5.15 with these coefficients gives an error that can be significant in the range used in the field measurements. Therefore a second order correction function,  $\delta L$ , has been calculated from the residuals. This resulted in:

$$\delta L = -0.0003T^2 + 0.19T - 27.595 \tag{5.17}$$

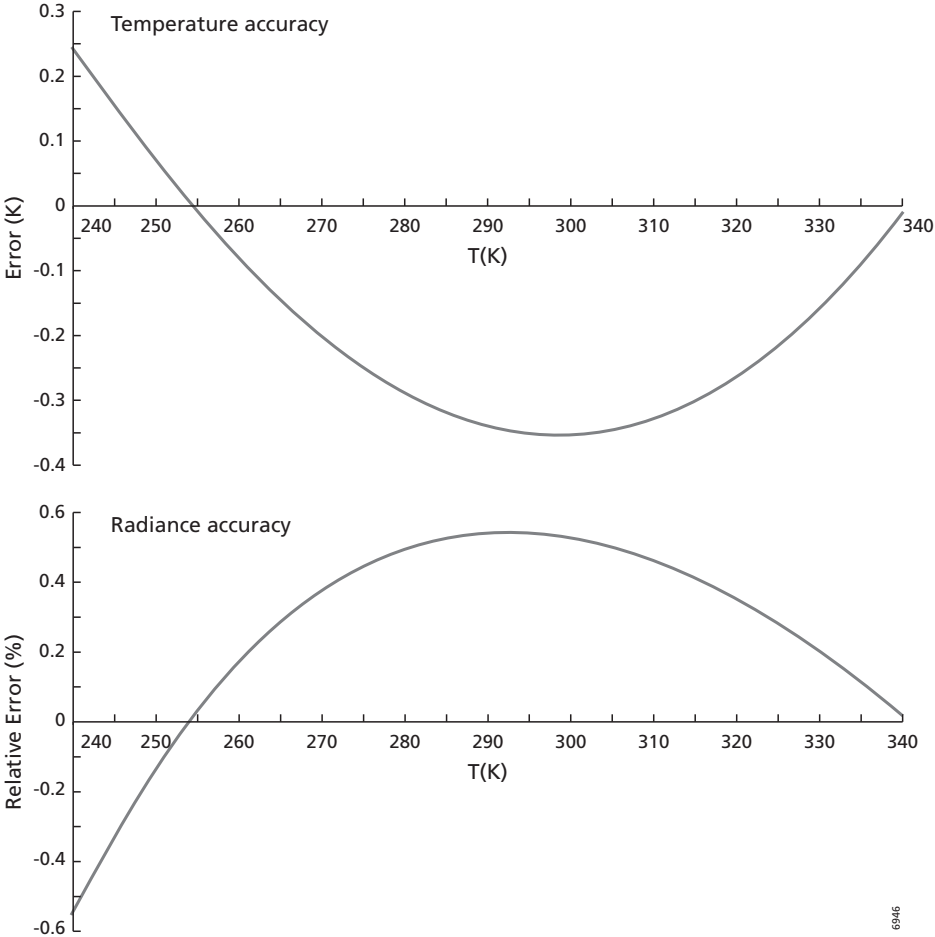


Figure 5.11 Temperature (a) and radiance (b) error when using eq. 5.18. Source: J. Manuel (Thermodynamics Department, Faculty of Physics, University of Valencia).

Combined with eq. 5.15 and the derived coefficients the equation to convert measured radiance temperature to band integrated radiance becomes:

$$L_{8-14} = 1.07 \cdot e^{\left(\frac{-1011}{T_b^{0.939}}\right)} + \delta L \quad (5.18)$$

This gives an  $r^2$  of 0.9932.  $T_b$  is the calibrated temperature measured with the infrared thermometer.

Now the infrared thermometer can be used with the two-lid box method to measure surface emissivity of soils and low vegetation. For high vegetation the composition should be simulated by making a bed of branches and leaves at the bottom of the box.

## 5.4 Results & Discussion

### 5.4.1 SEBS

The SEBS model has been run with the input data generated from the different satellite sensors. Additionally, meteorological data from a field station in the Sehoul study area has been used. The output of the SEBS model consists of maps representing net radiation, soil heat flux, sensible heat flux, latent heat flux, relative evaporation, evaporative fraction and actual evapotranspiration flux at the moment of satellite overpass. The spatial variability of the latent heat flux calculated with SEBS for the different satellite images will be discussed in detail. The actual evapotranspiration flux, which can be used in hydrological models, follows the same patterns.

The spatial variability of latent heat flux shows a clear relationship with land cover and topography for ASTER (figure 5.12a) and Landsat TM5 (figure 5.12b). Levees, wet valleys and irrigated fields have the largest latent heat flux, followed by the Forest of Mamora in the north of the study area and the Forest of Sehoul near the Grou River. Bare soils and fallow land have the lowest latent heat flux. Slopes, which are exposed to the south are dryer and consequently have a lower latent heat flux than slopes with an exposition to the north.

In the case of MODIS (figure 5.12c) the resolution of 1000 m makes it difficult to interpret the results at the scale of the Sehoul study area. Furthermore, missing pixels, caused by invalid temperature values due to cloud cover, disturb the pattern. In general coarse resolution images have less spatial variability than fine resolution images, because of averaging effects. In this case, however, the spatial variability of MODIS is larger, probably because of the large water bodies in the study area.

### 5.4.2 Emissivity

Figure 5.13 shows the emissivity derived from ASTER, Landsat TM5 and MODIS using the empirical relationship with NDVI (eq. 5.7). The spatial patterns in the results for the different satellite images are comparable: a high emissivity for semi-natural vegetation and a low emissivity for bare soils. The high resolution of ASTER and Landsat TM5 reveals the high emissivities for individual irrigated fields and valley bottoms.

Emissivity has been measured at seven locations in the study area, using the two-lid box method. At these sites repeated measurements have been made. Only emissivities between 0.9 and 1.0 have been selected, because they fall in the expected range for the measured surfaces. Furthermore, only the measurements in which  $L_3 > L_1 > L_2$  have been used. Measurements that

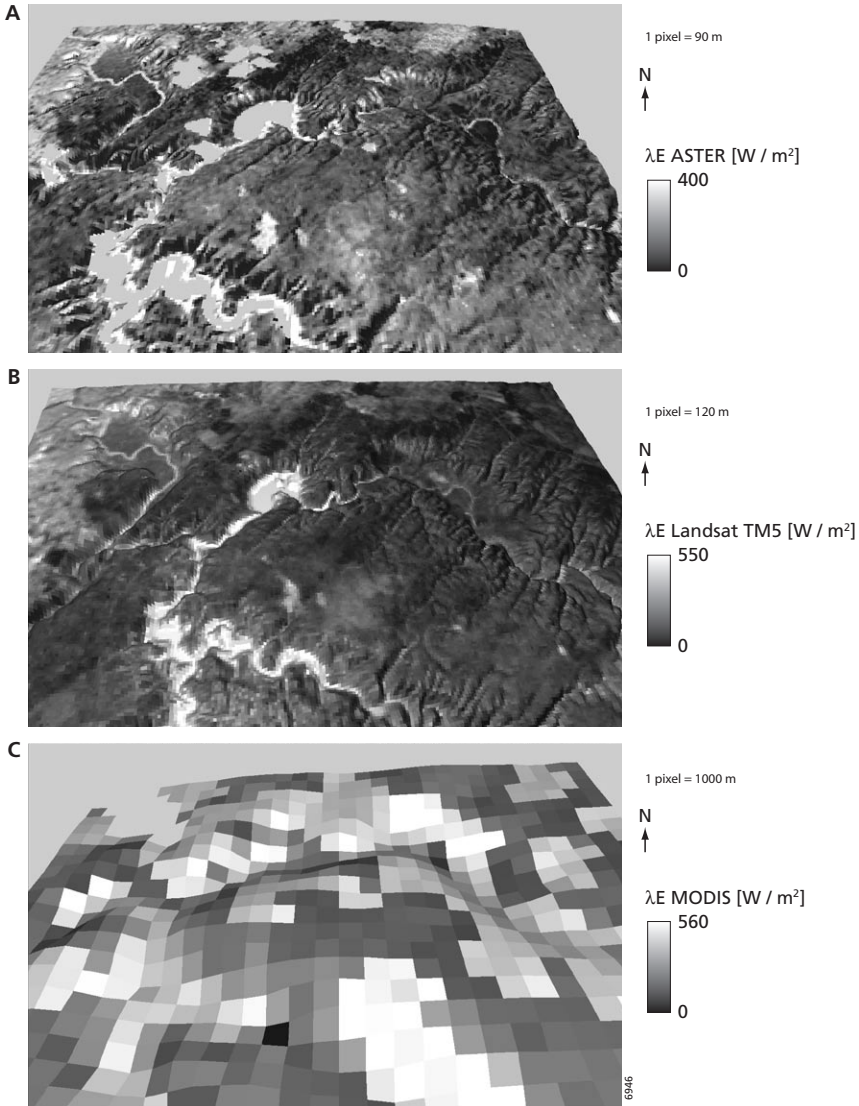


Figure 5.12 Latent heat flux calculated with SEBS for (a) ASTER (October 20<sup>th</sup> 2004), (b) Landsat TM5 (September 15<sup>th</sup> 2003) and (c) MODIS (October 20<sup>th</sup> 2004).

do not meet this requirement have been caused by changing temperatures of the sample, box and/or the lids during the measurement sequence. Because ambient temperatures are high, it is hard to heat the lid to 30 K above this temperature and keep the temperature of the lid constant during the measurements.

Furthermore,  $L_4$  should be less than  $L_2$ , but this selection has not been applied since many measurements showed  $L_4 > L_2$  because the box and cold lids had been warmed during the measurements. Therefore, in these cases the correction described in eq. 5.13 could not be applied.

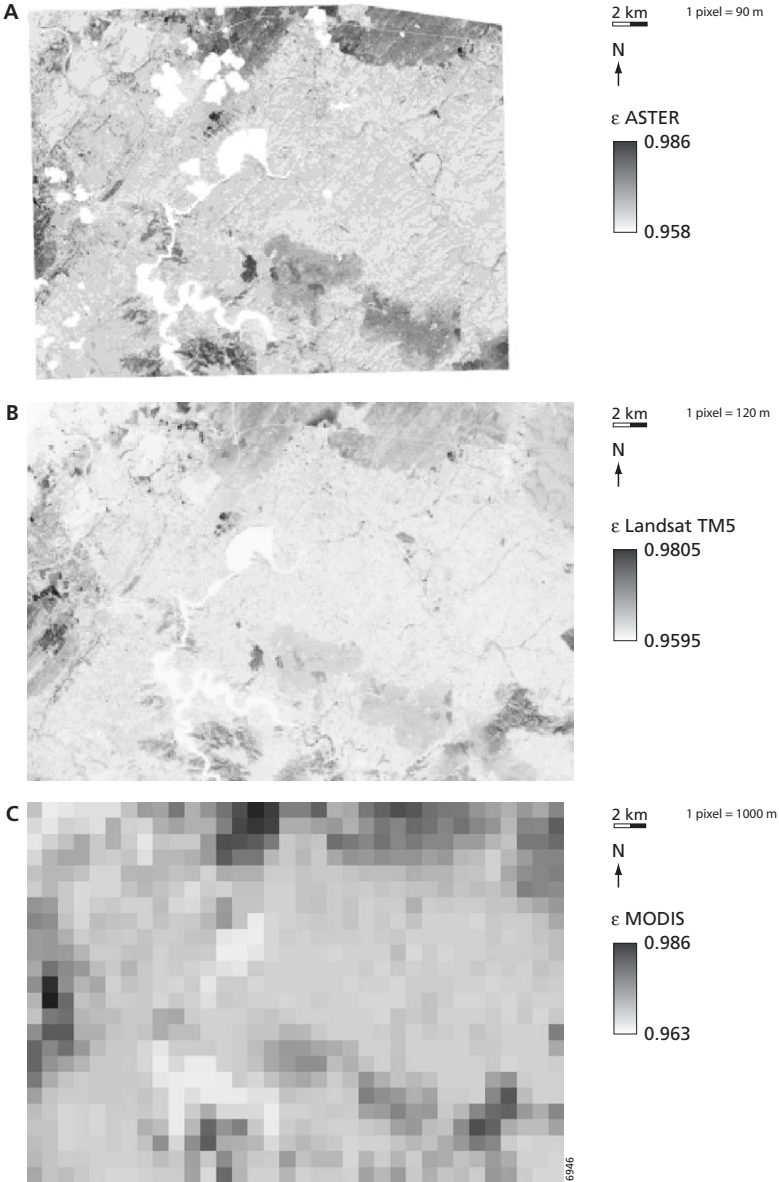


Figure 5.13 Results of the empirical derivation of emissivity for (a) ASTER (October 20<sup>th</sup> 2004), (b) Landsat TM5 (September 15<sup>th</sup> 2003) and (c) MODIS (October 20<sup>th</sup> 2004).

Table 5.4 shows a comparison between remote sensing derived emissivities and field measurements. Sometimes a number of field locations fall within one pixel of one or more satellite images. Because the satellite pixels have a large surface area, their emissivities are a mix of different land cover types. It can be seen that ASTER and Landsat give comparable results with

an RMSE of 0.002 and are correlated with a  $r^2$  of 0.59. The emissivities calculated from MODIS are slightly higher on average. The correlation with ASTER ( $r^2 = 0.20$ ) and Landsat ( $r^2 = 0.25$ ) is lower. Emissivities derived from the image are not correlated with field measurements of emissivity. Also, the field measurements always give a lower emissivity. The differences between field measurements and the remote sensing derived emissivities are caused by a combination of factors including: measurement errors, differences in support and short range variation and non-linearity.

The standard deviations of the field measurements are high ( $\sigma > 0.02$ ) except for the *sols fersiallitiques lessivé* and *sol fersiallitique lessivé à galets* (see chapter 8 for a description of soil types in the Sehoul study area). This is larger than errors reported by Rubio et al. (1997, 2003), who claim that this method can be used to measure emissivities with a standard deviation less than 0.6%.

Such a low standard deviation is probably the case in stable or controlled environments and with a different sampling strategy. In this study measurements were done at different locations within a land cover or soil type. Therefore, the reported standard deviation takes into account the variability within a plot. Another measurement strategy is to select a representative point in a land cover or soil type and to repeat measurements at this point many times. The standard deviations will be much lower, but do not represent the variability of emissivity within a larger area.

Upscaling of the highly variable emissivity by statistical techniques like kriging, would require many measurements at different locations, which is not feasible.

## 5.5 Conclusions

A procedure has been proposed for the derivation of input data for SEBS from three different satellite images. It is possible to derive albedo, emissivity, temperature and vegetation cover for ASTER, Landsat TM5 and MODIS images with algorithms found in literature and products that are available from NASA's Land Processes Distributed Active Archive Center (LP DAAC).

*Table 5.4* Comparison between emissivities derived from ASTER, Landsat TM5 and MODIS using the empirical relation with NDVI (eq. 5.7) and field measurements of emissivity using the box method. See chapter 8 for a description of the soil types.

	ASTER	Landsat TM5	MODIS	Box ( $\epsilon \pm \sigma$ )
Mint	0.965	0.963	0.965	$0.949 \pm 0.020$
Sols fersiallitiques lessivé	0.966	0.963	0.965	$0.951 \pm 0.009$
Sols isohumique gris couvrant les sols fersiallitiques sableux lessivé	0.962	0.961	0.965	$0.955 \pm 0.025$
Sols isohumique gris couvrant les sols fersiallitiques sableux lessivé	0.962	0.961	0.965	$0.943 \pm 0.021$
Sol fersiallitique lessivé à galets	0.962	0.961	0.964	$0.964 \pm 0.005$
Semi natural vegetation (Doum)	0.961	0.961	0.963	$0.950 \pm 0.024$
Wet valley	0.965	0.961	0.964	$0.944 \pm 0.025$

The modelled fluxes for ASTER and Landsat TM5 are of sufficient high resolution to show patterns caused by irrigated agricultural areas, differences in land cover, wet valleys and differences in exposition of slopes. The results for MODIS show only large-scale patterns, like the difference between the river floodplains and dry agricultural areas. In addition, missing values, resulting from invalid temperatures that have been filtered out from the MODIS MOD11 product, make it difficult to interpret spatial patterns at this scale. For operational use of daily MODIS images at the scale of agricultural areas like the Sehoul study area, upscaling procedures could provide a solution. This will be further investigated in chapter 7.

Emissivity estimated from the satellite images show the contrast in vegetation cover. Although the resolution of MODIS is 1000 m, the forests can still be discriminated from the agricultural areas. Minor differences are not visible in the MODIS derived emissivity map.

The box-method has been evaluated for in-situ measurement of emissivity. The results show no correlation with remote sensing derived emissivity. This is caused by errors in the measurement of thermal radiance of both a satellite remote sensing sensor and the box-method, a large difference in spatial support and short range variation and non-linearity. Results show that the standard deviation in emissivity of soils and vegetation measured in the Sehoul study area is larger than the variation reported by other researchers. The large standard deviation is mainly caused by the environment that causes a change in temperature of the box and the lids during most measurements. It was also difficult to maintain the high temperature of the hot lid due to a high ambient temperature. Emissivity measurements with the box during calm nights can solve these problems.

Even when measurements with the box-method are accurate, upscaling to effective pixel values is difficult. The large amount of measurements with the box-method required for upscaling to large areas using geostatistical interpolation techniques makes it not a feasible alternative for remote sensing based estimations of emissivity.

# 6 Evaluation of the Surface Energy Balance System (SEBS) using ASTER imagery at the SPARC 2004 site (Barrax, Spain)

Submitted to Hydrology and Earth System Sciences as: Van der Kwast, J., W.J. Timmermans, A.S.M. Gieske, Z. Su, A. Olioso, L. Jia, J. Elbers, D. Karssenberg & S. de Jong. Evaluation of the Surface Energy Balance System (SEBS) using ASTER imagery and flux-measurements at the SPARC 2004 site (Barrax, Spain).

## 6.1 Introduction

Research in the fields of hydrology, agronomy and meteorology depends upon accurate quantification of the amount of evapotranspiration and its spatial distribution. This information aids in precision irrigation, determining crop water stress and water use of vulnerable ecosystems, and predicting weather and climate change.

Because the surface processes contributing to evapotranspiration are complex and the relevant physical parameters are difficult to measure, accurate mapping of evapotranspiration remains an important challenge.

Evapotranspiration links the water balance to the surface energy balance. It is controlled by the availability of moisture and available energy at the surface. Models that parameterize the interaction between the land surface and the atmosphere are known as soil-vegetation-atmosphere transfer schemes (SVAT).

Conventional SVAT's are based on point measurements and give only reliable results at local scales. These models cannot be upscaled to larger areas because of the heterogeneity of land surfaces and the dynamic nature of heat transfer processes.

Recently, surface energy balance models have been developed using remote sensing data, e.g. TSEB (Norman et al., 1995), SEBAL (Bastiaanssen, 1998), and SEBS (Su, 2002). Remote sensing makes it possible to derive relevant physical parameters at different scales. Nowadays many sensors are available with different spectral and spatial resolutions, airborne and satellite based.

Outcomes of remote sensing based energy balance models are usually validated with a limited number of tower-based flux measurements (Bastiaanssen, 1998; Su, 2002; French et al., 2003), supported by some kind of footprint modelling (Horst and Weil, 1992). The validity of these models on a landscape scale is uncertain. This is of particular importance for a-typical and heterogeneous land cover types, because flux measurements are typically situated at homogeneous sites.

The objective of this study was to evaluate SEBS with distributed flux measurements at a landscape scale. The focus is on the sensible heat flux calculation as this is the most critical part of these types of models. The main research questions were:

1. How do SEBS estimated sensible heat fluxes relate to flux measurements at different land cover units?
2. Do the results of SEBS improve significantly by using field measurements or literature values of surface physical properties instead of empirical formulations?

In this study the turbulent sensible heat fluxes were modeled with SEBS, using images from the Advanced Spaceborne Thermal Emission and Reflection Radiometer (ASTER) in combination with field measurements collected during the SPARC2004 field campaign of July 2004 in Barrax, Spain (Su et al., 2008).

## 6.2 SEBS

The Surface Energy Balance System (SEBS) is a single source model, which estimates atmospheric turbulent fluxes and surface evaporative fraction from remote sensing data.

In the current setup SEBS requires three sets of input data: (1) Products derived from remote sensing data: albedo, emissivity, temperature and the Normalized Difference Vegetation Index (NDVI) to derive local surface roughness parameters; (2) Meteorological parameters collected at a reference site (air pressure, temperature, relative humidity, wind speed); (3) Radiation data (downward solar radiation, downward longwave radiation).

The SEBS algorithm (Su, 2002) was implemented in the PCRaster Environmental Modelling language with the Python Library (Karssenber, 2006). The model consists of three modules: (1) Derivation of energy balance terms; (2) Submodel to derive roughness length for heat transfer; (3) Submodel to derive stability parameters. Using these three modules, the energy balance for limiting cases (i.e. completely wet or dry pixels) can be resolved. Consequently, the energy balance terms, relative evaporation, evaporative fraction and evapotranspiration flux can be derived for all pixels.

For a detailed description of SEBS, the reader is referred to section 4.5 of this thesis.

## 6.3 Data description

The data set (Su et al., 2008) used by the model was collected during the ESA SPARC (SPectra bARrax Campaign) 2004 field experiment conducted at the Las Tiesas Experimental Farm test site at Barrax in the La-Mancha region in Spain, maintained by the Provincial Technical Agronomical Institute (ITAP).

The campaign took place during two weeks in mid-summer when natural surfaces are under water-stress. This agricultural area, which is partly irrigated, comprises of land covers ranging from completely bare soil to fully vegetated parcels with canopy heights from several centimetres up to two meters. Corn, sun flower and other crops are irrigated by pivots. The area is rather flat and is situated at an average of 700 meters above mean sea level.

### 6.3.1 Remote Sensing data

ASTER's capabilities for surface energy flux mapping (French et al., 2005) – 15m resolution in 3 visible, 30m resolution in 6 near-infrared and 90m resolution in 5 thermal infrared bands – are used from an overpass on July the 18<sup>th</sup> 2004 at 11.008 UTC (figure 6.1).

Surface temperature, broadband surface albedo, emissivity and vegetation cover have been calculated from ASTER, using the procedure described in section 5.3.2.

### 6.3.2 Ground data

Other input data for the SEBS model consisted of meteorological data and radiation measurements ( $T_a$ ,  $H_p$ ,  $u$ ,  $p$ ,  $K_s^\downarrow$ ). Furthermore, validation data has been acquired from flux towers at six locations in the study area. These consist of measurements of incoming ( $K_s^\downarrow$ ) and outgoing shortwave ( $K_s^\uparrow$ ) and longwave ( $L_s^\downarrow$  and  $L_s^\uparrow$ ) radiation as well as soil ( $G_0$ ) and sensible heat fluxes ( $H$ ) at six sites. Sensible heat flux measurements were done using Large Aperture Scintillometers (LAS), an eddy correlation system (EC), a sonic anemometer (SA) and fast response thermocouples and are described in detail by Su et al. (2008). The measurements were performed over typical land-cover units, comprising of a forest nursery (F), a wheat stubble field (W), vineyard (V-LAS and V-EC), and a sunflower field (S). An additional measurement was carried out at the edge of a corn field (C) adjacent to the vineyard site, covering either site depending on wind-direction. The locations of the flux measurements are indicated in figure 6.1.

A land cover map (figure 6.1) is derived from a combination of the SPARC2004 landuse database and a supervised classification of the 15 meter resolution ASTER imagery, which was afterwards resampled to the 90 meter gridsize. This land cover map was used to provide the aerodynamic surface properties. Assessment of canopy height,  $h_c$ , was done using field observations, whereas surface roughness for momentum transport,  $z_{0M}$ , and zero-plane displacement height,  $d_0$ , were assigned using tabulated values from existing literature (Brutsaert, 1982) (table 6.1).

For a successful interpretation of the turbulent fluxes, it is necessary to know the composition and extension of the up-wind source area. In the footprint methodology, see for example Horst & Weil (1992), Schmid (2002) and Schuepp et al. (1990), the flux measured at a particular height is considered as originating from an array of point sources where the relative weight depends

Table 6.1 Surface parameters for the different land cover types

#	Landcover	Canopy height, $h_c$ [m]	Roughness, $z_{0M}$ [m]	Displacement height, $d_0$ [m]
1	Bare soil	0.00	0.005	0.00
2	Wheat stubble	0.15	0.015	0.10
3	Forest nursery	0.35	0.06*	0.228
4	Vineyard	1.25	0.15*	0.813
5	Grassland	0.02	0.0025	0.013
6	Sunflower	1.00	0.125	0.65
7	Crops	0.25	0.03	0.163
8	Corn	2.00	0.25	1.30
9	Waterbody	0.00	0.00035	0.00

\*Note that the surface roughnesses for the forest nursery and the vineyard may vary considerably depending on wind parallel or across row-directions.

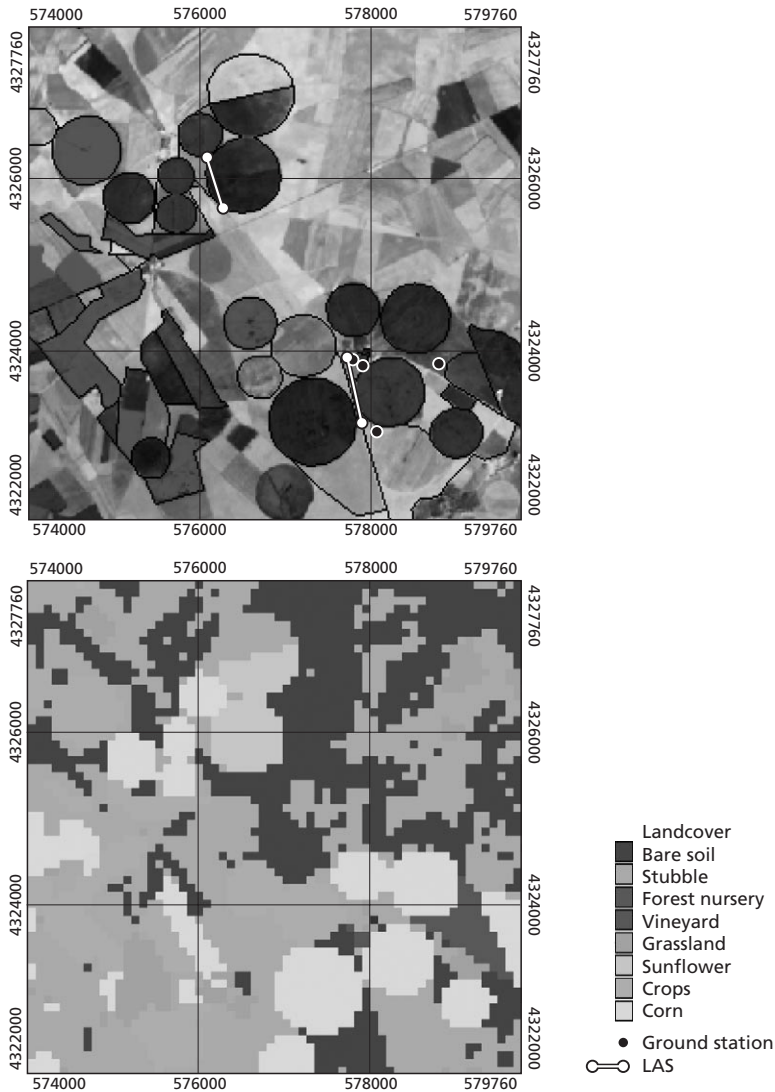


Figure 6.1 Top: ASTER image of July the 18<sup>th</sup> 2004 at 11.008 GMT with the positions of the ground measurements and fields used for experiments during the SPARC 2004 field campaign. LAS = Large Aperture Scintillometer. Bottom: landuse map with 90 m cells. Coordinate system: UTM Zone 29, Datum WGS-84.

on the location relative to the measuring instrument. By spatial integration of a source weight function, it is possible to determine the footprint, i.e. the spatial contribution by percentage of the total flux. Here, this relative contribution is calculated using the approximate analytical model described by Hsieh et al. (2000), using the distance along the main wind direction, the measuring height, the friction velocity and surface roughness at the tower sites. The comparison

of model results with tower observations is done by applying this relative contribution as a weighting function to the pixels concerned.

For the measurements by the Large Aperture Scintillometer (LAS) the situation is slightly different. The LAS consists of a transmitter and a receiver between which the scintillation, which is a measure for the turbulence, is measured along the pathlength between the transmitter and receiver. As such, the “location” of the instrument, in terms of determining the source area, is not a point but a line, and the source area is determined by assuming an array of point measurements along the pathlength. However, Wang et al. (1978) show that scintillations produced by turbulence near the centre of the pathlength contribute more to the signal measured than scintillations near the transmitter and receiver, according to a spatial weighting function. Therefore the relative contribution determined by the approximate analytical model is combined with this spatial weighting function as described in Meijninger (2003).

A footprint consists of 5 to 12 ASTER pixels of 90 m, depending on the vertical location and the type of the measuring device. For comparison with the field measurements of fluxes the weighted average flux,  $\hat{\mu}$  [ $\text{W m}^{-2}$ ], within the footprint is calculated using:

$$\hat{\mu} = \sum_{i=1}^N w_i x_i \quad (6.1)$$

where  $x_i$  is the modelled flux at location  $i$  with weight  $w_i$  for  $N$  pixels. The sum of the weights equals 1. The footprint weighted variance of the modelled fluxes can be calculated with (Gädke et al., 2005):

$$\hat{\sigma}^2 = \left( \frac{\sum_{i=1}^N w_i}{\left( \sum_{i=1}^N w_i \right)^2 - \sum_{i=1}^N (w_i)^2} \cdot \sum_{i=1}^N w_i (x_i - \hat{\mu})^2 \right) \cdot N^{-1} \quad (6.2)$$

## 6.4 Results

### 6.4.1 Model output

First, SEBS has been run without the use of lookup tables for  $z_{0MP}$ ,  $h_c$  and  $d_0$ , and a land cover map, but solely remote sensing and meteorological data. The output of the SEBS model consists of the spatial distribution of  $R_n$ ,  $G_0$ ,  $H$ ,  $\lambda E$  and  $\Lambda$  at the moment of satellite overpass (18<sup>th</sup> of July 2004, 11.008 UTC) (figure 6.2). Although the land cover map was not used as an input, the results have a clear relationship with land cover (figure 6.1). This can be explained by the sharp contrast between irrigated fields and their surroundings for the model inputs of surface temperature and NDVI.

Irrigated fields have a high latent heat flux and a low sensible heat flux. Inside the pivot irrigation fields the sensible heat flux is at times negative due to the oasis effect (Brutsaert, 1982; Stull, 1988). Because of the high vegetation cover,  $f_s$ , inside the pivots, the soil heat flux is low at the irrigated sites, following eq. 4.26. Net radiation is high in these areas, because the albedo of fully vegetated areas generally is much lower than for bare soils (see eq. 4.11).

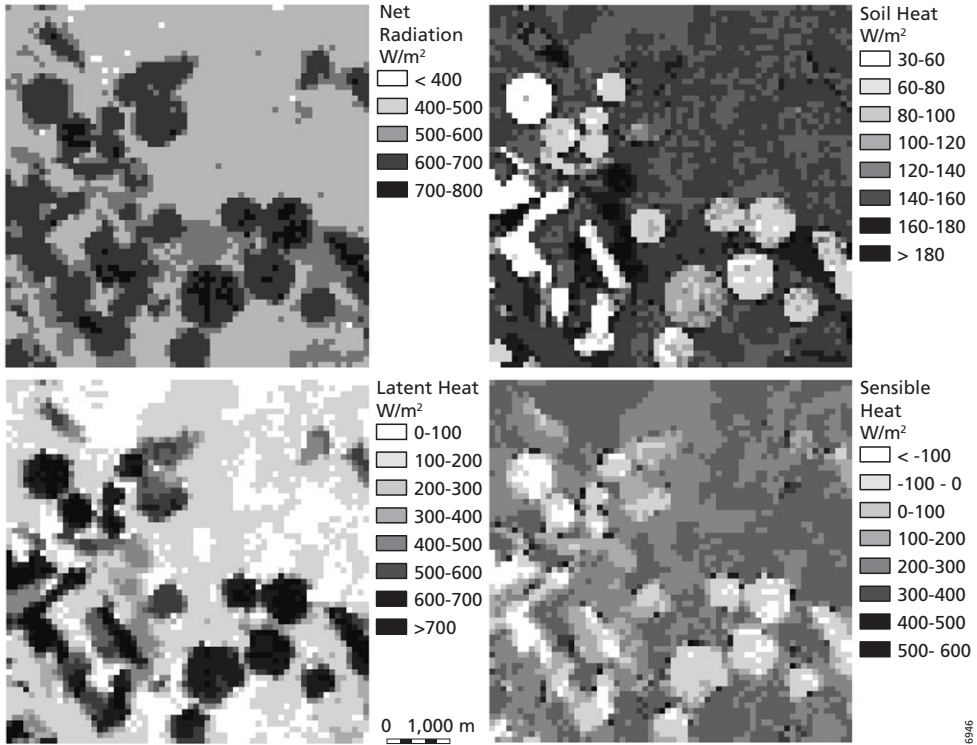


Figure 6.2 Net radiation flux ( $R_n$ ) (upper left), soil heat flux ( $G_0$ ) (upper right), latent heat flux ( $\lambda E$ ) (lower left) and sensible heat flux ( $H$ ) (lower right) as modelled by SEBS for 18 July 2004 at Barrax, Spain.

Sensible heat fluxes ( $H$ ) modelled for irrigated crops range from  $6 \text{ W m}^{-2}$  (standard deviation  $\sigma = 1.5 \text{ W m}^{-2}$ ) for corn to  $58 \text{ W m}^{-2}$  ( $\sigma = 0.9$ ) for sunflower. Other irrigated crops have a mean  $H$  flux of  $46 \text{ W m}^{-2}$  ( $\sigma = 1.5$ ). The highest sensible heat fluxes are modelled for the vineyard ( $209 \text{ W m}^{-2}$ ,  $\sigma = 1.2$ ), wheat stubble ( $191 \text{ W m}^{-2}$ ,  $\sigma = 0.7$ ), bare soil ( $187 \text{ W m}^{-2}$ ,  $\sigma = 0.4$ ) and forest nursery ( $184 \text{ W m}^{-2}$ ,  $\sigma = 1.0$ ). Grassland has an  $H$  flux of  $138 \text{ W m}^{-2}$  ( $\sigma = 1.4$ ).

#### 6.4.2 Model evaluation

Footprint modelling revealed that only the measurements over the sunflower field (S) and the forest nursery (F) cover most of these land cover types and are therefore representative for the land cover type. The source area of the instrument situated at the edge of the corn (C), is influenced by vineyard, while the measurement over wheat stubble (W) is very slightly influenced by corn, causing a lower sensible heat flux. The eddy correlation measurement in the vineyard (V-EC) is a little influenced by wheat stubble. The LAS over vineyard (V-LAS) measures a mix of different land covers and is also influenced by wheat stubble. This means that the comparison of flux measurements with modelled values is not necessarily related to one land cover type.

Comparison of the measured and modelled fluxes (weighted for the footprint) is shown in figure 6.3.

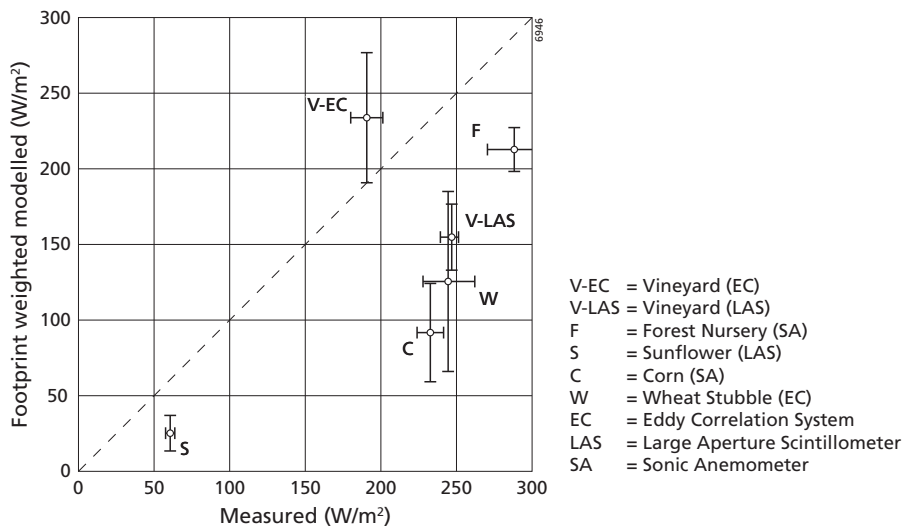


Figure 6.3 Measured versus modelled sensible heat flux ( $H$ ) for various land cover types. EC = Eddy Correlation system, LAS = Large Aperture Scintillometer and SA = Sonic Anemometer. The whiskers indicate 1 standard deviation.

The results show that measured and modelled  $H$  are in the same order of magnitude for the different sites. Also the trends are the same: the sun flower pivot (S) has a low  $H$  for both the model and the measurement, while other locations have a higher  $H$ . Results of the EC measurement in the vineyard (V-EC) and the LAS measurement in the sun flower pivot (S) are comparable with the model output.

There are also discrepancies between the modelled and measured  $H$ . The field measurements of  $H$  in most cases give higher values than the model. Sensible heat flux measurements over corn (C), vineyard (V-LAS), wheat stubble (W) and forest nursery (F) show an overestimation compared to the model outputs. Figure 6.3 also shows that the footprint-weighted standard deviation of the SEBS results is in the same order of magnitude as the standard deviation of the measurements.

These errors are probably introduced by the aggregation of heterogeneous surfaces to ASTER pixels. When all weighting pixels fall inside one land cover type, the results are better. This is the case for the eddy correlation measurements of sensible heat flux over the vineyard (V-EC) and the scintillometer measurement over the sunflower field (S), which show a difference with the modelled  $H$  of 43 and 36  $W m^{-2}$  respectively. The scintillometer measurement over the vineyard (V-LAS), however, shows a larger difference (91  $W m^{-2}$ ), because the footprint also partly covers bare soil and wheat stubble and pixels in the ASTER image are mixed.

The sonic anemometer that measured the corn field gave very high values of sensible heat flux for this irrigated field. The placement on the northern edge of the corn pivot in combination with a northern wind ( $5^\circ$ ) biases the measurement by including other land covers, mainly vineyard in the footprint.

Obviously, SEBS results are less comparable to flux measurements when the measurement footprint covers different land cover types. This could be caused by side effects in the footprint,

when sharp transitions between the land cover types exist, as is the case with pivots. Sharp transitions have a large effect on roughness, which is difficult to parameterize in surface energy balance models. Furthermore, SEBS and comparable models do not take into account wind direction, which influences  $z_{0M}$ . Moreover, care should be taken in these typical transition zones where the Monin-Obukhov similarity theory might be violated (Brutsaert, 1982).

At many locations SEBS underestimates the sensible heat flux; a phenomenon seen more often at high sensible heat flux rates when dealing with one source models (Kustas et al., 1996; Huntingford et al., 2000). Although the difference between flux measurements and SEBS results can be large, the difference between two field measurements in vineyard (V-LAS and V-EC) is also large. It seems that errors in field measurements are at least as important as errors in SEBS modelled fluxes.

### 6.4.3 Model sensitivity

The results shown in the previous paragraph are computed using many empirical relations included in SEBS. We hypothesize that SEBS results can be improved by replacing some of these functions by field estimates or literature values. First, however, we need to determine the most sensitive parameters.

Su (2002) derived the sensitivity of the sensible heat flux analytically. He estimated that the sensitivity is in the order of  $20 \text{ W m}^{-2}$  when the input variables are within 50% of their actual values, which is around 20% relative to the mean sensible heat flux.

We performed a sensitivity analysis on all input maps (surface temperature, emissivity, NDVI, albedo, DEM) and field measurements (reference temperature, wind speed, air pressure, relative humidity, height of boundary layer, incoming shortwave radiation).

Sensitivity ( $S_i$ , %) of an input factor in SEBS is defined here as:

$$S_i = \left( \frac{H_{\pm} - H_0}{H_0} \right) \times 100 \quad (6.3)$$

*Table 6.2* Input parameters of SEBS for which the sensitivity,  $S_i$  [%] (eq. 6.3) of sensible heat flux ( $H$ ) is less than 10% when a deviation of 25% is applied.  $H_+$  indicates a positive deviation and  $H_-$  indicates a negative deviation applied to the input parameter. DEM = Digital Elevation Model,  $\varepsilon$  = emissivity,  $NDVI$  = Normalized Difference Vegetation Index,  $\alpha$  = albedo,  $RH$  = relative humidity,  $K_S^\downarrow$  = shortwave incoming radiation and  $Z_{pbl}$  = height of the Planetary Boundary Layer (PBL).

	$S_i(H_+) [\%]$	$S_i(H_-) [\%]$
<i>DEM</i>	-0.9	0.9
$\varepsilon$	-0.3	0.0
<i>NDVI</i>	0.3	-0.4
$\alpha$	-0.5	0.0
<i>RH</i>	0.4	0.3
$K_S^\downarrow$	0.0	-7.4
$Z_{pbl}$	0.9	-1.1

where  $H_0$ ,  $H_+$  and  $H_-$  are the sensible heat fluxes predicted by SEBS when the input equals its reference value  $i_0$ ,  $1.25 \cdot i_0$  and  $0.75 \cdot i_0$ , respectively, with reference values used for all other inputs. For air temperature, however, a deviation of 1% was used, since a 25% deviation exceeds its physical limits. Furthermore absolute deviations of 0.1, 0.5 and 1.0 K were used for surface temperature. The sensitivity has been calculated for all validation locations separately (V-EC, V-LAS, S, F, W and C) and averaged.

Table 6.2 shows the parameters for which  $H$  modelled by SEBS is insensitive ( $S_i < 10\%$ ). The relative insensitivity to DEM (which is assumed not to vary spatially in the study area),  $\epsilon_s$ ,  $NDVI$ ,  $\alpha$ ,  $H_f$ ,  $K_s^\downarrow$  and  $Z_{pbl}$  was expected, because the derivation of sensible heat flux, by iteratively solving equations 4.15, 4.27 and 4.28 requires only meteorological parameters at reference height as well as surface temperature. This means that the calculation of  $H$  in SEBS is independent of other surface energy balance terms in contrary with most other models, e.g. SEBAL, TSEB.

In some cases, however, other input parameters can have an effect on the sensible heat flux estimation. This is the case where the calculation of  $H$  exceeds the model restriction that the minimal  $H$  is equal to the wet-limit sensible heat flux and the maximum of  $H$  equals the dry-limit sensible heat flux (section 4.5.5). This is determined using net radiation and soil heat flux calculations. The values of  $H$  outside the dry- and wet-limit are caused when the iteration does not converge. This happens with some land cover types when varying the  $K_s^\downarrow$  (figure 6.4).

Figure 6.5 shows the parameters for which  $H$  modelled by SEBS is sensitive ( $S_i > 10\%$ ): windspeed ( $u$ ), air temperature ( $T_a$ ) and air pressure ( $p$ ).

Most parameters show a comparable sensitivity at the different locations. Exceptions to this are the shortwave incoming radiation (figure 6.4) and temperature (figure 6.6). Sensible heat flux at the sunflower pivot (S) is especially sensitive to a small error in surface temperature.

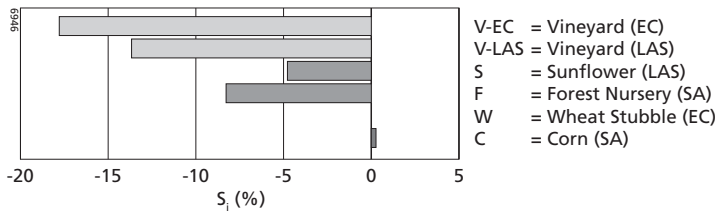


Figure 6.4 Sensitivity of sensible heat flux ( $H$ ) to 25% deviation in shortwave incoming radiation ( $K_s^\downarrow$ ), for all measurements. The sensitivity of shortwave incoming radiation depends on limitations of sensible heat flux between its dry and wet limit values. EC = Eddy Correlation system, LAS = Large Aperture Scintillometer and SA = Sonic Anemometer.

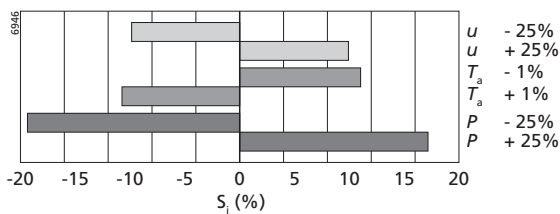


Figure 6.5 Mean sensitivity of sensible heat flux ( $H$ ) to most sensitive input parameters of SEBS (except for shortwave incoming radiation (figure 6.4) and surface temperature (figure 6.6)).

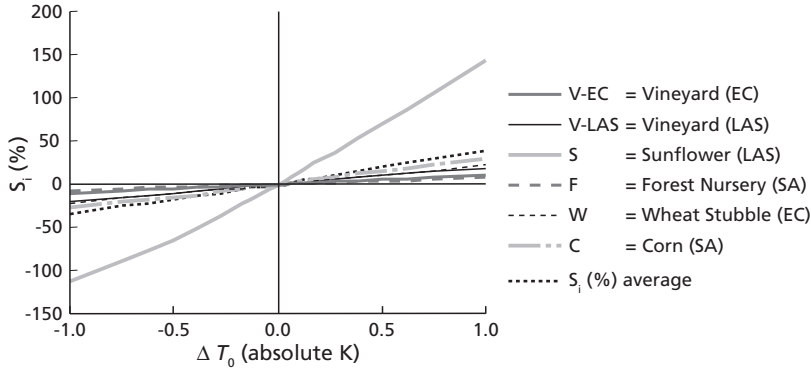


Figure 6.6 Sensitivity of sensible heat flux to surface temperature. EC = Eddy Correlation system, LAS = Large Aperture Scintillometer and SA = Sonic Anemometer.

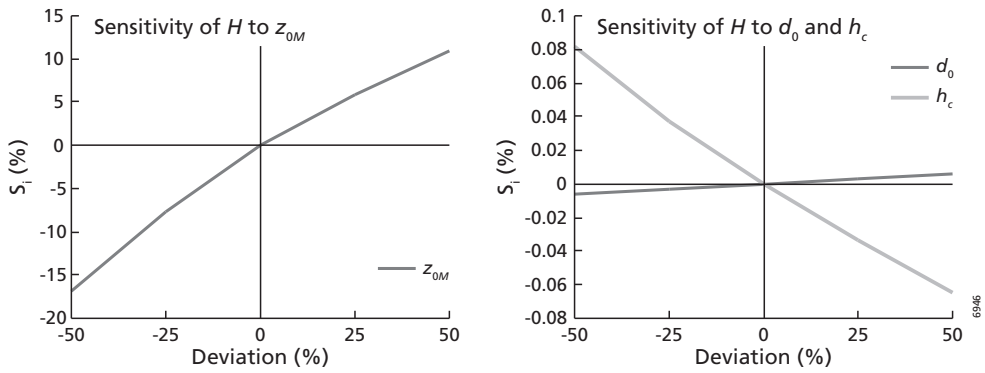


Figure 6.7 Mean sensitivity of sensible heat flux to  $z_{0M}$  (left),  $d_0$  and  $h_c$  (right).

Table 6.3 Field observations ( $h_c$ ) and literature-based ( $z_{0M}$  and  $d_0$ ) versus land use averaged modelled surface parameters.

Landcover	Canopy height, $h_c$ [m]	Modelled $h_c$ [m]	Roughness, $z_{0M}$ [m]	Modelled $z_{0M}$ [m]	Zero plane Displacement height $d_0$ [m]	Modelled $d_0$ [m]
Bare soil	0	0.14	0.005	0.019	0	0.095
Wheat stubble	0.15	0.26	0.015	0.036	0.1	0.18
Forest nursery	0.35	0.49	0.06	0.066	0.228	0.33
Vineyard	1.25	0.86	0.15	0.12	0.813	0.57
Grassland	0.02	1.22	0.0025	0.17	0.013	0.81
Sunflower	1	1.18	0.125	0.16	0.65	0.78
Crops	0.25	2.05	0.03	0.29	0.163	1.36
Corn	2	2.5	0.25	0.34	1.3	1.66
Waterbody	0	0.37	0.00035	0.051	0	0.25

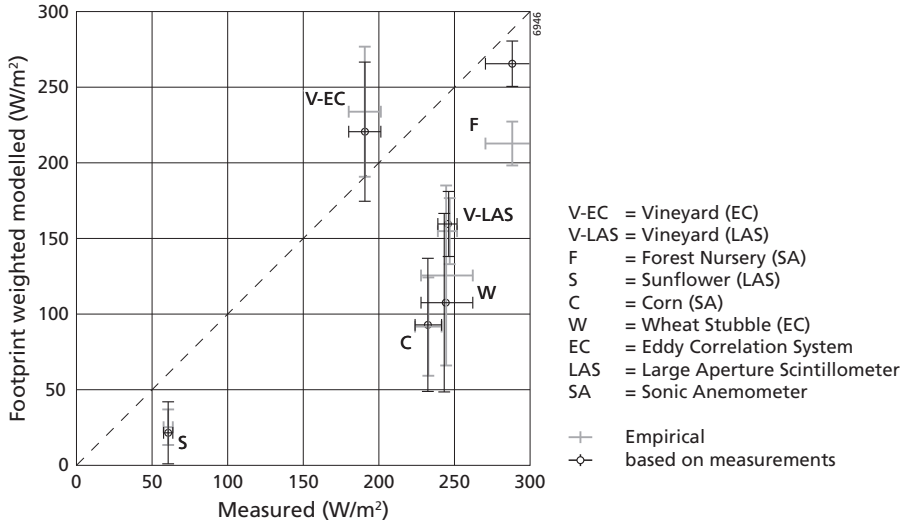


Figure 6.8 Modelled sensible heat flux ( $H$ ) compared to measured values. A comparison between  $H$  modelled with remote sensing based empirical functions and field measurement/literature values for  $z_{0M}$ ,  $h_c$  and  $d_0$ .

The sensitivity of  $H$  to the roughness height of momentum ( $z_{0M}$ ), zero plane displacement height ( $d_0$ ) and canopy height ( $h_c$ ) can be found in figure 6.7. These parameters are empirically derived from their relationship with NDVI (eq. 4.49, 4.50 and 4.51).

Table 6.3 shows that the differences between estimated values using NDVI and field estimations/literature values can differ more than the deviations used in the sensitivity analysis and the 50% limit stated by Su (2002). Furthermore, there is no relation between modelled and measured values of  $h_c$ ,  $z_{0M}$  and  $d_0$ . For example, the modelled  $z_{0M}$  of grassland is higher than vineyard, which means that homogeneous grassland is rougher than heterogeneous vineyard. The relation of  $z_{0M}$  with the arrangement of surface objects, their spacing and physical height is not well represented by the relation between NDVI and  $z_{0M}$  (eq. 4.49). This was also found by Tasumi et al. (2000), Hasager and Jensen (1999), Jasinski and Crago (1999) and Timmermans et al. (2007). The high  $z_{0M}$  value modelled for bare soil is probably related to errors in the classification.

New SEBS results are calculated by replacing the empirical functions for the calculation of canopy height ( $h_c$ ), surface roughness for momentum transport ( $z_{0M}$ ) and zero-plane displacement height ( $d_0$ ) with the values from table 6.1. A lowering of the sensible heat flux for most land cover types is expected, because of an overestimation of the roughness parameters by the empirical functions. Only for vineyard these parameters were underestimated. Figure 6.8 shows the results.

## 6.5 Discussion

In this study it has been assumed that the calculation of the footprint, using the approximate analytical model from Hsieh et al. (2000), does not have uncertainties. The evaluation of the quality of footprint models is outside the scope of this thesis, but should be addressed in further research.

From the sensitivity analysis it has been concluded that sensible heat flux modelled by SEBS is most sensitive to errors in surface temperature. Although sensitivity of SEBS derived sensible heat flux to errors in surface roughness parameters is much smaller compared to surface temperature, the errors in the estimation of these parameters from remote sensing images using empirical relations can be much larger and are significant for certain land cover types. In the previous paragraphs this has been investigated using two types of input data for the derivation of sensible heat flux from SEBS. First, solely remote sensing data is used for derivation of  $z_{0M}$ ,  $b_c$  and  $d_0$ . Next, lookup tables with field observations and literature values of these parameters were used in combination with a land cover map. The average sensible heat fluxes per land cover unit have been calculated for both cases. The lookup table approach shows a reduction compared to the empirical approach for bare soil, wheat stubble, grassland and water, as was expected from the overestimation of these parameters by the empirical functions. The increase of the average sensible heat flux for vineyard which was expected in the previous section due to higher  $z_{0M}$ ,  $b_c$  and  $d_0$  is visible in the model results

For forest nursery, crops and corn fields, however, an increase in sensible heat flux was found, which was not expected from a decrease in  $z_{0M}$ ,  $b_c$  and  $d_0$ . This could have been caused by misclassifications in the land cover map around the pivots. The round pivots, which in reality have sharp borders between wet and dry surfaces, are at 90 m resolution bordered by many mixed pixels, causing misclassifications at the edges of the pivots. Also the forest nursery is surrounded by pivots, which bias the results with mixed pixels. The results for sun flower pivots are comparable in both approaches.

Compared to the flux measurements (figure 6.8), the model results improve for forest nursery (F). Also vineyard (V-EC) results improve at the location of the eddy correlation system. The scintillometer measurement (V-LAS) remains unrepresentative for the vineyard, because of the footprint issue discussed before. Both approaches give similar results.

In addition, results for the sunflower field (S) and corn field (C) do not change much and the sensible heat flux estimates over the wheat stubble (W) get worse. This is related to the fact that pixels from a corn pivot are included in the footprint of the wheat stubble measurement, which gives side effects as explained before. Because the wheat stubble is very dry, the higher sensible heat flux measured by the eddy correlation system seems to be more realistic than both values modelled with SEBS.

The results for the sunflower field and the corn field are the same for both modelling cases. The algorithms seem to perform better for homogeneous covers instead of the heterogeneous surfaces they are developed for. The roughness parameters that have been derived empirically are comparable with literature/field values for these homogeneous covers (see table 6.3).

However, the difference between modelled and measured sensible heat flux over the corn field is large for both cases. This can be related to the measurement position and wind direction at satellite overpass, as stated before. Intuitively, the modelled values seem to be more appropriate because at the irrigated field the evapotranspiration is large, resulting in a high latent heat flux and a low, or even negative sensible heat flux.

The large improvement for the forest nursery by using field measurements can be explained by the fact that the footprint mainly covers the forest nursery plot and field estimated roughness values are representative. The same can be concluded for one of the vineyard pixels (V-EC). However, it should be noted that the surface roughness values as given for the forest nursery and particularly the vineyard may vary considerably depending on wind direction. This is due to the structure of these orchards, i.e. row orientation.

The results also suggest that relating field measurements to 90 m ASTER pixels, which have been chosen as the modelling resolution, can cause large differences between modelled and measured sensible heat flux at this scale. This is especially the case where the measurements are done in the neighbourhood of different land covers, which causes mixed pixels at 90 m resolution. This becomes an important issue when dealing with pivots. It is expected that results will improve with higher model resolution, which can be achieved by either using a disaggregation scheme (Kustas et al., 2003) or higher resolution imagery, for example the Airborne Hyperspectral Sensor (AHS).

## 6.6 Conclusions

In this chapter SEBS has been validated on a landscape scale, using distributed field measurements of sensible heat flux  $H$ . SEBS is capable of estimating  $H$  in the same order of magnitude as the field measurements. Furthermore, SEBS estimates the contrasts between well irrigated pivots and other land cover types comparable to the field measurements. Standard deviations in field measurements of  $H$  are similar to standard deviations of  $H$  modelled by SEBS.

SEBS estimated sensible heat fluxes relate well to measured fluxes when the footprint of the measurements covers only one land cover type. When different land cover types are included in the footprint, errors are introduced when land surface variables are aggregated to the size of an ASTER pixel. At the current modelling scale of 90 meters this becomes an important issue when dealing with e.g. pivot irrigation. Using higher resolution imagery or disaggregating surface temperature to a scale in accordance with the footprint of the flux measurements can give better validation results. However, when disaggregating surface temperature, this should be done very accurately as the sensitivity analysis showed that SEBS is most sensitive to the surface temperature. Especially in well irrigated fields, sensible heat flux estimates by SEBS can deviate up to 70% with 0.5 K difference in surface temperature.

We replaced empirically calculated surface roughness parameters  $z_{0MP}$ ,  $d_0$  and  $h_c$  in SEBS with field estimates or literature values, because these variables exceeded the 50% limit of input accuracy for many land cover types. This, however, only resulted in a small improvement where the field flux measurements are placed within one land cover type within the footprint. The land cover classification in combination with lookup tables for the roughness parameters can even worsen the result for mixed footprints, by creating sharp borders.

In order to get better correspondence between SEBS results and flux measurements that cover different land cover types, we suggest that the placement of flux measurements should be carefully planned and related to the modelling scale. On the other hand, the effect of wind direction on surface roughness for momentum transport should be incorporated in SEBS in order to relate SEBS results to flux measurements, independent of the location of the measurements. This should cope with edge effects and varying roughness for row crops.



# 7 Comparison of MODIS and ASTER derived surface temperatures and energy fluxes at different resolutions

To be submitted to Remote Sensing of Environment as: Van der Kwast, J, W.J. Timmermans, D. Karssenbergh, S.M. De Jong & Z. Su. Comparison of MODIS and ASTER derived surface temperatures and energy fluxes at different resolutions.

## 7.1 Introduction

Remote sensing based estimations of actual evapotranspiration play an increasingly important role in hydrological monitoring and modelling of agricultural fields at various spatial scales. A combination of optical and thermal remote sensing observations, and a limited number of meteorological station or field data enable quantitative estimates of actual evapotranspiration and its spatial distribution (Norman et al., 1995; Bastiaanssen, 1998; Su, 2002).

Agricultural fields generally have a size ranging between  $10^2$  and  $10^4$  m<sup>2</sup>. Consequently, quantitative estimates of actual evapotranspiration of these agricultural plots require high spatial resolution daily optical and thermal images at a comparable resolution. Sensors with pixels smaller than an agricultural field can detect spatial variation within a field, while sensors with pixels larger than the field size measure the emission and reflection from heterogeneous land cover within a pixel.

Because the energy from the earth's surface emitted in the thermal infrared part of the electromagnetic spectrum is much less than the solar energy reflected in the visual and near infrared (optical) part of the spectrum, the resolution of thermal infrared channels of a sensor is less than the resolution of the optical channels. The resolution of surface energy balance models, however, is restricted to the resolution of thermal infrared channels of the sensor that are used to calculate surface temperature input of the model. Resampling thermal images to the high resolution of the optical bands is difficult, because surface temperature is non-linearly related to radiation received by the sensor. Furthermore, surface temperature is the most sensitive parameter in surface energy balance modelling (chapter 6). Therefore, an accurate method for upscaling surface temperature to an appropriate resolution to detect differences in agricultural fields is indispensable.

Sensor systems such as Landsat Thematic Mapper (Landsat TM) and the Advanced Spaceborne Thermal Emission and Reflection Radiometer (ASTER) provide data at the required spatial resolution. The practical use of these TM and ASTER satellite observations for operational hydrological models is hampered by the poor temporal coverage of these systems due to their repeat cycles of 16 days. Moreover, the number of available images will in practice

be much lower than one per 16 days because unfavourable atmospheric circumstances hamper the accurate retrieval of radiometric surface temperature. A further limiting factor is that, for some of these satellite sensors like ASTER, the acquisition schedule is on-demand, meaning that data will only be collected over a location after a user request. This makes these sensor systems inadequate for use in event based modelling, i.e. after rainstorms, since it is impossible to anticipate on clouds and rainfall events when doing a data acquisition request. Satellite images with a better temporal coverage of for instance every day are available. However, these have much lower spatial resolutions of 1 to 5 km. Examples of such sensor systems are the Moderate Resolution Imaging Spectroradiometer (MODIS), the Advanced Very High Resolution Radiometer (AVHRR), the Geostationary Orbiting Environmental Satellite (GOES) and the Meteosat Second Generation (MSG). At these spatial resolutions of 1 to 5 km it is not any more possible to compute the actual evapotranspiration for individual agricultural fields. Especially the low resolution of the thermal bands hampers the operational use for evapotranspiration estimates at the scale of agricultural communities. The optical bands have a higher spatial resolution, for example 250 and 500 meters for MODIS, which could be used to improve the resolution of the thermal bands, as will be done here.

The objective of this chapter is 1) to present and apply methods to upscale daily available but low spatial resolution thermal satellite images using high optical spatial resolution images of the same platform; 2) to use the Surface Energy Balance System (SEBS; Su, 2002), explained in section 4.5, to estimate and compare the results of the original and upscaled images of both ASTER and MODIS, and 3) the comparison of average sensible heat flux for each land cover type, calculated using the original and upscaled images of both ASTER and MODIS. The upscaling algorithm and SEBS will be applied to the Barrax study area in Spain.

GOES, MSG and AVHRR are not used in this analysis, since NDVI cannot be calculated at a higher resolution than the thermal data, which is required for the upscaling algorithm. This research uses the same approach as Kustas et al. (2003) and Kustas et al. (2004), which has been applied to simulated satellite images. Here, the upscaling approach will be applied to operationally available satellite data, i.e. ASTER and MODIS.

## 7.2 Approach

In this study we compare the results of surface energy fluxes estimated by the SEBS model (Su, 2002) applied to different resolutions of satellite data. The resolution of surface energy balance models is restricted to the resolution of thermal infrared channels of the sensor that are used to calculate surface temperature input of the model. Resampling thermal images to the high resolution of the optical bands is difficult, because surface temperature is non-linearly related to radiation received by the sensor. A pixel of a remote sensing image consists of a mixture of land cover types, making its heterogeneity different for different image resolutions. The surface temperature within a pixel is an integral quantity that represents the mixed pixel. Uncertainties in the retrieval of surface temperature can be caused by atmospheric properties (Schmugge et al., 1998), the derivation of emissivity (see chapter 5) and spatial variations in temperature and emissivity (Wan et al., 2002). The relative contribution of each error source is unclear (Liu et al., 2006). The nonlinear effects due to heterogeneity may lead to markedly different representations of surface temperature at different resolutions (Jacob et al., 2004).

Sometimes no upscaling is applied, meaning that the temperature of a coarse resolution pixel is used, ignoring the spatial variability within the coarse pixel, while using other SEBS input data at the high resolution of the optical bands. A possible alternative has been proposed by Kustas et al. (2003). They developed a disaggregation procedure (DisTrad) for radiometric surface temperature by using the functional relationship between radiometric surface temperatures ( $T_R$ ) and the Normalized Difference Vegetation Index (NDVI). NDVI is commonly available at the higher resolution of the optical bands. With the NDVI –  $T_R$  relation,  $T_R$  can be calculated at the resolution of the NDVI image.

DisTrad has been applied to airborne remote sensing data collected during the Southern Great Plains Experiment (SGP97) in Oklahoma, USA (Kustas et al., 2003) with promising results for the application to upscaling of MODIS images. They demonstrated this by using simulated images. Later Agam et al. (2007) renamed the algorithm to TsHARP for the application of the algorithm on simulated MODIS and GOES images of the Walnut Creek agricultural area, Iowa, USA.

Here we apply the DisTrad upscaling algorithm and a uniform resampling method (UniTrad, Kustas et al., 2003) of radiometric surface temperature to real ASTER and MODIS images over the SPARC2004 site in Barrax in Spain. The DisTrad algorithm is compared with a procedure that increases the resolution of the surface temperature field without applying a upscaling algorithm. This procedure, referred to as UniTrad, assumes that all high resolution subpixel (i.e. pixels of a high resolution image that correspond with one coarse resolution pixel) surface temperature values are equal to the corresponding coarse resolution radiometric surface temperature observations of the satellite sensor. This ignores spatial variability within a pixel and is used here as a reference for comparison with DisTrad.

Surface temperature is the most sensitive parameter in surface energy balance modelling (chapter 6). The sensitivity analysis for SEBS, presented in the previous chapter, shows that a deviation in surface temperature of 0.5 K can give a  $S_i$  (eq. 6.3) for sensible heat flux of well irrigated pivots of up to 75%. The reported accuracy of the MODIS radiometric surface temperature product is 1 K at 1 km resolution under clear-sky conditions and has been validated by Wan et al. (2002). For the ASTER Surface Kinetic Temperature product the accuracy has been estimated to be within 1.5 K (Gillespie et al., 1999). These temperature accuracies of the sensors put restrictions on the accuracy of the model outcome as will be discussed.

The differences in  $T_R$  values and SEBS model outcomes are compared for the different methods and sensors in order to determine whether SEBS outputs improve when DisTrad is used instead of UniTrad. The study has been done for an irrigated agricultural area. We evaluate and judge the results and possible improvements using frequency distribution histograms, regression analysis, semivariograms and spatial pattern interpretations of  $T_R$  values and SEBS results.

### 7.3 Remote Sensing and Field Data

The ASTER and MODIS images used, were acquired simultaneously on the 18<sup>th</sup> of July 2004 coinciding with the SPARC2004 fieldcampaign at Barrax in Spain. The overpass time was 11.008 UTC. The ASTER and MODIS sensors are both aboard the Terra (EOS AM) satellite guaranteeing a simultaneous overpass and data acquisition time.

A detailed description of ASTER can be found in chapter 5 and Yamaguchi et al. (1988). In this study, two VNIR bands of 15 m (channel 2 and 3) are used to calculate NDVI (chapter 2, eq. 2.1) and the ASTER surface temperature product of 90 m resolution, derived from the TIR channels (chapter 5, section 5.3.2), will be used.

A detailed description of MODIS is provided in Justice et al. (1998). The NDVI product of 250 m resolution and the surface temperature product of 1000 m resolution (chapter 5, section 5.3.3) will be used in this research.

Ground-based measurements that provide inputs for SEBS consisted of standard meteorological measurements, and measurements of radiation and fluxes over different land covers. For a detailed description of the measurements during the SPARC2004 field campaign we refer to Su (2005).

## **7.4 Methods**

### **7.4.1 SEBS**

The Surface Energy Balance System (SEBS) is a single source model, which estimates atmospheric turbulent fluxes and surface evaporative fraction from remote sensing data.

In the current setup SEBS requires three sets of input data: (1) Data obtained from remote sensing observations: albedo, emissivity, temperature and the Normalized Difference Vegetation Index (NDVI) to derive local surface roughness parameters; (2) Meteorological parameters collected at a reference site (air pressure, temperature, relative humidity, wind speed); (3) Radiation data (downward solar radiation, downward longwave radiation).

The SEBS algorithm (Su, 2002) was implemented in the PCRaster Environmental Modelling language with the Python Library (Karssenbergh, 2006). The model consists of three modules: (1) Derivation of energy balance components; (2) Submodel to derive roughness length for heat transfer; (3) Submodel to derive stability parameters. Using these three modules, the energy balance for limiting cases (i.e. completely wet or dry pixels) can be resolved. Consequently, the energy balance terms, relative evaporation, evaporative fraction and evapotranspiration flux can be derived for all pixels.

The SEBS model is described in detail in section 4.5 and evaluated with flux measurements for the Barrax experimental site in Spain in chapter 6.

### **7.4.2 UniTrad**

UniTrad is a uniform resampling method assuming a linear relation between surface temperature at coarse resolution and at detailed resolution. UniTrad applies a straightforward linear upscaling to the coarse resolution images. It assumes that all high resolution subpixel surface temperature values are equal to the corresponding coarse resolution radiometric surface temperature observations of the satellite sensor. The spatial variability within a coarse resolution pixel is ignored.

### **7.4.3 DisTrad**

DisTrad is a procedure for disaggregating low resolution surface temperatures to the higher resolution NDVI-pixel resolution of sensor systems such as ASTER and MODIS (Kustas et al. 2003). The relationship between a vegetation index and radiometric surface temperatures has

been used in many studies of soil and vegetation water contents (e.g. Price, 1990; Carlson et al., 1994; Gillies and Carlson, 1995). DisTrad uses a regression between NDVI (the independent variable) and radiometric surface temperature (the dependent variable), comparable to the Temperature Vegetation Dryness Index (TVDI) or Temperature-Vegetation index plot (TVX) approach (Czajkowski et al., 2000). Figure 7.1 illustrates the relation between NDVI and surface temperature as used in DisTrad. The left hand side of this figure shows an NDVI image and a surface temperature image, the right hand side displays a scatterplot relating surface temperature to NDVI values for each pixel. Where NDVI values are high, an indication for healthy vegetation cover, the surface temperature usually is relatively low. The left hand side of the scatterplot, i.e. bare areas (low NDVI values) shows the variability in soil moisture present in bare soil areas. This variability causes a large variance of surface temperatures at low NDVI values. By fitting a linear regression to the NDVI- $T_R$  relation, the NDVI can be used to estimate radiometric surface temperature. The TVX approach was successfully used and tested with data from the HAPEX-Sahel (Andersen et al., 2002) and BOREAS (Czajkowski et al., 2000) field campaigns.

In this study DisTrad was applied to ASTER and MODIS images. First, NDVI images were calculated from a 15 meter resolution image for ASTER and a 250 meter resolution image for MODIS. These images will be referred to as NDVI<sub>15</sub> and NDVI<sub>250</sub> respectively in the DisTrad procedure. These two NDVI images are aggregated by area averaging to the coarse resolution  $T_R$  image of the sensor, i.e. 90 meters for ASTER and 1000 meters for MODIS. We refer to these images as NDVI<sub>90</sub> and NDVI<sub>1000</sub> respectively.

The DisTrad procedure of Kustas et al. (2003) was applied to these datasets using the following steps:

1. Classification of the aggregated NDVI images (NDVI<sub>90</sub> and NDVI<sub>1000</sub>) to three classes: sparse vegetation ( $0 < \text{NDVI} < 0.2$ ), partial canopy cover ( $0.2 < \text{NDVI} < 0.5$ ) and high

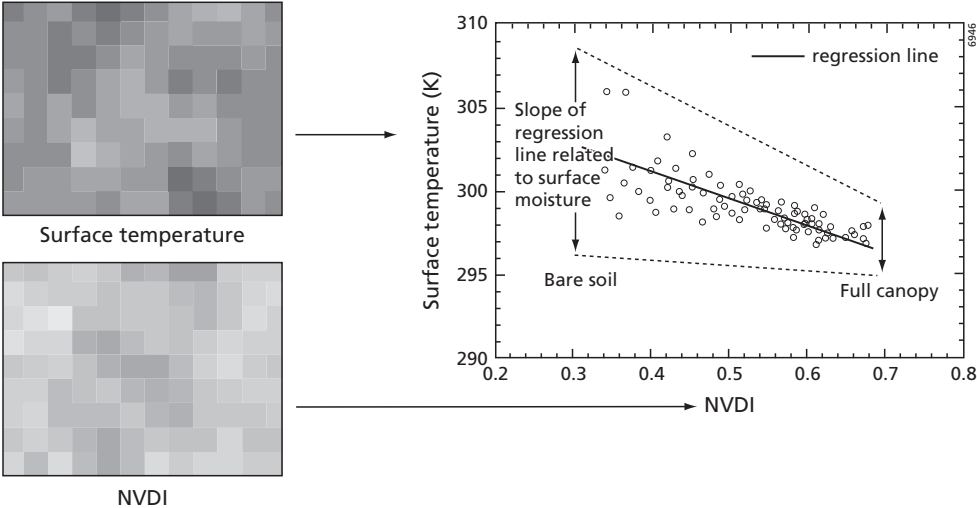


Figure 7.1 The relation between NDVI and surface temperature. Source: (Czajkowski et al., 2000). Low NDVI values can have a large variability in surface temperatures, caused by differences in soil moisture content. In full canopies, the effect of soil moisture is not present.

canopy cover (NDVI > 0.5). According to Kustas et al. (2003) the grouping of NDVI pixels into relatively uniform cover classes increases the local relations between surface temperature and NDVI compared to handling the dataset as a whole.

2. Selection of a fraction of approximately 25% of the pixels with the lowest coefficient of variance (CV) of NDVI values. In addition to the classification in the first step, this should also improve the relation between NDVI and  $T_R$ , by screening out coarse resolution NDVI pixels with a high sub-pixel variability (Kustas et al. 2003);
3. Calculation of a linear regression function on the selected data following:

$$\hat{T}_{R90}(\text{NDVI}_{90}) = a + b\text{NDVI}_{90} \quad (7.1a)$$

(ASTER)

$$\hat{T}_{R1000}(\text{NDVI}_{1000}) = c + d\text{NDVI}_{1000} \quad (7.1b)$$

(MODIS)

$\hat{T}_R$  [K] is the estimated radiometric surface temperature as a function of NDVI and  $a$ , and  $c$  are the intercepts and  $b$  and  $d$  are the regression coefficients.

4. Calculation of residuals, i.e. difference between the measured radiometric surface temperature ( $T_R$ ) and the estimation based on the regression ( $\hat{T}_R$ ):

$$\Delta\hat{T}_{R90} = T_{R90} - \hat{T}_{R90} \quad (7.2a)$$

$$\Delta\hat{T}_{R1000} = T_{R1000} - \hat{T}_{R1000} \quad (7.2b)$$

5. Estimation of  $T_R$  at the resolution of the corresponding original NDVI image for each  $i^{\text{th}}$  high resolution pixel within the low resolution pixel by substituting the high resolution NDVI image in the regression function of eq. 7.1a and 7.1b.

$$\hat{T}_{R15}(i) = a + b\text{NDVI}_{15} + \Delta\hat{T}_{R90} \quad (7.3a)$$

$$(i = 1, 2, 3 \dots 36) \text{ (ASTER)}$$

$$\hat{T}_{R250}(i) = a + b\text{NDVI}_{250} + \Delta\hat{T}_{R1000} \quad (7.3b)$$

$$(i = 1, 2, 3 \dots 16) \text{ (MODIS)}$$

The  $\Delta\hat{T}_R$  value of eq. 7.2a and 7.2b is added to the regression to account for variations in soil moisture in the image that is neglected by the average conditions calculated by the least-squares regressions (Kustas et al., 2003).

The uncertainty in subpixel temperatures derived with DisTrad has two components:

1. The discrepancy between remotely sensed coarse resolution temperatures and the temperatures resulting from the regression at coarse scale. This uncertainty has been completely removed by correcting with  $\Delta\hat{T}_R$ .
2. The uncertainty in subpixel temperatures within each coarse pixel caused by the regression applied at subpixel resolution.

The DisTrad method assumes that the correlation between NDVI and temperature is scale independent. Furthermore DisTrad assumes that NDVI can be linearly upscaled by area averaging. These assumptions cannot be proven, because temperature data at the high resolution is not available.

When using the upscaled ASTER or MODIS images derived with DisTrad for absolute flux computations, we need to account for the inherent sensor uncertainty of 1.5 K for ASTER (Gillespie et al., 1999) and 1 K for MODIS (Wan et al., 2002) under the assumptions of the DisTrad method.

#### 7.4.4 Analysis methods

DisTrad results for subpixel radiometric surface temperature were first analysed using scatterplots. Linear regression statistics were calculated. Next, a visual comparison between the different temperature images ( $T_{R1000}$ ,  $T_{R90}$ ,  $\hat{T}_{R250}$ ,  $\hat{T}_{R15}$  and the UniTrad images) has been done. Histograms of the frequency distribution of these six images have been calculated for further analysis. Spatial correlation within each image has been investigated using experimental semivariograms (Curran, 1988).

In an experimental semivariogram the variance of a class is plotted against the distance along a transect. The semivariance is a measure for the spatial variability between two points. Semivariance is calculated with:

$$s^2 = \frac{1}{2} [z(x) - z(x+h)]^2 \quad (7.4)$$

where  $z$  is the value of the feature on location  $x$  along a transect, and  $h$  is the distance between features. At a transect there are a number of pairs of features with the same distance  $h$ ; the semivariances of these pairs are averaged. This is plotted against the lag ( $h$ ) (figure 7.2). A semivariogram has several important features (Burrough and McDonnell, 1998):

1. Support: pixel size or resolution of sample distance along transect
2. Sill: maximum semivariance
3. Range: lag distance at which the sill is reached
4. Nugget variance: intercept with the y-axis, which is the variance of measurement errors combined with errors from spatial variation at distances smaller than the support that cannot be accounted for.

These properties of a semivariogram play an important role in their interpretation (Woodcock et al., 1998). The height of the sill depends on the spatial variation of the variable under consideration. The range determines the maximum distance along the transect at which objects are spatially correlated.

Nugget, spherical, exponential and Gaussian semivariogram models are used to fit the experimental semivariogram (Isaaks and Srivastava, 1989). Their properties can be found in chapter 9, table 9.7. The GSTAT (Pebesma and Wesseling, 1998) software has been used to automatically fit semivariogram models to the experimental semivariogram. GSTAT is also used to apply block kriging (Burrough and McDonnell, 1998) to fine resolution images for comparison with coarse resolution images.

Sensible heat flux has been modelled with SEBS using the six different input surface temperatures ( $T_{R1000}$ ,  $T_{R90}$ ,  $\hat{T}_{R250}$ ,  $\hat{T}_{R15}$  and UniTrad images) in combination with the measurements

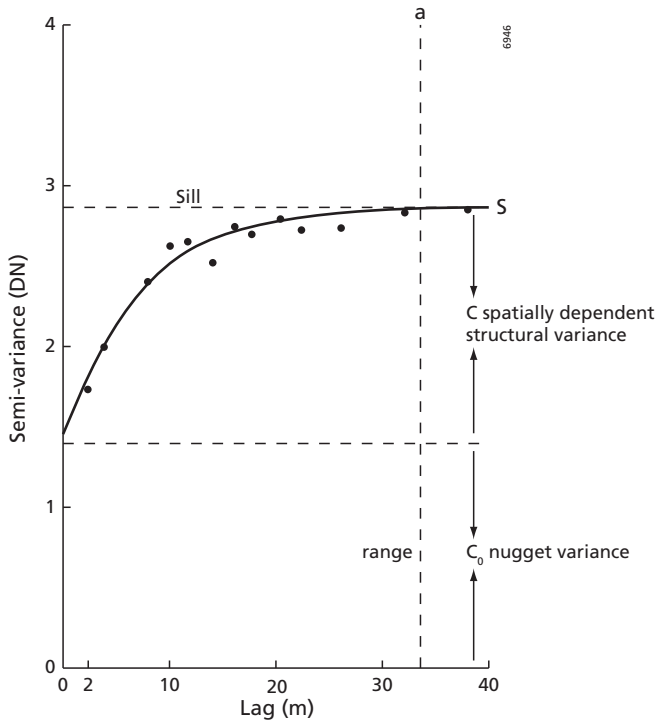


Figure 7.2 An experimental semivariogram with a fitted spherical semivariogram model (Curran, 1988).



Figure 7.3 Part of the RGB ASTER composite of July 18<sup>th</sup> 2004, 11.004 UTC over the SPARC 2004 site.

of meteorological parameters and radiance. The resulting maps of sensible heat flux are compared visually. Histograms and scatterplots have been calculated for further analysis. Finally, the results are analysed per land cover type. The land cover map has been derived from a combination of the SPARC2004 land use database and a supervised classification of the 15 meter resolution ASTER imagery (figure 7.3), which has been resampled afterwards to the 90 meter grid size (see chapter 6).

## 7.5 Results

### 7.5.1 Temperatures

The linear regression analyses of the DisTrad method (step 3) resulted in the following functions between sub-pixel radiometric surface temperature and NDVI (figure 7.4):

$$\hat{T}_{R15}(i) = 322.8 - 29.4NDVI(i) + \Delta\hat{T}_{R90} \quad (7.5a)$$

(ASTER)

$$\hat{T}_{R250}(i) = 322.0 - 20.6NDVI(i) + \Delta\hat{T}_{R1000} \quad (7.5b)$$

(MODIS)

The correlation coefficient,  $r^2$ , was 0.69 for ASTER and 0.61 for MODIS. Figure 7.4 shows the scatterplots of the regression in step 3 from which these functions were derived. Note that the scatterplot has a triangular shape in figure 7.4 which corresponds with the explanation mentioned in figure 7.1.

The radiometric surface temperature images derived from DisTrad, UniTrad and the original ASTER and MODIS temperature images are presented in figure 7.5. Visual inspection of figure 7.5 shows that the Barrax experimental site and its surrounding area contain many active pivot irrigation fields of different crops (see also figure 7.3). These fields have a diameter between 50 and 1500 meters. As the crops on these irrigated fields are actively evaporating during the satellite overpass, their temperatures are lower (~10 to 20 K) than their non-irrigated surroundings. The irrigated pivots are ideal test cases for this study because the contrast between pivot and non-pivot area is very large with respect to surface temperature and evapotranspiration and the geometric pattern is clearly visible. Visual inspection of the images reveals that in the case of MODIS the DisTrad procedure improves the spatial detail of surface temperature patterns. Individual pivots visible in the ASTER 90 and ASTER 15 temperature images are however not detectable in both MODIS images. The results for the ASTER images are less significant. Visually the gain of spatial detail is limited between the ASTER 90 image and the ASTER 15 image computed using the DisTrad approach. The spatial variability of temperature in the study area probably occurs at a scale between 90 and 250 resolution. The higher ASTER 15 resolution does not add much, because there is not much more spatial detail within 90 m. MODIS 1000 is too coarse to show spatial detail between 90 and 250 m. The variogram analysis will give further information on the scale of spatial variability of surface temperature in the study area.

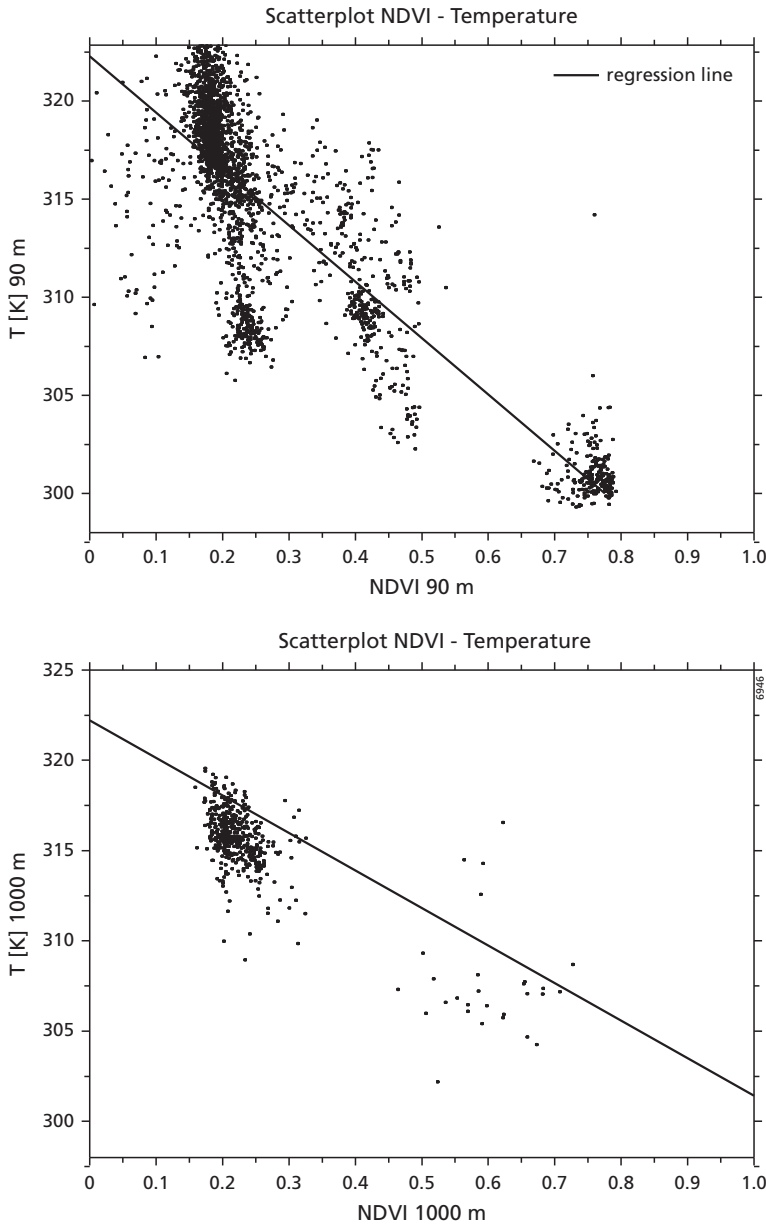


Figure 7.4 Scatterplots of NDVI-Temperature relations. Top: ASTER; bottom: MODIS. The correlation coefficients are 0.69 and 0.61 respectively. The three classes of step 1 in the DisTrad procedure are clearly visible as three clouds. The gaps between the clouds are a result of the selection in step 2 of the DisTrad procedure. This is more clear for ASTER than for MODIS.

The histograms of the temperature distributions are shown in figure 7.6 and reveal a bi-modal distribution in the ASTER 90 and ASTER 15 image. This bi-modal distribution is caused by the sharp contrast between the pivots and other areas. All active pivots are evaporating and hence colder and form the first peak in the histogram. Neither MODIS image shows bimodality, although the skewness of the MODIS 250 image suggests the presence of the pivots. The frequency distribution histogram of the MODIS 1000 image shows spikes for some temperatures. These are probably artefacts from the sensor or the temperature calibration procedure.

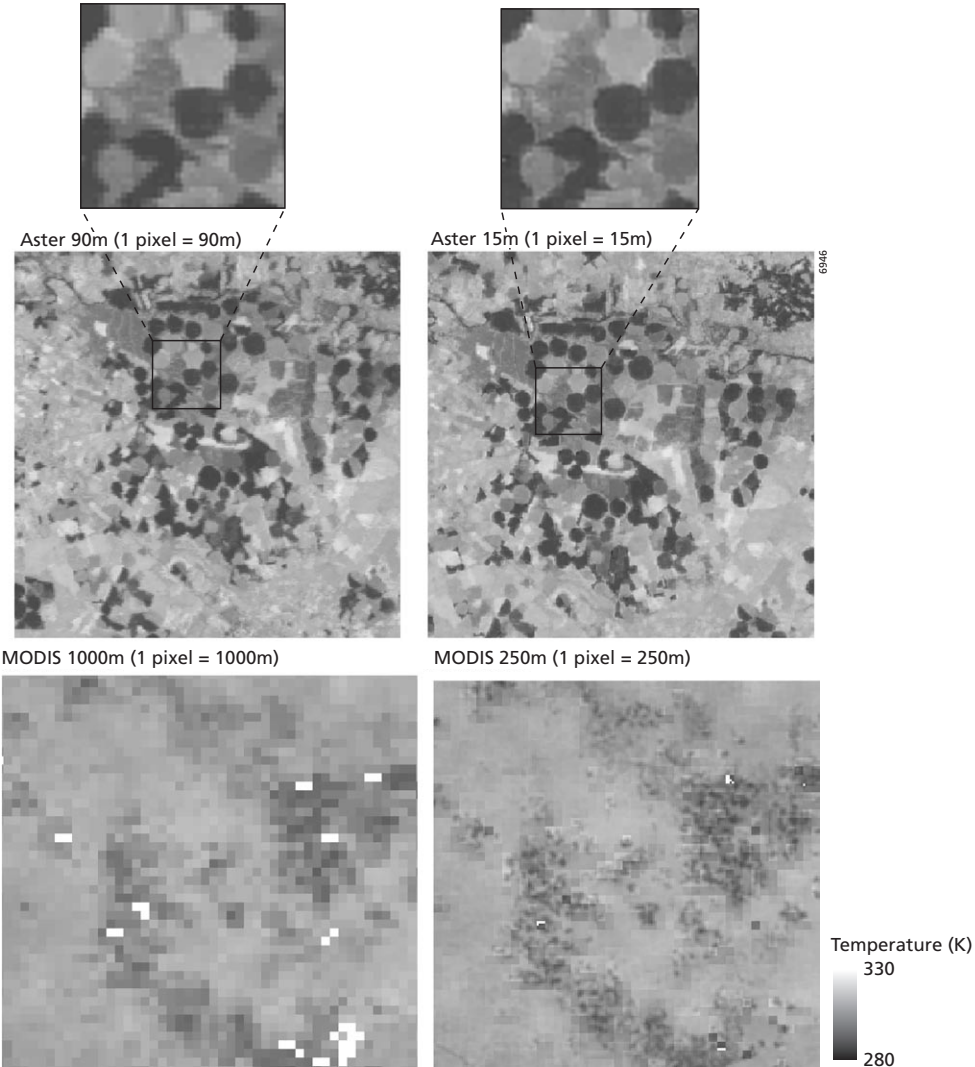


Figure 7.5 Radiometric surface temperatures from MODIS and ASTER at original resolution (left) and calculated with DisTrad (right).

Figure 7.7 shows difference images between the coarse resolution radiometric surface temperatures and the DisTrad calculation for ASTER and MODIS. The differences in the case of ASTER are obviously the largest at field borders and other sharp edges in the landscape (e.g. pivots, roads, channels and rivers). For MODIS this is not visible, but the overall pattern of irrigated versus non-irrigated areas remains visible. The visibility of the roads and other linear elements in the difference images proves that the upscaling of the surface temperature image is in principle successful. Note that the original MODIS temperature image contains missing

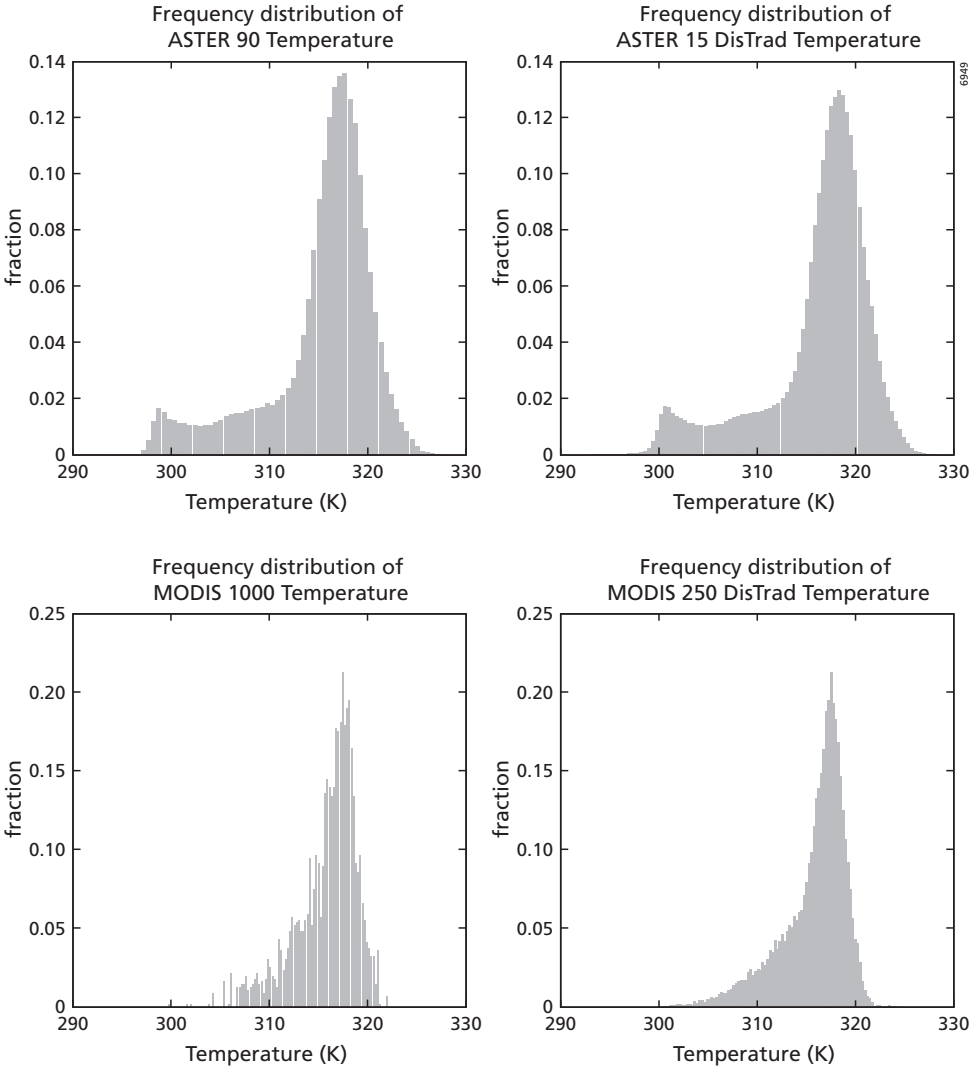
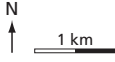
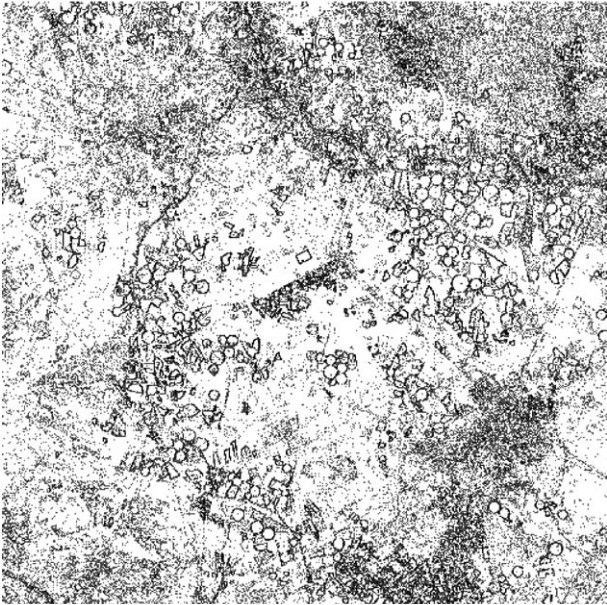
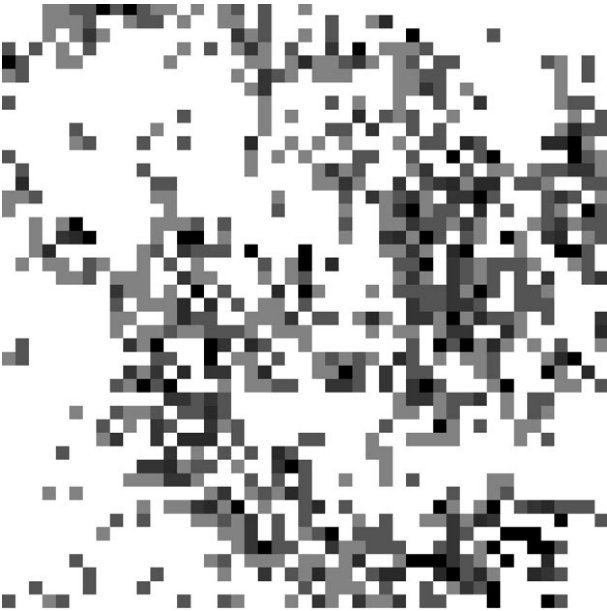
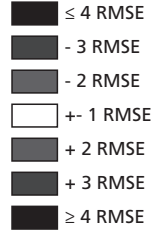


Figure 7.6 Histograms of the frequency distribution of the radiometric surface temperature for ASTER (bottom) and MODIS (top) at original resolution (left) and calculated with DisTrad (right).



Difference between  
ASTER 15 and ASTER 90

ASTER 15 - ASTER 90  
Kelvin



MODIS 250 - MODIS 1000

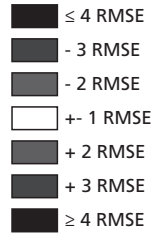


Figure 7.7 Difference between coarse resolution radiometric surface temperature and DisTrad results for ASTER and MODIS expressed in RMSE (see for calculation eq. 3.1).

6946

values, because of clouds or other factors that give invalid results in the temperature retrieval algorithm of MODIS. Using DisTrad, these artefacts are removed when high resolution NDVI pixels are available at the location of these missing temperature values.

The root mean squared error (RMSE, eq. 3.1) between UniTrad and DisTrad is 1.3 K for MODIS and 1.2 K for ASTER. Block kriging (Burrough and McDonnell, 1998) is applied to the ASTER 90 ( $T_{R90}$ ) image to predict radiometric surface temperatures for blocks of 1000 x 1000 m to be compared with the MODIS 1000 ( $T_{R1000}$ ) image and blocks of 250 x 250 m to be compared with MODIS 250 DisTrad and UniTrad images. Figure 7.8 shows scatterplots of the comparisons.

When we compare the original radiometric surface temperature measured by ASTER and MODIS (figure 7.8a), they have a low correlation coefficient ( $r^2 = 0.11$ ) and a high RMSE

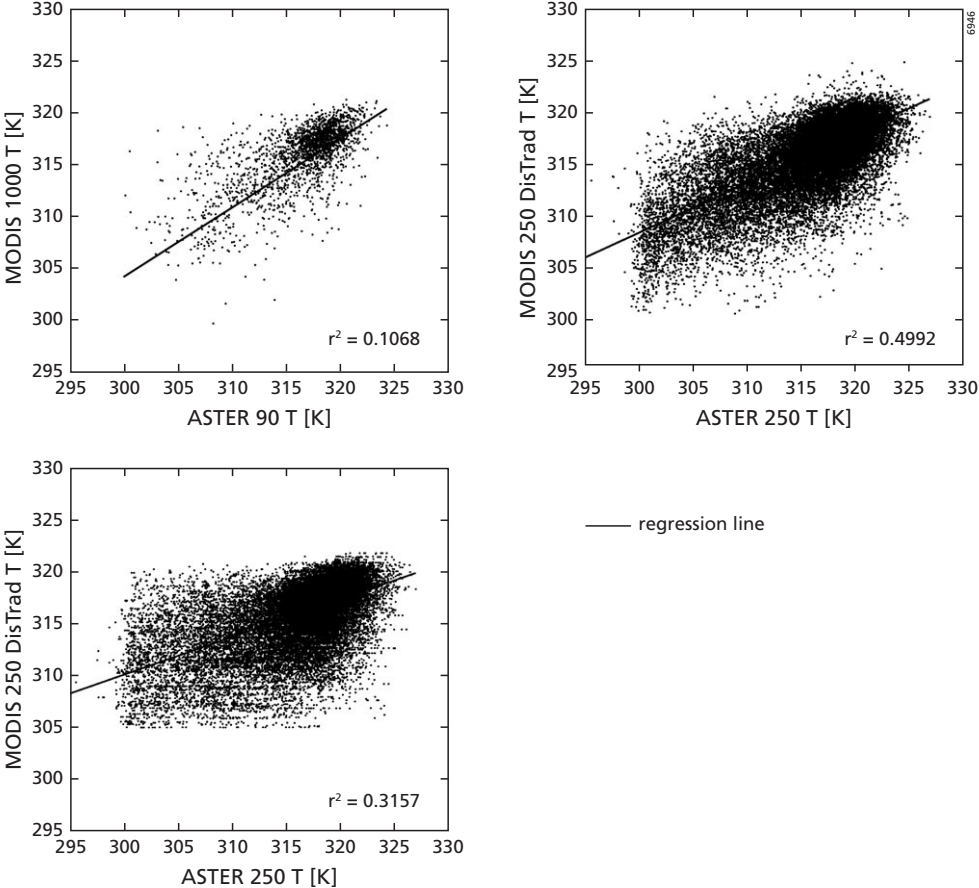


Figure 7.8 Scatterplots of radiometric surface temperatures: (a) ASTER 90 vs. MODIS 1000; (b) ASTER 250 vs. MODIS 250 DisTrad; (c) ASTER 250 vs. MODIS 250 UniTrad. Block kriging has been used to estimate the spatial variation of ASTER temperatures at the resolution of MODIS.

(RMSE = 7.9 K). These values confirm that the temperatures and their spatial correlation observed within an ASTER image are different from a MODIS image, because the radiation received by the sensor originates from a different mix of heterogeneous land cover within a pixel.

Figure 7.8b and c show the scatterplot of MODIS 250 DisTrad and UniTrad versus the ASTER 90 image that has been block kriged to a resolution of 250 m. The comparison of ASTER 90 with MODIS DisTrad shows a higher correlation ( $r^2 = 0.50$ ) and a lower RMSE (RMSE = 3.4 K) than with MODIS UniTrad. For MODIS UniTrad the correlation coefficient,  $r^2$ , is 0.32 and the RMSE is 4.0 K. This confirms that the DisTrad result is closer to radiometric surface temperatures observed at 250 m, than the UniTrad result. The RMSE of MODIS DisTrad compared to the ASTER image, however, is still high and their correlation is moderate. The relation between NDVI and surface temperature does not explain all variance in temperature. Other sources are the different errors of the sensors and errors caused by the DisTrad algorithm.

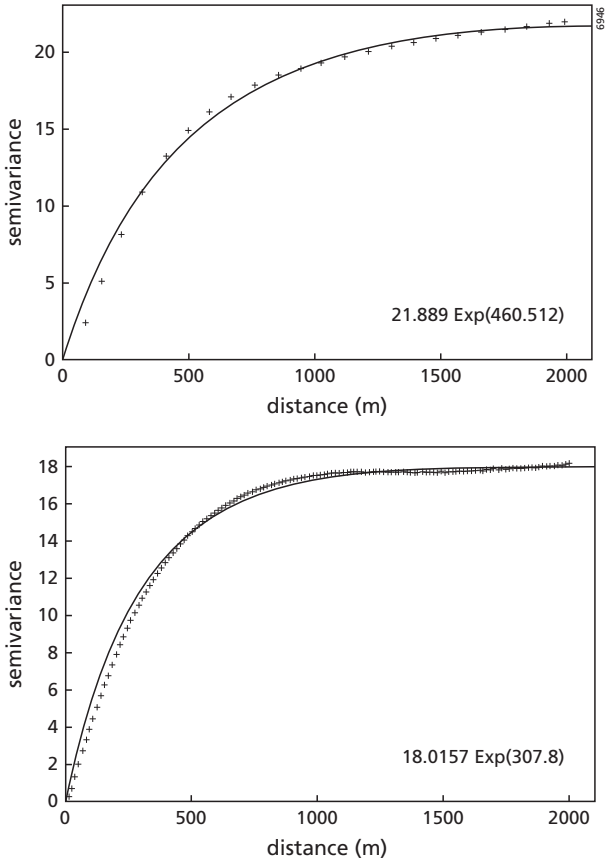


Figure 7.9 Experimental semivariogram (crosses) of radiometric surface temperature from ASTER 90 (top) and ASTER 15 DisTrad (bottom). The line shows the fitted variograms. The equation of the fitted semivariogram models are given in table 9.7, chapter 9.

Semi-variograms (Curran, 1988) were computed for the  $T_{R90}$  and  $\hat{T}_{R15}$  images and are shown in figure 7.9. Analysis of the properties of these semivariograms of surface radiometric temperature at the different scales show that for ASTER at resolutions of 15 and 90 meters the estimated effective range is 923 and 1380 meters respectively. Because more short distance variance is included at 15 m resolution, the range is smaller than for ASTER 90. The sill however is also smaller, which means that there is less spatial variance for the ASTER 15 DisTrad image.

Semivariograms of radiometric surface temperatures were also computed and analysed for the MODIS images at 1000 m and 250 m resolution. These variograms are presented in figure 7.10. The sill is lower for MODIS than for ASTER indicating that the MODIS temperature images contain less spatial variability compared to the ASTER images. Furthermore, the effective range distances for MODIS are approximately 12 km for both  $\hat{T}_{R250}$  and  $T_{R1000}$ . These ranges do not reflect individual pivots because the pivot size ranges from 50 to 1500 meters. Most likely the range distances are an indication for the spatial differentiation between irrigated areas and

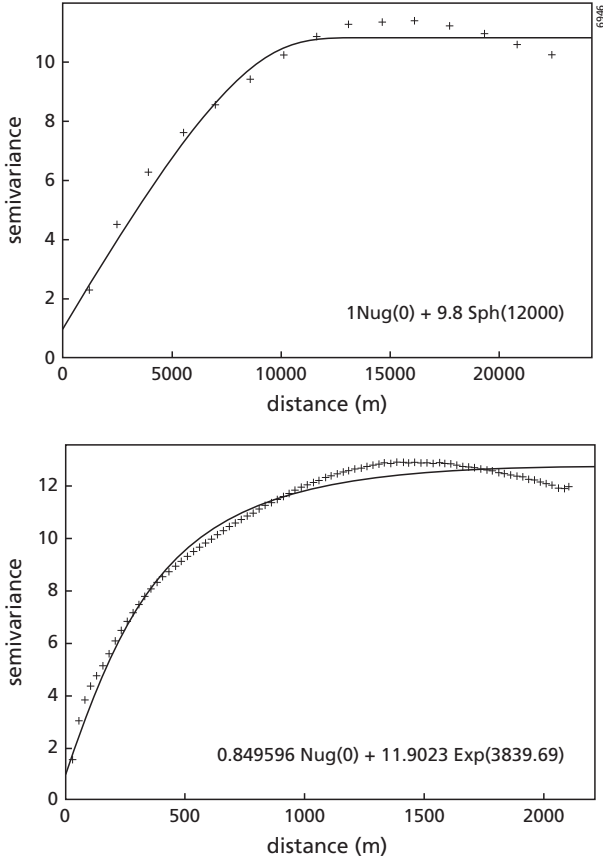


Figure 7.10 Experimental semivariograms (crosses) of radiometric surface temperature from MODIS 1000 (top) and MODIS 250 DisTrad (bottom). The lines show the fitted variograms. The equation of the fitted semivariogram models are given in table 9.7, chapter 9.

the dry non-irrigated areas. Some spatial variability is added when upscaling with DisTrad is applied, because the sill is higher at 250 m resolution and the semivariance at short lag distances is higher than at 1000 m. These results suggest that the spatial variability of surface temperature in the study area is better represented by MODIS 250 DisTrad image than by the original 1000 m image, which was also concluded from the histogram analysis.

It should be remarked that these results are typical for this agricultural region with large pivot irrigations. Other study sites, with differently sized agricultural plots can give other results for the variogram analysis.

### 7.5.2 Energy fluxes

The SEBS model has been run 6 times using each time another image to estimate the sensible heat flux, i.e. original resolution image, UniTrad or DisTrad upscaled images. Images used are respectively the  $T_{R1000}$ ,  $\hat{T}_{R250}$ ,  $T_{R90}$ ,  $\hat{T}_{R15}$  and UniTrad images. The SEBS outcomes for sensible heat flux at different scales are presented in figure 7.11. Similar results are found here for the sensible heat flux as for the radiometric surface temperature: in the case of MODIS the differences between the UniTrad and DisTrad approach are largest for irrigated areas. In case of ASTER the differences are most significant at sharp edges of individual agricultural fields and along roads.

The histograms of sensible heat flux at different resolutions (figure 7.12) were investigated, because of its direct relation with radiometric temperature. Histograms of latent heat flux distributions are not used in this analysis, because of the indirect relation with temperature.

The evaporating pivots are clearly visible around  $0 \text{ W m}^{-2}$  in the bi-modal distribution of ASTER 90, ASTER 15 DisTrad and ASTER 15 UniTrad (figure 7.12). The sensible heat flux distribution of MODIS 250 with DisTrad is unimodal and negative values are not present. Negative values of sensible heat flux are sometimes present and are caused by the so-called *oasis effect* (see chapter 4, figure 4.5). The oasis effect is likely to occur in areas like our study site where irrigated fields form a sharp evaporation gradient with the dry surroundings. Sensible heat energy is transported downwards and sideways to the evaporating crops. See section 4.3 for further details on the oasis effect.

The MODIS pixels can contain complete pivots and their surroundings. Because of this mixing, negative values of sensible heat flux are not present in the MODIS results. On the other hand, a pivot can contain more than one ASTER 90 pixel and ASTER 15 pixel, so at these resolutions a pivot can contain a mix of pixels with either a negative sensible heat flux or a small positive sensible heat flux.

Scatterplots of the combinations of the computed sensible heat fluxes are presented in figure 7.14. The scatterplot of the sensible heat flux modelled with the original ASTER and MODIS resolutions, i.e. 90 and 1000 meters respectively (figure 7.14), have a very low correlation ( $r^2 = 0.01$ ) and high RMSE ( $70 \text{ W m}^{-2}$ ). This is mainly caused by the different spatial resolution and non-linear relationship between surface radiometric temperature and sensible heat flux (figure 7.13). When MODIS 1000 results are compared with MODIS 250 (figure 7.14b and figure 7.14c), the DisTrad method has the lowest RMSE: 39 versus 47 for UniTrad. Correlations between all MODIS results are poor indicating that spatial scale does matter for surface energy balance computations.

ASTER results have a higher correlation: the 15 meter DisTrad image has an RMSE of  $17 \text{ W m}^{-2}$  compared to the 90 meter sensible heat flux image, while the 15 meter UniTrad image

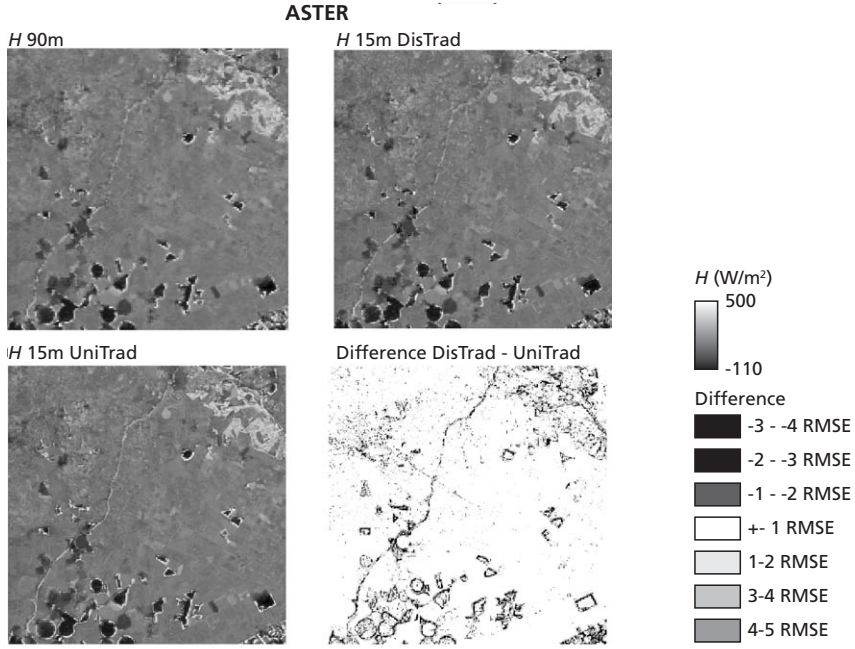
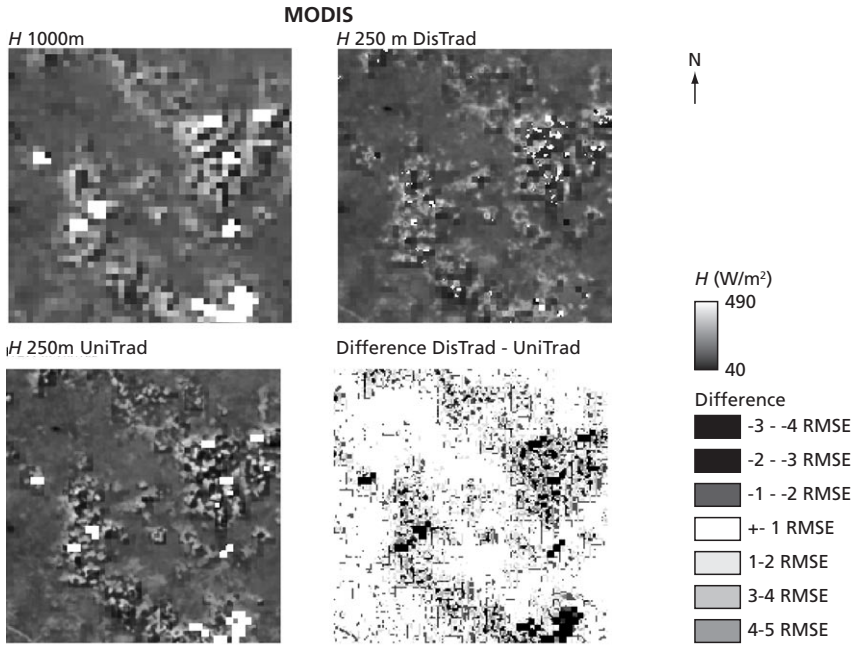


Figure 7.11 Sensible heat fluxes ( $H$ ) modelled with SEBS at different resolutions. Note that because of computer memory restrictions the calculations for ASTER were applied to a subset and cover a smaller area than the SEBS outputs for MODIS.

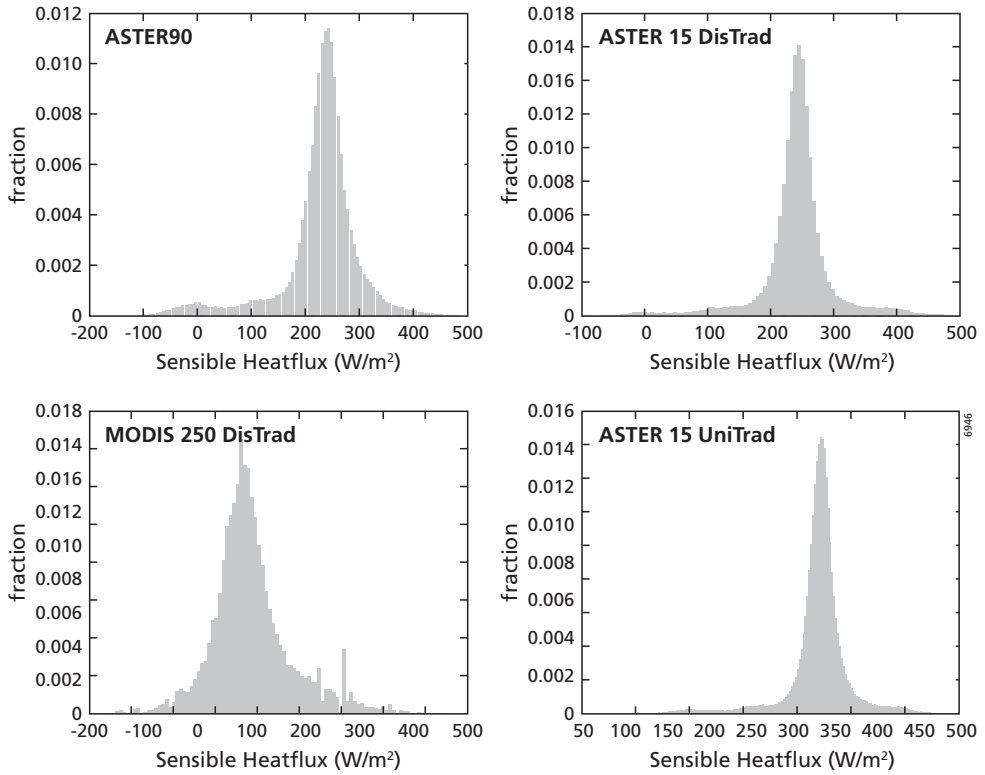


Figure 7.12 Histograms of sensible heat flux ( $W m^{-2}$ ) distribution. Clockwise starting from upper left: ASTER 90, ASTER 15 DisTrad, ASTER 15 UniTrad and MODIS 250 DisTrad.

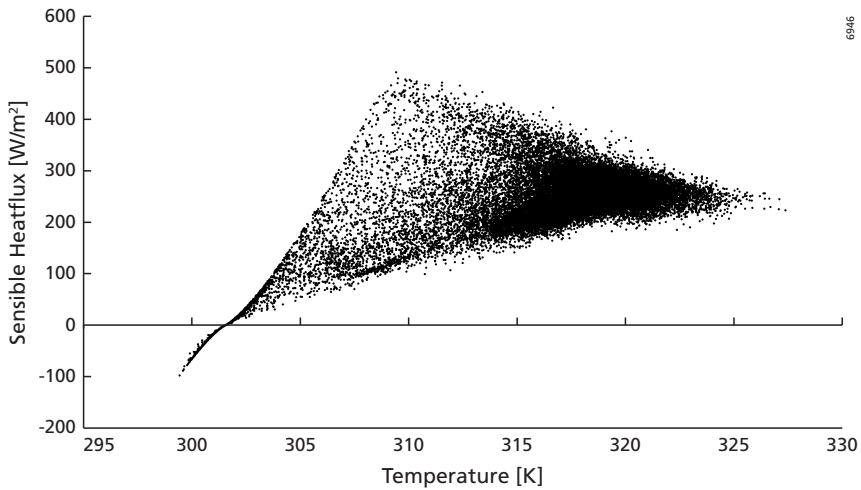


Figure 7.13 Relation between ASTER 90 radiometric surface temperature and corresponding sensible heat flux, modelled with SEBS.

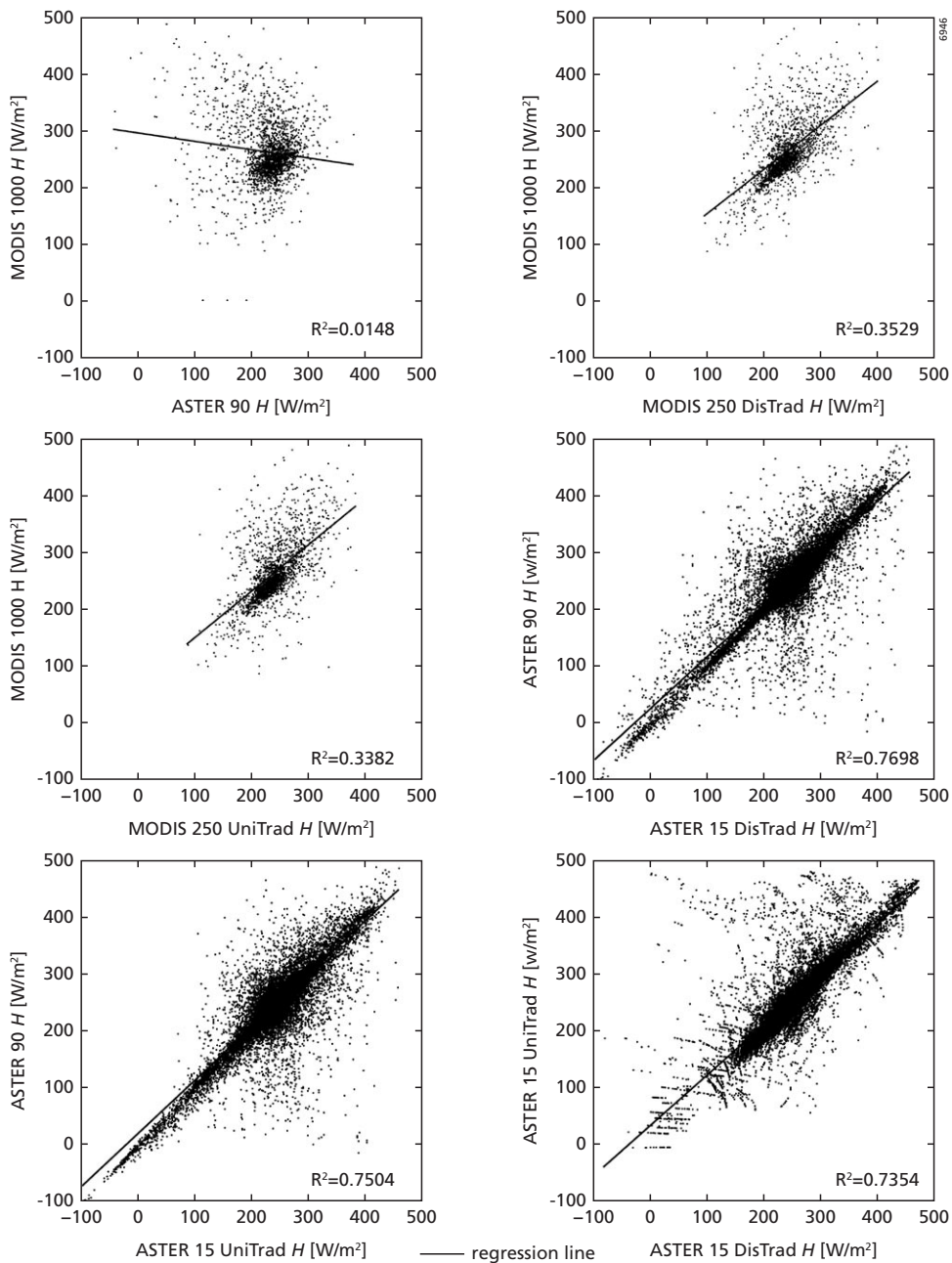


Figure 7.14 Scatterplots of sensible heatflux calculations. Block kriging has been used to estimate the spatial variation of fine resolution results at the resolution of coarse resolution results in order to make a comparison possible. Each dot represents a pixel at the coarse resolution.

has an RMSE of  $21 \text{ W m}^{-2}$  compared to ASTER 90. The  $r^2$  are respectively 0.77 and 0.75. The UniTrad versus DisTrad method gives a RMSE of  $30 \text{ W m}^{-2}$  and an  $r^2$  of 0.74. ASTER results represent the spatial variation of surface energy components in this study area much better than the MODIS results, because of the higher resolutions.

Next, the average sensible heat flux per land cover type was calculated for each resolution using the land cover map (90 m resolution, figure 6.1). Figure 7.15 presents the average sensible heat flux ( $\text{W m}^{-2}$ ) per land cover type as computed by SEBS for all six discussed combinations of MODIS and ASTER images, standard resolution, upscaled resolution by DisTrad and upscaled by UniTrad. Differences between MODIS and ASTER based sensible heat flux computations are larger for actively evaporating crops in pivots such as corn and sunflower than for dry surfaces with low or no evapotranspiration such as bare soil and wheat stubble. For MODIS the sensible heat flux is higher, because a MODIS pixel can contain partly the pivot with the evaporating crop and partly the dry surrounding, causing a mixed pixel. For forest nursery and vineyard, the outputs from ASTER show more effects of evaporating trees and vines than MODIS results, where the effect of dry soil is dominant. In fact, for these land cover types, there are no pure MODIS pixels.

For the ASTER DisTrad results sensible heat flux values are lower for evaporating agricultural fields than for the ASTER 90 and ASTER 15 UniTrad. The choice between the

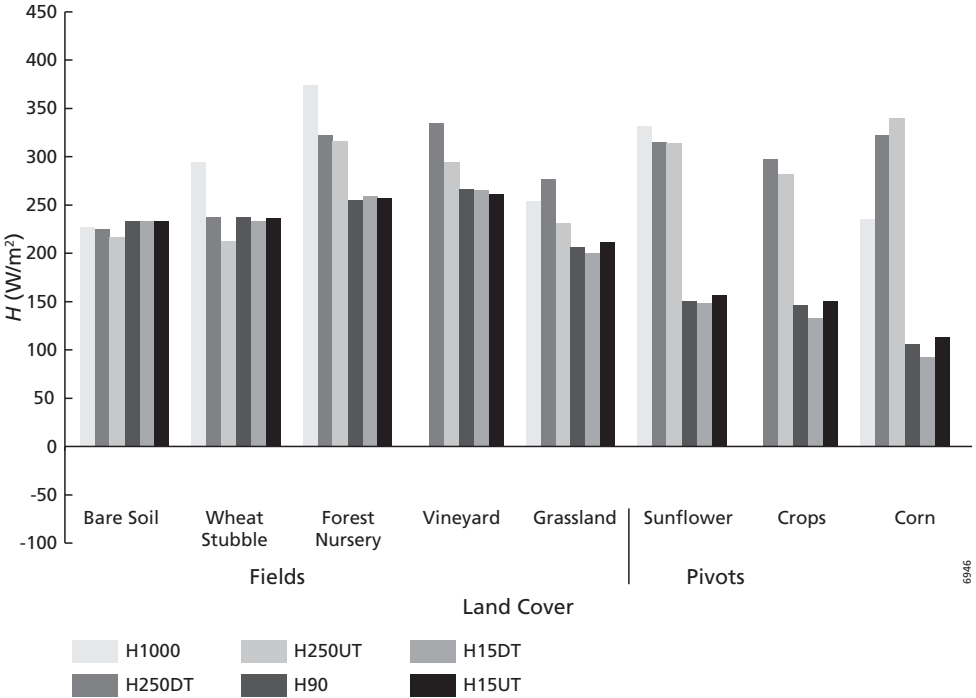


Figure 7.15 Sensible heatflux per land cover type at different resolutions. H1000 = MODIS 1000, H250DT = MODIS 250 DisTrad, H250UT = MODIS 250 UniTrad, H90 = ASTER 90, H15DT = ASTER 15 DisTrad and H15UT = ASTER 15 UniTrad.

three possible ASTER inputs is less relevant for the non-evaporating cover types because the differences are small.

In the case of MODIS, the UniTrad method gives the lowest estimations of sensible heat flux for most land covers, except corn. For dry surfaces, MODIS 1000 gives the highest sensible heat fluxes.

## 7.6 Discussion

The results of DisTrad applied to the MODIS image show that although the resolution of the surface radiometric temperature of MODIS was increased, it is still not possible to discriminate individual agricultural fields in the study area. Furthermore, the bi-modal temperature frequency distributions present in the histograms computed for the ASTER temperature images were not found in the MODIS images indicating that the MODIS resolution is too coarse to monitor energy fluxes for individual fields in the study area. However, the skewness of the frequency distribution of the MODIS DisTrad image suggests that the upscaling improves the identification of individual fields and results in a slight improvement in the modelling of sensible heat flux from evaporating crops. The semivariogram analyses of upscaled ASTER and MODIS images also suggest that spatial detail is added by using DisTrad, because variogram range values calculated from ASTER temperature images are larger (approximately 1000 m) than the MODIS DisTrad pixel size (250 m). Semivariogram analysis of the MODIS images revealed only large ranges (12 km), but the semivariance at short lag distances is larger in the case of the MODIS 250 m imagery. Although some detail is added by applying DisTrad to MODIS, the MODIS 250 m imagery is not suitable for modelling detailed temperature variances between and within individual pivots. From the semivariogram analysis it can be concluded that mixing of temperatures from evaporating crops and its dry surroundings diminishes the variance on at least 250 m resolution.

The SEBS outputs for sensible heat flux confirm the observations for surface radiometric temperature. The histograms of all MODIS derived outputs show few low sensible heat flux values, while the pivots are actively evaporating. Low and at times even negative fluxes, caused by the oasis effect, have been measured at the pivots in the study area (Su et al., 2005). The low correlation between ASTER and MODIS derived sensible heat fluxes are caused by differences in spatial detail and because of the non linear behaviour of surface radiometric temperature (figure 7.13).

The analysis of modelled sensible heat flux per land cover type showed that the choice between MODIS and ASTER becomes more relevant when modelling irrigated crops in pivots instead of regional studies. ASTER gives a more realistic evapotranspiration within a pivot. The DisTrad method and the UniTrad method perform equally well for this case study since both methods give comparable means for each land cover type and the differences are within the modelling error (typically around  $50 \text{ W m}^{-2}$ ) for both sensors. Therefore, the method requiring the least computational effort, i.e. UniTrad must be preferred for daily operational use of upscaling and energy flux estimates.

It should be noted that the results from this research are area specific and should only be applied with the utmost care to other areas. Further research is required on the use of DisTrad over different types of landscapes, with different sensors.

## 7.7 Conclusions

In this study it has been hypothesized that the estimation of sub-pixel surface temperatures may improve the modelling of evapotranspiration from individual agricultural fields with sensors having a coarse spatial resolution and a high temporal resolution. A method for upscaling operational MODIS and ASTER satellite images was applied and analysed in this chapter.

It can be concluded that SEBS outputs for MODIS and ASTER results for temperature and sensible heat flux differ significantly. The DisTrad algorithm enhances the differences between irrigated and non irrigated areas for MODIS, while with ASTER typical individual field edges are enhanced. ASTER can show variations of sensible heatflux within pivots in the study area. The choice for DisTrad or UniTrad is unimportant for ASTER over dry areas. However, it does have a significant influence at the pivot areas. DisTrad results for MODIS show a slight improvement in the estimation of sensible heat flux.

Although DisTrad does not give much improvement in the study area where pivots ranging from 100 to 1500 m diameter are present, our results suggest that for areas where larger agricultural plots and less contrast between irrigated and non-irrigated areas are present sub-pixel radiometric temperature estimates from MODIS at 250 m resolution can bridge the scale between daily available MODIS 1000 m resolution images and infrequent ASTER images at 90 m resolution. Further research should quantify the improvements for these types of agricultural areas.



## **Part III**

# **Soil moisture modelling with a process-based model**



# 8 Process-based soil moisture modelling using the Soil Moisture System (SOMS) model

## 8.1 Introduction

It has been reported that in the last decades of the past century precipitation has decreased throughout the southern Mediterranean region, while the demands of fresh water are rising due to expansion of irrigated areas and urban development (Grenon and Batisse, 1988; Zeng et al., 1999; Van Dijck et al., 2005). Climate models predict even a further reduction in precipitation and an increase of the annual temperature (Van Dijck et al., 2005). To cope with the economic pressure on water resources and a changing climate, scientists need to provide water management tools to guarantee a sustained availability of fresh water. A key variable both in agricultural land use and in degradation processes such as erosion and desertification is the spatial and temporal distribution of soil moisture.

Process-based soil moisture models are capable of simulating soil moisture at any required temporal resolution. Spatially, however, they are often lacking the required resolution. The main reason is that these models have been calibrated with soil moisture measurements with a limited spatial support (see section 1.2.2). Spatial soil moisture estimates of these models are based on interpolations between a limited amount of point locations for which the model was calibrated, introducing large spatial uncertainties.

The incorporation of spatially consistent data from remote sensing in soil moisture modelling could improve the spatial predictions of soil moisture models. Many studies have been done into the integration of remote sensing in soil moisture modelling (Houser et al., 1998; Galantowicz et al., 1999; Hoeben and Troch, 2000; Reichle et al., 2001a, 2001c, 2002; Schuurmans et al., 2003). Most studies were applied to large regions and used microwave remote sensing.

In this chapter the Soil Moisture System (SOMS) model is presented and evaluated. The model has been developed for the integration of a remote sensing based surface energy balance model (SEBS, see Part II for details) at the scale of an agricultural community. The aim of SOMS is to simulate the spatial and temporal patterns of top soil moisture after rainfall events. The model simulates top soil moisture, on an hourly basis, with a resolution of 125 meters. The top soil moisture is defined here as the upper 15 cm of the soil, since this is the support of the calibration and evaluation field measurements of soil moisture and represents the layer that interacts with surface processes. The modelled area is 50 km<sup>2</sup>. Additionally, the model should simulate the actual evapotranspiration flux in order to assimilate this with the outcome of SEBS.

There are many possible choices for the process descriptions in a soil moisture model, ranging from a finite difference solution of the Richards equation, such as is done for instance in Hydrus (Simunek et al., 1998a), to a simple single layer storage model. The approach chosen here is a

compromise between the need to model the actual evapotranspiration in a sufficiently detailed way for comparison with the outcomes of the surface energy balance model, while keeping in mind the lack of available spatial data of soil physical characteristics and soil moisture dynamics. The model is explained and applied to the Sehoul study area, comparing model simulations to point measurements of soil moisture at various locations. The data assimilation and link to SEBS are explained in chapter 10.

## 8.2 Site description

The area considered in the model is located in the north of the community of Sehoul, Morocco (figure 8.1). The community is about 20 km south-east from Rabat, in the prefecture of Sala al Jadida, Wilaya of Rabat-Salé-Zemmour-Zaër. It is bordered by the highway from Rabat to Fès in the north and the Bou Regreg River in the south. The eastern and western borders are the community borders. The largest village in the community is El Arjat. In the south-west of the study area, the large reservoir lake Sidi Mohamed ben Abdellah is located, that provides drinking water for the coastal cities between Rabat and Casablanca.

### 8.2.1 Climate

The Sehoul study area is characterised by a sub-humid to semi-arid climate, with short rainfall events occurring mainly in winter and spring. The average annual rainfall is between

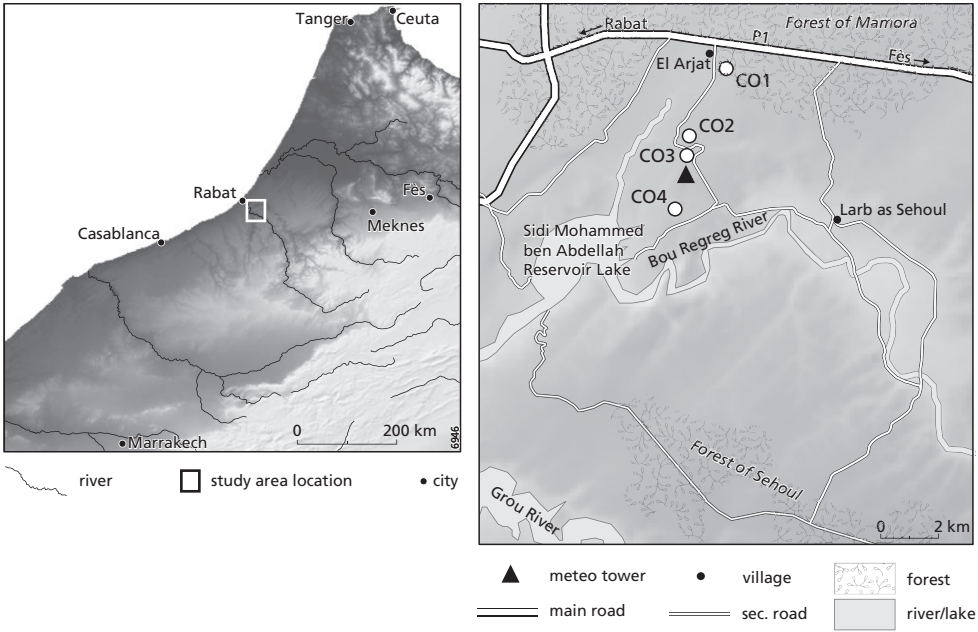


Figure 8.1 Left: the location of the Sehoul study area in Morocco. Right: The Sehoul study area. C01 to C04 are calibration sites for SOMS.

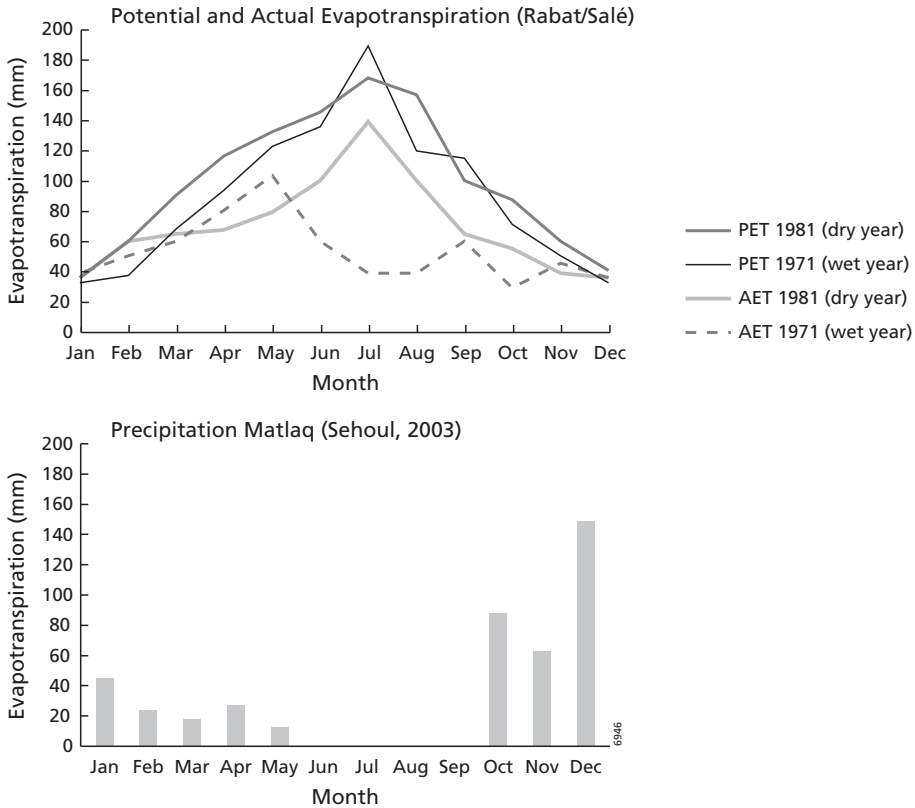


Figure 8.2 Top: Potential evapotranspiration (PET) and actual evapotranspiration (AET) for a wet and a dry year (Rabat/Salé). Source: Nafaa (2002); Bottom: Precipitation in Sehoul in 2003 (Antari, 2007).

500 and 550 mm. The potential annual evapotranspiration is around 1127 mm (Nafaa, 2002). These circumstances lead to predominantly low actual evapotranspiration fluxes in the rain season (figure 8.2), which requires that the soil moisture model is able to estimate actual evapotranspiration as low as 0.05 mm/h.

### 8.2.2 Geomorphology and soils

A generalised soil map (scale 1:25000) (figure 8.4) has been derived from research done by Watfeh (1986) and Nafaa (2002).

The northern part of the study area is part of the Plateau of Mamora. This shelving landscape is covered by the *beige and gray sands of Mamora*. They originate from plio-quaternary dunes that cover the ancient red sandy-clay soils that are called the *red formation of Mamora*. The soils in this part are the *sols sableux fersiallitiques lessivés* (sandy leached fersiallitic soils). *Fersiallitique* means that the soil mainly consists of smectite clay. The soils are rich in iron and aluminium, but also a large amount of silicium is present (Baize and Girard, 1995). Reference site C01 is located in a *sol isohumique gris couvrant les sols sableux fersiallitiques lessivés* (isohumic sands covering the

Table 8.1 Soil profile of the *Sols isohumique gris couvrant les sols sableux fersiallitiques lessivés* (Nafaa, 2002).

Horizon	Depth (cm)	Description
A1:	0- 60	Homogeneous grey sands, rich in organic matter
A2:	60-120	Homogeneous beige sands with a low clay content (loamy sands)
Bt1:	120-240	Illuvial horizon, consisting of sandy clays, ochre colour
Bt2:	> 240	Ancient red eluviation horizon, poor in clay and iron oxides, with white and yellow speckles
Bt3:		Solid clayey sands, possibly with pebble layers
R:		Layered, red coloured, fluvialite deposits from the early Quaternary.

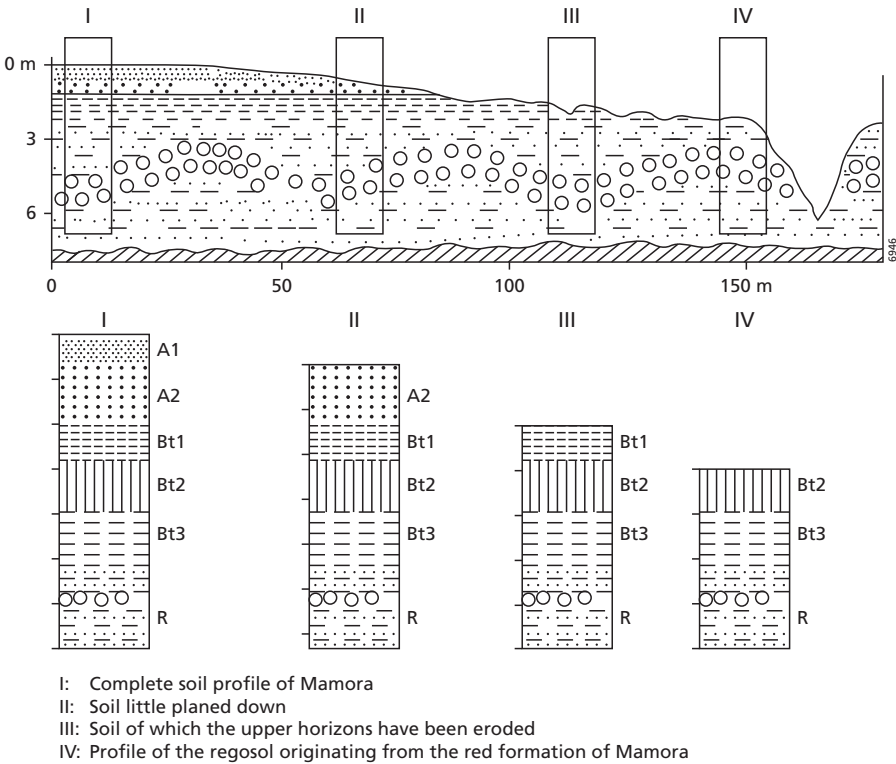


Figure 8.3 Cross section through Oued Arjat Seghir in the south of the Plateau of Mamora at Rouichat (see figure 8.4) (Nafaa, 2002). See table 8.1 for the description of the legend.

sandy leached fersiallitic soils). This is the complete soil profile of the Plateau of Mamora, which is shown in figure 8.3 as type I and described in table 8.1 (Nafaa, 2002). C02 has essentially the same profile, but the grey sands of the A1 horizon have been eroded. Its profile is presented in figure 8.3 as type II.

Table 8.2 Soil profile of the *Sols fersiallitique lessivé à galets*.

Horizon	Depth (cm)	Description
A	0-130	matrix of loamy sand (sable beige) with pebbles
B	130-180	Clayey sands (alteration of sandstones)
R	>180	Parent rock: calcareous arenaceous sandstone

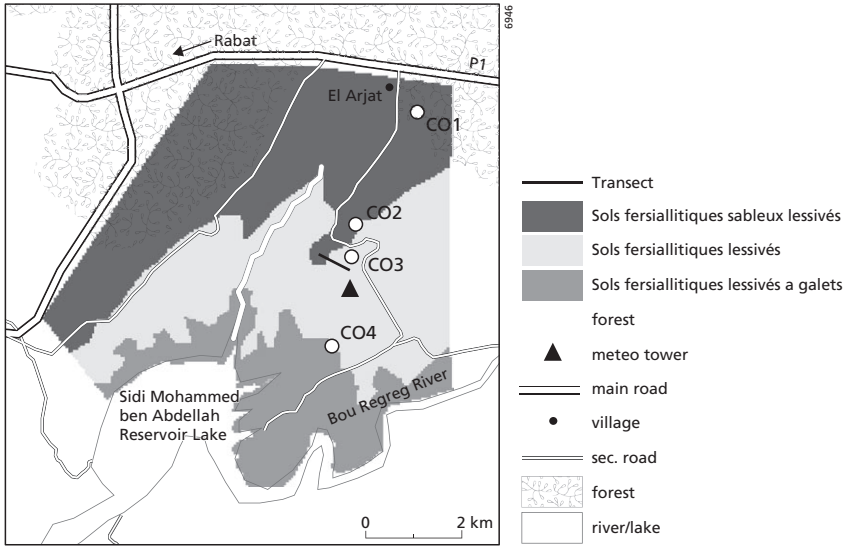


Figure 8.4 Generalised soil map of northern Sehoul, based on Watfeh (1986) and Nafaa (2002). The calibration sites C01, C02, C03 and C04 are indicated as well as the transect of figure 8.3.

In the middle part of the study area the sandy A horizon gets thinner and mixes with the beheaded soil profiles of the *red formation*. These profiles resemble type III in figure 8.3, which is the profile of reference site C03. Type IV can be found in gullies, where the recent soils have been removed. This soil profile is omitted from the model and generalized map, because of the spatial resolution of the model, i.e. at 125 m resolution, these features of approximately 10 m radius do not dominate the model grid cell.

The southern part of the study area consists largely of alluvial terraces deposited by the Bou Regreg River onto Miocene marls and Pliocene calcretes (Fetah et al., 1989). Table 8.2 gives the general soil profile in this region.

### 8.2.3 Land cover

Most of the study area is in use for agriculture. Exceptions are the northern and western border that are covered by cork oak (*Quercus suber*) forest, which is part of the Forest of Mamora. In some small areas within the agricultural area semi-natural vegetation exists, mainly doum palm (*Hyphaene thebaica*), which remains below 50 cm since it is eaten by cattle. Furthermore, little

*Eucalyptus* plantations exist for fire wood and construction. Traditionally, the agricultural plots are fenced by prickly pears (*Opuntia spp.*), a cactus that also provides edible fruits.

Agricultural activities in the community of Sehoul are dependent on precipitation. Land use comprises rainfed wheat, maize and horticulture. Some small (<0.5 ha) plots are irrigated, using traditional irrigation schemes such as submersion or drip irrigation, using water collected from wells (Van Dijck et al., 2005). The availability of sufficient soil moisture in this area is indispensable for obtaining sufficient crop yield.

### 8.3 Methods

#### 8.3.1 The SOMS model

The algorithms used in the Soil Moisture System (SOMS) model are partly dictated by climate, soils, land cover and relief in the study area. The soil moisture model only describes vertical flow. Lateral flow is not included in the model, because it is assumed that on the Plateau of Sehoul only vertical flow takes place. Furthermore, it is assumed that vertical flow is only a function of the gravitational potential, neglecting the matric potential. This means that percolation is determined by gravitational flow only. Groundwater levels in the study area are usually very deep (> 10 m) (Loos and Schipper, 2003) and therefore the influence of groundwater is not considered in the model. Runoff is neglected in the model. Runoff only occurs at the edge of the Plateau of Sehoul. Although active erosion takes place there and the fraction of runoff can be around 8% during an event (Antari, 2007), this is only a few percent on an annual basis. It is therefore assumed that the redistribution of water by overland flow on the plateau itself can be neglected.

The low actual evapotranspiration rates caused by the climate of the study area, which has been discussed in section 8.2.1, requires a multi-layer model with a detailed calculation of the

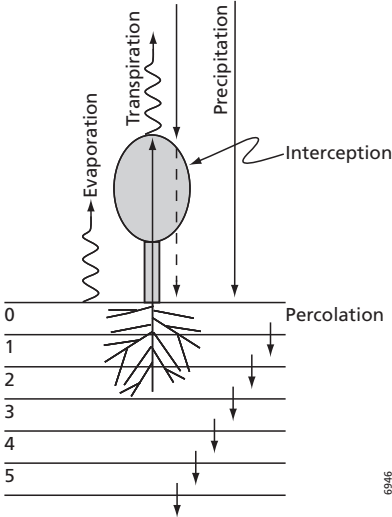


Figure 8.5 6 layer soil moisture model: arrows are the fluxes simulated in the model.

evapotranspiration flux, based on a separation between bare soil and vegetated areas with a vertical root zone distribution.

Within the study area four representative model calibration sites were selected in such a way that they cover the most common land cover and soil combinations and have a size of 1 ha (C01 to C04). Their location is shown in figure 8.1.

This section will give the mathematical description of the SOMS model. Table 8.3 shows the input variables and parameters needed in the model and gives their sources, which will be explained in the following sections.

The SOMS model estimates soil moisture in 6 soil layers (figure 8.5). For the first five layers the thickness,  $\Delta z$ , is 15 cm. The bottom layer has a thickness of 50 cm. Soil moisture is calculated in discrete timesteps of 1 hour ( $\Delta t = 1 \text{ h}$ ) and for discrete grid cells of 125 m length.

Table 8.3 Input variables and parameters used in the SOMS model.

Input variable	Description	Source
$t_a(t)$ [°C]	Air temperature	Meteorological station
$H_f(t)$ [-]	Relative humidity	Meteorological station
$K_s^{\downarrow}(t)$ [W m <sup>-2</sup> ]	Incoming shortwave radiation	Meteorological station
$p(t)$ [Pa]	Air pressure	Meteorological station
$u(t)$ [m s <sup>-1</sup> ]	Wind speed	Meteorological station
$\theta(0)$ [m/m]	Initial soil moisture content	Field measurements (TDR)
$P(t)$ [m]	Precipitation	Tipping bucket
Input parameters	Description	Source
$\chi$ [m <sup>2</sup> /m <sup>2</sup> ]	Leaf Area Index	Field measurements (Hemispherical photographs)
$f_c$ [-]	Fractional vegetation cover	Field estimates (Land cover map)
$\theta_s$ [m/m]	Saturated moisture content	Field measurements (TDR)
$k_{sat}$ [m s <sup>-1</sup> ]	Saturated hydraulic conductivity	Calibration (initialized from field measurements with double ring infiltrometer)
$\zeta$ [-]	Parameter of the soil water retention curve	Calibration
$h_A$ [m]	Air entry value	Assumption
$\tau$ [-]	Tortuosity	Literature: Millington and Quirk, 1959, 1961
$\alpha$ [-]	Albedo	Calculated from ASTER image
$z_{meso}$ [m]	Height of mesostrophic wind	Assumption
$h_c$ [m]	Height of canopy	Field estimates (Land cover map)
$r_{s,min}$ [s m <sup>-1</sup> ]	minimal stomatal resistance	Assumption
$R_p$ [W m <sup>-2</sup> ]	minimum radiation for photosynthesis	Assumption
$r_{s,max}$ [s m <sup>-1</sup> ]	maximum stomatal resistance	Jacquemin and Noilhan, 1990
$w_i$	rootzone distribution for transpiration	Assumption
$h_{50}$ [m]	matrix potential at 50% reduction of potential evapotranspiration	Simunek et al, 1988a

The soil moisture content is calculated by:

$$\theta_i(t+1) = \theta_i(t) + \frac{(P_n(t) - E(t) - T_i(t) - I_i(t) + I_{i-1}(t)) \cdot \Delta t + X(t)}{\Delta z} \quad (8.1)$$

where  $\theta_i$  [m/m] is the actual volumetric soil moisture content of layer  $i$  ( $i = 0, \dots, 5$ ),  $P_n$  [ $\text{m s}^{-1}$ ] is the net precipitation (based on interception, see below),  $E$  [ $\text{m s}^{-1}$ ] is the actual evaporation,  $T_i$  [ $\text{m s}^{-1}$ ] is the actual transpiration from layer  $i$ ,  $I_i$  [ $\text{m s}^{-1}$ ] is the percolation from layer  $i$  to the next layer,  $I_{i-1}$  [ $\text{m s}^{-1}$ ] is the percolation received from the layer above or from the surface storage  $X$  [m] for  $i = 0$ . For  $i = 1, \dots, 5$ ,  $P_n(t) = 0$ ,  $E(t) = 0$  and  $X(t) = 0$  m. The individual components of the SOMS model are discussed in the next sections.

### Net rain

The net rainfall is defined as:

$$P_n(t) = P(t) - S(t) + D(t) \quad (8.2)$$

where  $D$  [m] is throughfall and  $S$  [m] is the interception, which is:

$$S(t) = S_{max} - C(t) \quad (8.3)$$

The intercepted amount of rain ( $C$  [m]) is limited by the maximum canopy storage capacity ( $S_{max}$  [m]) which is calculated using the method by Von Hoyningen-Huene (1983):

$$S_{max} = (0.935 + 0.498 \chi - 0.00575 \chi^2) \cdot f_c \cdot 0.001 \quad (8.4)$$

where  $\chi$  [ $\text{m}^2/\text{m}^2$ ] is the leaf area index (LAI) and  $f_c$  is the fraction of canopy cover in a gridcell.

At the beginning of the first rainfall event  $C = 0$  m. It increases when rainfall is added until  $S_{max}$  is reached and  $C$  decreases through evaporation ( $E_{Int}$  [m]) until its minimum value 0:

$$C(t+1) = C(t) + (P(t+1) - E_{Int}(t+1)) \cdot f_c \cdot \Delta t \text{ for each } t \text{ and } 0 \leq C \leq S_{max} \quad (8.5)$$

If  $C(t) < T_p(t)$ :

$$E_{Int}(t) = C(t) \quad (8.6)$$

If  $C(t) \geq T_p(t)$ :

$$E_{Int}(t) = T_p(t) \cdot \Delta t \quad (8.7)$$

where  $T_p$  [m/s] is the potential transpiration, which is calculated with eq. 8.34.

When the canopy cannot store more water, i.e.  $C = S_{max}$ , the remaining rainfall reaches the soil as throughfall ( $D$  [m]). Throughfall is calculated by:

$$D(t) = f_c \cdot P(t) - (S_{max} - C(t)) \quad (8.8)$$

### Percolation

The calculation of the percolation is based on the relative degree of saturation ( $\theta_{E,i}$  [-]). The relative degree of saturation of layer  $i$  is defined as (Kutilek and Nielsen, 1994):

$$\theta_{E,i}(t) = \frac{\theta_i(t) - \theta_{r,i}}{\theta_{s,i} - \theta_{r,i}} \quad (8.9)$$

where  $\theta_{s,i}$  [m/m], is the saturated moisture content of layer  $i$  and  $\theta_{r,i}$  [m/m] is the residual moisture content of layer  $i$  (assumed 1% of  $\theta_s$ ).

The percolation from each layer to the next layer is determined by the unsaturated hydraulic conductivity ( $k_i(\theta_{E,i})$  [-]), based on the soil water retention curve (SWRC) model by Farrel and Larson (1972):

$$h_i(t) = h_A \exp[\zeta(1 - \theta_{E,i}(t))] \quad (8.10)$$

where  $h$  is the matric suction in [m],  $h_A$  is the air entry matric suction in [m] and  $\zeta$  is the dimensionless slope of the log-linear relationship between  $\ln(h/h_A)$  and  $(1 - \theta_{E,i})$ . The log-linear relation is true when  $h < h_A$  (both are negative).  $h_A$  has been assumed to be -0.04 m.

The unsaturated hydraulic conductivity is expressed as the relative unsaturated hydraulic conductivity ( $k_{r,i}(\theta_{E,i})$  [-]) (Millington and Quirk, 1959, 1961). Together with the SWRC model of Farrel and Larson (1972), the unsaturated hydraulic conductivity becomes:

$$k_{r,i}(\theta_{E,i}, t) = \theta_{E,i}(t)^\tau \cdot \frac{e^{2\zeta\theta_{E,i}(t)} - 2\zeta\theta_{E,i}(t) - 1}{e^{2\zeta} - 2\zeta - 1} \quad (8.11)$$

where  $\tau$  [-] is the ‘‘tortuosity’’, which is set to 4/3 (Millington and Quirk, 1959, 1961). The relative unsaturated hydraulic conductivity ( $k_{r,i}$ ) forms an analogue with filled capillaries that represent filled pores in the soil at different suction levels. It is zero at the residual soil moisture content and unity when the soil is completely saturated. By multiplying the relative unsaturated hydraulic conductivity with  $k_{sat,i}$  [ $\text{m}\cdot\text{s}^{-1}$ ], the absolute unsaturated hydraulic conductivity ( $k_i(\theta_{E,i})$  [ $\text{m}\cdot\text{s}^{-1}$ ]) is calculated:

$$k_i(\theta_{E,i}, t) = k_{sat,i}(t) \cdot k_{r,i}(\theta_{E,i}, t) \quad (8.12)$$

Percolation from each layer is calculated by using the geometric mean of  $k_i(\theta_{E,i})$  between two timesteps:

$$I_i(t+1) = \sqrt{(k_i(\theta_{E,i}, t) \cdot k_i(\theta_{E,i}, t+1))} \quad (8.13)$$

The geometric mean between two timesteps is used to prevent total drainage of the pore space when the unsaturated hydraulic conductivity at one timestep becomes too large, which is unrealistic (Van Beek, 2002). In addition, the percolation for layer  $i$  cannot be larger than the available pore space in layer  $i+1$ .

### Evapotranspiration

The evaporation ( $E$ ) and transpiration ( $T$ ), are calculated separately and weighted proportionally to vegetation cover ( $f_v$ ). Evaporation takes place from the canopy (intercepted rainfall,  $E_{Int}$ ) and

from the first soil layer for the bare part of the soil (eq. 8.1). Transpiration takes place from the first three soil layers according to the root distribution (see below, eq. 8.36) assuming that the bulk of the roots occur in the upper 0.45 m of the soil. Both are determined by the potential evapotranspiration ( $E_p$  [ $\text{m s}^{-1}$ ]) which is calculated using the combination equation of Penman-Monteith (Monteith, 1981):

$$E_p(t) = \frac{1}{\lambda} \left( \frac{R_n(t) \cdot \delta(t) + \rho_a c_p v(t) / r_a(t)}{\delta(t) + \gamma(1 + r_s(t) / r_a(t))} \right) \quad (8.14)$$

where  $R_n$  [ $\text{W m}^{-2}$ ] is the net radiation,  $v$  [Pa] is the vapour pressure deficit of the air,  $\rho_a$  [ $\text{kg m}^{-3}$ ] is the mean air density at constant pressure,  $c_p$  [ $\text{J kg}^{-1} \text{K}^{-1}$ ] is the specific heat of the air at constant pressure,  $\delta$  [ $\text{Pa K}^{-1}$ ] is the slope of the saturation vapour pressure-temperature relationship,  $\gamma$  [ $\text{Pa K}^{-1}$ ] is the psychrometric constant,  $\lambda$  [ $\text{J kg}^{-1}$ ] is the latent heat of vaporization of water, and  $r_s$  and  $r_a$  are the (bulk) surface and aerodynamic resistances [ $\text{s m}^{-1}$ ]. Note that for the evaporation fluxes at bare soils  $r_s$  is zero.

The SOMS model calculates the net radiation,  $R_n$ , and the aerodynamic parameters  $r_s$  and  $r_a$  of the Penman-Monteith equation in separate modules.

The net radiation module calculates the net radiation with the radiation balance equation (see also eq. 4.5-4.11):

$$R_n(t) = K_s^\downarrow(t)(1 - \alpha) - L_n(t) \quad (8.15)$$

where  $K_s^\downarrow$  [ $\text{W m}^{-2}$ ] is the incoming shortwave radiation as measured at the meteorological station,  $\alpha$  is the albedo [-], and  $L_n$  [ $\text{W m}^{-2}$ ] is the net longwave radiation, which is calculated according to Feddes et al. (1983):

$$L_n(t) = L_p(t) \cdot (0.56 - 0.008\sqrt{e_a(t)}) (0.1 + 0.9c_f(t)) \quad (8.16)$$

where  $e_a$  [Pa] is the actual vapour pressure,  $c_f$  [-] is the cloud factor and  $L_p$  [ $\text{W m}^{-2}$ ] is the potential longwave radiation. The actual vapour pressure is calculated with:

$$e_a(t) = H_f(t) \cdot e_s(t) \quad (8.17)$$

where  $H_f$  [-] is the relative humidity measured by the meteorological station and  $e_s$  [Pa] is the saturated vapour pressure that is related to air temperature measured at the meteorological station ( $t_a$  [ $^{\circ}\text{C}$ ]) by (Allen et al., 1998):

$$e_s(t) = 611 \cdot e^{\frac{17.27t_a(t)}{237.3 + t_a(t)}} \quad (8.18)$$

The cloudfactor ( $c_f$ ) in eq. 8.16 is determined by dividing the actual incoming shortwave radiation ( $K_s^\downarrow$ ) by the potential incoming shortwave radiation ( $K_p^\downarrow$  [ $\text{W m}^{-2}$ ]) based on latitude, time of day and day of the year (see e.g. WOFOST (Boogaard et al., 1998)):

$$c_f(t) = \frac{K_s^\downarrow(t)}{K_p^\downarrow(t)} \quad (8.19)$$

$L_p$  [ $\text{W m}^{-2}$ ] in eq. 8.16 is the potential longwave radiation of a blackbody with a temperature  $T_b$  [K] and can be calculated using Stefan-Boltzmann's law (see also eq. 4.2):

$$L_p(t) = \sigma(t_a(t) + 273.15)^4 \quad (8.20)$$

where  $\sigma$  is the Stefan-Boltzmann constant ( $5.670400 \cdot 10^{-8} \text{ J s}^{-1} \text{ m}^{-2} \text{ K}^{-4}$ ).

The SOMS module for calculating the aerodynamic parameters first calculates the aerodynamic resistance ( $r_a$ ):

$$r_a(t) = \frac{\ln((z_{meso} - d_0)/z_0)^2}{k^2 \cdot u(t) \cdot \eta} \quad (8.21)$$

$z_{meso}$  [m] is the height of the mesostrophic wind and is assumed 10 m,  $u$  [ $\text{m s}^{-1}$ ] is the wind speed and  $k$  [-] is the Von Karman's constant, which is 0.41.  $d_0$  [m] and  $z_0$  [m] are the displacement height and aerodynamic roughness respectively, which are related to vegetation height ( $h_c$  [m]) according to Rutter (1975):

$$d_0 = 0.75 h_c \quad (8.22)$$

$$z_0 = 0.1 h_c \quad (8.23)$$

The wind extrapolation factor,  $\eta$  [-] is 1 for  $h_c \leq z_{meso}$  and bare soils. If  $h_c > z_{meso}$ ,  $\eta$  is calculated with:

$$\eta = \frac{\ln((z_{meso} - d_{met})/z_{0met})}{\ln((z_{met} - d_{met})/z_{0met})} \quad (8.24)$$

where  $d_{met}$  and  $z_{0met}$  are the displacement height [m] and aerodynamic roughness [m] at the wind measurement height ( $z_{met}$  [m]).

Next, for vegetation the stomatal resistance ( $r_s$ ) is calculated, using the Jarvis, Noilhan and Planton (JNP) scheme (Nyogi and Raman, 1997) based on Jarvis' model (Jarvis, 1976) and extended by Noilhan and Planton (1989). In this model the resistance of vegetation to transpire is modelled. This model has been chosen, because it can be run with measured meteorological and land cover parameters. The main equation of the model is:

$$r_s(t) = \frac{r_{s,min} \cdot F_1(t)}{\chi \cdot F_2(t) \cdot F_3(t) \cdot F_4(t)} \quad (8.25)$$

The stomatal resistance depends on (Jarvis, 1976):

- $r_{s,min}$ , the minimal stomatal resistance, which is assumed to be  $60 \text{ s m}^{-1}$ .
- $F_1$ , a function of the amount of photosynthetically active radiation (PAR) available for the vegetation.
- $F_2$ , a function of air temperature to calculate the heat stress of the vegetation.
- $F_3$ , a function of air humidity to calculate the dry air stress of the vegetation.
- $F_4$ , a function of soil moisture to calculate stress caused by a dry soil.

$F_1$  is calculated as:

$$F_1(t) = \frac{1 + f(t)}{f(t) + r_{s,\min} / r_{s,\max}} \quad (8.26)$$

where

$$f(t) = 0.55 \frac{2R_n(t)}{R_p \cdot \chi} \quad (8.27)$$

where  $R_n$  is the solar radiation flux [ $\text{W m}^{-2}$ ] that reaches the foliage and  $R_p$  is the minimum radiation for photosynthesis, which is assumed to be  $100 \text{ W m}^{-2}$ .  $r_{s,\max}$  is the maximum stomatal resistance and is set to  $5000 \text{ s m}^{-1}$  (Jacquemin and Noilhan, 1990).

$F_2$  depends on the volumetric moisture content at 1 m depth and the SWRC curve. In our model  $F_2$  has been set to 1, because we assume that deep soil moisture conditions have no influence on stomatal resistance, since our root zone is confined to the upper 0.45 m.

$F_3$  is computed using the following equation:

$$F_3(t) = 1 - 0.025 \vartheta(t) \quad (8.28)$$

where the vapour pressure deficit ( $\vartheta$ ) is calculated by:

$$\vartheta(t) = e_s(t) - e_a(t) \quad (8.29)$$

The last variable  $F_4$  is based on the air temperature:

$$F_4(t) = 1 - 0.0016(298.0 - (273.15 + t_a(t)))^2 \quad (8.30)$$

In order to solve  $E_p$  from the Penman-Monteith combination equation (eq. 8.14) the slope of the saturation vapour pressure temperature relationship ( $\delta$ ) the latent heat of vaporization of water ( $\lambda$ ) and the psychrometric constant ( $\gamma$ ) are needed.  $\delta$  is calculated with:

$$\delta = \frac{4098 \cdot e_s}{(237.3 + t_a)^2} \cdot \frac{1}{274.15} \quad (8.31)$$

$\lambda$  is calculated with:

$$\lambda = 2.501 \cdot 10^6 - 2370.0 t_a \quad (8.32)$$

$\gamma$  is determined with:

$$\gamma = \left( \frac{c_p \cdot p}{0.622 \lambda} \right) \cdot \frac{1}{274.15} \quad (8.33)$$

$E_p$  is assumed 0 m/s at night and during rainfall events. The total potential transpiration ( $T_p$  [m/s]) for vegetation is calculated with:

$$T_p(t) = E_p(t) \cdot f_c \quad (8.34)$$

From the total potential transpiration, first the evaporation from the actual interception storage is subtracted. The potential transpiration that remains for the root zone ( $T_r$  [m/s]) is given by:

$$T_r = T_p(t) - \frac{E_{Int}(t)}{\Delta t} \quad (8.35)$$

The potential transpiration from each rootzone layer ( $T_{p,i}$  [m/s]) is calculated with:

$$T_{p,i}(t) = w_i \cdot T_r(t) \quad (8.36)$$

where  $w_i$  defines the rootzone distribution of transpiration:  $w_0 = 0.4$ ,  $w_1 = 0.3$ ,  $w_2 = 0.3$  and  $w_3$  to  $w_5$  are 0.

The potential evaporation for the unvegetated fraction of a grid cell ( $V_p$  [m/s]) can be calculated with:

$$V_p(t) = E_p(t) \cdot (1 - f_c) \quad (8.37)$$

The actual evaporation and transpiration from different soil layers are calculated respectively by:

$$E(t) = \beta_0 \cdot V_p(t) \quad (8.38)$$

$$T_i(t) = \beta_i \cdot T_{p,i}(t) \quad (8.39)$$

$\beta_i$  is a moisture dependent evapotranspiration reduction factor (Van Genuchten, 1978), which is calculated for layer  $i$  using:

$$\beta_i = \frac{1}{1 + \left( \frac{h_i(t)}{h_{50}} \right)^3} \quad (8.40)$$

Where  $h_i$  is known from eq. 8.10.  $h_{50}$  [m] is the matrix potential at a 50% reduction of the potential evapotranspiration, i.e.  $\beta_i = 0.5$ . It is set to -8 m, the average value adopted in Hydrus 1D (Simunek et al., 1998a) for crops.

Now, eq. 8.1 can be solved and the top soil moisture content ( $\theta_0$ ) can be calculated. When  $\theta_0 > \theta_s$  the excess soil moisture is added to the surface storage ( $X$ ):

$$X(t) = (\theta_0(t) - \theta_s) \cdot \Delta z \quad \text{for } \theta_0 > \theta_s \quad (8.41)$$

For other model layers  $\theta_i$  is between  $\theta_r$  and  $\theta_s$ .

Additionally, the SOMS model calculates the actual surface evapotranspiration,  $E_0$  [m s<sup>-1</sup>], that can be used for data-assimilation with remote sensing based  $E_0$  predictions:

$$E_0(t) = E(t) + \sum_{i=0}^N T_i(t) \quad (8.42)$$

where  $N = 2$  in order to calculate the total transpiration for the three rootzone layers.

### 8.3.2 Field data

During field campaigns in November and December of 2004 and 2005 field data was collected. Four representative sites were selected in the north of the community of Schoul. These sites were located in such a way that they cover the most common land cover and soil combinations in the study area and have a size of 1 ha. Their location has been presented in figure 8.1. Table 8.4 gives the main properties of the sites. An overview of the measurements at each site can be found in table 8.5.

#### *Soil moisture measurements*

At the four reference sites soil moisture was measured on a daily basis, using a Fieldsout TDR 300 with an attached handheld GPS (Garmin eTrex) (figure 8.6). The accuracy of the TDR is  $\pm 3\%$  (Spectrum, 2003). The sampling time on each day was chosen close to satellite overpass time: all sites were sampled between 9.00 and 12.00 am GMT. Soil moisture was sampled on a regular grid, with a gridspacing of 20 m. The TDR gives the average volumetric soil moisture content between 0 and 12 cm depth. The soil moisture measurements under cork oak forest have been done in winter 2005. Therefore the model has been separately calibrated with data from 2005 for this location (C01). The calibration procedure will be explained in section 8.3.3. For each plot of 1 ha the daily average top soil moisture content and its standard deviation were calculated from the daily grid measurements. It is assumed that small differences in sampling times give a negligible bias to the measured top soil moisture content. Under the forest at location C01 it was difficult to sample on a grid, because the GPS receiver could not always receive enough satellite signals.

*Table 8.4* Calibration sites. See figure 8.1 for the locations of the calibration sites.  $f_c$  = vegetation cover,  $\chi$  = leaf area index and  $h_c$  = canopy height. See section 8.2.2 for an explanation of soil types.

ID	Soil	Land cover type	$f_c$ %	$\chi$ [m <sup>2</sup> /m <sup>2</sup> ]	$h_c$ [m]
C01 (2005)	Sols isohumique gris couvrant les sols fersiallitique sableux lessivés	Semi-Natural (Cork oak forest)	50	1.0	8.75
C02 (2004)	sols fersiallitique sableux lessivés	Agriculture (harvested cereals)	5	0.1	0.05
C03 (2004)	Sols fersiallitiques lessivés	Agriculture (grassland)	20	0.5	0.05
C04 (2004)	Sols fersiallitiques lessivés à galets	Agriculture (grassland)	75	0.5	0.05

*Table 8.5* Measurement periods of top soil moisture content with a TDR ( $\theta_0$ ), residual soil moisture content ( $\theta_r$ ) and saturated soil moisture content ( $\theta_s$ ) from samples, saturated hydraulic conductivity ( $k_{sat}$ ) with the double ring infiltrometer and leaf area index ( $\chi$ ) with hemispherical photographs at the calibration sites (see figure 8.1 for locations).

Site	$\theta_0$	$\theta_r$	$\theta_s$	$k_{sat}$	$\chi$
C01	2005, 13 days	-	-	2005	2004
C02	2004, 31 days	2003	2003	2005	-
C03	2004, 28 days	-	-	2005	-
C04	2004, 29 days	-	-	2005	-



Figure 8.6 TDR with handheld GPS.

*Saturated hydraulic conductivity ( $k_{sat}$ )*

At the reference sites hydraulic conductivity values were derived from three infiltration measurements per site using a double ring infiltrometer (figure 8.7). The infiltration rate is the amount of water that penetrates the soil per surface area and time unit in the inner ring. The outer ring prevents lateral flow. The first infiltration volume in the inner ring is measured after 2 minutes and then at 5 minutes intervals, from which the infiltration rates can be calculated. When the infiltration rate reaches a steady state condition, it infiltrates with a rate that equals the saturated hydraulic conductivity ( $k_{sat}$ ). For practical reasons a falling head was used inside the inner ring during the measurements. Two to three measurements per site have been done, from which the most stable results have been chosen. Results for the four reference sites are presented in figure 8.8 and table 8.6. The measured  $k_{sat}$  values have been assumed to be constant for all model layers. It is generally known that  $k_{sat}$  has a large variability (Karssenbergh, 2006). Therefore the value of  $k_{sat}$  will be optimized in the calibration procedure explained in section 8.3.3.

The double ring infiltrometer is a simple method. The measurement results, can be biased by the presence of surface vegetation, soil compaction and different soil layers. At site C03 it was difficult to reach a steady-state condition, which can be related to surface vegetation and bioturbation.

Table 8.6 Measured saturated hydraulic conductivity ( $k_{sat}$ ).

Site	$k_{sat}$ [mm/h]
C01	240
C02	228
C03	336
C04	252



Figure 8.7 The double ring infiltrometer.

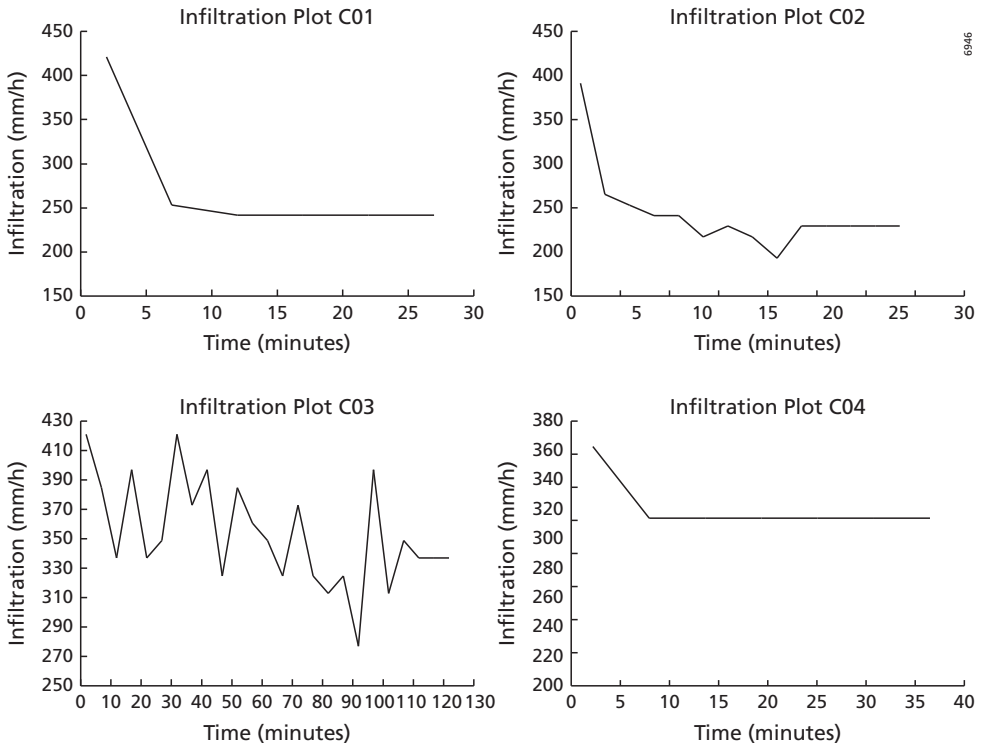


Figure 8.8 Example curves of infiltration at the four calibration sites. For locations see figure 8.1.

In 2003 2 soil samples from the *sable beige de Mamora* were analyzed in the laboratory. The soil water retention curve (SWRC) was determined, using the evaporation method (Simunek et al., 1998b). The SWRC is plotted in figure 8.9.

It can be seen that the  $k_{sat}$  from this method is different from the double ring infiltrometer data: 152 mm/h (evaporation method) versus 228 mm/h (double ring infiltrometer). A possible reason for this could be that the size of the double ring test is much larger, possibly including

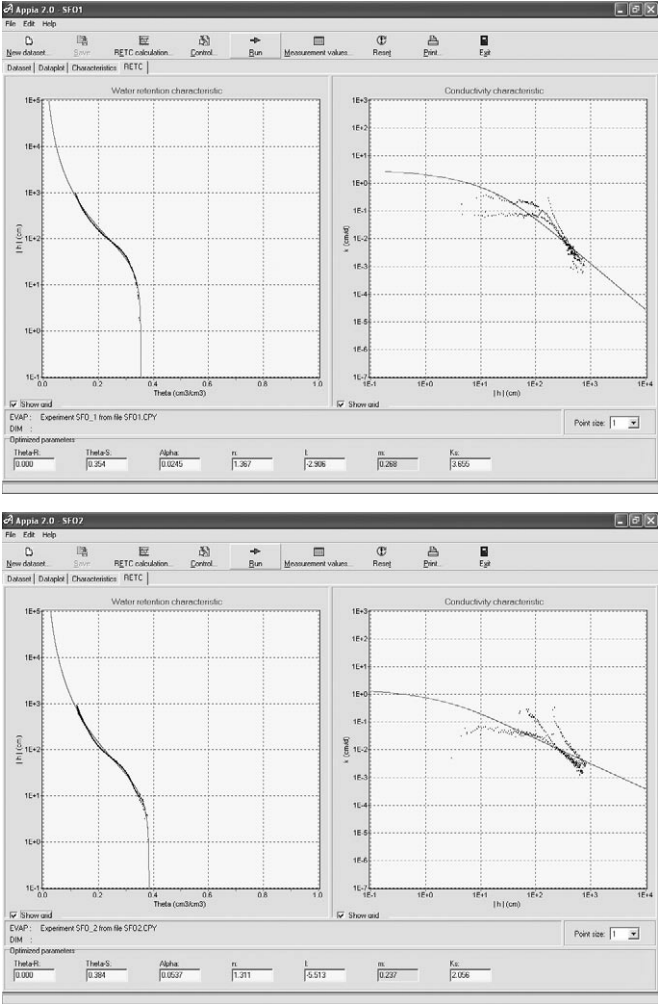


Figure 8.9 Soil Water Retention Curves for two samples from the *sable beige de Mamora*. The laboratory results show the water retention characteristic of the sample (left) and the conductivity of the soil (right). Below the graphs, the fitted parameters are reported: Theta-R = residual soil moisture content [cm<sup>3</sup>/cm<sup>3</sup>], Theta-S = saturated soil moisture content [cm<sup>3</sup>/cm<sup>3</sup>], Alpha, n, l and m are Van Genuchten parameters (Van Genuchten, 1980) of the fitted soil water retention curve and Ks= saturated hydraulic conductivity [cm/day]. Source: Alterra.

macropores, and possibly there is a hysteresis effect because the field experiments are wetting experiments while the lab tests are drying experiments. The scatter in the hydraulic conductivity graphs is very large and extrapolation to the saturated hydraulic conductivity value is not reliable. Therefore the  $k_{sat}$  results of the double ring infiltrometer will be used as initial values in the model calibration. The residual and saturated soil moisture contents are estimated based on all measurements.

#### *Land cover data ( $f$ , $\chi$ )*

Land cover data was collected at a range of land use and vegetation sites in the study area (104 in 2003 and 65 in 2004), in order to provide input for a supervised remote sensing-based land cover classification. The land cover survey consisted of the observation of land cover type, visual estimation of the fractional vegetation cover ( $f$ ) and measurement of the LAI ( $\chi$ ).

LAI was measured for semi-natural vegetation, using hemispherical photographs and WINPHOT software (Ter Steeghe, 1997). LAI is defined as the amount of leaf area per unit of ground area. Direct measurement can be done by clipping all foliage, but is very laborious, especially with trees. WINPHOT estimates LAI from the gap fraction in the zenithal view angle by assuming that leaves are small, randomly distributed, have no azimuthal preference and do not transmit light.

The inputs for WINPHOT are black and white hemispherical photographs that are created manually by thresholding grayscale photographs (figure 8.10).

Table 8.7 shows the results for all measurements for *Quercus suber* in the Forest of Mamora and a *Eucalyptus spp.* plantation near the meteorological station. WINPHOT results are very sensitive to the thresholding of the hemispherical photographs, which is a manual operation and therefore subjective. The CAN\_EYE software of INRA, which became available since November 2004, might give better results since subjectivity is reduced by an image classification on colour photographs (Jonckheere et al., 2004; Weiss et al., 2004).



Figure 8.10 Hemispherical photographs of *Quercus suber* (left) and *Eucalyptus* (right).

Table 8.7 LAI estimations using WINPHOT on four samples per vegetation type.

Vegetation	LAI [m <sup>2</sup> /m <sup>2</sup> ]
<i>Quercus suber</i>	1.01
<i>Quercus suber</i>	0.81
<i>Quercus suber</i>	1.07
<i>Quercus suber</i>	0.98
<i>Eucalyptus</i>	1.22
<i>Eucalyptus</i>	1.10
<i>Eucalyptus</i>	1.02
<i>Eucalyptus</i>	1.18

Average values of measured LAI are used for semi-natural vegetation. For grasslands and crops the LAI has been derived from literature values (Scurlock et al., 2001).

Table 8.8 shows the values used in the model.

*Meteorological measurements, rainfall and soilmoisture*

During the field campaigns of 2004 and 2005 a meteorological station (figure 8.11) measured air temperature ( $t_a$ ) relative humidity ( $H_p$ ) air pressure ( $p$ ), incoming solar radiation ( $K_s^\downarrow$ ) and wind speed ( $u$ ) at a representative location in the study area (figure 8.1). A tipping bucket rain gauge measured the precipitation intensity ( $P$ ).



Figure 8.11 The meteorological field station in the Sehouli study area. For location see figure 8.1.

Rainfall and soil moisture of the calibration sites are shown in figure 8.12 and figure 8.13. The SOMS model will be applied to a period starting from October 15<sup>th</sup> to November 23<sup>rd</sup> 2004. For location C01 only soil moisture data from 2005 exists.

The total rainfall during the modelling period was 78.1 mm. Until October 27<sup>th</sup> 2004, at the end of the dry season, the volumetric soil moisture content at all calibration sites is  $\pm 5\%$ . The first rain of the season has been registered on October 28<sup>th</sup>, 6.00 pm. The humidity of the soils rises to 25.9% for the *sol fersiallitique lessivé à galets* at site C04 and around 32% for the soils at site C02 and C03. This rise in soil moisture content is not immediate, which may be the result of the rainfall not being measured exactly at the same time, or a delayed response of the soil profile.

After a rapid wetting of the soils during the first rainfall event, the soils start drying. The first two or three days the soils dry rapidly because percolation is important, than it takes about eight more days to return to their dry initial state, mainly by evapotranspiration. The agricultural site on aeolian deposits of Mamora (*sable beige*), C02, stays dryer than the other sites, because of the large percolation rates of the precipitation into the sandy soil, which is approximately 80 cm thick. The soil at site C03 (*sol fersiallitique lessivé*), is much thinner (30 cm). Clay has been leached from the A horizon into the Bt horizon, which reduces the percolation in the Bt horizon. This forms an obstruction for percolation from the A horizon. Therefore the top soil at site C03 wettens faster than C02 and dries more slowly because of the higher water retention capabilities of the clayey Bt horizon. The site located at a quaternary terrace of the Bou Regreg River, C04, is much thicker than C03: between 1.3 and 1.8 m (Antari, 2007). The terrace deposits are very stony (*sol fersiallitique lessivé à galets*), which reduces the porosity. As a result, this site takes an intermediate position regarding its top soil moisture content, compared to the other sites.

The soil moisture measurements of calibration site C01 were done under the cork oak forest of Mamora in the winter of 2005. Although a little more rain fell during the first events of the season (a total amount of 73.2 mm on November 13<sup>th</sup> and 14<sup>th</sup> 2005), soil moisture content was lower than from measurements at C02 in 2004, which is located in the same soil type. This indicates a higher evapotranspiration of the top soil, probably from the water stored in litter that covers the soil. Location C01 is further away from the meteorological station so the rainfall of the oak forest may be slightly different from the measured rainfall.

Figure 8.15a to d shows the measurements at each calibration site with their standard error ( $SE_x$ ). The standard error of the mean of the measurements is calculated with:

$$SE_x = \frac{s}{\sqrt{n}} \quad (8.43)$$

where  $s$  is the sample standard deviation and  $n$  is the number of soil moisture measurements.

Generally, it can be seen that  $SE_x$  increases with a wetter soil. At the homogeneous aeolian deposits at sites C01 and C02,  $SE_x$  is low and more uniform than at the more heterogeneous soils at sites C03 and C04. The  $SE_x$  values are at a maximum at rainy days, as was expected.

### *Spatial model input*

The SOMS model is in fact a point model. The model parameters can be extrapolated to the entire study area by assigning parameter values to each unique soil type/land cover combination derived from the generalised soil map (figure 8.4) and land cover map (figure 8.14). In this way the point model is run for every model grid cell.

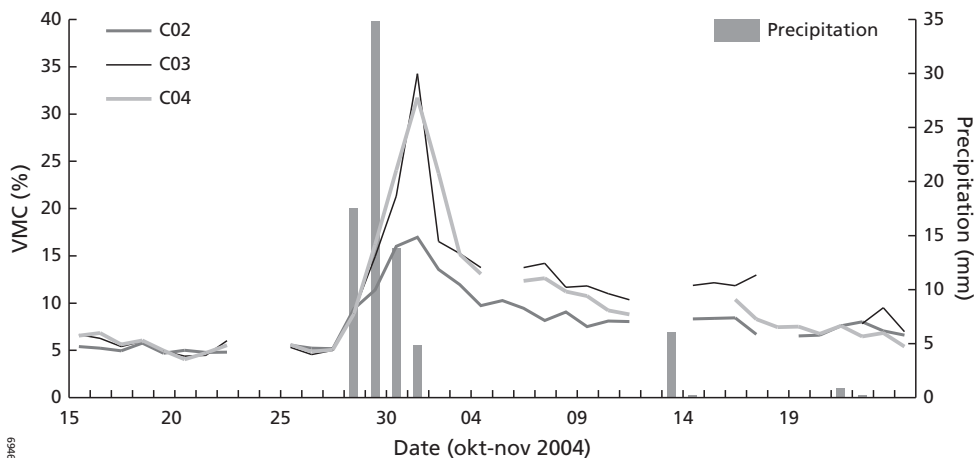


Figure 8.12 Daily precipitation and volumetric soil moisture content measured late morning at the calibration sites, winter 2004. Details about the calibration sites are given in the text and table 8.4.

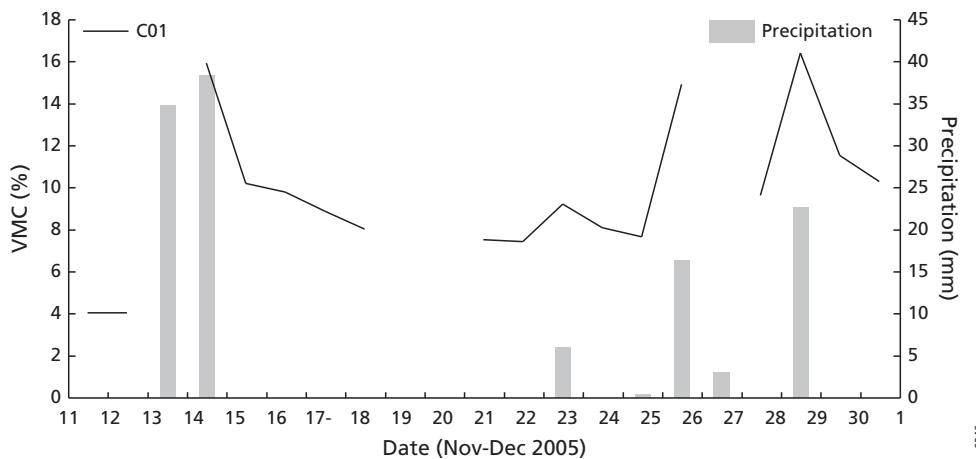


Figure 8.13 Daily precipitation and volumetric soil moisture content measured late morning at the calibration site, winter 2005 (C01), the cork oak Forest of Mamora. Details about the calibration site are given in the text and table 8.4.

The parameters connected to the soil map are the initial soil moisture content  $\theta_0(1)$ , saturated hydraulic conductivity ( $k_{sat}$ ), porosity ( $\theta_s$ ) and of the fitting parameters of the soil water retention curve ( $h_A$  and  $\zeta$  in eq. 8.10). It is assumed that the soil physical parameters and initial soil moisture of the calibration sites are representative for its soil type/land cover combination and for the whole soil profile.

The parameters that are linked to the land cover map are LAI ( $\chi$ ), vegetation cover ( $f$ ) and albedo ( $\alpha$ ).

The land cover map has been derived from a supervised land cover classification of an image from the Advanced Spaceborne Thermal Emission Radiometer (ASTER) of October 20<sup>th</sup> 2004, 11.13 am. All optical channels and a segmentation layer (with mean reflectance and its standard deviation for each segment), created with eCognition (Definiens-Imaging, 2008), have been used in a minimum distance to mean classification. Areas under clouds and their shadows have been masked in the classification and were afterwards digitized from aerial photographs from June 1996. The difference in date was not problematic, since most of these areas consist of semi-natural vegetation that did not change much in time.

Albedo has been calculated using the empirical equation of Liang (2000):

$$\alpha = 0.484\alpha_1 + 0.335\alpha_3 - 0.324\alpha_5 + 0.551\alpha_6 + 0.305\alpha_8 - 0.367\alpha_9 - 0.0015 \tag{8.44}$$

Where  $\alpha$  is the total broadband shortwave albedo and  $\alpha_n$  is the surface reflection of ASTER band  $n$ . In Liang et al. (2003) the equation was validated and shows an  $r^2$  of 0.839 compared to field measurements at several dates and land cover types. An average albedo value for each land cover class was calculated.

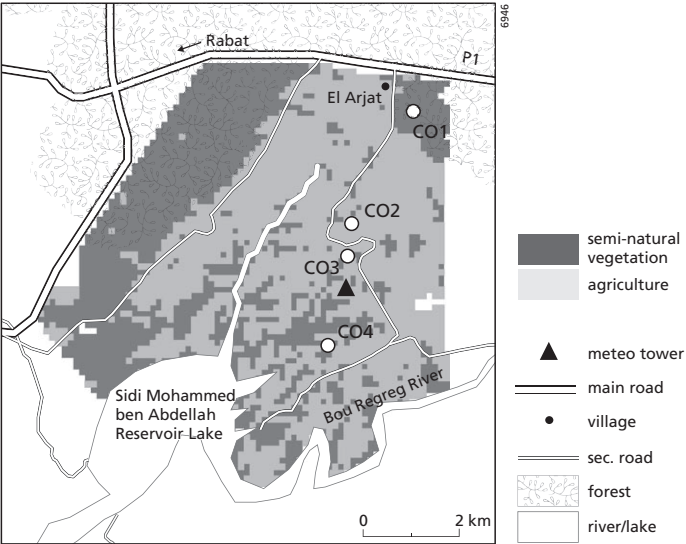


Figure 8.14 Land cover map with calibration sites and location of the meteorological station.

Table 8.8 Average land cover properties assigned to the land cover map (figure 8.14). Albedo ( $\alpha$ ), fractional vegetation cover ( $f_c$ ) and leaf area index ( $\chi$ ). The standard deviation ( $\sigma$ ) of  $\alpha$  is determined for all pixels of the albedo map within a land cover class.

Land cover	$\alpha \pm \sigma$	$f_c$ (%)	$\chi$ (m <sup>2</sup> /m <sup>2</sup> )
Rainfed agriculture	0.21 ± 0.02	60	0.5
Semi-natural vegetation	0.16 ± 0.03	50	1.0

The mean values for  $\chi$ ,  $fc$  and  $\alpha$  were assigned to the three land cover classes (figure 8.14, table 8.8).

### 8.3.3 Model calibration

The SOMS model needs to be calibrated to account for uncertainties in parameter values, initial conditions and boundary conditions used in the model.

The SOMS model was calibrated for each of the four calibration sites separately, by optimizing the predicted top soil moisture content ( $\hat{\theta}_0$ ), against the measured daily soil moisture content  $\theta_0$ . Automatic model calibration was done with the PEST (Parameter ESTimation) software package (Doherty, 2002). PEST is a model independent inverse modelling optimization suit, which is based on the Leven-Marquardt algorithm. PEST minimizes the following objective function:

$$\Phi = \sum_{t=1}^T (w(t) \cdot r(t))^2 \quad (8.45)$$

where  $T$  is the total number of field measurements and  $r(t)$  is the residual at timestep  $t$ , expressing the difference between the model prediction  $\hat{\theta}_0$  and the field measurement  $\theta_0$  at timestep  $t$ :

$$r(t) = \hat{\theta}_0(t) - \theta_0(t) \quad (8.46)$$

The weights  $w(t)$  are the inverse of the standard error of the mean of the grid measurements ( $n > 20$  per site) of soil moisture. Because the standard errors of wet soils are high (figure 8.15), they cause a low weight. The use of weights results in better calibration results for drying soils compared to wetting soils.

The soil moisture model uses many parameters that were measured during the field campaign. It was decided to calibrate the saturated hydraulic conductivity  $k_{sat}$  and  $\zeta$ , because (1) the model is very sensitive to these parameters; (2) accurate field measurements were lacking, and (3) they have a large natural variability.

First, the initial value of the calibration parameter is given as an input to PEST. The measured values of  $k_{sat}$  (table 8.6) and an intermediate value of  $\zeta = 6.2$  have been used. As  $k_{sat}$  and  $\zeta$  have lognormal distributions, within PEST a logarithmic transformation has been applied.

Next, PEST runs the model iteratively. Each iteration step starts with the linearization of the relationship between the calibration parameters and the model outcomes for which the objective equation (eq. 8.45) will be minimized using field observations of soil moisture. This is done by expanding the currently best parameter set with a Taylor series, requiring the calculation of the derivatives of all observations with respect to all parameters, using finite differences.

The model is run once for each calibration parameter during every optimisation iteration and a small increment is added to the parameters. The changes of the new model results are divided by this increment for calculation of their derivatives with respect to the parameter.

When the objective equation is minimal, PEST reports the corresponding  $k_{sat}$  and  $\zeta$  together with their covariance and correlation matrix.

## 8.4 Results, calibration and evaluation

First the results of the calibration of the model at each of the four calibration sites will be discussed. Next, the soil moisture estimations of the SOMS model with the spatial stratification of parameters are evaluated using an independent set of soil moisture measurements.

### 8.4.1 Calibration

The model has been run for each of the four calibration sites using meteorological data of 2005 for site C01 and 2004 for sites C02 to C04. 2004 contains 3 rainfall events, while there are 4 in 2005.

The saturated hydraulic conductivity ( $k_{sat}$ ) estimated by PEST is 1082 mm h<sup>-1</sup> for C01, 17192 mm h<sup>-1</sup> for C02, 420 mm h<sup>-1</sup> for C03 and 1209 mm h<sup>-1</sup> for C04. The high  $k_{sat}$  values are likely a result of over-dimensioning of the system, with which is meant that several combinations of parameter values can lead to a minimum of the objective function (eq. 8.45) in PEST. PEST reports a correlation of 0.3 between  $\zeta$  (eq. 8.10) and  $k_{sat}$ . The calibrated values of  $\zeta$  give realistic values for the texture classes found in the study area (Van Beek, personal communication). However, because of the low moisture content (5-7%) this leads to very small fluxes (< 1·10<sup>-6</sup> mm h<sup>-1</sup>) that cannot cause the correct model response. The PEST algorithm compensates by increasing  $k_{sat}$  to extreme values in order to simulate a percolation flux that can influence the moisture dynamics. Simulations were done with a low  $\zeta$  value and lower  $k_{sat}$  values, but this lead to a rapid drying out of the soil resulting in a low ( $\theta_s$ ) moisture content outside the rainfall periods. The reason for this can be that the Farrel and Larson equation (eq. 8.10) is a log-linear estimate of the SWRC curve, which fits well in the central part of the SWRC curve, but less well at both ends (saturation and extreme dryness). The flux at the dry end will be over-estimated with low values of  $\zeta$ . We therefore selected the combination of modelling parameters that lead to the best simulation results: high  $\zeta$  and  $k_{sat}$  values.

For each of the calibration sites timeseries of measured and modelled top soil moisture values were produced and are presented in figure 8.15a to d. The graphs show the average measured top soil moisture and its standard deviation.

The calibrated model results for soil drying after a rainfall event compare well with measured values. The model results show that model predictions during rainy days is poor compared to dry days. In all cases, except for C01, the model underestimates the top soil moisture content at rainy days. On the other hand, the standard errors in soil moisture measurements are also higher for wet soils. The modelled values are mostly within one standard error of the field measurements.

In the scatterplots of figure 8.16 predictions are plotted against observed soil moisture measurements.

For each calibration site the error variance,  $\sigma_E^2$ , is calculated as a goodness of fit measure. It is defined as:

$$\sigma_E^2 = \frac{1}{T-1} \sum_{t=1}^T (\hat{\theta}_0(t) - \theta_0(t))^2 \quad (8.47)$$

Additionally, the modelling efficiency (Nash and Sutcliffe, 1970) has been calculated with:

$$\Xi = \left[ 1 - \frac{\sigma_E^2}{\sigma_0^2} \right] \quad (8.48)$$

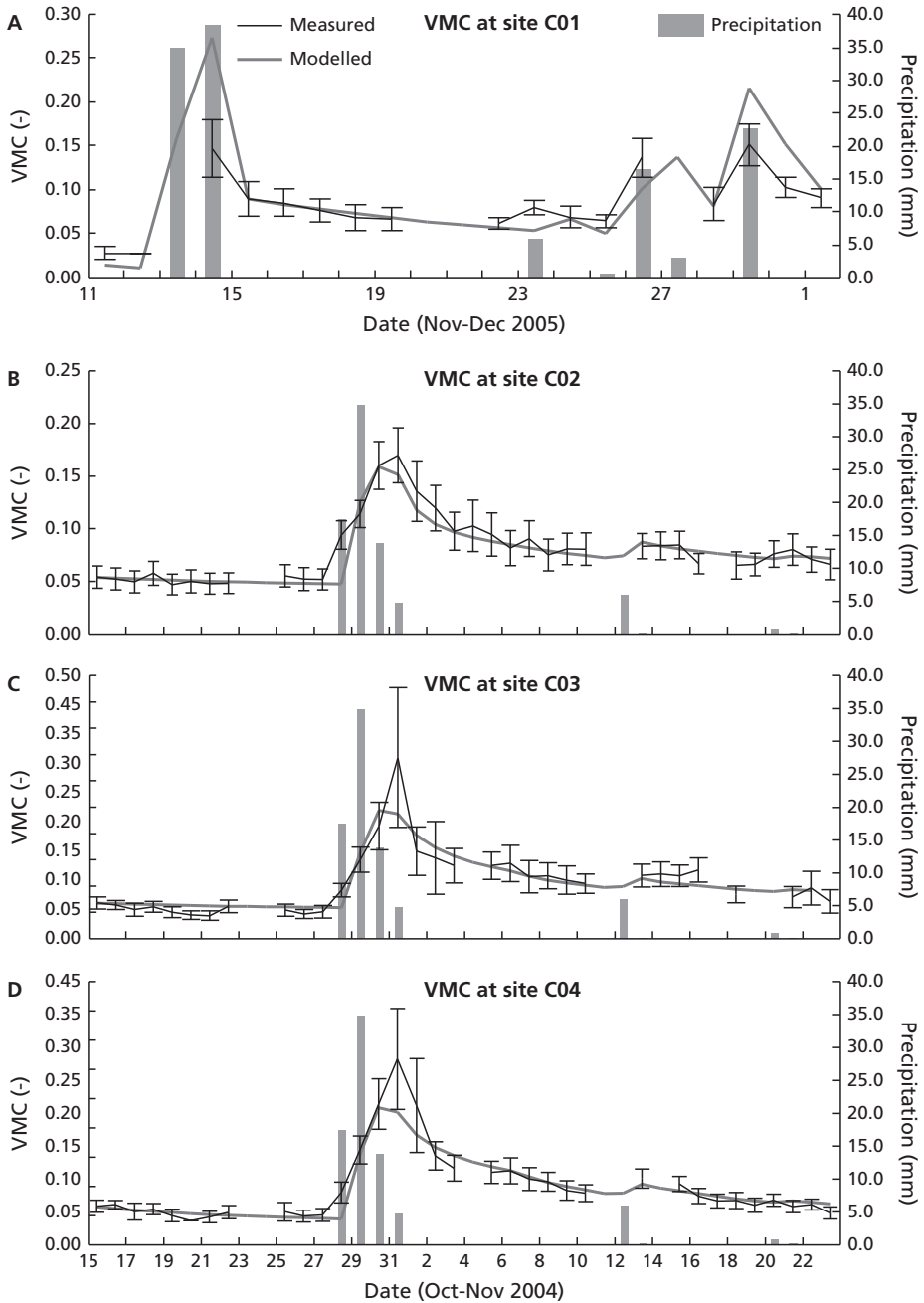


Figure 8.15 Measured and modelled top soil moisture for the four reference sites C01, C02, C03 and C04. Details about the calibration sites are given in the text and table 8.4. The whiskers of the measurements indicate 1 standard error (eq. 8.43).

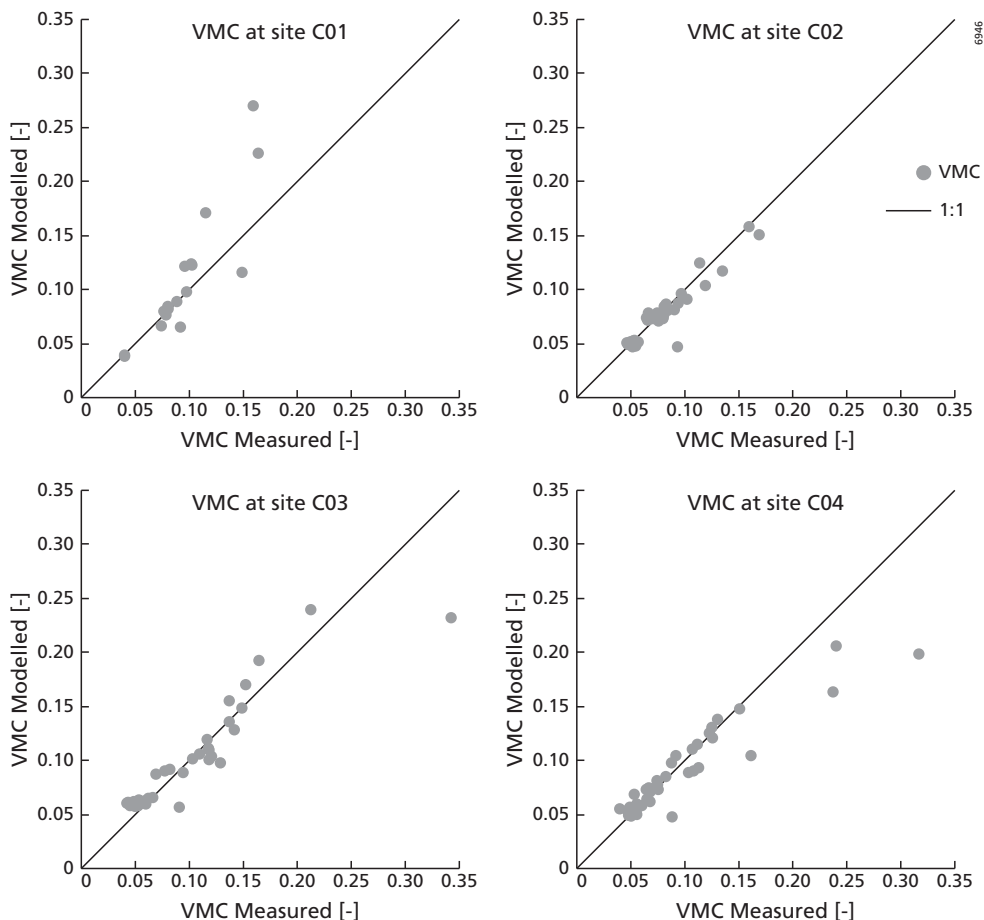


Figure 8.16 Scatterplots of measured versus modelled soil moisture values.

where  $\sigma_0^2$  is the variance of the measured soil moisture. A value of 1 means a perfect fit, while 0 or negative is a bad fit. Additionally the Root Mean Square Error (RMSE, eq. 3.1) and  $r^2$  are given in table 8.9.

The automatic calibration performed well for all sites. However, for C01 the model has the poorest fit, shown by a negative modelling efficiency and high RMSE and Error Variance.

This difference can be explained by the fact that C01 has a much higher LAI with a relatively high vegetation cover, compared to the other sites. Probably, the evapotranspiration or interception algorithms cause larger errors in this case.

#### 8.4.2 Evaluation

The model has been evaluated with an independent dataset, collected during the field campaign of 2004. The assumption that vegetation cover and LAI are constant during the modelling period probably holds for 2004, because precipitation was too low for rapid crop growth during the

Table 8.9 Goodness of fit of the calibration.  $\sigma_E^2$  is the error variance,  $\Xi$  is the modelling efficiency and  $T$  is the number of days.

Site	$\sigma_E^2$	RMSE	$\Xi$	$r^2$	$T$
C01	$1.43 \cdot 10^{-3}$	0.037	-0.15	0.78	17
C02	$1.33 \cdot 10^{-4}$	0.012	0.86	0.88	35
C03	$6.14 \cdot 10^{-4}$	0.025	0.83	0.84	32
C04	$8.31 \cdot 10^{-4}$	0.029	0.77	0.86	34

Table 8.10 Evaluation results with an independent dataset of 2004. RMSE = Root Mean Squared Error (eq. 3.1),  $T$  = number of measurements

Validation site	RMSE	$T$
V02	0.035	26
V03	0.010	4
V04	0.007	4

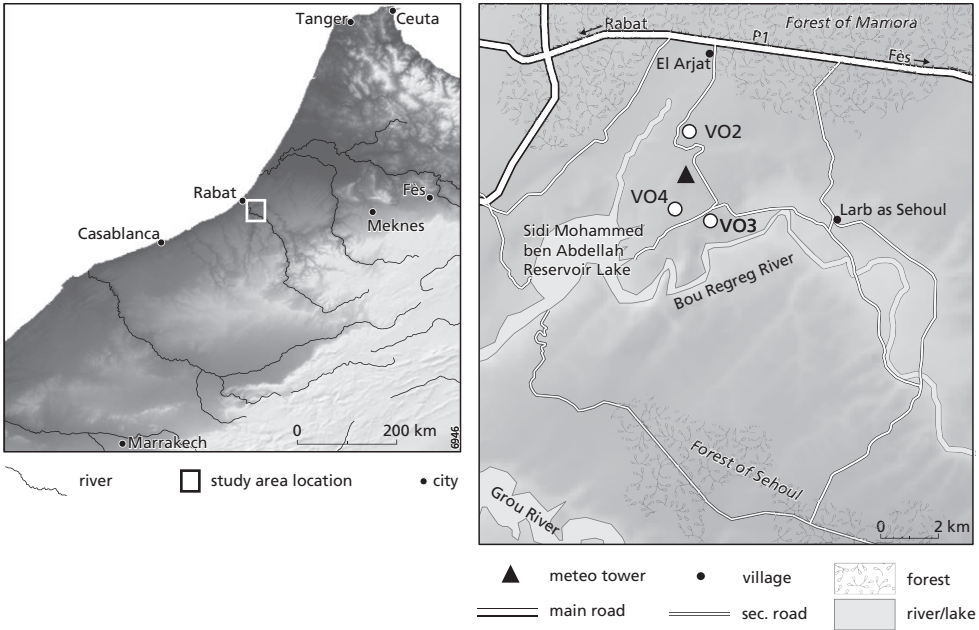


Figure 8.17 Validation sites.

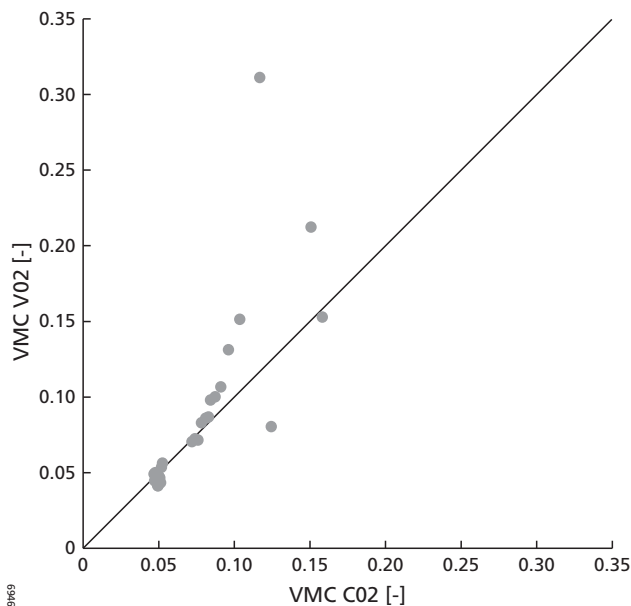


Figure 8.18 Scatterplot of validation of the model results for site C02.

measurement period, after the first rainfall events of the season. In wetter years, like 2005, land cover can change rapidly. Farmers plough the soil with different means and crops start growing shortly after ploughing when favourable conditions exist. This could be the explanation why the model does not perform well for 2005 if soil moisture measurements are compared with model outcomes.

The location of the evaluation sites can be found in figure 8.17. The land cover/soil type combination of V02, V03 and V04 corresponds to C02, C03 and C04 respectively, which can be found in table 8.4. V02 has been measured during 26 days, V03 and V04 have been measured for four days.

Figure 8.19 shows the timeseries of the model and validation data. Table 8.10 gives the RMSE of the evaluation with data from 2004. Evaluation results of V03 and V04 are within the standard deviation of the evaluation measurements of top soil moisture and within the reported measurement accuracy of the TDR. The higher RMSE for site V02 are due to measurements in wet periods, when the standard deviations of individual measurements are higher as can also be seen in the scatterplot of figure 8.18. The other evaluation data are from dry days at the end of the modelling period.

### 8.4.3 Spatial results

In fact SOMS is a point model that is distributed by means of a combination between a land cover and a soil map. This stratification is clearly visible in the model results. Smooth boundaries and variance within soil and land cover types were not modelled.

Figure 8.20 shows the initial top soil moisture in the study area and the predictions for four sites that are comparable with the calibration sites. For three sites (2, 3 and 4) the spatio-

temporal model is identical to the calibration data, because it uses the same data and no spatial variation is taken into account. The soil moisture predictions under semi-natural vegetation for 2004 cannot be validated, but give reasonable results.

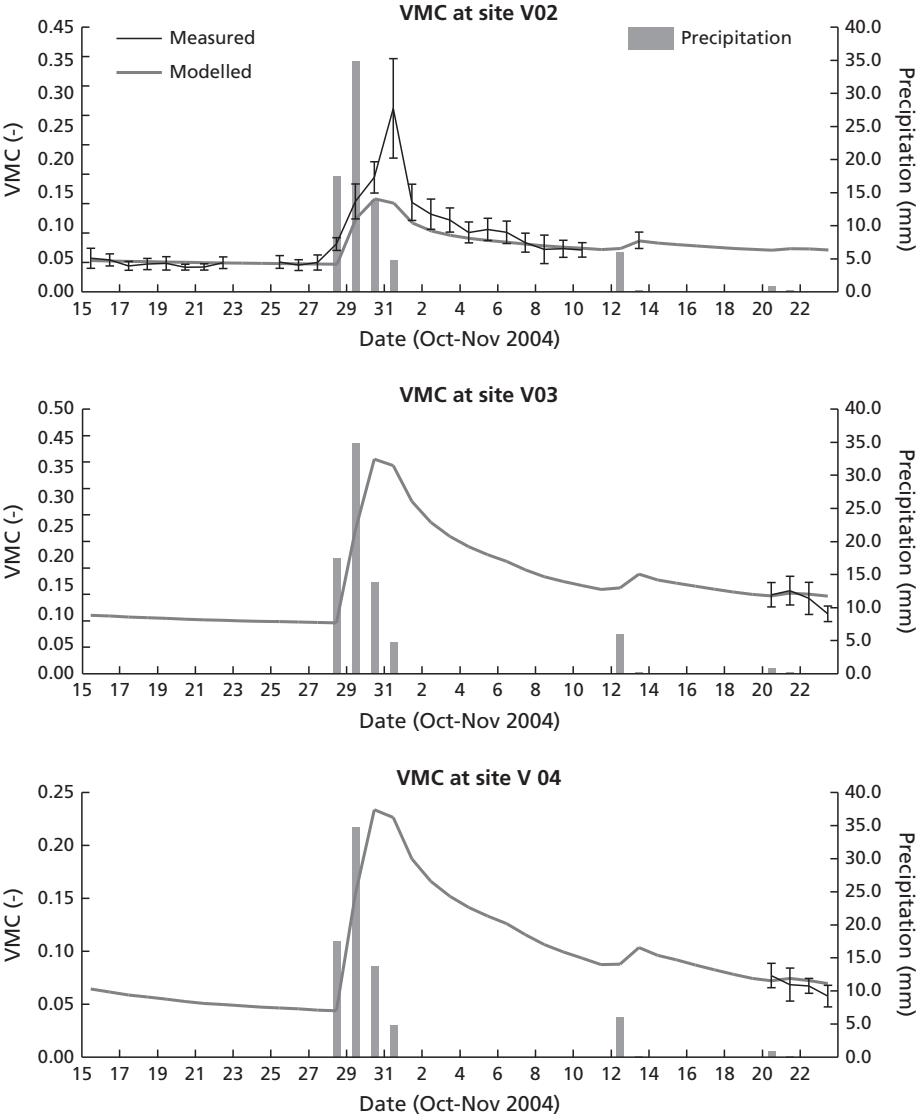


Figure 8.19 Modelled versus measured volumetric soil moisture content (VMC) at the validation sites V02, V03 and V04.

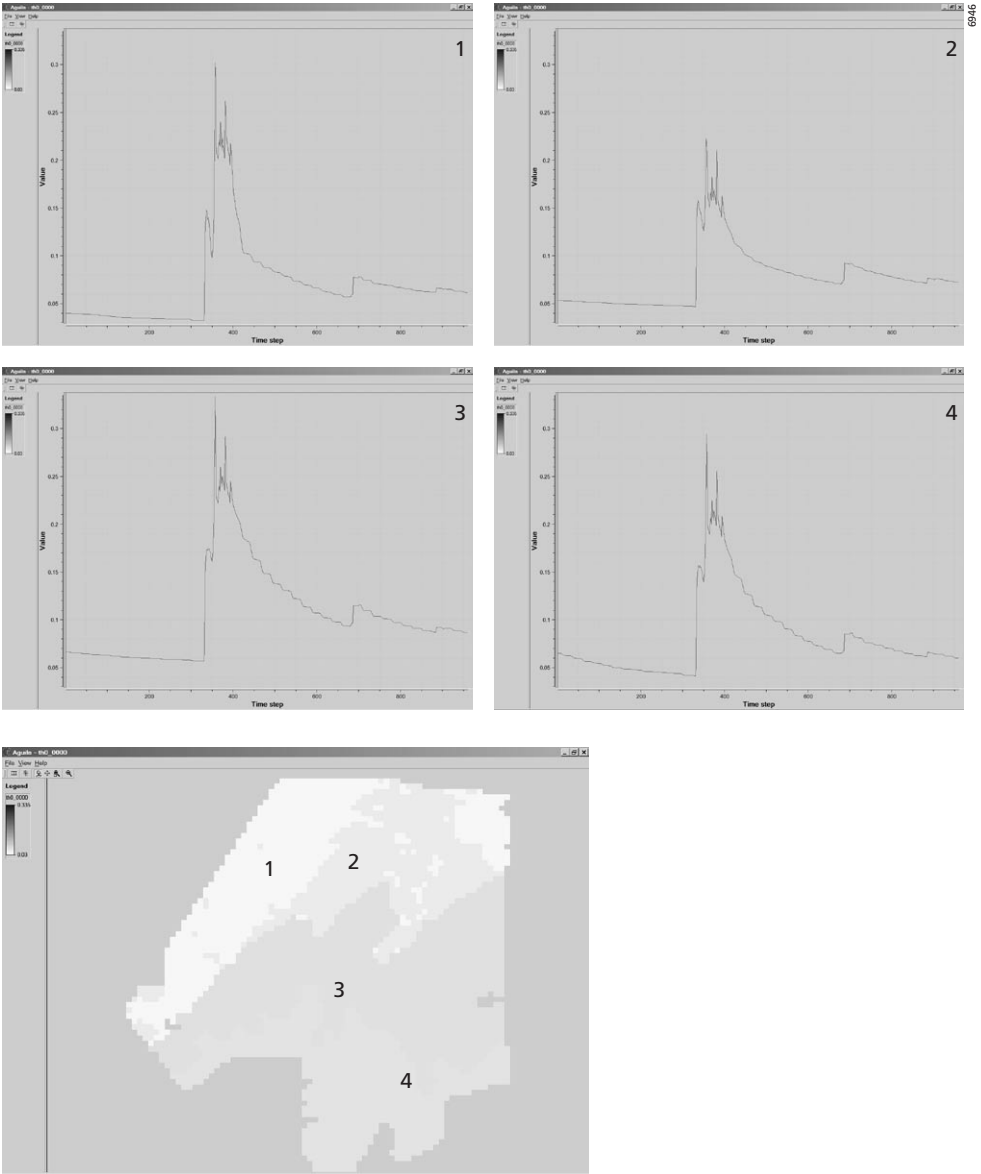


Figure 8.20 Spatial modelling of top soil moisture using PCRaster.

## 8.5 Discussion

The soil moisture model described in the previous paragraphs is capable of predicting top soil moisture with a RMSE between 0.007 and 0.037 for agricultural areas in the community of Sehoul in winter 2004. For dry periods the accuracy of the modelled top soil moisture is within the reported measurement accuracy of the TDR, which is 0.03. We were unable to validate the model predictions for semi-natural vegetation, because soil moisture measurements on this land cover type were not available in 2004. When the model is applied to the situation of 2005, it does not give reliable results for sites C02 to C04. To apply the model to different years, a new calibration is needed. This is a common problem with many models (Beven, 2002). Therefore the results for C01, which has been calibrated with data from 2005, should be interpreted with care.

Model predictions, as well as field measurements are not reliable during rainfall events. Field measurements are sparse during rainfall events and standard deviations of the measurements are large, causing a low weight in the automatic calibration by PEST. However, for the purposes of soil moisture modelling, the prediction of soil moisture patterns after and in-between rainfall events is more important than during rainfall events. The integration with remote sensing based evapotranspiration can only take place on days with clear skies. Because at satellite overpass moments the model will be optimized, it is important that soil moisture estimates of SOMS are better at other moments. The estimation of evapotranspiration, however, should be optimized for satellite overpass times, because this is the variable used for data assimilation.

In this model the influence of dew has been neglected. Dew is very common in this region at times that moist air from the Atlantic Ocean condensates when temperatures are low around sunrise. It has been frequently observed during the model period.

Because top soil moisture was only measured on a daily schedule, the diurnal variation in top soil moisture is unknown. The temporal resolution of the model (hours) does not match the temporal resolution of calibration and validation measurements (days). Model estimations and field measurements have been evaluated for values at noon. It is not clear if the diurnal variation in top soil moisture can be neglected.

To improve the model for soil moisture predictions in agricultural areas in the growing season, a simple plant growth model should be applied and several land cover maps should be used. A linear, crop specific increase in LAI could improve the results in a simple manner.

Soil physical parameters used in this model, i.e. hydraulic conductivity and SWRC characteristics, are based on a very limited set of field and laboratory measurements. Therefore the exponential relation between soil moisture and hydraulic conductivity has been calibrated by optimizing the saturated hydraulic conductivity and assumed to be uniform over the soil profile.

Although the soils in the study area are quite homogeneous, the lateral and vertical variability of these parameters should at least be known for a proper extrapolation over the whole study area. In this research it is anticipated that the assimilation of remote sensing data improves the representation of the spatial variability in soil moisture within the soil and land cover units of the model.

## 8.6 Conclusions

In this study we prepared a spatio-temporal soil moisture model for the integration of a remote sensing based surface energy balance model at the scale of an agricultural community. The calibrated soil moisture model is capable of simulating the spatial and temporal patterns of top soil moisture for agricultural and semi-natural areas after rainfall events on an hourly basis. For agricultural areas the model results are comparable with independent measurements. The model is also capable to simulate the actual evapotranspiration flux that should form the basis for assimilation with evapotranspiration modelled by a remote sensing based energy balance model. In the present situation PEST is needed to find the best combination of parameters. Possibly PEST would not be needed when more and/or better soil physical property data are available to give a better calibration of the unsaturated hydraulic conductivity function. The model can be improved when the spatial variation of soil physical parameters and input variables is known. Results for semi-natural vegetation should be interpreted with care, since for this land cover type the model was calibrated with data from a different year.

An increase of the temporal resolution of the soil moisture measurements for calibration can improve the model predictions of the diurnal variation in top soil moisture.

Looking at the error bars of the measured soil moisture curves, it is clear that the variability of soil moisture within a field is fairly large, while a spatial pattern of the predicted soil moisture based on a combination of soil units and land use gives a uniform soil moisture field per stratum. In the next chapter, the integration of a remote sensing based energy balance model and this soil moisture model will be explained. It is hypothesised that in this way, the spatial predictions of soil moisture patterns by this model will be improved.

## **Part IV**

# **Integration of remote sensing data in a soil moisture model**



# 9 Error propagation in SEBS and SOMS using Monte Carlo simulations

## 9.1 Introduction

In Part II and III the Surface Energy Balance System (SEBS) and the Soil Moisture System (SOMS) model have been introduced. Both are deterministic, process-based, models that predict a variable, depending on deterministic input variables and parameters. SOMS predicts the volumetric soil moisture content (VMC) and actual evapotranspiration (AET), SEBS estimates AET.

The propagation of errors in input variables and parameters used in the model will affect the accuracy of the model predictions (Heuvelink et al., 1989). Quantification of these errors is important for practical application of the model predictions, for comparison of different modelling approaches to investigate which model results in the smallest output uncertainty and for improving the process descriptions in the model.

The aims of this chapter are (1) to determine the uncertainty in model output and to compare the output error of AET as predicted by SEBS and SOMS; (2) to determine the range of uncertainty of model predictions for different input scenarios of data availability; (3) to determine if field measurements are within the uncertainty range of the different error propagation scenarios, and (4) to compare the uncertainty of VMC predicted by SOMS with uncertainty in field measurements of VMC.

A number of studies have been done on the error propagation of soil moisture models (Leenhardt et al., 1994; Leenhardt, 1995; Heuvelink and Pebesma, 1999; Crosetto et al., 2000; Christiaens and Feyen, 2001; Margulis, 2001; Mölders et al., 2005). This is, however, the first study that includes all error sources in a process-based soil moisture model and that evaluates the performance of the model in terms of predicted mean and uncertainty, compared to field measurements.

Different scenarios of data availability will be evaluated. The following scenarios have been defined:

1. SOMS – Data Rich Scenario: representing a scenario with measurement data available from field measurements, maps, and satellite images. The error models are representative for these data sources.
2. SOMS – Data Poor Scenario: representing a scenario without field data. Only data from remote sensing images, maps and a meteorological station are used. The errors in unknown variables and parameters have been increased for the error models in this scenario, compared to the SOMS – Data Rich Scenario.
3. SEBS – Large Error Scenario: this scenario assumes that the measurement and upscaling of surface radiometric temperature introduces a large error, and other error sources are

negligible. Furthermore, SEBS results are most sensitive to errors in surface radiometric temperature (chapter 6).

4. SEBS – Small Error Scenario: this scenario assumes that only a small measurement error in surface radiometric temperature causes errors in SEBS estimates, and other error sources are negligible.

The same error propagation scenarios will be used in the chapter 10, where the Monte Carlo approach is used in a data assimilation algorithm in order to improve estimations of top soil moisture.

## 9.2 Methods

Environmental models can contain six types of error sources: attribute errors, positional errors, lineage, logical consistency, completeness and temporal accuracy (DCDSTF, 1988; Guptill and Morrison, 1995). It is assumed that positional errors are small because input maps are georeferenced to each other and the satellite images. The positional accuracy will be within a model gridcell of 125 meters. Logical consistency and completeness have been checked by water and energy budgets. Other errors in the mathematical model descriptions will show up when distributions of the predicted variable differ significantly from field measurements. The temporal accuracy is determined by the synchronisation of temporal input data and the model timestep. These errors are assumed to be small and are ignored. Therefore, the only errors considered here are attribute errors.

To quantify the model output error, input variables and parameters need to be described as a set of random fields. The description of a static model, like SEBS, becomes (Karssenbergh and De Jong, 2005):

$$A(x) = f(I(x), P(x)) \text{ for all } x \in D \quad (9.1)$$

The description of a forward dynamic model, like SOMS, becomes:

$$A(x, t+1) = f(A(x, t), I(x, t), P(x)) \text{ for all } x \in D \text{ and each } t \quad (9.2)$$

where  $A$  is a set of stochastic state variables, which is a function ( $f$ ) of a set of stochastic input variables  $I$  and a set of stochastic model parameters  $P$ . For SEBS,  $f$  is the model described in section 4.5. In the case of SOMS,  $f$  is the model description in section 8.3.1. The distributions of  $A$ ,  $I$  and  $P$  are defined by the error model of each input variable or model parameter. The estimation of the variance of a model prediction is a commonly used indicator of model error and spread of the probability density of a model output (Van Leeuwen, 2003).

$A$ ,  $I$  and  $P$  are spatial, with  $x$  the spatial index, referring to a grid cell with discrete coordinates within the domain of interest  $D: D \subset \mathfrak{R}^2$ . In eq. 9.2,  $A$ ,  $P$  and  $I$  are temporal, with  $t$ , the discrete model timestep.

The different scenarios of error propagation differ in the way  $I$  and  $P$  are defined. The next sections describe the different error propagation scenarios.

The set of stochastic state variables,  $A$ , can be estimated using the Monte Carlo method (Hammersley and Handscomb, 1979; Lewis and Orav, 1989). The Monte Carlo method

computes the process based model  $N$  times with input variables and parameters that are realisations from  $I$  and  $P$  (Heuvelink, 1998). After  $N$  runs, the model results form a random sample from the distribution of  $A(x)$  (eq. 9.1) or  $A(x,t)$  (eq. 9.2). From this sample the mean and variance of the distribution of  $A(x)$  or  $A(x,t)$  can be estimated if  $N$  is large enough.

Schematically the Monte Carlo method works as follows (Heuvelink, 1998; Karssenbergh and De Jong, 2005):

1. For each Monte Carlo run  $s$ ,  $s=1\dots N$  (lower-case variables will be used to represent realisations of random variables given as upper-case in eq. 9.1 and 9.2):
  - a. Generate realisations for each stochastic input variable, and realisations for each stochastic model parameter, for each time step  $t$  (in the case of a dynamic model).
  - b. For this set of realisations, run  $f(\cdot)$  (eq. 9.1 or 9.2), and store the realisations of the model output variables  $a$  that are of interest, for all time steps in the case of a dynamic model.
2. Compute and store sample statistics (e.g. mean, variance) from the  $N$  model outputs, for each model variable and each time step  $t$ , or for a selection of model variables and time steps.

The larger the number of Monte Carlo runs ( $N$ ), the more accurate the estimations of sample statistics are. In this study a number of  $N = 200$  runs is used for the error propagation of both SEBS and SOMS. This is a trade-off between accuracy of the estimation and model runtime. In order to test all scenarios, the run-times had to be limited. It is assumed that 200 Monte Carlo runs give results that are sufficiently accurate for the error propagation models used in this research, while keeping runtimes below 72 hours for the SOMS scenarios.

The realisations of  $I$  and  $P$  are obtained by transforming independent realisations from a univariate uniform distribution created with a pseudo random number generator (Lewis and Orav, 1989; Press et al., 1992) to the desired distribution of  $I$  and  $P$  (Devroye, 1986). The GSTAT (Pebesma and Wesseling, 1998) software has been used to generate random fields and the tools used for the Monte Carlo simulation have been developed by Karssenbergh and De Jong (2005).

### 9.2.1 SOMS – Data Rich Scenario

Heuvelink (1998) describes various ways to model errors in model inputs and parameters, depending on their nature, being spatial, temporal or spatio-temporal. Spatial error models can be further subdivided into continuous, discrete or mixed models. Table 9.1 lists the input variables and model parameters used in the SOMS – Data Rich Scenario for error propagation of the soil moisture model. The error models will be explained below.

#### *Non-Spatial Error Model*

Temporal inputs that are considered as non-spatial, are represented with the non-spatial error model (NSEM):

$$Z(t) = \mu(t) + \varepsilon(t) + \varepsilon_g + \mu(t) \cdot \varepsilon_r(t) \quad (9.3)$$

where  $Z(t)$  is the non-spatial, temporal stochastic input variable or parameter.  $\mu(t)$  is the measured deterministic variable at timestep  $t$ .  $\varepsilon(t)$  is a random variable that represents the non-systematical error in the measured variable and  $\varepsilon_g$  is a random variable representing the systematic error or bias (Heuvelink, 1998), induced for instance by a measuring instrument.  $\varepsilon_r(t)$

Table 9.1 Input variables and parameters modelled with error in the soil moisture model. NSEM = Non Spatial Error Model, DMSV = Discrete Model of Spatial Variation, CMSV = Continuous Model of Spatial Variation and MMSV = Mixed Model of Spatial Variation.

Input variable ( $I(x,t)$ )	Description	Type	Model
$T_a$	Air temperature	Non-spatial, temporal	NSEM
$H_f$	Relative humidity	Non-spatial, temporal	NSEM
$K_S^{\downarrow}$	Incoming shortwave radiation	Non-spatial, temporal	NSEM
$p$	Air pressure	Non-spatial, temporal	NSEM
$u$	Wind speed	Non-spatial, temporal	NSEM
$\theta_0$	Initial volumetric soil moisture content	Spatial	DMSV
$P$	Precipitation	Spatial, temporal	CMSV
$E_p$	Potential evapotranspiration	Spatial, static	MMSV
Parameters ( $P(x)$ )	Description	Type	Model
$k_{sat}$	Saturated hydraulic conductivity	Spatial, static	DMSV
$\zeta$	Parameter of soil water retention curve	Spatial, static	DMSV
$\theta_s$	Saturated volumetric soil moisture content	Spatial, static	DMSV
$S_{int}$	Maximum interception storage	Spatial, static	MMSV

Table 9.2 Non-Spatial Error Model (NSEM) parameters for the meteorological measurements.  $Z(t)$  are the random input variables,  $C=\text{var}(\epsilon(t))$ ,  $C_g=\text{var}(\epsilon_g)$  en  $C_r=\text{var}(\epsilon_r)$

Input	Explanation	Instrument	C	$C_g$	$C_r$	range	Unit
$T_a$	Air temperature	HMP35D	$2.5 \cdot 10^{-3}$	0.25	0	0-60	Celsius
$H_f$	Relative humidity	HMP35D	$2.5 \cdot 10^{-3}$	$9.0 \cdot 10^{-4}$	0	0-1	[-]
$K_S^{\downarrow}$	Incoming shortwave radiation	KIPP CM3	4.0	163.84	0	> 0	W·m <sup>-2</sup>
$p$	Air pressure	Keller PAB/8556.1-1.1	1.56	1.21	0	900-1100	mBar
$u$	Wind speed	Vector Instruments A100R	$2.5 \cdot 10^{-3}$	0.36	$2.5 \cdot 10^{-5}$	>0	m·s <sup>-1</sup>

is a random variable that represents the non-systematical error in the measured variable, relative to the measured value. The assumptions hereby are that:

1.  $\epsilon_g$  is a non-temporal, non-spatial random variable with zero mean and variance  $\text{var}(\epsilon_g) = C_g$ .
2.  $\epsilon(t)$  is a temporal, non-spatial random variable with zero mean and variance  $\text{var}(\epsilon(t)) = C$ . It is independent for each timestep.
3.  $\epsilon_r(t)$  is a temporal, non-spatial, random variable with a mean of one and variance  $\text{var}(\epsilon_r(t)) = C_r$ . It is independent for each timestep.

NSEM has been applied to the meteorological input data, except precipitation. The meteorological input data varies in time, but it has been assumed that the measurements have zero spatial variation. This assumption had to be done, because only one meteorological station

has been used and no data on the spatial variability of meteorological variables were available for the study area. It should however be noted that the spatial variability in air temperature ( $T_a$ ) and wind speed ( $u$ ) might be large due to the variation in land cover.  $\mu(t)$  is the value measured by the instrument,  $\epsilon_g$  is the measurement error of the instrument as reported by the manufacturer and  $\epsilon(t)$  is the non-systematical error, derived from an intercalibration of the instruments used in this research with instruments from the Royal Netherlands Meteorological Institute (KNMI) at Cabauw, the Netherlands. The NSEM parameters are reported in table 9.2. For wind speed,  $u$ , the relative noise term  $\epsilon_r(t)$  has been added because friction within the anemometer causes a lag before it starts to measure.

*General Model of Spatial Variation*

The following sections will describe the errors in spatial attributes. In general spatial random fields used in this chapter will be referred to as  $Z(x)$ . Spatial inputs to GIS models have a spatial variation that generally can be modelled by the general model of spatial variation (GMSV) (Heuvelink, 1998):

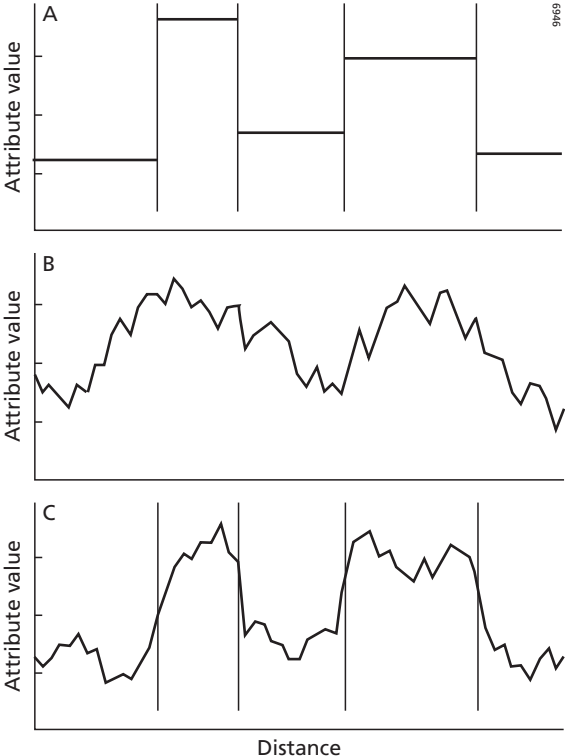


Figure 9.1 Example realisations along a transect of a spatial attribute satisfying the: (a) Discrete Model of Spatial Variation (DMSV), (b) Continuous Model of Spatial Variation (CMSV), (c) Mixed Model of Spatial Variation (MMSV). Vertical lines represent boundaries between mapping units. Source: Heuvelink (1998).

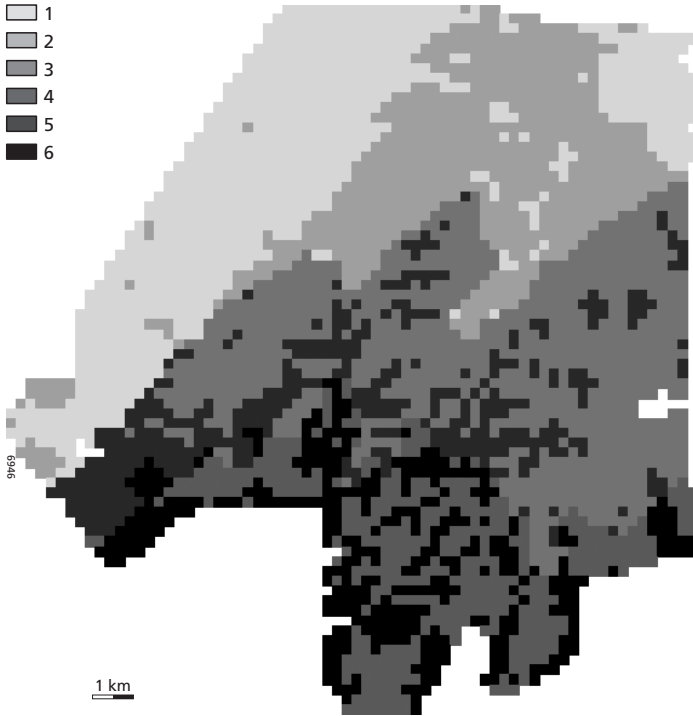


Figure 9.2 Map of unique land cover and soil type combinations within the study area used for the error modeling of  $\theta_0, k_{sat}, \zeta$  using DMSV. The classes 1 to 6 are described in table 9.3.

$$Z(x) = \mu(x) + \varepsilon(x) \text{ for all } x \in D \tag{9.4}$$

where  $\mu(x)$  is the (deterministic) mean, or trend, of attribute  $Z(x)$ . It represents the large-scale fluctuation.  $\varepsilon(x)$  is a zero-mean, spatially autocorrelated residual that represents the small-scale fluctuation (Cressie, 1991).

In order to quantify  $\mu(x)$  and  $\varepsilon(x)$  from measurements, assumptions need to be made and the GMSV should be modified (Heuvelink, 1998). For the modelling of spatial variation in the soil moisture model, three models of spatial variation, derived from the GMSV, have been used: the discrete model of spatial variation (DMSV), the continuous model of spatial variation (CMSV) and the mixed model of spatial variation (MMSV) (Bregt, 1992; Anselin et al., 1994; Heuvelink, 1996; Heuvelink and Huisman, 1996). Figure 9.1 illustrates the difference between the spatial error models.

*Discrete Model of Spatial Variation, single variable*

In the DMSV, the spatial domain  $D$  is divided into  $K$  mutually exclusive units  $D_k (k = 1, \dots, K)$ . The following assumptions are made on the GMSV of eq. 9.4:

1.  $\mu(x) = \beta(k)$  for all  $x \in D_k (k = 1, \dots, K)$ .
2.  $\varepsilon(x) = \varepsilon(k)$  for all  $x \in D_k (k = 1, \dots, K)$ .
3.  $\text{var}(\varepsilon(k)) = C_0(k)$  for all  $x \in D_k$ .

Table 9.3 Land cover and soil type combinations. For further specifications, see Part III, chapter 8.

<i>k</i>	Land cover type	Soil Type
1	Semi-natural vegetation	Sols isohumiques gris couvrant les sols fersiallitiques sableux lessivés
2	Agricultural	Sols fersiallitiques sableux lessivés
3	Agricultural	Sols fersiallitique lessivé
4	Agricultural	Sols fersiallitique lessivé à galets
5	Semi-natural vegetation	Sols fersiallitique lessivé
6	Semi-natural vegetation	Sols fersiallitique lessivé à galets

The DMSV assumes that the model area  $D$  can be stratified into a finite number of homogeneous classes  $D_k$ .  $\beta(k)$  is the unit-dependent mean. The residual noise term  $\varepsilon(k)$  is uncorrelated with neighbouring classes and it represents noise per class, not per cell, which is in contrast with the definition of DMSV in Heuvelink (1998).

DMSV has been used for the error propagation modelling of the volumetric soil moisture content,  $\theta_0$  [-]. This input parameter of the soil moisture model has been stratified according to unique combinations of soil types and land cover, based on the soil map (Part III, chapter 8, figure 8.4) and land cover map (Part III, chapter 8, figure 8.13). The combinations,  $k = 1 \dots 6$ , are presented in figure 9.2 and summarized in table 9.3. Combinations 1 to 4 correspond to calibration site C01 to C04 as explained in the previous chapter. Combinations 5 and 6 are other combinations that contain no field measurements, but their properties have been derived by combining data from the other areas.

The parameters of the DMSV model for  $\theta_0$  in each domain  $D_k$  are given in table 9.4.  $\beta(k)$  is the average of a unit, calculated from the field measurements of volumetric soil moisture (see section 8.3.2) and  $C_0(k)$  is the variance of the mean volumetric moisture content within a unit  $k$ ,  $s_{\bar{X}}^2(k)$ , which is calculated by:

$$s_{\bar{X}}^2(k) = s^2(k)/N(k) \quad (9.5)$$

where  $N$  is the number of observations and  $s^2(k)$  is the sample variance, which is calculated by:

$$s^2(k) = \frac{\sum_{i=1}^N (X_i(k) - \bar{X}(k))^2}{N(k)} \quad (9.6)$$

where  $X_i$  is the  $i^{\text{th}}$  observation and  $\bar{X}$  is the mean and equals  $\beta(k)$ .

#### DMSV, two variables

When modelling the error of two correlated variables,  $z_1$  and  $z_2$ , extra assumptions are made for the DMSV:

1.  $\mu_1(x) = \beta_1(k)$  and  $\mu_2(x) = \beta_2(k)$  for all  $x \in D_k$  ( $k = 1, \dots, K$ ).
2.  $\varepsilon_1(x) = \varepsilon_1(k)$  and  $\varepsilon_2(x) = \varepsilon_2(k)$  for all  $x \in D_k$  ( $k = 1, \dots, K$ ).
3.  $\text{var}(\varepsilon_1(k)) = C_1(k)$  and  $\text{var}(\varepsilon_2(k)) = C_2(k)$  for all  $x \in D_k$  ( $k = 1, \dots, K$ ).
4.  $\text{cov}(\varepsilon_1(k), \varepsilon_2(k)) = C_{z_1 z_2}(k)$  for all  $x \in D_k$  ( $k = 1, \dots, K$ ).

The covariance is calculated by:

$$C_{z_1 z_2}(k) = E((z_1(k) - \mu_1(k))(z_2(k) - \mu_2(k))) \text{ for all } x \in D_k \text{ (} k = 1, \dots, K) \quad (9.7)$$

where  $z_1$  and  $z_2$  are correlated variables with respectively a mean of  $\mu_1$  and  $\mu_2$ .

Saturated hydraulic conductivity,  $k_{sat}$  [ $\text{cm s}^{-1}$ ], and the soil water retention curve (SWRC) parameter,  $\zeta$  [-], are modelled with this form of DMSV in combination with the stratification map of figure 9.2, because they are correlated with each other and related to a soil type/land cover combination. The DMSV parameters for  $k_{sat}$  and  $\zeta$  are given in table 9.5. The parameters are derived from the PEST calibration, which has been described in the previous chapter.

$k_{sat}$  and  $\zeta$  are modelled as a lognormal distribution, because their distributions are closer to lognormal than to normal. For the same reason, a logtransformation has been used in the

Table 9.4 Parameters used in the application of DMSV for  $\theta_0(x)$ .  $k$  is the land use/soil type combination (table 9.3),  $\beta(k)$  is the mean  $\theta_0(x)$  and  $C_0(k)$  is the variance of  $\theta_0(x)$ .

$k$	$\beta(k)$	$C_0(k)$
1	0.066	$1.45 \cdot 10^{-7}$
2	0.053	$1.80 \cdot 10^{-8}$
3	0.066	$8.84 \cdot 10^{-9}$
4	0.065	$1.20 \cdot 10^{-7}$
5	0.066	$8.84 \cdot 10^{-9}$
6	0.065	$1.20 \cdot 10^{-7}$

Table 9.5 Parameters for the DMSV model applied to the correlated variables  $k_{sat}(x)$  and  $\zeta(x)$ . Subscript 1 denotes parameters for  $\log(k_{sat}(x))$ , subscript 2 has been used for  $\log(\zeta(x))$  parameters.

$k$	$\beta_1(k)$ [cm/s]	$C_1(k)$	$\beta_2(k)$ [-]	$C_2(k)$	$C_{z_1 z_2}(k)$
1	0.03007	0.1691	7.65583	$8.2614 \cdot 10^{-5}$	$1.4930 \cdot 10^{-3}$
2	0.47755	$7.0160 \cdot 10^{-2}$	7.49682	$1.4763 \cdot 10^{-4}$	$3.0453 \cdot 10^{-3}$
3	0.01167	$3.9384 \cdot 10^{-2}$	7.4609	$3.9244 \cdot 10^{-5}$	$7.2590 \cdot 10^{-4}$
4	0.03358	$1.6042 \cdot 10^{-2}$	6.91387	$3.5931 \cdot 10^{-5}$	$5.7889 \cdot 10^{-4}$
5	0.01167	$3.9384 \cdot 10^{-2}$	7.4609	$3.9244 \cdot 10^{-5}$	$7.2590 \cdot 10^{-4}$
6	0.03358	$1.6042 \cdot 10^{-2}$	6.91387	$3.5931 \cdot 10^{-5}$	$5.7889 \cdot 10^{-4}$

Table 9.6 Model restrictions for initial volumetric soil moisture content ( $\theta_0$ ), saturated hydraulic conductivity ( $k_{sat}$ ), and the soil water retention curve parameter ( $\zeta$ ). Realisations outside these ranges are physically impossible and not used in the error propagation model.  $\theta_r$  is the residual soil moisture content and  $\theta_s$  is the saturated soil moisture content.

Parameter	Model restriction
$\theta_0$ [-]	$\theta_r < \theta_0 < \theta_s$
$k_{sat}$ [cm/s]	$> 0$
$\zeta$ [-]	$> 0$

calibration by PEST. The resulting random fields of  $k_{sat}$  and  $\zeta$  are back transformed to resolve the values for  $k_{sat}$  and  $\zeta$ .

Realisations of  $\theta_0$ ,  $k_{sat}$  and  $\zeta$  are calculated during the initialization of each Monte Carlo run. The distributions of these realisations have been bounded by the ranges given in table 9.6, to prevent random values that are physically impossible.

### Continuous Model of Spatial Variation

For the Continuous Model of Spatial Variation (CMSV) the following assumptions have been made related to  $Z(x)$  (eq. 9.4):

1.  $\mu(x) = \mu$  for all  $x \in D$
2.  $\varepsilon(x)$  is represented by  $\text{cov}(Z(x), Z(x+h)) = C_z(h)$  for all  $x, x+h \in D$

which means that it is assumed that  $Z(x)$  is a second order stationary random field, i.e. without trend, and the autocovariance function,  $C_z(h)$ , is a function of the distance ( $h$  [m]) between locations (Oliver and Webster, 1990; Cressie, 1991; Heuvelink, 1998). The spatial autocovariance structure of  $Z(x)$  is characterised by a semivariogram,  $\gamma(h)$ :

$$\gamma(h) = \frac{1}{2} E[(Z(x) - Z(x+h))^2] \text{ for all } x, x+h \in D \quad (9.8)$$

Note that the autocovariance function and the semivariogram are related by:

$$\gamma(h) = C_z(0) - C_z(h) \quad (9.9)$$

Nugget, spherical, exponential and Gaussian semivariogram models are used to fit to the experimental semivariogram (Isaaks and Srivastava, 1989). Their properties can be found in table 9.7.

CMSV has been applied to the modelling of errors in saturated volumetric soil moisture content,  $\theta_s$  [-]. A nugget semivariogram model has been assumed. The sill value and assumed

Table 9.7 Semivariogram models used in this chapter.  $a$  is the range distance in meters and  $s^2$  is the variance that represents the sill.  $h$  is the lag distance in meters.

Spherical model	$\gamma(h) = \begin{cases} s^2 \left[ \frac{3}{2} \left( \frac{h}{a} \right) + \frac{1}{2} \left( \frac{h}{a} \right)^3 \right] & \text{if } h < a \\ s^2 & \text{if } h \geq a \end{cases}$	
	$h \geq 0; a, s^2 > 0$	
Exponential model	$\gamma(h) = s^2 [1 - e^{-(h/a)}]$	$h \geq 0; a, s^2 > 0$
Gaussian model	$\gamma(h) = s^2 [1 - e^{-(h^2/a^2)}]$	$h \geq 0; a, s^2 > 0$
Nugget model	$\gamma(h) = \begin{cases} 0 & \text{if } h = 0 \\ s^2 & \text{if } h > 0 \end{cases}$	
	$s^2 > 0$	

Table 9.8 Parameter values for the application of CMSV to saturated volumetric soil moisture content ( $\theta_s$  [-]). The parameter  $s^2$  is the variance that represents the sill of the nugget semivariogram model.

$\mu$ [-]	$s^2$	Model restriction
0.4	0.01	$0.1 < \theta_s < 0.6$

mean of the random field are given in table 9.8. The assumptions are based on measurements of volumetric soil moisture at soils saturated after infiltration tests (chapter 8).

CMSV has also been applied to the precipitation data, because precipitation varies continuously in space independent of land cover. Some additional assumptions on CMSV were made to allow application to the available data:

1. Each event  $i$  is represented by a random field  $Z_i(x)$  [cm], which is the total rainfall during the event, with  $\mu_i(x) = \mu_{event}$  and  $C_{z,i}(h) = C_{event}(h)$ . Where  $\mu_{event}$  is the measured total rainfall for the event and  $C_{event}(h)$  represents the spatial covariance for the rainfall event.
2.  $Z_i(x)$  is conditioned to the total amount of rainfall measured during the event  $i$  at the meteorological station.
3. The distribution of the total precipitation of an event over the timesteps of that event, per cell, is proportional to the distribution of precipitation in time at the meteorological station:

$$P_i(x, t) = \frac{Z_i(x) \cdot P_{m,i}(t)}{\sum P_{m,i}(t)} \tag{9.10}$$

where  $P_i(x, t)$  [cm] is the amount of precipitation at a time step  $t$  at location  $x$ ,  $P_{m,i}(t)$  is the amount of precipitation measured at the meteorological station ( $m$ ) at the time step,  $\sum P_{m,i}(t)$  is the total amount of precipitation measured for event  $i$  at the location of the meteorological station.

4. The random fields are generated using block kriging in order to get grid cells of 125 m. Because semivariograms of precipitation were not available for the study area, data from measurements in the Netherlands were used in the following way. The spatial variability for each of the three rainfall events was estimated using data from two tipping bucket rain gauges in the study area and a semivariogram estimated by Schuurmans et al. (2007), who fitted pooled spherical semivariogram models to data from 330 rain gauges with a density of approximately 1 station per 100 km<sup>2</sup> and a selection of 74 rainfall events between March and October 2004. The estimated pooled semivariogram, therefore, should represent the total rainfall during an event. The daily rainfall is measured by volunteers at 8.00 am and the data is published on the website of the Royal Netherlands Meteorological Institute (KNMI, 2008).

Schuurmans et al. (2007) concluded that the use of a pooled semivariogram for each event does not imply a loss of accuracy when compared to event-based semivariogram models and it can be used when data for semivariogram estimation is not available for areas that have precipitation conditions comparable with the Netherlands. This is assumed for the Sehoul study area, because no data exists on spatial rainfall variability in this area.

It is assumed that the shape of the pooled semivariogram model  $\gamma_U$  is applicable to each of the three rainfall events included in the soil moisture model, but that the vertical scale, i.e. semivariance should be scaled for each rainfall event proportional to the semivariance of the total precipitation during the rainfall event.

The semivariance for each event has been derived from the two tipping bucket rain gauges. First the semivariance corresponding with the distance between the two rain gauges ( $b = 3699$  m) has been derived from pooled nested semivariogram model  $\gamma_U$  (figure 9.3, Schuurmans, 2007) resulting in  $\gamma_U(3699) = 0.148$ . By calculating the semivariance between the two measurement sites for each rainfall event,  $\gamma(event)$ , a scaling factor,  $f$ , has been calculated:

$$f = \frac{\gamma(event)}{\gamma(3699)} \tag{9.11}$$

Since only the vertical scale of semivariogram  $\gamma_U$  should be adapted, the scaling factor has been applied to the sill ( $s_z^2$ ) and nugget values of the nested semivariogram model  $\gamma_U$ . This resulted in the semivariograms  $\gamma_{P1}$ ,  $\gamma_{P2}$  and  $\gamma_{P3}$  for the three rainfall events. Their parameter values are reported in table 9.9.

*Mixed Model of Spatial Variation*

The Mixed Model of Spatial Variation, MMSV, is a combination of DMSV and CMSV. The assumptions of MMSV are:

*Table 9.9 Semivariogram model parameters used in the CMSV for precipitation.  $a$  and  $s_z^2$  correspond with the model fitting parameters in table 9.7. These semivariograms are nested, therefore the nugget and two spherical models should be added to obtain the entire semivariogram model.  $\gamma_U$  is the pooled semivariogram determined by Schuurmans et al. (2007),  $\gamma_{P1}$ ,  $\gamma_{P2}$  and  $\gamma_{P3}$  are the semivariograms of the three modelled rainfall events.*

	<b>Nugget</b>	<b>Spherical (<math>a = 23</math> km)</b>	<b>Spherical (<math>a = 156</math> km)</b>
$\gamma_U$	$s_z^2 = 0.053$	$s_z^2 = 0.281$	$s_z^2 = 0.795$
$\gamma_{P1}$	$s_z^2 = 0.00031$	$s_z^2 = 0.0017$	$s_z^2 = 0.0047$
$\gamma_{P2}$	$s_z^2 = 0.00019$	$s_z^2 = 0.00102$	$s_z^2 = 0.0029$
$\gamma_{P3}$	$s_z^2 = 0.08$	$s_z^2 = 0.42$	$s_z^2 = 1.2$

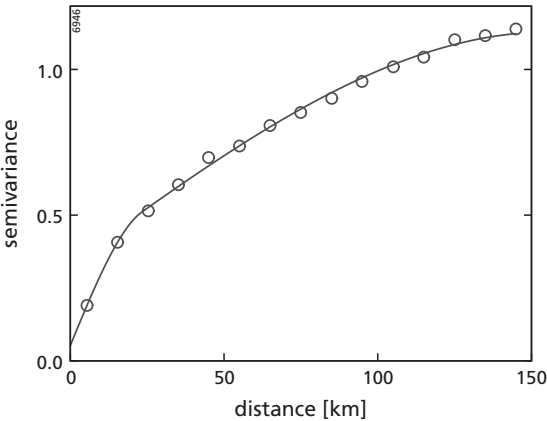


*Figure 9.3 Nested pooled semivariogram model ( $\gamma_U$  in table 9.9) calculated from standardized non-zero square root transformed daily rainfall data. Source: Schuurmans et al. (2007).*

1.  $\mu(x) = \beta(k)$  for all  $x \in D_k$
2.  $\text{Cov}(Z(x), Z(x+h)) = C_{z,k}(h)$  for all  $k, k+h \in D$ . This means that for each land cover/soil class a different semivariogram will be used.

The MMSV model has been applied to the maximum interception storage ( $S_{int}$  [cm]) and the potential evapotranspiration ( $ET_p$  [cm/h]), because it is assumed that these parameters vary continuously within a land cover/soil class and the pattern differs for each class. The semivariograms of  $S_{int}$  were derived from an image from the Advanced Spaceborne Thermal Emission and Reflection Radiometer (ASTER) of October 20<sup>th</sup> 2004.  $S_{int}$  values were derived by using the NDVI-LAI relationship as discussed in eq. 4.48 in Part II, chapter 4 and then applying eq. 8.3 of chapter 8. In order to match the model resolution, the derived  $S_{int}$  has been resampled from the original 15 m to 125 m pixels. For each combination  $k$  of land cover and soil type a unit dependent mean,  $\beta(k)$ , and semivariogram model has been estimated (table 9.10).

The meteorological inputs are used to calculate the potential evaporation, using the Penman-Monteith equation (Monteith, 1981) (see eq. 8.14, chapter 8). Since the meteorological parameters are measured at only one location these data could not be used to calculate semivariograms. Instead, average semivariograms were estimated from potential evapotranspiration, spatially modelled by SEBS using the MODIS images at the three

Table 9.10 MMSV parameters for maximum interception storage,  $S_{int}$ . Sill ( $s_z^2$ ) and range ( $a$ ) parameters correspond with models described in table 9.7. The models are summed to get the total semivariogram model.

$k$	$\beta(k)$ [cm]	Nugget	Exponential		Gaussian	
		$s_z^2$	$s_z^2$	$a$ [m]	$s_z^2$	$a$ [m]
1	0.71	$2.0 \cdot 10^{-4}$	-	-	$9.2 \cdot 10^{-3}$	350.8
2	0.22	$1.0 \cdot 10^{-5}$	$7.1 \cdot 10^{-5}$	225.0	-	-
3	0.24	$1.0 \cdot 10^{-5}$	$7.1 \cdot 10^{-5}$	225.0	-	-
4	0.89	$4.8 \cdot 10^{-5}$	$2.5 \cdot 10^{-4}$	245.0	-	-
5	0.71	$2.0 \cdot 10^{-4}$	-	-	$9.2 \cdot 10^{-3}$	350.8
6	0.71	$2.0 \cdot 10^{-4}$	-	-	$9.2 \cdot 10^{-3}$	350.8

Table 9.11 Parameters of semivariogram model for potential evaporation ( $ET_{ps}(x)$ ). Sill ( $s_z^2$ ) and range ( $a$ ) parameters for models described in table 9.7.

$k$	Nugget	Spherical	
	$s_z^2$	$s_z^2$	$a$ [m]
1	$1.0 \cdot 10^{-4}$	$6.0 \cdot 10^{-5}$	4000
2	$6.0 \cdot 10^{-7}$	$8.3 \cdot 10^{-6}$	1933
3	$6.0 \cdot 10^{-7}$	$8.3 \cdot 10^{-6}$	1933
4	$6.0 \cdot 10^{-7}$	$8.3 \cdot 10^{-6}$	1933
5	$1.0 \cdot 10^{-4}$	$6.0 \cdot 10^{-5}$	4000
6	$1.0 \cdot 10^{-4}$	$6.0 \cdot 10^{-5}$	4000

overpasses. For each class in the land cover map a semivariogram model was fitted, based on all cells of each class. The parameters are provided in table 9.11. Realisations of fields of potential evapotranspiration modelled by SEBS ( $ET_{ps}(x)$  [cm/timestep]) are generated at the start of each Monte Carlo loop and are used for each timestep.

First the total potential evapotranspiration,  $ET_{ptot}$  [cm/timestep], is calculated by adding the potential evaporation from bare soil,  $E_p$  [cm/timestep], to the potential evapotranspiration from vegetation,  $ET_p$  [cm/timestep], both temporal stochastic variables:

$$ET_{ptot}(t) = ET_p(t) + E_p(t) \quad (9.12)$$

Next, the noise in the potential evapotranspiration,  $ET_{ptotn}$  [cm/timestep] is calculated:

$$ET_{ptotn}(x, t) = Z(x) \cdot \left( \frac{ET_{ptot}(t)}{ET_{ps}(x)} \right) \quad (9.13)$$

where  $Z(x)$  is the spatial random field with zero mean and a variance  $\text{var}(Z(x))$  calculated from the semivariogram models in table 9.11.  $ET_{ptot}(t)$  is a temporal stochastic variable, calculated using NSEM results for the hourly meteorological point data as described before.

Next, the noise  $ET_{ptotn}(x, t)$  is separated for vegetated areas,  $ET_{pn}$  [cm/timestep], and bare areas,  $E_{pn}$  [cm/timestep]. The calculation for vegetated areas is:

$$ET_{pn}(x, t) = ET_{ptotn}(x, t) \cdot \left( \frac{ET_p(t)}{ET_{ptot}(t)} \right) \quad (9.14)$$

and for bare soil:

$$E_{pn}(x, t) = ET_{ptotn}(x, t) \cdot \left( \frac{E_p(t)}{ET_{ptot}(t)} \right) \quad (9.15)$$

Finally, the spatio-temporal random fields of potential evapotranspiration for the vegetated part of a grid cell can be calculated with:

$$ET_p(x, t) = ET_p(t) + ET_{pn}(x, t) \quad (9.16)$$

and for the bare soil fraction with:

$$E_p(x, t) = E_p(t) + E_{pn}(x, t) \quad (9.17)$$

### 9.2.2 SOMS – Data Poor Scenario

In, or near, most study areas basic meteorological measurements are available. Soil physical data, like measurements of  $k_{sat}$ ,  $\theta_r$  and  $\theta_s$  and land cover data like  $S_{imp}$ , however, are often not available and are derived from literature, maps or remote sensing data. The SOMS – Data Poor Scenario of the error propagation model has been developed to show the uncertainty in VMC predictions if only meteorological data, maps and remote sensing images are available.

Changes have been made in the parameters of the error model of initial VMC ( $\theta_0$ ), saturated hydraulic conductivity ( $k_{sat}$ ), soil water retention curve parameter  $\zeta$  and saturated volumetric moisture content ( $\theta_s$ ).

The same DMSV error models as in the SOMS – Data Rich Scenario have been used. The mean and variance of  $\theta_0$ ,  $k_{sat}$  and  $\zeta$ , however, have been changed and are kept constant in all six land cover/soil type units. For  $\theta_0$  the parameters are  $\beta(k) = 0.2$  and  $C_0(k) = 0.2$  for  $k = 1, \dots, K$ . This is an assumption for an intermediate VMC without prior knowledge on precipitation events. For  $k_{sat}$  and  $\zeta$  the parameters of the two variable DMSV are given in table 9.12. For the mean value of  $k_{sat}$  values for sand ( $k = 1$ ) and loamy sand ( $k = 2, \dots, K$ ) reported by USDA (Jetten, 1994) have been used. Since  $k_{sat}$  is highly variable, a standard deviation of 70% is assumed. The mean of  $\zeta$  is assumed to be 10 with a standard deviation of 70%.

Table 9.13 gives the values applied for  $\theta_s$  in the SOMS – Data Poor Scenario. The sill and mean value are derived from literature (USDA).

### 9.2.3 SEBS – Large Error scenario

Upscaling of surface radiometric temperature introduces a large error. This scenario models the effect of propagation of errors in the input of SEBS on the uncertainty in the output of actual evapotranspiration of SEBS (AET). The implementation of SEBS used for estimating AET from MODIS images for the Sehoul study area uses three sets of input data: (1) Data derived from remote sensing: albedo, emissivity, temperature and Normalized Difference Vegetation Index (NDVI); (2) Meteorological parameters measured at a meteorological station: air pressure, air temperature, relative humidity, wind speed; (3) Radiation data: downward solar radiation and downward longwave radiation.

In Part II, chapter 6 we concluded that the sensible heat flux calculation in SEBS is most sensitive to surface radiance temperature as measured by the satellite. A deviation of only 0.5 K can result in a deviation of up to 70% in the estimated sensible heat flux for some land cover types. Compared to surface radiance temperature, the errors in other inputs are of minor importance for the errors in estimated sensible heat flux.

Table 9.12 Parameters for the DMSV model applied to the correlated variables  $k_{sat}(x)$  and  $\zeta(x)$  for the SOMS – Data Poor Scenario. Subscript 1 denotes parameters for  $\log(k_{sat}(x))$ , subscript 2 has been used for  $\log(\zeta(x))$  parameters.  $C_{z1z1}(k)$  is calculated in the same manner as for the SOMS – Data Rich Scenario (eq. 9.7).

$k$	$\beta_1(k)$ [cm/s]	$C_1(k)$	$\beta_2(k)$ [-]	$C_2(k)$	$C_{z1z2}(k)$
1	0.00825	$3.33506 \cdot 10^{-05}$	10	0.023262	$2.64 \cdot 10^{-4}$
2	0.004053	$8.04857 \cdot 10^{-06}$	10	0.023262	$1.30 \cdot 10^{-4}$
3	0.004053	$8.04857 \cdot 10^{-06}$	10	0.023262	$1.30 \cdot 10^{-4}$
4	0.004053	$8.04857 \cdot 10^{-06}$	10	0.023262	$1.30 \cdot 10^{-4}$
5	0.004053	$8.04857 \cdot 10^{-06}$	10	0.023262	$1.30 \cdot 10^{-4}$
6	0.004053	$8.04857 \cdot 10^{-06}$	10	0.023262	$1.30 \cdot 10^{-4}$

Table 9.13 Assumed parameter values for the application of CMSV to  $\theta_s$  [-] in the SOMS – Data Poor Scenario.

$\mu$ [-]	$s^2$	Model restriction
0.4	0.03	$0.1 < \theta_s < 0.6$

The error in latent heat flux and SEBS estimated actual evapotranspiration (AET) are related to the errors in the sensible heat flux calculation, since the sensible heatflux, the latent heat flux and the soil heat flux should be equal to the net radiation (Part II, chapter 4, eq. 4.12).

The accuracy of the radiometric surface temperatures measured by MODIS is reported as 1 K at 1 km resolution under clear-sky conditions and has been validated by Wan et al. (2002). An additional error occurred when applying DisTrad to the 1 km data for the estimation of the radiometric surface temperature at 250 m resolution as discussed in Part II, chapter 7, and upscaling to 125 m to compare with the resolution of the soil moisture model.

Only the variance from the DisTrad calculations has been used, because other sources of error are relatively small. Since radiometric surface temperature is the most sensitive parameter in SEBS, it is assumed in this scenario that this is the only input of SEBS with error, while all other inputs are assumed to have zero error. The error model used for the radiometric surface temperature is GMSV (eq. 9.4) with the assumption that  $\varepsilon(x)$  is not spatially autocorrelated.

In the error model for radiometric surface temperature we assume that  $\mu(x) = \hat{T}_{R250}(x)$  and  $\text{var}(\varepsilon(x)) = f(\text{NDVI}(x))$ .  $\hat{T}_{R250}$  [K] is the surface temperature image from MODIS at 250 meter resolution after application of DisTrad.  $\text{var}(\varepsilon(x))$  is the variance in radiometric surface temperature, derived from DisTrad calculations for each satellite overpass. It is a linear regression function of NDVI:

$$\text{var}(\varepsilon(x)) = a \cdot \text{NDVI}(x) + b \quad (9.18)$$

with  $a, b$ , regression parameters.

One regression function has been fitted for each overpass, using three values of NDVI and the variance in  $\hat{T}_{R250}$ . The three values are the  $\hat{T}_{R250}$  variances that correspond with the class mean of each NDVI class used in the DisTrad regression, i.e.  $0 < \text{NDVI} < 0.2$  (sparse vegetation),  $0.2 < \text{NDVI} < 0.5$  (partial canopy cover),  $\text{NDVI} > 0.5$  (high canopy cover). The results are shown in figure 9.4a to c.

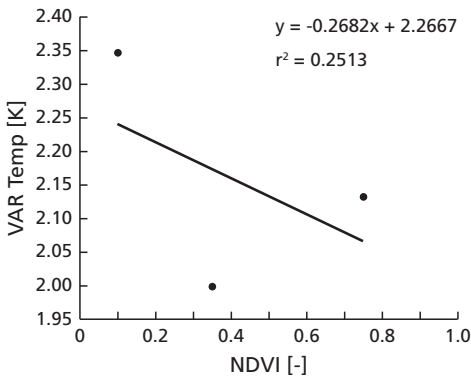
The graphs show a large difference between the satellite overpasses. Only the result for overpass day 328 shows what was expected from the Temperature-Vegetation Index plot (TVX) approach (Czajkowski et al., 2000) as discussed in Part II, section 7.4.2 and figure 7.1: a high variance of surface temperature at low NDVI values and a significant negative correlation with a  $r^2$  of 0.98. At the other overpass days also a negative correlation has been found, but the  $r^2$  values are much lower and the partial canopy cover seems to have the lowest temperatures. In the wettest situation (overpass day 307), the variances are very small: 2 – 2.35. At day 322 the soils are dryer and the variance in surface temperatures is larger. Day 328 is the driest and the variance of surface temperatures ranges between 13.6 and 15.4. Note that this relation is clearer when volumetric soil moisture content is plotted against the variance of surface temperature at the three overpasses. In figure 9.4d this is done for site C04 (see chapter 8). This pattern has been observed at all locations, so in general we can state that wetter soils have a higher variance in their volumetric soil moisture content and a lower variance in their radiometric surface temperature.

The regression equations are used to generate variance images for each overpass, based on NDVI (eq. 9.18). Table 9.14 shows the coefficients of the regression function in eq. 9.18.

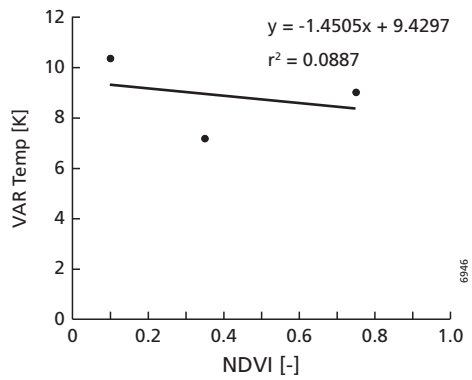
Table 9.14 Coefficients of the regression function (eq. 9.18).

Overpass Day Nr. (2004)	a	b
307	-0.2682	2.2667
322	-1.4505	9.4297
328	-2.889	15.83

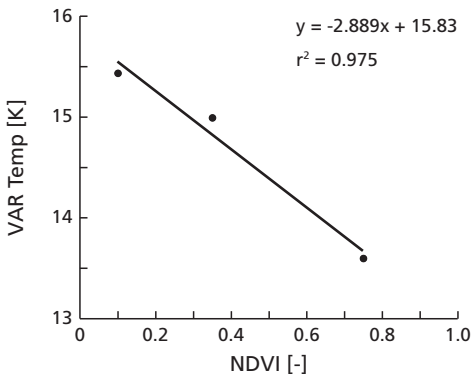
a. MODIS overpass day 307



b. MODIS overpass day 322



c. MODIS overpass day 328



d. Soil moisture content and variance of surface temperature

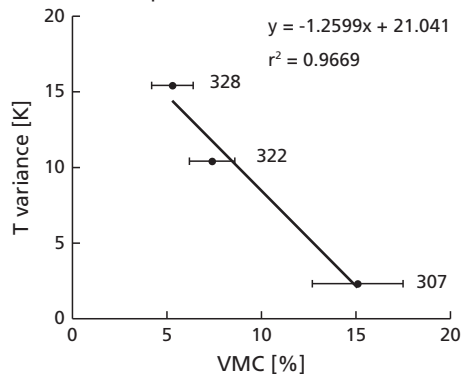


Figure 9.4 Regression between variance in radiometric surface temperature at 250 meter resolution and NDVI for the three MODIS overpasses (a to c). Each point reflects the center of the NDVI class used to calculate the variance. In d the soil moisture content at calibration site C04 (see previous chapter) is plotted against the temperature variance at the three overpasses. Note that the vertical scale is different between the graphs.

The resulting average and variance images of actual evapotranspiration [ $\text{cm h}^{-1}$ ] are resampled from 250 m resolution to the resolution of the soil moisture model, i.e. 125 meters. These are later used in the data assimilation procedure (chapter 10).

#### 9.2.4 SEBS – Small Error scenario

In the ‘small error’ scenario only the error in surface radiometric temperature caused by the MODIS sensor system is included, to show the difference with the ‘large error model’. The reported error of 1 K at 1 km resolution under clear-sky conditions (Wan et al., 2002) has been propagated through the model. The GMSV model has been used (eq. 9.4) with  $\text{var}(\varepsilon(x)) = 1$ , which is not spatially autocorrelated. For  $\mu(x)$  the MODIS LST (MOD11 – Land Surface Temperature 5-Min L2 Swath 1km) product has been used. As with the ‘large error scenario’, the DisTrad method has been applied to deliver 250 m resolution input data for the SEBS error propagation model. The resulting average and variance images of actual evapotranspiration [ $\text{cm/h}$ ] are resampled to the resolution of the soil moisture model, i.e. 125 meters. These are later used in the data assimilation procedure.

### 9.3 Results and discussion

Both SOMS and SEBS have been run in error propagation mode, with 200 Monte Carlo runs. For SOMS the average volumetric moisture content (VMC) ( $\theta_0(t)$ , eq. 8.1, chapter 8) and average actual evapotranspiration (AET) ( $E_0(t)$ , eq. 8.42, chapter 8) were calculated, together with their standard deviation, while for SEBS the error propagation model resulted in maps of average actual evapotranspiration (AET) ( $E$ , eq. 4.63, chapter 4) and its standard deviation for each pixel at each satellite overpass. AET of both SOMS and SEBS will be used in the next chapter as filter data in a particle filter data assimilation algorithm, in order to improve the spatio-temporal estimation of  $\theta_0$ . The analysis of timeseries of the results has been done at the calibration locations C01 to C04 (figure 8.1) and validation locations V02 to V04 (figure 8.16).

#### 9.3.1 SOMS – Data Rich Scenario

Figure 9.5 shows the output of the SOMS error propagation model for all sites, while figure 9.6 shows the Coefficient of Variation ( $CV$ ) of VMC for all sites.  $CV$  is calculated with:

$$CV = \frac{s}{\bar{X}} \quad (9.19)$$

where  $s$  is the standard deviation (eq. 9.6). The  $CV$  makes it easier to compare the degree of variation among the sites, even if their means are very different from each other.

The volumetric moisture content in the first layer, and its associated error band, shows the same trend through time for all sites. The error bandwidth at  $t=0$  is very narrow, because in this scenario the initial soil moisture measurements, used as input to SOMS, have a low uncertainty. Each timestep some error is introduced resulting in an increase of  $CV$  in time. Rain temporarily decreases the error. This can be caused by a combination of factors, e.g. when saturation occurs, the error in VMC is only determined by  $\theta_s$  or the model assumption that potential evapotranspiration ( $E_p$ , chapter 8 eq. 8.14) in SOMS is zero during rainfall events. The difference in width of the error bands between the sites (e.g. C01 and C04) is mainly caused by differences

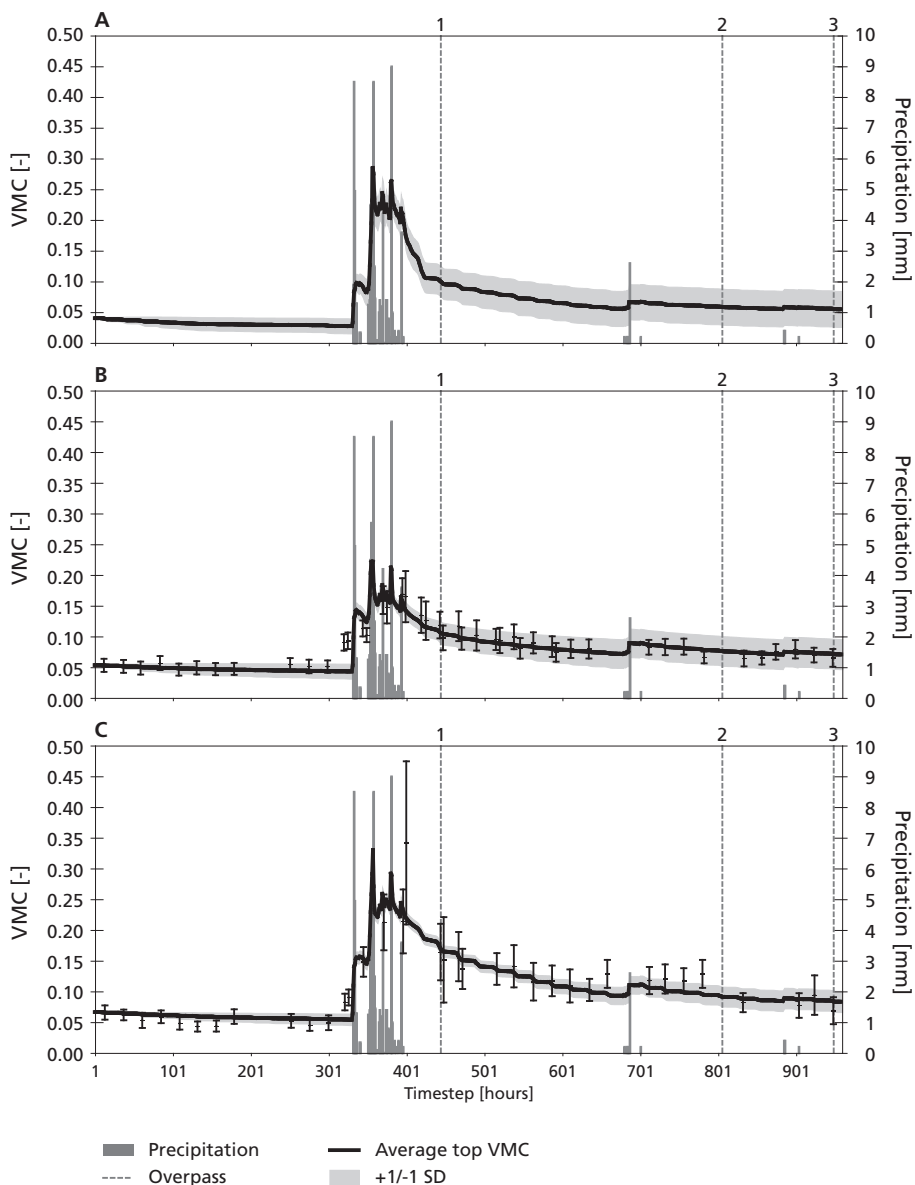
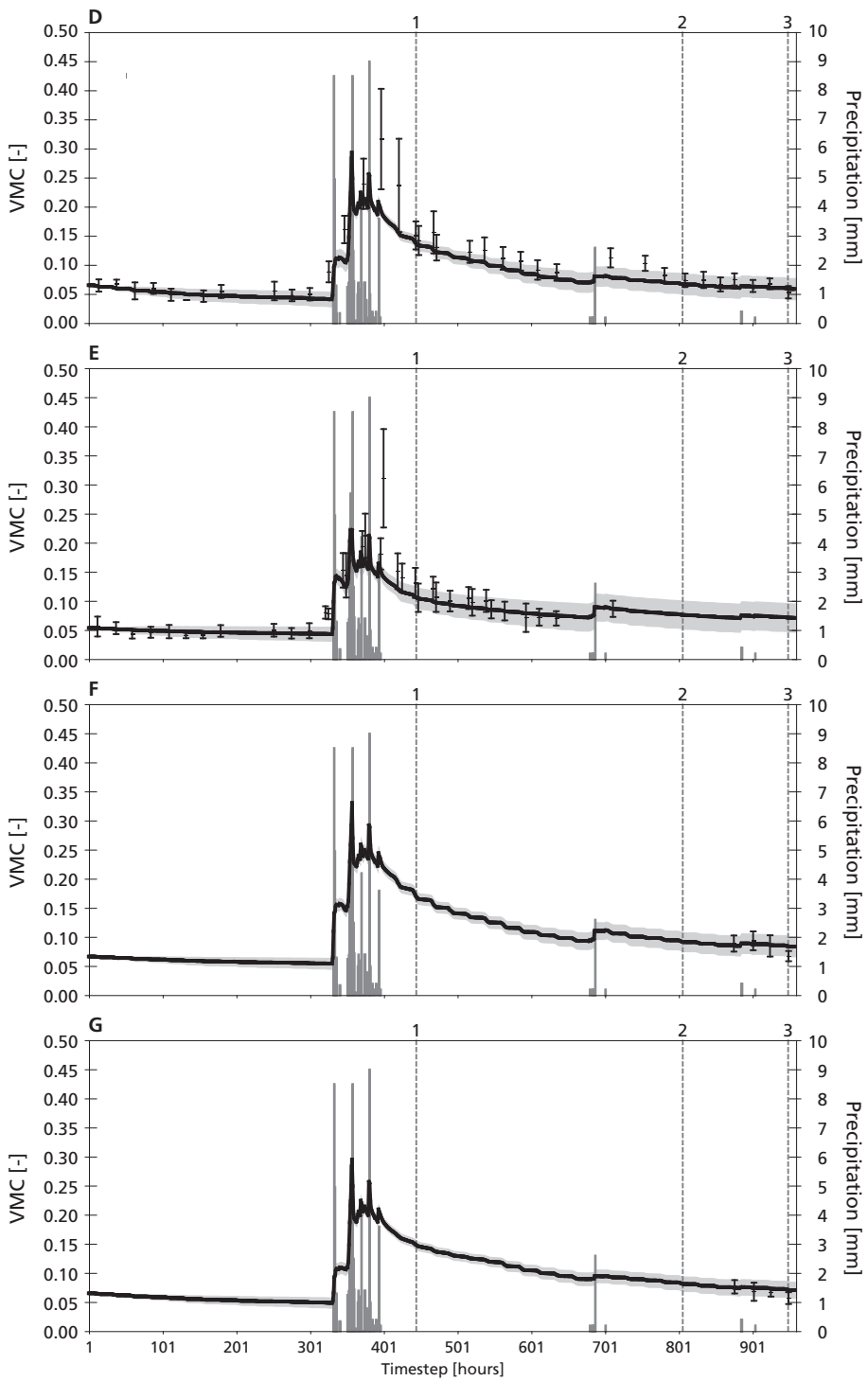


Figure 9.5 Timeseries of the average volumetric soil moisture content (VMC) in the first model layer (0-15 cm) at the calibration and validation sites (see figure 8.1 and 8.16) for the SOMS-Data Rich Scenario. A) C01, B) C02, C) C03, D) C04, E) V02, F) V03, G) V04. Rainfall events and satellite overpasses are indicated in the graphs. Field measurements are plotted as points. The whiskers indicate 1 standard error from the average of the soil moisture measurements in an agricultural parcel (chapter 8, eq. 8.43).



9689

in vegetation cover. The interception of the forest at C01 introduces more uncertainty than the land use at the other locations. A day/night cycle can also be recognised in both the VMC and the  $CV$  graphs: the VMC and its  $CV$  are almost constant during the night, because  $E_p$  is also assumed 0 by night.

In figure 9.5 the field measurements of VMC and their standard deviations (see chapter 8 for details on the measurements) are also indicated when they are available. Most measurements fall within 2 standard deviations of the model predictions. At some timesteps after the first rainfall event, however, the model underestimates the VMC.

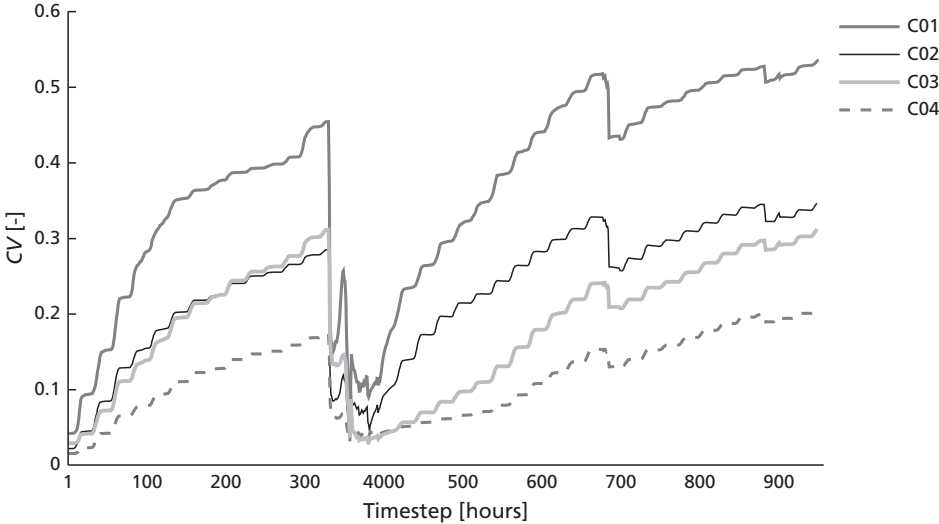


Figure 9.6 Timeseries of the Coefficient of Variation ( $CV$ , eq. 9.19) for VMC for locations C01, C02, C03 and C04 for the SOMS-Data Rich Scenario. The results for V02, V03 and V04 are comparable.

Table 9.15 Goodness of fit of error propagation results for the SOMS – Data Rich Scenario at the calibration sites C02, C03 and C04 and independent validation sites V02, V03 and V04. For C01 no field measurements were available during the modelled period. For the calculation of error variance and modelling efficiency ( $E$ ) see eq. 8.47 and 8.48 in chapter 8. The equation for the root mean squared error (RMSE) is given in eq. 3.1, chapter 3.  $r^2$  is the correlation of the regression between measured and modelled VMC and  $N$  gives the number of observations.

Site	Error variance	RMSE	$E$	$r^2$	$N$
C02	$2.09 \cdot 10^{-4}$	0.01	0.80	0.84	45
C03	$6.90 \cdot 10^{-4}$	0.03	0.81	0.82	36
C04	$9.54 \cdot 10^{-4}$	0.03	0.75	0.90	36
V02	$1.15 \cdot 10^{-3}$	0.03	0.67	0.80	34
V03	$1.11 \cdot 10^{-4}$	0.01	0.16	0.66	4
V04	$8.73 \cdot 10^{-5}$	0.01	-0.38	0.90	4

The predicted mean VMC and the goodness of fit results (table 9.15) are comparable with the results for the deterministic model (see table 8.8 and 8.9 in the previous chapter). This means that no large non-linear model responses occur when running the SOMS error propagation model. Maps of the estimated mean VMC and its uncertainty show very little spatial variation within the units defined in figure 9.2, because only for precipitation and evapotranspiration little spatial variation of errors within classes are modelled using respectively CMSV and MMSV.

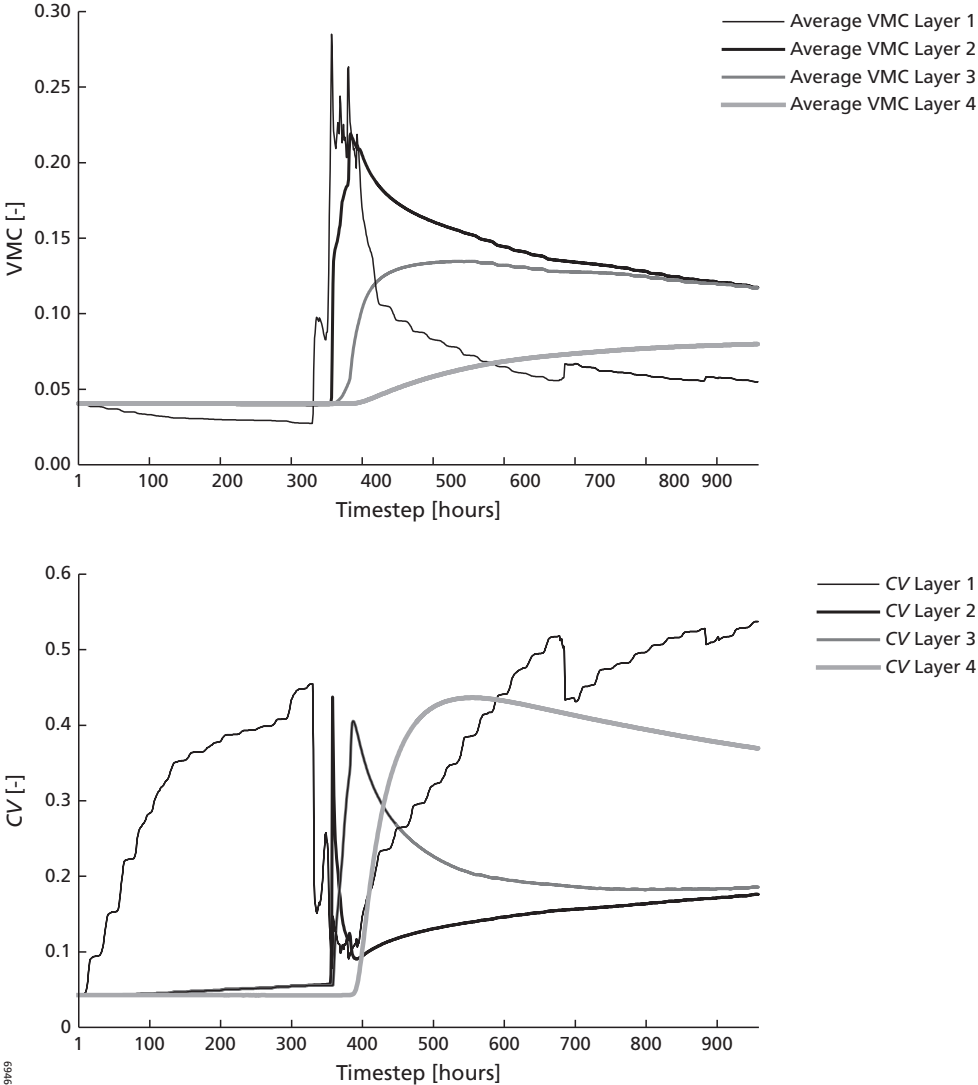


Figure 9.7 Average VMC (upper) and its CV (lower) at 4 model layers as modelled at location C01 using the SOMS-Data Rich Scenario.

Care should be taken with interpretation for sites V03 and V04, since they only have 4 measurements. The negative value for modelling efficiency,  $E$ , of site V04 indicates a bad fit, but the other goodness of fit statistics show a small error and a good correlation with field measurements.

The results of the SOMS – Data Rich Scenario show that uncertainty in VMC modelled with this scenario are in the same order of magnitude as the uncertainty of field TDR measurements, averaged over an agricultural parcel. The level of uncertainty of this scenario of the SOMS model will be acceptable for many applications. For example for agriculture in semi-arid areas, the start of the growing season coincides with the first rainfall event that provides sufficient soil moisture for the seeds to germinate. The SOMS – Data Rich Scenario of SOMS is well capable of accurately estimating soil moisture conditions after rainfall events. The accuracy, however, decreases within five to ten days from a rainfall event, but is often small compared to the error in field measurements.

Figure 9.7a shows the predicted volumetric soil moisture content for different model layers at location C01. It can be clearly seen that the first rainfall event causes a rapid wetting of the first layer. The temporal variation during the event is large for layer one. The second layer responds later and shows less temporal variation. The third and fourth layer show a further lag and are even smoother as can be expected from infiltration theory. The day and night cycle is only visible in layer one. Layer one is the wettest during the rainfall event and the driest layer at the end of the modelled period.

Figure 9.7b shows that for layer one the  $CV$  increases until the first rainfall event, while the  $CV$  of the other layers does not change much. This is caused by the uncertainty introduced by evaporation, which mainly affects layer one. The uncertainty in evaporation is high, because it depends on many uncertain variables (meteorological and soil physical). For layer one the  $CV$  is lowest during a rainfall event, while when the wetting front reaches the other layers, the  $CV$  becomes very high for those layers and is lower afterwards. This is caused by the uncertainty that accumulates in depth due to infiltration processes. The results for locations C02, C03 and C04 are comparable.

Variation in average actual evapotranspiration (AET) (figure 9.8) consists of two components: (1) Day and night cycles, because AET depends on solar radiation. The amplitudes at daytime increase with increasing soil moisture content (i.e. largest amplitudes during and after rainfall events). (2) the influence of rainfall events which have effect over a period of several days. During bright spells after a shower AET shows a strong increase, when the potential evapotranspiration ( $E_p$ ) is large enough (i.e. during daytime, clear sky and zero precipitation), because the supply of soil water is large. The AET predicted for the forest at C01 is higher than at other locations during the whole modelling period, because transpiration subtracts water available from deeper layers via the root system of the trees. The much higher AET at C01 during the first rainfall event is related to evaporation of intercepted water from the leaves of the trees. The AET diminishes after the rainfall events. The temporal variability is largest when bright spells are alternated with showers.

### 9.3.2 SOMS – Data Poor Scenario

The standard deviation of the volumetric moisture content estimated with the SOMS – Data Poor Scenario (figure 9.9) is 2 to 10 times larger than the standard deviation of the SOMS – Data Rich Scenario. Since the field measurements of initial VMC were not used in this

scenario, the error band is large during the initial timesteps and the average estimated VMC is high compared to the SOMS – Data Rich Scenario. This is a consequence of the assumption in this scenario that the time passed since the last rainfall event is unknown at the start of the model run. Therefore average literature values for initial VMC have been used with a relatively large uncertainty. During the first 10 hours the VMC decreases rapidly. All sites show the same trend for the mean VMC and the error bands. The same trends as in the SOMS – Data Rich Scenario are visible: the error bands increase in width over time, but are temporarily reduced during rainfall events. In this scenario the model overestimates the VMC on average, compared to field measurements, but most of the measurements fall within the error band of 1 standard deviation of the model prediction. During and shortly after the first rainfall event, when the error bands are narrow at all locations, few measurements fall outside the error bands of the model prediction. The standard deviation of VMC predictions in this scenario, however, is larger compared to the field measurements.

The goodness of fit results (table 9.16) for the SOMS – Data Poor Scenario show an average RMSE of 0.05, while the SOMS – Data Rich Scenario has an average RMSE of 0.02. The error variances are also higher and the model efficiency ( $E$ ) is lower. The high correlation coefficients ( $r^2$ ) indicate that the general trends are well represented by the model, except for site V03. Also here care should be taken with interpretation for sites V03 and V04, since these only have 4 measurements. This goodness of fit results are obvious, because the SOMS parameters have been calibrated for the deterministic SOMS model. When more error is introduced in the stochastic model scenarios, the goodness of fit will get worse.

For the SOMS – Data Poor Scenario, at all locations the initial average evapotranspiration (figure 9.10) is about 10 times higher compared to the SOMS – Data Rich Scenario, because the average VMC is also higher. Throughout the modelled period the AET remains higher for this scenario. Also the standard deviations of the VMC predictions are 10 times larger (figure 9.10). Furthermore, the contrast between rainfall events and dry periods is less in the SOMS – Data Poor Scenario.

There are also similarities with the SOMS – Data Rich Scenario. The day and night cycles are also clearly visible in this scenario and the same trends can be seen: AET increases after the first rainfall event, when the soil moisture content increases and AET predicted for the forest

*Table 9.16* Goodness of fit of error propagation results of the SOMS – Data Poor Scenario at the calibration sites C02, C03 and C04 and validation sites V02, V03 and V04. For C01 no field measurements were available during the modelled period. For the calculation of error variance and modelling efficiency ( $E$ ) it is referred to eq. 8.47 and 8.48 in chapter 8. The equation for the root mean squared error (RMSE) is given in eq. 3.1, chapter 3).  $r^2$  is the correlation of the regression between measured and modelled VMC and  $N$  gives the number of observations.

Site	Error variance	RMSE	$E$	$r^2$	$N$
C02	$3.66 \cdot 10^{-3}$	0.06	-2.47	0.82	45
C03	$1.31 \cdot 10^{-3}$	0.04	0.64	0.78	36
C04	$1.40 \cdot 10^{-3}$	0.04	0.63	0.78	36
V02	$3.07 \cdot 10^{-3}$	0.05	0.11	0.80	34
V03	$1.50 \cdot 10^{-3}$	0.03	-10.39	0.38	4
V04	$4.98 \cdot 10^{-3}$	0.06	-77.56	0.92	4

at C01 is much higher than at other locations during the whole modelled period. The temporal variability is largest during rainfall events.

### 9.3.3 SEBS error propagation results

The results for locations C01 to C04 can be found in figure 9.8, figure 9.10 and table 9.17. In these figures it can be seen that the SEBS – Large Error Scenario gives the highest actual evapotranspiration for all locations during overpass 1, while the SEBS – Small Error Scenario also gives a high actual evapotranspiration result during overpass 3. Both scenarios estimate the lowest AET at all locations during the second satellite overpass.

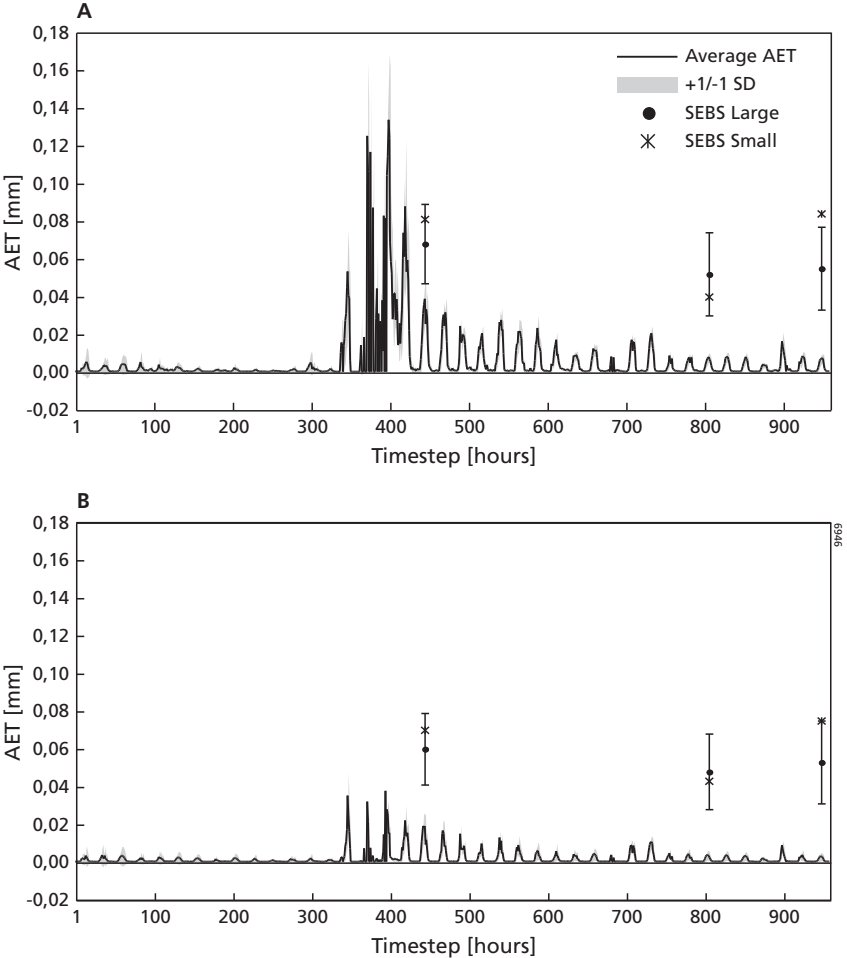
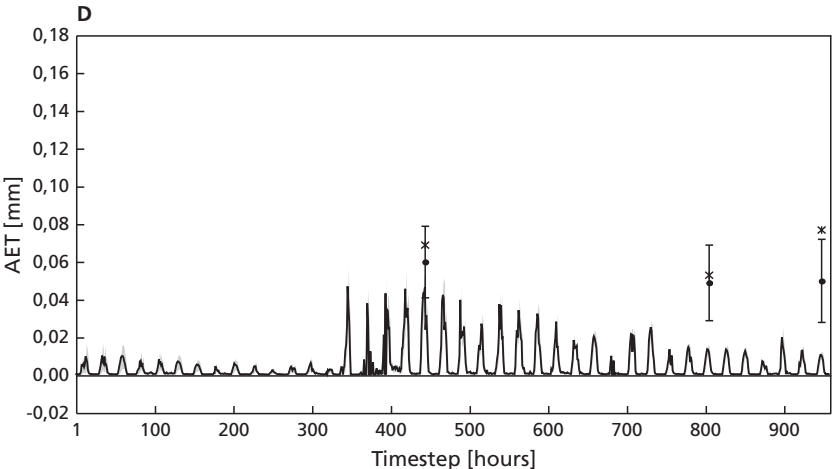
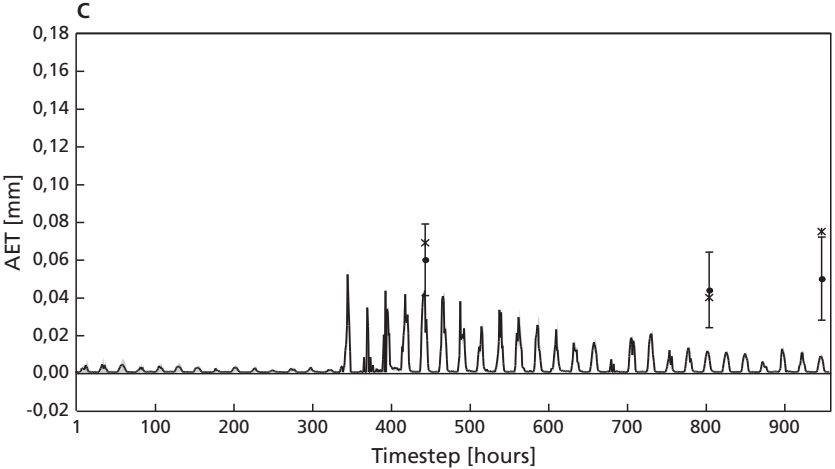


Figure 9.8 Actual evapotranspiration at locations C01 to C04 for the SOMS – Data Rich Scenario. Evapotranspiration estimated by both SEBS scenarios is also indicated in the graph with whiskers of 1 standard deviation.

The mean AET predicted by the SEBS – Large Error Scenario results show a relatively large spatial variability compared to the SEBS – Small Error Scenario (figure 9.11). The SEBS – Small Error Scenario is much smoother as can be expected, since only noise of 1 K in the accuracy of the satellite based measurement of surface kinetic temperature has been introduced. In the SEBS – Large Error Scenario, the non-linear response of AET to surface temperature as modelled with SEBS increases the spatial variability, because of the increased range in input surface temperatures.

The stratification present in the SOMS error propagation model cannot be recognised in the SEBS scenarios, except for the forest land cover class (at location C01), which has the highest



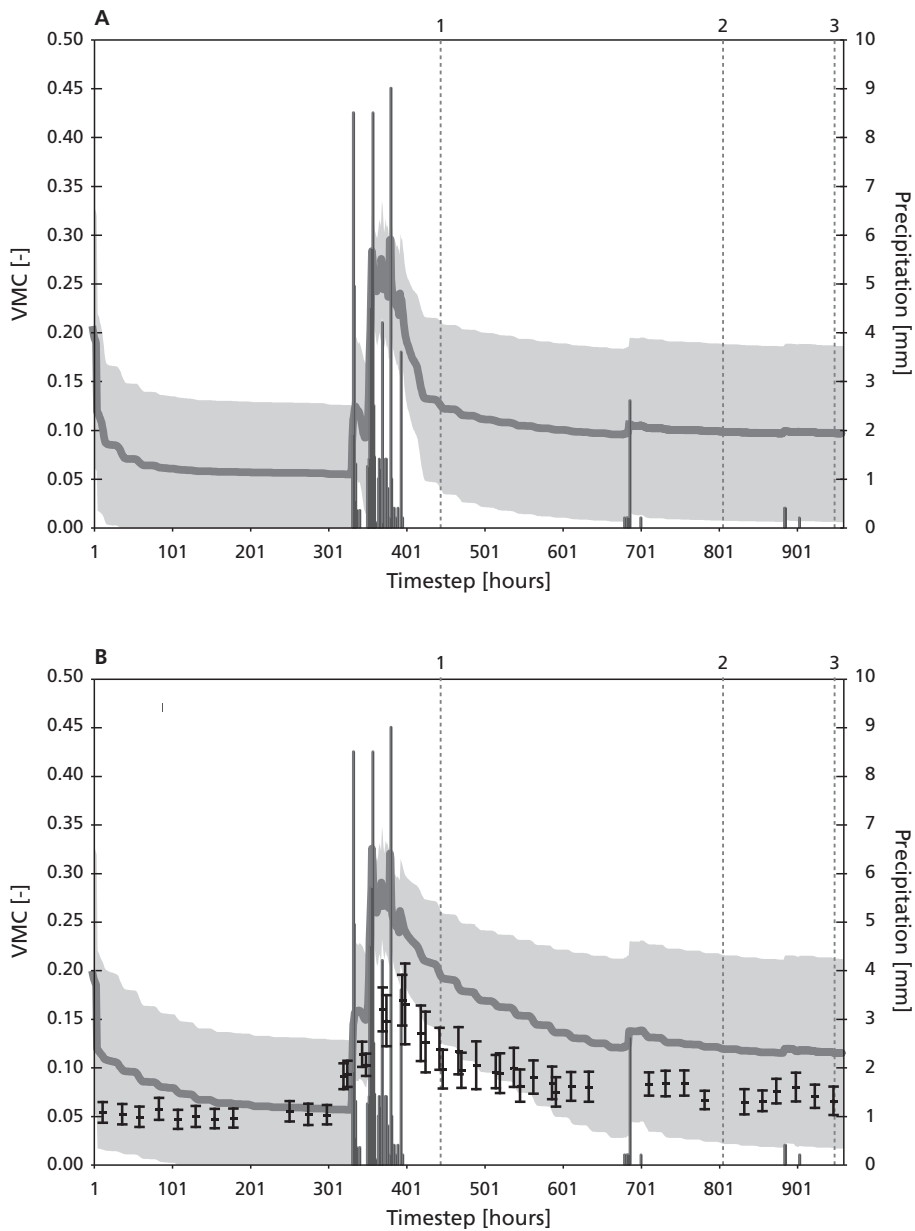
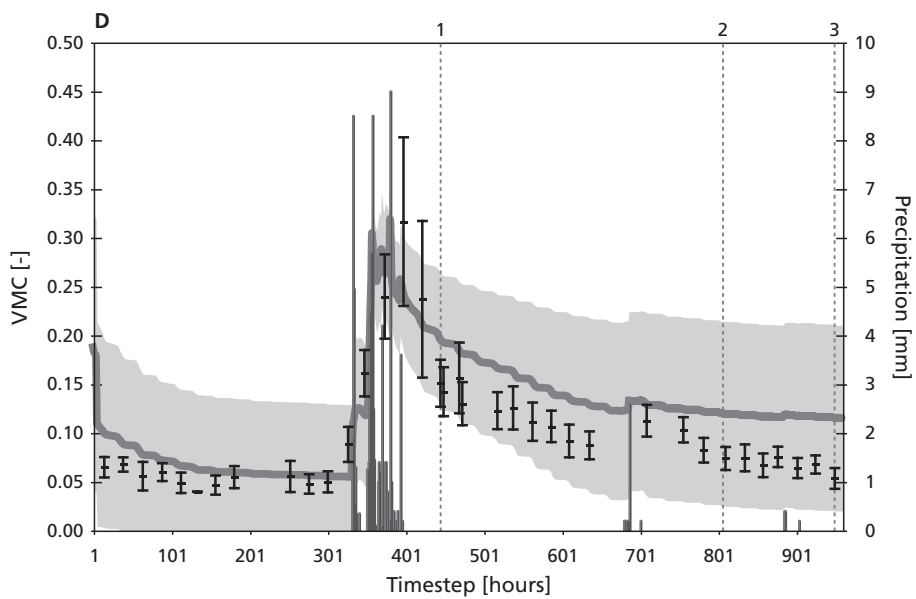
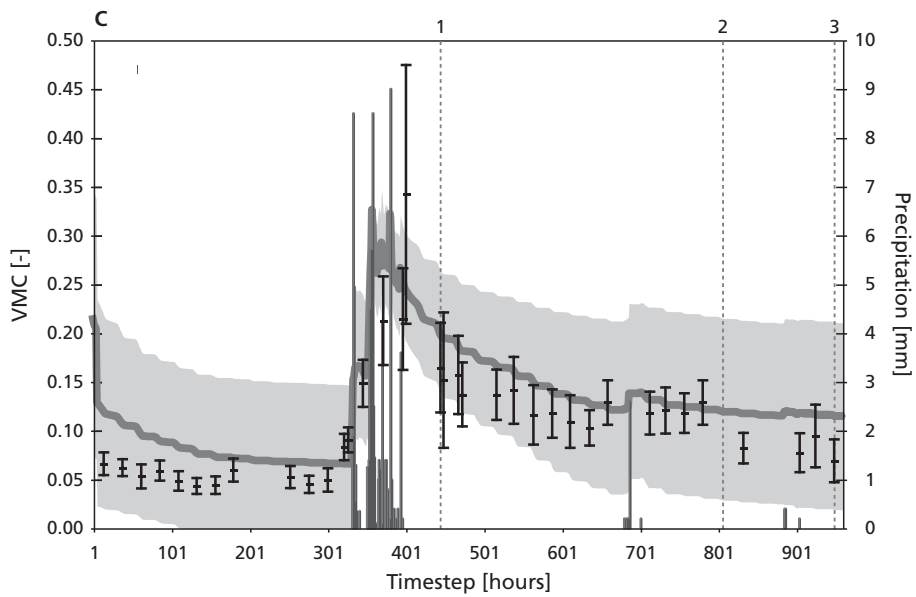
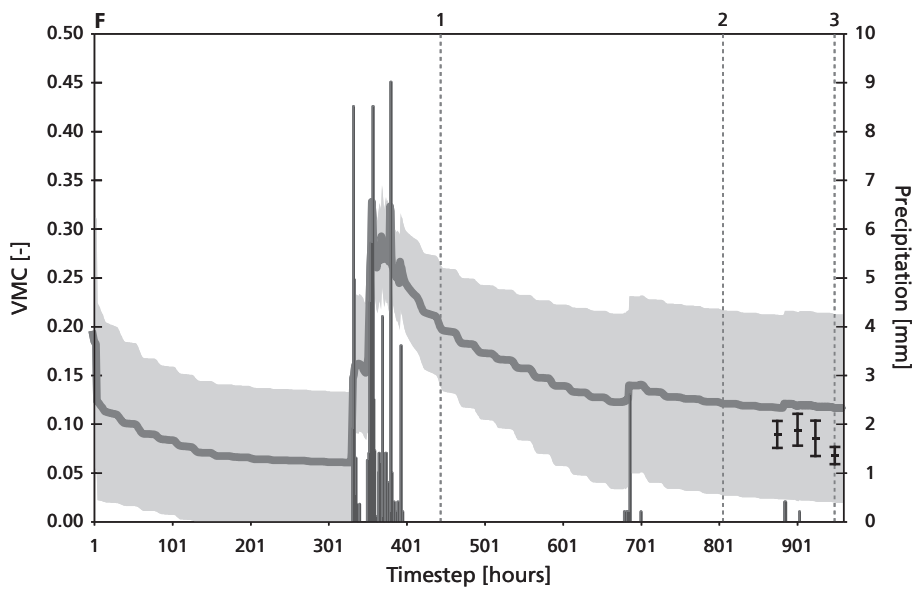
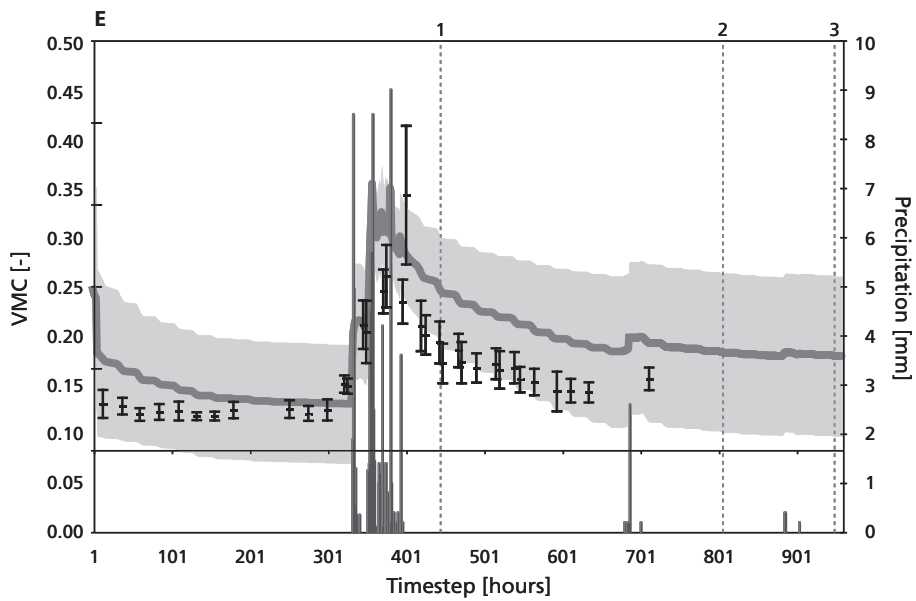


Figure 9.9 Timeseries of the average volumetric soil moisture content (VMC) in the first model layer (0-15 cm) at the calibration and validation sites (see figure 8.1 and 8.16) for the SOMS-Data Poor Scenario. A) C01, B) C02, C) C03, D) C04, E) V02, F) V03, G) V04. Rainfall events and satellite overpasses are indicated in the graphs. Field measurements are plotted as points. The whiskers indicate 1 standard error from the average of the soil moisture measurements in an agricultural parcel (chapter 8, eq. 8.43).



- Precipitation
- Overpass
- Average top VMC
- +1/-1 SD



(Figure 9.9 continued)

modelled AET during the overpass 1 as predicted by both SEBS error propagation scenarios (table 9.17). The SOMS error propagation model does not show this.

Table 9.17 shows that the spatial variability in mean AET for both error propagation scenarios is small. Also the difference in mean between the two scenarios is small except for the third overpass ( $t = 948$ ). The standard deviations of the estimated mean AET, however, are about 10 to 30 times higher for the SEBS – Large Error Scenario compared to the SEBS – Small Error Scenario.

**9.3.4 Comparison of SOMS and SEBS**

The simulated AET values of the SOMS and SEBS scenarios were also compared and are shown in figure 9.8, figure 9.10 and figure 9.11. It can be concluded that:

1. SEBS error propagation scenarios always estimates a higher average AET than the SOMS error propagation scenarios;
2. The standard deviation of all SOMS predictions of AET is smaller than the standard deviations of SEBS predictions;
3. The average AET has a higher spatial variability for the SOMS scenarios than for the SEBS scenarios.

The stratification present in the SOMS error propagation model cannot be recognised in the SEBS scenarios, except for the forest land cover class (at location C01), which has the highest modelled AET during the overpass 1 (both Small and Large Error Scenarios) and overpass 3 (Large Error Scenario) (table 9.17). The SOMS error propagation model does not show this.

The spatial variability of average AET predicted by SOMS is mainly caused by the stratification. Within the units there is little spatial variability. It was expected that the patterns

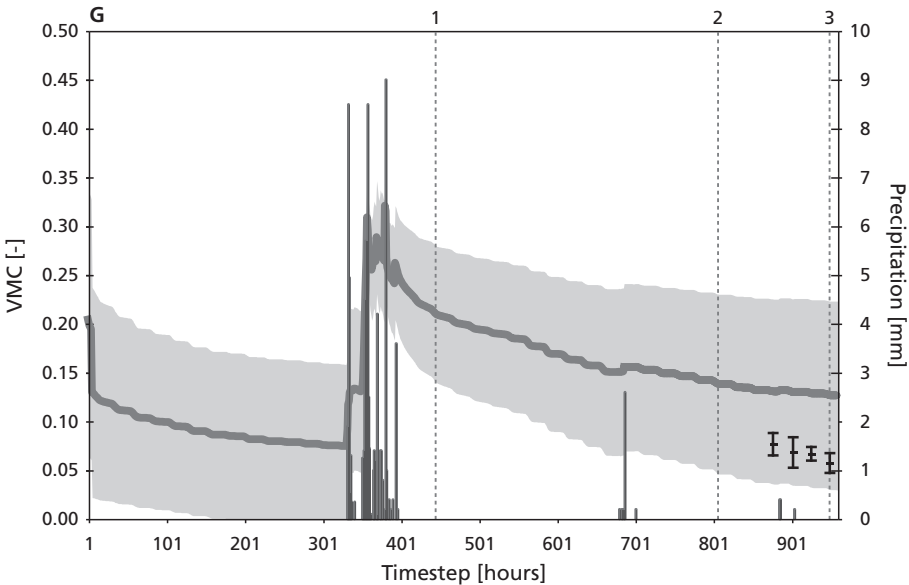


(Figure 9.9 continued)

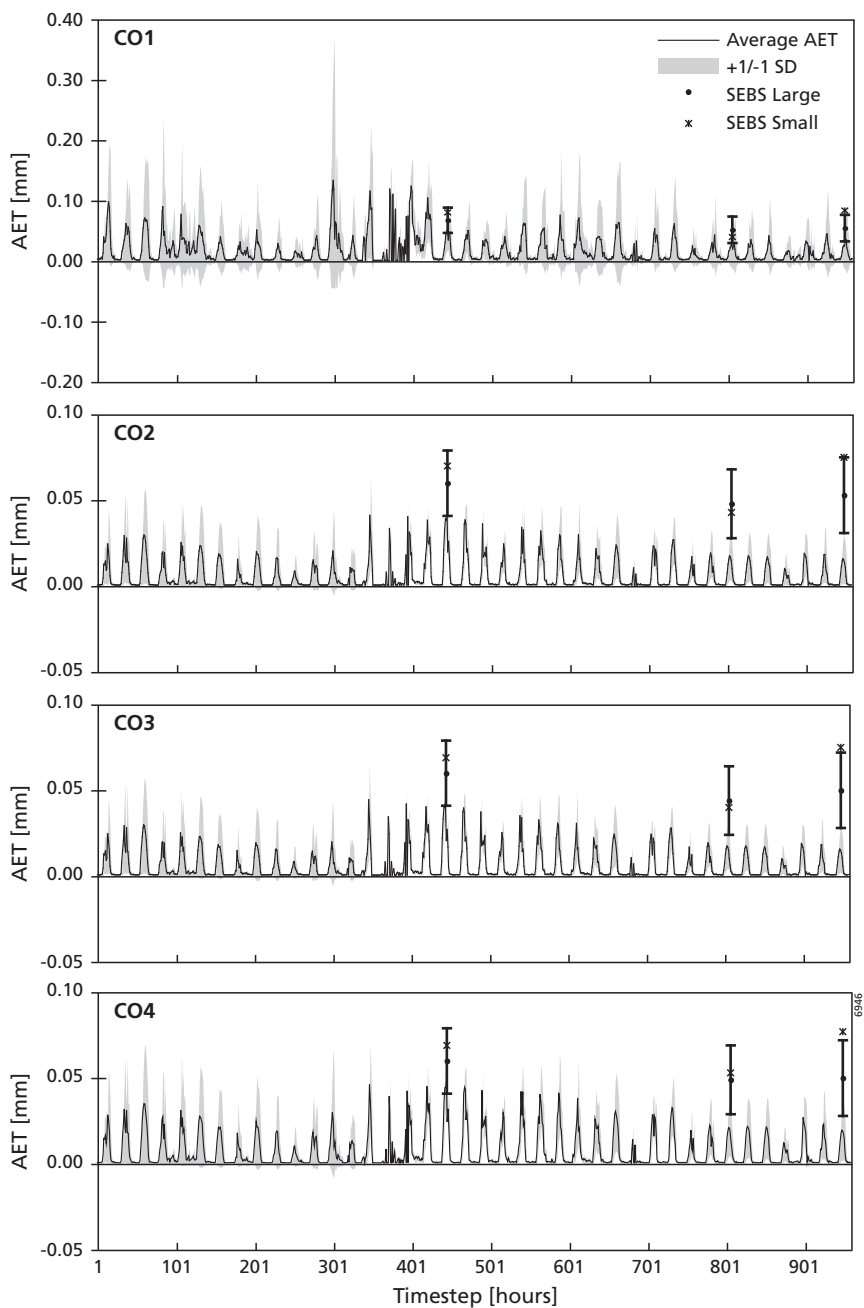


Figure 9.10 Average actual evapotranspiration and its standard deviation at locations CO1 to CO4 after 200 Monte Carlo runs for the SOMS – Data Poor Scenario. The actual evapotranspiration estimated for these locations by both SEBS scenarios are also indicated in the graph with whiskers of 1 standard deviation.

do not change with the error propagation modelling, because its base is a one-dimensional model consisting of a set of stochastic vectors (eq. 9.1) that are spatially correlated, but not conditioned to locations. Only precipitation is conditioned in the error propagation model, but the spatial patterns caused by the precipitation fields are not significant because of a small spatial variation.

Since the error bands are much larger in the SOMS – Data Poor Scenario (figure 9.10), the confidence interval of plus or minus one standard deviation overlaps with this interval of SEBS predicted AET. For location C01, all SEBS predictions of AET overlap with SOMS for this confidence interval. For the other locations some overlap exists with the SEBS – Large Error Scenario.

### 9.4 Conclusions

The two scenarios of the error propagation of the SOMS model and the error propagation in SEBS provide useful estimates of uncertainties in the predicted variables.

The SOMS – Data Rich Scenario shows small error bands compared to the SOMS – Data Poor Scenario. Most field validation and calibration field measurements in the SOMS – Data Rich Scenario fall within two standard deviations of the model predictions. Only shortly after the rainfall event the model underestimates the VMC, but the field measurements also show a large uncertainty at these timesteps. The estimated VMC and the goodness of fit statistics are

Table 9.17 AET [cm h<sup>-1</sup>] and standard deviation modelled by SEBS using the Small Error Scenario and the Large Error Scenario for all overpasses (t = 444, t = 805 and t = 948).

t = 444 Location	SEBS – Small Error Scenario		SEBS – Large Error Scenario	
	Mean	St.Dev.	Mean	St. Dev.
C01	0.08	2.0·10 <sup>-3</sup>	0.07	0.02
C02	0.07	6.0·10 <sup>-4</sup>	0.06	0.02
C03	0.07	6.1·10 <sup>-4</sup>	0.06	0.02
C04	0.07	1.4·10 <sup>-3</sup>	0.06	0.02
t = 805 Location	SEBS – Small Error Scenario		SEBS – Large Error Scenario	
	Mean	St.Dev.	Mean	St. Dev.
C01	0.04	1.2·10 <sup>-2</sup>	0.05	0.02
C02	0.04	7.2·10 <sup>-3</sup>	0.05	0.02
C03	0.04	7.6·10 <sup>-3</sup>	0.04	0.02
C04	0.05	6.0·10 <sup>-3</sup>	0.05	0.02
t = 948 Location	SEBS – Small Error Scenario		SEBS – Large Error Scenario	
	Mean	St.Dev.	Mean	St. Dev.
C01	0.08	2.0·10 <sup>-3</sup>	0.07	0.02
C02	0.08	5.2·10 <sup>-3</sup>	0.05	0.02
C03	0.08	4.8·10 <sup>-3</sup>	0.05	0.02
C04	0.08	4.1·10 <sup>-3</sup>	0.05	0.02

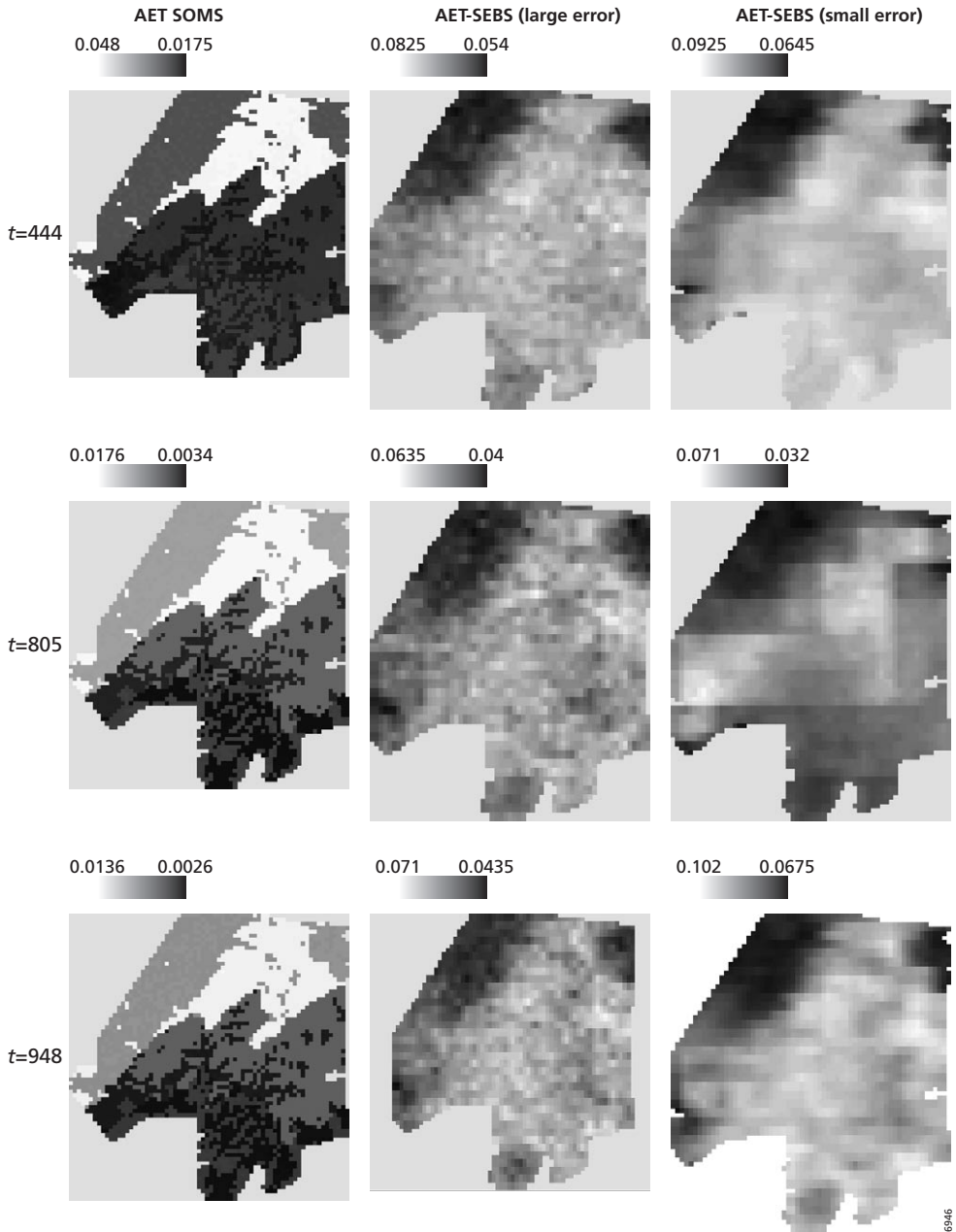


Figure 9.11 Realisation of actual evapotranspiration [ $\text{mm h}^{-1}$ ] at three overpass times (2, 17 and 23 November 2004) for the soil moisture model, SEBS – Large Error Scenario and SEBS – Small Error Scenario of the SEBS error propagation model.

comparable with the deterministic model, which means that the error-propagation model does not introduce large non-linear responses of the output.

In addition, the uncertainty in VMC modelled with the SOMS – Data Rich Scenario is in the same order of magnitude as the uncertainty of the field measurements at the scale of an agricultural parcel. Therefore, the uncertainty in VMC predictions by the SOMS – Data Rich Scenario will be acceptable for many applications. The good predictions suggest that it will be challenging for a data assimilation model to improve the patterns of VMC predicted when using the SOMS – Data Rich Scenario.

For the SOMS – Data Poor Scenario it can be concluded that the stochastic model predicts the trends in VMC patterns quite well, with an average  $r^2$  of 0.75. The average RMSE of 0.05, however is larger in comparison with the SOMS – Data Rich Scenario that has an average RMSE of 0.02. The uncertainty bands are much wider, but most observations fall inside one standard deviation from the predicted average VMC. It is hypothesised that in this case data-assimilation with remote sensing data can potentially improve the prediction of VMC patterns and decrease the uncertainties in the predictions. This will be investigated in the next chapter.

The two SEBS error propagation scenarios show very different results for the prediction of AET, compared to the two SOMS error propagation scenarios. The spatial variation in predicted AET is much larger in the SEBS – Large Error Scenario. The SEBS – Small Error Scenario is much smoother. In both scenarios only land cover/soil type combination 1 (forest) can be clearly recognised. Also the differences in the mean of the AET predictions are large between the two scenarios.

The difference between the AET distributions predicted by the error propagation models of SOMS and SEBS is large, which might give problems with the use of these models in data-assimilation. On the other hand, the higher spatial detail of SEBS estimated AET within the strata of the SOMS model has the potential of increasing the spatial detail of the sharply stratified SOMS model. This will be further investigated in the next chapter.



# 10 Integrating remote sensing observations in soil moisture modelling by means of a particle filter

## 10.1 Introduction

In the introduction of this thesis it was discussed that soil moisture is difficult to predict due to its large variation in both space and time. It is shown (chapter 8) that process-based models are capable of predicting temporal variation quite well, while spatial patterns within soil units are difficult to predict. It is also shown (chapter 2 and 6) that remote sensing can provide spatial inputs for process-based soil moisture models and can be used to calculate actual evapotranspiration (AET) that reflects soil moisture patterns. The temporal variation, however, cannot be represented by remote sensing imagery, since it is limited to satellite overpasses.

In this chapter the strength of both remote sensing derived data and a process-based model will be used by combining them with the use of a data assimilation algorithm. Such an algorithm aims at providing a process-based model with the best estimate of a model state at the timestep of a measurement (Walker, 1999) or when remote sensing data is available (Errico, 1999; Errico et al., 2000).

In many researches soil moisture estimates from microwave remote sensing have been assimilated in hydrological models with promising results, using Kalman Filters, e.g. Reichle et al. (2001b, 2001c), Pauwels et al. (2001), Margulis et al. (2002), Houser et al. (1998), Hoeben and Troch (2000), Walker et al. (2001). The approach followed by these authors has two disadvantages which will be targeted in this chapter:

1. The spatial resolution of radar estimated soil moisture ( $10^6$ - $10^7$  m) is not appropriate for the level of detail required in predictions of soil moisture at the scale of agricultural areas and small catchments ( $10^1$  –  $10^2$  m);
2. Kalman Filters use linearizations of non-linear model functions, introducing errors (Gelb, 1974). They also assume a Gaussian distribution of the prior probability density function (pdf) of model state variables, which is not necessarily true in hydrological modelling. Ensemble Kalman filters prevent this by propagating the non-linear model equations in Monte Carlo simulations (Evensen, 1994; Burgers et al., 1998; Margulis et al., 2002; Reichle et al., 2002). All Kalman Filters, however, modify the system state at the filter moment, which can cause a violation of the conservation of mass, momentum, and energy and therefore induce problems in the closure of water and energy budgets (Van Leeuwen, 2003). Furthermore, with a large amount of filter data such is the case when using remote sensing data, large matrices need to be inverted (Van Leeuwen, 2003).

To overcome the first issue, this study assimilates AET fluxes derived from optical and thermal remote sensing images that have higher resolutions than radar images. The second issue is tackled

by using a Particle Filter algorithm (PF), which can be applied to non-linear and non-Gaussian processes. Moreover, unlike a Kalman filter, a particle filter does not violate the conservation of mass, since it does not modify the system state after the filter moment.

A PF samples different realisations from a stochastic model in order to calculate the posterior probability density function (pdf), which is the pdf at a timestep when new data is available (Weerts and El Serafy, 2006). The samples of model runs are called *particles*.

At each timestep when an observation becomes available, called *filter moment*, the particles and their uncertainty are compared with the filter data and its uncertainty and weighted. The weights of the particles are called *importance weights*. The best set of particles is propagated, resulting in an approximation of stochastic model variables at each timestep, of which a mean and a variance can be calculated. It is expected that the use of a PF reduces the variance of the predictions.

Particle filters have only recently been introduced in the field of hydrology (Moradkhani et al., 2005; Weerts and El Serafy, 2006) and need an evaluation of their benefits and constraints, which is done in this chapter by applying a PF algorithm to the soil moisture model (SOMS, see chapter 8), using actual evapotranspiration derived from MODIS remote sensing images as filter data (SEBS, see section 4.5).

In this chapter the performance and restrictions of the implementation of a PF algorithm in soil moisture modelling will be investigated by analysing the mean and variance of the prediction variable (volumetric moisture content, VMC) calculated by the SOMS model and the filter data (AET) derived from SEBS, and the relationship between AET and VMC, using different scenarios of error propagation, which have been described in chapter 9.

First, the particle filter is explained as well as its implementation in the SOMS model. Next, the results for VMC and AET are analysed. VMC estimations from the different scenarios are compared with field measurements and with error propagation models without particle filtering. Finally, some restrictions specific for our implementation and for the particle filter in general will be discussed.

## 10.2 Methods

### 10.2.1 Particle Filter

In this study the Residual Resampling (RR) Particle Filter (Liu and Chen, 1998) will be used. The main advantage of an RR Particle Filter compared to other PF's is that it is computationally faster because smaller ensemble sizes can be used (Liu and Chen, 1998; Van Leeuwen, 2003). It has been evaluated in rainfall-runoff modelling (Weerts and El Serafy, 2006) and ocean modelling (Van Leeuwen, 2003).

All PF's combine pdf's of a model and additional data (*filter data*). In this way Bayesian statistics can be used to derive the posterior pdf (Van Leeuwen, 2003). The pdf resulting from the model is called the prior pdf,  $f_m(\psi)$ .  $\psi$  is the unknown model evolution, which is a value of a random variable  $\underline{\psi}$ . At model timesteps where filter data is available, the prior pdf can be conditioned to the new data  $\mathbf{d}$  to derive the posterior pdf (Van Leeuwen, 2003):

$$f_m(\psi|\mathbf{d}) = \frac{f_d(\mathbf{d}|\psi)f_m(\psi)}{\int f_d(\mathbf{d}|\psi)f_m(\psi)d\psi} \quad (10.1)$$

where  $f_d(\mathbf{d}|\psi)$  is the pdf of  $\mathbf{d}$  assuming that random variable  $\underline{\psi} = \psi$ . The denominator is normalization term consisting of the pdf of  $\mathbf{d}$  written as a marginal density of the combined density of the model and the filter data (Van Leeuwen, 2003).

The mean of the posterior pdf is calculated with (Van Leeuwen, 2003):

$$\bar{\psi} = \int \psi f_m(\psi|\mathbf{d}) d\psi \quad (10.2)$$

$\bar{\psi}$  can be approximated by using an ensemble of model realisations  $i$  ( $i=1, \dots, N$ ), the particles (Van Leeuwen, 2003). The total number of particles (ensemble size  $N$ ) should be defined in the algorithm and is determined by available computing power and model complexity. Eq. 10.3 gives the approximation of eq. 10.2:

$$\bar{\psi} = \sum_{i=1}^N \psi_i f_m(\psi_i|\mathbf{d}) \quad (10.3)$$

This can be rewritten as (Van Leeuwen, 2003):

$$\bar{\psi} = \frac{\sum_{i=1}^N \psi_i f_d(\mathbf{d}|\psi_i)}{\sum_{i=1}^N f_d(\mathbf{d}|\psi_i)} \quad (10.4)$$

This is in fact a weighting of each particle by its ‘‘distance’’ to the filter data. The weight  $w_i$  of particle  $\psi_i$  is calculated with (Van Leeuwen, 2003):

$$w_i = \frac{f_d(\mathbf{d}|\psi_i)}{\sum_{i=1}^N f_d(\mathbf{d}|\psi_i)} \quad (10.5)$$

When we assume that errors in the additional data are uncorrelated and have a Gaussian distribution, the weights can be calculated with (Van Leeuwen, 2003):

$$w_i = \frac{e^{-\left(\frac{(\mathbf{d}-H\psi_i)^2}{2\sigma^2}\right)}}{A} \quad (10.6)$$

where  $\sigma$  is the standard deviation of the distribution of  $\mathbf{d}$ ,  $H$  is the measurement operator, which can be strongly nonlinear (Van Leeuwen, 2003).  $A$  is a normalization constant that is calculated with:

$$A = \sum_{i=1}^N e^{-\left(\frac{(\mathbf{d}-H\psi_i)^2}{2\sigma^2}\right)} \quad (10.7)$$

In this study a distributed model will be used. Therefore,  $w_i$  is calculated for each model gridcell with eq. 10.6 and averaged for the entire model area.

Now the weight of each particle is known, the particles with largest weights can be selected (cloned) and propagated. The ensemble size  $N$  is constant for all model time steps. The selection procedure of particles that are cloned is called residual resampling (Van Leeuwen, 2003; Weerts and El Serafy, 2006):

1. Multiply the weights with the ensemble size  $N$ :

$$k_i = Nw_i \tag{10.8}$$

2. The particles with  $k_i > 1$  are selected and cloned according to the integer value of  $k_i$ . Suppose that particle  $i$  has a weight  $w_i = 0.115$  according to eq. 10.6 and the desired ensemble size  $N = 100$ , which results in  $k_i = 11.5$ . This means that particle  $i$  will be cloned 11 times, while a residual  $k_{i,r} = 0.5$  remains.
3. The residuals  $k_{i,r}$  form a new probability density distribution from which remaining particles of the ensemble are sampled to reach an ensemble size  $N$ .  
This procedure is illustrated in figure 10.1.

### 10.2.2 Implementation

In this research the Residual Resampling Particle Filter algorithm has been implemented using the PCRaster Python library (Karsenberg et al., 2007). In order to investigate the performance and limitations of the PF, two scenarios of the error propagation of the SOMS model (chapter 8), applied to the Sehoul study area, have been used with filter data from two scenarios of the error propagation of SEBS. The two scenarios of the SOMS model are the SOMS – Data Rich Scenario and SOMS – Data poor Scenario that have been modelled in chapter 9. The filter data,

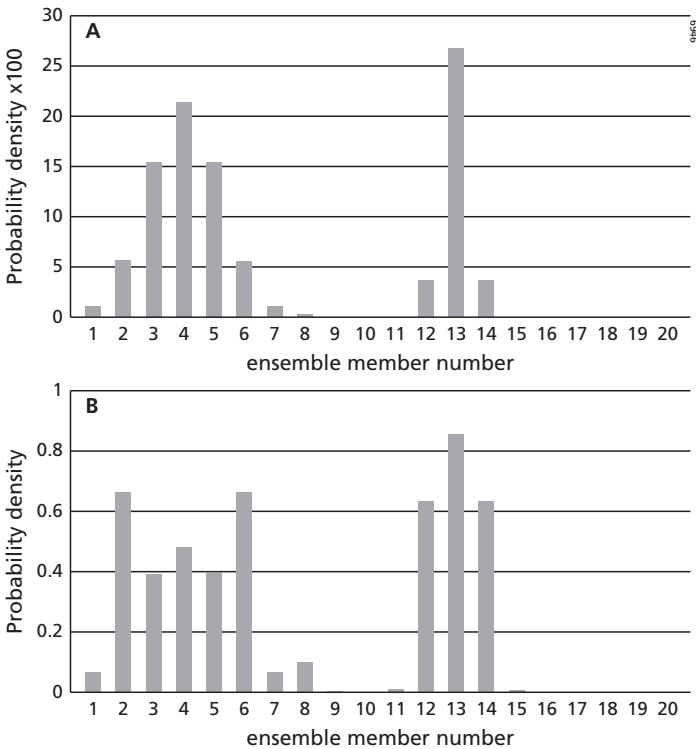


Figure 10.1 a) the posterior density ( $k_i$ ) before resampling, multiplied by the ensemble size (100); b) the modified posterior density ( $k_{i,r}$ ) after subtraction of the integer values in histogram a). The remainder of the ensemble is drawn from this density. Source: Van Leeuwen (2003).

consisting of the mean and variance of AET flux, have been derived from two scenarios of error propagation in SEBS that have been explained in the previous chapter. The filter data that is based on the error propagation modelling of downscaling of surface temperature is called the SEBS – Large Error filter data and the filter data that is based on the error propagation model in which only the error in the MODIS surface temperature product has been propagated is called the SEBS – Small Error filter data. The filter data is modelled at three satellite overpass times, which will be called the *filter moments*. The filter moments are at timesteps 444, 805 and 948 (hours). The number of particles used is 200.

All scenarios are evaluated with TDR field measurements of volumetric moisture content as described in section 8.3.2 at the model calibration locations C01-C04 (figure 8.1) and validation locations V02-V04 (figure 8.17). The same goodness of fit statistics (RMSE, Error Variance, modelling efficiency (*E*)) will be used as defined in section 8.4.1.

### 10.3 Results

#### 10.3.1 Filter results for actual evapotranspiration

The timeseries results for the filter variable AET using the four filter scenarios (figure 10.2) are comparable with the results for the same scenarios without the use of a particle filter (see section 9.3, figure 9.8). The error bands of the predicted AET with the SOMS – Data Poor Scenarios are much wider during initialisation and during daytime than the error bands of the SOMS – Data Rich Scenarios.

In chapter 9 it had been concluded that filtering probably has little effect on the estimation of AET using the SOMS – Data Rich Scenarios, because the distance between the probability distributions of modelled AET and the SEBS estimated AET are large. The chances were

*Table 10.1* Analysis of the change of mean estimated VMC after filtering. FM = Filter Moment, Large = SEBS – Large Error Filter Data, Small = SEBS – Small Error Filter Data. C01 to C04 are the calibration locations (fig. 8.1) and V02 to V04 are the validation locations (fig. 8.17).

FM	Data Rich/Large			Data Rich/Small			Data Poor/Large			Data Poor/Small		
	1	2	3	1	2	3	1	2	3	1	2	3
C01	+-	+-	+-	+-	-	+-	-	--	--	--	-	--
C02	+-	+-	+-	+-	+-	--	-	--	-	-	+-	+-
C03	+-	+-	+-	+-	+-	--	--	--	--	+-	--	-
C04	+-	+-	+-	+-	+	+	+-	-	+-	-	-	-
V02	+-	+-	-	-	+-	--	+-	-	-	-	+-	+
V03	+-	+-	+-	+-	+-	--	-	--	--	+-	--	-
V04	+-	+-	+-	+-	+-	+-	+-	--	-	-	-	+-

Legend:

Large decrease	Little decrease	No Change	Small increase	Large increase
--	-	+-	+	++
>0.01 m/m	0.003-0.01 m/m	0-0.003 m/m	0.003-0.01 m/m	>0.01 m/m

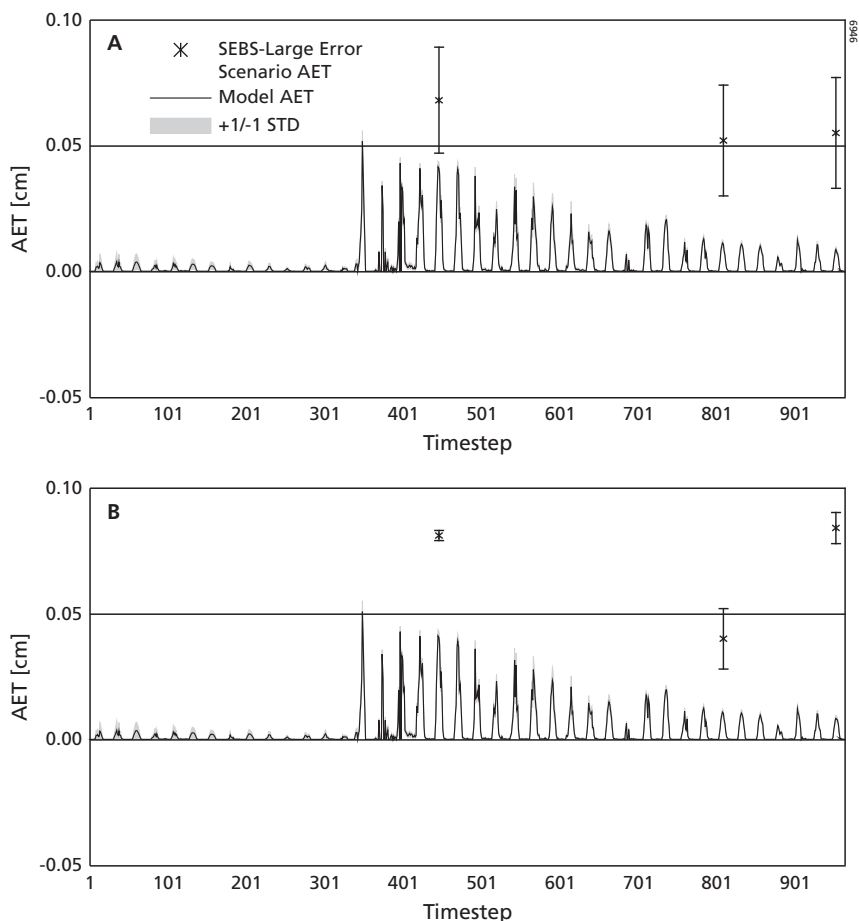
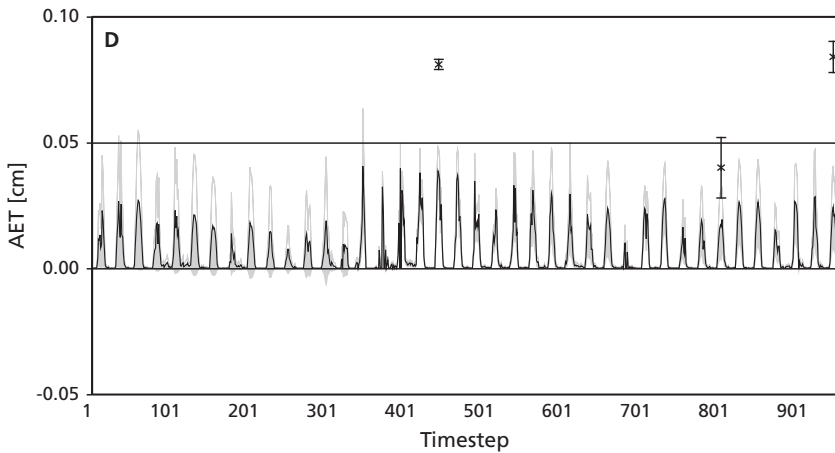
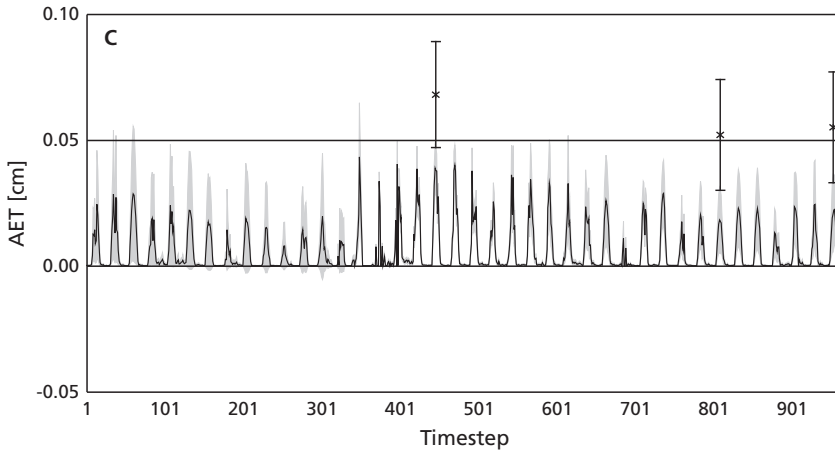


Figure 10.2 Modelled actual evapotranspiration (AET) at location C03 (see figure 8.1) using four scenarios. A) SOMS – Data Rich Scenario filtered with the SEBS – Large Error filter data; B) SOMS – Data Rich Scenario filtered with the SEBS – Small Error filter data; C) SOMS – Data Poor Scenario filtered with the SEBS – Large Error filter data; D) SOMS – Data Poor Scenario filtered with the SEBS – Small Error filter data. One standard deviation in the estimation of the average AET is indicated for SOMS as an uncertainty band and for SEBS as whiskers.

slightly higher for the SOMS – Data Poor Scenarios, because the distance between modelled AET and the filter data are smaller and some overlap existed for three filter moments with SEBS – Large Error filter data and the second filter moment with SEBS – Small Error filter data. Comparison of figure 10.2 with figure 9.8, however, reveals no large difference in the mean AET.

Also, the variance in AET shown in figure 10.2 and figure 9.8 is mainly caused by uncorrelated noise or short range variation (nugget variance), which means that the difference between model cells is very large, but averaged over the model area it gives almost the same



result for each particle. When the difference between particles is too small, the effect of filtering will be very small (see also figure 10.10).

Another way to compare the error propagation results of chapter 9 with the results of the PF scenarios is to analyse the ratio between the standard deviation of AET predicted using a PF and AET predicted by error propagation modelling without a PF. When the ratio becomes less than 1, the uncertainty in the AET predictions is lower after filtering than without filtering. Successful filtering should minimize the variance of AET predictions.

Figure 10.3a to c show the ratio plots for the locations where a change has been observed for certain filtering scenarios. Only filtering with the SEBS – Small Error filter data shows a change in AET uncertainty. Other location/scenario combinations showed no change and are comparable with figure 10.3d. The ratio plots show that:

- Filtering using the SOMS – Data Rich Scenarios has no effect at most locations except at location C03 with the SEBS – Small Error filter data. Figure 10.3a shows for this case a small decrease in the standard deviation after the first filter moment which means that the PF is successful here in reducing the error in estimated AET;

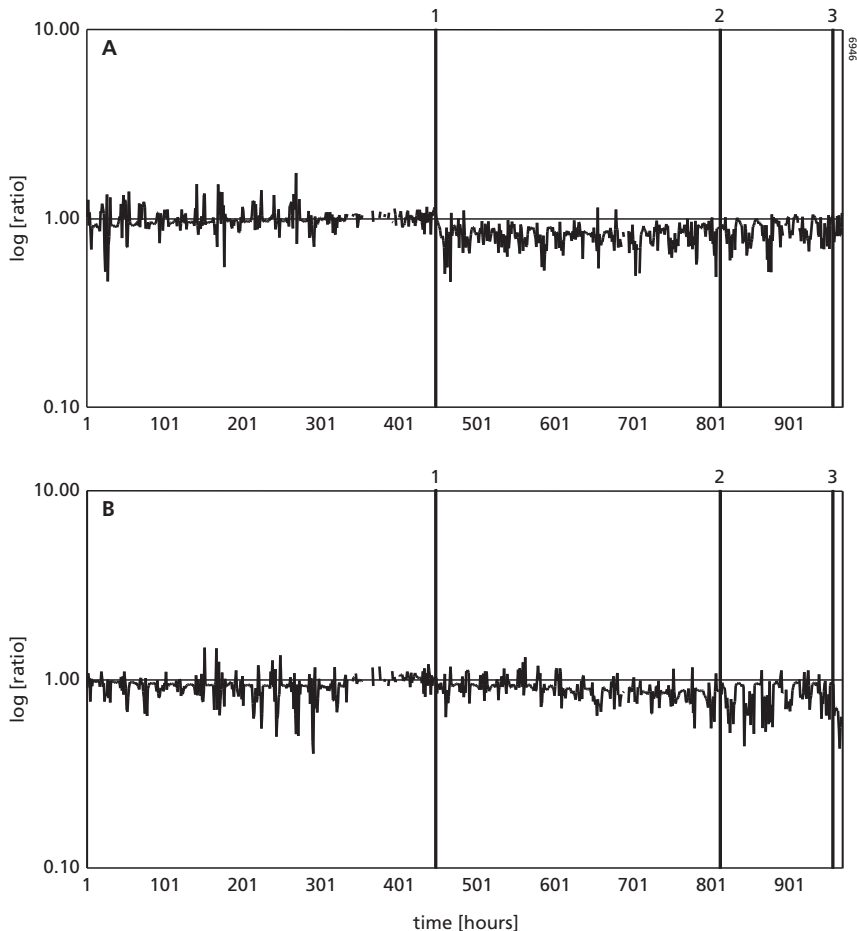
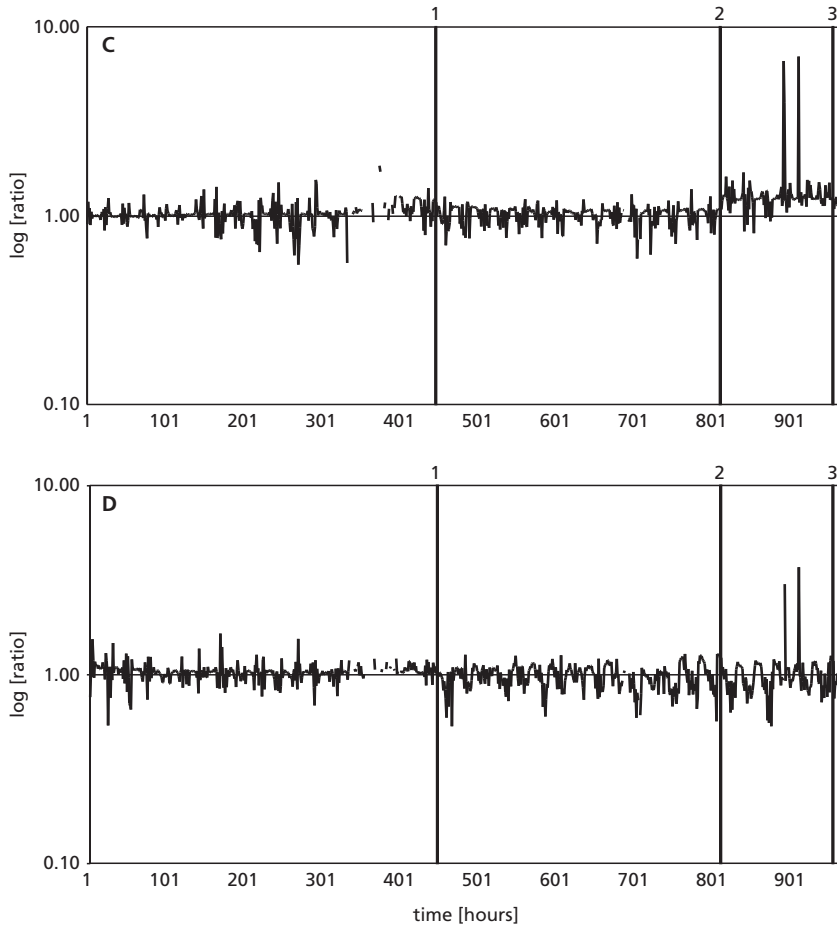


Figure 10.3  $\sigma_{VMCfilter}/\sigma_{VMC}$  ratio timeseries results. The ratio is plotted on a logarithmic scale. Results are shown for A) location C03: SOMS Data – Rich Scenarion with SEBS – Small Error filter data; B) location C02: SOMS – Data Poor Scenario with SEBS Small Error filter data; C) location C03: SOMS – Data Poor Scenario with SEBS – Small Error filter data; D) Location C04: SOMS – Data Rich Scenario with SEBS – Small Error filter data. Note that missing values are present during the first rainfall event, because the model assumes no evapotranspiration during rainfall events and consequently the standard deviation of AET is zero.

- Filtering with the SEBS – Small Error filter data and the SOMS – Data Poor Scenario shows a slightly decreasing trend in standard deviation at location C02, especially after the third filter moment (figure 10.3b), indicating a successful application of the PF;
- Filtering with the SEBS – Small Error filter data and the SOMS – Data Poor Scenario shows an increase of the standard deviation at location C03 after the second filter moment (figure 10.3c);



So in only three of the studied filter moments a little effect of filtering on the trend in AET is observed. In all other scenarios, for all locations, the effect of the PF on the standard deviation of AET is negligible. However, the  $\sigma_{\text{AETfilter}}/\sigma_{\text{AET}}$  ratio shows a large variation in time (figure 10.3) and could disguise changes induced by filtering, which could be in the same order of magnitude.

It seems that the effect of filtering does not only depend on the scenario, but also on the filter moment and the location within the study area.

### 10.3.2 Filtering results for Volumetric Moisture Content (VMC)

Analysis of timeseries (table 10.1) of modelled mean VMC in the first model layer, i.e. 0-15 cm, reveals that filtering reduces the mean VMC for most reference sites in the SOMS – Data Poor Scenarios. The larger error in this scenario causes a large variance of the VMC estimation of SOMS, which makes filtering more effective. Most reductions take place in the SOMS – Data Poor Scenario with SEBS – Large Error filter data (e.g. figure 10.4a, b and c). The improvements

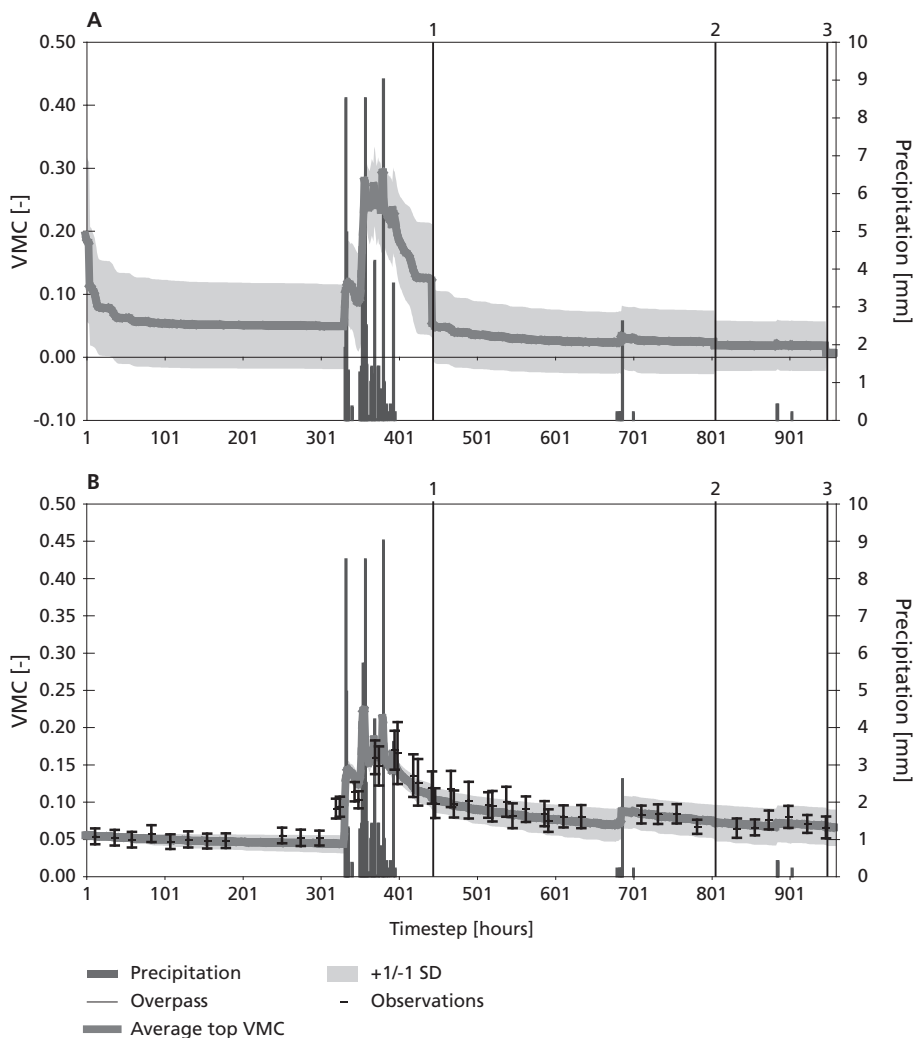
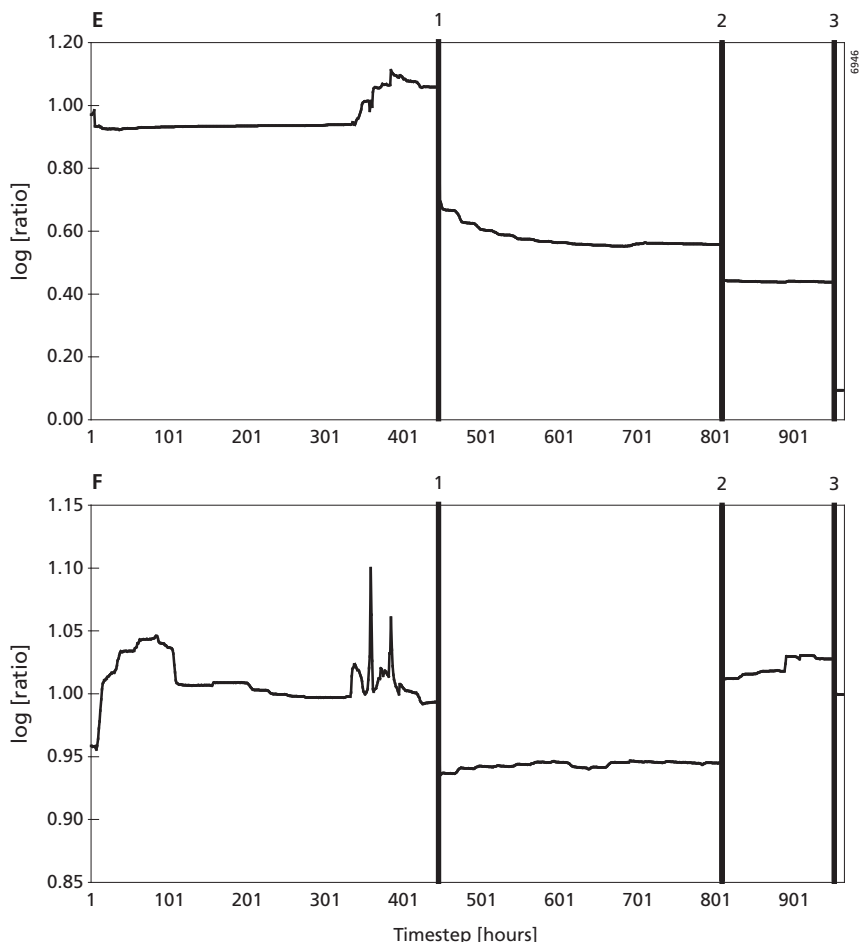


Figure 10.4 Left column: timeseries of model output for the average VMC in the first model layer (0-15 cm) after 200 Monte Carlo runs. The error bands indicate 1 standard deviation. Rainfall events and satellite overpasses are indicated in the graphs. At timesteps where field measurements are available, they are plotted with whiskers of 1 standard deviation. Right column:  $\sigma_{\text{VMC}_{\text{filter}}}/\sigma_{\text{VMC}}$  ratio timeseries results. Note that only after the first filter moment the standard deviation of VMC with filtering ( $\sigma_{\text{VMC}_{\text{filter}}}$ ) can be compared with the same scenario without filtering ( $\sigma_{\text{VMC}}$ ). The VMC at the other filter moments are influenced by the first filter moment. The results are shown for locations (a) C01 with the SOMS – Data Poor Scenario and SEBS – Small Error filter data; (b) C02 with the SOMS – Data Rich Scenario and SEBS – Large Error filter data; (c) C03 with the SOMS – Data Poor Scenario and SEBS – Large Error filter data; (d) V02 with the SOMS – Data Poor Scenario and SEBS – Small Error filter data.



(Figure 10.4 continued)

in predicted mean VMC, however, are small compared to the uncertainty in the estimation of the standard deviation when using 200 particles.

In the SOMS – Data Rich Scenario with SEBS – Small Error filter data an increase in VMC after filtering has been observed (e.g. figure 10.4d). Filtering has almost no effect on the SOMS – Data Rich scenario with SEBS Large Error filter data.

The PF modelling results of mean VMC have been evaluated with field measurements of VMC at sites C01 to C04 and V02 to V04. Figure 10.6 shows the goodness of fit statistics for the four particle filter scenarios and the two SOMS scenarios without a particle filter. It should be noted that these statistics are based only on the predicted VMC and do not include the predicted model uncertainty. Care should be taken with the interpretation of the statistics for locations V03 and V04, because they are based on only 4 observations and therefore not statistically significant.

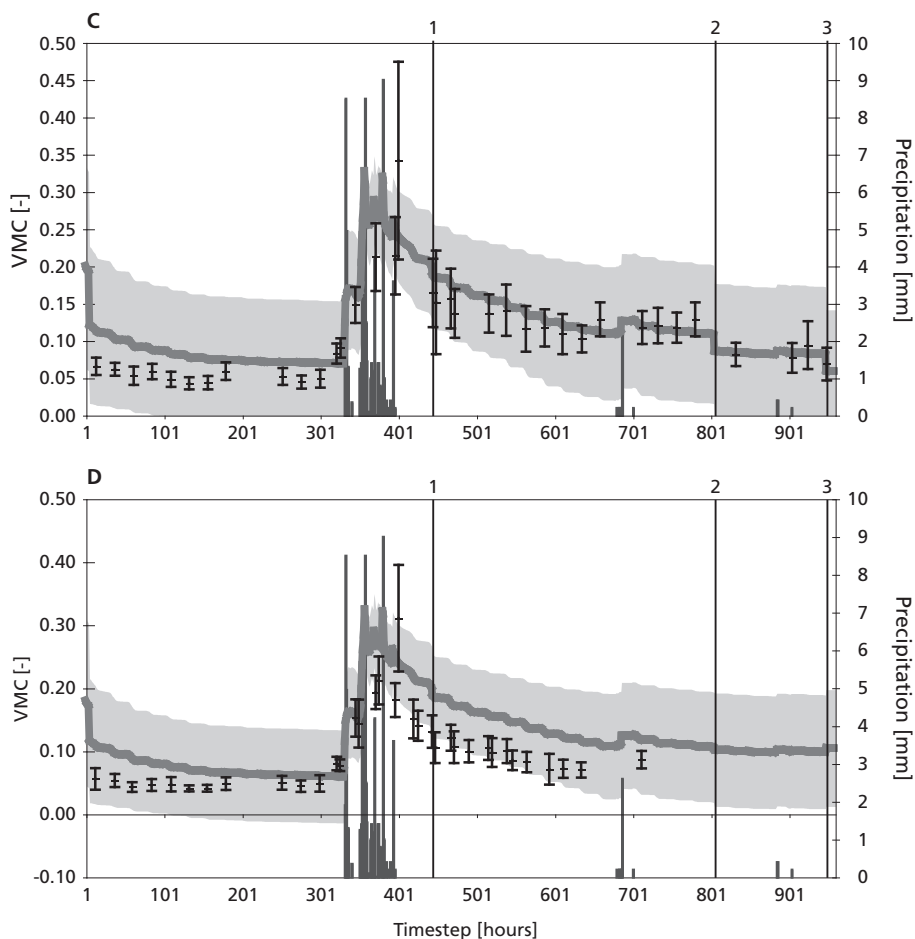


(Figure 10.4 continued)

Compared to the SOMS – Data Poor Scenarios, both with and without filtering, the SOMS – Data Rich scenarios perform better in terms of error variance, root mean squared error (RMSE), model efficiency and correlation with field data ( $r^2$ ). Most of the SOMS – Data Rich Scenarios are comparable with these for the scenarios without filtering. The SOMS – Data Poor Scenarios show some improvements:

- C03 and V03 have a lower RMSE and higher modelling efficiency with both scenarios of filter data (see also figure 10.4c);
- C04 shows a reduction in error variance and RMSE and an increase in modelling efficiency and  $r^2$  with SEBS – Small Error filter data;
- V04 shows in the case of small error filter data a reduction in error variance and RMSE and an increase in modelling efficiency, although this remains negative.

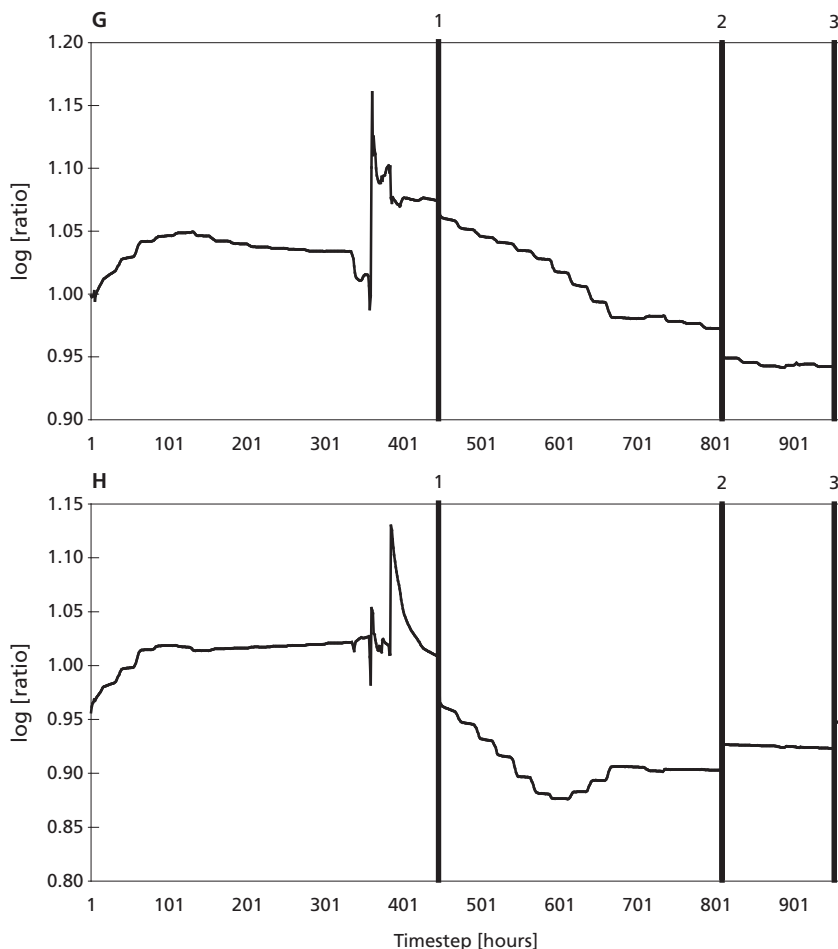


(Figure 10.4 continued)

Analysis of the spatial distribution of VMC in the output maps at each model timestep revealed that filtering does not add much extra spatial variability compared to the error propagation scenarios without the use of MODIS based filter data. This is caused by: 1) the mean AET estimated by SEBS does not have much more small scale variation compared to the mean AET estimated by SOMS, 2) the error structure of the AET estimated by SOMS is different from the AET estimated by SEBS, causing very different realisations (figure 9.11).

Figure 10.5, for example, shows the spatial result of the VMC at one timestep after the first filter moment ( $t = 445$ ) for the SOMS – Data Poor Scenario without filtering (figure 10.5a) and with filter data (figure 10.5b).

A Particle Filter is successful when the uncertainty of the estimated variable is reduced. In the same way as in section 10.3.1 this can also be investigated by plotting the ratio, in this case between the standard deviation of VMC predicted using a PF and VMC predicted by error

propagation modelling without a PF. When the ratio becomes less than 1, the uncertainty in the VMC predictions is lower after filtering than without filtering.

Table 10.2 shows the changes in standard deviation of VMC estimated after filtering. All scenarios show decreasing and, surprisingly, increasing standard deviations of VMC. The two SOMS – Data Poor Scenarios show more decreases in standard deviation (e.g. b) than the

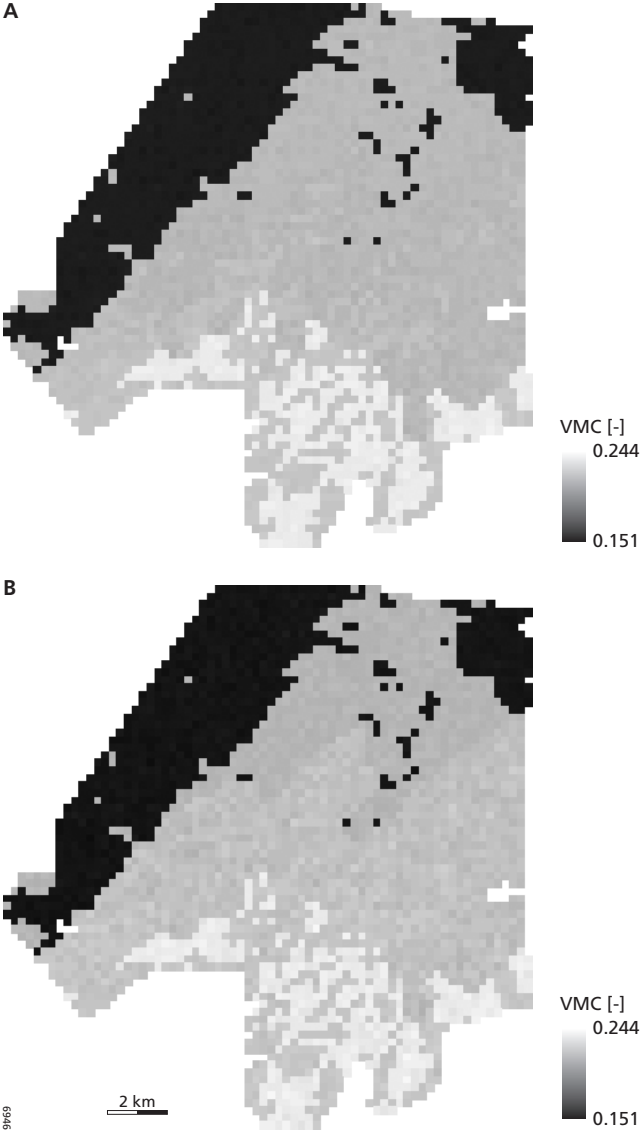


Figure 10.5 Average VMC map at  $t = 445$  (one timestep after the first filter moment) for a) Data Poor error propagation scenario without filtering, b) Data Poor error scenario with large error filter data.

Table 10.2 Analysis of the change of standard deviation of VMC after filtering. FM = Filter Moment, Large = Large Error Filter Data, Small = Small Error Filter Data. C01 to C04 are the calibration locations (fig. 8.1) and V02 to V04 are the validation locations (fig. 8.17). Absolute changes in standard deviation are in the order of  $10^{-3}$ - $10^{-5}$  mm.

FM	Data Rich/Large			Data Rich/Small			Data Poor/Large			Data Poor/Small		
	1	2	3	1	2	3	1	2	3	1	2	3
C01	--	-	-	--	-	--	+	-	--	--	--	--
C02	--	++	--	+	++	++	-	--	-	-	+	+
C03	--	++	--	--	++	--	-	--	--	-	--	--
C04	-	+	+-	+	--	--	+	-	+	-	+	--
V02	--	++	--	+	++	++	-	--	-	--	+	+
V03	--	+	--	--	++	--	-	-	-	--	--	-
V04	-	+	+	-	--	-	-	+	+	--	-	-

Legend:

Large decrease	Little decrease	No Change	Small increase	Large increase
--	-	+-	+	++
>10%	1 – 10%	0-1%	1-10%	>10%

SOMS – Data Rich Scenarios. In the SOMS – Data Rich Scenario with SEBS – Large Error filter data the standard deviation always increases after the second filter moment, except at location C01. Location C01 shows more decreases (e.g. figure 10.4a) than other locations, while location C02 and V02 show more increases in standard deviation (e.g. figure 10.4b and d). The increases in the standard deviation will be explained in the next section.

## 10.4 Discussion

### 10.4.1 Variance versus distribution of AET

In the introduction of this chapter it was hypothesised that the variance of modelled AET always decreases by using the PF. The results, however, show that this is not always the case. In most cases the variance of AET remains unchanged or sometimes increases. This increase is most probably caused by the large difference in distribution of SOMS predicted AET and the AET modelled by SEBS at the filter moments. The PF assumes a normal distribution of AET estimated by SEBS, while AET estimated by SOMS is not normally distributed. The filtering algorithm will give a higher weight to particles with a high AET. As a consequence, the frequency distribution of AET of the cloned ensemble can be skewed and will have an increased variance in comparison with runs without filtering. Figure 10.7 illustrates this for location C03 modelled with the SOMS – Data Poor Scenario. The AET frequency histogram shows a normal, Gaussian, distribution in the case of the SOMS – Data Poor error propagation scenario without filtering (figure 10.7a). When the small error PF scenario is used, the AET frequency histogram after filtering is non-Gaussian, resulting in an increased variance. This has also been described by

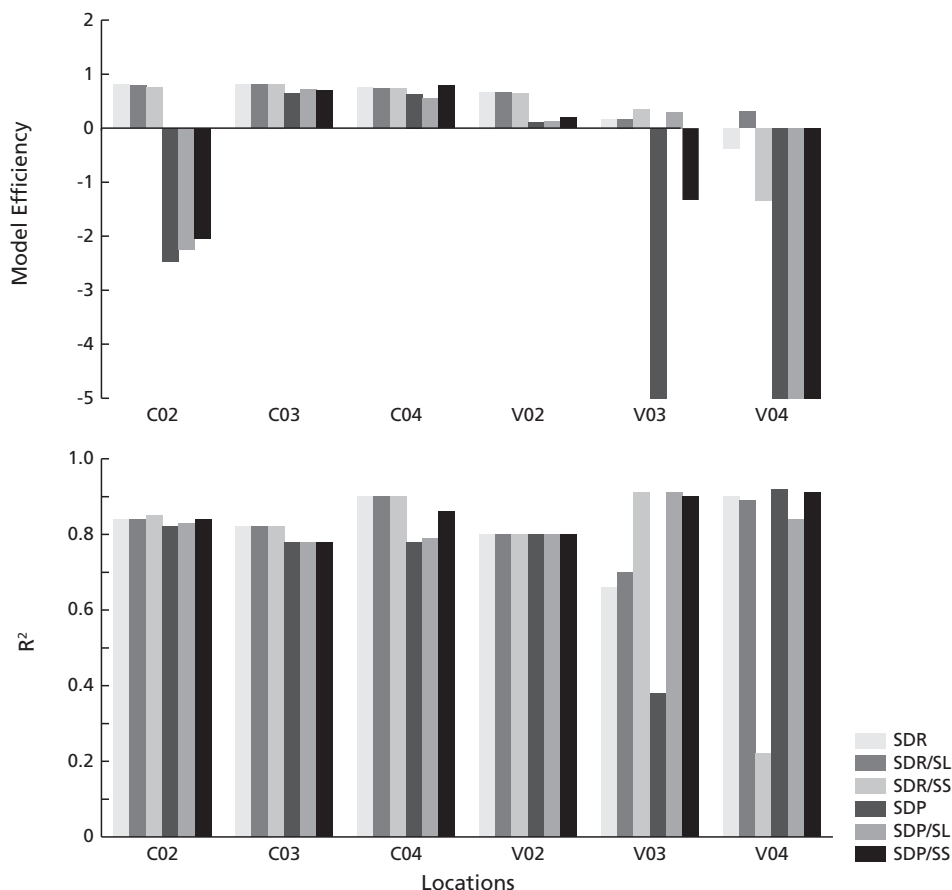
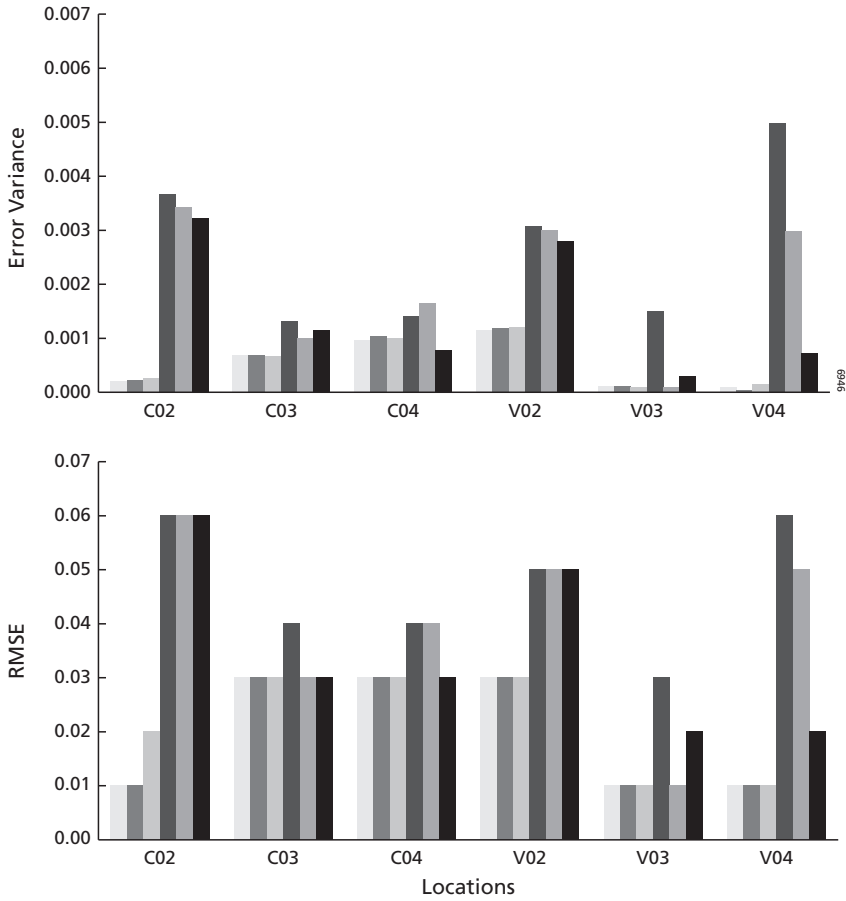


Figure 10.6 Goodness of fit of different model scenarios at the calibration sites C02, C03 and C04 and validation sites V02, V03 and V04. For C01 no field measurements were available during the modelled period. SDR = SOMS – Data Rich Error Propagation Scenario, SDP = SOMS – Data Poor Error Propagation Scenario, SL = filtering with the SEBS – Large Error Scenario filter data and SS = filtering with the SEBS – Small Error Scenario filter data.

Van Leeuwen (2003), who concludes that variance estimates of the posterior distribution is not always an appropriate measure to describe the accuracy for non-Gaussian distributed variables.

#### 10.4.2 Correlation between AET and VMC

During all filter moments, the average SEBS estimated AET is much higher than the SOMS predictions of average AET (figure 10.2). Filtering will therefore increase AET in the model. It was expected that this would cause a higher VMC after filtering. The results, however, show that in most cases the average VMC decreases after filtering, while only in some cases the average VMC increases (table 10.1). This means that the instantaneous AET and VMC, i.e. at one timestep over all realisations, have sometimes a positive and sometimes a negative correlation. The sign of the correlation (negative or positive) depends on which mechanism determines AET.



(Figure 10.6 continued)

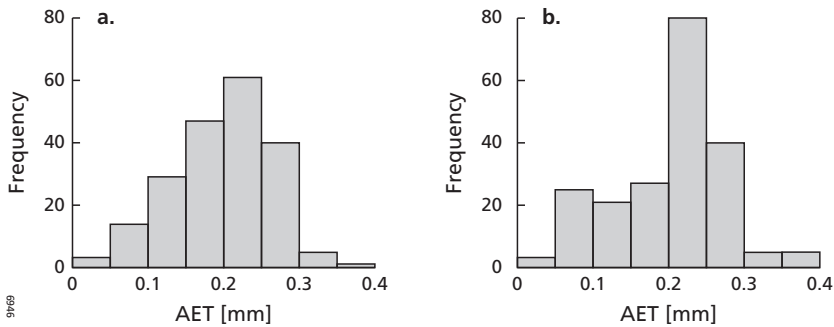


Figure 10.7 Effect of filtering on the frequency distribution of actual evapotranspiration at  $t = 445$ , one hour after the first filter moment. a) SOMS – Data Poor error propagation scenario without filtering,  $\sigma^2=4.3 \cdot 10^{-3}$ , b) SOMS – Data Poor Scenario with SEBS – Small Error filter data,  $\sigma^2=4.9 \cdot 10^{-3}$ .

In the case of a negative correlation between AET and VMC, an increase in AET causes a decrease in VMC. In this case AET is predominantly determined by other variables than AET. A higher AET causes drying of soils in this case. In the case of a positive correlation between AET and VMC, an increase in VMC causes an increase in AET. In this case AET is predominantly determined by VMC. When more VMC is available, more water can evapotranspire and AET will be higher in this case.

In the error propagation models of both the SOMs – Data Rich and SOMs – Data Poor scenarios, the uncertainty in meteorological parameters that determine potential

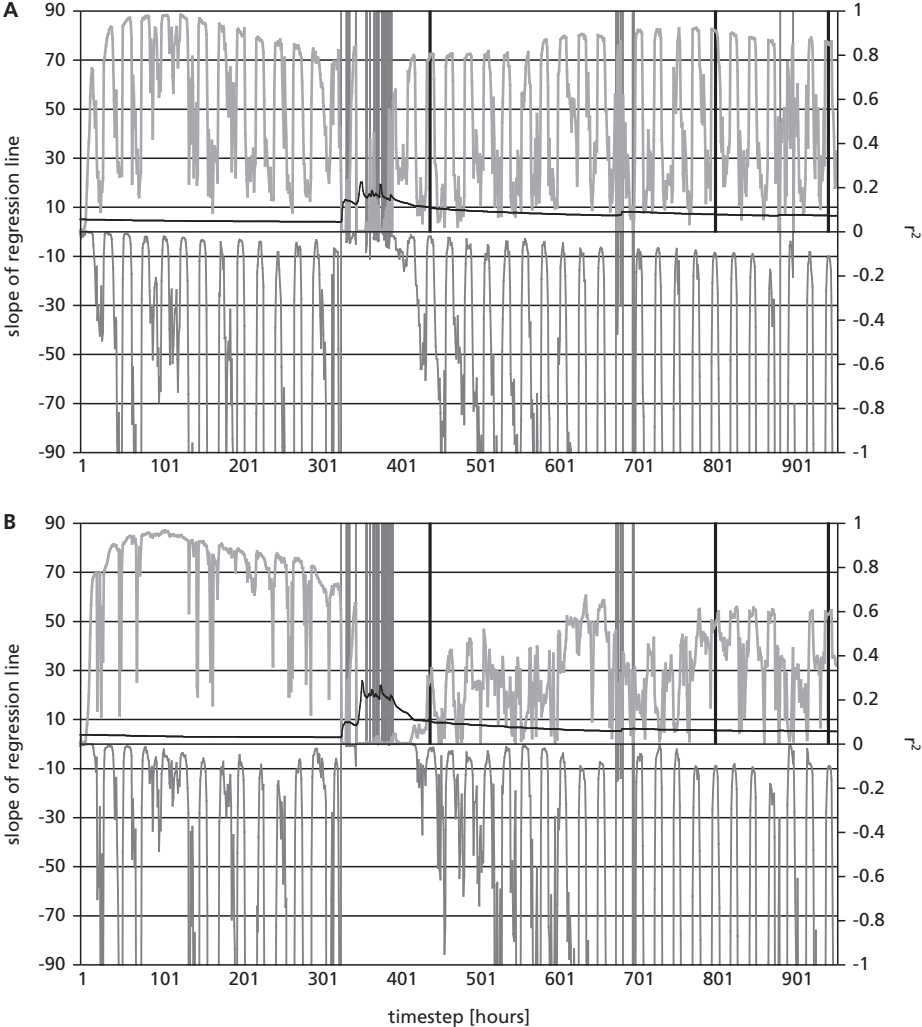
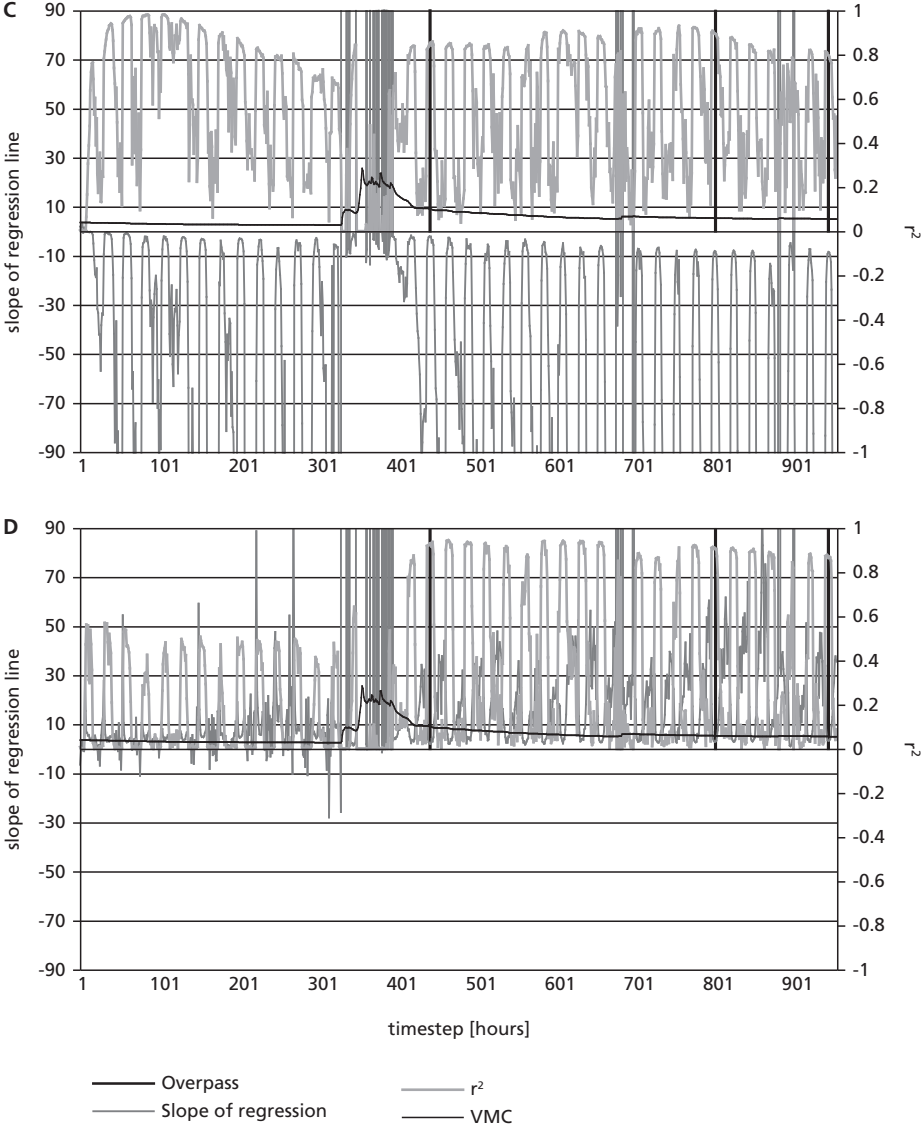


Figure 10.8 Regression analysis between VMC and AET at location CO2 for a) original Data Rich scenario, b) No meteo error scenario, c) No meteo and no pore space error scenario, d) Fixed  $\zeta$  scenario.

evapotranspiration (PET) in the SOMS model is much larger than the uncertainty in soil(moisture) parameters, which causes a larger uncertainty in the modelled PET than the modelled  $\beta$  evapotranspiration reduction factor (chapter 8, eq. 8.40). As a result, the correlation between AET and VMC is negative. As the AET derived from SEBS is greater than the AET derived from SOMS at filter moments, realisations with a higher PET are cloned more.

In order to confirm this explanation, three extra scenarios have been defined in which different errors in the error propagation model have been switched off in order to reduce the



6946

error in variables that determine AET, other than VMC, and analyse the effect on the correlation between AET and VMC:

1. No meteo error scenario: errors associated with the measurements at the meteorological station are assumed to be zero;
2. No meteo and no pore space error scenario: errors associated with the measurements at the meteorological station and errors in pore space ( $\theta_p$ ) are assumed to be zero;
3. Fixed  $\zeta$  scenario: same as No meteo no pore scenario, but with the  $\beta$  evapotranspiration reduction factor calculated by fixing  $\zeta$  in eq. 8.10 to  $\zeta = 7$ .  $\zeta$  has been chosen, because the

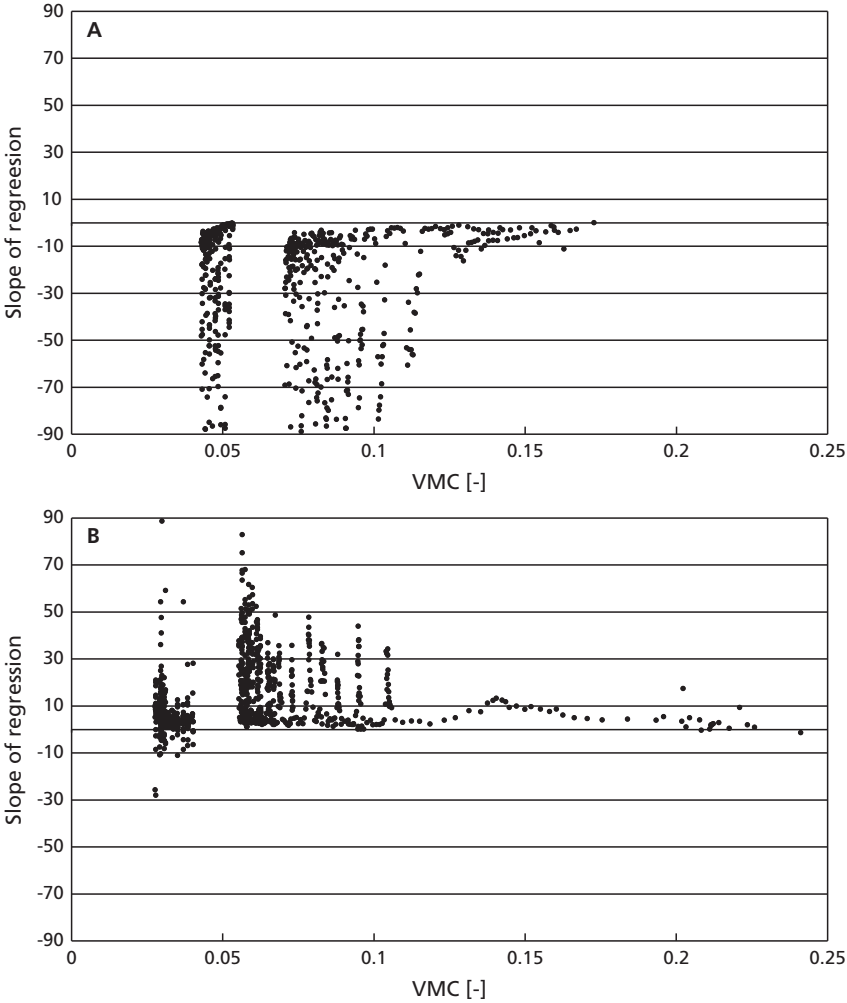


Figure 10.9 Scatterplot of VMC versus slope of the regression curve with AET for a) SOMS – Data Rich error propagation scenario and b) Fixed  $\zeta$  error propagation scenario. Each dot represents a model realisation at location C02.

model has been calibrated for this parameter, which is correlated with  $k_{sat}$ , and might have unrealistic values for the soils in the study area.

The other errors in the three scenarios are the same as in the SOMS – Data Rich error propagation scenario.

A regression analysis between AET and VMC calculated by the three new scenarios and the original Data Rich scenario has been done. It should be noted that a regression analysis assumes a normal distribution of the error terms, which is not the case for AET and VMC. The results (figure 10.8), however, are useful to investigate the effect of the different scenarios on the correlation between AET and VMC.

The scenarios have in common that the slope of the regression and the  $r^2$  follow a clear day-night rhythm. At night  $r^2$  is minimal indicating a bad correlation between AET and VMC. At noon, however,  $r^2$  can be high during clear days. During rainfall events the correlation is low and the slope switches to a positive correlation in all scenarios. All scenarios show a negative correlation between AET and VMC during clear days, except the fixed  $\zeta$  scenario. The negative correlation during clear days is caused by the relatively large errors in soil parameters compared

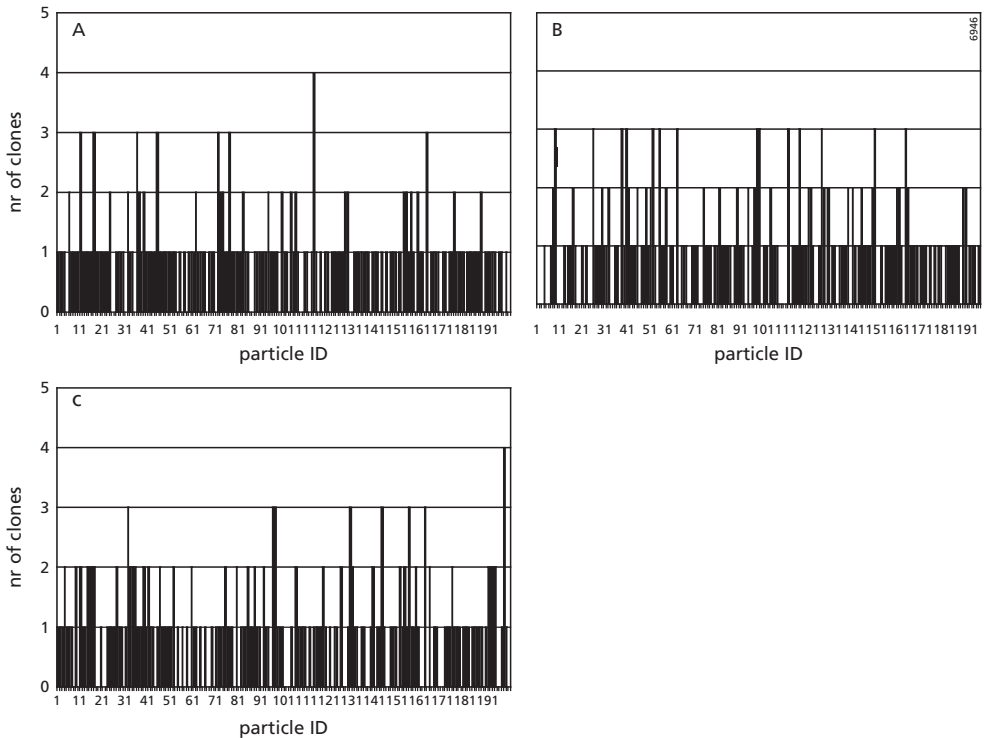


Figure 10.10 Distribution of the number of clones (y-axis) over the different realisations during the SOMS – Data Poor Scenario with the SEBS – Large Error filter data. a)  $t = 444$  (filter moment 1), b)  $t = 805$  (filter moment 2) and c)  $t = 948$  (filter moment 3). Not that the x-axis shows the particle ID, but this ID is re-assigned at each filter moment.

to the errors in meteorological parameters that determine PET. Therefore the ensemble members can predict low VMC values, while maintaining a large AET through uncertainties in soil parameters that determine the amount of AET ( $\zeta$ ,  $\theta_s$ ,  $\theta_r$ , etc.).

In the fixed  $\zeta$  scenario, the errors in the soil parameters are less important than the errors in the calculation of PET. In this case the VMC controls the AET, resulting in a positive correlation.

The scatterplots of figure 10.9 show the relation between the slope of the regression curve and VMC for the SOMS – Data Rich error propagation scenario (figure 10.9a) and the fixed  $\zeta$  error propagation scenario (figure 10.9b). It can be seen that both scenarios show a steep slope for  $VMC < 0.12$ , which is negative in the case of the Data Rich scenario and positive in the case of the fixed  $\zeta$  scenario. The small slope values observed in both scenarios for  $VMC > 0.12$  is caused by the rainfall events, when mean and variance of PET are very low.

The implication of this for particle filtering is that the direction of the state correction of VMC depends on the filter moment and can be either positive or negative, which has been observed in the results. The direction of the correlation is dependent on the model structure and the relative errors of the model input.

#### 10.4.3 Spatial variability of VMC after filtering

It was expected that the use of remote sensing derived filter data should add spatial variation within the strata defined in the inputs of the SOMS model. Not much increase in spatial variation of VMC within the strata, however, has been observed after filtering, compared to the SOMS results without filtering. This was the case for all filter scenarios. The reason is the low spatial variation of AET in the SEBS results for the two filter data scenarios, already shown in figure 9.11. In circumstances with more spatial contrast of SEBS predicted AET, e.g. the Barrax dataset (chapter 6 and 7), the filter algorithm will increase the spatial variation within the units of SOMS.

#### 10.4.4 Technical restrictions of the Particle Filter

The Particle Filter can only be applied successfully when the number of particles (ensemble size) is large enough for accurately estimating the posterior pdf. The choice of the ensemble size, however, is a trade-off between computing time, depending on computing power and model complexity, and statistical accuracy. In this application of the particle filter an ensemble size of 200 particles is used, because it keeps the computing time short enough to analyse different scenarios in reasonable time. It is however expected that with more particles the particle filter model gives better results.

A serious risk of a small particle size is the issue of ensemble collapse, discussed by Van Leeuwen (2003). In the case of ensemble collapse, the particle filter assigns a very high weight to only one particle in such a way that this is the only particle cloned and propagated. When the posterior density is determined of this new ensemble it will have a mean that is determined by the original particle and a variance close to zero. At the next filter moment the same problem arises. In this study ensemble collapse has not been observed. As an example figure 10.10 shows the distribution of the number of clones over the different realisations during the SOMS – Data Poor Scenario with the large error filter data. It can be seen that there are no dominant particles that can cause an ensemble collapse. This is also an indication that the particle filter does not improve the results of soil moisture prediction, because only a limited number of particles are

cloned, which means that the pdf before and after the filter moment does not change much and consequently the weight of each particle remains more or less constant.

A further technical restriction of the applied particle filter is the area averaging of the weight of the particles. Filtering will therefore be biased towards the largest area. Future research should investigate how to distribute the weights over all model pixels, while preserving short model calculation times.

## 10.5 Conclusions

It has been investigated here whether the use of a data assimilation algorithm can improve the predictions of top soil moisture in space and time, by providing a process-based model with the best estimate of a model state at the timestep when remote sensing data is available providing spatial data on soil moisture distribution.

In this chapter the Residual Resampling Particle Filter has been used to assimilate AET modelled by SEBS in the SOMS model for the spatio-temporal prediction of VMC in the Sehoul study area. Two scenarios of the stochastic SOMS model have been filtered by two scenarios of the stochastic SEBS model explained in chapter 9.

It can be concluded that in the majority of the analysed filter moments the variance of VMC is reduced after filtering. In few cases the variance has been reduced after all three filter moments. Concerning the goodness of fit of mean estimated VMC with field measurements, the SOMS – Data Rich filter scenarios do not show a significant improvement compared to the error propagation results. The SOMS – Data Poor Scenarios however show improvements at some locations, simply because the SOMS error propagation model performs much worse. This large uncertainty causes more overlap between the pdf of the filter data and the model.

Some important conclusions can be drawn from the analysis of the results from the applied PF:

1. The number and distribution of filter moments should be sufficient in order to frequently optimize the model.
2. The distance between the probability density function of the filter data and model prediction of the filter variable should not be too large. In this study, the probability density functions of the SEBS derived AET (both scenarios), were too different from the probability density functions of the SOMS derived AET.
3. The errors in variables and parameters should be well known. In this research we found that the direction of the correlation between VMC and AET depends on the dominance of the uncertainty in potential evapotranspiration (PET) or in the determination of soil moisture content. Most of the time the errors in soil parameters were much larger than the errors in meteorological parameters that determine PET, causing a negative correlation between VMC and AET. During rainfall events, however, the error in soil moisture parameters is relatively low and a positive correlation between VMC and AET exists. Because of this complex relation between the variable to be predicted (VMC) and the filter variable (AET), it would be easier to filter directly with VMC as filter variable, for example by using VMC derived from radar images. These data, however, are not available at the high resolution desired for agricultural areas of the scale of the Sehoul study area.

4. There should be a strong correlation between filter data (AET) and the objective variable (VMC). Filtering only has an effect when a strong correlation exists between filter data and the objective variable. This was the case at each of the filter moments used in this study.
5. The particle filter can both increase and decrease the variance of AET, because the distribution of AET can be non-Gaussian. This was observed in this study for several cases.
6. In this research the spatial variability of the SEBS filter data was too low to add much variability to the SOMS model. The study site consisted of a plateau with relatively homogeneous soils. This site was chosen for its simplicity for soil moisture modelling, but for the particle filter an area with more (natural) spatial variability would be more interesting. On the other hand, higher resolution satellite images can detect more spatial variation than MODIS images (see chapter 7).
7. In this study 200 particles have been used, because of limitations in computation time for all scenarios. Given the large number of uncertain input parameters for the SOMS model, the chances for finding particles with a good combination of input parameter values are small when only 200 particles are used. Furthermore, the estimation of variance is more accurate when using more particles.

Finally, it can be concluded that this PF approach does not significantly improve the spatio-temporal prediction of VMC in the present study, particularly for the SOMS – Data Rich scenario, but the technique may improve the estimation of VMC in space and time if the filter data show more spatial variability and a lower uncertainty, the pdf of the filter data is closer to the distribution of model data, the distribution of the filter variable is not so much skewed and there exists a strong correlation between the filter variable and the objective variable at each filter moment.

# 11 Conclusions

The earth's precious water sources are under pressure due to climate change and population pressure that increases the demands for drinking water and irrigation. Water availability is important for the world's food production, which is currently under threat. Too much water, however, can destroy fertile soils by erosion or flooding. The urgent need in the fields of earth sciences, meteorology, hydrology, agriculture and global change modelling for operational models that can accurately predict soil moisture patterns in space and time, has been explained in the introduction of this thesis. High spatial and temporal variability of soil moisture and its low degree of autocorrelation complicate the modelling using process-based models. Input data and parameters for these models are traditionally based on field measurements at point support and discontinuous, making it laborious and time consuming to get a spatio-temporal consistent dataset.

The aim of this research was to evaluate the performance of different methods that can be used for the estimation of top soil moisture patterns in space and time. Field measurements, process-based modelling and remote sensing based modelling have been evaluated. Additionally, a data assimilation approach that combines the advantages of each method for operational soil moisture modelling has been developed and evaluated. The predictions of top soil moisture (0-15 cm below the soil surface) have been done at a specific spatial resolution of 125 m and timesteps of 1 h, which is in accordance with processes related to agriculture in the study area.

The main research question was defined as:

*Top soil moisture patterns in space and time can be estimated using field methods, process-based models and remote sensing data. What is the performance, in terms of accuracy, resolution and coverage of operational spatio-temporal estimation of top soil moisture, of each method separately and a combined approach that uses a particle filter data assimilation algorithm?*

In order to answer this question, several sub-questions have been investigated in the different parts of this thesis. In this chapter the sub-questions will first be answered, followed by a discussion of the main research question.

## 11.1 Remote sensing data as input to process-based models

Part I investigated the following research question:

*Which spatial inputs for a process-based soil moisture model and a remote sensing based evapotranspiration model can be derived from remote sensing? Are these inputs available at a sufficient temporal and spatial resolution for the modelling of agricultural areas like the study sites?*

Figure 1.2 in chapter 1 shows the potential for the use of optical and thermal remote sensing in process-based soil moisture modelling. Furthermore, it indicates the use of remote sensing in the generation of Digital Elevation Models (DEMs). In part I, remote sensing techniques using optical and thermal remote sensing have been reviewed and a case study on DEM generation using photogrammetry techniques has been presented. The use of microwave remote sensing falls outside the scope of this thesis.

Optical remote sensing, using images in the visual, near infrared and shortwave infrared part of the electromagnetic spectrum, is a suitable tool to acquire vegetation properties such as vegetation cover, Leaf Area Index (LAI), aboveground biomass and structure, especially through spectral indices like the Normalized Difference Vegetation Index (NDVI). Vegetation indices, however, give only qualitative information. Empirical equations make it possible to derive maps of, for example, albedo and emissivity from the optical channels of a remote sensing image. Thematic classification of optical channels of remote sensing images results in raster-based land cover maps. In combination with lookup tables, these maps can provide spatial inputs for distributed hydrological models, like the SOMS model developed in chapter 8 of this thesis.

It is not feasible to directly derive soil moisture maps from optical remote sensing, because the signal received by the sensor is only representative for the upper few millimetres of the earth's surface. In addition, the received reflection is not only a function of soil moisture, but also a function of soil composition and soil physical properties. Vegetation and the atmosphere further distort the soil moisture signal.

Combined with thermal remote sensing, optical remote sensing can be more efficiently used to derive soil moisture patterns. Thermal remote sensing provides data on the surface radiance temperature, which can be converted to surface kinetic temperatures with emissivity derived from optical remote sensing. The spatial variation of surface temperature is highly correlated with soil moisture variability for bare soils. Soil moisture patterns for (partially) vegetated areas can be derived by using the negative correlation that exists between radiometric surface temperature and a spectral vegetation index, like NDVI. Although the results are promising, the methods are sensitive to atmospheric conditions and the empirical formulations should be calibrated for different seasons or crop growing stages, different land cover types, topography and meteorological conditions in order to get accurate absolute estimations of soil moisture content.

An alternative is to use albedo and NDVI from optical sensors in combination with data from thermal sensors as important inputs for surface energy balance models, like the Surface Energy Balance System (SEBS) model used in this thesis. Surface energy balance models estimate the evapotranspiration, which can be used in the prediction of soil moisture.

Digital Elevation Models (DEMs) can be derived at different resolutions from stereo aerial photos, stereo satellite images, laser altimetry (LIDAR) and radar interferometry. The accuracies from these sources differ and land cover is an important disturbing factor in the extraction of digital terrain models (DTMs) (see chapter 3). DTMs are important for the calculation of drainage networks, volume of surface runoff, surface ponding, assessment of incoming solar radiation, computation of wetness indices and many other important hydrology-related terrain variables.

The usefulness of remote sensing derived data for soil moisture modelling depends on the spatial resolution, temporal resolution and accuracy of the data required in the model.

Vegetation properties are calculated from the visual and near infrared channels of a remote sensing image, which have higher resolutions than the thermal channels used for energy balance

Table 11.1 Resolutions of different applications of remote sensing sensors. Units in meters. The resolutions are typical values.

Sensor	Vegetation parameters	Energy Balance Parameters	Digital Elevation Models
Aerial photographs	< 1	< 1	5-10
QuickBird	2.44	-	10
IKONOS	4	-	10
ASTER	15	90	30
SPOT (1-4,5)	10, 20	-	20
Landsat TM (5,7)	30	120, 60	-
MODIS	250	1000	-
SRTM	-	-	30, 90

calculations. Sensors that measure both optical and thermal channels at the same moment, make it possible to develop upscaling algorithms. An example is the DisTrad algorithm that derives sub-pixel temperatures by correlating radiometric surface temperature with NDVI (see chapter 7). Also, the resolution of DEMs depends much on the sensor used. Table 11.1 shows typical values of resolution for different applications of remote sensing platforms.

The temporal resolution also depends much on the sensor used. Generally, the higher the resolution required, the larger the repeat cycle of the sensor and the lower the spatial coverage. Acquisitions from aerial photographs, IKONOS and QuickBird do not have a global coverage with repeat cycles, but are completely on-demand. The ASTER sensor has a repeat cycle of 16 days, but acquisitions are scheduled using a data acquisition request (DAR). The chance that an image will be acquired, depends on the priorities of the ASTER science team, based on the available capacities and urgency of acquisition. Furthermore, acquisition does not take place when the predicted cloud cover exceeds a threshold. Landsat TM 5 has a more continuous acquisition schedule with a repeat cycle of 16 days. MODIS acquires data every one or two days. The usefulness, however, depends on the cloud cover. Table 1.1 in chapter 1 of this thesis showed the low success rates for the availability of useful MODIS or ASTER images.

Accuracies also depend on the sensor used. For energy balance applications, the temperature product of ASTER has an accuracy of 1.5 K and MODIS 1 K. The accuracies (RMSE) of height values of DEMs derived from aerial photographs, ASTER and SRTM are respectively: 18, 33 and 7 m (chapter 3).

It can be concluded that remote sensing is a suitable tool, and often the only available source, for deriving spatial inputs for process-based soil moisture models and remote sensing based evapotranspiration models, although it has a number of constraints.

## 11.2 Evapotranspiration modelling using remote sensing

The second part of this thesis investigated the use of remote sensing in modelling the actual evapotranspiration (AET), which can be used in soil moisture modelling. Chapter 4 explained the theory of the surface energy balance. The surface energy balance equation describes that the surface net radiation is the balance among all incoming and outgoing radiation. This energy is mainly distributed by three major fluxes: the soil heat flux, the sensible heat flux and the latent

heat flux. The soil heat flux is the energy flux used to heat the soil. The sensible heat flux is used to heat the atmosphere and the latent heat flux is used for the evaporation of water.

Many different types of surface energy balance models have been developed in order to estimate the fluxes in the surface energy balance equation. In this thesis the Surface Energy Balance System (SEBS) has been used. SEBS is a single source model, which estimates energy fluxes and actual evapotranspiration at scales ranging from agricultural plots and small catchments to continents.

*How can SEBS, the model selected for derivation of evapotranspiration from remote sensing, derive fluxes from satellite data and how accurate is this for different land cover types?*

The SEBS algorithm used in this thesis has been implemented with the PCRaster Python Library. The model consists of three modules: (1) Derivation of energy balance terms; (2) Submodel to derive roughness length for heat transfer; (3) Submodel to derive stability parameters. Using these three modules, the energy balance for limiting cases (i.e. completely wet or dry pixels) can be resolved. Consequently, the energy balance terms and evapotranspiration flux can be derived for all pixels. This model setup requires three sets of input data: (1) Data derived from remote sensing: albedo, emissivity, temperature and NDVI to derive local roughness parameters; (2) Meteorological parameters collected at a reference site: air pressure, air temperature, relative humidity and wind speed; (3) Radiation data: downward shortwave and longwave radiation.

Chapter 6 evaluated the results of the SEBS model used with ASTER imagery at the SPARC 2004 experimental field site in Barrax (Spain). The sensible heat flux is the most uncertain variable in the modelling of the surface fluxes and its accuracy has therefore been evaluated. SEBS results for sensible heat flux have been compared with field measurements of fluxes during the field campaign. In chapter 6 it has been concluded that SEBS is capable of estimating the sensible heat flux in the same order of magnitude as the field methods. Also the errors of SEBS and field measurements have the same order of magnitude. Both SEBS and field measurements give different results for well irrigated pivots and the other land cover types. The difference in sensible heat flux for an irrigated pivot and dry agriculture as measured and modelled can range from about 100 to 250 W m<sup>-2</sup> in the Barrax study area.

Field measurements, however, have a support that is limited to their footprints, while SEBS estimates fluxes for an entire satellite image, e.g. 3600 km<sup>2</sup> for ASTER. The shape and extent of the footprint of a flux measurement depends on the type of measurement, wind speed, wind direction and surface roughness. For evaluation of SEBS results with field measurements, a footprint weighted average of the pixels within a footprint should be compared with the measured value. At the 90 m resolution of ASTER, however, pixels can be partly within and outside the footprint. This causes a mix of aerodynamic properties that is different from the properties within a footprint. This is especially the case when modelling an area with pivot irrigation, which causes mixed pixels at the sharp edges of the pivots. The results suggest that the use of images with a higher resolution than ASTER can reduce the edge effects in accordance with the footprint of field measurements. The difficult modelling of aerodynamic properties causes differences in accuracy for different land covers.

When remote sensing based surface roughness parameters are replaced by field measurements and literature values, through lookup tables and a land cover map, the results for SEBS only

improve for homogeneous footprints. When footprints have mixed land covers, the results can even be worse, because sharp borders are created by the generalized land use map. A better correspondence between the SEBS results and the field flux measurements can be achieved by both increasing the resolution of the satellite image and the placement of measurements adequately for the resolution of SEBS, taking into account the location of the footprint of the measurements, which should not include sharp borders. Furthermore, SEBS can be improved by incorporating the effect of wind direction on surface roughness for momentum transport, which prevents bias from edge effects and varying roughness for row crops.

Another question answered in Part II is:

*Can we derive the inputs for SEBS from different satellite data, in order to include remote sensing based evapotranspiration in operational models?*

Chapter 5 describes the procedures of preprocessing to derive surface temperature, broadband surface albedo, emissivity, global radiation, NDVI and vegetation cover from Landsat TM5, ASTER and MODIS. It is possible to derive these input data for these images with algorithms found in literature and products available from NASA's Land Processes Distributed Active Archive Center (LPDAAC). The availability of data products reduces the time needed for preprocessing and makes these sensors useful for operational models. When the latent heat flux calculated with SEBS for the Sehoul study area are compared for the different sensors, it can be concluded that ASTER and Landsat TM5 are of sufficient high resolution to show patterns caused by irrigated agricultural areas, differences in land cover, wet valleys and differences in exposition of slopes. The results for MODIS, however, show only large scale patterns. Furthermore, missing values, resulting from invalid temperatures filtered out of the MOD11 data product, further confuses the results.

Emissivity, which is an important input in SEBS, is an earth surface property that is correlated with surface temperature and surface properties. Therefore it is difficult to directly derive emissivity from remote sensing images. The difference between emissivity estimated by a field method and using a remote sensing based algorithm has been investigated in chapter 5. Remote sensing derived emissivity is preferred, because field measurements of emissivity have a standard deviation of about 0.02, which is larger than the differences between the images (chapter 5, table 5.4) and field measurements are difficult to upscale to pixel sizes or land covers. The large amount of measurements required for using geostatistical interpolation techniques makes it laborious.

The last question answered in Part II is:

*Can we improve the spatial resolution of daily remote sensing images in order to provide data for an operational model at an appropriate scale?*

ASTER has a repeat cycle of 16 days, while MODIS provides daily images. However, the resolution of MODIS is problematic for modelling the surface energy balance of agricultural fields in areas like the Barrax field site and the Sehoul study area. In chapter 7 the DisTrad algorithm has been evaluated for the improvement of the resolution of MODIS and ASTER thermal images acquired at the same moment. From this evaluation it can be concluded that the

results for MODIS and ASTER differ significantly for both temperature and modelled sensible heat flux. In the case of MODIS the differences between irrigated and non-irrigated areas are enhanced by adding detail through application of the DisTrad algorithm, while in the case of ASTER edges of agricultural fields are enhanced. DisTrad does not significantly improve the detail in ASTER images. DisTrad results of MODIS show only a slight increase of detail in the estimation of sensible heat flux. Although the improvements for the Barrax study area are not very large, the results suggest that in areas with larger agricultural plots and less contrast between irrigated and non-irrigated areas, sub-pixel radiometric surface temperature estimates from MODIS at 250 m resolution can bridge the scale difference between daily available MODIS 1000 m resolution images and infrequent ASTER images at 90 m resolution. This approach should be evaluated in further research. Because ASTER images were not available, sub-pixel temperatures from MODIS were used in chapter 10 for the integration of SEBS derived evapotranspiration in the SOMS model for the Sehouli study area.

### 11.3 Soil moisture prediction using process-based models

*How accurate can a deterministic process-based soil moisture model predict patterns of top soil moisture in space and time, compared to field measurements of soil moisture?*

In Part III, chapter 8, the process-based Soil Moisture System (SOMS) model has been developed and calibrated and evaluated using field measurements from the Sehouli study area. The model has been specifically developed for the integration of a remote sensing based surface energy balance model at the scale of an agricultural community. The SOMS model estimates the hourly evolution of top soil moisture patterns for agricultural and semi-natural areas after rainfall events. After automatic calibration using PEST, estimates of top soil moisture in agricultural areas agree well with independent validation measurements. The calibrated saturated hydraulic conductivity ( $k_{sat}$ ) values are unfortunately unrealistic high. These high values probably result from the correlation between  $k_{sat}$  and the soil water retention curve parameter ( $\zeta$ ), leading to several combinations of parameters (equifinality) that minimize the objective function in PEST. The calibration factor  $\zeta$  is realistic for the soil texture classes found in the study area, but low soil moisture contents lead to too small percolation fluxes. This is compensated by PEST by choosing  $k_{sat}$  values that are extreme, but still give a percolation flux that can influence the moisture dynamics in the model and give the best simulation results.

Spatially, the model results show the sharp edges defined by the land cover and soil maps, which have been used to distribute the input variables and parameters. The model assumes no spatial variability of parameters within the combinations of soil and land cover and sharp boundaries between the units. Although the soils in the Sehouli study area are quite homogeneous, this assumption is unrealistic. It has been hypothesised in chapter 8 that the integration of remote sensing data could add spatial variability within the units.

### 11.4 Uncertainty analysis of SEBS and SOMS

Two other questions have been answered in part IV, chapter 9:

*What is the accuracy of SEBS predictions of actual evapotranspiration and what are the most important sources of uncertainty?*

*What is the uncertainty of the predictions of top soil moisture and actual evapotranspiration of the process-based soil moisture model when taking into account all errors in input variables and parameters, and what are the most important sources of uncertainty?*

In Part IV chapter 9 the uncertainty of actual evapotranspiration (AET) predictions of SEBS have been estimated for two error propagation scenarios. The SEBS – Large Error Scenario assumes that the measurement and upscaling of radiometric surface temperature induces a large error compared to other error sources, based on the results of Part II. The standard deviation of AET estimates in this scenario is  $0.02 \text{ cm hour}^{-1}$ . The SEBS – Small Error Scenario assumes that only a small measurement error in surface radiometric temperature causes errors in SEBS estimates. This results in AET estimates with an average standard deviation of  $0.004 \text{ cm hour}^{-1}$ .

In chapter 9 also the uncertainty in volumetric soil moisture content (VMC) and AET of SOMS predictions are estimated with two error propagation scenarios. The SOMS – Data Rich Scenario, in which all errors in field measurements, maps and satellite data are modelled, shows an average RMSE of  $0.02 \text{ m m}^{-1}$  compared to field measurements of VMC. The results also show that uncertainty in VMC modelled with this scenario are in the same order of magnitude as the uncertainty of field TDR measurements, averaged for an agricultural parcel. The level of uncertainty of this scenario of the SOMS model can be acceptable for many applications. The SOMS – Data Rich Scenario is well capable of accurately estimating soil moisture conditions after rainfall events. It can be used, for example, to predict the start of the growing season for crops in semi-arid areas. In these areas the start of the growing season coincides with the first rainfall event that provides sufficient soil moisture for the seeds to germinate. Shortly after the first rainfall event, however, the model underestimates the VMC, but the field measurements also show a large uncertainty at these timesteps. The goodness of fit values are comparable with the deterministic model results, indicating that there are no large non-linear responses in the error propagation model. The average standard deviation in estimated AET is  $0.0006 \text{ cm hour}^{-1}$ .

The SOMS – Data Poor Scenario, which assumes that the only data is available from remote sensing, land use and soil maps and a meteorological station, shows an average RMSE of  $0.05 \text{ m m}^{-1}$  for the predicted VMC, compared to field measurements. With this scenario SOMS also predicts the trends well when compared to field measurements, with an average  $r^2$  of 0.75. The goodness of fit measures give worse results compared to the SOMS – Data Rich Scenario. Although the uncertainty bands are much wider, most field measurements fall within one standard deviation from the predicted average VMC. Compared to the SOMS – Data Rich Scenario the standard deviation is about seven times higher in the SOMS – Data Poor Scenario. The average standard deviation in estimated AET is  $0.004 \text{ cm hour}^{-1}$ . This scenario can be used when field data on soil moisture and soil physical data is lacking as is the case in many data poor areas in the world. This scenario is able to predict patterns and trends, although the absolute accuracy is lower than for the SOMS – Data Rich Scenario.

The most important sources of uncertainty in SOMS are the spatial distribution and amount of precipitation and evapotranspiration, which depend on the meteorological measurements of only one meteorological station.

The AET distributions predicted by the scenarios are very different. The SEBS scenarios give a much higher mean AET than the SOMS scenarios. Also spatially the results differ. The SEBS scenarios of AET prediction show much less correlation with land cover or soil type than the AET estimations of the SOMS scenarios that use a stratification in land cover/soil type combinations with only short range spatial variation inside the strata. With SEBS only the Forest of Mamora can clearly be recognized. The cause of the large difference between SEBS and SOMS estimated AET remains unclear, but is probably related to the resolution of the SEBS estimates. Because field measurements of AET do not exist for the study area, AET results could not be validated. The large difference between SOMS and SEBS, combined with the low contrast in the SEBS results, can have a negative impact on the performance of the particle filter data assimilation algorithm.

### **11.5 Integrating remote sensing derived AET in a soil moisture model by means of a particle filter**

In chapter 10 a residual resampling particle filter data assimilation algorithm has been implemented in order to integrate AET modelled by the SEBS error propagation scenarios with the SOMS error propagation scenarios. The following questions were addressed in the analysis of the different data assimilation scenarios:

*Can the particle filter data assimilation of remote sensing based predictions of actual evapotranspiration in a process-based model improve the prediction of soil moisture patterns in space and time compared to methods that use field measurements, process-based models and remote sensing separately?*

*What are the requirements for successful application of a particle filter for the prediction of top soil moisture patterns?*

From chapter 10 it can be concluded that in most cases (67 %) filtering with the particle filter reduces the variance of VMC estimated by the SOMS model, using SEBS filter data. In a small number of cases the variance has been reduced after each of the three filter moments. In all these cases the reduction is small. When comparing the mean estimated VMC with field measurements, the SOMS – Data Rich scenario does not show significant improvement for both SEBS filter data scenarios, compared to the error propagation results without filtering. The SOMS – Data Poor scenarios, however, show improvements at some locations. The large uncertainty in the SOMS – Data Poor error propagation scenario causes more overlap between the probability density functions of the SOMS model and the SEBS derived filter data.

The success of the particle filter depends on a number of factors:

1. The number and distribution of filter moments should be sufficient in order to frequently optimize the model.
2. The distance between the probability density function of the filter data and model prediction of the filter variable should not be too large. In this study, the probability density functions of the SEBS derived AET (both scenarios), were too different from the probability density functions of the SOMS derived AET.

3. The errors in variables and parameters should be well known. In this research we found that the direction of the correlation between VMC and AET depends on the dominance of the uncertainty in potential evapotranspiration (PET) or in the determination of soil moisture content. Most of the time the errors in soil parameters were much larger than the errors in meteorological parameters that determine PET, causing a negative correlation between VMC and AET. During rainfall events, however, the error in soil moisture parameters is relatively low and a positive correlation between VMC and AET exists. Because of this complex relation between the variable to be predicted (VMC) and the filter variable (AET), it would be easier to filter directly with VMC as filter variable, for example by using VMC derived from radar images. These data, however, are not available at the high resolution desired for agricultural areas of the scale of the Sehoul study area.
4. Strength of the correlation between filter data (AET) and the objective variable (VMC). Filtering only has an effect when a strong correlation exists between filter data and the objective variable. This was the case at each of the filter moments used in this study.
5. The distribution of the filter data. The particle filter can both increase or decrease the variance of AET, because the distribution of AET can be non-Gaussian. This was observed in this study for several cases.
6. Spatial variability of the filter data. In this research the spatial variability of the SEBS filter data was too low to add much variability to the SOMS model. The study site consisted of a plateau with relatively homogeneous soils. This site was chosen for its simplicity for soil moisture modelling, but for the particle filter an area with more (natural) spatial variability would be more interesting. On the other hand, the Barrax test site would have been too variable. An intermediate study area can give the best results. On the other hand, higher resolution satellite images can detect more spatial variation than MODIS images (see chapter 7).
7. The number of particles is low. In this study 200 particles have been used, because of limitations in computation time for all scenarios. Given the large number of uncertain input parameters for the SOMS model, the chances for finding particles with a good combination of input parameter values are small when only 200 particles are used. Furthermore, the estimation of variance is more accurate when using more particles.

## 11.6 Main research question

*Top soil moisture patterns in space and time can be estimated using field methods, process-based models and remote sensing data. What is the performance, in terms of accuracy, resolution and coverage of operational spatio-temporal estimation of top soil moisture, of each method separately and a combined approach that uses a particle filter data assimilation algorithm?*

Table 11.2 summarizes the answer of the main research question. Field measurements of top soil moisture have been done using a TDR. The instrument has an error of  $0.03 \text{ m m}^{-1}$ . The measurements for a field of 1 ha show standard deviations of less than  $0.03 \text{ m m}^{-1}$ . During and shortly after rainfall events the standard deviations are higher. Although the uncertainty of field measurements is relatively low, the lateral support of the TDR measurements is also low,  $0.002 \text{ m}^2$ , requiring many measurements for a good coverage in space and time. The vertical coverage

of the field measurements is low, typically between 0 and 15 cm. The choice to make more measurements within the soil profile is often a trade-off with the choice to increase the lateral coverage, depending on the number of instruments. The temporal coverage can be increased by using data loggers.

Process-based models have a lateral support that depends on their resolution. In the case of the SOMS model the lateral support is 15625 m<sup>2</sup> (125 m gridcells). The model calculates VMC in a soil profile of 90 cm with timesteps of 1 hour for each gridcell in an area of 50 km<sup>2</sup>. This gives this method a good lateral, vertical and temporal coverage. The uncertainty depends on the location in the modelled area, because the model has been calibrated for a limited number of locations. The only source of spatial variation introduced in the process-based model is the stratification in soil type and land use class combinations. Modelled VMC, however, showed a good goodness of fit compared to independent measurements at other locations than the measurements used for calibration.

When optical and/or thermal remote sensing images are used for the estimation of soil moisture patterns, the uncertainty of the absolute soil moisture content values depends on the calibration of the empirical, and often non-linear, relationships between surface temperature, vegetation indices and soil moisture content. The calibration is needed to compensate for differences in atmospheric conditions, vegetation cover, land cover type, topography and meteorological variables. Qualitatively, soil moisture patterns in space, i.e. contrast in soil moisture content, can be well estimated for large areas, because the spatial coverage of these images is large. The lateral support of the images depends on the resolution of the sensor (table 11.1). The vertical coverage is low, because reflection and emission are only received from the upper few millimetres of the soil. The temporal coverage is low for high and medium resolution imagery (> 16 days) and high for coarse resolution images (< daily), making remote sensing methods difficult to apply for operational monitoring soil moisture patterns at the scale of an agricultural community, e.g. the Sehoul and Barrax study areas, after rainfall events. The lateral support of coarse resolution temperature images can be increased by using an upscaling algorithm, like DisTrad (chapter 7). These methods will increase the resolution, but also the uncertainty in the temperature estimation.

The aim of the integrated approach was to combine the good lateral coverage and support of remote sensing data with the vertical and temporal coverage of a process-based model. In the integrated approach, AET derived from remote sensing using SEBS has been assimilated in the SOMS model by means of a particle filter. In most cases the particle filter reduces the uncertainty in estimated VMC, although the reduction is small. The lateral support and coverage of the particle filter model has been chosen to be the same as the for the SOMS model. The

*Table 11.2* Performance of different methods for the estimation of soil moisture patterns in space and time, in terms of uncertainty, resolution and coverage.

	Field data	Process-based model	Remote sensing	Particle Filter
Uncertainty	-	-	+	-
Lateral support	-	+	++	++
Coverage				
Time	-	++	-	++
Lateral	+	+	++	++
Vertical	-	++	-	++

assimilation of remote sensing derived AET did not add much spatial variability to the VMC predictions, because the spatial variability in AET was low.

It can be concluded that the use of a particular method depends on the specific demands of the application in terms of support and coverage, and required accuracy of the estimates. Field measurements are well applicable in studies of in-situ top soil moisture estimation at the scale of individual plots. For the prediction of soil moisture at specific locations in an agricultural area, a calibrated process-based soil moisture model gives the best results. For applications demanding spatially distributed, operational, soil moisture predictions, the assimilation of all available data, either remote sensing data or field measurements, in a process-based model can benefit from the advantages of each method separately. In this case, the particle filter algorithm used in this study, can give good results when the requirements mentioned in the previous section are met. Further research is needed to confirm this.

The availability of field measurements of soil moisture and high resolution, cloudless, remote sensing images with a good temporal coverage remains a problem. Research should focus on the optimal use of the various datasets and satellite images available at various spatial and temporal resolutions in order to provide operational models for the many environmental problems that we are facing. New data assimilation algorithms can play an important role in this research.



# References

- Abbott, M.B., J.C. Bathurst, J.A. Cunge, P.E. O'Connell & J. Rasmussen (1986). An introduction to the European Hydrological System – système hydrologique européen, "SHE", 1. History and philosophy of a physically-based, distributed modelling system. *Journal of Hydrology* 87, pp. 45-59.
- Abrams, M., S.J. Hook & B. Ramachandran (2002). ASTER user handbook. Pasadena: Jet Propulsion Laboratory.
- Agam, N., W.P. Kustas, M.C. Anderson, F. Li & C.M.U. Neale (2007). A vegetation index based technique for spatial sharpening of thermal imagery. *Remote Sensing of Environment* 107, pp. 545-558.
- Al-Rousan, N. & G. Petrie (1998). System calibration, geometric accuracy testing and validation of DEM and orthoimage data extracted from SPOT stereopairs using commercially available image processing systems. *International Archives of Photogrammetry and Remote Sensing* 34, pp. 8-15.
- Allen, R.G., L.S. Pereira, D. Raes & M. Smith (1998). Crop evapotranspiration – guidelines for computing crop water requirements -. FAO Irrigation and drainage paper 56.
- Altmaier, A. & C. Kany (2002). Digital surface model generation from CORONA satellite images. *ISPRS Journal of Photogrammetry and Remote Sensing* 56, pp. 221-235.
- Andersen, J., I. Sandholt, K.H. Jensen, J.C. Refsgaard & H. Gupta (2002). Perspectives in using a remotely sensed dryness index in distributed hydrological models at the river-basin scale. *Hydrological Processes* 16, pp. 2973-2987.
- Anderson, G.P., A. Berk, P.K. Acharya, M.W. Matthew, L.S. Bernstein, J.J.H. Chetwynd, H. Dothe, S.M. Adler-Golden, A.J. Ratkowski, G.W. Felde, J.A. Gardner, M.L. Hoke, S.C. Richtsmeier, B. Pukall, J.B. Mello & L.S. Jeong (1999). MODTRAN4: Radiative transfer modeling for remote sensing. *Proceedings of the Optics in Atmospheric Propagation and Adaptive Systems III*, Florence, Italy.
- Anselin, L., R.F. Dodson & S. Hudak (1994). Linking GIS and spatial data analysis in practice. *Geographical Systems* 1, pp. 3-23.
- Antari, M. (2007). Mesure de l'érosion et du ruissellement dans le micro-bassin versant Matlaq et essai de modélisation (région de Rabat, Maroc). Rabat, Ph.D. thesis Université Mohammed V – Agdal.
- Asrar, G. (1989). *Theory and applications of optical remote sensing*. New York: John Wiley & Sons.
- ASTER (2008). Advanced Spaceborne Thermal Emission and Reflection radiometer. [08/12/2008] <http://asterweb.jpl.nasa.gov>.
- Baltsavias, E.P. (1996). Digital ortho-images – a powerful tool for the extraction of spatial- and geo-information. *ISPRS Journal of Photogrammetry and Remote Sensing* 51, pp. 63-77.
- Barnsley, M.J. & S.L. Barr (1996). Inferring urban land use from satellite sensor images using kernel-based analysis and classification. *Photogrammetric Engineering and Remote Sensing* 62, pp. 949-958.
- Basara, J.B. & K.C. Crawford (2002). Linear relationships between root-zone soil moisture and atmospheric processes in the planetary boundary layer. *Journal of Geophysical Research* 107, pp. 4274.
- Bastiaanssen, W.G.M. (1995). Regionalization of surface flux densities and moisture indicators in composite terrain – a remote sensing approach under clear skies in Mediterranean climates. Wageningen, Ph.D. thesis Landbouwniversiteit Wageningen.
- Bastiaanssen, W.G.M. (1998). A remote sensing surface energy balance algorithm for land (SEBAL): 2. Validation. *Journal of Hydrology* pp. 213-229.

- Becker, F. & Z.L. Li (1990). Towards a local split window method over land surfaces. *International Journal of Remote Sensing* 11, pp. 369-393.
- Beckett, P.H.T. & R. Webster (1971). Soil variability: A review. *Soils and Fertilizers* 34, pp. 1-15.
- Beecham, R. (1995). Patterns of spatial and temporal variability of factors affecting nutrient export from chaffey dam catchment. *Proceedings of the Proceedings of MODSIM 95 International Congress in Modelling and Simulation*, Newcastle.
- Beljaars, A.C.M. & A.A.M. Holtslag (1991). The parameterization of surface fluxes in large scale models under free convection. *Quarterly Journal of the Royal Meteorological Society* 12, pp. 255-270.
- Belmans, C., J.G. Wesseling & R.A. Feddes (1983). Simulation model of the water balance of a cropped soil: SWATRE. *Journal of Hydrology* 63, pp. 271-286.
- Betts, A.K., J.H. Ball, A.C.M. Baljaars, M.J. Miller & P. Viterbo (1994). Coupling between land-surface, boundary-layer parameterizations and rainfall on local and regional scales: Lessons from the wet summer of 1993. *Proceedings of the Fifth Conference on Global Change Studies: American Meteor. Soc., Nashville*.
- Beven, K. (1989). Changing ideas in hydrology – the case of physically-based models. *Journal of Hydrology* 105, pp. 157-172.
- Beven, K. & A. Binley (1992). The future of distributed models: Model calibration and uncertainty prediction. *Hydrological Processes* 6, pp. 279-298.
- Beven, K.J. (2002). Parameter estimation and predictive uncertainty. In: Beven, K.J. (Ed.) *Rainfall-runoff modelling the primer* pp. 217-233. Chichester: Wiley.
- Bierkens, M.F.P., P.A. Finke & P. de Willigen (2000). *Upscaling and downscaling methods for environmental research*. Dordrecht: Kluwer Academic Publishers.
- Blaschke, T., C. Burnett & A. Pekkarinen (2004). Image segmentation methods for object-based analysis and classification. In: De Jong, S.M. & F.D. van der Meer (Eds.) *Remote sensing analysis: Including the spatial domain*. pp. 211-236. Dordrecht: Kluwer academics. 5.
- Blöschl, G. & M. Sivapalan (1995). Scale issues in hydrological modelling: A review. *Hydrological Processes* 9, pp. 251-290.
- Boegh, E., M. Thorsen, M.B. Butts, S. Hansen, J.S. Christiansen, P. Abrahamsen, C.B. Hasager, N.O. Jensen, P. van der Keur, J.C. Refsgaard, K. Schelde, H. Soegaard & A. Thomsen (2004). Incorporating remote sensing data in physically based distributed agro-hydrological modelling. *Journal of Hydrology* 287, pp. 279-299.
- Boltzmann, L. (1884). Ableitung des Stefan'schen gesetzes, betreffend die abhängigigkeit der wärmestrahlung von der temperatur aus der electromagnetischen lichttheorie. *Annalen der Physik und Chemie* 22, pp. 291-294.
- Boogaard, H., C. van Diepen, R.P. Rötter, J.M.C.A. Cabrera & H.H. van Laar (1998). *User's guide for the WOFOST 7.1 crop growth simulation model and WOFOST control center 1.5*. Wageningen: DLO-Winand Staring Centre.
- Boucher, K. (1997). Hydrological monitoring and measurement methods. In: Wilby, R.L. (Ed.) *Contemporary hydrology* pp. 107-149. Chichester: Wiley.
- Bregt, A.K. (1992). *Processing of soil survey data*. Wageningen, Ph.D. thesis Wageningen Agricultural University.
- Brutsaert, W. (1982). *Evaporation into the atmosphere*. Dordrecht, The Netherlands: Reidel.
- Brutsaert, W. (1999). Aspects of bulk atmospheric boundary layer similarity under free convective conditions. *Reviews of Geophysics* 37, pp. 439-451.
- Buettner, K.J.K. & C.D. Kern (1965). The determination of emissivities of terrestrial surfaces. *Journal of Geophysical Research* 70, pp. 173-189.
- Burgers, G., P. van Leeuwen & G. Evensen (1998). Analysis scheme in the ensemble Kalman filter. *Monthly Weather Review* 126, pp. 1719-1724.

- Burrough, P.A. & R.A. McDonnell (1998). Principles of geographical information systems. New York: Oxford University Press Inc.
- Carlson, T.N., R.R. Gillies & E.M. Perry (1994). A method to make use of thermal infrared temperature and ndvi measurements to infer soil water content and fractional vegetation cover. *Remote Sensing Reviews* 52, pp. 45-59.
- Carlson, T.N., R.R. Gillies & T.J. Schmugge (1995). An interpretation of methodologies for indirect measurement of soil water content. *Agricultural and Forest Meteorology* 77, pp. 191-205.
- Carlson, T.N. & D.A. Ripley (1997). On the relation between NDVI, fractional vegetation cover, and leaf area index. *Remote Sensing of Environment* 62, pp. 241-252.
- Caselles, V. & J.A. Sobrino (1989). Determination of frosts in orange groves from NOAA-AVHRR data. *Remote Sensing of Environment* 29, pp. 135-146.
- Cheng, X. (2003). Digital elevation model construction using ASTER stereo vnr in antarctic in-land ice sheet. *Proceedings of the International Geoscience and Remote Sensing Symposium (IGARSS'03)*, Toulouse, France.
- Christ, E.P. & R.C. Cicone (1984). A physically based transformation of thematic mapper data: The TM tasseled cap. *IEEE Transactions on Geoscience and Remote Sensing* GE-22, pp. 256-263.
- Christ, E.P. & R.J. Kauth (1986). The tasseled cap de-mystified. *Photogrammetric Engineering and Remote Sensing* 52, pp. 81-86.
- Christiaens, K. & J. Feyen (2001). Analysis of uncertainties associated with different methods to determine soil hydraulic properties and their propagation in the distributed hydrological mike she model. *Journal of Hydrology* 246, pp. 63-81.
- Colby, J.D. (1991). Topographic normalization in rugged terrain. *Photogrammetric Engineering and Remote Sensing* 57, pp. 521-537.
- Coll, C., E. Valor, V. Caselles & R. Niclos (2003). Adjusted normalized emissivity method for surface temperature and emissivity retrieval from optical and thermal infrared remote sensing data. *Journal of Geophysical Research-Atmospheres* 108.
- Combs, A.C., H.K. Weickmann, C. Mader & A. Tebo (1965). Application of infrared radiometers to meteorology. *Journal of Applied Meteorology* 4, pp. 253-262.
- Conaway, J. & C.H.M. van Bavel (1967). Evaporation from a wet surface calculated from radiometrically determined surface temperatures. *Journal of Applied Meteorology* 6, pp. 650-655.
- Cressie, N. (1991). *Statistics for spatial data*. New York: Wiley.
- Crosetto, M., S. Tarantola & A. Saltelli (2000). Sensitivity and uncertainty analysis in spatial modelling based on GIS. *Agriculture, Ecosystems & Environment* 81, pp. 71-79.
- Curran, P.J. (1985). *Principles of remote sensing*. Hong Kong: Longman Group Ltd.
- Curran, P.J. (1988). The semivariogram in remote sensing: An introduction. *Remote Sensing of Environment* 24, pp. 493-507.
- Czajkowski, K.P., S.N. Goward, T. Mulhem, S.J. Goetz, A. Walz, D. Shirey, S. Stadler, S.D. Prince & R.O. Dubayah (2000). Estimating environmental variables using thermal remote sensing. In: Quattrochi, D.A. & J.C. Luvall (Eds.) *Thermal remote sensing in land surface processes* pp. 11-32. Boca Raton: CRC Press.
- Dana, R.W. (1969). Measurement of 8-14 micron emissivity of igneous rocks and mineral surfaces. *NASA Science Report NSG-632*. Greenbelt: Goddard Space Flight Center.
- Dankers, R. (2002). Sub-arctic hydrology and climate change: A case study of the tana river basin in northern fennoscandia. Utrecht, Ph.D. thesis (Nederlandse Geografische Studies 251).
- DCDSTF (1988). Digital cartographic data standards task forces. The proposed standard for digital cartographic data. *The American Cartographer* 15, pp. 1-140.

- De Jong, S.M. (1994). Derivation of vegetative variables from a landsat tm image for erosion modelling. *Earth Surface Processes and Landforms* 19, pp. 165-178.
- De Jong, S.M., A. Bagre, P.B.M. van Teeffelen & W.P.A. van Deursen (2000). Monitoring trends in urban growth and surveying city quarters in Ouagadougou, Burkina Faso using SPOT-XS. *Geocarto International* 15, pp. 61-67.
- De Jong, S.M. & P.A. Burrough (1995). A fractal approach to the classification of Mediterranean vegetation types in remotely sensed images. *Photogrammetric Engineering and Remote Sensing* 68, pp. 1041-1053.
- De Jong, S.M., T. Hornstra & H.G. Maas (2001). An integrated spatial and spectral approach to the classification of Mediterranean land cover types: The SSC method. *International Journal of Applied Geosciences* 3, pp. 176-183.
- De Jong, S.M., E.J. Pebesma & B. Lacaze (2003). Above-ground biomass assessment of Mediterranean forests using airborne imaging spectrometry: The DAIS Payne experiment. *International Journal of Remote Sensing* 24, pp. 1505-1520.
- De Roo, A., C.G. Wesseling, V. Jetten & C.J. Ritsema (1992). Limburg soil erosion model. [07-12-2008] <http://www.itc.nl/lisem>.
- Definiens-Imaging (2008). E-cognition. [7/12/2008] <http://www.definiens.com>.
- Devroye, L. (1986). *Non-uniform random variate generation*. New York: Springer.
- Dickinson, R.E. (1986). *Biosphere-atmosphere transfer scheme (BATS) for the ncar community climate model*. Boulder, CO: National Center for Atmospheric Research.
- DKD (1996). Kalibrierschein 0392 DKD-K-05202 96-02. Deutscher Kalibrierdienst.
- Doherty, J. (2002). *PEST model independent parameter estimation. User manual*.
- Doucet, A., S. Godsill & C. Andrieu (2000). On sequential Monte Carlo sampling methods for Bayesian filtering. *Statistics and Computing* 10, pp. 197-208.
- Duguay, C.R. & E.F. LeDrew (1991). Mapping surface albedo in the east slope of the Colorado Front Range, U.S.A., with Landsat Thematic Mapper. *Arctic and Alpine Research* 23, pp. 213-223.
- Dupigny-Giroux, L.-A. & J.E. Lewis (1999). A moisture index for surface characterization over a semiarid area. *Photogrammetric Engineering and Remote Sensing* 65, pp. 937-945.
- Engman, E.T. (1990). Progress in microwave remote sensing of soil moisture. *Canadian Journal of Remote Sensing* 16, pp. 6-14.
- Engman, E.T. (1992). Soil moisture needs in earth sciences. *Proceedings of the Proceedings of the International Geoscience and Remote Sensing Symposium (IGARSS)*,
- Engman, E.T. & N. Chauhan (1995). Status of microwave soil moisture measurements with remote sensing. *Remote Sensing of Environment* 51, pp. 189-198.
- Entekhabi, D., H. Nakamura & E.G. Njoku (1993). Retrieval of soil moisture by combined remote sensing and modeling. *Proceedings of the ESA/NASA International Workshop on Passive Microwave Remote Sensing Research related to Land-Atmosphere Interactions, St. Lary, France*.
- Errico, R.M. (1999). Workshop on assimilation of satellite data. *Bull. Amer. Meteor. Soc.* 80, pp. 463-471.
- Errico, R.M., G. Ohring, J. Derber & J. Joiner (2000). NOAA-NASA-DOD workshop on satellite data assimilation. *Bull. Amer. Meteor. Soc.* 81, pp. 2457-2462.
- ERSDAC (2002). Aster user's guide part-III, DEM product (L4A01) (ver. 1.0). Earth Remote Sensing Data Analysis Center.
- Evensen, G. (1994). Sequential data assimilation with a nonlinear quasi-geostrophic model using Monte-Carlo methods to forecast error statistics. *Journal of Geophysical Research-Oceans* 99, pp. 10143-10162.
- Evensen, G. & P.J. van Leeuwen (1996). Assimilation of GEOSAT altimeter data for the Agulhas current using the ensemble Kalman filter with a quasigeostrophic model. *Monthly Weather Review* 124, pp. 85-86.

- Farr, T.G. & M. Kobrick (2000). Shuttle Radar Topography Mission produces a wealth of data. *Amer. Geophys. Union Eos* 81, pp. 583-585.
- Farrel, D. & W. Larson (1972). Modeling the pore structure of porous media. *Water Resources Research* 8, pp. 699-705.
- Fast, J.D. & M.D. McCorcle (1991). The effect of heterogeneous soil moisture on a summer baroclinic circulation in the central United States. *Monthly Weather Review* 119, pp. 2140-2167.
- Fetah, S.E.M., M. Bensaid & M. Dahmani (1989). Carte géologique du Maroc, Rommani, 1/100 000. Rabat: Royaume du Maroc, Ministère de l'Énergie et des Mines, Direction de la Géologie, Editions du Service Géologique du Maroc.
- Fitzjohn, C., J.L. Ternan & A.G. Williams (1998). Soil moisture variability in a semi-arid gully catchment: Implications for runoff and erosion control. *Catena* 32, pp. 55-71.
- Fox, D., W. Burgard, F. Dellaert & S. Thrun (1999). Monte Carlo localization: Efficient position estimation for mobile robots. *Proceedings of the Proc. of the National Conference on Artificial Intelligence*,
- Franklin, S.E. & D.R. Peddle (1990). Classification of SPOT HRV imagery and texture features. *International Journal of Remote Sensing* 11, pp. 551-556.
- French, A.N., F. Jacob, M.C. Anderson, W.P. Kustas, W. Timmermans, A. Gieske, Z. Su, H. Su, M.F. McCabe, F. Li, J. Prueger & N. Brunzell (2005). Surface energy fluxes with the Advanced Spaceborne Thermal Emission and Reflection Radiometer (ASTER) at the Iowa 2002 SMACEX site (USA). *Remote Sensing of Environment* 99, pp. 55-65.
- French, A.N., T.J. Schmugge, W.P. Kustas, K.L. Brubaker & J. Prueger (2003). Surface energy fluxes over El Reno, Oklahoma, using high-resolution remotely sensed data. *Water Resources research* 39, pp. 1164-1176.
- Friedl, M.A. (2002). Forward and inverse modeling of land surface energy balance using surface temperature measurements. *Remote Sensing of Environment* 79, pp. 344-354.
- Friedl, M.A. & F.W. Davis (1994). Sources of variation in radiometric surface temperature over a tallgrass prairie. *Remote Sensing of Environment* 48, pp. 1-17.
- Gädke, A., J. Küpper, S. Maret & P. Schnizer (2005). Pygsl reference manual. [08/12/2008] <http://pygsl.sourceforge.net>.
- Galantowicz, J.F., D. Entekhabi & E.G. Njoku (1999). Tests of sequential data assimilation for retrieving profile soilmoisture and temperature from observed L-band radiobrightness. *IEEE Transactions on Geoscience and Remote Sensing* 37, pp. 1860-1870.
- Gardner, W.H. (1986). Water content. In: Klute, A. (Ed.) *Methods of soil analysis, I. Physical and mineralogical methods*. pp. 493-544. Madison, Wis.: ASA/SSSA.
- Giacomelli, A., U. Bacchiega, P.A. Troch & M. Mancini (1995). Evaluation of surface soil moisture distribution by means of sar remote sensing techniques and conceptual hydrological modelling. *Journal of Hydrology* 166, pp. 445-459.
- Gillespie, A.R. (1986). Lithologic mapping of silicate rocks using tims. *Proceedings of the TIMS Data Users' Workshop*,
- Gillespie, A.R., S. Rokugawa, S.J. Hook, T. Matsunaga & A.B. Kahle (1999). Temperature/emissivity separation algorithm theoretical basis document, version 2.4. NAS5-31372: NASA.
- Gillespie, A.R., S. Rokugawa, T. Matsunaga, J.S. Cothorn, S.J. Hook & A.B. Kahle (1998). A temperature and emissivity separation algorithm for Advanced Spaceborne Thermal Emission and Reflection Radiometer (ASTER) images. *IEEE Transactions on Geoscience and Remote Sensing* 36, pp. 1113-1126.
- Gillies, R.R. & T.N. Carlson (1995). Thermal remote sensing of surface soil water content with partial vegetation cover for incorporation into climate models. *Journal of Applied Meteorology* 34, pp. 745-756.

- Gomez-Plaza, A., M. Martinez-Mena, J. Albaladejo & V.M. Castillo (2001). Factors regulating spatial distribution of soil water content in small semiarid catchments. *Journal of Hydrology* 253, pp. 211-226.
- Gordon, N.J., D.J. Salmond & A.F.M. Smith (1993). Novel-approach to nonlinear non-Gaussian Bayesian state estimation. *IEEE Proceedings-F Radar and Signal Processing* 140, pp. 107-113.
- Goward, S.N., Y. Xue & K.P. Czajkowski (2002). Evaluating land surface moisture conditions from the remotely sensed temperature/vegetation index measurements: An exploration with the simplified simple biosphere model. *Remote Sensing of Environment* 79, pp. 225-242.
- Grayson, R.B., A.W. Western & F.H.S. Chiew (1997). Preferred states in spatial soil moisture patterns: Local and nonlocal controls. *Water Resources Research* 33, pp. 2897-2908.
- Grayson, R.B., A.W. Western, J.P. Walker, D.D. Kandel, J.F. Costelloe & D.J. Wilson (2006). Controls on patterns of soil moisture in arid and semi-arid systems. In: D'Ordorico, P. & A. Porporato (Eds.) *Ecohydrology of semi-arid ecosystems* pp. 341. Amsterdam: Springer.
- Grenon, M. & M. Batisse (1988). *Le plan bleu: Avenirs du bassin Méditerranéen*. Paris: PNUE, Economica.
- Hammersley, J.M. & D.C. Handscomb (1979). *Monte Carlo methods*. London: Chapman & Hall.
- Hasager, C.B. & N.O. Jensen (1999). Surface flux aggregation in heterogeneous terrain. *Quarterly Journal of the Royal Meteorological Society* 125, pp. 2075-2102.
- Hassan, Q.K., C.P.-A. Bourque, F.-R. Meng & R.M. Cox (2007). A wetness index using terrain-corrected surface temperature and normalized difference vegetation index derived from standard MODIS products: An evaluation of its use in a humid forest-dominated region of eastern Canada. *Sensors* 7, pp. 2028-2048.
- Herman, B.M. & S.R. Browning (1965). A numerical solution to the equation of radiative transfer. *Journal of Atmospheric Sciences* 22, pp. 559-566.
- Heuvelink, G.B.M. (1996). Identification of field attribute error under different models of spatial variation. *International Journal of GIS* 10, pp. 921-935.
- Heuvelink, G.B.M. (1998). *Error propagation in environmental modelling with GIS*. London: Taylor & Francis Ltd.
- Heuvelink, G.B.M., P.A. Burrough & A. Stein (1989). Propagation of errors in spatial modelling with GIS. *International Journal of GIS* 3, pp. 303-322.
- Heuvelink, G.B.M. & J.A. Huisman (1996). Choosing between abrupt and gradual spatial variation? In: Mowrer, H.T., R.L. Czaplewski & R.H. Hamre (Eds.) *Spatial accuracy assessment in natural resources and environmental sciences* pp. 243-50. Fort Collins: USDA Forest Service technical report RM-GTR-277.
- Heuvelink, G.B.M. & E.J. Pebesma (1999). Spatial aggregation and soil process modelling. *Geoderma* 89, pp. 47-65.
- Hirano, A., R. Welch & H. Lang (2003). Mapping from ASTER stereo image data: DEM validation and accuracy assessment. *ISPRS Journal of Photogrammetry and Remote Sensing* 57, pp. 356-370.
- Hoeben, R. & P.A. Troch (2000). Assimilation of active microwave observation data for soil moisture profile estimation. *Water Resources research* 34, pp. 3405-20.
- Hoekstra, P. & A. Delaney (1974). Dielectric properties of soils at UHF and microwave frequencies. *Journal of Geophysical Research* 79, pp. 1699-1708.
- Horst, T.W. & J.C. Weil (1992). Footprint estimation for scalar flux measurements in the atmospheric surface layer. *Boundary-Layer Meteorology* 59, pp. 279.
- Houser, P.R., W.J. Shuttleworth, J.S. Famiglietti, H.V. Gupta, K.H. Syed & D.C. Goodrich (1998). Integration of soil moisture remote sensing and hydrologic modeling using data assimilation. *Water Resources Research* 34, pp. 3405-3420.
- Houtekamer, P.L. & H.L. Mitchell (1998). Data assimilation using an ensemble Kalman filter technique. *Monthly Weather Review* 126, pp. 796-811.

- Hsieh, C.-I., G. Katul & T.-w. Chi (2000). An approximate analytical model for footprint estimation of scalar fluxes in thermally stratified atmospheric flows. *Advances in Water Resources* 23, pp. 765-772.
- Hue, C., J.-P. Le Cadre & P. Perez (2002). Tracking multiple objects with particle filtering. *IEEE Transactions on Aerospace and Electronic Systems* 38, pp. 791-812.
- Huete, A.R. (1989). Soil influences in remotely sensed vegetation canopy spectra. In: Asrar, G. (Ed.) *Theory and applications of optical remote sensing*. pp. 107-141. New York: John Wiley & Sons.
- Huntingford, C., A. Verhoef & J. Stewart (2000). Dual versus single source models for estimating surface temperature of African savannah. *Hydrology and Earth System Sciences* 4, pp. 185-191.
- Hurcom, S.J. & A.R. Harrison (1998). The NDVI and spectral decomposition for semi-arid vegetation abundance estimation. *International Journal of Remote Sensing* 19, pp. 3109-3125.
- HyVista (2008). HyVista corporation website. [08/12/2008] <http://www.hyvista.com>.
- ICAO (1993). *Manual of the ICAO standard atmosphere (extended to 80 kilometres (262 500 feet))*, doc 7488-CD, third edition.
- IGN (2008). IGN – institut géographique national. [08/12/2008] <http://www.ign.fr>.
- Isaaks, E.H. & R.M. Srivastava (1989). *An introduction to applied geostatistics*. Oxford: Oxford University Press.
- Jackson, T.J. (1982). Survey applications of passive microwave remote sensing for soil moisture in the ussr. *EOS Transactions of the American Geophysical Union* 63, pp. 497-499.
- Jackson, T.J., M.E. Hawley & P.E. O'Neill (1987). Preplanting soil moisture using passive microwave sensors. *Water Resources Bulletin* 23, pp. 11-19.
- Jackson, T.J., T.J. Schmugge, A.D. Nicks, G.A. Coleman & E.T. Engman (1981). Soil moisture updating and microwave remote sensing for hydrological simulation. *Hydrological Sciences Bulletin* 26, pp. 305-319.
- Jacob, F., F. Petitcolin, T. Schmugge, E. Vermote, A. French & K. Ogawa (2004). Comparison of land surface emissivity and radiometric temperature derived from MODIS and ASTER sensors. *Remote Sensing of Environment* 90, pp. 137.
- Jacquemin, B. & J.L. Noilhan (1990). Sensitivity study and validation of a land surface parameterization using the HAPEX-mobilhy data set. *Boundary-Layer Meteorology* 52, pp. 93.
- Janssen, P.H.M. (1995). Calibration of process-oriented models. *Ecological Modelling* 83, pp. 55-66.
- Jarvis, P. (1976). The interpretation of leaf water potential and stomatal conductance found in canopies in the field. *Philos. Trans. Roy. Soc. London B* 273, pp. 593-610.
- Jasinski, M.F. & R.D. Crago (1999). Estimation of vegetation aerodynamic roughness of natural regions using frontal area density determined from satellite imagery. *Agricultural and Forest Meteorology* 94, pp. 65-77.
- Jetten (1994). *Soil, atmosphere plant model – a one dimensional water balance model for a forest environment*, Tropenbos Technical Series 5. Wageningen: The Tropenbos Foundation.
- Jia, L. (2004). *Modeling heat exchanges at the land-atmosphere interface using multi-angular thermal infrared measurements*. Wageningen, Ph.D. Thesis Wageningen University.
- Jonckheere, I., S. Fleck, K. Nackaerts, B. Muysa, P. Copin, M. Weiss & F. Baret (2004). Part I Theories, sensors and hemispherical photography. *Agricultural and Forest Meteorology* 121, pp. 19-35.
- Justice, C.O., E. Vermote, J.R.G. Townshend, R. Defries, D.P. Roy, D.K. Hall, V.V. Salomonson, J.L. Privette, G. Riggs, A. Strahler, W. Lucht, R.B. Myeni, Y. Knyazikhin, S.W. Running, R.R. Nemani, Z.M. Wan, A.R. Huete, W. van Leeuwen, R.E. Wolfe, L. Giglio, J.-P. Muller, P. Lewis & M.J. Barnsley (1998). The Moderate Resolution Imaging Spectroradiometer (MODIS): Land remote sensing for global change research. *IEEE Transactions on Geoscience and Remote Sensing* 36, pp. 1228-1249.
- Kääb, A. (2002). Monitoring high-mountain terrain deformation from repeated air- and spaceborne optical data: Examples using digital aerial imagery and ASTER data. *ISPRS Journal of Photogrammetry and Remote Sensing* 57, pp. 39-52.

- Kalman, R.E. (1960). A new approach to linear filtering and prediction problems. *Trans. ASME. J. Basic Eng.* 82, pp. 35-45.
- Karssenberg, D. (2002). Building dynamic spatial environmental models. Utrecht, Ph.D. Thesis Utrecht University. (Nederlandse Geografische Studies 305).
- Karssenberg, D. (2006). Upscaling of saturated conductivity for Hortonian runoff modelling. *Advances in Water Resources* 29, pp. 735-759.
- Karssenberg, D. & K. de Jong (2005). Dynamic environmental modelling in GIS: 2. Modelling error propagation. *International Journal of Geographical Information Science* 19, pp. 623-637.
- Karssenberg, D.J., K. de Jong & J. van der Kwast (2007). Modelling landscape dynamics with Python. *International Journal of Geographical Information Science* 21, pp. 483-495.
- Keppenne, C.L. (2000). Data assimilation into a primitive-equation model with a parallel ensemble Kalman filter. *Monthly Weather Review* 128, pp. 1971-1981.
- KNMI (2008). KNMI catalogus. [08/12/2008] <http://www.knmi.nl>.
- Koorevaar, P., G. Menelik & C. Dirksen (1983). *Elements of soil physics*. Amsterdam: Elsevier science publishers B.V.
- Köppen, W. (1936). *Das geographische System der Klimate*.
- Kroon, L.J.M. & H.A.R. de Bruin (1993). Atmosphere-vegetation interaction in local advection conditions: Effect of lower boundary conditions. *Agricultural and Forest Meteorology* 64, pp. 1-28.
- Kustas, W.P. (1990). Estimates of evapotranspiration with a one- and two-layer model of heat transfer over partial canopy cover. *Journal of applied meteorology* 29, pp. 704.
- Kustas, W.P. & C.S.T. Daughtry (1990). Estimation of the soil heat flux/net radiation ratio from spectral data. *Agricultural and Forest Meteorology* 49, pp. 205.
- Kustas, W.P., K.S. Humes, J.M. Norman & M.S. Moran (1996). Single- and dual-source modeling of surface energy fluxes with radiometric surface temperature. *Journal of Applied Meteorology* 35, pp. 110-121.
- Kustas, W.P., F. Li, T.J. Jackson, J.H. Prueger, J.I. MacPherson & M. Wolde (2004). Effects of remote sensing pixel resolution on modeled energy flux variability of croplands in Iowa. *Remote Sensing of Environment* 92, pp. 535.
- Kustas, W.P. & J.M. Norman (2000). A two-source energy balance approach using directional radiometric temperature observations for sparse canopy covered surfaces. *Agronomy Journal* 92, pp. 847-854.
- Kustas, W.P., J.M. Norman, M.C. Anderson & A.N. French (2003). Estimating subpixel surface temperatures and energy fluxes from the Vegetation Index – radiometric temperature relationship. *Remote Sensing of Environment* 85, pp. 429-440.
- Kutilek, M. & D.R. Nielsen (1994). *Soil hydrology*. Cremlingen-Destedt: Catena Verlag.
- Lambers, H., F. Stuart Chapin III & T. Pons (1998). *Plant physiological ecology*. New York: Springer-Verlag.
- Lambin, E.F. & D. Ehrlich (1996). The surface Temperature-Vegetation Index space for land cover and land-cover change analysis. *International Journal of Remote Sensing* 17, pp. 463-488.
- LANDSAT (2008). USGS Landsat project. [08/12/2008] <http://landsat.gsfc.nasa.gov>.
- Leenhardt, D. (1995). Errors in the estimation of soil water properties and their propagation through a hydrological model. *Soil Use and Management* 11, pp. 15-21.
- Leenhardt, D., M. Voltz & M. Bornand (1994). Propagation of the error of spatial prediction of soil properties in simulating crop evapotranspiration. *European Journal of Soil Science* 45, pp. 303-310.
- Leica (2003). *Leica Photogrammetry Suite Orthobase & Orthobase Pro user's guide*. Atlanta, Georgia: Leica Geosystems GIS & Mapping, LLC.
- Lermusiaux, P.F.J. (1999). Data assimilation via error subspace statistical estimation. Part II: Middle Atlantic bight shelfbreak front simulations and esse validation. *Monthly Weather Review* 127, pp. 1408-1432.

- Lewis, P.A.W. & E.J. Orav (1989). Simulation methodology for statisticians, operations analysts, and engineers. Pacific Grove, California: Wadsworth and Brooks/Cole.
- Liang, S. (2000). Narrowband to broadband conversions of land surface albedo I: Algorithms. *Remote Sensing of Environment* 76, pp. 213-238.
- Liang, S., C.J. Shuey, A.L. Russ, H. Fang, M. Chen, C.L. Walthall, C.S.T. Daughtry & J. R. Hunt Jr. (2003). Narrowband to broadband conversions of land surface albedo: II. Validation. *Remote Sensing of Environment* 84, pp. 25-41.
- Lillesand, T.M. & R.W. Kiefer (1994). Remote sensing and image interpretation. John Wiley & Sons, Inc.
- Liu, J.S. & R. Chen (1998). Sequential Monte Carlo methods for dynamic systems. *Journal of the American Statistical Association* 93, pp. 1032-1044.
- Liu, Y., T. Hiyama & Y. Yamaguchi (2006). Scaling of land surface temperature using satellite data: A case examination on ASTER and MODIS products over a heterogeneous terrain area. *Remote Sensing of Environment* 105, pp. 115-128.
- Loos, S. & A.M. Schipper (2003). Investigation of the effect of future climate conditions on groundwater levels in the commune of sehoul (Morocco). Internship report Alterra Wageningen.
- LPDAAC (2006). MODIS reprojection tool swath user's manual release 2.1. Land Processes DAAC, USGS Center for Earth Resources Observation and Science (EROS).
- Madsen, H. & R. Canizares (1999). Comparison of extended and ensemble Kalman filters for data assimilation in coastal area modelling. *International Journal for Numerical Methods in Fluids* 31, pp. 961-981.
- Margulis, S.A. (2001). Temporal disaggregation of satellite-derived monthly precipitation estimates and the resulting propagation of error in partitioning of water at the land surface. *Hydrology & Earth System Sciences* 5, pp. 27-38.
- Margulis, S.A., D. McLaughlin, D. Entekhabi & S. Dunne (2002). Land data assimilation and estimation of soil moisture using measurements from the Southern Great Plains 1997 field experiment. *Water Resources research* 38, pp. 1-18.
- Markham, B.L. & J.L. Barker (1986). Landsat MSS and TM post-calibration dynamic ranges, exoatmospheric reflectances and at-satellite temperatures. *EOSAT Landsat Technical Notes* 1, pp. 3-8.
- Massman, W.J. (1999a). A model study of  $KB^{-1}$  for vegetated surfaces using 'localized near-field' Lagrangian theory. *Journal of Hydrology* 223, pp. 27-43.
- Massman, W.J. (1999b). Molecular diffusivities of Hg vapor in air, O<sub>2</sub> and N<sub>2</sub> near stp and the kinematic viscosity and the thermal diffusivity of air near stp. *Atmos. Environ.* 33, pp. 453-457.
- McDonald, R.A. (1997). CORONA, between the sun & the earth: The first NRO reconnaissance eye in space. Bethesda, Maryland: American Society for Photogrammetry and Remote Sensing.
- Meijninger, W.M.L. (2003). Surface fluxes over natural landscapes using scintillometry. Wageningen, Ph.D. thesis Wageningen University.
- Menenti, M. (1984). Physical aspects of and determination of evaporation in deserts applying remote sensing techniques. Report 10 (special issue). Institute for Land and Water Management Research (ICW).
- Mikhail, E.M., J.S. Bethel & J.C. McCole (2001). Introduction to modern photogrammetry. New York: John Wiley & Sons.
- Millington, R.J. & J.P. Quirk (1959). Permeability of porous media. *Nature* 183, pp. 387-388.
- Millington, R.J. & J.P. Quirk (1961). Permeability of porous media. *Transactions of the Faraday Society* 57, pp. 1200-1207.
- MODIS (2008). The moderate resolution imaging spectroradiometer website. [08/12/2008] <http://modis.gsfc.nasa.gov/>.

- Mohanty, B.P. & T.H. Skaggs (2001). Spatio-temporal evolution and time-stable characteristics of soil moisture within remote sensing footprints with varying soil, slope, and vegetation. *Advances in Water Resources* 24, pp. 1051-1067.
- Mölders, N., M. Jankov & G. Kramm (2005). Application of Gaussian error propagation principles for theoretical assessment of model uncertainty in simulated soil processes caused by thermal and hydraulic parameters. *Journal of Hydrometeorology* 6, pp. 1045-1062.
- Molero, F., M. Pujadas, J.C. Fortea, J.L. Gómez-Amo, V. Estellés, M.P. Utrillas & J.A. Martínez-Lozano (2005). Vertical profiles of atmospheric constituents from LIDAR and sounding measurements. Proceedings of the SPARC Final Workshop, ITC Enschede, the Netherlands.
- Monin, A.S. & A.M. Obukhov (1954). Basic laws of turbulent mixing in the ground layer of the atmosphere. *Trans. Geophys. Inst. Akad. Nauk. USSR* 151, pp. 163-187.
- Monteith, J.L. (1965). Evaporation and environment. *Symposia of the Society for Experimental Biology* 19, pp. 205-234.
- Monteith, J.L. (1981). Evaporation and surface temperature. *Quarterly Journal of the Royal Meteorological Society* 107, pp. 1-27.
- Moradkhani, H., K.L. Hsu, H. Gupta & S. Sorooshian (2005). Uncertainty assessment of hydrologic model states and parameters: Sequential data assimilation using the particle filter. *Water Resources Research* 41, pp. -.
- Moran, M.S., C.D. Peters-Lidard, J.M. Watts & S. McElroy (2004). Estimating soil moisture at the watershed scale with satellite-based radar and land surface models. *Canadian journal of remote sensing* 30, pp. 805-826.
- Nafaa, R. (2002). Dynamique du milieu naturel de la Mamora. Mohammedia, Ph.D. thesis Université Hassan II.
- Narayanan, R.M. & P.P. Hirsave (2001). Soil moisture estimation models using SIR-C SAR data: A case study in New Hampshire, USA. *Remote Sensing of Environment* pp. 385-396.
- NASA (2008). Shuttle Radar Topography Mission. [08/12/2008] <http://www2.jpl.nasa.gov/srtm/>.
- Nash, J.E. & J.V. Sutcliffe (1970). River flow forecasting through conceptual models part I – a discussion of principles. *Journal of Hydrology* 10, pp. 282-290.
- Nemani, R., L. Pierce & S. Running (1993). Developing satellite-derived estimates of surface moisture status. *Journal of Applied Meteorology* 32, pp. 548-557.
- Newton, R.W., J.L. Heilman & C.H.M. van Bavel (1983). Integrating passive microwave measurements with a soil moisture/heat flow model. *Agricultural Water Management* 7, pp. 379-389.
- Nichols, W.E. & R.H. Cuenca (1993). Evaluation of the Evaporative Fraction for parameterization of the surface energy balance. *Water Resources Research* 29 pp. 3681-3690.
- Noilhan, J. & S. Planton (1989). A simple parameterization of land surface processes for meteorological models. *Monthly Weather Review* 117, pp. 536-549.
- Norman, J.M., W.P. Kustas & K.S. Humes (1995). A two-source approach for estimating soil and vegetation energy fluxes in observations of directional radiometric surface temperature. *Agricultural and Forest Meteorology* 77, pp. 263.
- Nyogi, D.S. & S. Raman (1997). Comparison of four different stomatal resistance schemes using FIFE observations. *American Meteorological Society* pp. 903-917.
- Ogawa, K., T. Schmugge & F. Jacob (2003). Estimation of land surface window (8-12 $\mu$ m) emissivity from multispectral thermal infrared remote sensing – a case study in a part of Sahara desert. *Geophysical Research Letters* 30, pp. 4.
- Ogawa, K., T. Schmugge, F. Jacob & A.N. French (2002). Estimation of broadband land surface emissivity from multi-spectral thermal infrared remote sensing. *Agronomie* 22, pp. 19-20.
- Oke, T.R. (1978). *Boundary layer climates*. London: Methuen & Co Ltd.

- Oliver, M.A. & R. Webster (1990). Kriging: A method of interpolation for geographical information systems. *International Journal of GIS* 4, pp. 313-332.
- Oreskes, N., K. Shrader-Frechette & K. Belitz (1994). Verification, validation, and confirmation of numerical models in the earth sciences. *Science* 263, pp. 641-646.
- Ottlé, C. & D. Vidal-Madjar (1994). Assimilation of soil moisture inferred from infrared remote sensing in a hydrological model over the HAPEX-MOBILHY region. *Journal of Hydrology* 158, pp. 241-264.
- Paparoditis, N. & O. Dissard (2002). 3D data acquisition from visible images. In: Kasser, M. & Y. Egels (Eds.) *Digital photogrammetry* pp. 168-220. London: Taylor & Francis.
- Paparoditis, N. & L. Polidori (2002). Overview of digital surface models. In: Kasser, M. & Y. Egels (Eds.) *Digital photogrammetry* pp. 159-168. London: Taylor & Francis.
- Pauwels, V.R.N., R. Hoeben, N.E.C. Verhoest & F.P. De Troch (2001). The importance of the spatial patterns of remotely sensed soil moisture in the improvement of discharge predictions for small-scale basins through data assimilation. *Journal of Hydrology* pp. 88-102.
- PCRaster (2008). PCRaster homepage. [08/12/2008] <http://pcraster.geo.uu.nl>.
- Pebesma, E.J. & C.G. Wesseling (1998). GSTAT: A program for geostatistical modelling, prediction and simulation. *Computers & Geosciences* 24, pp. 17-31.
- Piironen, A.K. (1994). Analysis of volume imaging LIDAR signals. Joensuu, Finland, Ph.D. thesis University of Joensuu.
- Press, W.H., S.A. Teukolsky, W.Y. Vetterling & B.P. Flannery (1992). *Numerical recipes in C*, 2nd edition. Cambridge: Cambridge University Press.
- Price, J.C. (1990). Using spatial context in satellite data to infer regional scale evapotranspiration. *IEEE Transactions on Geoscience and Remote Sensing* GE-28, pp. 940-948.
- Qin, Z., A. Karnieli & P. Berliner (2001). A mono-window algorithm for retrieving land surface temperature from Landsat TM data and its application to the Israel-Egypt border region. *International Journal of Remote Sensing* 22, pp. 3719-3746.
- Rabus, B., M. Eineder, A. Roth & R. Bamler (2003). The Shuttle Radar Topography Mission – a new class of digital elevation models acquired by spaceborne radar. *ISPRS Journal of Photogrammetry and Remote Sensing* 57, pp. 241-262.
- Rao, T.C.M., K.V. Rao, A.R. Kumar, D.P. Rao & B.L. Deekshatula (1996). Digital Terrain Model (DTM) from Indian Remote Sensing (IRS) satellite data from the overlap of two adjacent paths using digital photogrammetric techniques. *Photogrammetric Engineering and Remote Sensing* 62, pp. 727-731.
- Reichle, R.H., D. Entekhabi & D.B. McLaughlin (2001a). Downscaling of radio brightness measurements for soil moisture estimation: A four-dimensional variational data assimilation approach. *Water Resources Research* 37, pp. 2353-2364.
- Reichle, R.H., D.B. McLaughlin & D. Entekhabi (2001b). Hydrologic data assimilation with the ensemble Kalman filter. *Monthly Weather Review* 130, pp. 103-114.
- Reichle, R.H., D.B. McLaughlin & D. Entekhabi (2001c). Variational data assimilation of microwave radiobrightness observations for land surface hydrology applications. *IEEE Transactions on Geoscience and Remote Sensing* 39, pp. 1708-1718.
- Reichle, R.H., D.B. McLaughlin & D. Entekhabi (2002). Hydrologic data assimilation with the ensemble Kalman filter. *Monthly Weather Review* 130, pp. 103-114.
- Richardson, A.J. & C.L. Wiegand (1977). Distinguishing vegetation from soil background. *Photogrammetric Engineering and Remote Sensing* 43, pp. 1541-1552.
- Rowell, D.L. (1994). *Soil science: Methods and applications*. Harlow: Longman.

- Rubio, E., V. Caselles & C. Badenas (1997). Emissivity measurements of several soils and vegetation types in the 8-14  $\mu\text{m}$  wave band: Analysis of two field methods. *Remote Sensing of Environment* 59, pp. 490-521.
- Rubio, E., V. Caselles, C. Coll, E. Valour & F. Sospedra (2003). Thermal-infrared emissivities of natural surfaces: Improvements on the experimental set-up and new measurements. *International Journal of Remote Sensing* 24, pp. 5379-5390.
- Rutter, A.J. (1975). The hydrological cycle in vegetation. In: Monteith, J.L. (Ed.) *Vegetation and the atmosphere* pp. 11-114. London: Academic Press. 1.
- Saha, S.K. (1995). Assessment of regional soil moisture conditions by coupling satellite sensor data with a soil-plant system heat and moisture balance model. *International Journal of Remote Sensing* 16, pp. 973-980.
- Salisbury, J.W. & D.M. D'Aria (1992). Emissivity of terrestrial materials in the 8-14  $\mu\text{m}$  atmospheric window. *Remote Sensing of Environment* 42, pp. 83-106.
- Sandholt, I., K. Rasmussen & J. Andersen (2002). A simple interpretation of the Surface Temperature/Vegetation Index space for assessment of surface moisture status. *Remote Sensing of Environment* 79, pp. 213-224.
- Schmid, H.P. (2002). Footprint modeling for vegetation atmosphere exchange studies: A review and perspective. *Agricultural and Forest Meteorology* 113, pp. 159-183.
- Schmugge, T. (1978). Remote sensing of surface soil moisture. *Journal of Applied Meteorology* 17, pp. 1549-1557.
- Schmugge, T., S.J. Hook & C. Coll (1998). Recovering surface temperature and emissivity from thermal infrared multispectral data. *Remote Sensing of Environment* 65, pp. 121-131.
- Schowengerdt, R.A. (1997). *Remote sensing: Models and methods for image processing*. London: Academic Press Ltd.
- Schuupp, P.H., M.Y. Leclerc, J.I. Macpherson & R.L. Desjardins (1990). Footprint prediction of scalar fluxes from analytical solutions of the diffusion equation. *Boundary-layer meteorology* 50, pp. 355-373.
- Schuurmans, J.M., M.F.P. Bierkens, E.J. Pebesma & R. Uijlenhoet (2007). Automatic prediction of high-resolution daily rainfall fields for multiple extents: The potential of operational radar. *Journal of Hydrometeorology* pp.1204-1224.
- Schuurmans, J.M., P.A. Troch, A.A. Veldhuizen, W.G.M. Bastiaanssen & M.F.P. Bierkens (2003). Assimilation of remotely sensed latent heat flux in a distributed hydrological model. *Advances in Water Resources* 26, pp. 151-159.
- Scurlock, J.M.O., G.P. Asner & S.T. Gower (2001). Worldwide historical estimates and bibliography of leaf area index, 1932-2000. ORNL Technical Memorandum TM-2001/268. Oak Ridge, Tennessee: Oak Ridge National Laboratory.
- Sellers, P.J., Y. Mintz, Y.C. Sud & A. Dalcher (1986). A simple biosphere model (SIB) for use within general circulation models. *Journal of Atmospheric Sciences* 43, pp. 505-531.
- Simunek, J., M. Sejna & M.T. van Genuchten (1998a). Hydrus 1D. Software package for simulating one-dimensional movement of water, heat and multiple solutes in variably saturated media. Version 2.0.
- Simunek, J., O. Wendroth & M.T. van Genuchten (1998b). Parameter estimation analysis of the evaporation method for determining soil hydraulic properties. *Soil Science Society of America Journal* 62, pp. 894-905.
- Sluiter, R. (2005). *Mediterranean land cover change. Modelling and monitoring natural vegetation using GIS and remote sensing*. Utrecht: Ph.D. thesis. (Nederlandse Geografische Studies 333)
- Sluiter, R., S.M. de Jong, J. van der Kwast & J. Walstra (2004). A contextual approach to classify Mediterranean heterogeneous vegetation using the spatial reclassification kernel (SPARK) and DAIS7915 imagery. In: De Jong, S.M. & F.D. van der Meer (Eds.) *Remote sensing image analysis: Including the spatial domain* pp. 291-310. Dordrecht: Kluwer Academic Publishers. 5.
- Smith, J.A., T.L. Lin & K.J. Ranson (1980). The Lambertian assumption and Landsat data. *Photogrammetric Engineering and Remote Sensing* 46, pp. 1183-1189.

- Smith, R.C.G. & B.J. Choudhury (1991). Analysis of normalized difference and surface temperature observations over southeastern Australia. *International Journal of Remote Sensing* 12, pp. 2021-2044.
- Sobrino, J.A. & V. Caselles (1993). A field method for measuring the thermal infrared emissivity. *ISPRS Journal of Photogrammetry and Remote Sensing* 48, pp. 24-31.
- Sobrino, J.A., Z.L. Li, M.P. Stoll & F. Becker (1994). Improvements in the split-window technique for land-surface temperature determination. *Ieee Transactions on Geoscience and Remote Sensing* 32, pp. 243-253.
- SPARK (2008). Pcraster website: Spark [08/12/2008] <http://pcraster.geo.uu.nl/projects/spark/index.html>.
- Spectrum (2003). Fieldscout TDR 300 soil moisture meter user's manual. Catalog #6430fs. Spectrum Technologies, Inc.
- Srivastava, S.K., N. Yograjan, V. Jayaraman, P.P.N. Rao & M.G. Chandrasekhar (1997). On the relationship between ERS-1 SAR/backscatter and surface/sub-surface soil moisture variations in vertisols. *Acta Astronautica* 40, pp. 693-699.
- Stefan, J. (1879). Über die Beziehung zwischen Wärmestrahlung und der Temperatur. *Sitzungsberichte der mathematisch-naturwissenschaftlichen Classe der kaiserlichen Akademie der Wissenschaften* 79, pp. 391-428.
- Strobl, P., R. Richter, A. Mueller, F. Lehmann, D. Oertel, S. Tischler & A. Nielsen (1996). DAIS7915 system performance – first results of the 1995 evaluation campaigns. *Proceedings of the 2<sup>nd</sup> International Airborne Remote Sensing Conference and Exhibition, San Francisco 2*,
- Stull, R.B. (1988). *An introduction to boundary layer meteorology*. Kluwer Academic Publishers.
- Su, Z. (1996). *Remote sensing applied to hydrology: The Sauer river basin study*. Bochum, Ph.D. Thesis Faculty of Civil Engineering, Ruhr University Bochum, Germany.
- Su, Z. (2000). Remote sensing of land use and vegetation for mesoscale hydrological studies. *International Journal of Remote Sensing* 21, pp. 213-233.
- Su, Z. (2001). A Surface Energy Balance System (SEBS) for estimation of turbulent heat fluxes from point to continental scale. In: Su, Z. & C.E. Jacobs (Eds.) *Advanced earth observation – land surface climate, final report*. pp. 184: Publications of the National Remote Sensing Board (BCRS). USP-2.
- Su, Z. (2002). The Surface Energy Balance System (SEBS) for estimation of turbulent heat fluxes. *Hydrology & Earth System Sciences* 6, pp. 85-99.
- Su, Z., L. Jia, A.S. Gieske, W.J. Timmermans, X. Jin, J. Elbers, J. van der Kwast, A. Olioso, J.A. Sobrino, F. Nerry, D. Sabol & J. Moreno (2005). In-situ measurements of land-atmosphere exchanges of water, energy and carbon dioxide in space and time over the heterogeneous Barrax site during SPARC2004. *Proceedings of the SPARC Final Workshop, ITC Enschede, The Netherlands*.
- Su, Z., T. Schmugge, W.P. Kustas & W.J. Massman (2001). An evaluation of two models for estimation of the roughness height for heat transfer between the land surface and the atmosphere. *Journal of Applied Meteorology* 40, pp. 1933-1951.
- Su, Z., W. Timmermans, A. Gieske, L. Jia, J. Elbers, A. Olioso, J. Timmermans, R. van der Velde, X. Jin, H. van der Kwast, F. Nerry, D. Sabol, J.A. Sobrino, J. Moreno & R. Bianchi (2008). Quantification of land-atmosphere exchanges of water, energy and carbon dioxide in space and time over the heterogeneous Barrax site. *International Journal of Remote Sensing* 29, pp. 5215-5235.
- Su, Z., P.A. Troch & F.P. De Troch (1997). A method for retrieving soil moisture using active microwave data. *Physics and Chemistry of The Earth* 22, pp. 235-239.
- Su, Z., P.A. Troch, F.P. De Troch, L. Nochtergale & B. Cosyn (1995). Preliminary results of soil moisture retrieval from ESAR (EMAC 94) and ERS-1/SAR, part II: Soil moisture retrieval. *Proceedings of the second workshop on hydrological and microwave scattering modelling for spatial and temporal soil moisture*

- mapping from ERS-1 and JERS-1 SAR data and macroscale hydrological modeling (EV5V-CT94-0446). Institut National de la Recherche Agronomique, Unité de Science du Sol et de Bioclimatologie, France.
- Tasumi, M., R.G. Allen & W.G.M. Bastiaanssen (2000). The theoretical basis of SEBAL. In: Morse, A., M. Tasumi, R.G. Allen & W.J. Kramber (Eds.) Application of the SEBAL methodology for estimating consumptive use of water and streamflow depletion in the bear river basin of idaho through remote sensing, final report pp. 107: Raytheon Systems Company, Earth Observation System Data and Information System Project, Idaho Department of Water Resources and University of Idaho.
- Ter Steeghe, H. (1997). WinPhot. A windows 3.1 programme to analyse vegetation indices, light and light quality from hemispherical photographs. Tropenbos-Guyana Programme 97-3. Georgetown, Guyana: Tropenbos-Guyana Reports.
- Thom, A.S. (1972). Momentum, mass, and heat exchange in vegetation. *Quarterly Journal of the Royal Meteorological Society* 98, pp. 124-134.
- Thome, K. (1999). Algorithm theoretical basis document for ASTER level 2B1 – surface radiance and ASTER level 2B5 – surface reflectance. Tucson, Arizona: University of Arizona.
- Timmermans, W.J., W.P. Kustas, M.C. Anderson & A.N. French (2007). An intercomparison of the Surface Energy Balance Algorithm for Land (SEBAL) and the Two-Source Energy Balance (TSEB) modeling schemes. *Remote Sensing of Environment* 108, pp. 369-384.
- Timmermans, W.J., J. van der Kwast, A.S. Gieske, Z. Su, A. Olioso, L. Jia & J. Elbers (2005b). Intercomparison of energy flux models using ASTER imagery at the SPARC 2004 site (barrax, spain). Proceedings of the SPARC Final Workshop, ITC Enschede, The Netherlands.
- Tomaselli, R. (1981). Main physiognomic types and geographic distribution of shrub systems related to Mediterranean climates. In: Di Castri, F. (Ed.) *Ecosystems of the world, II Mediterranean-type shrublands* pp. 95-106: Elsevier.
- Topp, G.C. & J.L. Davis (1985). Measurement of soil water content using Time-Domain Reflectometry (TDR): A field evaluation. *Soil Science Society of America Journal* 49, pp. 19-24.
- Topp, G.C., J.L. Davis & A.P. Annan (1980). Electromagnetic determination of soil water content: Measurements in coaxial transmission lines. *Water Resources Research* 16, pp. 574-582.
- Troufleau, D., J.P. Lhomme, B. Monteny & A. Vidal (1997). Sensible heat flux and radiometric surface temperature over sparse Sahelian vegetation. I. An experimental analysis of the  $k_B^{-1}$  parameter. *Journal of Hydrology* 188-189, pp. 815-838.
- Tucker, C.J. (1979). Red and photographic infrared linear combinations for monitoring vegetation. *Remote Sensing of Environment* 8, pp. 127-150.
- Ulaby, F.T., P.C. Dubois & J. van Zyl (1996). Radar mapping of surface soil moisture. *Journal of Hydrology* 184, pp. 57-84.
- Valor, E. & V. Caselles (1996). Mapping land surface emissivity from NDVI: Application to European, African, and South American areas. *Remote Sensing of Environment* 57, pp. 167-184.
- Van Asch, T.W.J., S.J.E. van Dijk & M.R. Hendriks (2001). The role of overland flow and subsurface flow on the spatial distribution of soil moisture in the topsoil. *Hydrological Processes* 15, pp. 2325-2340.
- Van Beek, L.P.H. (2002). Assessment of the influence of changes in land use and climate on landslide activity in a Mediterranean environment. Utrecht, Ph.D. Thesis Utrecht University. (Nederlandse Geografische Studies 294)
- Van Dam, O. (2000). Modelling incoming potential radiation on a land surface with PCRaster: Potrad5.Mod manual. Faculty of Geosciences, Utrecht University, the Netherlands.
- Van Dam, O. (2001). Forest filled with gaps: Effects of gap size on water and nutrient cycling in tropical rain forest: A study in guyana. Utrecht: Ph.D. thesis Utrecht University.

- Van de Griend, A.A. & E.T. Engman (1985). Partial area hydrology and remote sensing. *Journal of Hydrology* 81, pp. 211-251.
- Van der Meer, F.D. & S.M. de Jong (2001). *Imaging spectroscopy: Basic principles and prospective applications*. Dordrecht: Kluwer Academic Publishers.
- Van Dijk, S.J.E., A. Laouina, A.V. Carvalho, S. Loos, A.M. Schipper, J. van der Kwast, R. Nafaa, M. Antari, A. Rocha, C. Borrego & C.J. Ritsema (2005). Surface runoff and groundwater recharge under climate change in semi-arid agricultural land (Rabat region, Morocco).. In: Kepner, W.G., J.L. Rubio, D.A. Mouat & F. Pedrazzini (Eds.) *Desertification in the Mediterranean region. A security issue*. pp. 605. Heidelberg: Springer Publishers. 3.
- Van Genuchten, M.T. (1978). Calculating the unsaturated hydraulic conductivity with a new, closed-form analytical model. Research report 78-WR-08. Water resources program. Princeton: Dep. of Civil Engineering, Princeton University.
- Van Genuchten, M.T. (1980). A closed-form equation for predicting the hydraulic conductivity of unsaturated soils. *Soil Sci Soc Am J* 44, pp. 892-898.
- Van Leeuwen, P. (2003). A variance-minimizing filter for large-scale applications. *Monthly Weather Review* 131, pp. 2071-2084.
- Van Oevelen, P.J. (2000). Estimation of areal soil water content through microwave remote sensing. Wageningen, Ph.D. thesis Landbouwwuniversiteit Wageningen.
- Verhoef, W., H.A.R. de Bruin & B.J.J.M. van den Hurk (1997). Some practical notes on the parameter  $kB^{-1}$  for sparse vegetation. *Journal of Applied Meteorology* 36, pp. 560-572.
- Von Hoyningen-Huene, J. (1983). *Die Interzeption des Niederschlags in landwirtschaftlichen Pflanzenbeständen*. Braunschweig: DVWK.
- Wagner, W., A. Ullrich, T. Melzer, C. Briese & K. Kraus (2005). *From single-pulse to full-waveform airborne laser scanners: Potential and practical challenges*. Vienna: Vienna University of Technology.
- Walker, J.P. (1999). Estimating soil moisture profile dynamics from near-surface soil moisture measurements and standard meteorological data. Newcastle, Ph.D. thesis University of Newcastle.
- Walker, J.P., G.R. Willgoose & J.D. Kalma (2001). One-dimensional soil moisture profile retrieval by assimilation of near-surface measurements: A simplified soil moisture model and field application. *Journal of Hydrometeorology* 2, pp. 356-373.
- Wan, Z., Y. Zhang, Q. Zhang & Z.-l. Li (2002). Validation of the land-surface temperature products retrieved from Terra Moderate Resolution Imaging Spectroradiometer data. *Remote Sensing of Environment* 83, pp. 163.
- Wang, K.C., Z.M. Wan, P.C. Wang, M. Sparrow, J.M. Liu, X.J. Zhou & S. Haginoya (2005). Estimation of surface long wave radiation and broadband emissivity using Moderate Resolution Imaging Spectroradiometer (MODIS) land surface temperature/emissivity products. *Journal of Geophysical Research-Atmospheres* 110.
- Wang, T.i., G.R. Ochs & S.F. Clifford (1978). A saturation-resistant optical scintillometer to measure  $CN_2$ . *Journal of the Optical Society of America* 69, pp. 334-338.
- Ward, R.C. & M. Robinson (1989). *Principles of hydrology*. Berkshire: McGraw-Hill.
- Watfeh, A. (1986). *Etude géomorphologique de la région de l'Arbaa Essechoul*. Rabat, Thèse 3ème cycle Université Mohammed V.
- Weerts, A.H. & G.Y.H. El Serafy (2006). Particle filtering and ensemble Kalman filtering for state updating with hydrological conceptual rainfall-runoff models. *Water Resources Research* 42.
- Weiss, M., F. Baret, G.J. Smith, I. Jonckheere & P. Coppin (2004). Part II. Estimation of LAI, errors and sampling. *Agricultural and Forest Meteorology* 121, pp. 37-53.

- Wesseling, C.G., D.J. Karssenbergh, P.A. Burrough & W.P.A. van Deursen (1996). Integrating dynamic environmental models in GIS: The development of a dynamic modelling language. *Transactions in GIS* 1, pp. 40-48.
- Western, A.W., R.B. Grayson, G. Blöschl, G.R. Willgoose & T.A. McMahon (1999). Observed spatial organisation of soil moisture and its relation to terrain indices. *Water Resources Research* 35, pp. 797-810.
- Western, A.W., T.R. Green & R.B. Grayson (1997). Hydrological modelling of the Tarrawarra catchment; use of soil moisture patterns. *Proceedings of the MODSIM 97 International Congress on Modelling and Simulation*, Hobart, Australia.
- Western, A.W., H. Richter, F.H.S. Chiew, R.I. Young, G. Mills, R.B. Grayson, M. Manton & T.A. McMahon (2002). Testing the Australian Bureau of Meteorology's land surface scheme using soil moisture observations from the Murrumbidgee catchment. *Proceedings of the Hydrology and Water Resources Symposium*,
- Wharton, S.W. (1982). A contextual classification method for recognizing land use patterns in high resolution remotely sensed data. *Pattern Recognition* 15, pp. 317-324.
- Wieringa, J. (1986). Roughness-dependent geographical interpolation of surface wind speed averages. *Quarterly Journal of the Royal Meteorological Society* 112, pp. 867-889.
- Wigneron, J.P., T. Schmugge, A. Chanzy, J.C. Calvet & Y. Kerr (1998). Use of passive microwave remote sensing to monitor soil moisture. *Agronomie* 18, pp. 27-43.
- Williams, A.G., J.L. Ternan, C. Fitzjohn, S. de Alba & A. Perez-Gonzalez (2003). Soil moisture variability and land use in a seasonally arid environment. *Hydrological Processes* 17, pp. 225-235.
- Woodcock, C.E., A.H. Strahler & D.L.B. Jupp (1998). The use of variograms in remote sensing: II. Real digital images. *Remote Sensing of Environment* 25, pp. 349-379.
- Yamaguchi, Y., A.B. Kahle, H. Tsu, T. Kawakami & M. Pniel (1988). Overview of Advanced Spaceborne Thermal Emission and Reflection Radiometer (ASTER). *IEEE Transactions on Geoscience and Remote Sensing* 36, pp. 1062-1071.
- Yu, J. (2005). On leverage in a stochastic volatility model. *Journal of Econometrics* 127, pp. 165-178.
- Zeng, N., J.D. Neelin, K.M. Lau & C.J. Tucker (1999). Enhancement of interdecadal climate variability in the Sahel by vegetation interaction. *Science* 286, pp. 1537-1540.
- Zhou, S.K., R. Chellappa & B. Moghaddam (2004). Visual tracking and recognition using appearance-adaptive models in particle filters. *IEEE Transactions on Image Processing* 13, pp. 1491-1506.
- Zomer, R., S. Ustin & J. Ives (2002). Using satellite remote sensing for DEM extraction in complex mountainous terrain: Landscape analysis of the Makalu Barun national park of Eastern Nepal. *International Journal of Remote Sensing* 23, pp. 125-143.
- Zribi, M. & M. Dechambre (2003). A new empirical model to retrieve soil moisture and roughness from C-band radar data. *Remote Sensing of Environment* 84, pp. 42-52.

# Summary

The earth's precious water sources are under pressure due to climate change and population pressure, increasing the demands for drinking water and irrigation. Water availability is essential for the world's food production, currently under threat. Too much water, however, can destroy fertile soils by erosion or flooding. Knowledge about the spatial and temporal variation of soil moisture is indispensable to predict and prevent such hazards. There is an urgent need in the fields of earth sciences, meteorology, hydrology, agriculture and global change modelling for operational models that can accurately predict soil moisture patterns in space and time. High spatial and temporal variability of soil moisture and its low degree of autocorrelation complicate the modelling using process-based models.

The aim of this research was to evaluate the performance of different methods that estimate top soil moisture patterns in space and time. Field measurements, process-based modelling and remote sensing based modelling were evaluated. Additionally, a data assimilation approach that combines the advantages of each method for operational soil moisture modelling was developed and evaluated. The predictions of top soil moisture (0-15 cm below the soil surface) were done at a specific spatial resolution of 125 m and timesteps of 1 hour. The main research question was defined as:

*Top soil moisture patterns in space and time can be estimated using field methods, process-based models and remote sensing data. What is the performance, in terms of accuracy, support and coverage of operational spatio-temporal estimation of top soil moisture, of each method separately and a combined approach that uses a particle filter data assimilation algorithm?*

The term support is defined here as the area (or volume) and time interval for which the measured properties are considered homogeneous, and for which only the average value is measured and not the variation within. Coverage is defined as the sampling intensity in space and/or time.

In this research three study sites, Barrax (Spain), Sehoul (Morocco) and La Peyne (France) were used for different purposes. The Barrax field site is located in the La-Mancha region in Spain. This flat agricultural area shows a large contrast between pivot irrigated crops and dry areas, which made it very suitable for the evaluation of a remote sensing derived surface energy balance model. During the ESA funded SPARC 2004 field campaign input data for the surface energy balance model was collected, which makes this a "data rich" area. Because the water balance in this region is human controlled, the site has not been used for soil moisture modelling. Agriculture in the Sehoul study area is more dependent on precipitation, which made it interesting for the measurement and modelling of soil moisture patterns. The study area is located in the north of the agricultural community of Sehoul in Morocco, approximately 20 km south-east of Rabat. Although the climate is comparable with the Barrax study area, the land use is very different. In the Sehoul study area land use comprises rainfed wheat, maize and

horticulture. Some traditional irrigation is present. Because soils are relatively homogeneous with low spatial variation and little relief, this site was chosen for soil moisture modelling. Meteorological measurements, soil moisture measurements and land cover mapping were done during several field campaigns from 2003 to 2006. Nevertheless, this study area is 'data poor' in the sense that only inexpensive practical measurements have been done and the use of remote sensing is necessary for the spatio-temporal predictions of soil moisture. The La Peyne study area is only used in a case study on DEM generation using remote sensing. The site is located in southern France, approximately 60 km west of the city of Montpellier. This area was selected because a large set of high quality aerial photographs was available as well as images from the Advanced Spaceborne Thermal Emission and Reflection Radiometer (ASTER). Furthermore, a large ground truth database exists for this area.

In this study, field measurements of top soil moisture were done using Time Domain Reflectometry (TDR). The instrument has an error of  $0.03 \text{ m m}^{-1}$ . The measurements for a field of 1 ha show standard deviations of less than  $0.03 \text{ m m}^{-1}$ . During and shortly after rainfall events the standard deviations are higher. Although the uncertainty of field measurements is relatively low, the lateral support of the TDR measurements is also low,  $0.002 \text{ m}^2$ , requiring many measurements for a good coverage in space and time. Also the vertical coverage of the field measurements is low, typically between 0 and 15 cm. The choice to make more measurements within the soil profile is often a trade-off with the choice to increase the lateral coverage, depending on the number of instruments. The temporal coverage can be increased by using data loggers.

The process-based Soil Moisture System (SOMS) model was developed in this research. The model was specifically developed for the integration of a remote sensing based surface energy balance model at the scale of an agricultural community. The SOMS model estimates the evolution of top soil moisture patterns for agricultural and semi-natural areas after rainfall events. Process-based models have a lateral support that depends on their resolution. In the case of the SOMS model, the lateral support is  $15625 \text{ m}^2$  ( $125 \text{ m}$  gridcells). The model calculates the volumetric moisture content (VMC) in a soil profile of 90 cm with timesteps of 1 hour for each gridcell in an area of  $50 \text{ km}^2$ . This gives this method a good lateral, vertical and temporal coverage. The uncertainty depends on the location in the modelled area, because the model has been calibrated for a limited number of locations, using PEST. The only source of spatial variation introduced in the process-based model is the stratification of input data and parameters, using a map with unique soil type and land use class combinations. Modelled VMC, however, showed a good goodness of fit compared to independent TDR measurements at locations other than the measurements used for calibration. SOMS is capable of predicting top soil moisture with a RMSE between  $0.007 \text{ m m}^{-1}$  and  $0.037 \text{ m m}^{-1}$  for agricultural areas in the Sehoul study area in winter 2004. For dry periods, the accuracy of the modelled top soil moisture is within the reported measurement accuracy of the TDR, which is  $0.03 \text{ m m}^{-1}$ .

Optical and thermal remote sensing can be used to estimate soil moisture patterns in space by using empirical, non-linear, relationships between surface temperature, vegetation indices and soil moisture content. In order to obtain accurate quantities of soil moisture, the empirical functions should be calibrated to compensate for differences in atmospheric conditions, vegetation cover, land cover type, topography and meteorological variables. On the other hand, remote sensing can provide spatial input data for process-based models, e.g. land cover data, albedo and evapotranspiration. In this research remote sensing was used to derive

surface temperature, emissivity, albedo, fractional vegetation cover, Leaf Area Index, NDVI, surface aerodynamic parameters and elevation. The lateral support of remote sensing methods depends on the resolution of the sensor. The lateral coverage is large, but the vertical coverage is low. The temporal coverage is low for high and medium resolution imagery (> 16 days) and high for coarse resolution imagery (< daily). An upscaling algorithm, DisTrad, was used to increase the resolution of surface temperature derived from the Moderate Resolution Imaging Spectroradiometer (MODIS) and ASTER by correlating low resolution temperature images with high resolution NDVI images calculated with data from the same platform. This algorithm is able to increase the resolution of the temperature image, but also its uncertainty.

For the integrated approach, which uses field measurements (TDR), a process-based model (SOMS) and remote sensing data from MODIS, a residual resampling particle filter data assimilation algorithm has been implemented. The algorithm integrates actual evapotranspiration (AET) derived from remote sensing using error propagation scenarios of the Surface Energy Balance System (SEBS) surface energy balance model with error propagation scenarios of SOMS.

The SEBS algorithm was implemented with the PCRaster Python library. SEBS calculates the energy balance terms, relative evaporation, evaporative fraction and evapotranspiration flux for all pixels of a remote sensing image, using its optical and thermal bands, in combination with meteorological measurements, radiation measurements and additional field data, when available.

The uncertainty of AET predicted by SEBS has been estimated for two error propagation scenarios. The SEBS – Large Error Scenario assumes that the measurement and upscaling of radiometric surface temperature, using the DisTrad procedure, induces a large error compared to other error sources. The standard deviation of AET estimates in this scenario is 0.02 cm hour<sup>-1</sup>. The SEBS – Small Error Scenario assumes that only a small measurement error in surface radiometric temperature causes errors in SEBS estimates. This results in AET estimates with an average standard deviation of 0.004 cm hour<sup>-1</sup>.

Also the uncertainty in VMC and AET of SOMS predictions was estimated with two error propagation scenarios. The SOMS – Data Rich Scenario, in which all errors in field measurements, maps and satellite data are modelled, shows an average RMSE of 0.02 m m<sup>-1</sup> compared to field measurements of VMC. The results also show that uncertainty in VMC modelled with this scenario are in the same order of magnitude as the uncertainty of field TDR measurements, averaged for an agricultural parcel. The level of uncertainty of this scenario of the SOMS model can be acceptable for many applications. The SOMS – Data Rich Scenario is well capable of accurately estimating soil moisture conditions after rainfall events. The goodness of fit values are comparable with the deterministic model results, indicating that there are no large non-linear responses in the error propagation model. The average standard deviation in estimated AET is 0.0006 cm hour<sup>-1</sup>. The SOMS – Data Poor Scenario, which assumes that the only data is available from remote sensing, land use and soil maps and a meteorological station, shows an average RMSE of 0.05 m m<sup>-1</sup> for the predicted VMC, compared to field measurements. With this scenario SOMS also predicts the trends well when compared to field measurements, with an average r<sup>2</sup> of 0.75. The goodness of fit measures give worse results compared to the SOMS – Data Rich Scenario. Although the uncertainty bands are much wider, most field measurements fall within one standard deviation from the predicted average VMC. Compared to the SOMS – Data Rich Scenario, the standard deviation is about seven times higher in the SOMS – Data Poor Scenario. The average standard deviation in estimated AET is 0.004 cm hour<sup>-1</sup>. This

scenario can be used when field data on soil moisture and soil physical data is lacking as is the case in many data poor areas in the world. This scenario is able to predict patterns and trends, although the absolute accuracy is lower than for the SOMS – Data Rich Scenario.

The particle filter approach reduces the variance of VMC estimated by the SOMS model, using SEBS filter data, in most of the cases. In all these cases, however, the reduction is small. The SOMS – Data Rich Scenario does not show significant improvement for both SEBS filter data scenarios, compared to the error propagation results without filtering. The SOMS – Data Poor scenarios, however, show improvements at some locations. An evaluation of the particle filter revealed that its successful application depends on a number of factors: the number and distribution of filter moments, the distance between the probability density function of the filter data and model prediction of the filter variable, knowledge of errors in variables and parameters, strength of the correlation between filter data and the objective variable, distribution of the filter data, spatial variability of the filter data and the number of particles.

It can be concluded that the use of a particular method for the derivation of soil moisture patterns in space and time depends on the specific demands of the application in terms of support and coverage and required accuracy of the estimates. Field measurements are well applicable in studies of in-situ top soil moisture estimation at the scale of individual plots. For the prediction of soil moisture at specific locations in an agricultural area, a calibrated process-based soil moisture model gives the best results. For applications demanding spatially distributed, operational, soil moisture predictions, the assimilation of all available data, either remote sensing data or field measurements, in a process-based model can benefit from the advantages of each method separately. In this case, the particle filter algorithm used in this study, can give good results when the above mentioned factors for successful filtering are considered. Further research is needed to confirm this.

The availability of field measurements of soil moisture and high resolution, cloudless, remote sensing images with a good temporal coverage remains a problem. Research should focus on the optimal use of the various datasets and satellite images available at various spatial and temporal resolutions in order to provide operational models for the many environmental problems that we are facing. New data assimilation algorithms can play an important role in this research.

# Samenvatting

## Kwantificering van bodemvochtpatronen

*Evaluatie van veldmethoden, proces-gebaseerde modellering, remote sensing en een geïntegreerde benadering*

Klimaatveranderingen en bevolkingsdruk zorgen voor een toename in de vraag naar drinkwater en water voor irrigatie, met als gevolg dat de waterbeschikbaarheid onder druk komt te staan. Waterbeschikbaarheid is belangrijk voor de wereld voedselproductie, die momenteel onder druk staat. Te veel water, echter, kan vruchtbare bodems verwijderen door erosie en overstromingen. Begrip van de ruimtelijke en temporele variatie van bodemvocht is noodzakelijk om de schadelijke effecten van dergelijke processen te kunnen voorspellen en te voorkomen. Binnen de aardwetenschappen, meteorologie, hydrologie, landbouwkunde en studies naar global change, bestaat een dringende behoefte aan operationele modellen die nauwkeurig bodemvochtpatronen in ruimte en tijd kunnen voorspellen. De hoge ruimtelijke en temporele variabiliteit van bodemvocht en complexe ruimtelijke autocorrelatie bemoeilijken echter het modelleren van bodemvocht door middel van proces gebaseerde modellen.

Het doel van deze studie was het evalueren van de performance van verschillende methoden die gebruikt kunnen worden voor de bepaling van bodemvochtpatronen aan het aardoppervlak in ruimte en tijd. Veldmetingen, proces gebaseerde modelleren en remote sensing gebaseerde modelleren werden geëvalueerd. Verder werd een data assimilatie benadering ontwikkeld en geëvalueerd die de voordelen van elke methode combineert voor het operationeel modelleren van bodemvocht. De bodemvochtvoorspellingen aan het oppervlak (0-15 cm onder het maaiveld) werden gedaan met een specifieke resolutie van 125 m en tijdstappen van 1 uur, wat overeenkomt met processen die gerelateerd zijn aan landbouwactiviteiten in het studiegebied. De centrale onderzoeksvraag luidt:

*Ruimtelijke en temporele patronen van bodemvocht bij het aardoppervlak kunnen worden bepaald met veldmetingen, proces gebaseerde modellen en remote sensing data. Wat is de performance, in termen van nauwkeurigheid, support en coverage, voor operationele, ruimtelijk-temporele voorspellingen van bodemvocht aan het oppervlak, voor iedere methode apart en een gecombineerde benadering die een particle filter data assimilatie algoritme gebruikt?*

De term *support* is gedefinieerd als het oppervlak (of volume) en tijdsinterval waarvoor de gemeten eigenschap homogeen kan worden beschouwd en waarvoor alleen de gemiddelde waarde is gemeten en niet de variatie er binnen.

Het onderzoek heeft plaatsgevonden in drie studiegebieden: Barrax (Spanje), Sehoul (Marokko) en La Peyne (Frankrijk). De gebieden zijn voor verschillende onderdelen van het onderzoek gebruikt. Barrax ligt in de La Mancha regio in Spanje. In het vlakke landbouwgebied

zijn grote contrasten te zien tussen pivot geïrrigeerde gewassen en droge gebieden, wat het gebied erg geschikt maakt voor de evaluatie van een remote sensing gebaseerd oppervlakte energiebalans model. Tijdens de door ESA gefinancierde SPARC 2004 veldcampagne werden metingen verricht voor het oppervlakte energiebalans model. Hierdoor is dit studiegebied “rijk aan data” te noemen. Omdat de waterbalans in dit gebied door de mens wordt bepaald, kan het niet worden gebruikt voor het modelleren van bodemvocht. Landbouw in het Sehoul studiegebied is afhankelijk van neerslag, waardoor het gebied interessant is voor het meten en modelleren van bodemvochtpatronen. Het studiegebied ligt in het noorden van de gemeente Sehoul in Marokko, ongeveer 20 km ten zuidoosten van de hoofdstad Rabat. Hoewel het klimaat vergelijkbaar is met het Barrax studiegebied, is het landgebruik erg verschillend. In Sehoul bestaat het landgebruik voor uit door neerslag gevoede tarwe, mais en tuinbouw. Ook enkele traditioneel geïrrigeerde percelen zijn er te vinden. Omdat de bodems relatief homogeen zijn en er weinig reliëf is, is dit gebied gekozen voor het modelleren van bodemvocht. Tijdens verschillende veldcampagnes tussen 2003 en 2006 zijn meteorologische metingen en bodemvochtmetingen verricht en is het landgebruik gekarteerd. Desondanks kan het gebied beschouwd worden als “arm aan data”, omdat er alleen goedkope praktische metingen zijn gedaan en het gebruik van remote sensing noodzakelijk is voor ruimtelijk-temporele voorspellingen van bodemvocht. Het La Peyne studiegebied is alleen gebruikt in de case study over DEM extractie uit remote sensing data. Het gebied is geselecteerd omdat een grote hoeveelheid luchtfoto's en satellietbeelden beschikbaar zijn. Tevens is er een uitgebreide database met veldgegevens beschikbaar.

In dit onderzoek zijn veldmetingen van bodemvocht verricht met behulp van Time Domain Reflectometry (TDR). Het instrument heeft een meetfout van  $0,03 \text{ m m}^{-1}$ . De standaard deviaties van alle metingen gemiddeld over een veld van 1 ha zijn kleiner dan  $0,03 \text{ m m}^{-1}$ . Tijdens en na regenbuien zijn de standaard deviaties groter. Hoewel de onzekerheid van de veldmetingen relatief klein is, is de horizontale support van de TDR metingen ook klein ( $0,002 \text{ m}^2$ ), waardoor veel metingen nodig zijn voor een goede coverage in ruimte en tijd. Ook de verticale coverage van de veldmetingen is klein, typisch tussen 0 en 15 cm. Het is een afweging om meer metingen in het bodemprofiel te maken ten op zichte van meer metingen in de ruimte, afhankelijk van het aantal beschikbare meetinstrumenten. De temporele coverage kan worden verbeterd door gebruik te maken van dataloggers.

Het proces gebaseerde Soil Moisture System (SOMS) model is speciaal ontwikkeld voor dit onderzoek, om de integratie van een remote sensing gebaseerd oppervlakte energy balansmodel mogelijk te maken. Het SOMS model berekent de evolutie van het bodemvocht na een regenbui voor landbouwgebieden en semi-natuurlijke gebieden. Proces gebaseerde modellen hebben een support die bepaald wordt door de gekozen resolutie. Voor het SOMS model is de horizontale support  $15625 \text{ m}^2$  (125 m gridcells). Het model berekent het volumetrisch vochtgehalte in een bodemprofiel van 90 cm met tijdstappen van 1 uur voor iedere cel in een gebied van  $50 \text{ km}^2$ . Hierdoor heeft deze methode een goede horizontale, verticale en temporele coverage. De onzekerheid van de voorspellingen hangen echter af van de locatie in het gemodelleerde gebied, omdat het model is gekalibreerd voor een beperkt aantal locaties, door middel van PEST. De enige bron van ruimtelijke variatie in het model is de stratificatie van input data en parameters door middel van units met een unieke landgebruik en bodemtype combinatie. Desondanks komt het gemodelleerde bodemvocht aan het oppervlak goed overeen met waarden gemeten op andere locaties dan de kalibratiepunten. Met SOMS is het mogelijk om bodemvocht aan het oppervlak te voorspellen met een RMSE tussen  $0,007 \text{ m m}^{-1}$  en  $0,037 \text{ m m}^{-1}$  voor landbouwgebieden in

het Sehoul studiegebied in de winter van 2004. Voor droge periodes is de nauwkeurigheid van het gemodelleerde bodemvocht vergelijkbaar met de meetfout van de TDR.

Optische en thermische remote sensing kunnen worden gebruikt om bodemvocht patronen te voorspellen in de ruimte met behulp van empirische, non-lineaire, relaties tussen temperatuur van het aardoppervlak, vegetatie indices en bodemvochtgehalte. Om de absolute hoeveelheid bodemvocht te berekenen, moeten de empirische functies worden gekalibreerd om te compenseren voor verschillen in atmosferische condities, vegetatiebedekking, type landgebruik, reliëf en meteorologische variabelen. Remote sensing kan echter ook gebruikt worden voor de ruimtelijke input van proces gebaseerde modellen, bijvoorbeeld landgebruik, albedo en evapotranspiratie. De horizontale coverage is groot, terwijl de verticale coverage klein is. De temporele coverage is klein voor hoge en medium resolutie beelden (< 16 dagen) en groot voor beelden met een grove resolutie ( $\leq$  dagelijks). Een opschalingsalgoritme, zoals DisTrad, kan gebruikt worden om de resolutie van beelden van oppervlakte temperatuur te verhogen, echter ten koste van de nauwkeurigheid.

Voor de geïntegreerde benadering, waarbij veldmetingen (TDR), een proces gebaseerd model (SOMS) en remote sensing data van de Moderate Resolution Imaging Spectrometer (MODIS) wordt gebruikt, is een residual resampling particle filter data assimilation algoritme geïmplementeerd. Het algoritme integreert actuele evapotranspiratie (AET), berekend met foutenpropagatie scenario's van het Surface Energy Balance System (SEBS) model, met foutenpropagatie scenario's van SOMS. De onzekerheid van AET berekend met SEBS is geschat voor twee foutenpropagatie scenario's. Het SEBS – Large Error Scenario veronderstelt dat de meting en opschaling van radiometrische oppervlakte temperatuur met DisTrad de grootste foutenbronnen zijn. De standaard deviatie van AET in dit scenario is gemiddeld  $0,02 \text{ cm uur}^{-1}$ . Het SEBS – Small Error Scenario veronderstelt dat er slechts een kleine meetfout is in de bepaling vanuit het remote sensing beeld. Dit scenario resulteert in een standaard deviatie van AET van  $0,004 \text{ cm uur}^{-1}$ . Ook de onzekerheid in bodemvochtgehalte en AET voorspeld door het SOMS model zijn geschat door middel van twee foutenpropagatie scenario's. Het SOMS – Data Rich Scenario, waarin alle foutenbronnen in veldmetingen, kaarten en remote sensing data zijn gemodelleerd, geeft een gemiddelde RMSE van  $0,02 \text{ m m}^{-1}$  vergeleken met veldmetingen van bodemvocht. De resultaten laten ook zien dat de onzekerheid in bodemvocht gemodelleerd met dit scenario overeen komt met de onzekerheid in veldmetingen, gemiddeld voor een akker. De nauwkeurigheid van dit scenario kan acceptabel zijn voor veel toepassingen. De goodness of fit waarden met de veldmetingen zijn te vergelijkbaar met de deterministische modelresultaten, wat betekent dat er geen grote non-lineaire respons is in het foutenpropagatie model. De gemiddelde standaard deviatie van AET is  $0,0006 \text{ cm uur}^{-1}$ . Het SOMS – Data Poor Scenario veronderstelt dat er alleen remote sensing data, een landgebruikskaart, een bodemkaart en een meteorologisch station beschikbaar is. Dit scenario geeft een RMSE van  $0,05 \text{ m m}^{-1}$  voor het voorspelde bodemvochtgehalte, in vergelijking met veldmetingen. Trends worden voorspeld met een gemiddelde  $r^2$  van  $0,75$ . De goodness of fit waarden zijn slechter in vergelijking met het SOMS – Data Rich Scenario. Hoewel de onzekerheidsbanden breder zijn, vallen de veldmetingen binnen 1 standaard deviatie van de voorspelling van het bodemvocht. Vergelijken met het SOMS – Data Rich Scenario is de standaard deviatie ongeveer zeven keer hoger in het SOMS – Data Poor Scenario. De gemiddelde standaard deviatie in AET is  $0,004 \text{ cm uur}^{-1}$ . Dit scenario kan worden gebruikt als veldgegevens over bodemvocht en bodemfysica ontbreken,

zoals in veel gebieden op de wereld. Met dit scenario is het mogelijk om patronen en trends te berekenen, hoewel de absolute nauwkeurigheid lager is dan bij het SOMS – Data Rich Scenario.

In de meeste gevallen reduceert het particle filter algoritme met SEBS filter data de onzekerheid in het door SOMS voorspelde bodemvochtgehalte. De reductie is echter klein. Het SOMS – Data Rich Scenario laat geen significante verbetering zien voor beide SEBS filter data scenario's, in vergelijking met de resultaten foutenpropagatie zonder het particle filter algoritme. De SOMS – Data Poor scenario's laten echter verbetering zien op sommige locaties in het studiegebied. Een analyse van de performance van het particle filter algoritme liet zien dat het succes van het algoritme afhangt van een aantal factoren: het aantal en de verdeling in de tijd van filter momenten, de afstand tussen de probability density function van de filter data en de modelvoorspellingen, kennis van onzekerheid in variabelen en parameters, grootte van de correlatie tussen filter data en de doelvariabele, verdeling van de filter data, ruimtelijke variabiliteit van filter data en het aantal particles.

Er kan worden geconcludeerd dat het gebruik van een bepaalde methode om bodemvochtpatronen in ruimte en tijd te bepalen afhangt van de specifieke eisen van de toepassing in termen van support en coverage, in relatie met de onzekerheid van de methode. Veldmetingen zijn goed toepasbaar voor studie betreffende in-situ bepaling van het bodemvochtgehalte op de schaal van individuele plotjes. Voor de voorspelling van bodemvocht op bepaalde locaties in een landbouwgebied kan het best een gekalibreerd proces gebaseerd model worden gebruikt. Voor toepassingen die ruimtelijk gedistribueerde, operationele, bodemvochtvoorspellingen nodig hebben, kan de assimilatie van alle beschikbare data, zowel remote sensing data als veldgegevens, in een proces gebaseerd model de beste resultaten geven door de voordelen van de verschillende methoden te combineren. In dit geval kan een particle filter algoritme, zoals gebruikt in dit onderzoek, goede resultaten geven, mits bovengenoemde factoren in ogenschouw worden genomen. Nader onderzoek is nodig om dit te bevestigen.

Omdat de beschikbaarheid van veldmetingen van bodemvocht en hoge resolutie, wolkenloze remote sensing beelden met een goede temporele coverage een probleem blijft, moet vervolgonderzoek zich toespitsen op het optimale gebruik van de vele beschikbare datasets en remote sensing beelden om operationele modellen te ontwikkelen ter voorspelling en voorkoming van milieuproblemen. Nieuwe data assimilatie algoritmen kunnen een belangrijke rol spelen in dit onderzoek.

# Résumé

## **“Quantification des variations de l’humidité de surface du sol”**

*Evaluation des méthodes de mesure sur le terrain, la modélisation basée sur des processus, la télédétection et l’approche intégrée.*

De nos jours, les ressources en eau sont soumises à de multiples pressions dues aux effets des changements climatiques et à la poussée démographique entraînant un accroissement de la demande en eau potable et d’irrigation. La production alimentaire mondiale, étroitement liée aux ressources en eau est actuellement plus menacée. Un excès d’eau, peut ainsi affecter négativement la fertilité des sols par érosion hydrique ou par inondation. Pour prévenir de tels dangers, la connaissance de la variabilité spatio-temporelle de l’humidité du sol s’avère indispensable. Ainsi, on note un besoin urgent dans le champ des sciences de la terre, la météorologie, l’hydrologie, l’agriculture et la modélisation du changement global en terme de modèles opérationnels qui peuvent prévoir, précisément, la variabilité spatio-temporelle de l’humidité. La forte variabilité spatio-temporelle de l’humidité du sol et son faible degré d’auto-corrélation complique davantage la modélisation de ces processus.

Le but de cette recherche est d’évaluer la performance de différentes méthodes d’estimation de variabilité spatiotemporelle de l’humidité de surface. Les mesures de terrain, la modélisation des processus et la modélisation à base de la télédétection ont été évaluées. En outre, l’approche d’assimilation des données qui combine les avantages de chaque méthode pour une modélisation opérationnelle de l’humidité du sol a été développée et évaluée. Les prévisions de l’humidité de surface (0-15 cm de la surface du sol) ont été faites avec une résolution spatiale spécifique de 125 m et à un pas de temps de 1 heure. La question principale de cette recherche est définie comme suit:

*La variabilité spatio-temporelle de l’humidité de surface peut être estimée par des mesures de terrain, des modèles basés sur des processus et des données de télédétection. Quelle est la performance, en terme de précision, de support et de couverture d’une estimation spatio-temporelle opérationnelle de l’humidité de surface, pour chaque méthode à part et une approche combinée qui utilise un algorithme d’assimilation de données à filtre particulière?*

Dans cette recherche, trois sites d’étude, Barrax (en Espagne), Sehoul (au Maroc) et la Peyne (en France) ont été choisis à des fins différentes. Le site de Barrax est situé dans la région La-Mancha en Espagne. Cette plaine agricole a montré un large contraste entre les champs irrigués à pivot et les zones sèches, ce qui la rend très appropriée pour l’évaluation d’un modèle de bilan énergétique de surface dérivé de la télédétection. Les données d’entrée du modèle du bilan énergétique de surface ont été collectées durant la campagne de terrain SPARC 2004 financée par ESA, ce qui rend ce site « riche en données ». Le site n’a pas été utilisé pour la modélisation de l’humidité du sol du fait que le bilan d’eau dans cette région est contrôlé par la population. Au niveau du

site de Sehoul, l'agriculture est beaucoup plus dépendante des précipitations, ce qui rend ce site plus intéressant pour les mesures et la modélisation des variations de l'humidité du sol. La zone d'étude est située au nord de la commune rurale de Sehoul (Maroc), à environ 20 km au sud-est de Rabat. Bien que le climat soit comparable à celui de Barrax, l'utilisation des terres reste très différente. Dans le site de Sehoul, l'utilisation des terres est dominée par la céréaliculture en bour, le maïs et l'horticulture. L'irrigation traditionnelle est très limitée. Etant donné la présence des sols relativement homogènes avec une faible variabilité spatiale et un faible relief, ce site a été choisi pour la modélisation de l'humidité du sol. Les mesures météorologiques et de l'humidité du sol en plus de la cartographie du couvert végétal ont été réalisées durant plusieurs campagnes de terrain entre 2003 et 2006. Néanmoins, ce site est pauvre en données, dans le sens où seulement des mesures pratiques peu coûteuses ont été investiguées et l'utilisation de la télédétection est nécessaire pour des prévisions spatio-temporelles de l'humidité du sol. Le site La Peyne a été utilisé comme une étude de cas pour la génération d'un MNT par télédétection. Ce site est situé au sud de la France, environ 60 km à l'ouest de Montpellier. Cette zone d'étude a été sélectionnée pour la raison qu'une large série de photos aériennes de haute qualité sont disponibles, ainsi que des images satellites ASTER (*Advanced Spaceborne Thermal Emission and Reflection Radiometer*). En outre, une importante base de données est également disponible dans ce site.

Dans cette étude, les mesures in situ de l'humidité de surface du sol ont été réalisées à l'aide d'un TDR (Time Domain Reflectometry) ayant une erreur de  $0,03 \text{ m m}^{-1}$ . Les mesures effectuées sur une parcelle de 1ha ont montré des écarts type inférieurs à  $0,03 \text{ m m}^{-1}$ . Durant et juste après la pluie, les écarts type sont élevés. Bien que l'incertitude des mesures de terrain soit relativement faible, le support latéral des mesures à l'aide du TDR est aussi faible,  $0,002 \text{ m}^2$ , exigeant un grand nombre de mesures pour une bonne répartition dans l'espace et dans le temps. De même, la répartition verticale des mesures dans le sol est faible, typiquement entre 0 et 15 cm. Le choix d'augmenter le nombre de mesures dans le profil du sol est souvent lié au choix d'augmenter la répartition latérale, selon le nombre d'instruments. La répartition temporelle peut être augmentée par l'utilisation des enregistreurs (data loggers).

Développé dans le cadre de cette recherche, le modèle SOMS (process-based Soil Moisture System) a été spécialement conçu pour intégrer le modèle du bilan énergétique de surface, basé sur la télédétection, à l'échelle de la commune rurale de Sehoul. Ce modèle permet d'estimer l'évolution de l'humidité de surface du sol dans les zones agricoles et semi-naturelles après les événements pluvieux. Les modèles basés sur des processus ont un support latéral qui dépend de leurs résolutions. Dans le cas du modèle SOMS, le support latéral est de  $15625 \text{ m}^2$  (cellule de 125 m). Le modèle calcule l'humidité volumétrique (VMC) dans un profil de sol de 90 cm avec un pas de temps d'une heure pour chaque cellule, sur une surface de  $50 \text{ km}^2$  ce qui donne une bonne répartition latérale, verticale et temporelle. L'incertitude dépend de l'emplacement dans la zone modélisée car la calibration du modèle a été faite pour un nombre limité de points, en utilisant PEST.

La seule source de variation introduite dans le modèle est la stratification des données d'entrée et des paramètres, en utilisant une carte de combinaisons d'un seul type de sol et des classes d'utilisation du sol. L'humidité volumétrique (VMC) modélisée, comparée avec les mesures faites au TDR au niveau de différents points, a cependant montré des résultats plus bons que les mesures utilisés pour la calibration. Le modèle SOMS s'est révélé capable de donner des prévisions de l'humidité de la surface du sol avec un RMSE qui varie entre  $0.007 \text{ m m}^{-1}$

et  $0,037 \text{ m m}^{-1}$  pour les zones agricoles de la région des Sehou (hiver 2004). Pour les saisons sèches, la précision de l'humidité du sol modélisée est comprise dans l'intervalle de précision de mesure reportée du TDR ( $\pm 0,03 \text{ m m}^{-1}$ ).

La télédétection optique ou thermique peut être utilisée pour estimer la variation de l'humidité du sol dans l'espace par l'utilisation des relations empiriques et non-linéaires entre la température de la surface, les indices de végétation et la teneur du sol en humidité. Dans le but d'obtenir des quantités précises d'humidité du sol, les fonctions empiriques doivent être calibrées pour compenser les différences dans les conditions atmosphériques, le couvert végétal, le type du couvert végétal, la topographie et les variables météorologiques. D'autre part, la télédétection peut fournir des données d'entrée spatiales pour des modèles basés sur des processus (ex. les données du couvert végétal, l'albédo et l'évapotranspiration). Dans notre recherche, la télédétection a été utilisée pour dériver la température de la surface, l'émissivité, l'albédo, la fraction du couvert végétal, l'index foliaire, le NDVI, l'élévation et les paramètres aérodynamiques de surface. Le support latéral des méthodes de télédétection dépend de la résolution du capteur. La couverture latérale est large, mais la couverture verticale est faible. La couverture temporelle est faible pour les images à résolution élevée et moyenne ( $>16$  jours) et élevée pour les images à faible résolution ( $< \text{jour}$ ). Un algorithme d'agrandissement d'échelle, DisTrad, a été utilisé pour augmenter la résolution de la température de surface, dérivée de MODIS (Moderate Resolution Imaging Spectroradiometer) et ASTER en corrélant les images de température à faible résolution avec des images de NDVI à haute résolution, calculées avec des données de la même plateforme. Cet algorithme est capable d'augmenter la résolution de l'image de température, mais aussi son incertitude.

Pour l'approche intégrée utilisant les mesures faites au TDR, le modèle basé sur des processus (SOMS) et les données de télédétection de MODIS, un algorithme d'assimilation de données, filtre particulaire à rééchantillonnage par résidu, a été appliqué. L'algorithme intègre l'évapotranspiration actuelle (AET) dérivée de la télédétection, utilisant les scénarios de propagation d'erreur du modèle de bilan énergétique de surface (Surface Energy Balance System, SEBS) avec les scénarios de propagation d'erreur de SOMS.

L'algorithme SEBS a été exécuté avec la bibliothèque PCRaster Python. SEBS calcule les conditions du bilan énergétique, l'évaporation relative, la fraction d'évaporation et le flux d'évapotranspiration pour tous les pixels de l'image satellite, en utilisant ses bandes optique et thermique en combinaison avec les mesures météorologiques, les mesures du rayonnement et d'autres mesures de terrain, quand cela est possible.

L'incertitude de l'AET prévu par SEBS a été estimée pour deux scénarios de propagation d'erreurs. Le scénario SEBS à large erreur suppose que les mesures et l'agrandissement d'échelle de température radiométrique de surface, utilisant la procédure DisTrad, provoque une large erreur en comparaison avec d'autres sources d'erreur. L'écart type des estimations de l'AET dans ce scénario est de  $0,02 \text{ cm heure}^{-1}$ . Le scénario SEBS à petite erreur estime qu'une petite erreur de mesure de la température radiométrique de surface cause des erreurs dans les estimations de SEBS. Ceci résulte en des estimations d'AET avec un écart type moyen de  $0,004 \text{ cm heure}^{-1}$ .

Aussi, l'incertitude en VMC et AET des prévisions de SOMS est estimée avec deux scénarios de propagation d'erreur. Le scénario SOMS riche en données, dans lequel toutes les erreurs issues des mesures de terrain, des cartes et des données satellites sont modélisées, montre un RMSE moyen de  $0,02 \text{ mm}^{-1}$ , en comparaison avec le VMC mesuré sur le terrain. Les résultats montrent aussi que les incertitudes en VMC modélisée avec ce scénario sont du même ordre

de magnitude que l'incertitude moyenne des mesures avec le TDR, pour une parcelle agricole. Le niveau d'incertitude de ce scénario du modèle SOMS peut être acceptable pour plusieurs applications. Le scénario SOMS riche en données est bien capable d'estimer avec précision les conditions d'humidité du sol après les événements pluvieux. Les valeurs d'ajustement sont comparables aux résultats du modèle déterministic, indiquant qu'il n'ya pas de larges réponses non-linéaires dans le modèle de propagation d'erreurs. L'écart type moyen dans l'AET estimé est de  $0,0006 \text{ cm heure}^{-1}$ . Le scénario SOMS pauvre en données, qui suppose que les données sont seulement disponibles de la télédétection, la carte des sols, la carte d'occupation et la station météorologique, montre un RMSE moyen de  $0,05 \text{ m m}^{-1}$  pour le VMC prévu, en comparaison avec les mesures de terrain. En plus, avec ce scénario, SOMS prévoit bien les tendances quand elles sont comparées aux mesures de terrain, avec un  $r^2$  moyen de  $0,75$ . Les mesures d'ajustement donnent de plus mauvais résultats, comparés au scénario SOMS riche en données. Bien que les bandes d'incertitude soient beaucoup plus larges, la plupart des mesures de terrain font partie d'un écart type du VMC moyen prévu. Comparé au scénario SOMS riche en données, l'écart type est d'environ sept fois plus élevé dans le scénario SOMS pauvre en données. L'écart type moyen dans l'AET estimé est de  $0,004 \text{ cm heure}^{-1}$ . Ce scénario peut être utilisé quand les données de mesure de l'humidité du sol et les données physiques du sol manquent. C'est le cas de plusieurs régions pauvres en données dans le monde. Ce scénario est capable de prévoir les changements et les tendances même si la précision absolue est plus faible pour le scénario SOMS riche en données.

L'approche filtre particulière réduit la variance du VMC estimé par le modèle SOMS, utilisant les données du filtre SEBS dans la plupart des cas. Dans tous ces cas, la réduction est petite. Le scénario SOMS riche en données ne montre pas une amélioration importante pour les deux scénarios de données du filtre SEBS, comparée aux résultats de propagation d'erreur sans filtrage. Le scénario SOMS pauvre en données montre, cependant, des améliorations dans certains points. Une évaluation du filtre particulière a indiqué que la réussite de son application dépend d'un certain nombre de facteurs: le nombre et la distribution des moments du filtre, la distance entre la fonction de densité de probabilité des données du filtre et le modèle de prévision du filtre variable, la connaissance des erreurs dans les variables et les paramètres, le niveau de corrélation entre les données du filtre et la variable objective, la distribution des données du filtre, la variabilité spatiale des données du filtre et le nombre de particules.

En conclusion, l'utilisation d'une méthode particulière pour la dérivation des changements de l'humidité du sol dans l'espace et dans le temps dépend des demandes spécifiques de l'application en termes d'appui, de couverture et la précision des estimations demandée. Les mesures de terrain sont bien applicables dans des études d'estimation in-situ de l'humidité de surface du sol à l'échelle d'une parcelle. Pour les prévisions de l'humidité du sols dans les zones agricoles et à des lieux spécifiques, un modèle calibré d'humidité du sol donne de bons résultats. Pour les applications demandant des prévisions d'humidité du sol spatialement distribuées et opérationnelles, l'assimilation de toutes les données disponibles, soit des données de télédétection ou des mesures de terrain, dans un modèle basé sur des processus, peut profiter des avantages de chaque méthode séparément. Dans ce cas, l'algorithme à filtre particulière utilisé dans cette étude peut donner de bons résultats, quand les facteurs sus-mentionnés pour un filtrage réussi sont considérés. Ainsi, une autre recherche doit confirmer ceci.

La disponibilité des mesures de terrain de l'humidité du sol et des images satellites à haute résolution et sans nuages avec une couverture dans le temps reste un problème. La recherche

doit focaliser sur l'utilisation optimale de diverses séries de données et des images satellites disponibles à des résolutions spatio-temporelles différentes, dans le but de fournir des modèles opérationnels pour le nombre élevé de problèmes environnementaux que nous affrontons. De nouveaux algorithmes d'assimilation de données peuvent jouer un rôle important dans cette recherche.



# القياس الكمي لتغيرات رطوبة سطح التربة

## تقييم منهجيات القياس الميداني، النمذجة المعتمدة على أساليب الاستشعار عن بعد و النهج المتكامل.

تخضع الموارد المائية لمجموعة من الإكراهات ترتبط أساساً بالتغيرات المناخية من جهة، وبالضغط الديمغرافي و ما يرافقه من تزايد الطلب على الماء الشروب وماء السقي من جهة ثانية. إن تزايد الطلب على إنتاج الغذاء العالمي يجعل الموارد المائية معرضة أكثر لضغوط الاستغلال. يضاف إلى ذلك أن الوفرة الزائدة للماء يمكن أن تلعب دوراً سلبياً في خصوبة التربة عبر الفيضانات والتعرية المائية التي يمكن أن تسببها.

ولتحديد طبيعة الأخطار المتوقعة و الحد منها، نرى أن معرفة التغيرات المجالية المؤقتة لرطوبة سطح التربة تشكل أمراً مهماً، لهذا هناك حاجة ماسة في مجال علوم الأرض، علوم التنبؤات المتعلقة بالأحوال الجوية، الهيدرولوجية، الفلاحة ونمذجة التغيرات العالمية لتطوير نماذج عملية يمكنها أن تنتبها بدقة بالتغيرات المجالية المؤقتة لرطوبة سطح التربة. إن هذه التغيرات و ضعف ارتباطها التلقائي يعقد أكثر نمذجة الأساليب.

يهدف البحث إلى تقييم أداء أفضل المناهج لتقدير التغيرات المجالية المؤقتة لرطوبة سطح التربة عبر القياسات الميدانية ونمذجة الأساليب من جهة، والنمذجة المعتمدة على تحليل صور الأقمار الصناعية من جهة ثانية. إضافة إلى ذلك تم تطوير و تقييم مقارنة تعتمد على تقليد المعطيات التي تمزج إيجابيات كل منهجية من أجل نمذجة عملية لرطوبة التربة على عمق يتراوح بين 0 و 15 سم، وذلك بوضوح مجالي يقدر بنقطة كل 125 متر وبمجال زمني بحدود ساعة واحدة.

إشكالية البحث تتمثل في تحديد المنهجية الأفضل والأكثر دقة لاختيار نموذجي يسمح بتقدير التغيرات المجالية المؤقتة لرطوبة سطح التربة بواسطة القياسات الميدانية لاستخلاص نماذج مبنية على الأساليب أو بواسطة النمذجة المعتمدة على تحليل صور الأقمار الصناعية. ما هي إذن قوة الأداء من حيث الدقة، التحمل وتغطية التقديرات المجالية المؤقتة لرطوبة التربة لكل منهجية من جهة، ومقاربة تركيبية تعتمد على خوارزمية خاصة لتقليد المعطيات ( *algorithm* ) *d'assimilation de données à filtre particulaire* من جهة أخرى؟

لقد اعتمد البحث على ثلاث مواقع للدراسة ذات أهداف مختلفة في كل من أسبانيا و فرنسا و المغرب. الموقع الأول (باراكس) بإسبانيا-منطقة لامنتشا- و هو عبارة عن سهل زراعي يبدو فيه تفاوت كبير بين الحقول المسقية بالأذرع المحورية والمجالات الجافة، وهذا يناسب عملية تقييم نموذج الحصيلة الطاقية للسطح، المستخرجة من تحليل صور الأقمار الصناعية. وقد استعملت معطيات مستقاة من العمل الميداني SPARC لسنة 2004 و الممول من طرف ESA، مما يجعل هذا الموقع غنيا بالمعطيات. لكن الموقع لم يستعمل لنمذجة رطوبة التربة لأن الموارد المائية في المنطقة يتم تدبيرها من طرف السكان.

الموقع الثاني (السهول) بالمغرب، ويقع في شمال الجماعة القروية/السهول على بعد حوالي 20 كلم جنوب شرق الرباط. يتمتع هذا الموقع بمناخ شبيه بما هو عليه في باراكس الإسبانية لكن استعمال التربة جد مختلف حيث تغلب في السهول زراعة الحبوب البورية والذرة والبقوليات، مع مجال سقوي تقليدي محدود مجالياً. وقد تم إنجاز مجموعة من الدراسات المساعدة خلال الفترة 2003-2006 (القياسات المطرية، رطوبة التربة، خرائط الغطاء النباتي). لهذا اختير موقع السهول على الرغم من كونه فقير بالمعطيات حيث أنجزت فقط القياسات الأقل تكلفة. لذا، كان لا بد من استعمال تحليل صور الأقمار الصناعية من أجل التنبؤات المجالية لرطوبة سطح التربة.

الموقع الثالث (لابين) بفرنسا، ويقع على بعد حوالي 60 كلم غرب مدينة مونبلييه في الجنوب الفرنسي، استعملت فقط كدراسة حالة من أجل إنجاز نموذج رقمي للميدان MNT بواسطة الإشعار عن بعد، وذلك لتوفره على سلسلة كبيرة من الصور الجوية الجديدة بالإضافة إلى صور الأقمار الصناعية للموقع (نوع ASTER).

استعملنا في هذه الدراسة القياسات المحلية لرطوبة سطح التربة والتي أنجزت بواسطة TDR ذات هامش خطأ  $mm^{-1}$  0,03، حيث تمت القياسات فوق مساحة هكتار واحد مع انحراف معياري أقل من  $0,03 mm^{-1}$ . لكن خلال أو مباشرة بعد تساقط الأمطار الإنحراف المعياري يصبح مرتفعاً. مع أن عدم دقة القياسات الميدانية يبقى نسبياً صغيراً، فإن التحمل الجانبي للقياسات بواسطة TDR هو صغير أيضاً ( $0,002 m^2$ )، و يتطلب عدداً كبيراً من القياسات من

أجل توزيع مجالي و زمني جيد. التوزيع العمودي لقياسات رطوبة التربة هو أيضا ضعيف (ما بين 0 و 15سم). اختيار رفع عدد قياسات الرطوبة بالقطاع الترابي هو مرتبط برفع التوزيع الجانبي، و ذلك حسب عدد آلات القياس. بالنسبة للتوزيع الزمني، يمكن رفعه باستعمال آلات التسجيل (data loggers).

يسمح نموذج SOMS ( Process-based Soil Moisture System )، الذي تم تطويره في إطار هذا البحث من أجل دمج نموذج الحصيلة الطاقية لسطح التربة معتمدة على تحليل الصور الجوية لجامعة السهول، بتقدير تطور رطوبة سطح التربة بعد الأحداث المطرية في كل من المجال الزراعي والمجال الشبه طبيعي. إن النماذج المعتمدة على الأساليب لها تحمل جانبي مرتبط بوضوح الشاشة. النموذج SOMS له تحمل جانبي يقدر ب 15625م<sup>2</sup> (خلية 125م)، كما يسمح بحساب الرطوبة الحجمية (VMC) في قطاع ترابي عمقه 90 سم خلال مدة ساعة واحدة بالنسبة لكل خلية موزعة على مساحة 50 كلم<sup>2</sup>، مما يسمح بتوزيع جيد (مجال و زمني وعمودي). عدم اليقين يتوقف على الموقع في المنطقة الذي تمت فيه النمذجة لأن معايرة النموذج تمت وفق عدد محدود من الأماكن، باستعمال PEST. ويكون المصدر الوحيد للتغيرات هو تراتب المعطيات المدخلة باستعمال خريطة تركيبيية نوع ترابي واحد واستعمالات متعددة للتربة. وقد تمت مقارنة الرطوبة الحجمية التي تم نمذجتها بالقياسات المنجزة ميدانياً بواسطة TDR بالنسبة لمختلف النقاط، حيث أعطت نتائج أحسن من النتائج المستعملة للمعايرة. نموذج SOMS أبان على قدرته على إعطاء تنبؤات لرطوبة سطح التربة مع هامش للخطأ RMSE يتراوح بين 0,007 mm<sup>-1</sup> و 0,037 mm<sup>-1</sup> بالمجالات الزراعية لمنطقة/السهول (شطاء 2004). بالنسبة للفصول الجافة، دقة الرطوبة المنمذجة تتواجد ضمن مجال دقة القياس TDR ب (0,03 mm<sup>-1</sup> +/-).

كما يمكن استعمال تحاليل صور الأقمار الصناعية أو الحرارية لتقدير تغيرات رطوبة سطح التربة في المجال باستعمال العلاقات التجريبية بين حرارة السطح ومؤشر الغطاء النباتي ومنسوب رطوبة التربة. من أجل الحصول على قياسات دقيقة لرطوبة السطح، لابد من معايرة هذه العلاقات التجريبية من أجل تعويض الاختلافات على مستوى الظروف المناخية، الغطاء النباتي، نوع الغطاء النباتي، الطوبوغرافيا والمتغيرات الجوية. يضاف إلى ذلك أن الاستشعار عن بعد يمكن من إنتاج معطيات جديدة يمكن استعمالها في نماذج تعتمد على أساليب (الإشعاع والأليبدو والتغطية النباتية... إلخ). في هذا البحث، استعمل تحليل صور الأقمار الصناعية في استخراج حرارة السطح، الإشعاع، الأليبدو، NDVI، العلو و البارامترات الإيرودينامية السطح. التحمل الجانبي لتقنيات الاستشعار عن بعد مرتبط بدرجة وضوح المحسس. التغطية الجانبية تعد واسعة، لكن التغطية العمودية ضعيفة. التغطية الزمنية ضعيفة بالنسبة للصور ذات درجة وضوح جيدة ومتوسطة (< 16 يوما)، و مرتفعة بالنسبة للصور الضعيفة الوضوح (> يوم). و قد استعملت خوارزمية تكبير المقياس (Distrad) من أجل رفع درجة وضوح حرارة السطح المستخرجة من صور MODIS و ASTER عن طريق ربط صور الحرارة ذات الوضوح الضعيف بصور NDVI ذات الوضوح الجيد. هذه الخوارزمية قادرة على الرفع من درجة وضوح صور الحرارة.

وفي إطار المقاربة المنمذجة باستعمال القياسات المنجزة ميدانياً بواسطة TDR ونموذج (SOMS) المعتمد على معطيات صور القمر الصناعي (MODIS)، تم استعمال خوارزمية خاصة لتقليد المعطيات (Filtre particulaire de rééchantillonnage par résidu). الخوارزمية تدمج معطيات النتج الحالي (AET) المستخلصة بواسطة الاستشعار عن بعد و باستعمال سيناريوهات انتشار أخطاء نموذج الحصيلة الطاقية لسطح (Surface Energy - SEBS) مع سيناريوهات انتشار أخطاء النموذج SOMS.

تم تشغيل الخوارزمية SEBS مع الخزانة PCRaster Python. يقوم SEBS بحساب ظروف الحصيلة الطاقية، النتج النسبي، أجزاء النتج، سيولة النتج... إلخ لكل نقطة شاشة بالصورة القمرية، وذلك باستعمال أشرطتها البصرية و الحرارية معاً مع القياسات الجوية و قياسات الإشعاع و قياسات ميدانية أخرى. لقد تم تقدير عدم يقين AET المنتبأ بواسطة SEBS لنوعين من السيناريوهات المعتمدة على انتشار الخطأ. السيناريو SEBS ذو الخطأ الواسع يفترض أن القياسات و تكبير مقياس الحرارة المنبعثة من السطح باستعمال Distrad ينتج عنه خطأ كبير بالمقارنة مع مصادر خطأ أخرى. الانحراف المعياري لتقديرات AET في هذا السيناريو يقدر ب 0,02 سم/ساعة. السيناريو SEBS ذو الخطأ الضعيف يقدر أن خطأ صغير في قياس الحرارة المنبعثة من السطح يسبب أخطاء في تقديرات SEBS. هذا ينتج عنه تقديرات ل AET بانحراف معياري متوسط يقدر ب 0,004 سم/ساعة.

يقدر عدم اليقين بالنسبة للرطوبة الحجمية (VMC) والنتح (AET) في تنبؤات النموذج SOMS بواسطة نوعين من السيناريوهات. بالنسبة للسيناريو SOMS غني بالمعطيات، فإن كل الأخطاء الناتجة عن القياسات الميدانية، الخرائط و معطيات القمر الصناعي تبين خطأ RMSE متوسط يقدر بـ  $0,02 \text{ mm}^{-1}$  مقارنة مع VMC المقاس بالميدان. كذلك، توضح النتائج أن عدم اليقين بالنسبة للرطوبة الحجمية المنمذجة بهذا السيناريو يقارب جداً عدم يقين القياسات بواسطة TDR، وذلك على مستوى مشاركة زراعية. يمكن قبول عدم يقين هذا السيناريو لنموذج SOMS في عدة تطبيقات. السيناريو SOMS غني بالمعطيات قادر على تقدير دقيق لظروف رطوبة التربة بعد الحوادث المطرية. تعد قيم التعديل شبيهة بنتائج النموذج الحتمي Déterministic، مشيراً بأنه ليس هناك إجابات لا خطية كبيرة في نموذج انتشار الخطأ. يقدر الانحراف المعياري بالنسبة ل AET بـ  $0,0006 \text{ سم/ساعة}$ .

السيناريو SOMS فقير بالمعطيات، أي لا يتوفر سوى على معطيات الاستشعار عن بعد وخرائط التربة و استعمال الأراضي و المعطيات المناخية، له خطأ RMSE متوسط يقدر بـ  $0,05 \text{ mm}^{-1}$  بالنسبة للرطوبة الحجمية المنتبأة بالمقارنة مع القياسات الميدانية. بالإضافة إلى ذلك، SOMS يتنبأ جيداً نزعة التطور حين مقارنتها بالقياسات الميدانية، مع  $r^2 = 0,75$ . قياسات التعديل أعطت نتائج رديئة مقارنة مع السيناريو SOMS غني بالمعطيات. الانحراف المعياري للسيناريو SOMS فقير بالمعطيات يقدر بحوالي 7 مرات أكبر بالمقارنة مع السيناريو SOMS غني بالمعطيات. الانحراف المعياري المتوسط ل AET يقدر بـ  $0,004 \text{ سم/ساعة}$ . يمكن استعمال هذا السيناريو عند غياب قياسات رطوبة التربة و المعطيات الفيزيائية للتربة. هذا السيناريو قادر على تنبأ التغيرات و نزعة التطور و لو أن الدقة المطلقة أصغر بالنسبة للسيناريو SOMS غني بالمعطيات.

المقاربة بواسطة المرشح الجزئي Filtre particulaire تنقص من التباين (Variance) بالنسبة للرطوبة الحجمية المنتبأة بواسطة النموذج SOMS باستعمال معطيات المرشح SEBS في أغلب الحالات. السيناريو SOMS غني بالمعطيات لا يظهر أي تحسن بالنسبة لكلا السيناريوهين للمرشح SEBS، مقارنة مع نتائج انتشار الخطأ بدون ترشح. السيناريو SOMS فقير بالمعطيات يظهر تحسناً في بعض النقط. تقييم المرشح الجزئي أظهر أن نجاح تطبيقه رهين ببعض العوامل: عدد و توزيع عزم المرشح، المسافة بين دالة كثافة احتمال معطيات المرشح و نموذج تنبأ المرشح، معرفة أخطاء المتغيرات و البارامترات، مستوى الارتباط بين معطيات المرشح و المتغير الهدف، توزيع معطيات المرشح و التغير المكاني لمعطيات المرشح و عدد الجزينات.

إن استعمال منهجية خاصة من أجل معرفة تغيرات رطوبة سطح التربة في المجال والزمان يتعلّق بمتطلبات خاصة بالتطبيق من حيث الدعم، تغطية و دقة التقديرات المطلوبة. إن القياسات الميدانية تكون دائماً قابلة للتطبيق خصوصاً عندما تكون ضمن دراسات قياس رطوبة التربة على صعيد مشاركة محددة. بالنسبة للتوقعات المستقبلية لرطوبة التربة في مجال زراعي ذو موقع خاص، توفر نموذج معير لرطوبة التربة يمكن أن يعطي نتائج جيدة. بالنسبة للتطبيقات التي تتطلب توقعات لرطوبة التربة موزعة مجالياً، تقليد كل المعطيات المتوفرة سواء منها القمرية أو الميدانية في نموذج يركز على أساليب، يمكنه أن يستفيد من إيجابيات كل منهجية على حدٍ. في هذه الحالة، يمكن للخوارزمية ذات المرشح الجزئي المستعملة في هذه الدراسة أن تعطي نتائج جيدة عندما تؤخذ بعين الاعتبار العوامل المذكورة أعلاه. يجب إثبات هذا بدراسة أخرى.

لكن يبقى المشكل الأساسي هو إمكانية توفر قياسات ميدانية لرطوبة التربة من جهة، ووجود صور للأقمار الصناعية ذات درجة وضوح عالية وبدون سحب. و أخيراً نرى أن الأبحاث في المستقبل يجب أن تركز على الاستعمال المثالي لمختلف سلاسل المعطيات وصور الأقمار الصناعية المتوفرة ذات درجة وضوح مختلفة من أجل استخلاص نماذج عملية للعديد من المشاكل البيئية التي تواجهها. يمكن لخوارزميات أخرى لتقليد المعطيات أن تلعب دوراً مهماً في هذه الدراسة.



# Acknowledgements

When I started this Ph.D. research in January 2003, I could not foresee its impact on my scientific and social life. Although the proverbial Local Drain Direction map that led me from the start of my research to the outflow point (this thesis) contained a lot of pits, during the flow I accumulated a lot of knowledge, colleagues and friends and eventually the catchment of my research was delineated. In these final words I would like to acknowledge all colleagues, friends and family who made this thesis possible.

Since I did my research on a multidisciplinary topic, comprising physics, (geo)statistics, (stochastical) hydrology, physical geography, climatology, remote sensing, geoinformatics, environmental modelling, an intense cooperation with different groups and people was necessary. Research comprising all these fields and linking them together in one thesis was not possible without the great effort and patience of my promoters and co-promotor. Prof. Steven de Jong, thank you for having confidence in me from the beginning of this research project. Your enthusiasm and broad knowledge of remote sensing and related fields were important ingredients for the success of this thesis. Prof. Bob Su, thank you for introducing me to the interesting and evolving field of remote sensing and surface energy balance modelling. You supported me with the SEBS model and gave me the opportunity to join your groups from ITC and ALTERRA to participate in the SPARC 2004 and EAGLE 2006 field campaigns, which was very useful and pleasant. Victor Jetten, I am very grateful for your help in programming the SOMS soil moisture model and its calibration. Special thanks go to Derek Karssenbergh. Although you were not involved in the first years of this research, your participation was crucial for the finalization of this thesis. Without your knowledge on stochastical modelling I would probably not have completed this research endeavour with the application of a sophisticated particle filter data assimilation algorithm. I appreciated very much your patience in thoroughly reviewing the text of my thesis, even if I was abroad, in Morocco or Belgium.

Soon after the start of my research I got in touch with Simone van Dijck and Coen Ritsema from ALTERRA, who needed internship students for a research on groundwater recharge in the Sehoul study area in Morocco as part of the EU funded CLIMED project. Thanks to their efforts, in the end of summer 2003 I drove for the first time with my black Polo, packed with equipment, to Morocco, not knowing that I would return there many times...

The fieldworks in Morocco were only possible with the help of many people. First I would like to thank Prof. Abdellah Laouina (UNESCO Chairholder at Université Mohammed V in Rabat) and Prof. Rachida Nafaa (Dean of the Human sciences School of Mohammedia at Université Hassan II, Mohammedia) for their support during the fieldworks, giving me access to facilities of the university and introducing me to the study area. Most importantly, they gave me the opportunity to cooperate with their excellent and enthusiastic (ex) Ph.D. students: my friends Mostafa Antari, Issam Machmachi and Fouzia Laazari. Thanks to their knowledge of the study area, languages and culture, and practical skills, each fieldwork was a success, even when satellite images or rain were lacking. During the fieldworks we learned a lot from each

other: their chances to work with new methods, software and equipment and my opportunity to acquire profound awareness of the environmental problems for which we are doing all this research on drought and erosion.

Fieldwork in an agricultural community like Sehoul is only possible with the trust and help of the local authorities and farmers. Therefore I would like to thank the Caïd and Moquadem of the community of Sehoul. Many thanks go to all the people in the community of Sehoul, for their help and hospitality. In particular I would like to thank the Bentounsi family: Mohammed, Tahra, Ilham, Khadija, Ashraf, Siham, Miloud, Youssef and, last but not least, Jamila “Wardadyal Meghrib”. I was always welcome in their beautiful traditional farm. Thanks to them my equipment was in good hands, I had some extra help with the measurements and I learned a lot about the local culture. I will never forget the delicious harira, couscous, marqa and bread prepared by Tahra, shokran! Other inhabitants of Sehoul to be thanked are Jilali, Youssef and the children who were a good team in the measurements with the emissivity box. I appreciate the help, hospitality and delicious tajines (Saïd) offered by the people of El Arjat in the period when I was with my students based in the village in 2003 and 2004. Many thanks go to these students that helped me with the fieldworks of 2003 and 2004: Sander Loos and Aafke Schipper who did an internship for ALTERRA and Antoanella Domnisoru and Heleen Genders who did their M.Sc. research on erosion in the Matlaq catchment of Sehoul. I thank Koen Rutten for writing an internship report on groundwater modelling in Sehoul. Other people to be thanked for the fieldworks in Morocco are staff members of the Université Mohammed V in Rabat, in particular Miloud Chaker, head of the Department of Geography, and Fatima Hajjaji and Mohammed Sfa for all their support. Furthermore I thank Prof. Mohamed Sabir of the Ecole Nationale Forestière d'Ingénieurs for making use of his laboratory.

Fieldwork is only possible with good equipment maintained by skilled personnel. I am indebted to Theo Tiemissen, Chris Roosendaal, Hassan Arab, Marcel van Maarseveen, Henk Markies, Bas van Dam, Jaap van Barneveld and Kees Klawer of the Laboratory of Physical Geography of Utrecht University, who provided technical support for the meteorological station, TDR's, emissivity box, and many other field gadgets. The development of the emissivity box by the laboratory was only possible thanks to the help from Rachel Niclos, Juan Manual and Enric Valor of the Thermodynamics Department of the University of Valencia and John Register from Raytek cooperation. Thanks also go to Philip Wenting of Wageningen University for providing a DGPS for the fieldworks.

I am very grateful to Wim Timmermans and Ambro Gieske from ITC and Li Jia from ALTERRA-WUR for their support on surface energy balance modelling. I was happy to program the SEBS model with your help in the nice international environment of ITC. Thanks to Loes Colebrander and Anke Walet, the cooperation with ITC was well organized. I learned a lot about measuring fluxes and surface parameters when ITC and ALTERRA gave me the opportunity to participate with them in the SPARC 2004 field campaign in Barrax (Spain). Here I also met many helpful new colleagues, who I want to thank: Eva Rubio, for her help with the box method, Don Sabol for his help with the ASTER requests for Morocco, Mireia Romaguera, Yves Julien and Xiaomei Jin for their support during the field measurements.

Thanks to all the colleagues of the department of Physical Geography, who made the office work as pleasant as the fieldworks. Special thanks go to the colleagues with whom I shared the office: Daniël Mourad, Sander Borghuis, Raymond Sluiter, Lara van den Bosch and Leonie van der Maesen. I also enjoyed the birthday cakes and discussions in the coffee corner. From these

discussions the Heidelberggruppe was founded. I would like to thank the co-members: Gilles Erkens, Pim van Santen, Ivo Thonon and Daniël Mourad.

The PCRaster team was always helpful when I got stuck with Linux, Python or PCRaster, thank you Kor de Jong and Oliver Schmitz. I am also grateful for the support by the secretariat of the Department of Physical Geography: Irene Esser, Anina Koopmans and Juul Beltman. Other colleagues that I would like to thank are: Edzer, Martin, Rudolf, Theo, Ed, Pim, Wladimir, Thom, Rens, Paulien, Marcel, Marc, Susanne, Elisabeth, Menno, Hanneke, Paul, Wiebe, Sanneke, Kim, Piet, Joachim, Ate, Sibren, Jan-Rik, Loes, Job, Pieter-Jan, Arien, Reinder, Ingwer, Frans, Hans Dürr, Hans Middelkoop, Roy, Maarten, Franca, Ton, Gerben, Esther and Marjan.

I should also acknowledge my former colleagues of the faculty helpdesk (FAD) who helped me out of many computer problems, but moreover they supported me in hard times. Thank you Maarten Zeijlmans van Emmichoven (also for your large expertise in GIS analysis and our pleasant cooperation in GIS education), Harm Deters, Gerlach van Beinum, Michel van Schaik, Tom de Jong and Jan Jaap Harts.

Besides work I enjoyed the nice student life in Utrecht, thanks to Drift '66 student association (Koen & Koen, Lisette, Eefje, Jikke, Japke, Femke, Matthijs, Hanna, Dion, Deon, Sanne, Jolanthe, Miriam, Saskia, and many others) and the Orchestra and Choir of Utrecht University (USKO). More specifically, thanks to paranimf Remi Klinkum, paranimf Sander Hol, Lucas Keijning, Gerrit Maas, Lieke en Judith for their pleasant and musical company after work. We were a great team in organising the tour around the Gulf of Finland, "Pieken aan de Finse Golf"! The proverb that music connects people is also demonstrated by the support that I always have got from my friends from the Rotterdams Jongemannenkoor De Coolsingers and their conductor Arie Hoek. Thanks also go to my room-mates Ralf Schrijvers and Tommy Wils and friends Jan Walstra, Martijn Stiekema and Anabelle de Jager for the pleasant times after work.

My new colleagues from the Flemish Institute for Technological Research (VITO) helped me getting through the final part of my thesis. Thank you for the support. I really enjoy the pleasant atmosphere at VITO and the opportunities to do interesting, relevant and state-of-the-art research.

Thanks to the examination committee for their encouraging response to this thesis and Geomedia (especially Rien Rabbers and Margot Stoete) for making the illustrations and layout of this thesis. Issam Machmachi and Professor Abderrahim Watfeh did an excellent job in translating the summary to French and Arabic.

Last, but not least, a great thanks to my parents who always stimulated and supported me to study and develop myself in different fields, and provided the means to do so. I have seen many places in the world and know that the role of parents in the self-development and raising of their children is very important and not self-evident.

Mol (B), December 2008

# Curriculum Vitae

Johannes (Hans) van der Kwast was born on March 2<sup>nd</sup>, 1979 and grew up in Rotterdam, the Netherlands. From 1991 to 1997 he attended the Comenius College (Grammar School) in Capelle aan den IJssel, graduating in Dutch, English, German, Geography, Mathematics, Physics, Chemistry and Biology. In 1997 he started studying Physical Geography at Utrecht University. His MSc research focused on the contextual classification of heterogeneous Mediterranean vegetation in the La Peyne study area in southern France. The study consisted of the collection of ground-truth data during two months of fieldwork and the analysis of hyperspectral airborne images from the DAIS7915 sensor using a contextual classification algorithm. In 2001 he did an internship at the World Agroforestry Centre (ICRAF) in Nairobi and Kisumu (Kenya). This included a fieldwork of three months to collect ground truth data for the production of a land cover and elevation map (DEM) of the Lake Victoria Basin in Western Kenya, using SPOT and Landsat images. After his graduation in September 2002, he was appointed at the Faculty of Geosciences as an Assistant Professor in GIS, lecturing theory and concepts of GIS and Remote Sensing to MSc students. Furthermore he developed and supervised computer-assisted courses on image processing and GIS. He was also employed at the computer helpdesk for the Faculty of Geosciences. In January 2003 he started his PhD research at the department of Physical Geography in Utrecht in cooperation with the International Institute for Geo-Information Science and Earth Observation (ITC, Enschede). During his PhD research he organised three field campaigns of two months in the Sehoul study area in Morocco in cooperation with Alterra (Wageningen, the Netherlands) and the UNESCO Chair in Sustainable Development (University Mohammed V, Rabat, Morocco). Apart from data collection for his PhD research, he supervised MSc and internship students and gave guest lectures at the University Mohammed V in Rabat. In 2003 he cooperated in the organisation of the HyMap calibration field campaign in the La Peyne study area (France). During this field campaign DGPS measurements and measurements of spectra of vegetation and soils were done in order to correct images from the HyMap hyperspectral airborne sensor. In 2004 he participated in the EU financed ESA SPARC-2004 field campaign in Barrax (Spain) and in 2006 he assisted in the EU financed EAGLE field campaign in the Netherlands. During these field campaigns surface roughness, emissivity, LAI, surface energy fluxes and meteorological variables were measured. During his MSc and PhD research, he participated in teaching remote sensing, GIS, environmental modelling, statistics and the supervision of a geological, geomorphological and hydrological fieldwork in France. He also was a member of the Physical Geography students' council during one year.

Since September 2007, Hans works for the Flemisch Institute for Technological Research (VITO) in Mol (Belgium) where he is appointed as a researcher in spatial and dynamical environmental modelling. In his spare time Hans enjoys singing classical music in a choir (Rotterdams Jongenskoor, De Coolingers, Utrechts Studenten Koor en Orkest and different projects), and learning languages (Moroccan Arabic, Swahili, French, Spanish).

# Publications

## Peer-reviewed

- Sluiter, R., Jong, S.M. de, Kwast, J. van der, & Walstra, D.J.R. (2004). A Contextual Approach to Classify Mediterranean Heterogeneous Vegetation using the Spatial Reclassification Kernel (SPARK) and DAIS7915 Imagery. In: S.M. Jong & F.D. van der Meer (Eds.), *Remote Sensing Image Analysis: Including the Spatial Domain (Remote Sensing and Digital Image Processing, Vol. 5, pp. 291-310)*. Dordrecht: Kluwer Academic Publishers.
- Van Dijk, S.J.E., Laouina, A., Carvalho, A.V., Loos, S., Schipper, A.M., Van der Kwast, J., Nafaa, R., Antari, M., Rocha, A., Borrego, C., Ritsema, C.J. (2005). Surface runoff and groundwater recharge under climate change in semi-arid agricultural land (Rabat region, Morocco). In: W.G. Kepner, J.L. Rubio, D.A. Mouat, and F. Pedrazzini (Eds.). *Desertification in the Mediterranean Region. A Security Issue. NATO Security through Science Series, Volume 3, 605p.*, Springer Publishers, Germany
- Nick, F., Van der Kwast, J., Oerlemans, J. (2007). Numerical modelling on Breidamerjokull. *Journal of Geophysical Research* 112, 1-12.
- Karssenber, D., De Jong, K., Van der Kwast, J. (2007). Modelling landscape dynamics with Python. *International Journal of Geographical Information Science* 5, 483-495.
- Jetten, V.G., De Jong, S.M. and Van der Kwast, H. (2008) Can soil moisture patterns in semi-arid areas be predicted? A case study of Morocco. In: Mamadouh, V., De Jong, S.M., Thissen, F., Van der Schee, J. and Van Meeteren, M. (Eds.). *Dutch windows on the Mediterranean; Dutch Geography 2004-2008. KNAG/IGU Section The Netherlands, Utrecht*.
- Su, Z., Timmermans, W.J., Gieske, A., Jia, L., Elbers, J.A., Oliso, A., Timmermans, J. Van der Velde, R., Jin, X., Van der Kwast, J., Nerry, F.M., Sabol, D., Sobrino, J.A., Moreno, J., Bianchi, R. (2008). Quantification of land-atmosphere exchanges of water, energy and carbon dioxide in space and time over the heterogeneous Barrax site. *International Journal of Remote Sensing*, 29:17, 5215-5235
- De Jong, S.M., Van der Kwast, J., Addink, E. & Su, B. (2008). Remote sensing for hydrological studies. In: Bierkens, M.F.P., Dolman, A.J. & Troch, P.A. (Eds.). *Climate and the hydrological cycle. IAHS Special Publication, Vol. 8. pp.297-321*.

## (To be) submitted

- Van der Kwast, J., Timmermans, W.J., Gieske, A.S.M., Su, Z., Oliso, A., Jia, L., Elbers, J., Karssenber, D. & De Jong, S. (submitted). Evaluation of the Surface Energy Balance System (SEBS) using ASTER imagery at the SPARC 2004 site (Barrax, Spain). In: Su, Z., Wen, J. & Wagner, W. (Eds.). *Special Issue "Advances in land surface hydrological processes – field observations, modeling and data assimilation"*. *Hydrology and Earth System Sciences*.
- Van der Kwast, J., Timmermans, W.J., Karssenber, D., De Jong, S.M. & Su, Z. (in prep.). Comparison of MODIS and ASTER derived surface temperatures and energy fluxes at different resolutions. *Remote Sensing of Environment*.

## Conference abstracts and papers

- Kwast, J. van der, & Jong, S.M. de (2004). Modelling evapotranspiration using the surface energy balance system (SEBS) and Landsat TM data (Rabat region, Morocco). 3rd Workshop of the EARSeL Special Interest Group on Remote Sensing for Developing Countries: Cairo – Egypt (09-26-2004 – 09-29-2004).
- Su, Z., Jia, L., Jin, X., Elbers, J., Gieske, A.S.M., Timmermans, W.J., Van der Kwast, J., Oliso, A., Sobrino, J.A., Moreno, J., Nerry, F., Sabol, D. (2004) Land-atmosphere exchanges of water and energy in space and time over a heterogeneous land surface. In: Proceedings of the 2nd international CAHMDA workshop on: the terrestrial water cycle: modelling and data assimilation across catchment scales, October 25-27, Princeton./ed. by A.J. Teuling, H. Leijnse, P.A. Troch, J. Sheffield and E.F. Wood. pp. 129-130.
- Sobrino, J.A., Romaguera, M., Sòria, G., Zaragoza, M.M., Gómez, M., Cuenca, J., Julián, Y., Jiménez-Muñoz, J.C., Su, Z., Jia, L., Gieske, A., Timmermans, W., Van der Kwast, J., Oliso, A., Nerry, F., Sabol, D., Moreno, J. (2005). Thermal measurements in the framework of SPARC. SPARC Final Workshop. ESA Proceedings WPP-250, ITC Enschede, The Netherlands.
- Su, Z., Jia, L., Gieske, A., Timmermans, W., Jin, X., Elbers, J., Van der Kwast, J., Oliso, A., Sobrino, J.A., Nerry, F., Sabol, D., Moreno, J. (2005). In-situ measurements of land-atmosphere exchanges of water, energy and carbon dioxide in space and time over the heterogeneous barrax site during SPARC 2004. SPARC Final Workshop. ESA Proceedings WPP-250, ITC Enschede, The Netherlands.
- Timmermans, W.J., Van der Kwast, J., Gieske, A.S.M., Su, Z., Oliso, A., Jia, L., Elbers, J. (2005). Intercomparison of energy flux models using ASTER imagery at the SPARC 2004 site (Barrax, Spain), SPARC Final Workshop. ESA Proceedings WPP-250, ITC Enschede, The Netherlands.
- Van der Kwast, J. and Jetten, V.G. (2006) Predicting medium scale soil moisture patterns by integrating remote sensing based energy balance modelling with soil water balance modelling in Morocco; In: ISCO 2006: 14th international soil conservation organization conference: water management and soil conservation in semi-arid environments: proceedings, Marrakech, Morocco, May 14-19, 2006.
- Van der Kwast, J. and Engelen, G. (2008). Evaluation of spatial metrics derived from remote sensing at different levels of abstraction for the calibration of urban land use change models, Proceedings of the i-SUP2008 conference, 22-25 April, Bruges.
- Van der Kwast, J. and Engelen, G. (accepted 2009). Calibration of land use change models: the potential of spatial metrics. Proceedings of the 28th EARSeL Symposium, 2-5 June 2008, Istanbul.
- Van der Kwast, J., Van de Voorde, T., Canters, F., Uljee, I., Engelen, G. and Lavallo, C. (accepted 2009). Using remote sensing derived spatial metrics for the calibration of land-use change models. Proceedings of the Joint Urban Remote Sensing Event 2009, 20-22 May 2009, Shanghai.
- Van de Voorde, T., Van der Kwast, J., Canters, F., Binard, M., Cornet, Y. and Engelen, G. (accepted 2009). Quantifying intra-urban morphology of the Greater Dublin area with spatial metrics derived from medium resolution remote sensing data. Proceedings of the Joint Urban Remote Sensing Event 2009, 20-22 May 2009, Shanghai.
- Van der Kwast, J., Karssenbergh, D. and De Jong, S.M. (2008). Quantification of top soil moisture patterns: evaluation of field methods, process-based modeling, remote sensing and an integrated approach. 1<sup>st</sup> Luxembourg Earth Observation Day, Remote sensing applications in hydrology, 19 November 2008, Bourglinster.

## Reports

- Van der Kwast, J. & Walstra, J. (2001). Contextual vegetation classification. Using the Spatial Reclassification Kernel to classify heterogeneous vegetation from DAIS images. MSc. thesis. Department of Physical Geography, Utrecht University.

Van der Kwast, J. & Zomer, R. (2002). Land cover classification and DEM generation: Using SPOT and Landsat images in the Lake Victoria basin, western Kenya. ICRAF, Nairobi.

**NEDERLANDSE GEOGRAFISCHE STUDIES / NETHERLANDS GEOGRAPHICAL STUDIES**

- 350 Z FÖLDI Neighbourhood dynamics in Inner-Budapest; A realist approach -- Utrecht 2006: Knag/Faculteit Geowetenschappen Universiteit Utrecht. 345 pp, 72 figs, 10 tabs, 34 pics. ISBN: 978-90-6809-391-9, Euro 35,00
- 351 S AGTERBOSCH Empowering wind power; On social and institutional conditions affecting the performance of entrepreneurs in the wind power supply market in the Netherlands -- Utrecht 2006: Knag/Copernicus Institute. 246 pp, 36 figs, 8 tabs. ISBN: 978-90-6809-392-6, Euro 27,50
- 352 C RINZIN On the middle path; The social basis for sustainable development in Bhutan -- Utrecht 2006: Knag/Copernicus Institute. 204 pp, 18 figs, 37 tabs, 5 box. ISBN: 90-6809-393-2, Euro 22,50
- 353 M VAN WIJK Airports as cityports in the city-region; Spatial-economic and institutional positions and institutional learning in Randstad-Schiphol (AMS), Frankfurt Rhein-Main (FRA), Tokyo Haneda (HND) and Narita (NRT) --Utrecht 2007: Knag/Faculteit Geowetenschappen Universiteit Utrecht. 323 pp, 59 figs, 18 tabs. ISBN: 978-90-6809-394-0, Euro 35,00
- 354 A C HELDERMAN Continuities in homeownership and residential relocations -- Utrecht/Amsterdam 2007: Knag/ Faculteit der Maatschappij- en Gedragwetenschappen Universiteit van Amsterdam. 125 pp, 15 figs, 14 tabs. ISBN: 978-90-6809-395-7, Euro 19,00
- 355 W BORREN Carbon exchange in Western Siberian watershed mires and implication for the greenhouse effect; A spatial temporal modeling approach -- Utrecht 2007: Knag/Faculteit Geowetenschappen Universiteit Utrecht. 125 pp, 36 figs, 17 tabs. ISBN: 978-90-6809-396-4, Euro 13,00
- 356 S O NEGRO Dynamics of technological innovation systems; The case of biomass energy -- Utrecht 2007: Knag/Copernicus Institute. 166 pp, 24 figs, 17 tabs. ISBN: 978-90-6809-397-1, Euro 18,00
- 357 R NAHUIS The politics of innovation in public transport; Issues, settings and displacements -- Utrecht 2007: Knag/Copernicus Institute. 184 pp, 9 figs, 40 tabs, 4 box. ISBN 978-90-6809-398-8, Euro 20,00
- 358 M STRAATSMAN Hydrodynamic roughnesses of floodplain vegetation; Airborne parameterization and field validation -- Utrecht 2007: Knag/Faculteit Geowetenschappen Universiteit Utrecht. 180 pp, 55 figs, 28 tabs. ISBN: 978-90-6809-399-5, Euro 23,00
- 359 H KRUIZE On environmental equity; Exploring the distribution of environment quality among socio-economic categories in the Netherlands -- Utrecht 2007: Knag/Copernicus Institute. 219 pp, 76 figs, 25 tabs. ISBN: 978-90-6809-401-5, Euro 25,00
- 360 T VAN DER VALK Technology dynamics, network dynamics and partnering; The case of Dutch dedicated life sciences firms -- Utrecht 2007: Knag/Copernicus Institute. 143 pp, 23 figs, 25 tabs. ISBN: 978-90-6809-402-2, Euro 15,00
- 361 M A SCHOUTEN Patterns in biodiversity; Spatial organisation of biodiversity in the Netherlands -- Utrecht 2007: Knag/Copernicus Institute. 152 pp, 16 figs, 20 tabs. ISBN: 978-90-6809-403-9, Euro 20,00
- 362 M H J W VAN AMSTEL – VAN SAANE Twilight on self-regulation; A socio-legal evaluation of conservation and sustainable use of agrobiodiversity by industry self-regulation -- Utrecht 2007: Knag/Copernicus Institute. 167 pp, 15 figs, 13 tabs, 5 box. ISBN: 978-90-6809-404-6, Euro 20,00
- 363 S MUHAMMAD Future urbanization patterns in the Netherlands, under the influence of information and communication technologies -- Utrecht 2007: Knag/Faculteit Geowetenschappen Universiteit Utrecht. 187 pp, 82 figs, 20 tabs. ISBN: 978-90-6809-405-3, Euro 20,00
- 364 M GOUW Alluvial architecture of the Holocene Rhine-Meuse delta (The Netherlands) and the Lower Mississippi Valley (U.S.A.) -- Utrecht 2007: Knag/Faculteit Geowetenschappen Universiteit Utrecht. 192 pp, 55 figs, 14 tabs. ISBN: 978-90-6809-406-0, Euro 22,00
- 365 E HEERE & M STORMS Ormeling's cartography; Presented to Ferjan Ormeling on the occasion of his 65<sup>th</sup> birthday and his retirement as Professor of Cartography -- Utrecht 2007: Knag/Faculteit Geowetenschappen Universiteit Utrecht. ISBN: 978-90-6809-407-7, Euro 20,00
- 366 S QUARTEL Beachwatch; The effect of daily morphodynamics on seasonal beach evolution -- Utrecht 2007: Knag/Faculteit Geowetenschappen Universiteit Utrecht. 125 pp, 39 figs, 7 tabs. ISBN: 978-90-6809-408-4, Euro 12,50
- 367 R O VAN MERKERK Intervening in emerging nanotechnologies; A CTA of Lab-on-a-chip technology regulation -- Utrecht 2007: Knag/Copernicus Institute. 206 pp, 19 box, 35 figs, 12 tabs. ISBN: 978-90-6809-409-1, Euro 20,00
- 368 R M FRINGS From gravel to sand; Downstream fining of bed sediments in the lower river Rhine -- Utrecht 2007: Knag/Faculteit Geowetenschappen Universiteit Utrecht. ISBN: 978-90-6809-410-7, Euro 25,00
- 369 W IMMERZEEL Spatial modelling of the hydrological cycle, climate change and agriculture in mountainous basins -- Utrecht 2008: Knag/Faculteit Geowetenschappen Universiteit Utrecht. 147 pp, 54 figs, 12 tabs. ISBN: 978-90-6809-411-4, Euro 25,00

- 370 D S J MOURAD Patterns of nutrient transfer in lowland catchments; A case study from northeastern Europe -- Utrecht 2008: Knag/Faculteit Geowetenschappen Universiteit Utrecht. 176 pp, 44 figs, 19 tabs. ISBN: 978-90-6809-412-1, Euro 20,00
- 371 M M H CHAPPIN Opening the black box of environmental innovation; Governmental policy and learning in the Dutch paper and board industry -- Utrecht 2008: Knag/Copernicus Institute. 202 pp, 41 figs, 30 tabs. ISBN: 978-90-6809-413-8, Euro 22,50
- 372 R P ODDENS & M VAN EGMOND Ormelings atlasen; Catalogus van atlasen geschenken aan de Universiteit Utrecht door de hoogleraren F.J. Ormeling sr. en jr. -- Utrecht 2008: Knag/Faculteit Geowetenschappen Universiteit Utrechts. ISBN: 978-90-6809-415-2, Euro 15,00
- 373 R VAN MELIK Changing public space; The recent redevelopment of Dutch city squares -- Utrecht 2008: Knag/Faculteit Geowetenschappen Universiteit Utrecht. 323 pp, 47 figs, 32 tabs. ISBN: 978-90-6809-416-9, Euro 20,00
- 374 E ANDRIESSE Institutions and regional development in Southeast Asia; A comparative analysis of Satun (Thailand) and Perlis (Malaysia) -- Utrecht 2008: Knag/Faculteit Geowetenschappen Universiteit Utrecht. 250 pp, 42 figs, 43 tabs, 18 box. ISBN: 978-90-6809-417-6, Euro 25,00
- 375 E HEERE GIS voor historisch landschapsonderzoek; Opzet en gebruik van een historisch GIS voor prekadastrale kaarten -- Utrecht 2008: Knag/Faculteit Geowetenschappen Universiteit Utrecht. 231 pp, 73 figs, 13 tabs. ISBN: 978-90-6809-418-3, Euro 30,00
- 376 V D MAMADOUH, S M DE JONG, J F C M THISSEN & J A VAN DER SCHEE Dutch windows on the Mediterranean; Dutch Geography 2004-2008 -- Utrecht 2008: Knag/International Geographical Union Section The Netherlands. 104 pp + cd-rom, 38 figs, 9 tabs. ISBN: 978-90-6809-419-0, Euro 10,00
- 377 E VAN MARISSING Buurten bij beleidsmakers; Stedelijke beleidsprocessen, bewonersparticipatie en sociale cohesie in vroeg-naoorlogse stadswijken in Nederland -- Utrecht 2008: Knag/Faculteit Geowetenschappen Universiteit Utrecht. 230 pp, 6 figs, 31 tabs. ISBN: 978-90-6809-420-6, Euro 25,00
- 378 M DE BEER, R C L BUITING, D J VAN DRUNEN & A J T GOORTS (Eds.) Water Wegen; Op zoek naar de balans in de ruimtelijke ordening -- Utrecht 2008: Knag/VUGS/Faculteit Geowetenschappen Universiteit Utrecht. 91 pp, 18 figs, 1 tab. ISBN: 978-90-6809-421-3, Euro 10,00
- 379 J M SCHUURMANS Hydrological now- and forecasting; Integration of operationally available remotely sensed and forecasted hydrometeorological variables into distributed hydrological models -- Utrecht 2008: Knag/Faculteit Geowetenschappen Universiteit Utrecht. 154 pp, 65 figs, 12 tabs. ISBN 978-90-6809-422-0, Euro 15,00
- 380 M VAN DEN BROECKE Ortelius' *Theatrum Orbis Terrarum* (1570-1641); Characteristics and development of a sample of *on verso* map texts. Knag/Faculteit Geowetenschappen Universiteit Utrecht. ISBN 978-90-6809-423-7, Euro 30,00
- 381 J VAN DER KWAST Quantification of top soil moisture patterns; Evaluation of field methods, process-based modelling, remote sensing and an integrated approach. Knag/Faculteit Geowetenschappen Universiteit Utrecht. ISBN 978-90-6809-424-4, Euro 30,00

For a complete list of NGS titles please visit [www.knag.nl](http://www.knag.nl). Publications of this series can be ordered from KNAG / NETHERLANDS GEOGRAPHICAL STUDIES, P.O. Box 80123, 3508 TC Utrecht, The Netherlands (E-mail [info@knag.nl](mailto:info@knag.nl); Fax +31 30 253 5523). Prices include packing and postage by surface mail. Orders should be prepaid, with cheques made payable to "Netherlands Geographical Studies". Please ensure that all banking charges are prepaid. Alternatively, American Express, Eurocard, Access, MasterCard, BankAmericard and Visa credit cards are accepted (please specify card number, name as on card, and expiration date with your signed order).